UNIVERSITÀ DEGLI STUDI DI TRIESTE

UNIVERSITÀ DEGLI STUDI DI TRIESTE

XXXIV CICLO DEL DOTTORATO DI RICERCA IN

NANOTECNOLOGIE

Synthesis, Characterization and Applications of Nanoparticles and Nanomaterials with Controlled Properties

Settore scientifico-disciplinare: **CHIM/06 – CHIMICA ORGANICA**

DOTTORANDO
MARIO DAKA

COORDINATORE
CHIAR.MO PROF. ALBERTO MORGANTE

SUPERVISORE DI TESI
CHIAR.MO PROF. LUCIA PASQUATO

CO-SUPERVISORE DI TESI
CHIAR.MO PROF. PAOLO FORNASIERO

TUTORI
PROF. PAOLO PENGO
PROF. TIZIANO MONTINI

ANNO ACCADEMICO 2021/2022

Se tu miri ad una meta
e durante la strada ti fermi
per tirare pietre ad ogni cane
che ti abbaia contro,
non arriverai mai alla meta.

Antico proverbio mediorientale

Contents

Abstract

Along the last decades, the fields of catalysis and nanotechnology have grown side by side and deeply entangled to the extent of creating fruitful contact points that led to the development of nano-catalysis. This new field is based on the use of nanostructured materials for the design and development of well-defined highly active and selective catalysts with controlled properties exploited in manifold of chemical transformations. At the nanoscale level, the properties of a material are strictly related to its size and shape, hence the control of this two parameters can have a tremendous impact on the nanomaterial behaviour and determine its potential in catalytic applications. In this thesis work, the nano-catalysis philosophy was applied for the development of engineered catalytic nanomaterials based on transition metal nanoparticles (NPs) and nanoclusters (NCs). State of the art protocols and synthetic techniques were employed through the use of organic surfactants and ligands, combined with fine tuning of the kinetic and thermodynamic parameters, for the control of surface features in Pt NPs and atomicity in Pd and Au NCs.

Porous multifaceted Pt NPs were designed and synthesised *via* wet-chemical approach meant for the expression of porous features characterized by extended regular planes as surface features. The peculiar porous structure of platinum NPs decorated with faceted crystallites arose from controlled growth of small seeds through progressive evolution that could be monitored by TEM experiments. Control experiments were performed to support the selected reaction conditions as the optimal in delivering the desired features and to corroborate the needful use of a defined surfactant mixture composition for the successful NPs formation. The property control on these NPs, through surface modification, was confirmed by the catalytic tests performed in electrochemical oxygen reduction reaction (ORR) and methanol oxidation reaction (MOR) achieving superior performances compared to a commercial and a non-porous benchmark catalysts.

Concerning the control of properties through size engineering, Pd_8/Al_2O_3 catalyst was prepared and studied through a rational design approach, starting from the synthesis of $Pd_8(SCH_2COOMe)_{16}$ complex. Unlike the conventional preparation of small metal clusters, in this work the atomicity control was attained by the use of organometallic chemistry. The Pd(II) complex, having a defined nuclearity, can provide highly active unprotected clusters once removal of ligands and reduction of Pd is performed. After complex deposition onto alumina by UV irradiation, working at low Pd concentration in order to preserve the atomicity, the pre-catalyst was reduced at high temperature with hydrogen to deliver metallic Pd clusters. Extensive

characterization, through the various steps of catalyst preparation, performed by TEM, XPS and EXAFS, confirmed the small size of the clusters and their metallic nature. The nanostructured catalyst was used in Suzuki coupling reactions of aryl bromides and phenylboronic acid, resulting in very high activity and selectivity. Additionally, the catalyst was able to deliver substituted biphenyls with great tolerance toward the use of various substituted bromobenzenes and demonstrated enhanced stability as evinced by the recycling and leaching tests.

Lastly, atomically precise Au NCs were applied in the preparation of photocatalysts to exploit their potential in the production of hydrogen from ethanol. Au NCs with different atomicity were employed in order to study their size influence on the activity. At the sub-nanometric level, the electronic properties of Au NCs have a non-monotonic oscillation that consequently can influence the performance of a catalyst, thus studies on the size/activity relationship are pivotal to provide a deeper understanding of the behaviour of such metal nanoobjects in catalysis. In this study Au_{11}, Au_{18}, Au_{23} and Au_{25} thiolate and phosphine protected clusters were synthesised and dispersed on TiO_2 by two different approaches based on UV irradiation and in situ impregnation. The two sets of catalysts were tested in the photocatalytic hydrogen production resulting superior in activity and stability toward a photodeposited Au/TiO_2 benchmark catalyst.

Riassunto

Negli ultimi decenni, i settori scientifici della catalisi e delle nanotecnologie si sono sviluppati fianco a fianco e profondamente intrecciati, arrivando a creare dei punti di contatto che hanno portato alla nascita della nano-catalisi. Questo nuovo settore scientifico fonda le sue radici sull'impiego di materiali nanostrutturati per la progettazione e lo sviluppo di catalizzatori strutturalmente definiti, attivi e selettivi, utili per l'impiego in molteplici reazioni chimiche. Su scala nanometrica, le proprietà di un materiale sono strettamente influenzate dalla forma e dimensione, che hanno un enorme impatto nel determinare il potere catalitico ed e le applicazioni del materiale stesso. In questo lavoro di tesi, l'approccio della nano-catalisi è stato impiegato nello sviluppo di nanomateriali catalitici a base di nanoparticelle e nano-cluster dei metalli di transizione. Strategie sintetiche e protocolli *ad hoc* sono stati impiegati, insieme all'utilizzo di surfattanti, leganti organici ed una attenta combinazione di parametri cinetici e termodinamici per il controllo morfologico della superficie esposta in nanoparticelle di Pt ed il controllo dell'atomicità in cluster di Pd e Au.

Nanoparticelle di Pt porose e sfaccettate sono state concepite e sintetizzate attraverso l'impiego di tecniche chimiche in fase liquida, atte a risaltare la porosità delle nanoparticelle e, nel contempo, a promuovere l'esposizione di determinati piani cristallini sulla superficie. La peculiare struttura porosa delle nanoparticelle, decorata da piccoli cristalliti sfaccettati, è stata sviluppata a partire dall'evoluzione di piccoli nuclei cristallini. Tale evoluzione durante la sintesi è stata monitorata tramite esperimenti di microscopia elettronica. Esperimenti di controllo sono stati svolti a sostegno della scelta delle condizioni di reazione adottate e a supporto della necessità di un appropriato rapporto OLAM/OLAC per garantire l'effettiva riuscita della sintesi. L'effettivo controllo delle proprietà, ottenute attraverso l'ingegnerizzazione della superficie delle nanoparticelle, è stato corroborato da test catalitici sull'elettro-riduzione dell'ossigeno e l'ossidazione di metanolo, da cui è risultata una performance superiore delle nanoparticelle porose rispetto ad un catalizzatore commerciale ed uno non poroso.

Riguardo il controllo di proprietà attraverso il confinamento dimensionale, un catalizzatore a base di cluster di palladio (Pd_8/Al_2O_3) è stato preparato e studiato tramite un approccio di progettazione razionale a partire dalla sintesi del complesso $Pd_8(SCH_2COOMe)_{16}$. A differenza dei convenzionali cluster metallici, in questo studio, il controllo sull'atomicità è stato raggiunto tramite l'impiego della chimica metallorganica. Il complesso di Pd(II), avente una nuclearità altamente definita, può essere fonte di cluster non protetti estremamente attivi dopo il processo di riduzione atto alla rimozione dei leganti organici e dello zolfo. In seguito alla deposizione del complesso, eseguita per irraggiamento di luce UV e con l'uso di basse concentrazioni di Pd in

modo da escludere fenomeni di aggregazione, il pre-catalizzatore è stato in seguito ridotto ad alte temperature in idrogeno favorendo la generazione di cluster metallici di palladio. Approfondite caratterizzazioni, lungo tutto il processo di preparazione del catalizzatore, sono state svolte tramite l'utilizzo di tecniche TEM, XPS ed EXAFS, confermando la ridotta dimensione dei cluster e la loro natura metallica. Il catalizzatore nanostrutturato è stato sottoposto a reazioni di cross coupling di Suzuki, con bromuri arilici e acido fenilboronico, mostrando una spiccata attività e selettività. In aggiunta, il catalizzatore si è dimostrato tollerante verso vari gruppi funzionali durante l'analisi del campo di applicabilità della reazione e molto stabile nei test di riciclo e di disattivazione causato da rilascio di specie metalliche in fase liquida.

Infine, cluster di oro ad atomicità precisa sono stati applicati nella preparazione di foto-catalizzatori atti alla produzione di idrogeno da foto-ossidazione di etanolo. Questi cluster di oro a diversa atomicità sono stati impiegati in uno studio di correlazione attività/dimensione. Al livello sub-nanometrico, le proprietà elettroniche dei cluster di oro non hanno una variazione lineare con la dimensione e di conseguenza questo influisce notevolmente sulle performance catalitiche. Ne consegue che studi correlanti l'attività con la dimensione dei cluster sono prioritari in determinare il potere catalitico dei cluster metallici. In questo studio, i cluster Au_{11}, Au_{18}, Au_{23} and Au_{25} protetti da leganti tiolati o fosfinici, sono stati preparati ed ancorati su TiO_2 utilizzando due diversi approcci basati su irraggiamento con luce UV e impregnazione diretta. I due set di catalizzatori, generati dalle diverse preparazioni, sono stati infine testati per la foto-generazione di idrogeno risultando in superiori attività e stabilità catalitiche rispetto ad un analogo catalizzatore foto-deposto usato come riferimento.

Abbreviations

(*hkl*)	Crystallographic plane/facet
C_{min}^{nu}	Critical concentration for nucleation
< *hkl* >	Crystallographic direction
0-D	Zero dimension
1-D	One dimension
2-D	Two dimension
Ac	Acetyl
acac	Acetylacetonate, 1,5-pentanedionate
API	Active pharmaceutical ingredient
BBSH	4-*tert*-Butylbenzylmercaptan
BET	Brunauer–Emmett–Teller
BF	Bright field
BFP	Back focal plane
BMIM	1-butyl-3-methylimidazolium
BP7A	Ac-ThrLeu-His-Val-Ser-Ser-Tyr-$CONH_2$
CN	Coordination number
CPC	Cetylpyridinium chloride
CTAB	Cetyltrimethylammonium bromide
CTAC	Cetyltrimethylammonium chloride
CVD	Chemical vapour deposition
DABCO	1,4-Diazabicyclo[2.2.2]octane
DDA	Dodecylamine
DEG	Diethylene glycol
DES	Deep eutectic solvents
DF	Dark field
DIPEA	N,N-Diisopropylethylamine
DMAP	4-Dimethylaminopyridine
DMF	Dimethylformamide
DMSO	Dimethyl sulfoxide
DNA	Deoxyribonucleic acid
DOS	Density of states
dppe	Diphenylphosphinoethane

dppm	Diphenylphosphinomethane
dppo	Diphenylphosphinooctane
dppp	Diphenylphosphinopropane
ECSA	Electrochemical surface area
EDTA	Ethylenediaminetetraacetate
EDX	Energy dispersive X-ray spectroscopy
EMA	European Medicines Agency
EPR	Enhanced permeability and retention
EXAFS	Extended X-ray absorption fine structure
fcc	Face centred cubic
FDA	Food and Drug Administration
FEG	Field emission gun
FG	Functional group
FT	Fourier transform
FWHM	Full width at half maximum
HAADF	High angle annular dark field
HDA	Hexadecylamine
Hdppa	*N*,*N*-bis(diphenylphosphino)amine
hkl	Miller's indexes
HOH	Hexoctahedra(l)
HOMO	Highest occupied molecular orbital
HPLC	High performance/pressure liquid chromatography
HR	High resolution
IUPAC	International union of pure and applied chemistry
LEIST	Ligand exchange-induced size transformation
LLC(s)	Lyotropic liquid crystal(s)
LUMO	Lowest unoccupied molecular orbital
MA	Mass activity
MBA	Mercaptobenzoic acid
MOR	Methanol oxidation reaction
MBT	Methylbenzenethiol
MSA	Mercaptosuccinic acid
mtet	2-Methylthioethanethiolate
NAP	Near ambient pressure

NCs	Nanocluster(s)
NHCs	N-heterocyclic carbenes
NPs	Nanoparticles
ODA	Octadecylamine
OLAC	Oleic acid
OLAM	Oleylamine
ORR	Oxygen reduction reaction
PAA	Polyacrylic acid
PAM	Polyacrylamide
PDDA	Poly(diallyldimethylammonium) chloride
PEG	Polyethylene glycol
PEO	Polyethylene oxide
PET	Phenylethanethiol
PVA	Polyvinyl alcohol
PVDF	Polyvinylidene fluoride
PVP	Polyvinylpyrrolidone
S7	Ac–Ser–Ser–Phe–Pro–Gln–Pro–Asn–$CONH_2$
SA	Specific activity
SAED	Selected area electron diffraction
SAED	Selected-area electron diffraction
SAM(s)	Self-assembled monolayer(s)
SDS	Sodium dodecylsulphate
SEM	Scanning electron microscopy
SERS	Surface-enhanced raman scattering
SGH	Glutathione
SPR	Surface plasmon resonance
STEM	Scanning transmission electron microscopy
T7	Ac–Thr–Leu–Thr–Thr–Leu–Thr– Asn–$CONH_2$
TBBT	4-*tert*-butylbenzenethiol
TEA	Triethylamine
TEG	Triethylene glycol
TEM	Transmission electron microscopy
TetraEG	Tetraethylene glycol
TFA	Trifluoroacetate/trifluoroacetic acid

THH	Tetrahexahedra(l)
TOAB	Tetraoctylammonium bromide
TOH	Trisoctahedra(l)
TOP	Trioctylphosphine
TOPO	Trioctylphosphine oxide
TPH	Trapezohedra(l)
TTAB	Tetradecyltrimethylammonium bromide
UHV	Ultra-high vacuum
UV	Ultraviolet
$V_{deposition}$	Deposition rate
$V_{diffusion}$	Diffusion rate
XAFS	X-ray absorption fine structure
XANES	X-ray absorption near-edge structure
XAS	X-ray absorption spectroscopy
XPS	X-ray photoelectron spectroscopy
XRD	X-ray diffraction
γ	Surface free energy

1. Introduction

1.1 The importance of Nanotechnology

For those working on nanomaterials and nanosciences field, Feynman's "There's plenty of room at the bottom" lecture[1] given before the America Physical Society members in 1959 is probably one of the most recurring examples in which the coming of the Nanotechnologies was correctly envisioned though with a little scepticism. While today the concept of manipulation at the nanoscale is fully comprehended and digested and Feynman's lecture is now acclaimed as visionary, back then the idea was somewhat futuristic because of a lack of knowledge and instrumentation limits. Luckily, Feynman's prediction has now become the everyday reality for thousands of scientists around the world that deal with Nanotechnology applied in different research fields. Particularly, in the last decades, the interest in going "nano" has grown exponentially thanks to the wide range of possible applications in various fields. Up to now, an increasing variety of nanomaterials have found their way to the real world with beneficial contributions ranging from medicine[2–5] to electronics[6–9] to industrial processes[10–13] and other areas (Figure 1.1). Although numerous benefits of nanotechnology are known and divulgated by the media, such those concerning the use in electronics and medicine, many others remain shaded because less understood and conceptualised by society.

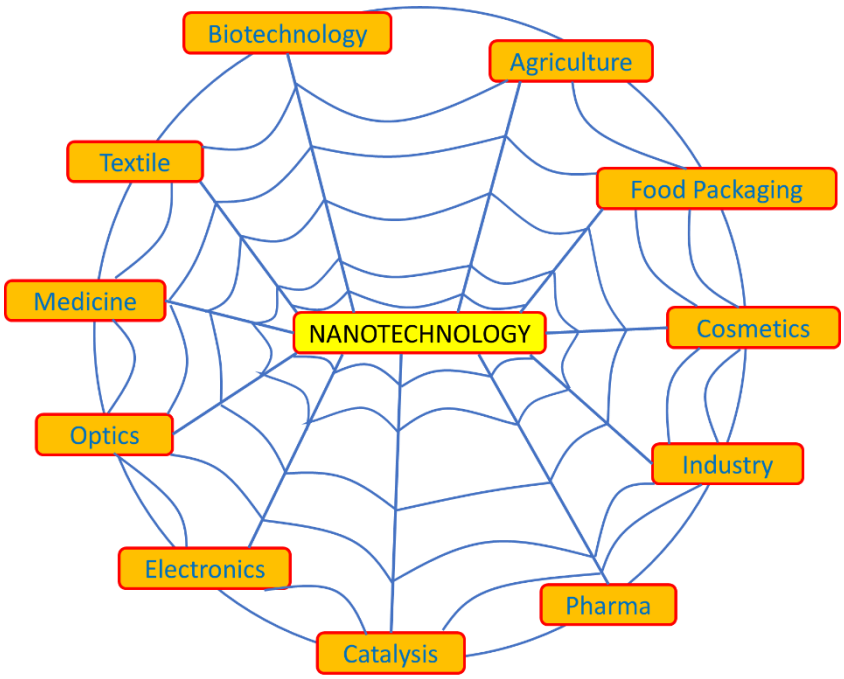

Figure 1.1. Some relevant areas in which nanotechnologies have found established applications.

The first applications of nanotechnology were observed in the field of electronics. [6–9] In the early ’60 Atalla and co-workers achieved the fabrication of a metal-semiconductor junction transistor based on 10 nm gold thin films.[14] Years later, in search of improved transistors, IBM was able to develop a metal-oxide-semiconductor field-effect transistor (MOSFET) with a 10 nm tungsten oxide gate by the use of nano-lithography. The study of various metal based semiconductors such as metal-chalcogenides, quantum dots and carbonaceous nanostructures, integrated with the advent of new instruments for nanofabrication (electron beam lithography, sputtering and nanoscale imprinting) contributed to the growth of the nano-electronics, especially during the ’90 at the research level.[15,16] However the commercial use of transistors and sensors based on nano-sized circuits began only in the 2010s with their implementation in daily devices such as computers, smartphones and automotive vehicles.

Medicine is also another field where nanotechnology has found room for innovative applications regarding treatment and/or diagnosis. Until 2016, more than 50 nanomaterial-based drug systems have been approved by the FDA for medical treatment in the USA while EMA has approved 48 nano medicines for clinical trial in the EU.[17] The nanomaterial-based drug systems or nano medicines currently used in the medicinal field differ from one another based on the formulation that also determines the properties related to pharmacokinetics and the enhanced permeability and retention (EPR) effect of the system itself.[18,19] A general classification can be extrapolated from the carrier composition of the nano medicine which is considered the transporter for an active pharmaceutical ingredient (API) and, in the majority of cases, the real nanomaterial in the formulation. Along the years various carriers have been studied and categorized in 5 main classes: dendrimers,[20,21] engineered nanoparticles (NPs),[4,22,23] lipids (emulsions, liposomes, solid lipid NPs),[2,24–27] micelles and polymeric NPs.[28–31] The benefits related to the use of nano-carriers are many, such as: enhanced stability, targeted delivery, solubility, oral bioavailability of the API; longer circulation times and higher blood concentration of the drugs allow enhanced binding capacity to biomolecules and higher accumulation in target tissues. This resulted in an increased efficacy and safety concerning the use of cytotoxic drugs for cancer therapy.[32]

Other sectors have also taken advantage of nanotechnologies like the food and agricultural industry even though the general population is not aware of that.[33] Agricultural sciences have started studying a pool of nanomaterials for various purposes like wastewater treatment, genetic improvement, soil improvement, plant protection and stress tolerance. Nano-photocatalysts (TiO_2 and other metal or metal oxides) for degradation of organic and inorganic pollutants[34–37] and nano-sorbents (carbon-based, polymeric nanostructures)[38–42] for contaminants trapping are two of the most privileged nanomaterials for water treatment. Plant genetic engineering has been achieved at

research level with promising results using nanomaterials binding DNA fragments for efficient transport and internalization.[43,44] Typical nano-carriers studied for this purpose are metal NPs, carbon based nanomaterials and polymeric NPs.[45–49] A main issue in the agricultural sector is the extensive use of fertilizers that can lead to deterioration of the natural ecosystem[50] (e.g. eutrophication) or to over-fertilization with toxic effects for the crop. The use of NPs as direct source of nutrients or as a slow-release devices have proved to be an efficient alternative to the direct delivery of nutrients.[51] This also avoids unnecessary waste thanks to the effective retention of the fertilizer in the nano-system that favours a gradual delivery without compromising the plant vital course.[52,53] Of higher concern, the extensive use of pesticides in agriculture and their implication with risks for the environment and the human health,[54–56] have directed researchers in studying new safer ways of administration. Formulations of pesticides entrapped or encapsulated in nano-matrixes are emerging as an efficient alternative to direct use of active ingredients.[57] The advantages in using nano-based pesticides range from controlled release in the crop and improved solubility of the active components to delayed degradation of the pesticide itself.[58–63] Crop growth in depleted or unsuitable soils, particularly in certain global regions, is also a rising issue in agriculture; various nanomaterials are being studied and tested for the progress of farming in these difficult areas. In particular, additives based on NPs have been developed for stress resistance to salinity and water deficiency, CO_2 assimilation and nutrient uptake enhancement.[64–66]

Food packaging is also touched by the nanotechnology expansion and growth witnessed by a multitude of applications in this branch. The unique properties of some nano-sized materials have been exploited for biodegradable packaging reinforcement with physico-mechanical properties improvement and for antimicrobial application increasing the safety and quality shelf life of the product.[67,68] Worth of mention, carbohydrate-based (e.g. cellulose, chitosan)[69,70] nanomaterials and protein (e.g. gelatin, gluten, alginate)[71] based ones are privileged for packaging applications, while inorganic NPs (e.g. Ag, Cu, TiO_2, ZnO, TiN) are used for their antimicrobial potential.[72–74]

Concerning the industrial applications, NPs and nanomaterials have been widely employed even before the term nano was coined, in particular in the chemical industry. One classic example is carbon black, which was developed in the 20th century and now serves in a manifold of industrial processes.[75,76] Beside carbon black, other nanomaterials have been intensively used in the past and still nowadays applied in the manufacturing of consumer goods. Titania and metal oxide nanostructures are some of the many nanomaterials exploited as much as carbon black in the industry with a multitude of applications like textile dyes,[12] UV filters,[77,78] self-cleaning surfaces,[79] additives as anti-caking agents[80] and of course heterogeneous catalysis.[81,82] Metal NPs, along with being employed as catalysts[83,84] in industrial chemical transformations, are also applied for other

purposes like the Ag NPs used for their antimicrobial properties incorporated in filters or household appliances.[85] Likewise, Au NPs embedded in proper matrixes are used for air pollutant decomposition.[86–88]

The great efforts made in the field of nanotechnology are giving birth to new applications every year, and with a constant demand for greener, eco-friendly, and at the same time, efficient goods an increased interest toward nanomaterials is to be expected.

1.2 Synthesis of transition metal nanoparticles and nanoclusters

The interest in transition metal nanostructures has exponentially grown over the last decades, aided by the development of state of the art instruments for their characterization. Additionally, the possibility offered by the manipulation of size and shape of these nano-objects has further captured the attention of material scientists. NPs are seen as the gap fillers between bulk and molecular materials as they display unique properties deriving from the quantum confinement (or quantum size effect). The properties of metal NPs are determined by a set of parameters that include size, morphology and composition above the others. Indeed, when NPs with specific properties are needed, the researchers must consider the aforementioned parameters when designing the nanomaterials. For instance, in catalysis it is well known that the activity of a metal NP is related to its size thus by reducing the dimension an enhanced activity is observed.[89–91] Selectivity, on the other hand, is driven by the arrangement of the atoms on the surface, namely the shape of the NP.[92–94] Worth of mention is the hydrogenation of benzene to cyclohexane and cyclohexene promoted by cuboctahedral Pt NPs while only cyclohexane is obtained when cubic NPs are employed.[95]

The procedures for metal NPs preparation are many and in constant increase, however a line can be drawn to distinguish these procedures in two categories: top down and bottom up procedures (Figure 1.2). Top down approaches rely on hard physical techniques for the processing and reduction of bulk materials to the nanoscale. Typical techniques developed for top down production of nanomaterials are mechanical milling,[96,97] lithography,[98–101] sputtering,[102,103] electrospinning,[104] and laser ablation.[105,106] Conversely, bottom up approaches combine chemical and physical procedures to build nanomaterials from their constituent units: atoms and/or molecules.

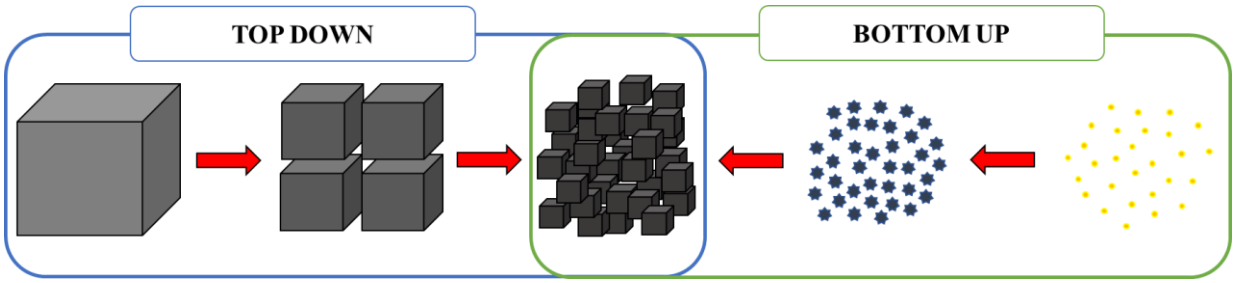

Figure 1.2. Schematic illustration of top down and bottom up approaches for NPs preparation.

Common strategies used in the bottom up production of nano-objects are chemical vapor deposition (CVD),[107–109] electrodeposition,[110] pyrolysis (for metal oxide NPs)[111,112] and wet chemical procedures, including solvothermal and hydrothermal methods, sol-gel and template assisted methods. [113–117] Due to extensive abundance of reported procedures and techniques for the production of metal NPs and NCs in literature, in this chapter, only wet chemical procedures will be discussed with a focus on colloidal synthesis, in accordance with the scope of the PhD project.

1.2.1. Transition metal NPs with controlled morphology

The tremendous work of material scientists in the past decades has brought to a myriad of procedures and methods for the synthesis of size- and shape-controlled metal NPs. Nanocrystals with distinctive size and shapes can be easily produced including 2-D NPs such as nanoplates and prisms, 1-D NPs like rods, bars and wires, and 0-D NPs with a huge variety in morphology such as spheres, cubes, cuboctahedrons, octahedrons, tetrahedrons, rhombododecahedrons, icosahedrons, stars, branched NPs, and concave ones. The great diversity in shape is governed by thermodynamic (surface capping agents, reduction potentials) and kinetic (temperature, stirring speed, concentration, foreign ions) parameters involved during the formation of such NPs. The choice and tuning of such parameters can drastically alter the outcome of the final NPs size and shape. For colloidal synthesis, three crucial steps can be outlined: nucleation, seeds formation and growth to the final NPs. The first step (nucleation) is particularly crucial for the definition of the product, and it is strongly governed by the aforementioned thermodynamics and kinetics, that at this stage are challenging to study and investigate which has clouded the understanding of the mechanisms involved during the first moments of colloidal syntheses. Nevertheless, various models have been developed to describe the dynamics involved in the nucleation phase like the LaMer model based on the synthesis of sulfur colloids.[118] The model can be stretched for the interpretation of metal nanocrystals homogeneous nucleation (Figure 1.3). After the metal precursor is reduced, the metal atom concentration in solution is expected to increase over time and as the critical concentration value for nucleation (C_{min}^{nu}) is exceeded, atoms will spontaneously aggregate to form nuclei. The

assembly of the atoms into nuclei causes their quick decrease in concentration and, when the concentration falls below C_{min}^{nu}, homogeneous nucleation ceases. Though, if new metal precursor is provided in the reaction solution and new metal atoms are reduced, nucleation can be restored.

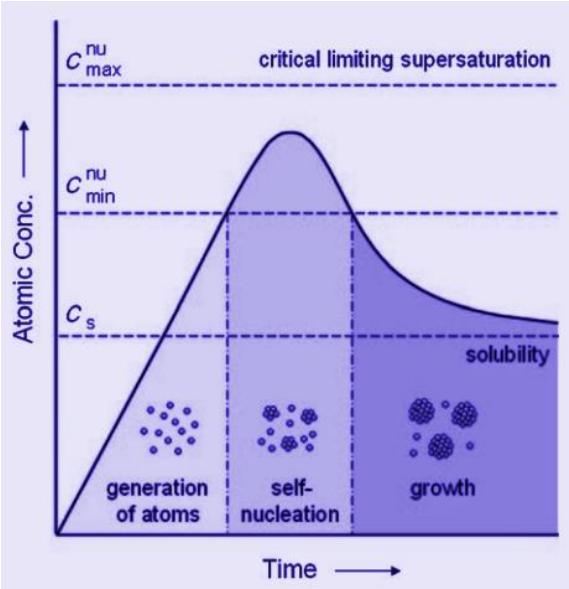

Figure 1.3. Plot of atomic concentration *vs* time extrapolated from LaMer model for the interpretation of NPs formation starting from homogeneous nucleation. Adapted with permission from ref. [117] (Copyright 2009 Wiley-VCH) and ref. [118] (Copyright 1950 American Chemical Society).

However, only one nucleation step is recommended as multiple nucleation steps may cause size polydispersity due to different growth intervals. Despite the flaws and oversimplified conjectures of the LaMer model, it has been essential in delivering a qualitative knowledge of colloidal synthesis for metal NPs and useful tips for the production of monodispersed nanocrystals. However, with the advent of computational methods and improved instrumentations the LaMer model has been questioned due to the discrepancies between predicted and experimental observations. New unconventional mechanisms based on multiple steps nucleation were suggested, involving metastable liquids[119] or amorphous structures[120] as the intermediates in the first moments of the reaction. In another study, it was suggested that nucleation stage involves the formation of clusters, by partial reduction of the metal precursor, that gradually evolve to nuclei.[121] To this point, only a few numbers of studies focused on nonclassical nucleation for colloidal NPs have been reported, yet leaving uncovered important atomistic aspects involved in the primary stage of the synthesis. On the other hand, in the seed-mediated colloidal synthesis, small nanocrystals (seeds), having a single crystal structure or well defined facets, act as heterogeneous substrate for the deposition of metal atoms and later growth of NPs. In this case a defined structure is already provided to which metal precursors in solution are reduced allowing a pre-established deposition and growth direction, thus avoiding the issues related to the nucleation stage. In this context, several approaches have been

developed for the manipulation of seed fractions that can evolve into different sizes and shapes. In a combined computational and experimental study, Barnard and co-workers shed light on the thermodynamics of Au seed evolution demonstrating a correlation of the internal crystallinity with the seed size (Figure 1.4A).[122] Another study recognised the importance of the initial reduction rate for the control of twin structures in Pd seeds. Stacking-fault-lined, multiply twinned, singly twinned and single crystal internal structures are observed in the seeds with the increasing initial reduction rate (Figure 1.4B).[123]

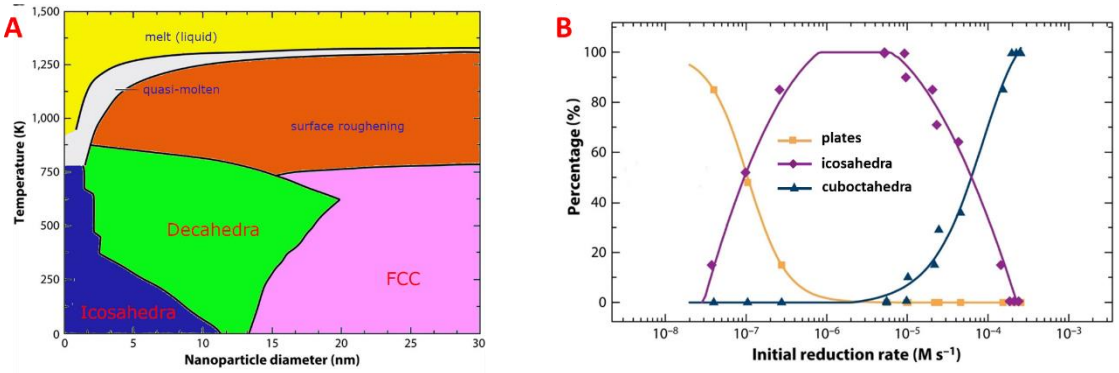

Figure 1.4. Phase diagram of Au seed as a function of temperature *vs* nanoparticle diameter (A) and population of Pd nanocrystals plotted *vs* the initial reduction rate showing the formation of plates with stacking faults (orange), multiply twinned icosahedra (purple) and single-crystal cuboctahedra (blue). (A) Adapted with permission from ref. [122]. Copyright 2009 American Chemical Society. (B) Adapted with permission from ref. [123]. Copyright 2015 American Chemical Society.

Regardless of the approach used for the preparation of metal NPs, whether homogeneous nucleation or seed-mediated strategies, the material scientists must rely on the fine tuning of thermodynamic and kinetic parameters that govern the dynamics tangled to the morphology control.

A thermodynamic control on NPs syntheses is based on the minimization of the global surface energy of the system. Atoms are arranged and packed in an ordered way driving the system to an equilibrium, defined by the chosen experimental parameters, leading to a defined shape. Usually, thermodynamic control is achieved by long aging periods of the NPs or by the temperature manipulation or both. In colloidal synthesis, the use of capping agents is probably the most known and used strategy for thermodynamic control on shaped NPs. A capping agent is defined as a foreign atom or molecule (which may not necessarily by incorporated in the final nanoparticle structure) that interacts with nanoparticle surface during all the stages of the synthesis promoting one growth direction with respect to the others. When a capping agent is introduced in a reaction system, it interacts with a specific facet lowering its specific surface energy, thus such facets will be predominant in the final shape of the NPs. A graphical example is represented in Figure 1.5 by the growth of a truncated octahedron in presence of two different capping agents that selectively interact with (100) and (111) facets. Naming γ the surface free energy, for a capping agent that

preferentially binds to (100) facets, the surface energy trend will be $\gamma_{(100)} < \gamma_{(111)}$ with a faster growth rate along the <111> direction. Due to the difference in the growth rate, the nanoparticle surface will be enriched in (100) facets delivering cubic shaped NPs. On the other hand, the use of capping agents for (111) facets will minimize $\gamma_{(111)}$ increasing the growth rate on <100> direction to finally produce octahedral NPs.

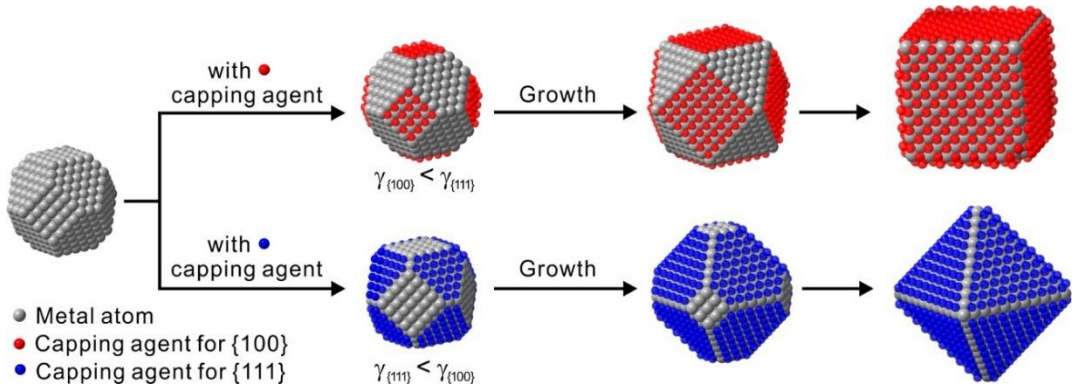

Figure 1.5. Schematic representation depicting the growth evolution of a fcc single-crystal influenced by capping agents specific for (100) facets (red) and for (111) facets (blue). Reproduced with permission from ref. [113]. Copyright 2015 American Chemical Society.

Contrary to the thermodynamic control, working under kinetically-controlled conditions allows the production of NPs with less favourable shapes, thus morphologies not having a minimized global surface energy. Typically, when deposition occurs, atoms are initially adsorbed on sites with high surface energy (the most active) and subsequently migrate or diffuse to sites having lower surface energy, if the system drives to a thermodynamic equilibrium. When thermodynamic equilibrium is not favoured, diffusion of the adsorbed atoms does not occur and the system is trapped in one of the local minima, not having the lowest surface free energy, giving rise to the formation of "kinetic NPs". Two main parameters influence the outcome of kinetic products: atom deposition rate ($V_{\text{deposition}}$) and surface diffusion rate ($V_{\text{diffusion}}$). For example, the growth of a cubic seed in presence of capping agents will take place firstly with the deposition on the highly energetic sites like corners and the newly adsorbed adatoms can follow two paths depending on $V_{\text{deposition}}$ and $V_{\text{diffusion}}$ (Figure 1.6). When $V_{\text{deposition}} / V_{\text{diffusion}} << 1$, surface diffusion will prevail guiding the growth on (100) and (110) facets promoting thermodynamic control (Figure 1.6A). On the contrary, if $V_{\text{deposition}} / V_{\text{diffusion}} >> 1$, surface diffusion is neglected with respect to atom deposition rate and growth is favoured on the <111> under kinetic control (Figure 1.6D). An analogous discussion can be applied for the intermediate cases where $V_{\text{deposition}} / V_{\text{diffusion}}$ is slightly above or below 1 and NPs display features less marked with respect to the extreme cases (Figure 1.6B, 1.6C).

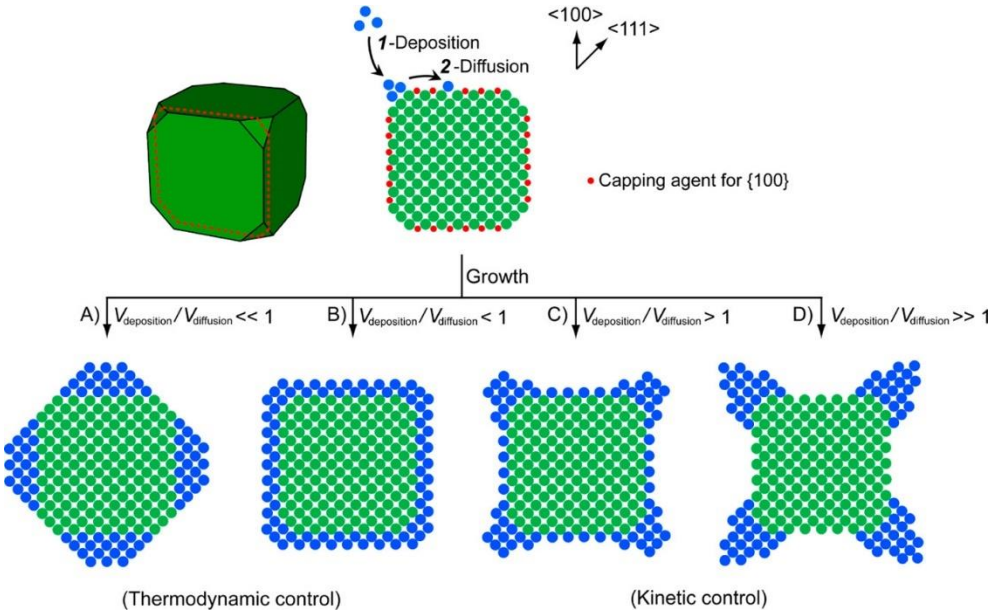

Figure 1.6. Schematic representation of the shape development of cubic seeds at four different kinetic conditions. Reprinted with permission from ref. [113]. Copyright 2015 American Chemical Society.

1.2.1.1. Capping agents

In addition to reactants, other substances can be introduced in the reaction system affecting the NPs morphology. Impurities, even in traces, and oxygen in the reaction environment can modulate the surface structure of the particles.[124,125] Various additives such as cationic/anionic species, surfactants, macromolecules (polymers), biomolecules and organic ligands have been employed in the syntheses of metal NPs (Figure 1.7). Originally, surfactants, polymers and ligands were adopted as stabilizers for colloidal solution of NPs to avoid aggregation and only later on, their real potential has been disclosed as growth directing agents and as size modulators. Nowadays all these additives that perturb the morphology of NPs interacting with the surface are called capping agents. Capping agents retain an important role in colloidal synthesis as they exhibit a dual function of stabilizers and shaped-selective growth. They preferentially adsorb or compete for binding to different particle surfaces. Their primary function is facets stabilization to which they bind with the consequence of surface free energy minimization and modulation of growth rates of the particle.

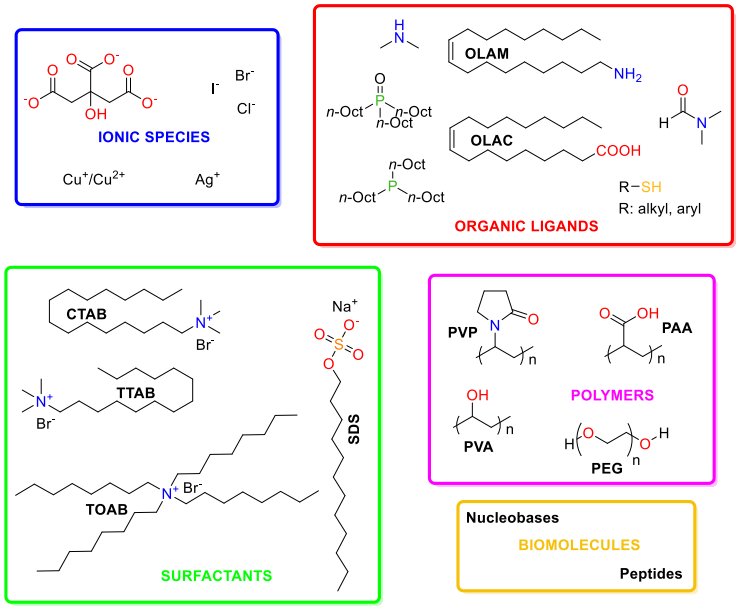

Figure 1.7. Most common used capping agents for the synthesis of metal NPs grouped by categories.

Common capping agents used in colloidal syntheses are cationic/anionic species, either organic or inorganic, neutral organic molecules, macromolecules (polymers) and biomolecules. Inorganic ionic species as capping agents have been widely reported including Ag^+, Cu^{2+}, Cl^-, Br^-, I^- and have been employed for the synthesis of various metal NPs. [126–133] The use of foreign ions as capping agents can influence growth and shape by facet passivation and minimization of specific surface free energy or by defect generation. One of the first reported examples involving the use of ions as capping agents was presented by Song *et al.* where the use of Ag^+ ions at varying concentrations delivered cubic-, cuboctahedra- and octahedra-shaped Pt NPs. The preferential adsorption of Ag^+ for (111) facets in Pt surfaces favoured the growth rates of cuboctahedrons, starting from cubic seeds, and consecutively to octahedral particles.[126] Another example is the synthesis of cuboids and decahedrons in presence of Cu^{2+} ions at increasing concentration. By binding to the (111) facets, Cu^{2+} retards the growth rate along the <111> direction boosting the growth rate along <100> to produce cuboids. Additionally increasing the Cu^{2+} concentration and the global growth rate, decahedrons bound by the stabilized (111) facets were produced.[132] Surfactants are another class of capping agents extensively used in the synthesis of shaped metal NPs. Regularly employed surfactants in particles production are cetyltrimethylammonium bromide (CTAB), tetraoctylammonium bromide (TOAB), sodium dodecylsulfate (SDS), tetradecyltrimethylammonium bromide (TTAB) and so on.[95,134–140] The use of cationic surfactants is predominant in the production of metal NPs, especially in aqueous solutions. For instance, the use of CTAB in NPs synthesis has been reported in a myriad of procedures. Palladium NPs with variable morphologies were reported by the use of CTAB as surfactant at increasing concentration

of sodium citrate. CTAB it is known to stabilize (100) Pd surfaces, thus directing metal reduction over (111) and (110) facets delivering cubic NPs, cuboids and eventually rods.[137] Another interesting application concerns the synthesis of gold multipods by a seed mediated approach reported by Huang and co-workers. Here the authors studied the formation of branched NPs by the reduction of $HAuCl_4$ with sodium citrate in presence of the surfactant SDS as capping agent. It was found that SDS selectively adsorbs on (110) gold facets favouring the preferential growth along <111> directions generating nanostructured bipods, tripods, tetra- and pentapods.[135]

Organic molecules with the ability to chemisorb to metals are called ligands. In nanomaterials, these molecules are pivotal in various studies such as those concerning: the formation of self-assembled monolayers (SAMs),[141] surface passivation,[142,143] and stabilisation.[144,145] Organic ligands feature a functional group able to bind the metal surface; the nature of the functional groups can vary depending on the application, although amines, phosphines, carboxylic acids and thiols are commonly used. Oleylamine (OLAM) and oleic acid (OLAC), in particular, have been broadly studied and applied for the colloidal synthesis of metal NP as confirmed by the large body of work found in literature.[146,147] The individual or concomitant use of OLAM and OLAC has generated a variety of shaped NPs exploiting distinctive reaction conditions. Kang *et al.* succeeded in producing Pt nanocubes, Pd nanospheres and Au nanowires using OLAM and OLAC as capping agents and carbon monoxide for a fast reduction. The authors used different combinations of OLAM/OLAC ratios to selectively deliver monodispersed and well-defined nanocrystals.[148] Even though these two organic ligands are employed in the production of low index NPs, unconventional shapes have also been reported. Xia *et al.* reported the synthesis of high-index faceted Pt NPs in presence of OLAM. They studied the influence of OLAM at variable concentrations on the morphology of Pt NPs. It was observed that by aging a solution of H_2PtCl_6 in dimethylformamide (DMF) at 160 °C with increasing concentrations of OLAM complex architectures were obtained starting from concave nanocubes to octapods and multibranched NPs.[149]

Recently, the use of polymers as additives in the synthesis of metal NPs has increased the interest in the scientific community thanks to the stabilization toward aggregation and the compatibility with both organic and aqueous media, depending on the polymer choice. Frequently used polymers as capping agents are polyvinylpyrrolidone (PVP), polyvinyl alcohol (PVA), polyacrylic acid (PAA), polyethylene oxide (PEO) and polyethylene glycol (PEG), although other more complex and unusual macromolecules have been used for the same purpose.[150–152] In addition to colloidal stabilization, polymers also act as templating agents in the NPs synthesis, and some of them can be used to promote directional growth. PVP it is widely used as capping agent in the production of nanostructures and for some metals, like Ag and Pd, it selectively adsorbs on specific facets. It has

been demonstrated that for Ag, PVP preferentially adsorbs on (100) facets delivering cubic shaped NPs.[153] The selective binding of PVP to Ag (100) was also computationally confirmed.[154] Similarly, El-Sayed and co-workers reported the use of PAA in the preparation of cubic and tetrahedral Pt NPs. [155] The shape selectivity was attributed to the use of the polymer at different concentrations: high concentrations of PAA stabilized the (111) Pt facets boosting the growth rate on the <100> directions thus generating tetrahedral NPs while low concentrations of PAA privileged growth on <111> direction resulting in cubic shaped NPs.[156]

Less reported, but very attractive capping agents for morphology control of nanostructures are biomolecules like peptides or nucleic acids.[157,158] For example, Chiu and co-workers investigated the use of two peptides, Ac–Thr–Leu–Thr–Thr–Leu–Thr– Asn–$CONH_2$ (T7) and Ac–Ser–Ser–Phe–Pro–Gln–Pro–Asn–$CONH_2$ (S7), in the synthesis of shaped Pt NPs. They demonstrated that the rational design of facet specific peptides for directed growth of nanocrystals can be achieved by studying the adsorption energies of the combined functional groups of the single aminoacidic unities constituting the peptides. T7 showed preferential adsorption on (100) Pt facets giving cubic shaped NPs, while S7 peptide stabilized (111) Pt facets allowing the obtainment of tetrahedral NPs as final product.[159] The use of capping agents in metal NPs production has been widely corroborated along the years and it is now at the basis of almost every new synthetic strategy adopted for morphology control at the nanoscale. However, some issues like their role in the primordial stages of nucleation and the post-synthetic surface preservation still need to be addressed and are now matter of study.

1.2.1.2. Size-controlled metal NPs

For a material to be labelled as “nano” it needs to have at least one of its dimensions in the range of 1-100 nm. As previously stated, reducing a material size to the nano-regime can drastically alter its electronic properties. For NPs exhibiting the same dimensions, the term “monodisperse” is applied: monodispersity refers to a size dispersion (standard deviation) that is less than 15% from the average size value while a deviation around 20% is considered a narrow size distribution for the NPs. A chemical procedure that focuses on the development of monodisperse NPs or with a narrow size distribution is typically called size-selective synthesis. Turkevich and co-workers were the first to report a size-selective synthesis for the preparation of colloidal metal NPs.[160] Employing the salt reduction method and using sodium citrate or sodium polyacrylate as stabilisers, they were able to reproducibly obtain monodisperse Au and Pd NPs of the desired size by exploiting different combinations of reducing agent and pH value.[160,161] Recently, the use of capping agents have become pivotal for size control and avoid aggregation. Occasionally, the capping agent or stabilizer

can also be the reducing agent in the synthesis, this is the case of sodium citrate in the preparation of gold NPs.[162] Sodium citrate reduces the metal salt, and at reaction completion it acts as stabilizer for the colloidal solution. [163] Size selectivity is an important parameter to be considered in the catalysis field because of the mass/specific activity relationship. This relationship strongly depends on the specific surface area that is inversely proportional to the size of the metal catalyst. In general, the size variation can affect the activity of a metal NP through two mechanisms: perturbation of the surface homogeneity (specifically the corner and edge atoms) and alteration of the electronic structure. It is well known that size reduction of a particle is accompanied by a change in the atoms coordination environment. For instance, when considering the nature of Au surface atoms at varying dimensions in an octahedral particle (Figure 1.8), a significant increase in corner and edge atoms is reported.[164,165] This abundance of low coordination number atoms at the surface lowers the degree of unsaturation which is directly related to the activity of a catalyst as reaction intermediates are easily formed and transformed into products.[166]

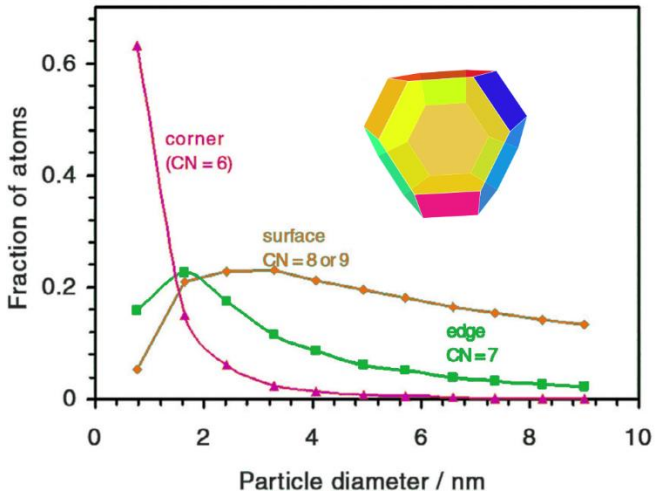

Figure 1.8. Calculated fraction of Au atoms at corners (purple), edges (green) and surface facets (orange) as a function of particle diameter. The calculations are performed on regular Au truncated octahedrons considering only the top half of the NPs. Adapted with permission from ref. [164]. Copyright 2007 Springer.

Along with mean coordination number, a change in the local electronic structure is also observed when altering the size of NPs. Such electronic perturbation triggers the separation of energy levels in the density of states (DOS) of a metal NP, especially when the size goes below a set threshold causing the separation of the electronic bands to the point where HOMO-LUMO gaps start to be appreciated and metal to non-metal transitions are observed, notably at the nanocluster regime.[167,168] Au on TiO_2 system perfectly exemplifies the change of electronic properties with the size. It was reported that the Fermi level of this nanocomposite increases with the decrease of Au NPs size causing an improved photoinduced charge separation thus affecting the global activity of the nanomaterial.[169]

Size-selective procedures can be applied to several transition metals and also to shaped NPs, even though most of the examples following will treat spherical or quasi-spherical NPs as those are the most frequently reported in literature for size confinement methods. Monodisperse NPs have been manufactured using various stabilizers like polymers, ligands, surfactants and so on. The polymer PVP has been effectively employed in the synthesis of size-controlled metal NPs.[170–174] The size of the particles can be narrowed by variation of the PVP concentration following the trend of higher concentration, smaller particle size. For example, Pd NPs with controlled dimensions ranging from 1.7 nm to 3 nm were obtained using PVP and alcohols as reducing agents in a one pot synthesis (Figure 1.9).[173] The same approach was also used to produce larger Pd particles in a seed-mediated synthesis involving a multistep reflux procedure of the PVP-stabilized seeds.[170]

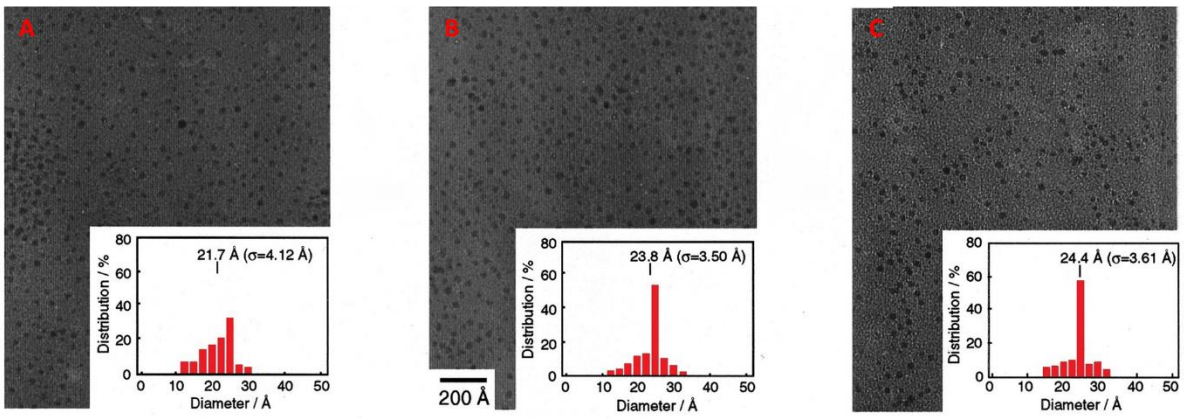

Figure 1.9. TEM micrographs and size distribution (inset) of monodispersed Pd NPs obtained by one-pot synthesis refluxing an aqueous solution of H_2PdCl_4 with PVP in water and ethanol for 15 min (A), 30 min (B) and 180 min (C). Adapted with permission from ref. [173]. Copyright 1998 American Chemical Society.

Other transition metal NPs of the platinum group have been fabricated with the use of PVP such as Pt,[172] Rh[175] and Ru. Organic ligands such as amines, thiols, carboxylic acids, phosphines, and bio-organic molecules have also been exploited for the size control of metal particles, among them of particular interest are the long chain alkyl amines and thiols.[141,146] Monodispersed colloidal Ni NPs, with size ranging from to 30 nm, were reported by Carenco *et al.* in presence of OLAM and trioctylphosphine (TOP) at high temperature (220 °C). The careful selection of TOP stoichiometry resulted in substantial changes in the NPs size granting fine dimensional selectivity. Similarly, Sun *et al.* reported the polyol synthesis of FePt bimetallic particles using OLAM and OLAC as capping agents in 1,2-hexadecanediol which acted as main reductant toward $Pt(acac)_2$ and $Fe(CO)_5$. Again, the procedure handed monodisperse (size deviation of 5%) particles in the range of 3 – 10 nm. The FePt NPs were tuned in dimension by simply growing the 3 nm particles in situ and then adding a desired amount of metal precursors which was directly reduced on the surface of the pre-synthetized particles. The chemical nature of thiols makes them a peculiar type of surfactant. Even though they

are mostly used in the synthesis of Au NPs,[176,177] it is not uncommon to find them employed in the synthesis of other transition metal NPs like Ag, Cu, Pd, Ir, Pt, Ru and many others.[178–182] In the preparation of metal NPs using thiol ligands the size restriction is easily achieved but particles bigger than 5 nm cannot be obtained as the bond strength between gold and sulfur do not allow a fast ligand desorption to promote a proper reduction rate for the additional growth of the particles. It follows that thiols are good ligands for the preparation of small and monodisperse NPs with an appealing application in catalysis.[183–185] Another interesting method for the production of monodisperse metal NPs is the use of microemulsions in aqueous solution consisting in reverse micelles.[186] The micelle itself is a first approximation of the size "confined vessel" which sets the upper growth limit of the particles. One of the key factors that influences the size of the final NPs prepared in micelles is the water-to-surfactant ratio: the lower the surfactant concentration, the bigger the particles obtained. With the reverse micelle technique numerous metal NPs were produced with controlled size including Fe, Cu, Rh, Pd, Pt and Au ones.[187–189] Still, a couple of drawbacks affect the outcome of the micellar syntheses like the poor yield of the final product and the polycrystallinity of the obtained NPs which is challenging to control or avoid as reactions are performed at low temperature to preserve the micellar structure.

1.2.1.3. Shape-controlled metal NPs

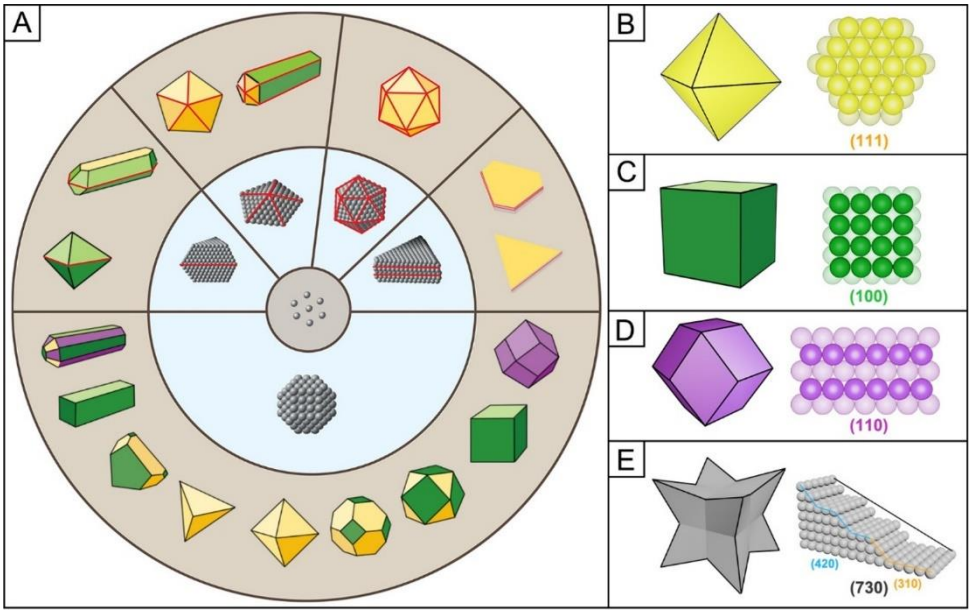

Figure 1.10. Shaped NPs obtained by growth of single-crystal or twinned seeds (A). Representative models of NPs shaped as octahedron, cube and rhombic dodecahedron with their atomic arrangement (B-D). Concave cube enclosed in (730) high-index facets and atomic model highlighting the presence of steps composed of (420) and (310) facets (E). Reproduced with permission from ref. [116]. Copyright 2021 American Chemical Society.

Along the decades, colloidal synthesis has been effectively exploited for the production of metal NPs in a wide range of shapes (Figure 1.10).[116,117,190–194] Obviously, the diverse shapes are the expression of different facets at the surface of the nanocrystals. In Figure 1.10B-D schematic representations of cubic, octahedral, and rhombic dodecahedral NPs of face centred cubic (fcc) metals are depicted, enclosed by low indexed facets like (100), (111) and (110) respectively. Certainly, the same kind of facets can be exposed on the surface of NPs with different shapes. For instance, the surface of a bar nanocrystal is enclosed in (100), just like the cubic nanocrystals. Penta-twinned rods and wires, in the same way, are enclosed by (100) facets on their side surface. The association of different shapes with the same facets can be useful as it provides access to a specific facet using differently shaped NPs. Nanocrystals having the same facets on the surface, but different geometries may also have different behaviours toward the same application because of the surface-to-volume ratio that particularly influences the properties of a nanomaterial, especially in catalysis. Compared to a bulk crystal, a nanocrystal can be easily enclosed in high-index facets that are enriched in low-coordination atoms which are extremely active in catalysing chemical transformations. High-index facets, symbolized by a set of Miller indexes (*hkl*) with at least one of the indexes being greater than one, are characterized by the abundant presence of steps, kinks and edges.[195] These are usually found on NPs with concave or convex surface, like the concave cube in

Figure 1.10E enclosed by (730) facets. High-index faceted NPs are produced by kinetic controlled process and have a total surface free energy that is higher compared to the low-index faceted ones. Even though metal NPs enriched in high-index facets are appealing for various applications in catalysis,[196,197] their production faces limitations mainly due to their instability and the scarcity of capping agents suitable for the stabilization of such facets.[198]

In this chapter, remarkable examples will be presented, and discussed, concerning the synthesis of faceted monometallic NPs, with a particular focus on noble metals in line with the scope of this thesis.

1.2.1.3.1. Low-index faceted metal NPs

Almost all the noble metals (exception made for Ru) have an fcc crystal structure and the low-index facets of a metal in this crystalline phase have specific surface energies that grow in the order of $\gamma\{111\} < \gamma\{100\} < \gamma\{110\}$. Nanoparticles enclosed in these facets are octahedra, cubes and rhombic dodecahedra, as previously mentioned. In the following, various metal NPs enclosed in (111), (100) and (110) facets will be discussed focusing on their synthesis.

Platinum

Platinum has been extensively studied in its various shapes for the production of NPs, this because of the simple and reproducible protocols developed to this end and for the high purity and crystallinity of the particles obtained. As an example: a great number of studies have reported the synthesis of Pt nanocubes. Generally, the cube is commonly observed in single-crystal NPs even though the exposed (100) facets are higher in surface energy compared to (111) facets because of the lower CN with respect to the latter (8 vs 9). The synthesis of Pt nanocubes usually involves a fast reduction process, in presence of capping agents suitable for the stabilization of (100) facets. The first protocol for the production of cubic shaped Pt NPs was reported in 1996 by El-Sayed and co-workers. The synthesis was based on the reduction of K_2PtCl_6 with hydrogen in presence of sodium polyacrylate as capping agent.[155,156] Despite the great accomplishment for the time, the integrity of the particles was not remarkable, which prompted others to improve the procedure. Later on, other capping agents were employed for the stabilization of (100) facets like OLAM and OLAC, CO, PVP and so on. For instance, Tilley and co-workers obtained Pt nanocubes in high purity reducing $Pt(acac)_2$ in presence OLAM, although with the drawback of having a significant size polydispersity.[199] In another study, Pt cubes were obtained using a combination of OLAM, OLAC and CO.[200] The strong adsorption of CO on Pt(100), rather than (111), promotes their

stabilization favouring the production of regular monodispersed cubes (Figure 1.11). When CO is generated from metal carbonyls, an issue about the metal ion role in the participation of the NP formation mechanism arises. It was suggested that CO instead of being the capping agent it only acts as reducing agent while the metal ions are the real facet stabilizers.[201,202]

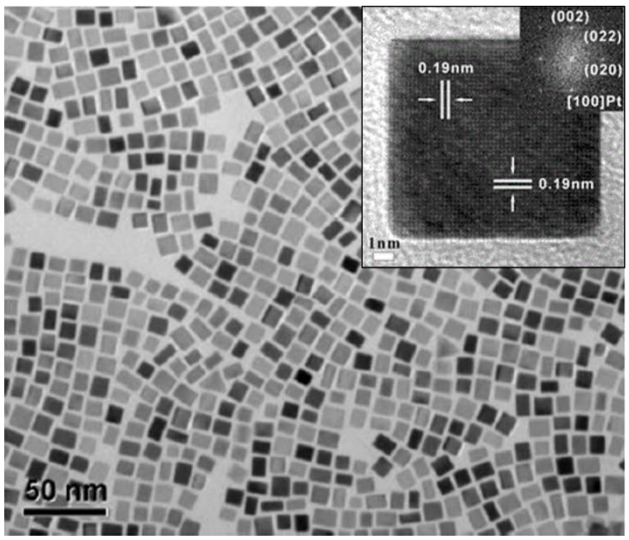

Figure 1.11. TEM micrograph of Pt nanocubes obtained by reduction of $Pt(acac)_2$ with CO in OLAM and OLAC. Inset: HR-TEM micrograph of a single particle with measured planar distances and SAED showing the fcc Pt reflections. Adapted with permission from ref. [200]. Copyright 2011 Royal Society of Chemistry.

Apart organic ligands for the synthesis of Pt cubes, other additives have been used for facet stabilization such as Ag+, polymers and peptides.[126,159,203] Just like cubes, also bars are enclosed in (100) facets and can be represented as elongated cubes. Unfortunately, few examples have been reported in literature for the synthesis of Pt bars. In one of those, Pt nanobars were produces by localized etching of nanocubes with the aim of capping agent removal in order to promote preferential growth only on one side.[204] Another work reported Pt bars exploiting the oriented attachment strategy. First, small particles were produced from $Pt(acac)_2$, OLAM, formic acid and benzyl alcohol, then the particles were assembled, through the process of coalescence, along the <100> direction until uniform bars were achieved.[205]

Complementary to cubes, octahedra are enclosed in (111) facets and, even though the $\gamma(111)$ is lower compared to $\gamma(100)$, the synthesis of octahedra is not so straightforward as cubes. The first high yield Pt octahedra synthesis was achieved by the use of Ag^+ ions in large quantity. It was speculated that Ag+ first stabilized Pt(100) facets and then were removed by displacement with Pt atoms promoting growth on the same facets to deliver octahedral NPs.[126] Monodisperse Pt octahedra were also produced by the use of $Mn_2(CO)_{10}$ with OLAM and OLAC in benzylether. Here the shape selectivity was attributed to the tuning of metal carbonyl/$Pt(acac)_2$ ratio, and to the reaction temperature which was maintained between 210 and 230 °C.[201,206] Beside Pt octahedra,

with this protocol various shaped Pt NPs were obtained like cubes, truncated cubes, cuboctahedra, icosahedra, spheres, tetrapods, octapods and multipods after a recrystallization step (Figure 1.12). Nanocrystals with small size are advantageous because they are optimized to deliver high mass-specific activity and are therefore good candidates for catalysis.

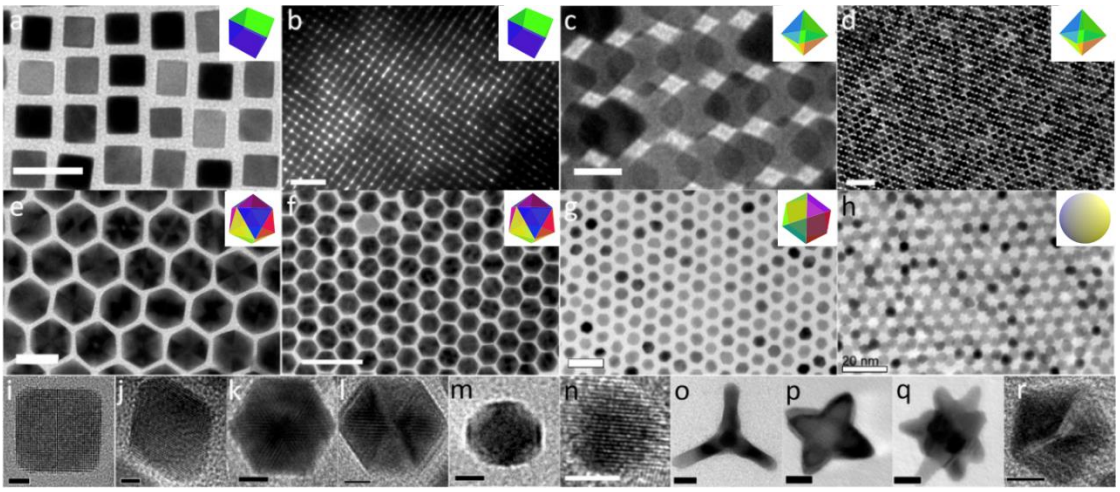

Figure 1.12. Representative TEM micrographs of Pt cubes (a, b), octahedra (c, d), icosahedra (e, f), cuboctahedra (g) and spheres (h). HR-TEM micrographs of Pt cube (i), octahedron (j), icosahedron (k, l), truncated cube (m), sphere (n), tetrapod (o), octapod (p), multipod (q) and decahedron (r) single particles. Scale bars: 20 nm (a, e, g, h), 50 nm (b, d, f), 10 nm (c, o, p, q), 2 nm (i, j), 5 nm (k, l, m, n, r). Adapted with permission from ref. [206]. Copyright 2013 American Chemical Society.

Sub-10 nm Pt octahedral NPs were recently reported by a modified procedure in water with the aid of PVP which served as capping agent and mild reductant for the Na_2PtCl_6 salt.[207] The synthesis was performed at 90 °C aging the solution for 48 hours after which 9 nm octahedra were collected. The shape evolution proceeds through spherical single-crystal seeds that evolve to octahedra covered in (111) facets that are favoured by thermodynamic conditions. Smaller Pt octahedra were also produced by Moglianetti *et al.* employing a seed-mediated growth protocol where Pt seeds were used with ascorbic acid and sodium citrate to deliver 7 nm NPs.[208] Computational studies have shown that citrate ions can adsorb on Pt(111) stabilizing the facets and driving the reaction to form octahedral NPs.[209] Also, the choice of temperature and reduction rate are crucial to the synthesis outcomes.

Platinum tetrahedra, also exposing (111) facets on the surface, have been early reported.[155] The synthesis, similar to the first cubic Pt NPs procedure, was performed in sodium polyacrylate with hydrogen for the reduction of K_2PtCl_4 using a higher surfactant concentration for the stabilization of (111) facets. The same behaviour was also observed when using PVP as capping agent: low concentrations of the polymer delivered Pt nanocubes whereas higher concentrations drove the shape to tetrahedra. Recently, also peptides have been used as capping agents for shape selectivity. It has been shown that a peptide of aminoacidic sequence Ac−Ser−Ser−Phe−Pro−Gln−Pro−Asn−

$CONH_2$ (S7) successfully promoted the synthesis of Pt(111) tetrahedra while a second peptide Ac-Thr-LeuThr-Thr-Leu-Thr-Asn-$CONH_2$ delivered Pt(100) cubes (Figure 1.13A).[159] Analogously to the last case, Pt bipyramids were also synthetized with the aid of peptides by the same group. The approach used here is a seed-mediated growth by which singly twinned seeds were produced employing the peptide Ac-ThrLeu-His-Val-Ser-Ser-Tyr-$CONH_2$ (BP7A) and used for the growth of (100) right bipyramids or (111) enclosed bipyramids in presence of peptide T7 or S7, respectively (Figure 1.13B).[210]

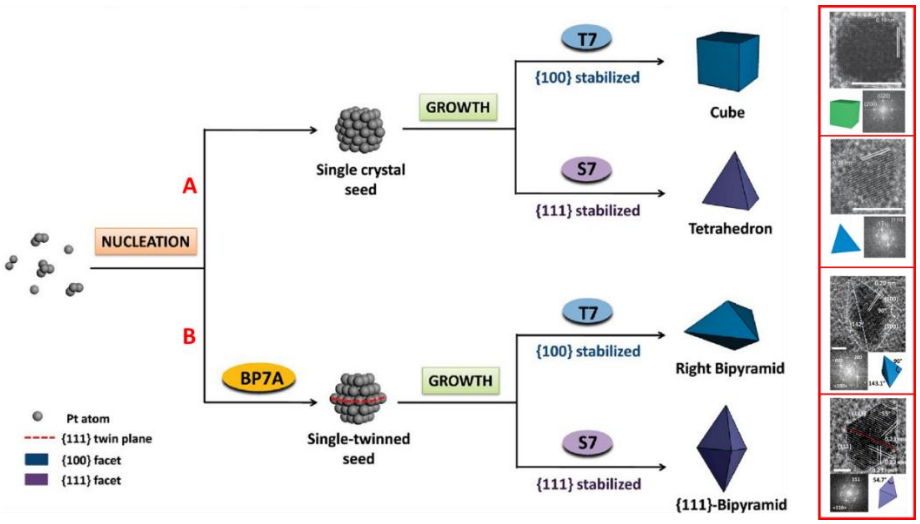

Figure 1.13. Schematic representation of the rational design with T7 and S7 peptides for the synthesis of Pt cubes or tetrahedrons from single-crystal seeds (A) and right bipyramids or (111)-bipyramids from single-twinned seeds (B). Inset on the right shows HR-TEM micrographs of the single particles. Scale bar: 5 nm (cube, tetrahedron), 2 nm (right bipyramid, (111)-bipyramid). Adapted with permission from ref. [159] (Copyright 2011 Springer) and ref. [210] (Copyright 2011 American Chemical Society).

Nanoparticles displaying more peculiar shapes can be isolated when twin defects are incorporated in the structure. Twin defects are created when the stacking sequence of the crystal lattice is interrupted and the two crystal lattices neighbouring the defect are mirror images of each other. Metals with fcc crystal structure are common to incorporate twin defects during crystallization as the decompensation in surface energy, generated by the presence of such defects, is negligible. For platinum, two shapes have been reported that present tween defects and low-index facets, decahedra and icosahedra. Decahedral NPs were isolated by a slow reduction of $[Pt(NH_3)_4][PtCl_4]$ with OLAM aging the solution for 7 days at 130 °C (Figure 1.14A, B).[211] With the same procedure Pt icosahedra were also produced by simply changing the Pt precursor to $[Pt(CH_3NH_2)_4][PtCl_4]$ and increasing the reaction temperature at 150 °C (Figure 1.14C, D). The preparation of icosahedral Pt nanocrystals have been reported also by other different procedures, such the fast reduction of $Pt(acac)_2$ with CO in dodecylamine (DDA), OLAM, diphenyl ether and with the addition of $Y(acac)_3$[212] or reduction with $Mn_2(CO)_{10}$.[201] Another slow reduction method requiring the use of

tetraethylene glycol (TetraEG) and PVP as capping agent was recently reported. The slow reduction of $Pt(acac)_2$ by TetraEG was described as the key factor for the formation of multiply twinned structures.[213]

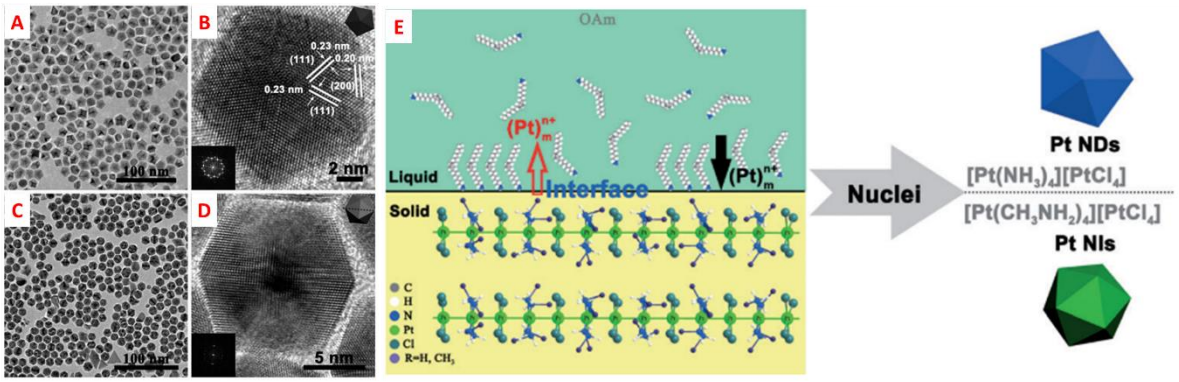

Figure 1.14. TEM and HR-TEM micrographs of Pt decahedra (A, B) and icosahedra (C, D) obtained by the reduction with OLAM at 130 °C and 150 °C, respectively. Schematic illustration of the plausible growth mechanism for Pt decahedra and icosahedra in OLAM (E). Modified with permission from ref. 208. Copyright 2012 Wiley-VCH.

Palladium

Like platinum, also palladium NPs have been extensively reported in several shapes and typical protocols for Pt NPs have been adapted to the synthesis of Pd NPs. A conventional synthesis for cubic Pd NPs consists in the addition of aqueous Pd salt solution to a mixture of reductant, PVP and halogen ions.[152,214,215] Here PVP provides stabilization against aggregation while Cl^-, Br^- or I^- are involved in multiple events such the selective (100) facet stabilization, the oxidative etching of twin defects and the reduction rate deceleration. Through oxidative etching it is also possible to obtain Pd nanobars. In one synthesis, nanobars were supplied by the polyol reduction of Na_2PdCl_4 with ethylene glycol (EG) in presence of PVP and KBr.[204] The anisotropic growth is associated to the selective oxidative etching of Br^- ions by oxygen which exposes specific cubic Pd facets and allows the deposition of new metal atoms.[216] Other mechanisms of anisotropic growth of nanobars can be the oriented attachment of small Pd nanocrystals along one direction or preferential growth promoted by kinetic conditions.[217]

Most of the Pd octahedral and tetrahedral NPs can be prepared by various procedures and some of them are suitable for both shapes which can be selectively obtained by minor changes in the reaction conditions. For example, Wang *et al.* reported a seed-mediated synthesis of both Pd octahedral and tetrahedral NPs selecting one shape with respect to the other by simply changing the platinum precursor (Figure 1.15a). [218] Here, Pd cuboctahedra seeds (Figure 1.15b) were used as substrate for the deposition of Pd atoms in a solution of $Pd(acac)_2$, PVP and TetraEG to generate

tetrahedral Pd NPs (Figure 1.15d). Shifting to Na_2PdCl_4 as metal precursor, octahedral NPs (Figure 1.15c) were obtained thanks to the slow reduction rate of Na_2PdCl_4 that ensures thermodynamic control on the growth. The weak coordination of acetylacetonate to Pd^{2+}, on the other hand, leads to a much faster reduction of Pd^{2+} favouring the kinetic product.

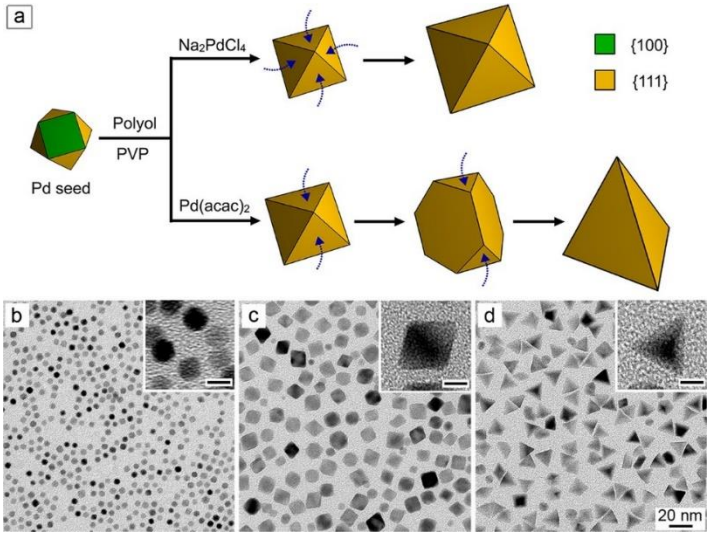

Figure 1.15. Schematic illustration showing the formation of Pd octahedral and tetrahedral NPs (a). TEM micrographs of cuboctahedral seeds (b) and the final octahedral (c) and tetrahedral (d) NPs. Insets show the particles at higher magnification. Scale bars insets: 5 nm. Reproduced with permission from ref. [218]. Copyright 2013 American Chemical Society.

Commonly, Pd octahedra can also be obtained by one-pot synthesis slowly aging the nanoparticles to allow achieving the thermodynamic products. For example, 20 nm Pd octahedral particles were produced from Na_2PdCl_4 salt after 26 hours of aging at 90 °C with PVP and citric acid as capping agents in water.[219] Citric acid is known to strongly adsorb on Pd(111) facets providing stabilization, thus favouring the growth along <100> direction. Another strategy for the preparation of Pd octahedra relies on oxidative etching. It has been demonstrated that by using HCl and oxygen Pd atoms can be redeposited on (100) facets from corner sites allowing the evolution from cubic to octahedral NPs.[220]

Contrary to nanocubes and octahedra, Pd rhombic dodecahedra are not so common in literature, although a few examples have been reported. A seed-mediated synthesis provided Pd rhombic dodecahedral NPs starting from cubes and using CTAB and KI as capping agents, which the authors considered to work synergically for the stabilization of (110) facets.[221,222] Another way to produce rhombic dodecahedra Pd NPs has been reported using an aqueous solution of PVP and glucose.[223]

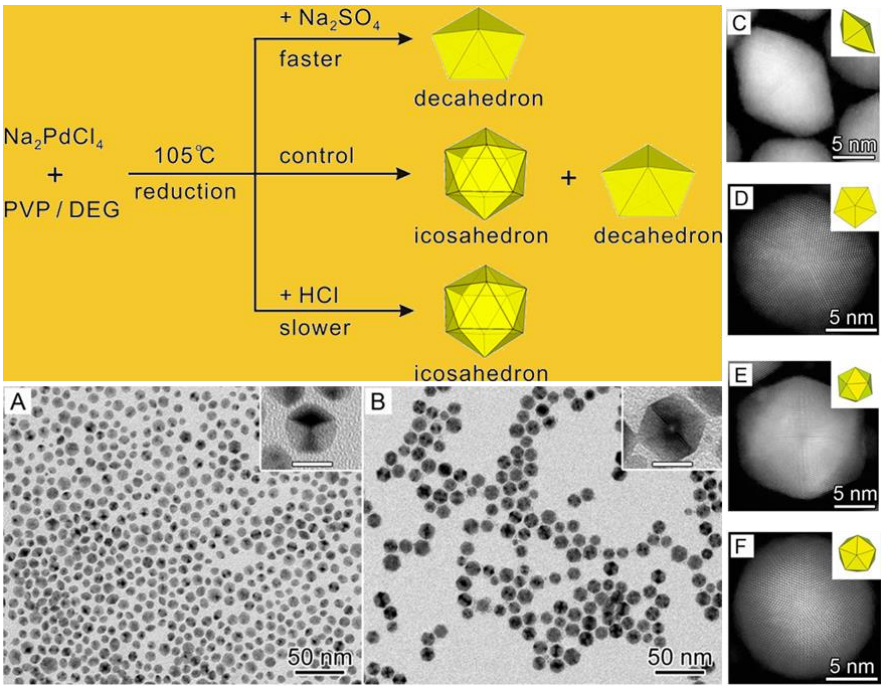

Figure 1.16. Schematic representation of the synthetic paths for the formation of Pd decahedral and icosahedral nanocrystals. Representative TEM images of Pd decahedra (A) and icosahedra (B). HAADF-STEM images of decahedral single particle seen from side (C) and top (D) and icosahedral single particle from side (E) and top (F). Scale bar inset A and B: 10 nm. Adapted with permission from ref. [224]. Copyright 2014 American Chemical Society.

Surprisingly, several Pd shapes deriving from engineered planar defects have been reported in literature. Pd decahedra for example, have been produced by addition of palladium salt in a mixture of PVP, Na_2SO_4 and diethylene glycol. Replacing Na_2SO_4 with HCl resulted in the formation of icosahedral particles (Figure 1.16).[224] Nanoplates also emerge from planar defects that are parallel to the basal plane of the plates. In general, their production requires a low reduction rate for the construction of the 2-D structure. Pd nanoplates have been obtained both in triangular and hexagonal shape. A protocol has been reported for both shapes that could be selectively prepared by tuning the concentration of $FeCl_3$ in an EG solution of Na_2PdCl_4, PVP and HCl (Figure 1.17). Low concentrations of $FeCl_3$ produced Pd triangular plates, while high concentrations of the salt delivered hexagonal plates. Both shapes were enclosed in (111) facets that arose thanks to the Fe^{3+} and Cl^- ions acting as etchants in the presence of oxygen.[225] Pd plates with a reduced thickness have been reported by Hang *et al.* Hexagonal Pd nanoplates made of few atomic layers were reported in a synthetic protocol based on the reduction of $Pd(acac)_2$ with CO using PVP and CTAB as capping agents in *N*,*N*-dimethypropionamide/water mixture.[226]

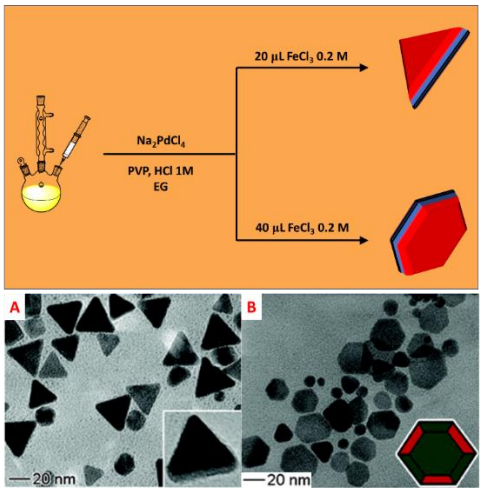

Figure 1.17. Schematic illustration of the synthetic procedure for the preparation of Pd plates with stacking faults and TEM images of the as prepared triangular plates (A) and hexagonal plates (B). Adapted with permission from ref. [225]. Copyright 2005 American Chemical Society.

Silver

Silver is another noble metal that was subjected to extensive studies in the field of selective formation of shaped nanostructures because of the availability and modest cost of the metal precursors. Various protocols for shaped Ag NPs rely on the polyol or aqueous synthesis although procedures employing organic solvents have also been developed. Cubic Ag nanocrystals have been synthetized employing different polyols including EG, DEG, 1,3-butylene glycol and 1,5-pentanediol.[227–231] The typical polyol protocol involves the use of capping agents and high temperature to ensure an appropriate reduction rate. A common procedure for the production of Ag nanocubes is carried out by reducing $AgNO_3$ in presence of Ag spherical or cubic seeds and PVP, in a EG solution, at high temperature.[227] PVP concentration was reported to be crucial for the morphology selection with only high concentrations of capping agent leading to the formation of nanocubes Figure (1.18).[232] Extremely uniform Ag nanocubes were also obtained by introducing Cl^- ions in the reaction (NaCl or HCl) to enhance oxidative etching and prevent the formation of twinned seed while privileging only single-crystal seeds formation.[228] Another method was reported for the fast production of cubic Ag NPs consisting in the use of hydrosulfide or sulfide ions in traces to promote the formation of Ag_2S clusters which then rapidly grow in the final particles.[233] d Here, the formation of 15 nm Ag nanocubes was achieved by a concomitant participation of different species in the mechanism. NaCl was used to prevent the HS^- consumption by protons thus favouring the formation of Ag_2S. NaBr, on the other hand, served as capping agent for the stabilization of (100) facets. Surprisingly, changing the Ag precursor from $AgNO_3$ to AgTFA (TFA: trifluoroacetate) revealed an improved control on the reproducibility. The use of AgTFA also

demonstrated the scalability for the production of Ag nanocubes by working under a blanket of inert atmosphere.[234]

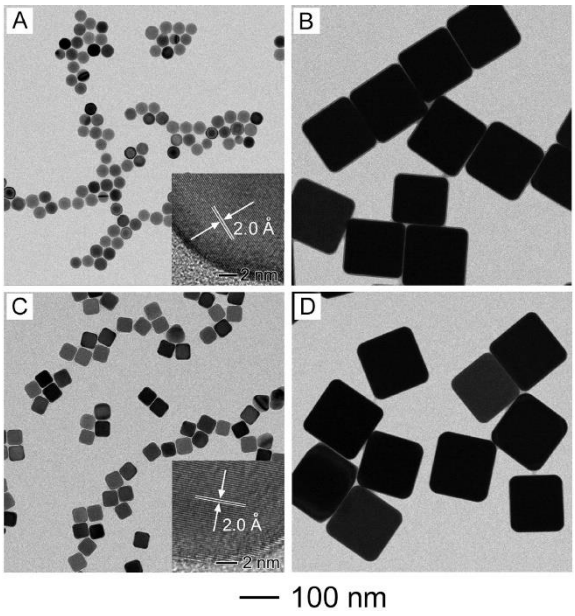

Figure 1.18. TEM images of Pd nanocubes (B, D) obtained by a polyol seed-mediated protocol in EG with PVP using both spherical (A) and cubic (C) seeds. Reproduced with permission from ref. [232]. Copyright 2010 American Chemical Society.

Octahedral Ag NPs have been produced both by homogeneous nucleation and seed-mediated growth. For example, Ag octahedra have been reported by reduction of $AgNO_3$ in presence of PVP and $CuCl_2$ at high temperature for 2 hours.[231] A morphological transition was observed during the reaction progress going from cubes to cuboctahedra and finally octahedra Figure 1.19).

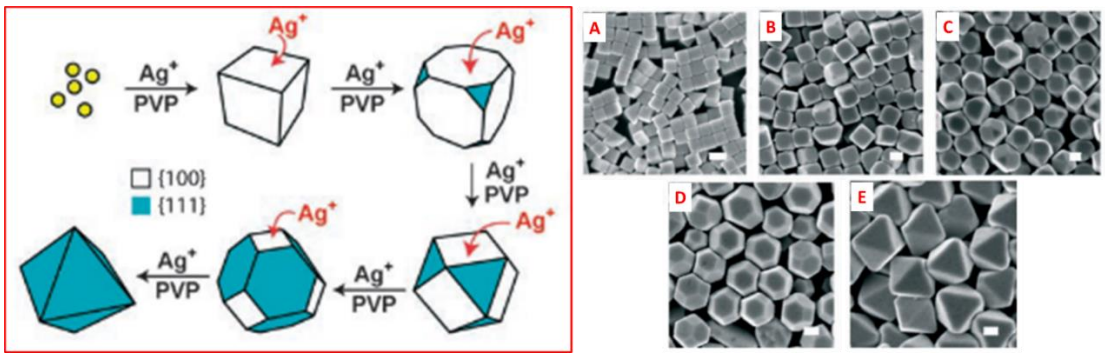

Figure 1.19. Schematic illustration of the shape evolution highlighting the Ag deposition on (100) facets (left panel) and SEM images of cubes (A), truncated cubes (B), cuboctahedra (C), truncated octahedra (D) and octahedra (E), respectively. Scale bars: 100 nm. Adapted with permission from ref. [231]. Copyright 2006 Wiley-VCH.

Citrate it is known to selectively bind (111) facets of fcc metal crystals, and it was also successfully employed for the synthesis of Ag octahedra. The protocol consisted of the use of Ag seeds (spherical of cubic) to deliver octahedral NPs by the reduction of AgTFA with ascorbic acid in presence of sodium citrate.[235]

As discussed above, shaped NPs with planar defects are obtained by a preliminary slow nucleation that allows the formation of twinned defects in the seed's crystal structure, followed by a moderate growth process. With this approach various Ag twinned NPs have been reported such as bipyramids, decahedra, icosahedra, penta-twinned rods and plates by the use of different surfactants and reducing agents.[236–243]

Gold

The use of gold for the preparation of shaped NPs has not flourished as much as other noble metals mainly due to the lack of suitable capping/directing agents for the preferential growth of specific facets. Nevertheless, remarkable examples of protocols and modified procedures have been provided along the years for some shaped Au nanocrystals. Au nanocubes were firstly reported by a polyol reduction of $HAuCl_4$ in EG and shape-directed by Ag^+ ions with PVP as stabilizer.[244] The addition of $AgNO_3$ to deliver Ag^+ was suggested to positively influence the directional growth over (111) facets thus stabilizing (100) ones and increasing amounts of Ag salt resulted in a morphological transition going through octahedra, cuboctahedra to finally produce cubes as final shape. Additionally, a seed-mediated procedure was also reported for cube-shaped Au NPs (Figure 1.20). In this protocol, Au nanospheres were employed as seeds and $HAuCl_4$ was reduced by ascorbic acid in an aqueous solution of CTAC and NaBr.[245] Bromide ions were suggested to be involved in the (100) facet stabilization.

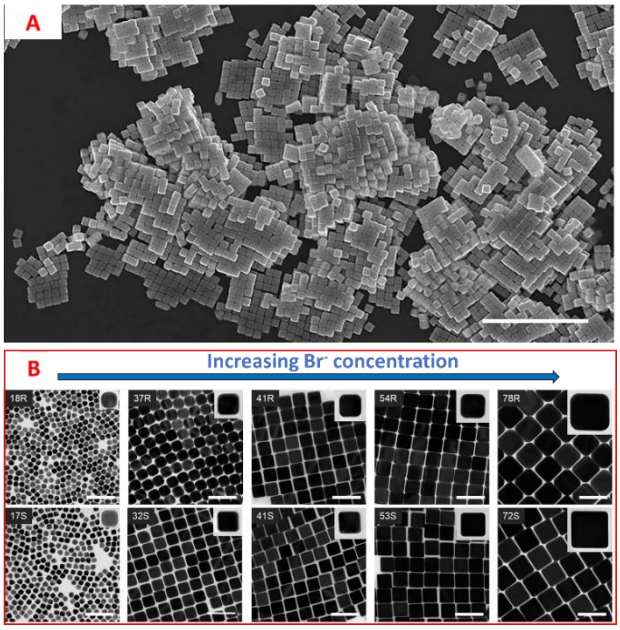

Figure 1.20. SEM image showing Au nanocubes self-assembled in ordered domains (A) and TEM images of the Au nanocubes obtained at increasing Br- concentration by the seed-mediated protocol in water with CTAC and NaBr. Scale bars: 1 μm (A), 100 nm (B). Adapted with permission from ref. [245]. Copyright 2018 American Chemical Society.

A seed-mediated approach was also adopted for the synthesis of Au octahedra: starting from spherical seeds, it was possible to obtain octahedra by reducing the Au precursor in presence of PVP.[246] Other methods for the preparation of Au octahedra rely on homogeneous growth, like the polyol synthesis in presence of poly(diallyldimethylammonium) chloride (PDDA), which stabilized Au(111) facets.[140] The pH control was essential to obtain a high yield of nanocrystals. The authors suggested an adduct formation between PDDA and $AuCl_4^-$ that decreased the reduction rate favouring the formation of octahedral particles (Figure 1.21, left panel). Moreover, size selectivity was achieved by controlling the added amount of HCl solution (Figure 1.21, right panel).

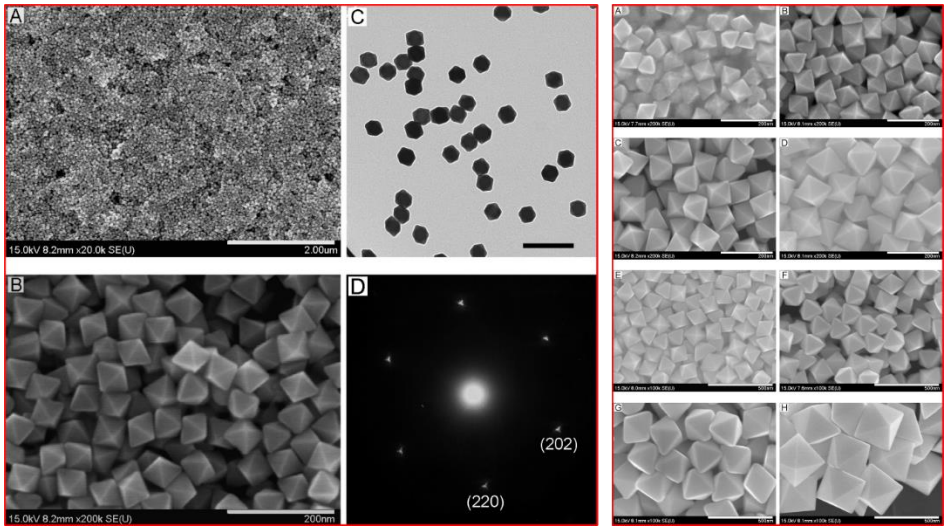

Figure 1.21. Left panel: SEM low (A) and high (B) magnification images, TEM (C) and SAED (D) of the octahedral Au NPs. Scale bars: 2 μm (A) 200 nm (B, C). Right panel: SEM images of Au octahedra obtained with increasing volume additions of HCl 1M to the reaction. Scale bars: 200 nm (A-D), 500 nm (E-H). Adapted with permission from ref. [140]. Copyright 2008 American Chemical Society.

Another interesting procedure for the production of Au octahedra is described by a simple protocol requiring the use of H_2O_2 to boost the ascorbic acid reduction ability. The synthesis was performed in water with CTAB as stabilizer, ascorbic acid as reductant adding trace amounts of H_2O_2. The reaction mixture was incubated for 3 hours at RT, after which, the solution was sonicated at 40 °C for 90 minutes to finally provide octahedral particles with a mean edge length of 52 nm.[247] By employing the previously discussed protocol for Au nanocubes aided by $AgNO_3$, with due modifications, it is also possible to obtain Au tetrahedra enclosed in (111) facets. With the complete exclusion of Ag salt and a small variation of the Au precursor and PVP concentrations it is possible to select octahedral NPs as main product.[244]

Au rhombic dodecahedra, enclosed in (110) facets, have been described by both one-pot and seed-mediated syntheses. Worth of mention, a surfactant free one-pot protocol for rhombic dodecahedral Au NPs has been devised in DMF (Figure 1.22). Here, the solvent acted both as reductant and plausibly as stabilizer for the Au particles. $HAuCl_4$ was heated in DMF at 90 °C for 15 hours for a

slow reduction process that favoured kinetic control over the particles growth.[248] An interesting alternative to this one-pot approach is the seed-mediated procedure based on the use of cetylpyridinium chloride (CPC) to selectively generate Au rhombic dodecahedra.[249] A low concentration of CPC combined with a high concentration of ascorbic acid (reductant) resulted on the blockage of (110) facets and growth along <111> direction, while inverting the surfactant and reductant concentrations provided octahedral Au particles.

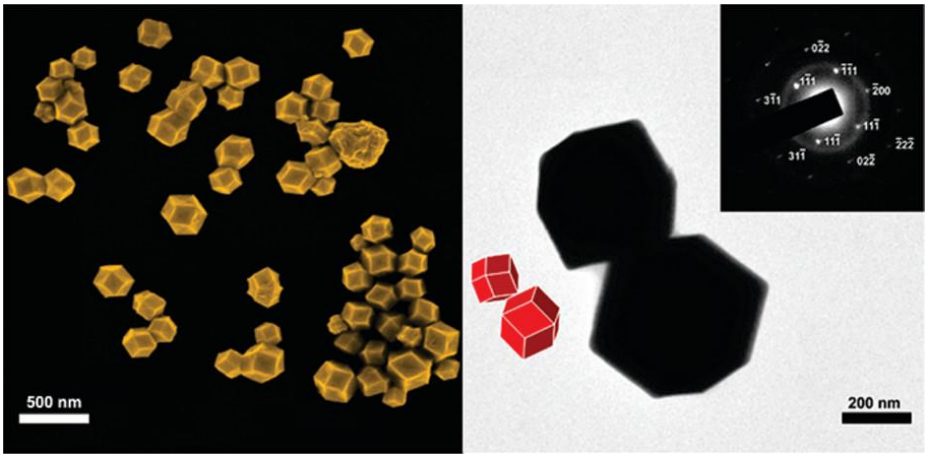

Figure 1.22. Representative SEM, TEM and SAED (inset) images of Au rhombic dodecahedra synthetized in DMF as reductant and capping agent. Reproduced with permission from ref. [248]. Copyright 2009 American Chemical Society.

Apart from single-crystal shaped Au NPs, nanocrystals embedding twin defects have also been reported. One of the first reports provided by Liz-Marzán and co-workers exploited the DMF reducing properties to grow Au decahedra starting from 3 nm seeds by ultrasonication process.[250] An additional example of Au decahedra relies on the homogeneous nucleation of twinned seeds in diethylene glycol (DEG) capped with PVP (Figure 1.23).[251] Of vital importance for the synthesis success is the large excess of PVP used, useful for the protection of twinned nuclei toward oxidative etching. The same procedure was applied to the synthesis of Au icosahedra (Figure 1.23h-k) and single-crystalline triangular plates (Figure 1.23l-o) by significantly lowering the surfactant concentration.

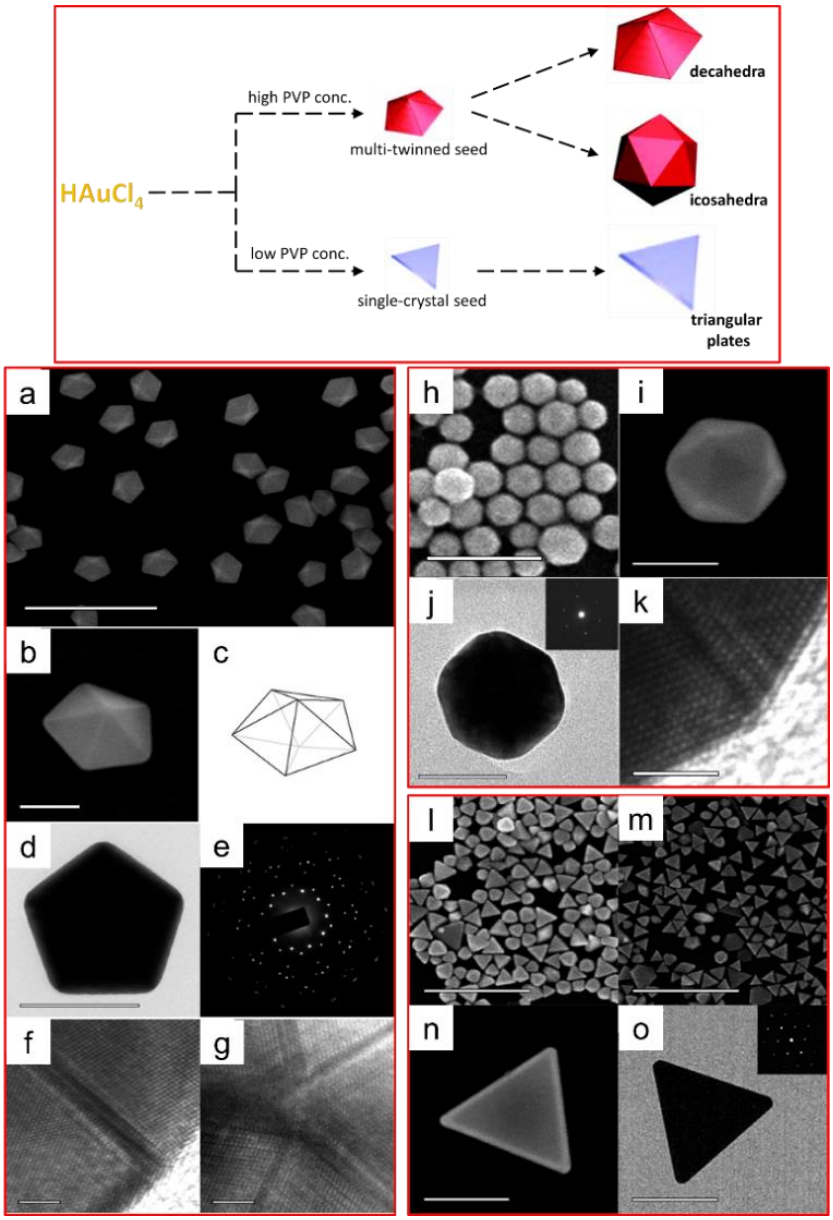

Figure 1.23. Schematic representation of the growth process for the production of multi-twinned and single crystal shaped Au nanocrystals in presence of PVP (upper panel). Microscopic characterization of the as prepared Au decahedra (a-g), icosahedra (h-k) and triangular plates (l-o). Scale bars: 500 nm (a, l, m), 200 nm (h, n, o), 100 nm (b, d, i, j), 2 nm (f, g, k). Adapted with permission from ref. [251]. Copyright 2008 American Chemical Society.

Other metals

Among all the other transition metals not considered until now, very few are eligible for the formation of monometallic NPs due to their instability at the nanoscale (tendency to form metal oxide NPs) or to the high dissociation bond energy and surface free energy of the NPs. In this section, only copper and rhodium will be treated because for these two metals there are well documented studies on faceted NPs.

Copper has been widely investigated in the formation of nanostructures (Figure 1.24), particularly those enclosed in low-index facets. Cubic Cu NPs are typically produced in organic phase at high temperature by the reduction of Cu(I) salts. For instance, the synthesis of Cu nanocubes in high purity was reported using OLAM, trioctylphosphine (TOP) and octadecylamine (ODA) at 330 °C. TOP and ODA have the main function of stabilizing the nanocrystals while OLAM serves as real directing agent for the newly reduced Cu atoms.[252] Cu nanocubes were also synthesised at lower temperature (260 °C) by treating CuBr in OLAM and trioctylphosphine oxide (TOPO).[253] The weaker coordination energy of TOPO (compared to TOP) could induce a faster reduction promoting the nucleation of seeds at lower temperature. In addition, water-based syntheses of Cu nanocubes were reported as-well. In one study, $CuCl_2$ was reduced by glucose in a refluxing aqueous solution of hexadecylamine (HDA).[254] This procedure allowed the production of cubic Cu particles at 100 °C which is far more convenient with respect to the organic phase approach. A combination of oxidative etching (Cl^-/O_2) and HDA stabilization accounted for the successful synthesis. Similar to the organic phase synthesis of Cu nanocubes, octahedral Cu NPs were also obtained. The reduction of CuCl was carried out at 335 °C in a solution of OLAM and TOP.[255] The Cu(111) facet stabilization was proposed to be favoured by TOP, although the weak interaction of the bulky amine with Cu surface could not completely exclude the facet stabilization by a merely thermodynamic factor. By a similar procedure, Buonsanti and co-workers reported the synthesis of Cu tetrahedral NPs performed in inert atmosphere by hot-injecting a solution of CuBr, TOPO in OLAM (solvent) to a preheated (300 °C) OLAM solution.[256] Concerning the production of twinned Cu NPs, a major obstacle limits the development of robust protocols: the tendency of Cu to oxidise that prevents highly energetic twin defects to be formed. Yet, examples of Cu decahedra, icosahedra and penta-twinned rods are reported. Cu decahedra were produced in oil-phase by a slow reduction of $Cu(acac)_2$ with ascorbic acid in OLAM.[257] A relevant aspect to mention is that the synthesis was carefully carried out in inert atmosphere and the solvent was priorly degassed to prevent oxidative etching of the penta-twinned seeds. As for Cu decahedrons, the synthesis of penta-twinned Cu rods is privileged in inert atmosphere.

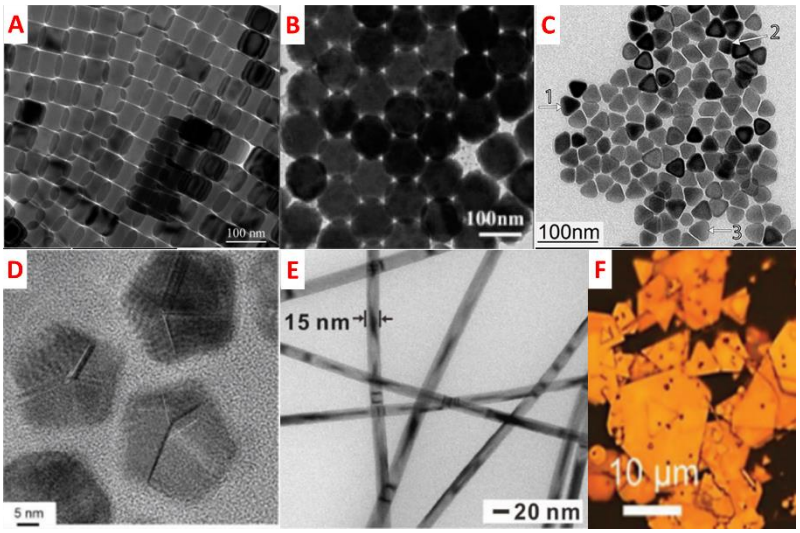

Figure 1.24. Low-index faceted Cu NPs obtained by wet chemical protocols. Cubes (A), octahedra (B), tetrahedra (C), decahedra (D), penta-twinned wires (E) and 2D plates (F). Adapted with permission from ref. [252] (A) (Copyright 2014 American Chemical Society), ref. [255] (B) (Copyright 2015 American Chemical Society), ref. [256] (C) (Copyright 2019 American Chemical Society), ref. [257] (D) (Copyright 2019 Wiley-VCH), ref. [258] (E) (Copyright 2017 Wiley-VCH) and ref. [259] (F) (Copyright 2018 Wiley-VCH).

One particular protocol for penta-twinned Cu rods involves the decomposition of $CuCl_2$ in an aqueous solution of HDA and glucose at 120 °C for 3 hours.[258] A high reductant concentration favoured the initial formation of decahedral seeds that evolved in rod-like Cu NPs. The authors further studied the reaction to elucidate the mechanism involved finding a correlation between chloride ions and anisotropic growth of the Cu penta-twinned rods that was initially attributed to HDA.[260] Cu plates incorporating planar defects with stacking faults on the side facets have been widely documented. It has been demonstrated that iodide ions combined with a slow reduction rate delivered triangular and hexagonal plates, selectively.[259] The slow reduction performed with glucose was fundamental in stabilizing the twinned seeds. Another well-known method for the production of Cu nanoplates involves a slow reduction of Cu precursor with hydrazine. For example, an aerobic synthesis of hexagonal Cu plates, enclosed in (111) facets, was reported in DMF at 60 °C by reduction of $Cu(OAc)_2$ with hydrazine.[261]

As for copper, also for rhodium there has been a lack of solid protocols to achieve nanomaterials with precise morphology. Nevertheless, acknowledged strategies applied to other shaped metal NPs can also be transposed to rhodium. For instance, the well-known polyol synthesis was applied to the assembly of Rh nanocubes through a seed-mediated growth. $RhCl_3$ was subjected to reduction by EG with PVP as stabilizer at 190 °C delivering truncated cubes with a lack in shape definition.[262] The protocol was later improved by the use of tetradecyltrimethylammonium bromide (TTAB) which provided Br^- ions, known to stabilize (100) facets in fcc metals, into the reaction environment.[263] Rh nanocubes have also been produced by the use of $RhBr_3$ as precursor in another

polyol protocol where the reductant is DEG.[264] With the same protocol, Rh octahedra were reported by simply switching from DEG to PEG300 that contributed in modifying the reduction rate thus the kinetics of the reaction favouring octahedral NPs as product. Another strategy also effective for controlling Rh NPs shape is the introduction of foreign metal ions to the reaction mixture. The use of $AgNO_3$ significantly improved the polyol synthesis of Rh octahedra in EG and PVP, increasing the NPs yield up to 90%.[265] Tetrahedral Rh NPs were also reported by the reduction of $[Rh(CO)_2Cl]_2$ in OLAM[266] or $Rh(acac)_3$ in a mixture of glucose, OLAM and DMF.[267]

Recently, decahedral Rh NPs have been synthetized in TetraEG which acted as both reducing agent and solvent.[268] Here, uniform Rh decahedra with controllable size ranging from 5 to 28 nm were obtained by finely tuning the Rh precursor and PVP concentrations. A modification in the protocol for Rh nanocubes allowed to obtain small icosahedral NPs (5 nm) in a polyol reduction of $Rh_2(TFA)_4$ with EG.[264] Larger icosahedra were also produced applying a protocol in which $Rh(acac)_3$ was slowly reduced by PVP (acting as both stabilizer and mild reducing agent) in benzyl alcohol.[269]

The extensive production of both single-crystal and twinned metal NPs enclosed in low-index facets has generated a considerable variety of shapes, thanks also to the low surface free energy of these facets and to the availability of suitable capping agents for their stabilization.

1.2.1.3.2. High-index faceted metal NPs

Metal NPs exposing high-index facets are usually characterized by uncommon polyhedral shapes, most of which are concave and convex nanostructures, multipods, nanostars and branched structures. The high-index facets decorating such NPs can be represented by Miller's indices (hkl) with at least one index being greater than 1. Four varieties of high-index facets that are (hk0), (hkk), (hhl) and (hkl) can be built which generate tetrahexahedral (THH), trapezohedral (TPH), trisoctahedral (TOH), and hexoctahedral (HOH) NPs, respectively (Figure 1.25). These NPs usually bear low-coordinated atoms on the surface that consecutively increase the overall surface free energy of the particles making them appealing for catalytic applications. Typical approaches for the stabilization of highly energetic nanocrystals rely on the manipulation of kinetics (reduction rate in particular) and surface diffusion, coupled with the introduction of suitable capping agents.[195] As for low-index faceted NPs, only selected monometallic high-indexed NPs will be concisely discussed in this sub-chapter.

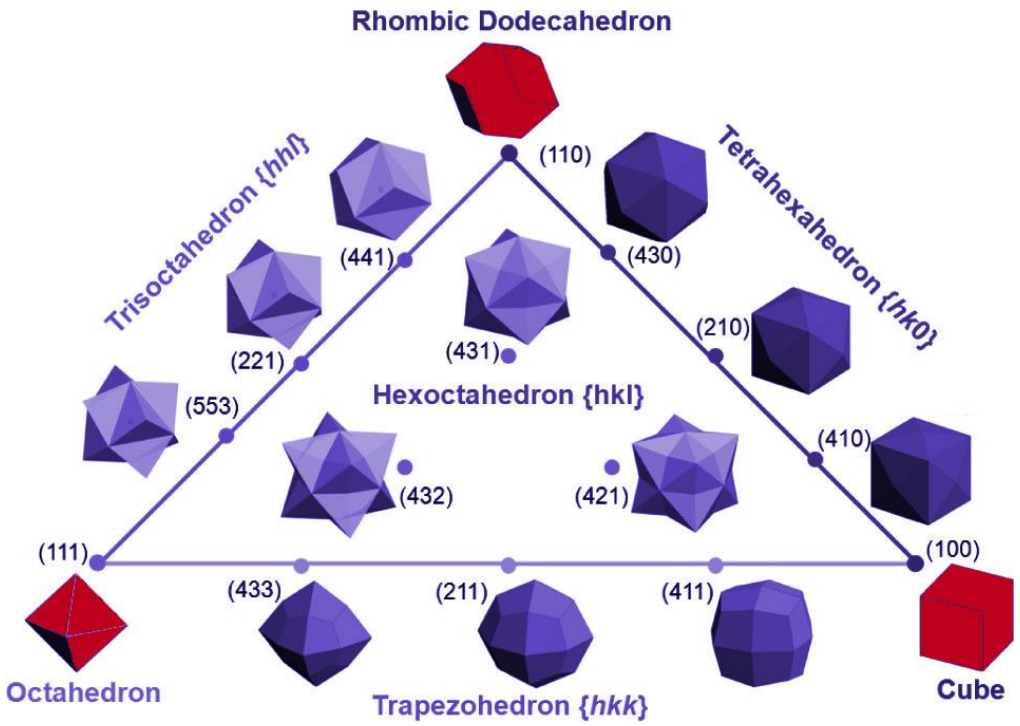

Figure 1.25. Schematic representation of polyhedral NPs enclosed by high-index facets. Adapted with permission from ref. [195]. Copyright 2012 American Chemical Society.

Palladium

Pd NPs exposing high-index facets have been reported as either concave or convex structures adopting various strategies (Figure 1.26). For the generation of concave surfaces, a high deposition rate is usually needed in order to overcome surface diffusion that leads to the formation of more stable low-indexed structures. Concave Pd nanocubes enclosed in (730) facets were achieved through a seed-mediated procedure by deposition of Pd atoms on the surface of Pd nanocubes in water in the presence of PVP, ascorbic acid and KBr.[270] A low concentration of KBr was described as key factor for a fast deposition on the cubic corners that were subjected to overgrowth delivering concave nanocubes. Pd nanocubes with concave morphology and high-index facets were also obtained by one-pot homogeneous nucleation strategy: the synthesis involved the reduction of H_2PdCl_4 by ascorbic acid in an aqueous solution of CTAC and CTAB at 30 °C for 7 hours.[271] In this study, a shape transition was observed going from nanocubes to elongated nanocubes and finally concave nanocubes enclosed in (730), (610), (410) and (310) facets. Other more complex concave Pd structures were also prepared by electrochemical methods applying a square-wave potential to aqueous solutions containing the Pd salt precursor. With this method oxygen adsorption-desorption cycles were induced to selectively direct the nanocrystals growth through periodic oxidation/dissolution and reduction/crystallization. With the square-wave potential method

concave HOH, enclosed in (321) facets, concave-disdyakis triacontahedral, enclosed in (631) facets, convex trapezohedral and tetrahexahedral Pd NPs were also reported.[272–274] Recently, the preparation of tetrahexahedral Pd NPs was reported by a dealloying protocol, without the use of any capping agent, in which bimetallic NPs of Pd-Sb, Pd-Bi or Pd-Te were dealloyed at high temperature leaving shaped Pd nanostructures covered in (210) planes. The shape selectivity of this procedure resulted from the evaporative process of Sb, Bi, or Te.[197]

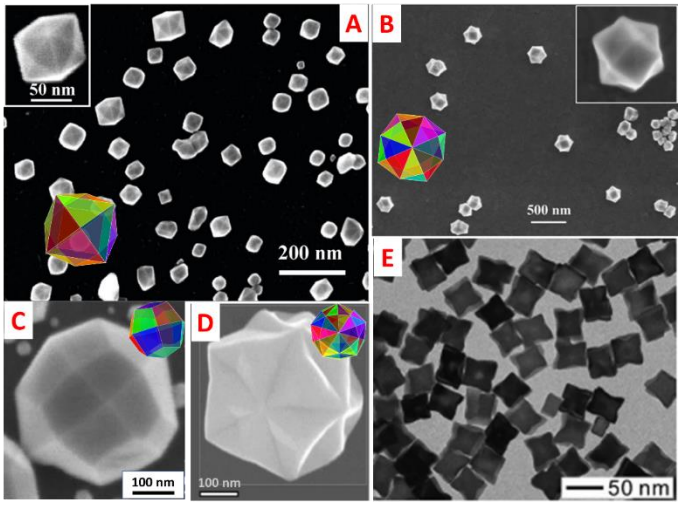

Figure 1.26. Representative TEM (STEM) images of high-index faceted Pd THH (A), HOH (B), TPH (C), DTH (D) and elongated cubes (E). Adapted with permission from ref. [270] (Copyright 2011 Wiley-VCH), ref. [272] (Copyright 2009 Royal Society of Chemistry), ref. [273] (Copyright 2016 American Chemical Society) and ref. [274] (Copyright 2010 American Chemical Society).

Platinum

Pt shares a similarity with Pd since its concave nanoparticles are mainly nanocubes enclosed in the high-index facets NPs. The development of concave structure depends on the tuning of reduction kinetics with a reduction process that has to be fast, combined with a high concentration of Pt precursor, that is of paramount importance for the suppression of Pt surface diffusion. For example, a high concentration of Na_2PtCl_6 and glucose in CTAB and OLAM resulted in the formation of concave Pt nanocubes enclosed in (720) facets after treatment at 160 °C for 3 hours.[275] In another example, Pt concave cubes were obtained by hydrothermal synthesis reducing H_2PtCl_6 with glycine in presence of PVP at 200 °C.[276] Both glycine and PVP served as reductants and capping agents favouring the formation of high-index facets on the concave nanostructures. Electrochemical protocols with the application of square-wave potentials were also used for the synthesis of concave tetrahexahedral Pt NPs in deep eutectic solvents (DES). The combination of electrochemical method and DES delivered uniform nanostructures covered in (910) facets (Figure 1.27A).[277] The

same approach was used also for the synthesis of triambic icosahedral Pt NPs enclosed in (771) facets and trapezohedral Pt NPs enclosed in (522) facets (Figure 1.27B, C).[278,279]

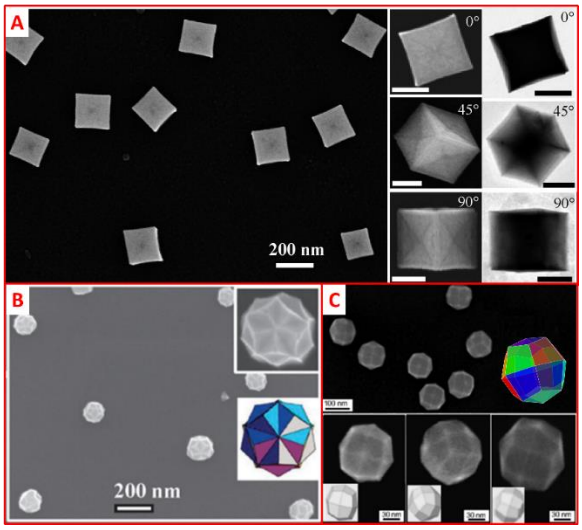

Figure 1.27. Microscopic characterization of high-index faceted Pt THH (A), triambic icosahedra (B) and TPH (C) NPs prepared by electrochemical square wave potential methods. Adapted with permission from ref. [277] (Copyright 2011 American Chemical Society), ref. [278] (Copyright 2013 Royal society of Chemistry) and ref. [279] (Copyright 2012 Royal Society of Chemistry).

Similarly, the first synthesis for the tetrahexahedral Pt NPs was performed by an electrochemical protocol using square-wave potentials to shape polycrystalline spherical NPs.[280] The high-index facets exposed on the nanocrystals were determined to be (730). Pt tetrahexahedra were also obtained by the same dealloying process used for Pd tetrahexahedra. The protocol was found to be suitable also for large scale production of Pt THH.[197] The great versatility of electrochemical methods for the preparation of shaped nanocrystals was confirmed also by the synthesis of hexoctahedral Pt NPs, which is a relatively rare structure reported in literature. Pt HOH NPs were electrodeposited to a glassy-carbon electrode by applying SWP to an acidic solution of H_2PtCl_6.[281] A shape evolution was observed when tuning the upper and lower potential that resulted in the formation of Pt THH and Pt TPH NPs as additional shapes. The HOH particles were confirmed to be bounded by (15 5 3) facets after careful HRTEM measurements. In accordance with the previously discussed shapes, multipods exposing high-index facets are extremely appealing for catalysis because of the high specific surface area and the low-coordination sites. These multipods are usually produced by wet-chemical approaches in presence of capping agents used for the stabilization of the highly energetic facets emerging from a fast reduction process. A solvothermal protocol for the synthesis of Pt multipods has been reported heating $Pt(acac)_2$ in 1-octyamine at 200 °C for 3 hours.[282] The amine served as solvent, reductant and capping agent stabilizing monoatomic step edges that resulted in the construction of (211) facets.

Gold

Compared to other metals, faceted Au nanocrystals are much easier to be obtained because of the lower surface energy of Au nanostructures. It follows that also Au NPs with high-index facets can be easily obtained applying milder reaction conditions with respect to the other metal NPs. For example, concave Au nanocubes have been reported under very common reaction conditions for the generation of other faceted metal NPs. In the protocol, spherical Au seeds were introduced in a growth aqueous solution composed of $HAuCl_4$, $AgNO_3$, ascorbic acid, HCl and CTAC and left react overnight without stirring.[283] The generation of (720) high-index facets in the concave Au cubes was attributed to a combination of Ag^+ and Cl^- ions. Another common Au structures decorated by high-index facets are TOH. Au TOH NPs can be produced by wet-chemical methods reducing a solution of $HAuCl_4$ with ascorbic acid in presence of CTAC as stabilizer (Figure 1.28).[284]

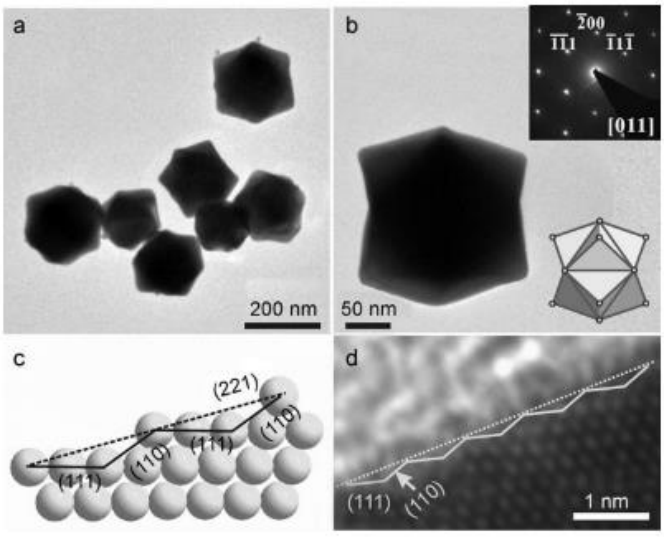

Figure 1.28. Low mag (a) and high mag (b) TEM images of Au TOH NPs obtained by the reduction of Au salt in presence of CTAC. Atomic model of the (221) surface seen as a combination of (111) terraces and (110) steps (c) and HR-TEM image highlighting (221) plane with (111) terraces and (110) steps. Reproduced with permission from ref. [284]. Copyright 2008 Wiley-VCH.

Despite the large size of the NPs obtained by this method (100-200 nm), regular (221) facets were observed on the surface. Recently, Au TOH were reported with smaller sizes (20-80 nm) by a slow reduction of Au(I)-EDTA complex (formed in situ) with ascorbic acid in presence of 10 nm Au seeds.[285] The as-prepared TOH NPs exposed a mixture of (11 11 7), (331), and (221) high-index facets on the surface. Au convex nanostructures like THH and TPH can be prepared with wet-chemical seed-mediated protocols as well. In one report, Au THH NPs exposing (730) facets were delivered by a seed-mediated growth of Au nanospheres in an aqueous solution of Au precursor, ascorbic acid, $AgNO_3$ and CTAB.[286] Importantly, keeping the pH value of the growth solution below 2 was necessary to ensure the successful production of Au THH. A seed-mediated approach

was also used to synthesise Au TPH NPs, with regular (311) facets, starting from cubic or octahedral seeds. The seeds solution was rapidly added to a pre-heated DMSO solution containing PVP, formic acid and $HAuCl_4$ and left reacting for 20 min at 120 °C.[287] With the same procedure, Au bipyramids enclosed in (311) facets were obtained by switching to nanorod seeds. Another seed-mediated procedure, employing icosahedral Au seeds, was used for the production of high-index faceted nanostars.[288] In this study, two DMF solutions of Au seeds and $HAuCl_4$ were subsequently added to a third DMF solution made of PVP, dimethylamine and HCl and stirred at 80 °C for 4 hours delivering highly symmetrical nanostars enclosed in (321) facets (Figure 1.29). Dimethylamine was suggested to be crucial in stabilizing these facets in concomitance with the appropriate choice of solution pH and temperature.

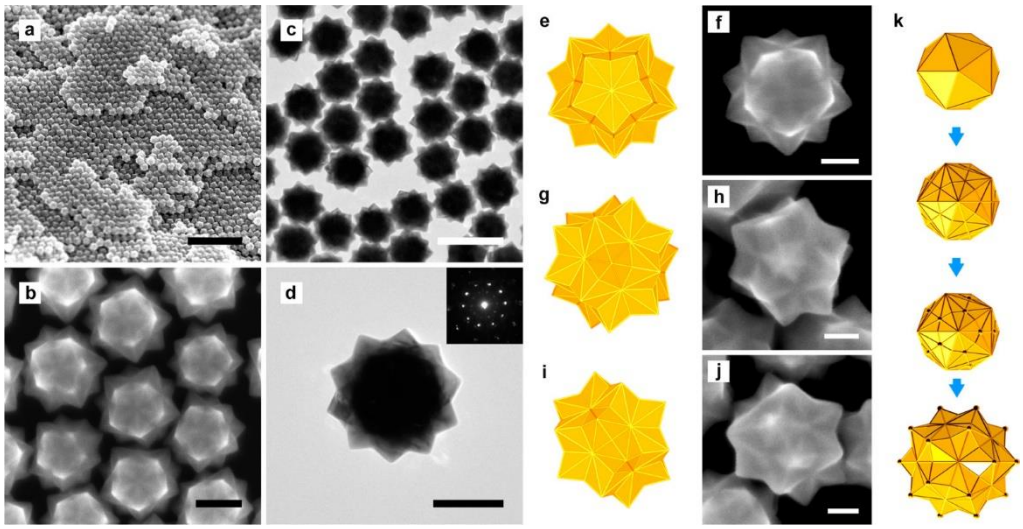

Figure 1.29. SEM and TEM micrographs of Au nanostars enclosed in (321) facets (a-c). High magnification TEM image of a single particle and SAED (d). SEM images and corresponding 3D models of the Au nanostars viewed from different zone axes (e-j). Growth evolution scheme showing the shape transition from icosahedron to nanostar. Scale bars: 1 μm (a), 200 nm (c), 100 nm (b, d), 50 nm (f, h, j). Reproduced with permission from ref. [288]. Copyright 2015 American Chemical Society.

1.2.1.4. (Meso)Porous/dendritic metal NPs

Nowadays, defined porous architectures have captured the attention because of the substantial adsorptive capacity due to their high specific surface area. Unfortunately, many of the porous nanomaterials have a restricted array of applications because their pore size, which is below 2 nm, falls in the microporous range. During the ’90, the discovery of mesoporous silica,[289] set a breakthrough for other mesoporous materials incrementing the interest toward these nanostructures with high surface area and tunable pore size. Mesopores have a diameter ranging from 2 to 50 nm and are relevant in processes requiring the transportation of guest species and increased availability of reaction sites. Materials of various nature and composition can be obtained with a porous texture

such as metal oxides, metals, hybrid organic-inorganic materials, carbonaceous materials and so on. Still, some aspects such as the pore tendency to collapse during crystallization hinder the successful obtainment of a good porosity grade. Porous metals have attracted enormous interests owing to their physicochemical properties that makes them eligible for many applications such as catalysis, energy storage, biosensors, SERS, SPR etc. Porous and dendritic metal nanostructures with specific properties can be produced by shape and morphology engineering adopting different approaches. In particular, two strategies have risen among the others: hard- and soft-templating methods and wet chemical methods.

The hard-templating method consists in depositing a metal on the surface of a porous template such as silica, carbon or other materials than can be easily decomposed or removed to expose the metal structure. The approach involves several steps including the template preparation, deposition of the metal/metal precursor (usually followed by a reduction step) and removal of the templating agent. The final porous metal structure is the upturned reproduction of the template. Ryoo and co-workers were the first to successfully report this method for the production of porous Pt nanostructures (Figure 1.30). The synthesis was performed by impregnating $Pt(NH_3)_4(NO_3)_2$ into MCM-48 silica that was then subjected to hydrogen flow at 300 °C and lastly the silica template was removed by acidic treatment with HF 10%.[290] Another interesting example of hard-templating synthesis was reported by Lu and co-workers who obtained nanostructured porous Pd films by electrochemical reduction/deposition of $PdCl_2$ into mesoporous silica which was removed by acidic washing steps.[291] Different types of mesostructured silica have been exploited as hard templates for the construction of porous metals such as MCM-41, MCM-48, SBA-15 and KIT-6.[292–295]

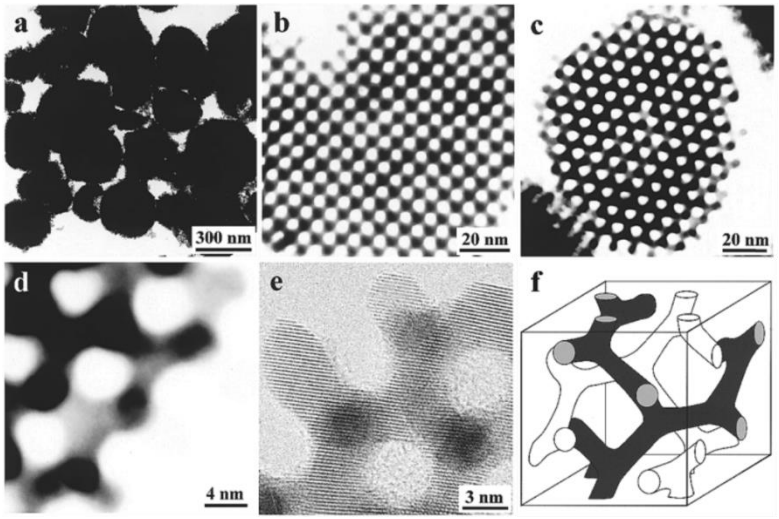

Figure 1.30. TEM micrographs of the mesoporous Pt nanostructures obtained by hard-templating protocol using MCM-48 as template (a-e). Schematic model showing the interconnected Pt structure (f). Adapted with permission from ref. [290]. Copyright 2001 American Chemical Society.

A common drawback in the hard-templating approach is the control of the deposition process that if not properly accomplished can drive to the growth of irregular metal structures. An improvement in this direction was firstly made by employing ascorbic acid as mild reducing agent in order to unsure a slow reduction rate required to give enough time to the metal precursor for a uniform diffusion in the template. Applying this strategy, uniform and monodispersed porous Pt NPs have been prepared with a high reproducibility.[296]

Soft-templating methods, on the contrary, are based on templating agents composed by organic molecules that, depending on the concentration in water or organic solvents, self-assemble in ordered and highly interconnected networks. Common soft-templates such as lyotropic liquid crystals (LLCs), block copolymers and micelles, have been exploited to achieve various nanoarchitectures including like nanowires, nanotubes, films and of course porous structures.[297,298] LLCs are formed when two incompatible component are phase segregated on the nanoscale generating long-range ordered structures. Typically, a highly concentrated micellar or polymeric aqueous solution can form a LLC phase and be employed as template for the synthesis of porous metals. The first reported use of LLCs for the synthesis of mesoporous metal structures was applied for the production of Pt films.[299] Since then, various soft-templating systems have been prepared and used in mesoporous materials synthesis. For example, Bartlett *et al.* reported the electrochemical deposition of mesoporous Pd films in LLCs composed of octaethyleneglycol monohexadecyl ether ($C_{16}E_8$) and decaethylene glycol hexadecyl ether (Brij 56).[300] The resulting Pd films contained regular hexagonal arrays of cylindrical pores and had a remarkable surface area of 91 $m^2\ g^{-1}$. Other studies employing LLCs as templating agents have been reported for the synthesis of mesostructured metals such as Cu, Ag, Cd, Ni and Sn.[301,302] Micellar confinement is another strategy reported for the synthesis of porous structures using ionic surfactants or polymers for the construction of nanoreactors in water at determined concentrations. In contrast with LLC, the micelle-assembly approach does not need high concentrations of surfactants since micelles can be formed already at low surfactant concentrations. One of the first reports using surfactants as stabilizers for porous NPs was described by Ullah *et al.* They reported the synthesis of porous Pt NPs in an acidic aqueous solution of CTAB and K_2PtCl_6 reduced by $NaBH_4$.[303] Yamauchi and co-workers have extended the protocols for porous metal NPs produced in micelles made of different surfactants[304–306] and polymers.[307,308] Other porous and branched NPs have been produced in solution phase with both surfactants and organic ligands for the stabilization of the porous/dendritic structure for metals like Pt, Pd, Au, Ag and Rh.[309]

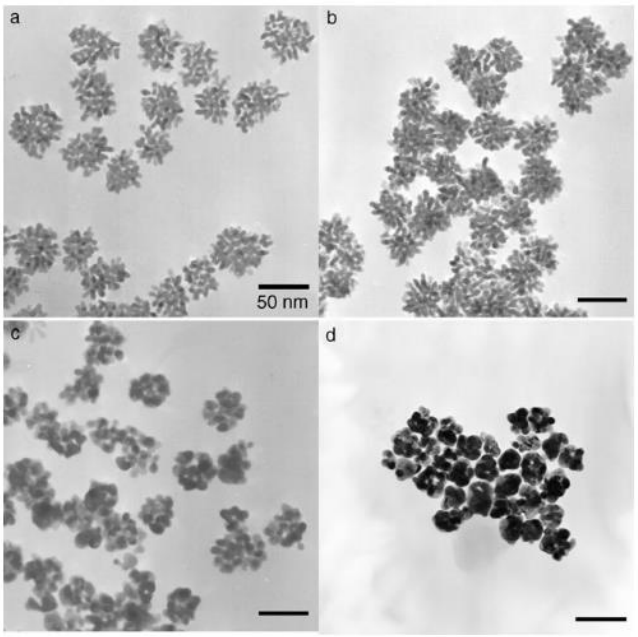

Figure 1.31. TEM images of porous Pt NPs recovered at 2 min (a), 3 min (b), 5 min (c), 20 min (d) and prepared in liquid phase employing 1-adamantanecarboxylic acid, 1,2-hexadecanediol and hexadecylamine in diphenyl ether. Reproduced with permission from ref. [310]. Copyright 2006 Wiley-VCH.

One interesting example is the concomitant use of 1-adamantanecarboxylic acid, 1,2-hexadecanediol and hexadecylamine for the synthesis of porous Pt NPs (Figure 1.31).[310] A fast autocatalytic process was speculated as the driving force for the formation of the porous structure. In general, the synthesis of porous metal colloids in solution phase is very challenging considering the number of variables that can influence the outcome of the reaction. Nevertheless, various methodologies based on different approaches such as controlled overgrowth, aggregation-based growth, selective oxidative etching and templated methods have been developed for metal colloids exhibiting porous structure or dendritic features.[311] A last strategy for the synthesis of porous particles and especially films, is the dealloying technique in which a bimetallic nanostructure is selectively depleted of one metal (the most electrochemically active) by a corrosion process. The first example of dealloying process for the formation of porous nanostructures was reported in the early 2000 when Erlebacher and co-workers reported Au nanosponges with an interconnected porous structure by electrochemical corrosion.[312] Since then various porous metal architectures have been produced with this technique.[313]

Overall, porous metal nanostructures can be provided in great variety by the use of different approaches increasing the availability of such singular NPs. The high surface area rich in pores and active sites make this NPs ideal candidates for many applications especially in the catalysis field in which their great potential can be exploited.

1.2.2. **Transition metal NCs**

In pursuing size control and monodispersity, chemist have applied different strategies to target uniform metal NPs resulting, in some cases, to the perfect monodispersity of molecular species with well-defined stoichiometry. Metal nanoclusters (NCs) can be considered as small NPs with dimensions that range between the sub-nanometer and 2.2 nm (Figure 1.32), composed by a strictly defined number of atoms (from 2 to 300 atoms) and with the peculiarity of having non-metallic properties; very often these compounds are referred to as atomically precise clusters. Two main approaches are used to obtain atomically precise metal nanoclusters: the first is based on the self-assembly process of ligands and metal atoms to form nanoclusters, while the second one is based on the metallorganic/coordination chemistry. The first one is similar to the self-assembling process in the synthesis of metal NPs, protected by organic ligands. Indeed, very often the synthesis of monolayer protected nanoparticles is accompanied by the formation of metal NCs of well-defined stoichiometry comprising a core, in which the metal is in the zero oxidation state, and an organic shell. On the other hand, the second strategy is based on transition metal complexes chemistry in which the clusters are real complexes without a defined core and shell but with an oligomeric structure in which the metal is in a higher oxidation state.

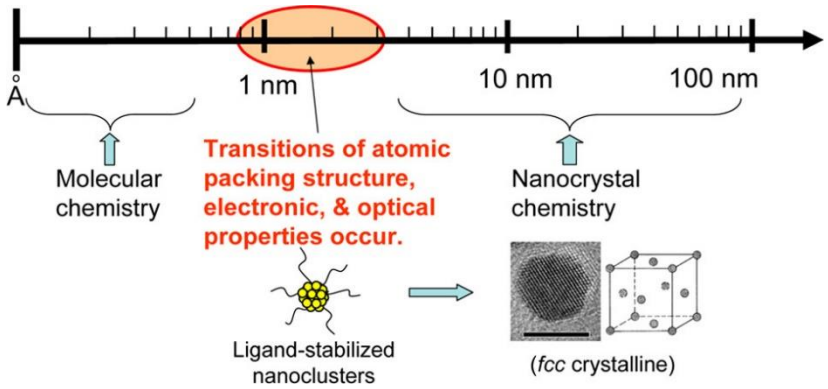

Figure 1.32. Metal clusters placed in a dimensional scale between NPs and molecules. Reproduced with permission from ref. 8. Copyright 2009 Royal Society of Chemistry.

Although cluster complexes have been known since the ’60 in the metallorganic community, their study has remained mainly focused on the synthesis and characterization without any particular mention on properties or applications, leaving this class of clusters in the shadow until modern days. In general, transition metal NCs have started to gain a lot of attention during the ’90 when the nanotechnologies were blooming and new opportunities were seen in the study of small nanoparticles with precise characteristics and properties. The study of metal clusters was also prompted by the isolation and characterization of small NCs in NPs matrixes, opening to the possibility of directly producing such small metal entities. Lately, metal NCs have become of great

interest to the scientific community because of their unusual properties. Indeed, NCs are considered to be the missing piece that bridge NPs to molecules because they express both nanoscale and molecular behaviour. In this chapter, examples of transition metal NCs will be provided for both zero oxidation state cluster and higher oxidation state clusters with a particular focus on the noble metal clusters.

1.2.2.1. Zerovalent Monolayer-protected NCs

As anticipated above, these clusters are characterized by a core where all the metal atoms are positioned, exception made for metal atoms directly involved in the construction of protecting shell of ligands. Various ligands such as thiols, alkynes, phosphines, organosilanes, NHCs and nitrogen containing molecules have been successfully used for the synthesis of metal NCs. The synthesis of these metal NCs rely on three methodologies: the widely used Brust-Schiffrin method developed for Au NPs,[314] the size-focusing[315] and the ligand exchange-induced size transformation (LEIST)[316] methods, these last two have been both mainly developed by Jin and co-workers. In this section, four monometallic monolayer protected NCs will be discussed, although other metal NCs have been described in literature.[317–320]

Gold

Au NCs have been widely studied and constantly reported along the years because of the robust protocols developed for their synthesis and to their high stability.[321] Au was the first to be reported in form of monolayer protected clusters and a large variety of Au NCs have been prepared displaying peculiar properties and interesting applications.[318–320] As mentioned above, the formation of well-defined NCs often accompanies the preparation of polydispersed monolayer protected nanoparticles. After the ground-breaking work of Brust and Schiffrin,[314] Murray and co-workers reported the first in depth characterization study of thiolate protected Au NPs[322] while Whetten and co-workers pinpointed the presence of nanoparticles with preferred “magic” composition in the crude NPs preparations.[323] Murray and co-workers reported in 2004 the isolation of a molecular cluster that was erroneously believed to be $Au_{38}(PET)_{24}$ (PET: $PhCH_2CH_2S$ residue)[324] while the correct structure was later established as $Au_{25}(PET)_{18}$ by high resolution mass analyses.[325,326] Another breakthrough was made in 2005 when through the determination of the precise masses by ESI-MS of $Au_n(SG)_m$, distinct NCs were unambiguously identified[327] and again allowed the correction of some previous wrongly assigned structures. In 2007 the first crystal structure of an Au

NC, namely Au_{102}(*p*-MBA)$_{44}$ (p-MBA: *p*-mercaptobenzoic acid) was reported by Kornberg and co-workers,[328] followed by the crystal structure of $Au_{25}(PET)_{18}$ reported independently by the groups of Murray and Jin.[329,330] These studies unveiled the structure of the gold core-ligand shell interface of these compounds highlighting how certain gold atoms belong to the ligand shell bridging different thiolate ligands in the so called staple motifs.

The early work on the synthesis of Au NCs mostly produced polydispersed clusters mixed with NPs that needed long purification steps like gel electrophoresis or HPLC[324,327] after which clusters were isolated in low yields. Things started to change with the development of the size focusing and LEIST methodologies.

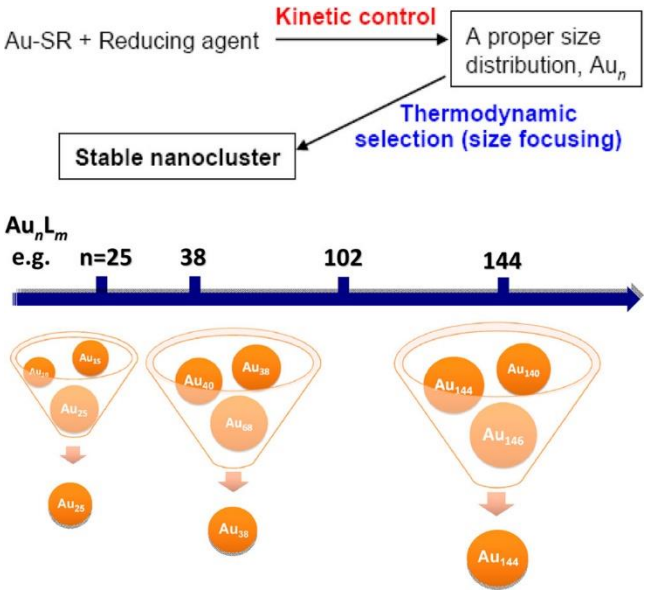

Figure 1.33. Schematic illustration of the size-focusing protocol applied to Au NCs. Reproduces with permission from ref. [315]. Copyright 2010 American Chemical Society.

Size focusing protocol is accompanied by fine tuning of the reaction conditions in order to increase the yield of atomically precise clusters (Figure 1.33). One of the first syntheses of this kind was reported in 2008 by Jin and co-workers for the assembly of $Au_{25}(PET)_{18}$ NCs in two phase solvent (water/toluene) or in THF only using TOAB as phase transfer and PET as ligand (Figure 1.34A).[331,332] The protocol demonstrated to be very productive in Au clusters (up to 50% yield, gold atom basis) and with a powerful size focusing ability since the distinct absorption bands (Figure 1.34B) of $Au_{25}(PET)_{18}$ at 670, 450 and 400 nm were visualized already in the crude product prior to any purification steps. The authors suggested the formation of Au(I)-SR polymeric complexes as the key factor for the high yield of the reaction, thus maximising the formation of these complexes the yield of Au_{25} NCs will dramatically increase. The size focusing protocol was extended to other thiolated Au clusters such as Au_{38} and Au_{144}. These two clusters, protected by dodecanethiolate, were reported in 2008 by Chaki *et al.* by the use of the Brust method, but in poor yields only.[333]

One year later Qian *et al.* improved the yield of the two clusters by using the size focusing method through aging of a narrowed mixture of Au NCs. $Au_{38}(SR)_{24}$ was prepared in high yield by first synthesising a mixture of $Au_n(SG)_m$ clusters that were subjected to size focusing in a mixture of water/toluene in which a new thiol (docecanethiol or phenylethanethiol) was dissolved.[334,335]

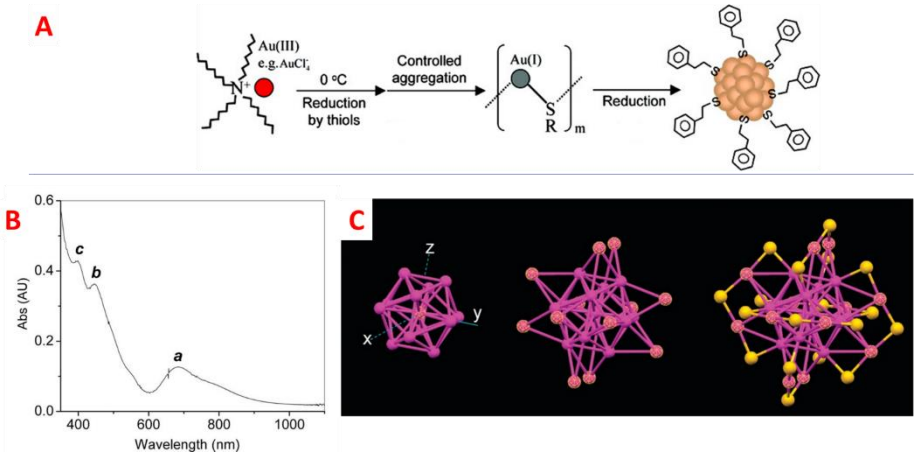

Figure 1.34. Synthetic scheme for the preparation of Au_{25} NCs (A), absorption spectrum of the isolated cluster with the main absorption bands indexed as a, b and c (B). Crystal structure of the $Au_{25}(PET)_{18}$ cluster with the Au_{13} core (left), core and exterior Au atoms (middle) and the complete structure with the sulfur atoms in yellow (right) (C). Adapted with permission from ref. [329] (Copyright 2008 American Chemical Society) and ref. [330] (Copyright 2008 American Chemical Society).

The mixture was heated in presence of oxygen favouring the gold core etching and transforming the $Au_n(SG)_m$ mixture in atomically precise $Au_{38}(SR)_{24}$ clusters. Relying on the same strategy, the authors were able to improve the synthesis of $Au_{144}(SR)_{60}$.[336] Also in this case, a two-step synthesis was adopted with some changes with respect to Au_{38} preparation. In the first step, instead of using SGH ligand, PET was selected to achieve a better control on the size distribution of the clusters. Subsequently, the size-narrowed clusters were heated at 80 °C in toluene for the size-focusing to Au_{144}. The size-focusing process was confirmed by UV-VIS monitoring of the reaction mixture in which the polydispersed clusters spectrum (without special features) evolved displaying prominent bands at 700 and 510 nm. Beside the control of the size range in the clusters prepared in the first step of the size-focusing method (which is pivotal in providing only one final product), other kinetic factors have to be considered for a good outcome. Temperature, solvent, reducing agents and reactant ratio (metal to ligand, in particular) are the factors to control in the first step of size-focusing method. The thiol etching, involved in the second step, in controlled by thermodynamics and here it was found that oxygen or a radical initiator is fundamental for the process.[337] Size-focusing was extended to the preparation of other Au clusters like $Au_{64}(SR)_{32}$, $Au_{99}(SR)_{42}$ and the nanoparticle $Au_{333}(SR)_{79}$[338–341] and it was also employed for aqueous synthesis with water soluble ligands.[342,343] Another peculiar example was reported by Chen *et al.* in which the authors were able

to control the atomicity of Au clusters by using the three isomers of methylbenzenethiol (MBT) in a size-focusing protocol at 80-90 °C (Figure 1.35).[344] They observed that the less sterically hindered *p*-MBT delivered the larger cluster Au_{130}(*p*-MBT)$_{50}$ while *m*-MBT and *o*-MBT produced Au_{104}(*m*-MBT)$_{41}$ and Au_{40}(*o*-MBT)$_{24}$, respectively, following the trend of size decrease with increased steric hindrance of the methyl position respect to the Au-S bond.

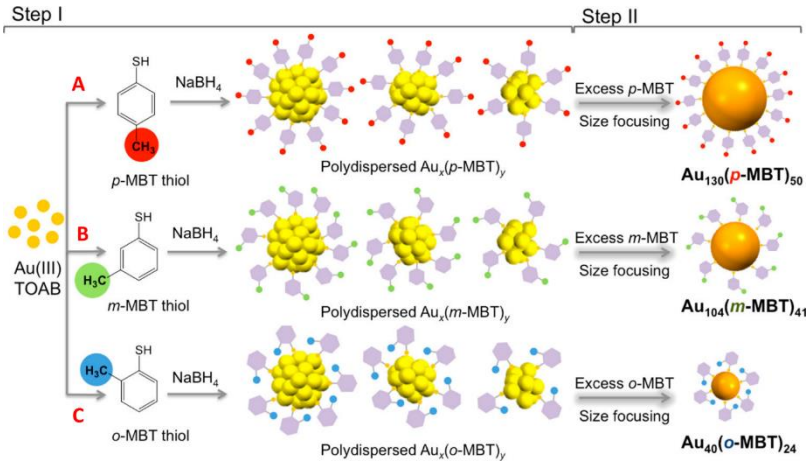

Figure 1.35. Schematic representation of the synthetic protocol for the synthesis of Au_{130}(*p*-MBT)$_{50}$ (A), Au_{104}(*m*-MBT)$_{41}$ (B) and Au_{40}(*o*-MBT)$_{24}$ (C) using *p*-MBT, *m*-MBT and *o*-MBT, respectively. The syntheses are divided in two steps consisting in the generation of polydispersed Au NCs (Step I), followed by the size-focusing protocol in excess thiol (Step II). Adapted with permission from ref. [344]. Copyright 2015 American Chemical Society.

Overall, the size-focusing methodology represents a starting point of expansion in the rational design of atomically precise metal NCs based on the selection of the most robust cluster. Nevertheless, the stability of one particular cluster with respect to the others is influenced by different aspects that are still a matter of study. However, some insight has been already given proposing a strong ligand impact on the selection of the number of metal atoms to be incorporated in the cluster.[344,345] The ligand influence is highlighted in the third approach that is based on ligand exchange that triggers the atomic redistribution to minimize the total surface free energy of the cluster.

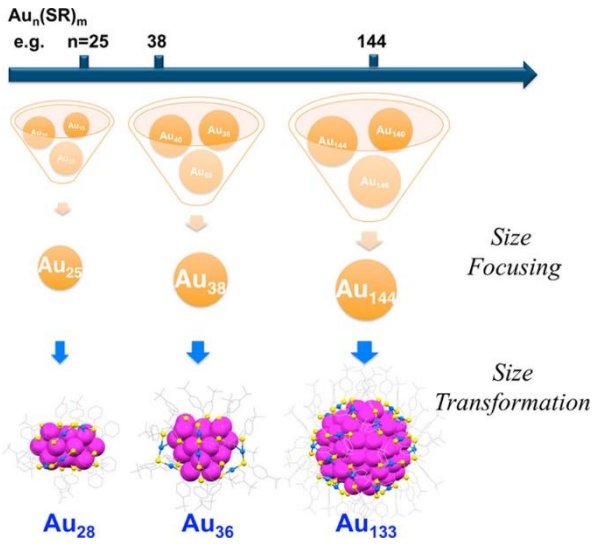

Figure 1.36. Schematic illustration depicting the preparation of three Au NCs by the LEIST protocol. Reproduced with permission from ref. [346]. Copyright 2015 American Chemical Society.

The ligand-exchange induced size/structure transformation (LEIST) is usually applied to clusters prepared by the size-focusing method for the generation of new magic sized NCs (Figure 1.36).[346] Compared to the common ligand exchange that affects the monolayer composition without altering the cluster core and atomicity, LEIST is a chemical transformation leading to cluster species with different atomicity and core structure. While in ligand exchange low temperatures and low ratios of new/exchanged ligand are used, in the LEIST process a large excess of new ligand is necessary and energy (heat) is often required since the transformation involves Au atoms loss or gain and not only a ligand displacement. Various thiolated Au NCs were obtained with this protocol like $Au_{28}(SR)_{20}$, $Au_{36}(SR)_{24}$ and $Au_{133}(SR)_{52}$. For instance, $Au_{28}(TBBT)_{20}$ was prepared starting from $Au_{25}(PET)_{18}$ by treating the latter at 80 °C with excess 4-*tert*-butylbenzenethiol (TBBT) obtaining the chiral cluster $Au_{28}(TBBT)_{20}$ in high yield (Figure 1.37A).[347] Interestingly, another chiral NCs was assembled by performing the LEIST on Au_{25} with TBBT at 40 °C, instead of 80 °C, producing $Au_{20}(TBBT)_{16}$ (Figure 1.37B).[348] The LEIST protocol was also applied to Au_{38} clusters to produce Au_{36} employing again TBBT (Figure 1.37C).[349] $Au_{36}(TBBT)_{24}$ NCs were produced by reacting $Au_{38}(PET)_{24}$ with TBBT at 80 °C for 12 hours favouring ligand exchange and Au atoms rearrangement. Again, TBBT resulted suitable in converting $Au_{144}(PET)_{60}$ in $Au_{133}(TBBT)_{52}$ by ligand exchange (Figure 1.37D).[350] The approach used here is the same for the Au_{36} and Au_{28} clusters, with the exception of applying a large excess of TBBT with respect to PET (370:1) and the ligand exchange was carried out in 4 days at 80 °C.

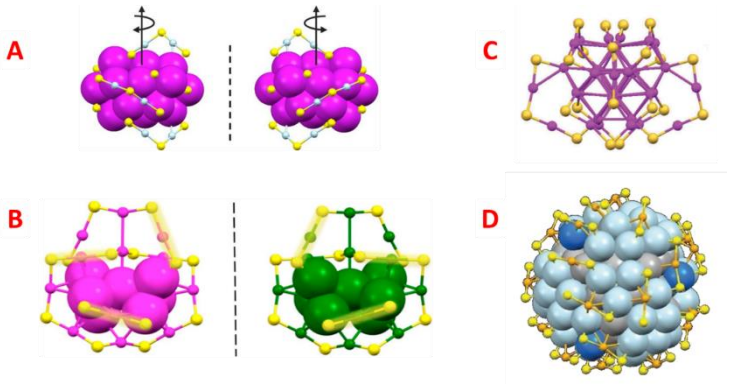

Figure 1.37. X-ray structures of the two chiral $Au_{28}(TBBT)_{20}$ (A) and $Au_{20}(TBBT)_{16}$ (B), $Au_{36}(TBBT)_{24}$ (C) and $Au_{133}(TBBT)_{52}$ (D) synthetised by LEIST procedure. Carbon atoms are omitted for visual clarity and sulfur atoms are depicted in yellow. Adapted with permission from ref. [347] (Copyright 2013 America Chemical Society), ref. [348] (Copyright 2014 American Chemical Society), ref. [349] (Copyright 2012 Wiley-VCH) and ref. [350] (Copyright 2015).

Beside the fact that thiolate protected Au clusters are the most known and studied, other ligands have been exploited in the construction of atomically precise NCs. For example, phosphines have been employed long before thiols as ligands for Au NCs. In the late '60 Malatesta and co-workers reported the synthesis and structural characterization of $Au_{11}(PPh_3)_7(SCN)_3$[351] while Mingos *et al.* reported the synthesis and X-ray structure of $Au_{13}(PMe_2Ph)_{10}Cl_2(PF_6)_3$ in the early '80.[352] Commonly, the synthesis of phosphine protected NCs is performed at room temperature and involves a reduction step, usually performed with $NaBH_4$. Great contribution to the phosphine protected Au NCs has also been brought by Konishi and Hutchinson groups. In particular, Konishi and co-workers reported the first diphosphine protected Au_{13}, Au_8 and Au_7 clusters employing a size focusing protocol for $[Au_{13}(dppe)_5Cl_2]Cl_3$ and a LEIST protocol for $[Au_8(dppp)_4Cl_2]^{2+}$ and $Au_7(dppp)_4(BF_4)_3$. [353–355] The group has also studied clusters composed by fused core subunits.[356,357] Hutchinson, on the other hand has focused more on the ligand exchange of phosphine Au NCs with thiols, particularly on Au_{11} clusters.[358–360] Also, in the same period larger diphosphine protected Au NCs such as $Au_{20}(PP_3)_4Cl_4$ (PP_3 = tris(2-(diphenylphosphino)ethyl)phosphine) bearing a tetradentate phosphine,[361,362] and $Au_{22}(dppo)_6$ (dppo: diphenylphosphinooctane) composed of two Au_{11} units were reported by other groups.[363]

Alkynyl protected Au NCs have also been studied along the years. These clusters have been reported both as mixed ligands (phosphines and alkynes) and alkynyl protected only. The first study in this topic described the synthesis of Au clusters protected by phenylacetylene by a ligand exchange starting from PVP protected small Au NPs.[364] The study reported $Au_n(C_2Ph)_m$ clusters with atomicity from 43 to 110 that were not isolated but characterized by MALDI-TOF spectrometry. One year later $Au_{54}(C_2Ph)_{26}$ was selectively prepared employing the same method for polydispersed clusters.[365] In this study, PVP-capped Au polydispersed clusters (d = 1.2 nm ± 0.2)

were treated with phenylacetylene in large excess in chloroform to obtain the desired Au cluster. Recently, Wang and co-workers reported the synthesis of a class of mixed phosphine and alkynyl protected Au clusters. Three atomically precise Au NCs were produced by the group, namely $Au_{19}(C_2Ph)_9(Hdppa)_3(SbF_6)_2$, $Au_{23}(C_2Ph)_9(Ph_3P)_6(SbF_6)_2$ and $Au_{24}(C_2Ph)_{14}(PPh_3)_4(SbF_6)_2$.[366–368] All the three clusters were synthetized by a similar procedure consisting in a first exchange of counterion in the gold complex (Cl^- with SbF_6^-), followed by a reduction step with $NaBH_4$.

Silver

Parallel to the development of Au NCs, silver clusters (Ag NCs) also emerged, and nowadays the studies on this topic lead to the development of a small library of atomically precise Ag NCs for which well-defined synthetic procedures and reliable characterisation data are available.[319] The first reports of Ag NCs appeared in 2009 and 2010 where various Ag NCs were prepared and detected by mass spectroscopies but not isolated.[369–371] Later, Stellacci and co-workers reported the preparation and characterization of $Ag_{44}(SR)_{30}^{4-}$ using 4-fluorothiophenol and 2-thionaphtalene (Figure1.38).[372,373] The synthesis was performed in liquid phase, similarly to the Au NCs preparation, by reducing a DMF solution of Ag salt in presence of thiols with $NaBH_4$ and leaving the crude product to age at -4 °C for one week. In the same period $Ag_7(MSA)_7$, $Ag_8(MSA)_8$ and $Ag_9(MSA)_7$ (MSA: mercaptosuccinic acid) were prepared through the reduction of $AgNO_3$ in methanol, in presence of the thiol ligand, and isolated by gel electrophoresis.[374,375]

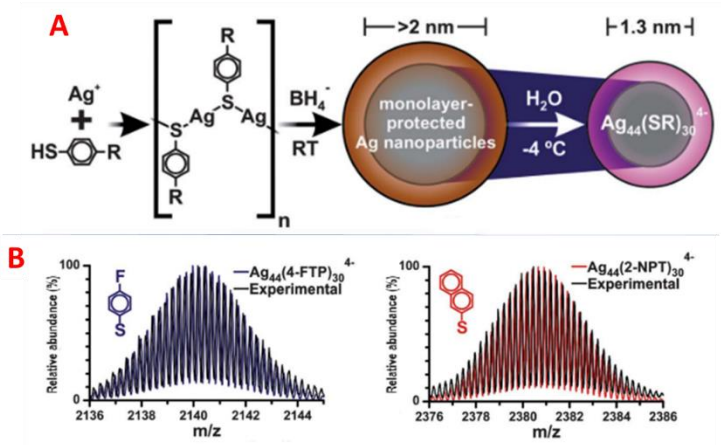

Figure 1.38. Synthetic scheme for the preparation of $Ag_{44}(SR)_{30}^{4-}$ NCs (A) and corresponding mass spectra for clusters protected by 4-fluorothiophenol and 2-thionaphtalene obtained by ESI-MS (B). Adapted with permission from ref. [372]. Copyright 2012 Royal Society of Chemistry.

Interestingly, the LEIST process was employed for the synthesis of $Ag_{44}(4\text{-FTP})_{30}$ (4-FTP: 4-fluorothiophenol) starting from $Ag_{35}(SG)_{18}$.[376] In recent years, new Ag NCs have been identified and isolated with various ligands. For example, $Ag_{19}(dppm)_3(C_2Ph)_{14}(SbF_6)_3$ (dppm: diphenylphosphinomethane) and $Ag_{25}(dpppe)_3(C_2PhOMe)_{20}(SbF_6)_3$ (dpppe: diphenylphosphinopentane) were prepared by a slow addition of $NaBH_4$ at room temperature and aging in absence of light and crystallized for structural characterization that revealed an Ag_{13} kernel with a particular anti-cuboctahedral symmetry.[377] Bigger Ag NCs like $Ag_{74}(C_2Ph)_{44}$ and $Ag_{78}(dppp)_6(SPhCF_3)_{42}$ (dppp: diphenylphosphinopropane) were also synthetised with bidentate phosphines or alkynes as ligands.[378,379] Of note, the $Ag_{74}(C_2Ph)_{44}$ cluster was prepared employing bidentate phosphines to firstly generate a silver-phosphine that delivers Ag(0) atoms finally protected by phenylacetylene. Ag_{14},[380] Ag_{15},[381] Ag_{23}[382] and Ag_{50}[383] have been also prepared, isolated and characterized by mass spectrometry techniques. Overall, the preparation and identification/characterization of atomically precise Ag NCs does not come without effort as these NCs lack in stability. Still, there is room for the introduction of new Ag NCs and the development of tailored protocols for the stabilisation of such nanomaterials.

Platinum

Compared to gold and silver NCs, platinum and palladium NCs are less reported because of their lower stability. Few studies can be found for Pt and Pd monolayer-protected clusters with the metals in the zero oxidation state mostly because the difficulties faced in the synthesis and characterization. The first reported synthesis of Pt NCs protected by thiolates was described by Chen *et al.* in a solution phase by reduction of H_2PtCl_6 in presence of mercaptosuccinic acid with $NaBH_4$.[384] The Pt NCs were obtained in a polydispersed range of atom number with a mean diameter of 2.5 nm. However, this first study set the ground for the future reports of atomically precise Pt NCs. Years later, very small Pt clusters were reported by Kawasaki *et al.* as a mixture of Pt_4, Pt_5 and Pt_6 in DMF.[385] The peculiarity of this work is the straightforward synthesis performed in DMF at 140 °C without ligands, thus making the solvent the stabilizing agent for the clusters. The NCs were identified in form of $Pt_4(MBT)_7$, $Pt_5(MBT)_7$ and $Pt_6(MBT)_7$ by MALDI-MS. In this study, 2-mercaptobenzothiazole (MBT) was used as the matrix for the mass analysis, but also provided the capping molecules stabilising the clusters and allowing their desorption from the specimen under analysis; here MBT displaced the weakly bound DMF molecules that originally protected the clusters. Another study by Schneider and co-workers reported Pt NCs protected by GSH with dimensions below 2 nm.[386] The NCs were produced following the LEIST process by

firstly preparing a colloidal solution of Pt NCs protected by mercaptosuccinic acid (MSA) that was subjected to etching by GSH at 65 °C for 6 days. Unfortunately, the authors were not able to identify the exact composition of the clusters due to ionisation issues of the Pt NCs with MALDI-TOF. $Pt_5(SCO_2Me)_7$ NCs have also been reported and isolated by HPLC from a mixture of clusters and NPs prepared by reduction of H_2PtCl_6 in presence of PAMAM (polyamidoamine) dendrimers.[387] Interestingly, atomically precise Pt_{11} NCs were reported by a solid state dry synthesis performed by milling platinum salt, 4-(*tert*-butyl)benzyl mercaptan (BBSH) and $NaBH_4$ in a mortar to yield crude $Pt_{11}(BBS)_8$ that was purified by HPLC and characterized by MALDI-MS.[388] Another peculiar strategy to achieve Pt NCs with precise atomicity was developed by Yamamoto and co-workers.[389] These authors exploited the complexation ability of phenylazomethine dendrimers to capture Pt ions at a maximum of 12 ions per dendrimer of assembled phenylazomethine units. The complexed ions were then reduced to Pt(0) that aggregated in NCs with precise atomicity (Figure 1.39A). The as-obtained NCs cannot be described as monolayer-protected because no ligand is bound to the metal surface, in fact the dendrimer has only the function of stabilization and preventing aggregation of the clusters. Using the same approach, the same group achieved the synthesis of a range of Pt NCs between 12 and 20 atoms by simply tuning the equivalents of platinum precursor (Figure 1.39B).[390] Recently, Zhuang *et al.* successfully produced $Pt_{21}(MSA)_{21}$ NCs by treating an aqueous solution of K_2PtCl_4 with mercaptosuccinic acid (MSA) at room temperature and isolated the NCs by dialysis.[391] Smaller Pt clusters capped with phosphine ligands such as $Pt_6(PPh_3)_4Cl_5$ have been reported by a mild reduction of H_2PtCl_6 with borane tert-butylamine complex.[392] Other Pt NCs have been reported although without strict control on the atomicity.[393–397]

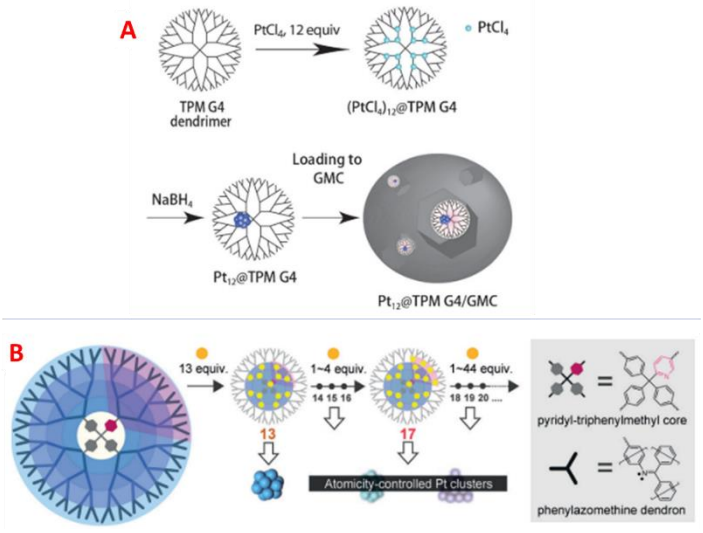

Figure 1.39. Schematic illustration of two protocols employing phenylazomethine dendrimers to control the atomicity of Pt NCs. Synthesis of Pt_{12} NCs (A) and synthesis of Pt_n (n: 12-20) NCs (B). Adapted with permission from ref. [389] (Copyright 2013 Wiley-VCH) and ref. [390] (Copyright 2015 Wiley-VCH).

Palladium

Similar to the case of platinum, also zerovalent monolayer-protected palladium NCs are mostly stabilized by thiolates, owing to the stability of M-S bond. In the early reports mostly polydispersed clusters, often contaminated by bigger NPs were described. Only in the last decade the synthetic protocols were refined to the point of obtaining atomically precise Pd NCs. The first study on Pd NCs was reported in early 2000 by Zamborini *et al.* in which the Brust-Schiffrin protocol was adopted to produce hexanethiol protected NCs.[398] In the same period, Negishi and co-workers prepared and characterized Pd NCs protected with octadecanethiol. From the mixture of clusters two major products were detected by MALDI-MS, namely $Pd_5(SC_{18}H_{37})_{10}$ and $Pd_{10}(SC_{18}H_{37})_{12}$.[399] More recently various atomically precise Pd NCs have been reported. For example, Jin and co-workers reported the one-pot synthesis of $Pd_{13–17}(SR)_{18–22}$ clusters by reduction of $Pd(OAc)_2$ in THF and TOAB employing various thiolated ligands such 4-*tert*-butylbenzenethiol, 1-adamantanethiol, 1-naphthalenethiol, and 2-naphthalenethiol.[400] Similarly, various Pd clusters protected with *N*-acetyl-L-cysteine were synthetised and isolated from the mixture by HPLC in the composition range between Pd_{10} and Pd_{20}.[401] With an optimized Brust-Schiffrin protocol, Dass and co-workers were able to isolate $Pd_{21}(PET)_{18}$ in high yield.[402] The synthesis was performed in two steps consisting in the preparation of a crude mixture of clusters enriched in Pd_{21} that were additionally size-focused by a thermal treatment in toluene and excess PET. In pursuing the synthesis of small atomically precise clusters, Chen and co-workers relied on a modified procedure for the synthesis of metal NPs to deliver $Pd_6(SC_{12}H_{25})_{11}$ NCs.[403] The procedure consisted in the reduction, under mild conditions, of $Pd(acac)_2$ in OLAM and excess 1-dodecanethiol at room temperature for 4 hours. Worth to be mentioned, the work of Dahl and Mednikov, which have extensively studied zerovalent Pd clusters coordinated to carbonyl ligands and phosphines.[404–407] Along the years their group have reported around 20 discrete Pd core geometries with Pd atoms ranging from 10 to 165. All the Pd NCs have been isolated and their crystal structure reported. The Pd carbonyl/phosphine ligand clusters bear very peculiar icosahedral or closed cubic/hexagonal packing geometries. Unfortunately, these Pd NCs are very reactive and can be preserved only under inert atmosphere or CO gas.

1.2.2.2. Polynuclear metal complexes

Polynuclear transition metal complexes are described as metallorganic molecules incorporating metal ions in oxidation states different from zero and with non-metallic properties like the monolayer protected clusters. Therefore, these clusters differ from the abovementioned ones for not having a defined core. The study of such complexes started in the last century and continues to current days with new clusters of various nuclearity and ligands being investigated. Widely used ligand for these complexes are thiols, phosphines, organosilanes, amines, carbon monoxide and so on.[408] In keeping with the objective of this thesis, this sub-chapter will be focused mainly on the thiolate coordinated metal complexes. A distinctive structural feature of thiolate coordinated metal complexes with nuclearity above four is the formation of closed rings with neighbouring metal centres doubly bridged by the ligands. These peculiar toroidal metallorganic structures have been named tiara-like complexes for resembling a crown and are typically reported for the group 10 transition metals (Ni, Pd, Pt).

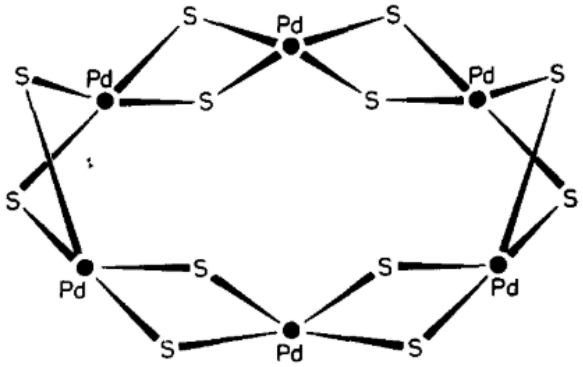

Figure 1.40. The first crystal structure of a $Pd_6(SR)_{12}$ tiara-like complex proposed by Hayter and co-workers. Reproduced with permission from ref. [409]. Copyright 1964 Elsevier.

The first report of such cyclic complexes dates to the mid '60,[409] even though studies on linear metal mercaptides have predicted their existence already in the '30.[410] The synthesis of these compounds usually involves the complexation of a metal salt with the thiol ligand by spontaneous coordination or promoted by a weak base. In the first example described by Hayter *et al.* in 1964, Pd tiara-like complexes of stoichiometry $Pd_6(SR)_{12}$ were formed by spontaneous complexation of $(NH_4)_2PdCl_4$ with ethanethiol, 1-propanethiol and 2-propanethiol in chloroform or benzene in a time span of 12 hours.[409] The complexes were recrystallized and characterized by single-crystal X-ray analysis (Figure 1.40) that confirmed their ring-closed structure. One year later, Dahl, Crosse and co-workers similarly reported the crystal structure of $Ni_6(SC_2H_5)_{12}$ (Figure 1.41) that was prepared by reacting a Ni(II) salt with bis (alkylthio)dialkyltin compounds.[411] The authors used the

same approach to prepare other hexanuclear tiara-like Ni complexes substituted by various thiolated ligands, in the same period.[412]

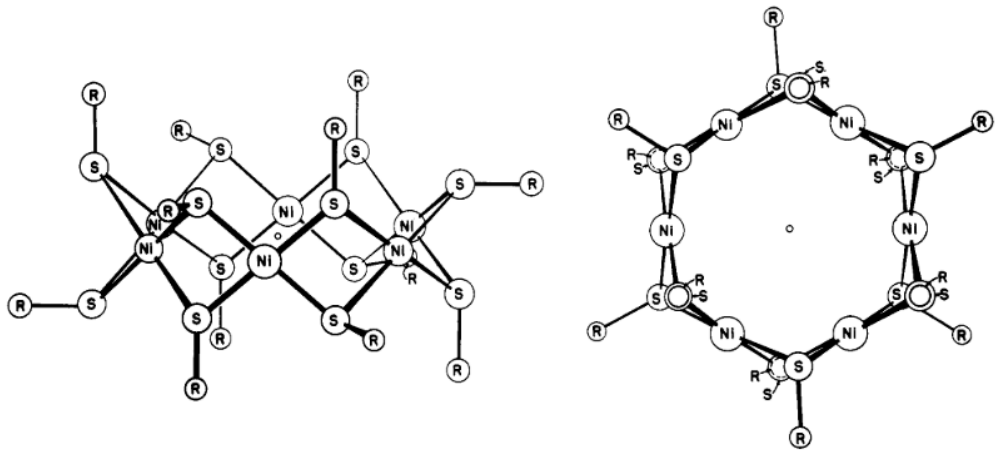

Figure 1.41. First crystal structure of a $Ni_6(SR)_{12}$ tiara-like complex reported by Dahl and co-workers. Reproduced with permission from ref. [411]. Copyright 1965 American Chemical Society.

In the following years various groups reported the preparation and crystal structure of diverse Pd, Ni, Cu, Ag, Fe, Co and Mn complexes enriching the library of thiolated tiara-like metal complexes.[413–424] More recently the tiara-like metal complexes have witnessed a revival not only because of their fascinating structure but also because of their unusual properties. In particular, thiolate coordinated complexes are of great interest because the strength of M-S bond confers to these clusters great stability toward oxidations and reductions.[425] Moreover, metal thiolates are interesting also from a bioinorganic aspect as they are involved in several key enzymes.[426,427] The latest studies of tiara-like complexes have mainly focused on the ligand influence toward the ring contraction or expansion, thus on the nuclearity of the clusters. An early example of ligand influence was reported by Tatsumi and co-workers in 2006 where they studied the Ni complex formation in presence of mixed thiolates.[428] A $Ni(mtet)_2$ (2-methylthioethanethiolate) complex was first prepared and subsequently reacted with potassium 2-propanathiolate or potassium *tert*-butanethiolate to yield cyclo-$[Ni(S\textit{i}Pr)(mtet)]_6$ and cyclo-$[Ni(S\textit{t}\text{-}Bu)(mtet)]_{10}$ respectively (Figure 1.42). Expansion of the ring from 6 to 10 atoms of Ni was attributed to the ligand effect and precisely to the bulkiness of tert-butanethiolate, with respect to 2-propanethiolate, that did not allow the ring closure at lower nuclearity because of the strain effect.

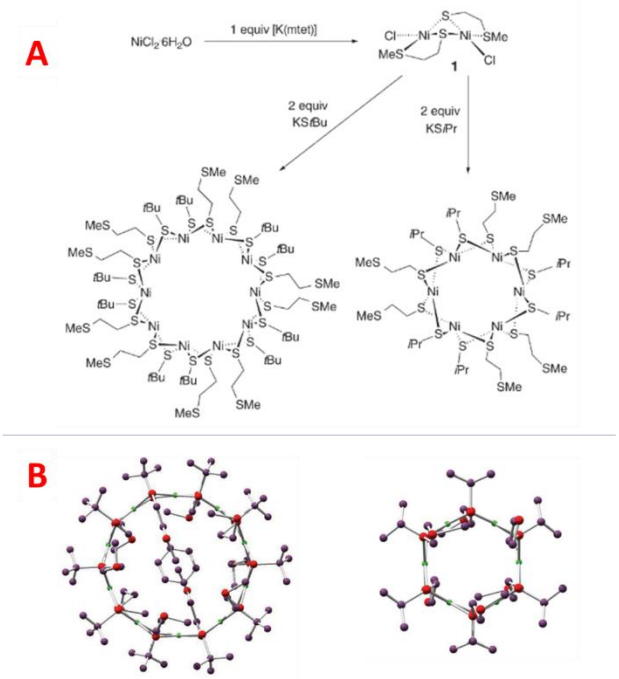

Figure 1.42. Synthetic scheme (A) of the cyclo-[Ni(S*i*Pr)(mtet)$_6$] and cyclo-[Ni(S*t*-Bu)(mtet)$_{10}$] and their respective crystal structure (B). Adapted with permission from ref. [428]. Copyright 2006 Wiley-VCH.

A similar study was reported also for Ni_6 tiara-like clusters employing mixed thiolates.[429] Four complexes were prepared by treating $Ni(ClO_4)_2$ with dimethyl disulfide (or diethyl disulfide) and 2-propanethiol or *tert*-butanethiol in ethanol at 120-130 °C with reaction times that were very sensitive to the nature of the ligand employed, spanning from a few hours to 24 hours. The obtained tiara-like Ni clusters, cyclo-[Ni(μ-SiPr)(μ-SMe)]$_6$, cyclo-[Ni(μ-StBu)(μ-SMe)]$_6$, cyclo-[Ni(μ-SiPr)(μ-SEt)]$_6$ and cyclo-[Ni(μ-StBu)(μ-SEt)]$_{10}$, were characterized by single-crystal X-ray diffraction highlighting the diverse Ni-Ni bond distances and the Ni-S-Ni bond angles that changed with the nature of the thiolated ligand. Another interesting example concerns Pt tiara-like complexes. Usually, Pt thiolates have the tendency to form polymeric complexes of indefinite length with the generic formula [Pt(SR)$_n$]$_\infty$ displaying an amorphous structure that makes these polymers insoluble and challenging to characterize.[430–433] By employing a derivatized symmetric ligand bearing two sulfide functions, [Pt(μ-$SCH_2CO_2Me)_2$]$_8$ was obtained refluxing $PtCl_2$ and the derivatized ligand in acetonitrile for 10 hours (Figure 1.43).[434] With the same procedure [Pd(μ-$SCH_2CO_2Me)_2$]$_8$ complexes were also reported.

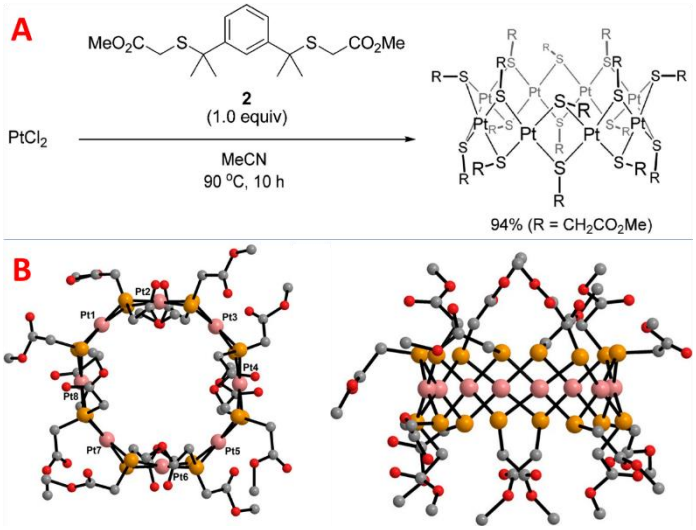

Figure 1.43. Synthetic scheme (A) of $[Pt(\mu\text{-}SCH_2CO_2Me)_2]_8$ and its molecular structure from top and side view (B). Adapted with permission from ref. [434]. Copyright 2014 American Chemical Society.

Pt tiara like clusters were also synthetised with nuclearities ranging from 5 to 13 (Figure 1.44).[435] The complexes were achieved in two steps: $PtCl_4$ was first treated with octanethiol and *N*,*N*-diisopropylethylamine (DIPEA) in chlorobenzene/acetonitrile at 90 °C for 1 hour and the resulting precipitate was refluxed again with excess octanethiol in chlorobenzene at 200 °C for 1 hour. $[Pt(SC_8H_{17})_{2n}]_n$ (with n: 5-13) were isolated by preparative HPLC and characterized with MALDI-TOF spectrometry, and the single crystal X-ray structure was solved for the Pt_6 and Pt_8 complexes. Another cyclic Pt complex was isolated recently in the hexameric form.[436] $[Pt(SC_{12}H_{25})_2]_6$ was prepared by thermal treatment at 210 °C for 2 days of a mixture composed by H_2PtCl_6 and docecanethiol in 4-*tert*-butyltoluene. Single-crystal X-ray diffraction confirmed the toroidal structure of the complex with each Pt atom displaying approximately a square planar configuration with four S atoms pointing at the edges (PtS_4).

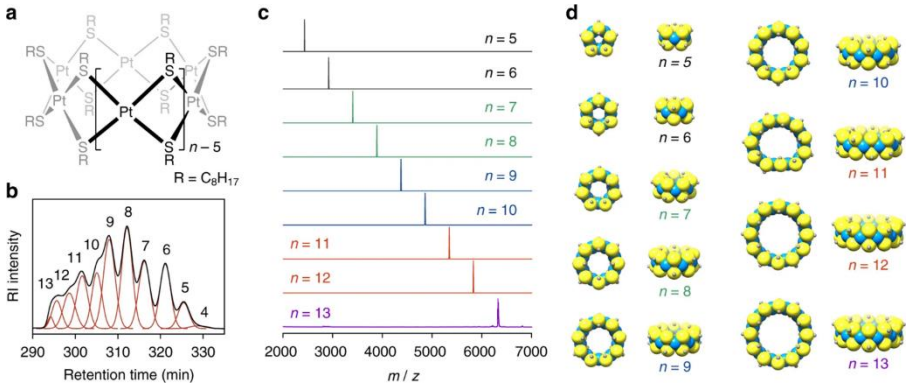

Figure 1.44. Chemical structure of the $[Pt(SC_8H_{17})_{2n}]_n$ complexes (a), chromatogram of the preparative HPLC separation by size-exclusion (b), MALDI-TOF mass spectra of the isolated Pt_n clusters and their relative structure modelled with DFT calculations (d). Reproduced with permission from ref. [435].

Interestingly, PET, that was widely used as thiolated ligand for monolayer protected cluster (e.g. $Au_{25}(PET)_{18}$), has also been employed for the preparation of tiara like complexes. Remarkable examples are Pd[425,437,438] and Ni[439–441] complexes coordinating PET prepared by different protocols providing complexes with various nuclearities. For example, $[Pd(PET)_{2n}]_n$ (n:5-20) have been prepared both by the Brust-Schiffrin protocol where the $NaBH_4$ acted as base on a solution of $Pd(OAc)_2$[438] in presence of PET, or by triethylamine treatment of $Pd(NO_3)_2$ also in presence of PET.[437] Although tiara-like clusters are mostly reported for the group 10 transition metals, examples with other transition metals such as Fe, Co, Ru and Os have also been reported.[442,443] Overall, tiara-like complexes are of great importance because they can be seen as a simple tool for controlling the atomicity of metal clusters in higher oxidation states. Moreover, recent studies have proved interesting light emitting[438] and catalytic[435,441] properties of such complexes opening the door to a multitude of future applications in various fields.

1.3 Catalytic applications of transition metal NPs and NCs

The pervasive role of catalysis in chemical research and chemical industry has led different approaches such as thermal, electro- and photo-catalysis to become well-established independent research areas with widespread applications. The central role of catalysis in chemical transformations is supported by the fact that about 90 % of products manufactured by chemical companies involve at least one catalytic step in their preparation, whether employing homogeneous or heterogeneous catalysts. The growth of heterogeneous catalysis was accompanied by various major historical advances (Figure 1.45). In particular, the concept of active site has been the focus point in many studies.[444–447] In the '20 Taylor pinpointed the role of a small portion, rather than the whole, of surface atoms as active centres and Schwab discussed the lattice defects activity and their involvement as active sites on the catalysts surface. Before Taylor and Schwab, Sabatier and Ostwald contributed to the fundamentals of physical and chemical adsorption in catalysis and they were awarded the Nobel prize in Chemistry in 1912 and 1909, respectively, for their discoveries. In 1916, Langmuir introduced the theory of chemisorption,[448] that together with the other findings at the beginning of the 20th century set the basis for the studies of catalytic systems and the introduction to surface science for the study of reaction mechanism's occurring on crystallographic facets and atomic scale features.[449]

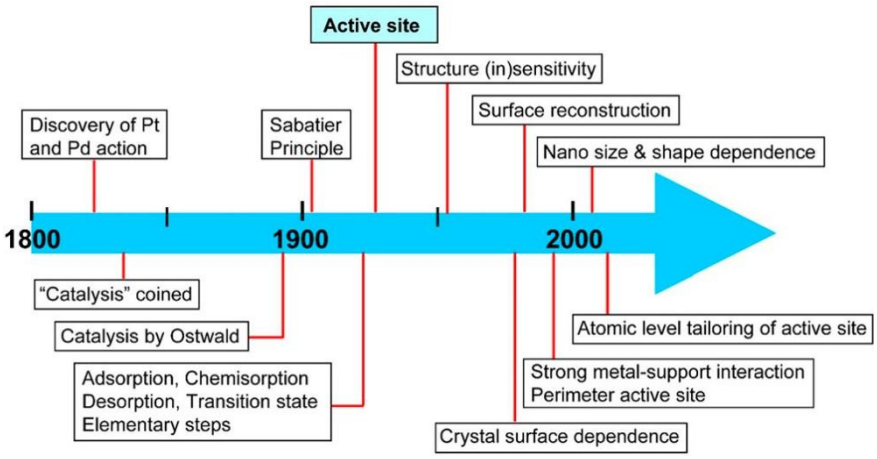

Figure 1.45. Historical and contemporary conceptual advances in heterogeneous catalysis. Reproduced with permission from ref. [450]. Copyright 2021 America Chemical Society.

Among all the catalytic materials, transition metals arise thanks to their redox properties that make them suitable catalysts for many oxidation and reduction reactions. Various established examples of industrial applications for heterogeneous catalysts can be found nowadays and most of them have been developed in the last century. Remarkable examples are catalysts based on copper for methanol production,[451,452] ruthenium for ammonia synthesis,[453,454] palladium and platinum for

hydrogenation of organic compounds,[455,456] silver for the epoxidation of ethylene[457] and so on. Moreover, platinum, palladium and rhodium are widely used in catalytic converters for the degradation of pollutants[458] and in fuel cells.[459] Although metal based catalysts have been used since long time, their preparation has not varied much and these catalysts are still produced by precipitation or impregnation methods followed by calcination and reduction at high temperatures. Despite being practical approaches for the production of well dispersed supported NPs with high surface area, these protocols still face some drawbacks. Firstly, a broad size distribution is often associated to these procedures causing Ostwald ripening of the NPs[460] that is one of the causes of mass/specific activity loss. Additionally, irregular and polycrystalline NPs obtained by the conventional preparations challenge the reproducibility control over activity and selectivity as many catalytic reactions are sensitive to the catalyst surface structure. For instance, it has been reported that NH_3 rate formation from N_2 and H_2 on Fe surface facets increases in the order of Fe(110) < Fe(100) < Fe(111).[461] For Pt nanostructures, it has been demonstrated that CO reduction is boosted on (100) and (210) facets[462,463] while electrochemical oxygen reduction rate in aqueous $HClO_4$ on single-crystal Pt follows the trend (100) < (111) < (110).[464] Despite these and other studies performed on single crystal metals, a structure gap is still present when comparing real catalysts to the ideal systems. This gap can be easily attributed to the difference in the catalyst preparation, which is accountable for the surface features on the metal[465] and it can be reduced by switching to colloidal metal NPs with controlled morphology. The control of metal NPs in terms of size and shape monodispersity have the potential of bridging the gap between the industrial catalysts and the single-crystal nanostructures studied in surface science.[466] Replacing the conventional polycrystalline NPs with uniformly shaped ones allows to improve the activity, selectivity and stability of a catalytic system. The concept of using monodispersed and shaped NPs in heterogeneous catalysis has been explored since the early 2000 with the development of various protocols for the syntheses of colloidal shaped NPs.[244,467,468] According to this, many studies have contributed to establish the relationship between surface structure and electronic properties enabling the development of new characterization techniques for probing active surfaces in catalytic reactions.[469,470] Another research line, based on the use on NCs, prompted the investigations of new catalytic systems. This was also encouraged by the fact that NPs, although having the same size and shape, still can be different by one or two atomic layers or by the number of defects present on the surface, thus never displaying the same precise structure. This drove the development of atomically precise catalysts as models for new structure-activity studies[450,471,472] since the electronic properties of metal NCs can significantly vary with the atomic composition of the cluster itself.

In general, the activity of a catalyst in solid phase is strongly related to the interaction of reactants with the catalyst surface generating the intermediates that evolve to products (Figure 1.46A). The Sabatier principle[473] suggests that such interaction in an optimal catalyst should be neither too weak nor too strong for the expression of a high activity. When the interaction is too weak, activation (dissociative adsorption) of the reactants will not occur and the reaction will not be promoted. On the opposite, if the interaction between reactant and surface atoms is too strong the catalyst will be poisoned as the intermediates will not be able to desorb from the surface. When plotting the reaction rate *vs* the heat of adsorption of an intermediate involved in the rate-limiting step a bell shaped curve is obtained in which the position of the maximum corresponds to the most active catalyst[474] (Figure 1.46B).

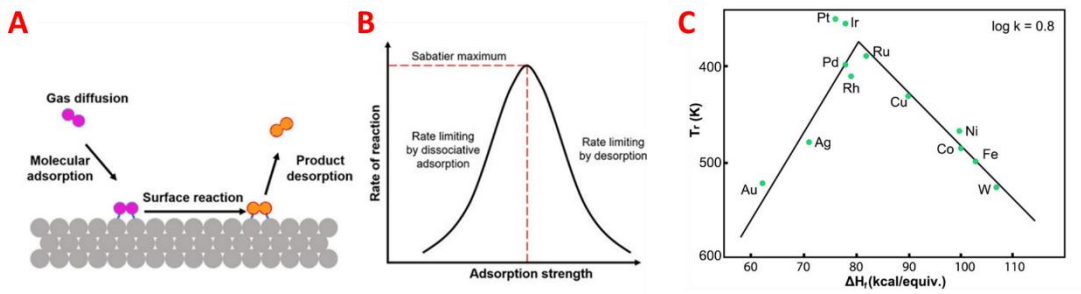

Figure 1.46. Elementary steps in a heterogeneous catalytic reaction (A), bell shaped plot derived from the Sabatier principle (B) and volcano plot showing the reaction rate of various metals toward the decomposition of formic acid (C). Adapted with permission from ref. [116]. Copyright 2021 American Chemical Society.

For example, a typical bell shaped plot can be drawn for the decomposition of formic acid with various metals in which the temperature (at rate constant log k = 0.8) is plotted *vs* the heat of formation (ΔH_f) of the intermediate (Figure 1.46C).[475] At low values of ΔH_f the reaction proceeds gradually, thus the adsorption is rate determining, while at high values of ΔH_f the opposite situation is favoured with desorption being the rate-limiting step. Taken together, the plot shows metals found in the intermediate ΔH_f values, with optimal combination of adsorption/desorption rate, are the most active catalysts for the decomposition of formic acid. A direct strategy for tuning the interaction strength of a catalyst consists in the modulation of its d-band center.[476] The d-band center theory describes the interaction of the metal d-states with the bonding and anti-bonding molecular orbitals of an adsorbate. Particularly it states that the d-band position with respect to the Fermi level of the metal determines the size of the bonding/anti-bonding energy shifts in the intermediate and the degree of filling of the antibonding states that consecutively reflects on the reaction rate. The d-band centre can be modulated through the engineering of the metal NPs and NCs surface structure by means of size, shape twin defects and elemental composition. A quantitative descriptor of the surface structure is the CN, that indicates the number of bonds an

atom forms with its nearest neighbours. The CN is directly related to the performance of a catalyst, including activity and selectivity, by altering the adsorption and dissociation energies of molecules on the surface.[477] Because the CN is dictated by the size, lattice structure and the exposed facets, NCs and shaped NPs are the perfect tool for the development of advanced catalytic systems with improved activity and selectivity.

In the next sections, various catalytic systems based on the use of shaped metal NPs and metal NCs will be described and discussed both from the activity (performance) and selectivity (type of reactions promoted) point of view. Due to the extensive number of works and studies reported for the application of shaped NPs and NCs in catalysis, only remarkable examples of some transition metals will be treated in the following three subparagraphs.

1.3.1. Organic transformations

CO oxidation

Since the pioneering work of Haruta about the low-temperature CO oxidation on gold catalysts,[478] a substantial number of studies have reported the development of new metal based heterogeneous catalysts for the conversion of CO to CO_2. Although it has been widely demonstrated that Au NPs with average size around 2-5 nm are very active in this transformation, the activation process is still unclear. Researchers have been focusing on various issues such as the support-NPs interaction, the active charge state of the supported NPs and the active sites on the NPs to shine light on the possible mechanisms involved in the transformation. Nevertheless, the participation of smaller particles (clusters and single atoms) in the reaction has been long debated triggering studies focused on sub-nanometric catalytic systems. In-between the end of the ’90 and the early 2000, Sanchez *et al.*[479] reported studies for the CO oxidation on unprotected Au_n clusters ($n \leq 20$) finding in Au_8 the minimum size for non-negligible activity while Anderson *et al.*[480] used Au clusters with atomicity from 1 to 7 for the same reaction observing that even smaller clusters down to Au_3 were active. These studies validated the hypothesis of the possible involvement of smaller species in CO oxidation. Later on, 0.5 nm Au NCs[481] and even bigger ones (1-3 nm)[482] were reported as active clusters in the oxidation process.

Even though nanoscale and sub-nanoscale gold is very efficient in oxidizing CO, other metal NCs have been employed as model catalysts for activity studies with this reaction. Anderson and co-workers, for example, studied the activity of Pd clusters supported on TiO_2 as a function of their atomicity considering a range between 1 and 25 atoms.[483] By XPS analysis, the authors observed a nonmonotonic charge variation with the cluster size, especially at smaller sizes, and naturally this

was also reflected on the NCs activity toward CO oxidation (Figure 1.47A). As for Pd, also for Pt a set of different NCs was used in temperature-dependent CO oxidation reactions for fundamental studies aimed at assessing the effect of NCs surface modification on the overall performance.

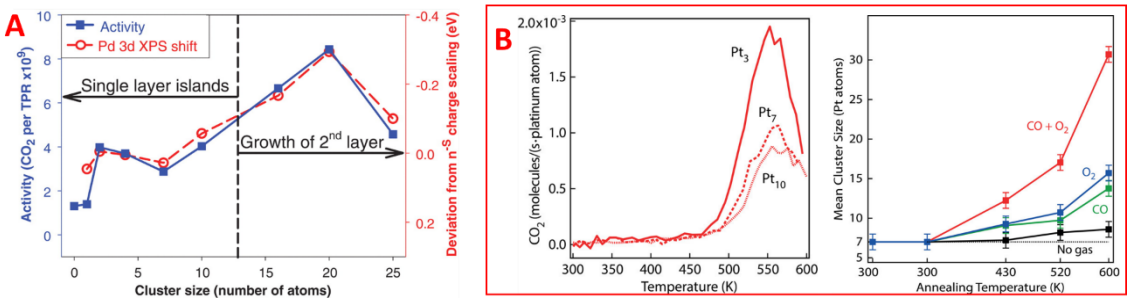

Figure 1.47. CO oxidation activities for Pd_n clusters compared with the shifts in Pd 3d binding energy (A). CO_2 production rates per Pt density as a function of cluster size and temperature and mean cluster size of Pt_7 after annealing in vacuum (black) and exposure to single (green and blue) and combined reactant gasses (red) (B). Adapted with permission from ref. [483] (copyright 2009 American Association for the Advancement of Science) and ref. [484] (copyright 2014 American Chemical Society).

Bonanni *et al.* determined the reaction rates for three Pt_n clusters (n: 3, 7, 10) on TiO_2(110) that decreased with the increasing atomicity (Figure 1.47B).[484] Size investigation before and after catalysis revealed a sintering process that involved all the clusters starting already at low temperatures while annealing of the clusters in absence of gasses resulted negligible. This aspect highlights the importance of stability testing when comparative performance studies are reported for catalysts.

Beside the aforementioned examples with clusters prepared in ultrahigh vacuum systems, NCs with defined crystal structure, gold especially, prepared by wet chemical protocols are also important model catalysts in pursuing new insights into the mechanism of CO oxidation. Since the breakthrough of supported $Au_{25}(PET)_{18}$ in CO oxidation reaction,[485] various efforts have been made to unveil the mechanistic details at the molecular scale. From this first study, an important role of the interface (Figure 1.48A) was established as $Au_{25}(SR)_{18}/CeO_2$ resulted in excellent conversion while $Au_{25}(SR)_{18}/TiO_2$ exhibited no activity at all. Additionally, oxygen pre-treatment of the catalyst resulted in the activation of the clusters since without this pre-treatment the protected Au_{25} NCs displayed no activity. The importance of oxygen pre-treatment was also observed in another study on protected and unprotected Au_{38} NCs.[486] Computational studies have suggested triangular Au_3 sites as active sites for the generation of active oxygen (Figure 1.48B) that favoured the oxidation of CO in Au NCs. However, Overbury *et al.* suggested an alternative perspective on the active site in Au NCs, based also on the ligand effect.[487] By studying the $Au_{25}(SR)_{18}/CeO_2$ catalytic system they noted a complete lack of activity for the protected NCs compared to unprotected NCs, while a partial ligand removal resulted in enhanced activity. Isotopic labelling experiments

indicated that active sites are at the interface and active oxygen species are not formed from molecular oxygen but derive from lattice oxygen of CeO_2, thus the catalysis was suggested to proceed via the Mars-Van Krevelen mechanism (Figure 1.48C) rather than Langmuir-Hinshelwood mechanism. The role of O_2 in the reaction was to replace the depleted lattice oxygen from ceria.

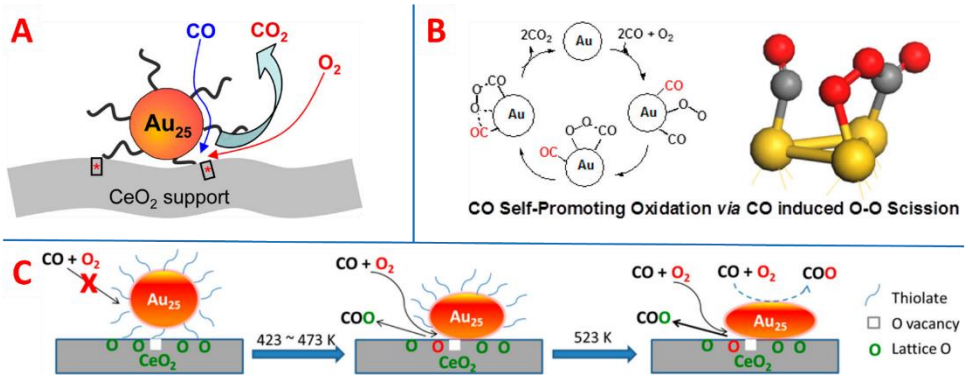

Figure 1.48. Proposed model for CO oxidation at the interface sites of $Au_{25}(SR)_{18}/CeO_2$ catalyst (A) and generation mechanism of active oxygen species and molecular model of the Au_3 active site (B). Proposed CO oxidation mechanism on protected, partially protected and unprotected Au_{25} NCs. Adapted with permission from ref. [485] (copyright 2012 American Chemical Society), ref. [486] (copyright 2013 American Chemical Society) and ref. [487] (copyright 2014 American Chemical Society).

However, the same group have developed a catalytic system with Au NCs bearing coordinatively unsaturated Au atoms in the structure that was active toward low temperature CO oxidation without the need of ligand removal.[488] $Au_{22}(dppo)_6$ (dppo: 1,8-(diphenylphosphino) octane) with 8 uncoordinated Au atoms, that are not susceptible to the phosphine charge transfer, was supported on different metal oxides (CeO_2, TiO_2, Al_2O_3) and used in the CO oxidation reaction demonstrating to be superior with respect to the $Au_{25}(PET)_{18}$ supported catalyst. The reaction mechanism still proceeded via redox transfer of lattice oxygen from the support at the interface. All these studies have offered a design strategy for the assembly of improved catalytic systems based on the engineering of atomically precise metal NCs and support/NCs interface that are still studied nowadays.

With metal NPs, low temperature CO oxidation starts to acquire significance only with reduced size (below 10 nm). At this size range the mechanisms can follow different paths, depending on temperature like in the case of Au NPs deposited on titania. At temperatures above 80 °C the oxidation can be promoted directly on Au surface where oxygen active species are generated, while at lower temperatures the reaction proceeds at the interface[489] and more interestingly, below -155 °C the CO can be directly adsorbed on TiO_2 from which it migrates at the interface to react with oxygen.[490] A study by Cargnello *et al.* on group 10 transition metals (Ni, Pd and Pt), supported on CeO_2, investigated the involvement of surface atoms at the interface during CO oxidation.[491] By

employing monodispersed NPs at different sizes the authors found corner atoms of the NPs at the interface as the active sites, thus smaller NPs presented superior activity because enriched in low coordinated corner atoms (Figure 1.49).

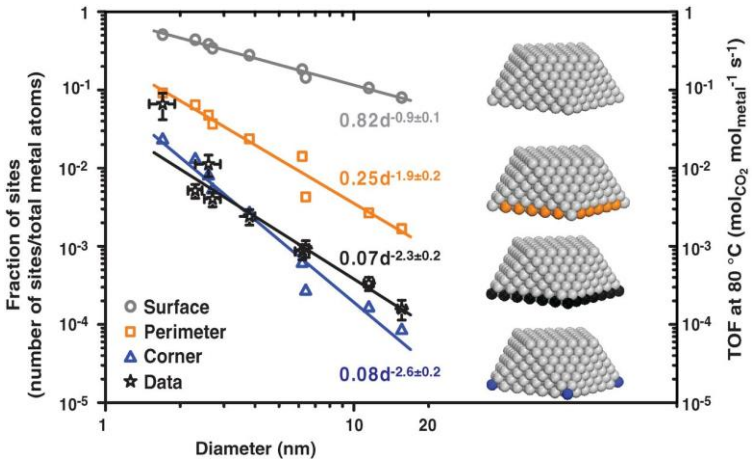

Figure 1.49. Calculated number of sites with a particular geometry (surface, perimeter or corner atoms at the support interface) as a function of size and TOF at 80°C of the ceria-based samples. Reproduced from ref. [491]. Copyright 2013 American Association for the Advancement of Science.

Contrary to polycrystalline NPs, for nanocrystals with well-defined geometry and facets the fraction of atoms with a particular geometry can be easily quantified. Figure 1.50 shows the fraction of surface atoms located at the (111) facets, (100) facets, vertexes and edges of Au cuboctahedral NPs with the edge length going from 0.5 to 10 nm. Atoms at the edges and vertexes have lower CN compared to facets and their presence naturally affects the catalytic activity of the NPs. This link was observed for the CO oxidation on Au cuboctahedra with variable size.[492] Here, dramatic increase in the CO conversion was observed when 3 nm cuboctahedral NPs were used instead of 6 nm NPs in keeping with the higher percentage of low-coordinated atoms at the vertexes and edges of smaller Au cuboctahedral NPs.

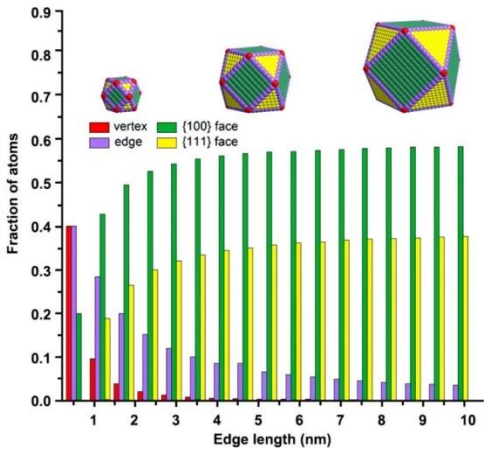

Figure 1.50. Fraction of surface atoms at the edges, vertexes, (111) and (100) facets at increasing size of Au cuboctahedrons. Reproduced with permission from ref. [493]. Copyright 2013 Elsevier.

Because the shape control of metal NPs is quite challenging at the size level required for the oxidation of CO at low temperatures, very few studies have been reported for faceted NPs in catalysing this reaction. However, as stated above, low coordination number sites are very active in converting CO to CO_2, thus NPs enclosed in high-indexed facets can be exploited for this purpose. In 2011 Xia and co-workers reported a synthetic protocol for Au rice-shaped NPs covered in (611) high-index facets with size around 50 nm.[494] These Au NPs were supported on ZnO and tested for CO oxidation demonstrating to be highly active and superior if compared to conventional Au nanospheres with the same dimension. More recently, Vinod and co-workers similarly compared the activity of high-indexes Pd NPs with Pd nanospheres.[495] The authors used (310) faceted flower-like and (311) faceted concave cubic Pd NPs enriched in steps and edges. They reported higher activities for flower like and concave cubic NPs compared to polycrystalline nanospheres with the same dimension (35 nm), while the use of smaller Pd nanospheres (6 nm) resulted in comparable activity to the high-indexed NPs (Figure 1.51A). Moreover, they performed size dependent tests on concave nanocubes finding an inverse correlation between size confinement and activity (Figure 1.51B) that suggested the importance of stability in bigger particles toward sintering and the presence of high-index facets for the boosting of CO oxidation.

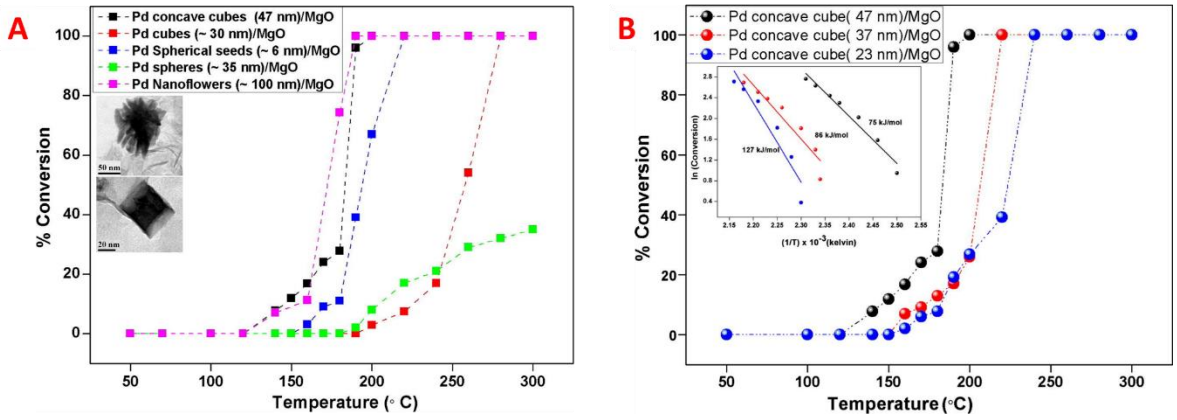

Figure 1.51. CO conversion activities of Pd concave cubes and nanoflowers compared with 35 and 6 nm spherical NPs (A). CO oxidation profile for concave nanocubes with different sizes and respective Arrhenius plots (inset) (B). Adapted with permission from ref. [495]. Copyright 2016 Elsevier.

Beside gold and group 10 metals, also ruthenium is considered a valid metal for CO oxidation.[496] Ruthenium is a peculiar metal since at the nanoscale it can be found in two distinct crystal structures, fcc and hcp, with the latter being predominant. The discrimination of one structure with respect to the other in the formation of Ru nanocrystals is governed by reduction kinetics that can be tuned through the use of different precursor and solvent. Kitagawa and co-workers reported the synthesis of both crystal phases NPs employing $RuCl_3$ and EG (solvent) for hcp phase and

$Ru(acac)_3$ and TEG (solvent) for fcc phase (Figure1.52A, B).[497] The as-prepared NPs were supported on γ-Al_2O_3 and tested for CO oxidation revealing a peculiar trend.

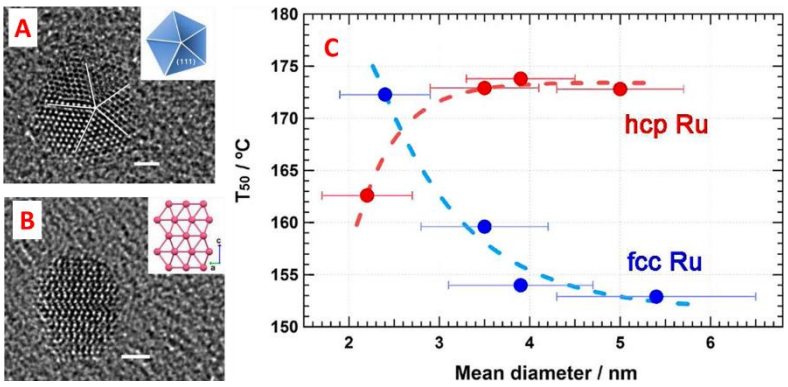

Figure 1.52. TEM images of fcc (A) and hcp (B) Ru NPs. Size dependence of the temperature for 50% conversion of the reaction with fcc NPs (blue) and hcp NPs (red). Adapted with permission from ref. [497]. Copyright 2013 American Chemical Society.

The temperature required for 50% conversion of CO to CO_2 (T50) was measured and compared for various Ru NPs sizes. For hcp Ru NPs, T50 increased with particle size while for fcc NPs T50 had the opposite trend. Above 3 nm in size fcc Ru NPs resulted superior in catalysing the reaction compared to hcp NPs (Figure 1.52C) and the authors attributed this behaviour to the presence of twin defects or lattice distortions in fcc structure.

Alcohol oxidation and alkene epoxidation.

The oxidation of alcohols is an important reaction for the production of aldehydes, ketones and carboxylic acids which are valuable building blocks for the synthesis of organic compounds both in research and industry. Although various oxidants have been developed along the years,[498] the use of molecular oxygen is encouraged and preferred as it is greener compared to organic/inorganic oxidants and generates no toxic by-products during the catalytic oxidation. In heterogeneous phase the oxidation takes place at the metal surface and metal/support interface with initial OH adsorption/activation to form followed β-hydride elimination to generate the carbonyl group and lastly, hydride abstraction by molecular oxygen closes the catalytic cycle (Scheme 1.1). Conventional metals used in this process are gold, palladium and platinum.

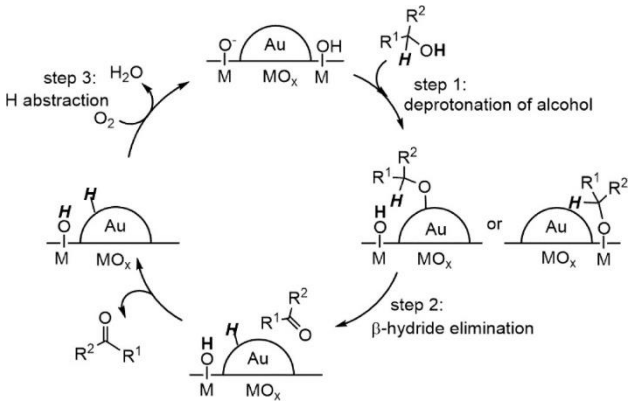

Scheme 1.1. Catalytic cycle for the aerobic oxidation of alcohols on supported Au NPs. Reproduced with permission from ref. [499]. Copyright 2019 American Chemical Society.

Even though, most of the heterogenous aerobic oxidations are performed with polycrystalline NPs,[499–501] in the last decades tailored catalysts based on atomically precise metal NCs and shaped NPs have been reported.[116,450] Gold NCs have been widely studied for the aerobic oxidation of alcohols with either ligand preservation on the cluster or with ligand removal before or during catalysis.[502–505] An interesting study was reported by Tsukuda and co-workers in which these authors studied the selectivity of protected and unprotected $Au_{25}(SC_{12}H_{25})_{18}$ NCs toward benzyl alcohol oxidation.[502] The authors observed that protected Au_{25} clusters displayed very low activity with 19% conversion of alcohol but at very high selectivity for benzaldehyde. With partial ligand removal, a higher conversion was observed, still favouring the benzaldehyde production with low amounts of benzoic acid and benzyl benzoate. Conversely, calcinated and unprotected Au_{25} clusters resulted highly active with almost quantitative conversion, but dominant chemo-selectivity for benzoic acid with benzaldehyde and benzyl benzoate being present as by-products (Figure 1.53). The selective oxidation to benzaldehyde was attributed to the thiolated ligands that lowered the oxidation ability of Au_{25} by electron withdrawal, thus promoting the formation of the less oxidised product only.

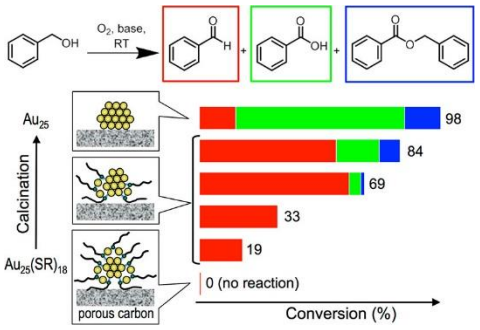

Figure 1.53. Conversion and selectivities for the protected, partially protected and unprotected Au_{25} NCs toward benzyl alcohol oxidation. Reproduced with permission from ref. [502]. Copyright 2014 American Chemical Society.

Unprotected platinum and palladium clusters have also been employed for the aerobic oxidation of alcohols.[506–509] An interesting study was described by Dun *et al.* on the oxidation of substituted benzylic alcohols with Pd clusters.[510] Pluronic P123 ($EO_{20}PO_{70}EO_{20}$) protected Pd clusters, were prepared by a wet chemical reduction in water and used as colloids for the catalytic oxidation (Figure 1.54). The clusters demonstrated to be active with variously substituted benzyl alcohols with a remarkable selectivity (100%) for the aldehyde products.

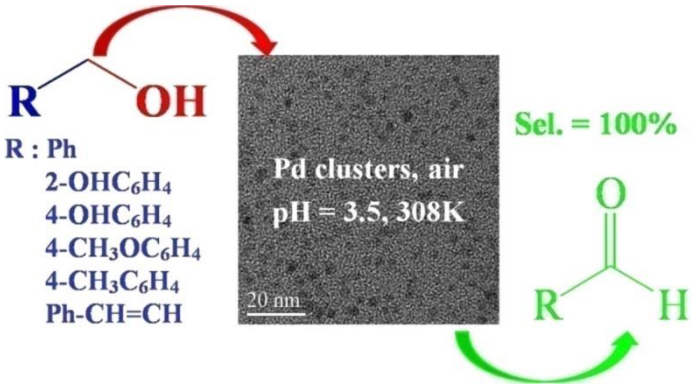

Figure 1.54. Aerobic oxidation of substituted benzyl alcohols promoted by polymer stabilized Pd cluster colloids. Reproduced with permission from ref. [510]. Copyright 2013 American Chemical Society.

Nanoparticles with controlled morphology have been extensively used for the aerobic oxidation of alcohols in electrocatalysis and these will be discussed in a following section. Unfortunately, very few examples of shaped NPs for thermal aerobic oxidation of alcohols can be found in literature. One of the first examples was reported by Corma and co-workers for the oxidation of 1-phenylethanol to acetophenone promoted by Pd nanostructures (Figure 1.55A).[511] Pd nanobars, nanorods and icosahedra were supported on TiO_2 or SiO_2 and tested at 110 °C until complete conversion. Pd nanobars/SiO_2 displayed the highest activity compared to the other catalysts with a good selectivity for benzaldehyde. In the same period, Tilley and co-workers exploited icosahedral Pd NPs with a gold core for the same reaction obtaining high selectivity for benzaldehyde.[512] Pd NPs exposing (110) faceted and deposited on flower-like hydroxyapatite were used for the thermal oxidation of neat primary alcohols displaying good conversions and high selectivity for the less oxidised product.[513] Recently, rhodium nanocubes were used for the selective conversion to aldehyde of benzyl alcohol through a room temperature photocatalytic process.[514] After deposition on silica nanospheres, the Rh nanocubes were tested both in dark and under illumination conditions confirming the higher performance of the photocatalysis (Figure 1.55B).

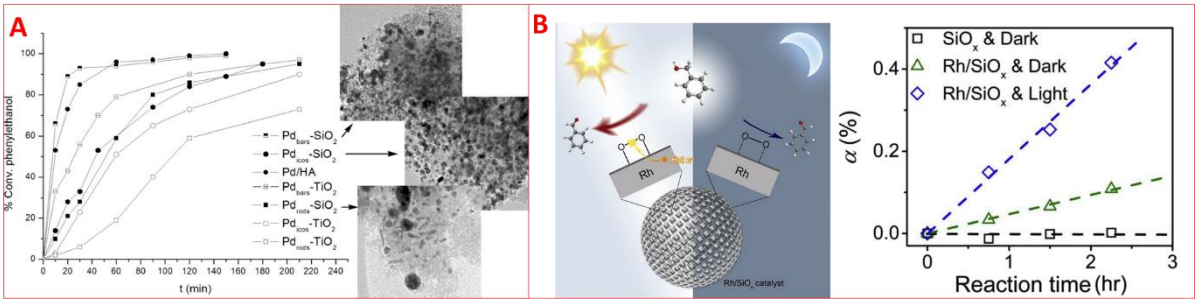

Figure 1.55. Conversion of 1-phenylethanol *vs* reaction time with the different Pd nanostructures supported on TiO_2 or SiO_2 (A). Representative scheme of the photocatalytic oxidation of benzyl alcohol promoted by Rh nanocubes/SiO_2 nanospheres and conversion efficiency vs reaction time comparisons for the reaction performed with light (blue), in dark (green) and without Rh nanocubes (black) (B). Adapted with permission from ref. [511] (copyright 2012 Elsevier) and ref. [514] (copyright 2018 Elsevier)

Epoxidation reactions are one of the most useful reactions in terms of applicability because epoxides, ethylene oxide in particular, are widely used building blocks in the polymer industry.[515–517] In the chemical industry the widely used catalyst for the synthesis of ethylene oxide is a fine dispersion of Ag NPs onto alumina. Supported metals in the form of NPs and NCs are still very appreciated because of their reusability and inferior toxicity, although metallorganic complexes[518,519] are applied for challenging epoxidations. In heterogenous catalysis the epoxidation reactions are mostly catalysed by gold and silver because of their oxophilic behaviour, that at the sub-nanoscale and nanoscale is not very marked, promotes a weak coordination of oxygen sufficient for the nucleophilic attack by an alkene. The epoxidations over metallic surfaces have been studied since the last century and a vast number of articles on this topic have been published.[520–523] More recently the research is directed on the use of atomically precise NCs and NPs enriched in well-defined facets for the investigation on activity and selectivity. Silver NPs are usually employed only for the epoxidation of ethylene and propylene because higher alkene molecules are not converted in the desired epoxide but tend to decompose in CO_2 and water during the catalytic reaction.[522] In addition, the size of the NPs is crucial for the successful conversion; smaller NPs are too active for the production of ethylene oxide and their use triggers the complete combustion of the reactant.[524] It has been reported that penta-twinned Ag nanowires, covered in (100) facets have a higher selectivity for ethylene epoxidation with respect to conventional polycrystalline Ag NPs (Figure 1.56A).[525] DFT calculations have been performed to investigate this behaviour and it has been found that the formation of a surface oxo-metallacycle intermediate is the key step for selectivity; interestingly, the evolution of this intermediate in ethylene oxide is more favoured on Ag(100) facets compared to Ag(111) that delivered CO_2 and water as major products (Figure 1.56B).

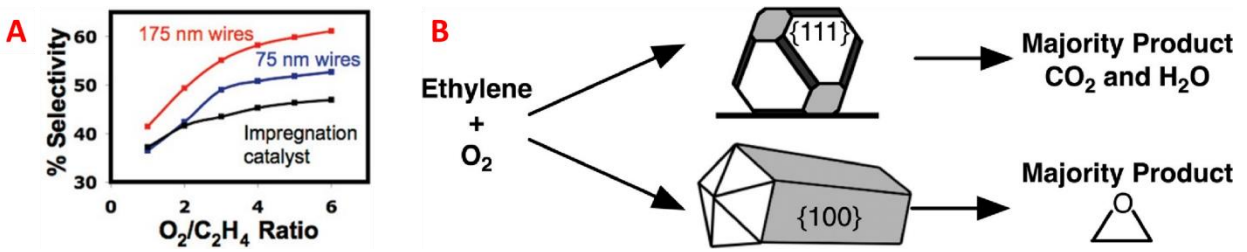

Figure 1.56. Selectivity vs ethylene/oxygen ratio plot for epoxidation reaction promoted by Ag nanowires (red and blue) and conventional Ag NPs on Al_2O_3 (A). Schematic illustration showing the products outcome for epoxidation performed on (111) and (100) enriched Ag NPs. Adapted with permission from ref. [525]. Copyright 2008 American Chemical Society.

For Ag, also the NPs shape influence was investigated for the selectivity of the reaction by comparing cubes, penta-twinned wires and polycrystalline NPs.[526] Experiments showed that Ag nanocubes had the higher selectivity, followed by nanowires and polycrystalline particles. The authors attributed this trend to the abundance of low-coordination number atoms that were present on the penta-twinned wires and polycrystalline surfaces. Under-coordinated atoms were responsible for the diminished selectivity because their higher reactivity caused the formation of CO_2.

Gold NPs have also been reported for epoxidation reactions, in particular for propene.[527,528] Nevertheless, atomically precise Au NCs have been exploited for the same reactions as-well. A peculiar study was conducted on the epoxidation of stilbene with $Au_n(PET)_m$ with n: 25, 38, 144. All three Au NCs displayed good conversions and high selectivity (> 90%) for the *trans*-epoxide regardless of the use of *cis*- or *trans*- stilbene as starting reagent. Internal alkenes are reported to be less prone to epoxidation with respect to terminal alkenes, thus these results suggest the high activity of Au NPs.

Hydrogenation reactions

Heterogeneous hydrogenations of organic compounds are well-known reactions, very used in industry and academic research for the conversion of olefines to alkanes, carbonyls to alcohols, nitro groups to amines and reduction of many other functional groups. Usually, these reduction reactions are performed by group 10 transition metals deposited on carbon or conventional metal oxide supports. The first preparations of a supported solid metal catalyst for reductions dates back to the early years of the 20th century which additionally supports their importance.[529] Nowadays heterogeneous hydrogenations are mainly studied as model reactions in surface science. Even though the concept of selective hydrogenations was largely investigated on solid phase during the '80 and '90,[530–532] with the development of tailored procedures for the synthesis of NPs with controlled morphology this concept was also transferred to the nanoscale. Somorjai and co-workers

reported one of the first studies on the selective hydrogenation of benzene over shaped Pt NPs (Figure 1.57).[95] They revealed a facet selectivity for the reduction of benzene to cyclohexane and cyclohexene based on the abundance of Pt(111) and Pt(100) active sites. Cubic NPs enriched in (100) facets were found to be highly selective for cyclohexene while cuboctahedral NPs, enclosed in (111) and (100) facets, produced a mixture of cyclohexane and cyclohexene. These results were in accordance with data obtained from single crystal studies,[533,534] however, activation energies on NPs were much lower compared to single crystals.

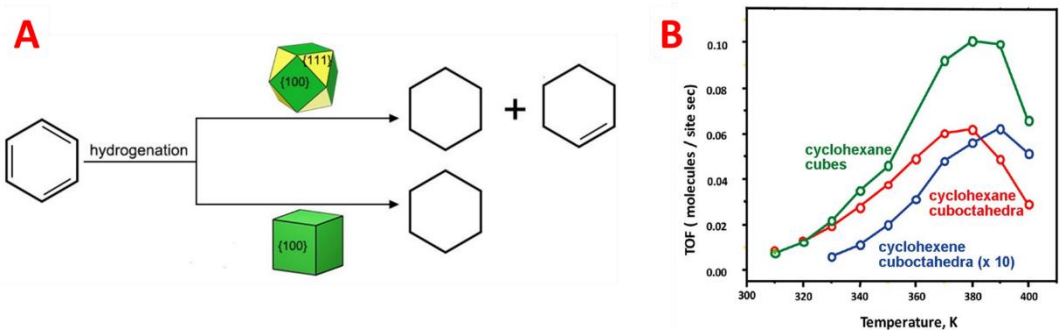

Figure 1.57. Schematic illustration for the selective hydrogenation of benzene on cuboctahedral and cubic Pt NPs (A). Activities of the Pt nanostructures as a function of temperature (B). Reproduced with permission from ref. [95]. Copyright 2007 American Chemical Society.

A similar study was conducted on the hydrogenation of pyrrole comparing the selectivity of sub-10 nm Pt nanocubes with polyhedral Pt NPs.[535] For pyrrole hydrogenation three different products can be obtained depending on the degree of reduction: pyrrolidine, *n*-butylamine or butane and ammonia. Here, Pt nanocubes gave higher selectivity and activity for the synthesis of *n*-butylamine with respect to polyhedral NPs (Figure 1.58).

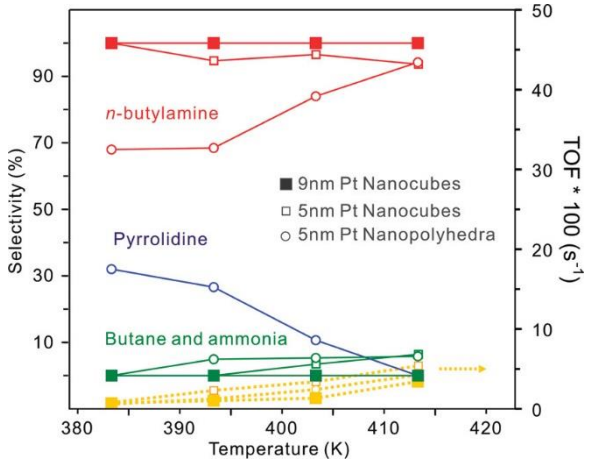

Figure 1.58. Pyrrole hydrogenation selectivity (left axis) and activity (right axis) for Pt nanocrystals with different size and shape plotted *vs* temperature. Reproduced with permission form ref. [535]. Copyright 2009 American Chemical Society.

Nanostructured Pd crystals can influence the selectivity of hydrogenations as well. A relevant study by Kiwi-Minsker and co-workers on the hydrogenation of 2-methyl-3-butyn-2-ol compared the selectivity of cubic, octahedral and cuboctahedral Pd NPs displaying (100), (111) and (100)/(111) facets on the surface, respectively.[536] At 50% conversion the selectivity toward the formation of 2-methyl-3-buten-2-ol was reported to be not regulated by the shape diversity of the particles. However, at higher conversion (90%) a substantial selectivity variation was observed depending on the shape of the nanocrystals. Because semi-hydrogenation was promoted on the side facets, regardless of the symmetry, NPs having higher fraction of uniform facets (cubes and octahedra) were reported to be more selective for 2-methyl-3-buten-2-ol. Therefore, Pd cuboctahedra resulted more active in delivering the over-hydrogenated 2-methylbutan-2-ol. According to the authors, the site-dependent selectivity was attributed to the difference in CN of the surface atoms: the high presence of corners and edges on the cuboctahedral Pd NPs made these shape the most effective in reducing the alkynol to the corresponding saturated alcohol.

A comprehensive study on the influence of differently shaped Pt NPs toward the activity and selectivity of enantioselective hydrogenations was proposed by Baiker and co-workers in 2009.[537] Heterogeneous enantioselective hydrogenations were studied since the ‘80 and during the ’90 and 2000 and great efforts were made[538] to shed light on these reductions as alternatives to conventional processes performed with chiral complexes in homogeneous phase. In this study cubic (100), octahedral (111) and cuboctahedral (100)/(111) Pt NPs with average size around 10 nm were deposited on Al_2O_3 or SiO_2 and tested for the enantioselective hydrogenation of ethyl pyruvate in presence of cinchona alkaloid derivatives as chiral modifiers (Figure 1.59). The authors discovered that in absence of the chiral modifier (cinchonidine CD or quinine QN) the rates and enantiomeric excesses did not deviate from the results obtained with a commercial Pt/Al_2O_3. However, the use of chiral modifiers increased the activity by a factor of 4-15 with QN giving better performance with respect to CD.

A

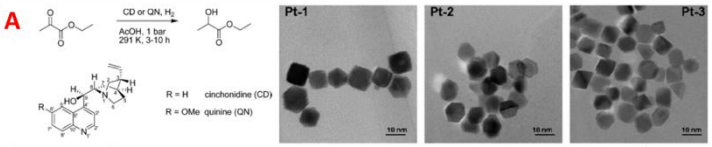

B

catalyst	chiral modifier	ee, %	TOF, h^{-1}	rate enhancement
Pt/Al_2O_3 (reference)	–	–	156	–
	CD	80	1200	7.7
	QN	85	1480	9.5
$Pt\text{-}1/SiO_2$ {100}	–	–	126	–
	CD	72	530	4.2
	QN	77	850	6.7
$Pt\text{-}1/Al_2O_3$ {100}	–	–	143	–
	CD	71	570	4.0
	QN	76	840	5.9
$Pt\text{-}2/SiO_2$ {100}+{111}	–	–	147	–
	CD	78	730	5.0
	QN	83	1380	9.4
$Pt\text{-}3/SiO_2$ {111}	–	–	127	–
	CD	86	1350	10.6
	QN	92	1890	14.8

Figure 1.59. Synthetic scheme for the enantioselective hydrogenation of ethyl pyruvate promoted by CD or QN and Pt NPs used for this study (Pt-1 cubic dominant, Pt-2 cuboctahedral dominant, Pt-3 octahedral dominant) (A). Performances of the three prepared catalysts compared with commercial Pt/Al_2O_3 as reference (B). Adapted with permission from ref. [537]. Copyright 2009 American Chemical Society.

Moreover, the chiral modifier has the role of transferring chirality to the reaction and it was observed that enantioselectivity increased with the increasing (111)/(100) ratio on the Pt surface with both CD and QN, thus octahedral NPs resulted superior in enhancing the enantiomeric excess. By DFT studies on the adsorption of CD on Pt surface, the authors further observed that rates and enantioselectivity were also strongly influenced by the adsorption mode of the cinchona alkaloids. The results suggested a stronger adsorption of CD on Pt(100) that made the chiral modifier more susceptible to hydrogenation of the aromatic ring, that is the part adsorbing to Pt, favouring desorption from the metal surface and deteriorating the overall performance.

Cross coupling reations

Carbon-carbon bond forming reactions are of paramount relevance for the construction of complex molecules starting from simple building blocks. One class of metal catalysed variation of these reactions are the cross coupling reactions. These organic transformations have had a great impact on the organic chemistry and have become fundamental in the industry and research, for the production of active ingredients, intermediates and fine chemicals at the extent that three chemists, Heck, Negishi and Suzuki, who first discovered these reactions, were awarded the Nobel prize in Chemistry in 2010. Heterogeneous cross coupling have been widely investigated since the last century,[539] although a big debate has risen over the effective solid phase promotion of these reactions.[540] Nowadays it is generally accepted the homogeneous nature of the reaction also with

the use of solid metal catalysts, which act as a reservoir for leached single atoms that catalyse the coupling in homogeneous phase.[541,542] Nevertheless, engineered NPs have been subjected to cross coupling during the last two decades with remarkable results for what concerns the activity. Even though not always explicitly stated, the following examples of NPs used in cross coupling are all affected by the leaching process, hence the activity is directly related to the sensitivity of the particles toward this phenomenon. One of the first studies on cross coupling with shaped Pt NPs was reported by El-Sayed and co-workers focusing on the shape evolution of the particles after being subjected to Suzuki coupling of phenylboronic acid with iodobenzene (Figure 1.60).[543] Nanoparticles enriched in tetrahedral shape (55 ± 4% regular tetrahedral, 22 ± 2% distorted tetrahedral, and 23 ± 2% spherical NPs) were used for this study revealing a morphological distortion already after the first recycle test. The shape evolution continued also in the second recycling test although less marked compared to the first cycle. Control experiments revealed that shape evolution was mainly promoted by iodobenzene that initiated the catalysis by oxidative addition to Pt surface atoms provoking the detachment and leaching. Conversely, refluxing of NPs in presence of phenylboronic acid only resulted in no morphology change.

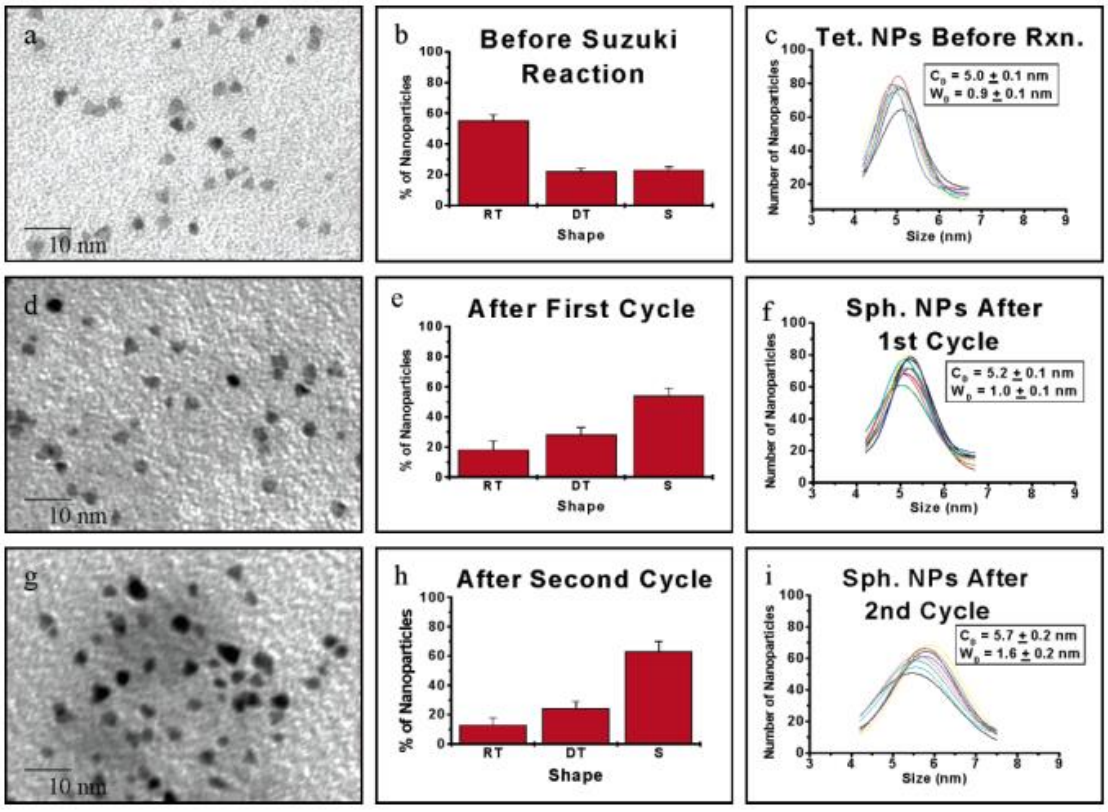

Figure 1.60. TEM micrographs, shape distribution (RT: regular tetrahedra, DT: distorted tetrahedra, S: spherical) and size distribution of the Pt NPs before catalysis (a-c), after first (d-f) and second (g-i) recycling tests. Reproduced with permission from ref. [543]. Copyright 2005 American Chemical Society.

Motivated by these findings, the same group expanded the study also to cubic and spherical Pt NPs comparing the behaviour with the previously reported tetrahedral NPs toward the electron transfer reaction between hexacyanoferrate (III) ions and thiosulfate ions and Suzuki coupling reactions.[93] Beside the study on morphology and activity evolution of shaped NPs, others have focused on the use of shaped NPs for the activity enhancement by enclosing the nanoparticle surface in facets displaying highly active metal atoms. In a systematic study, Xia and co-workers exploited high-index facets Pd concave nanocubes for the Suzuki coupling.[270] Concave nanocubes, enclosed in (730) high-index facets, exhibited a TOF 3.5 times higher than conventional Pd nanocubes toward the coupling of phenylboronic acid with iodobenzene. The higher reactivity of low-coordination number Pd atoms on concave nanocubes were more likely to be leached in solution with respect to atoms on cubic NPs. Another study by Holmes and McGlacken confirmed the importance of leaching for the promotion of coupling reactions by investigating the process in shaped Pd NPs. Here, cubic, cuboctahedral and octahedral NPs were employed as catalysts revealing a shape activity dependence that attributed to cubic NPs higher performance (Figure 1.61A).[544] Of course the enhanced activity was associated with the higher leaching susceptibility of cubic particles. On the other hand, size variations did not influence the activity as evinced by catalytic tests on 10 and 20 nm cubic NPs (Figure 1.61B). In addition, the authors found that molecular oxygen actively participates to the leaching process (Figure 1.61C) by delivering PdO in solution enhancing the global reaction rate.

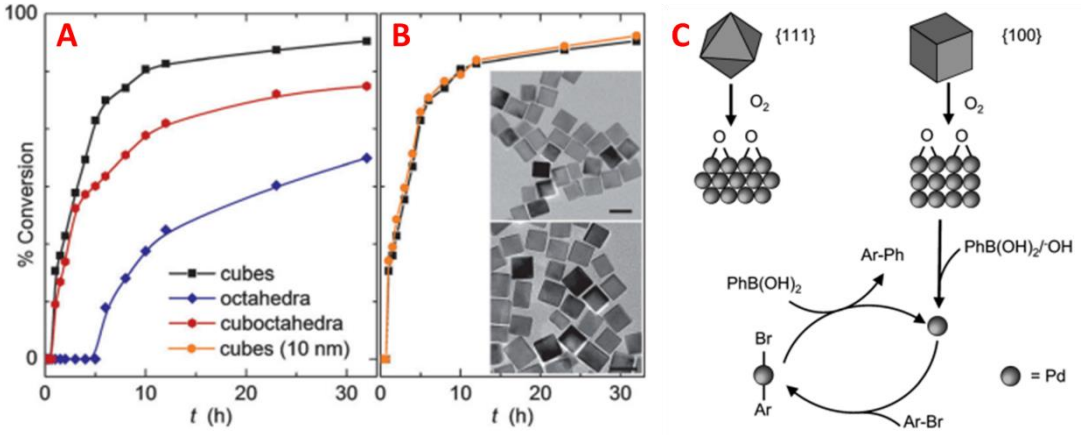

Figure 1.61. Conversion rates over time for shaped Pd NPs (A) and size effect tests on 10 and 20 nm cubic particles (scale bar: 20 nm)(B). Mechanism scheme for O_2-promoted leaching on Pd NPs (C). Adapted with permission from ref. [544]. Copyright 2014 Wiley-VCH.

Contrary to palladium or platinum NPs, the cross couplings reactions promoted by atomically precise ligand protected Au NCs are directly catalysed by the clusters themselves, therefore, these reactions can be considered heterogeneous. Jin and co-workers have pioneered the research line

based on the use of Au NCs in catalysis and have also studied coupling reactions, mainly promoted by Au_{25}.[545–548] The first example was reported for the promotion of Ullman coupling of aryl iodides by the use on $Au_{25}(PET)_{18}$ (Figure 1.62).[547] The Au NCs were first supported on various metal oxides (CeO_2, TiO_2, SiO_2, Al_2O_3) and tested for the coupling reaction; from the screening $Au_{25}(PET)_{18}/CeO_2$ system resulted the most active. The deposited Au NCs displayed a sizable activity also with substituted aryl iodides such as 4-iodoanisole, 1-iodo-4-nitrobenzene, 4-iodobenzaldehyde and 1-iodonaphtalene. Later on, the same group reported the Sonogashira coupling of substituted phenylacetylenes with 4-iodoanisole also promoted by $Au_{25}(PET)_{18}$.[548] Again the $Au_{25}(PET)_{18}/CeO_2$ resulted the most active delivering higher conversions and selectivities (cross coupling *vs* homocoupling) with respect to the cluster deposited on TiO_2, SiO_2 and MgO. Moreover, DFT modeling suggested a flat adsorption of the reactants on the open facet of Au_{25} with the aromatic rings facing an external gold atom. The adsorption energies of both reactants were strong enough (-0.40 to -0.48 eV) to activate them for the Sonogashira coupling. Sonogashira coupling reactions were also reported with Au NCs doped with Cu, Ag or Pt atoms.[549]

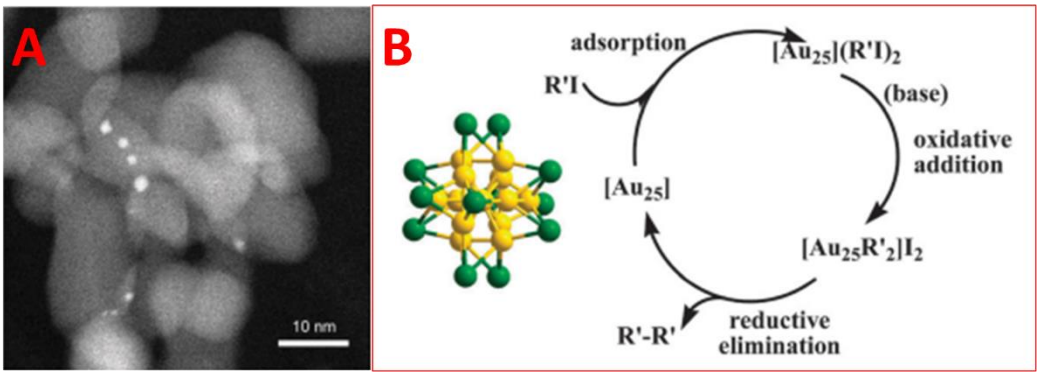

Figure 1.62. HAADF-STEM image of Au25 NCs supported on TiO_2 (A) and proposed catalytic cycle for the Ullman coupling of aryl iodides (B). Adapted with permission from ref. [547]. Copyright 2012 Royal Society of Chemistry.

Suzuki coupling reactions were also studied in presence of $Au_{25}(PET)_{18}$ supported on TiO_2 and ionic liquids (ILs) as solvent for the coupling of 4-iodoanisole with phenylboronic acid.[546] The reaction was tested with different solvents such as ethanol, xylene, toluene DMF and ILs with the latter giving higher conversion compared to the formers. With the use of 1-butyl-3-methylimidazolium X, with X = Br or Cl or BF_4 (BMIM X) the conversion increased up to 89-99% suggesting the ILs as promoter for the cross coupling reaction. Interestingly, the role of the counterion was pivotal in delivering high conversions since BMIM BF_4^- resulted in no conversion.

1.3.2. Electrochemical activation of small molecules

Noble-metal nanostructures are widely used catalysts for a large variety of electrochemical reactions, including those applied to the energy conversion devices such as fuel cells and metal-air batteries.[550] It is commonly accepted that the electrocatalyst's activity is affected by its interaction with the reactants and intermediates involved in the rate-determining step. Solid phase electrocatalysis on defined crystallographic surfaces has been extensively investigated along the decades by the use of single crystal metals,[551,552] however, a transition toward the use of metal nanostructures is in progress since the advent of nanotechnologies took place.[553–555] Nowadays metal nanoparticles are considered to be an optimal alternative to the use of single-crystal surfaces thanks to their superior surface area and to the possibility of controlling the expression of surface features. In this sub-chapter, different electrochemical reactions catalysed by well-defined metal NPs will be presented focusing on their performance.

Oxygen reduction reaction (ORR)

The ORR is a cathodic electrochemical transformation in which oxygen is reduced to water or hydrogen peroxide, very useful for energy production through the application in the proton-exchange membrane fuel cells (PEMFCs) or metal air batteries.[556] PEMFCs are seen as one of the most appealing alternatives for the production of green energy owing to the zero emissions and to the wide range of possible applications. Despite the advantages of such systems, the slow kinetics of the reaction demands a high quantity of material to be deposited on the cathode in order to generate a sufficient current density useful to power a device. The activity of the ORR is strongly related to the binding energy of the atomic oxygen intermediate (Figure 1.63A) resulting from the dissociation of molecular oxygen, as evinced by DFT calculations on various transition metals.[557] The volcano plot in Figure 1.63B shows the activity of various metals toward the ORR, with Pt being at the top. Despite the outstanding performance of this metal, Pt carries the drawback of being a scares metal which limits its use on large scale due to the unfavourable cost-effectiveness.

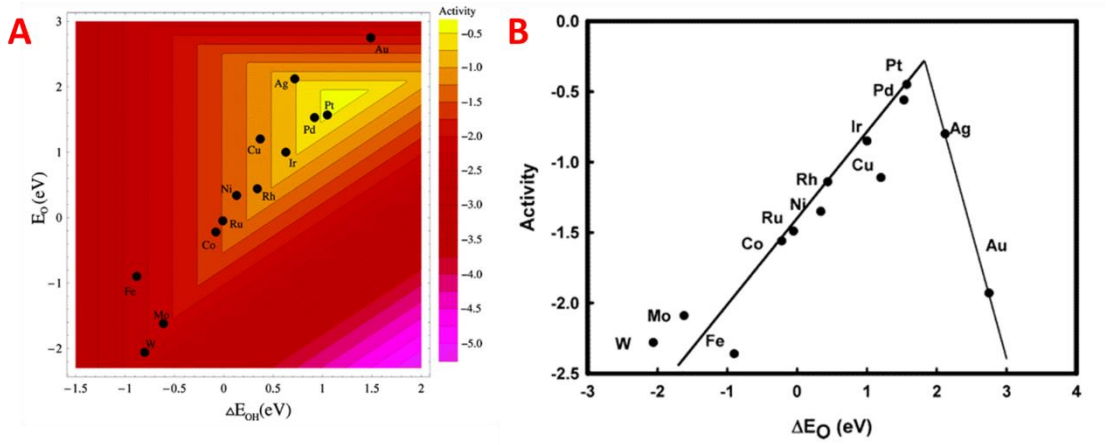

Figure 1.63. Trends in ORR activity of various transition metals as a function of both O and OH binding energies (A) and volcano plot for ORR activity as a function of O binding energy. Adapted with permission from ref. [557]. Copyright 2004 American Chemical Society.

One strategy to attenuate this issue relies on the use of engineered NPs as electrocatalysts; in particular, the arrangement of surface atoms alters the electronic structure of the particles consequently affecting the interaction with reactants. Studies performed on Pt single-crystal surfaces have demonstrated that the catalytic activity for ORR follows the trend of (100) << (111) < (110),[462] this was also corroborated by computational models that suggested a stronger binding energy of atomic oxygen on Pt(100), compared to Pt(111), which slows the removal of oxygenated species from the surface and lowers the catalytic activity.[558] In addition to the change in electronic structure, the reaction intermediates formed during the catalysis also differ depending on the surface. It was demonstrated that in acidic conditions generation of products went through the formation of HO_2• radical intermediate on Pt(111), whereas OH• radical was formed on both Pt(100) and Pt(110).[559] These studies suggested a central role of the surface structure in defining the proper electronic environment and reaction path for the improvement of catalytic activities. Encouraged by the results obtained with single-crystal electrodes, great effort has been made also with Pt NPs for the application in ORR.[560,561] One of the first studies on the comparison of shaped Pt NPs was reported by Wang *et al.* for the ORR catalyzed by Pt nanocubes, truncated nanocubes and nanospheres in 0.5 M H_2SO_4.[562] The authors reported the shape-dependent activity of the ORR ascribing the performance differences to the different adsorption energies of sulfate ions which was higher on Pt(111) compared to Pt(100) facets.

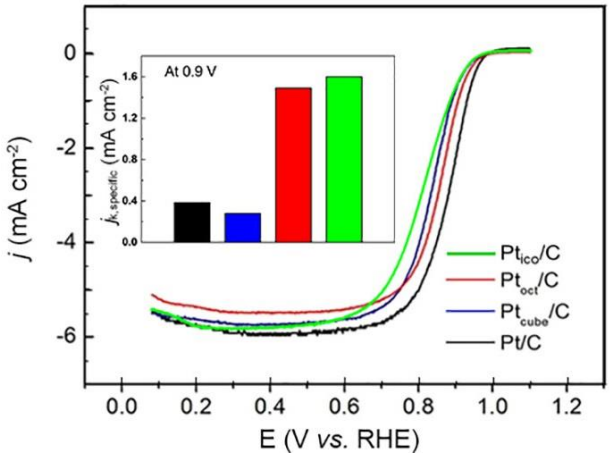

Figure 1.64. ORR polarization curves for cubic, octahedral and icosahedral Pt NPs compared with commercial Pt/C and their respective SAs (inset). Reproduced with permission from ref. 59 (Copyright 2021 American Chemical Society), ref. [212] (Copyright 2013 American Chemical Society), ref. [207] (Copyright 2017 Wiley-VCH) and ref. [213] (Copyright 2019 Wiley-VCH).

Pt nanocubes resulted in superior activity by 4 times compared to the spherical and truncated cubic NPs. The comparison of cubic,[212] octahedral[207] and icosahedral[213] Pt NPs highlighted different activities, with respect to commercial Pt/C, due to the facets exposed on the surface. Cubic nanocrystals had a specific activity (SA) 1.4 times lower with respect to commercial Pt/C while octahedral and icosahedral NPs showed enhanced SAs of 3.9 and 4.2 times higher, compared to commercial Pt/C, respectively (Figure 1.64). Although, octahedral and icosahedral NPs are both enclosed by (111) facets, the higher SA of the latter can be attributed to the presence of twin boundaries that cause tensile strain on the surface that additionally influence the electronic structure.

Beside NPs enclosed in low-index facets, those covered in high-index facets have also been explored for ORR. Pt concave nanocubes with (720) facets have been used for this purpose resulting in a very high SA that was 5.7 times higher that commercial Pt/C.[275] It must be pointed out that despite the outstanding SAs arising from shaped NPs, mass activity (MA) of these catalysts were usually only slightly higher or even lower to that of commercial Pt/C. This trend was attributed to the size of shaped nanocrystals which cannot be reduced to the size of commercial Pt/C that is a finely dispersed catalyst with NPs having size about 3-5 nm.

Other very interesting and appealing nanostructures for ORR are porous metals that exhibit a high surface area and increased number of active under-coordinated sites with respect to the non-porous counterparts. These nanostructures have been mainly explored for electrocatalytic applications.[563–566] Ullah *et al.* reported one of the first studies for ORR with porous Pt NPs protected by CTAB with marked activity.[303] Later on, Yu and co-workers studied the performances of Pd nanoflowers (NFs) and nanodendrites (NDs) demonstrating their superior activities compared to commercial

Pd/C.[565] SAs for NDs were reported to be 4.8 times higher with respect to commercial Pd/C while NFs had 2.6 fold SA compared to commercial Pd/C. Recently, Lu *et al.* reported the synthesis of porous Pt nanodendrites (NDs) with peculiar features arising from the use of halide ions (F^- and Cl^-) and tested the NPs for ORR (Figure 1.65).[566] Remarkably, both NPs resulted highly active for the activation of oxygen with NDs-F having MA 1.88-fold of NDs-Cl and 2.17-fold of commercial Pt/C. SAs followed the same trend with NDs-F 1.64 times higher than NDs-Cl and 4.14 higher than commercial Pt/C. Durability tests highlighted the good stress tolerance of NDs-F and NDs-Cl that after 5000 voltammetric cycles (CV) retained respectively 90% and 81% of the initial electrochemical surface areas (ECSAs) while commercial Pt/C retained 69% of initial ECSA.

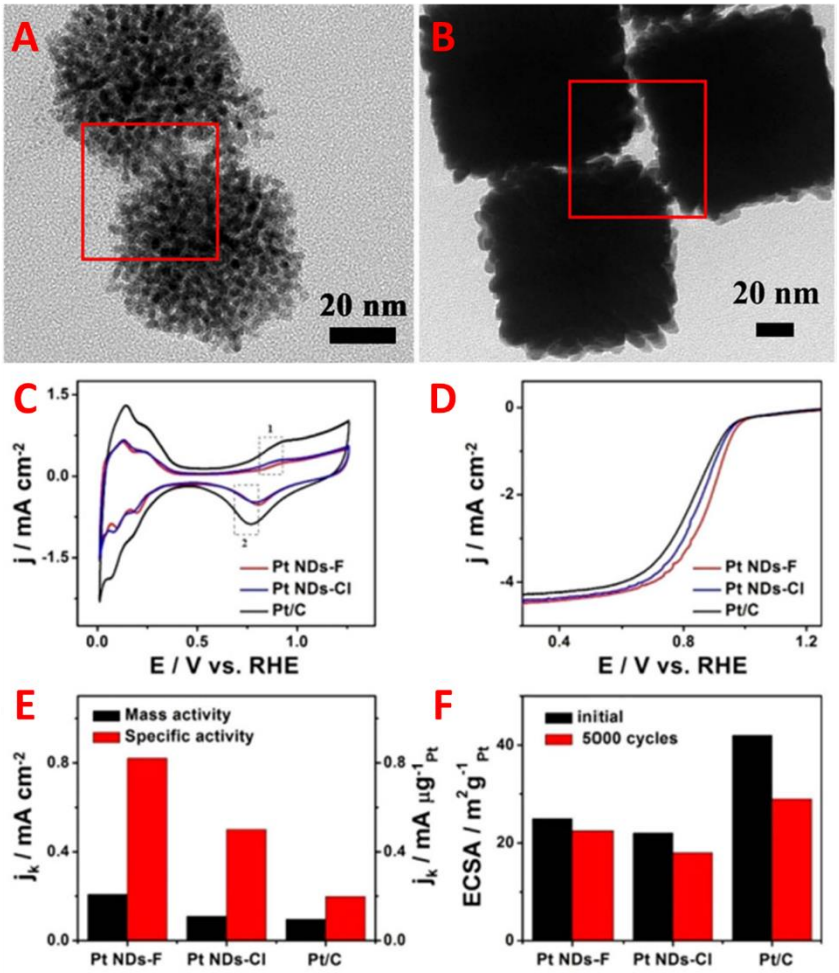

Figure 1.65. TEM images of Pt NDs-F (A) and Pt NDs-Cl (B) prepared in presence of F^- and Cl^- ions, respectively. CVs (C) and ORR polarization curves (D)for the Pt NDs and commercial Pt/C. MAs and SAs of the investigated Pt NDs compared with commercial Pt/C (E) and stress tests showing the initial and final ECSAs (F). Adapted with permission from ref. [566].

Metal NCs have also been subjected to the ORR with promising results thanks to their different electronic structure derived from the size confinement down to the sub-nanometric scale. Early studies on Pt NCs for ORR have been reported by Crooks and co-workers for a series of dendrimer stabilised NCs.[567,568] They subjected 1.4 nm Pt clusters, encapsulated in PAMAM dendrimers, to

ORR finding a stability up to 50 CV scans. In another work, the same group investigated the atomicity effect of Pt_n clusters (n: 55, 100, 147, 200, 240) on the activity for ORR with the larger clusters being more active.[567] Yamamoto *et al.* also reported studies on Pt_n clusters (n: 12, 28, 60) where the smallest Pt_{12} exhibited the highest activity for ORR (13 times higher than commercial Pt/C).[569] Clearly the catalytic activity of small NCs is not linearly dependent on the size and other factors may influence the overall behaviour such as number of surface atoms, edge structures and M-O binding energy. Contrary to Pt, Au NPs are less active in activating molecular oxygen, however, atomically precise Au NCs have demonstrated to be suitable for this reaction. For example, Wang *et al.* recently reported a study on the activities of carbon supported thiolate protected $Au_{25}(SR)_{18}$, $Au_{38}(SR)_{24}$ and $Au_{144}(SR)_{60}$ NCs toward ORR where an increasing trend in reactivity was observed with the decreasing of the NCs size.[570] Au_{25}^{q} NCs (q: -1, 0, +1) were also studied for the production of H_2O_2 in alkaline solutions with the use of a glassy carbon rotating ring-disk electrode (RRDE) to probe the formation of products (Figure 1.66).[571] CVs in saturated nitrogen electrolyte showed no reduction current for Au_{25}^{-} and a very marked change in current density was observed when oxygen was bubbled into the solution. In particular, a charge state dependence was observed on the activity with Au_{25}^{-} showing a more positive onset potential (-0.115 V) with respect to Au_{25}^{0} (-0.15 V) and Au_{25}^{+} (-0.18 V) and also a larger current density.

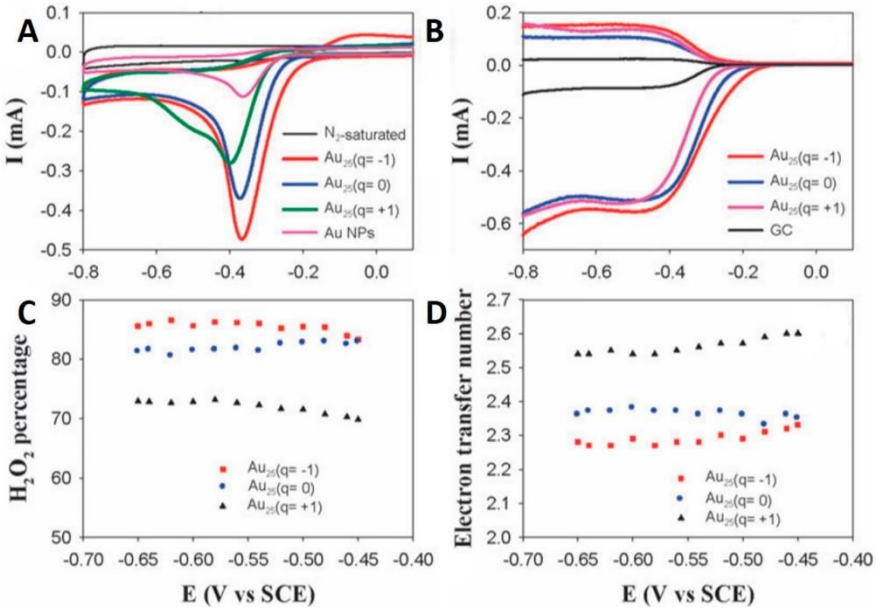

Figure 1.66. CVs or ORR for Au_{25} with different charge state compared to Au NPs (in 0.1 M KOH) (A). RRDE voltammograms in O_2 saturated 0.1 M KOH solution for blank glassy carbon and Au25 NCs supported on glassy carbon; scan rate 10 mV s^{-1}, ring potential 0.5 V, 1600 rpm (B). H2O2 percentage generation (C) and electron transfer number of Au_{25}^{q} as a function of applied potentials (D). Reproduced with permission from ref [571]. Copyright 2014 Royal Society of Chemistry.

Other studies reported for the ORR with protected or unprotected Au and Ag NCs can be found in literature deposited in supports and with remarkable activity.[572–576]

Alcohol oxidation reaction

Direct alcohol fuel cells are also a great alternative for the production of clean energy and, compared to hydrogen-based fuel cells are advantageous concerning the issue of storage, transportation and higher energy density. As for ORR also the anodic oxidation of alcohols is kinetically sluggish and demands for improved catalysts in order to be considered appealing. Palladium is the most active metal but its performance is strongly related to the surface structure, hence morphology-controlled (size and shape) Pd NPs are to be privileged when performing electrochemical alcohol oxidations. Various shaped Pd NPs have been reported with activities affected by the surface structure. For example, cubic, rhombic dodecahedral and octahedral Pd nanocrystals have been investigated for ethanol and ethylene glycol electrooxidation showing a dependence on the facets exposed.[577] For ethanol oxidation Pd nanocubes exhibited increased activity compared to the rhombic dodecahedral and octahedral NPs (Figure 1.67A). Computational analyses suggested that the improved activity of nanocubes is favoured by the lower activation energy barrier for the dehydrogenation of ethanol on (100) facets. In addition, durability test of the Pd NPs at 0.67 V for 1 hour showed an ECSA decrease to 59% with respect to the initial value for cubic particles while a drastic decay was observed for rhombic dodecahedral (82%) and octahedral (87%) NPs, respectively (Figure 1.67B). These results were validated by CO stripping and DFT calculations that attributed a superior stability to Pd nanocubes toward chemisorption of CO and other intermediate species. A similar trend in SAs and durability was also observed for the ethylene glycol electrooxidation.

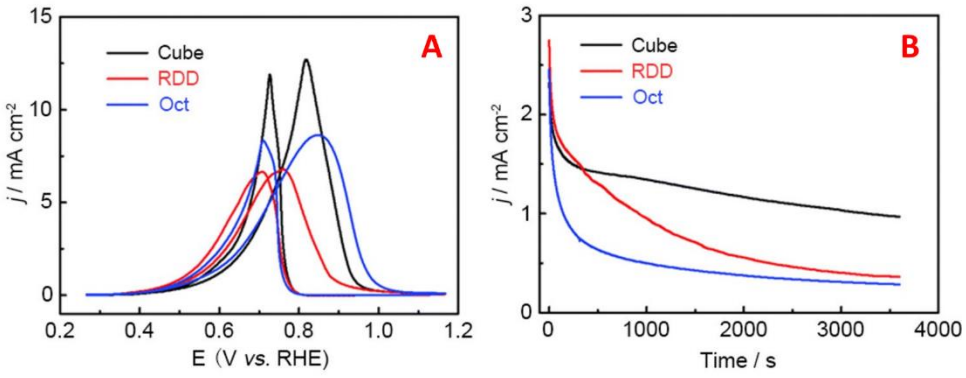

Figure 1.67. Ethanol electrooxidation CVs for cubic, rhombic dodecahedral (RDD) and octahedral Pd NPs recorded in 1.0 M NaOH + 1.0 EtOH (A) and chronoamperometric curves recorded at 0.67 V (B). Adapted with permission from ref. [577]. Copyright 2013 Royal Society of Chemistry.

In another interesting report, surfactant-free 3.5 nm Pt nanocubes were exploited for the oxidation of methanol and ethanol.[578] The reduced size and the clean surface delivered superior current densities when compared to commercial Pt/C catalyst. Stress tests also revealed a longer durability with respect to the commercial counterpart. The high resistance of these small nanocubes was attributed to the presence of (110) steps that easily adsorb HO• radical species that are very useful for the cleavage of carbonaceous intermediates on the surface that usually slow down the reaction rates. As for the ORR, porous metal NPs have been used also for the alcohol oxidation reaction. Many examples can be found in the literature, especially for the methanol and ethanol electrooxidation.[305,579–582]

Oxygen evolution reaction (OER)

Water splitting has gained a lot of attention in the last years owing to the possibility of generating O_2 and H_2 from renewable sources without the generation of by-products. The oxygen evolution reaction is the anodic half-reaction of water splitting where oxygen is produced by the recombined electrons in the cathode closing the circuit. Ruthenium is one of the metals of elections for the promotion of OER but its scarce abundance and the high price rise limit to its large scale use. Recently, Ru NPs with engineered facets and in fcc lattice phase were synthetised and applied in OER (Figure 1.68).[583] Concerning the phase influence, polycrystalline fcc Ru NPs resulted 1.4 times more active than hcp polycrystalline Ru NPs.

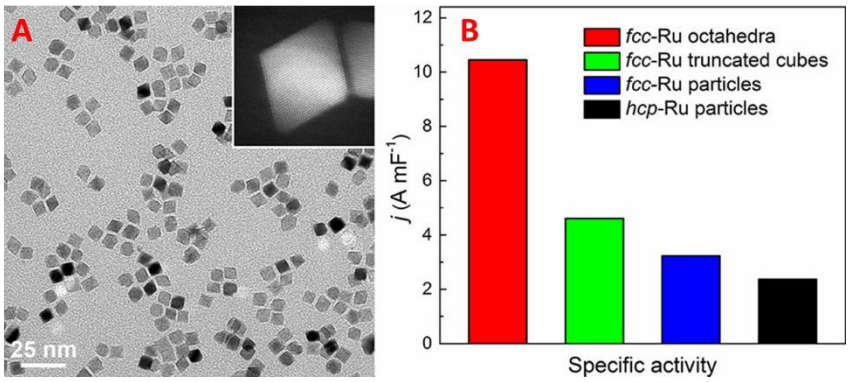

Figure 1.68. TEM image and HAADF-STEM (inset) of fcc octahedral Ru NPs (A). OER SAs for fcc Ru octahedra, truncated cubes, polycrystalline NPs and hcp polycrystalline NPs (B). Adapted with permission from ref. [583]. Copyright 2019 American Chemical Society.

Furthermore, fcc octahedral NPs with (111) facets displayed a SA 3.3 times superior compared to irregular fcc NPs suggesting a shape effect on the catalysis. Truncated cubes, in fcc phase, were also tested as catalyst for the OER showing an enhanced activity relative to the irregular fcc NPs but still lower to the fcc octahedral ones. From these results and considering a mix of (111)/(100)

facets exposed by truncated cubes, it was speculated that the Ru catalysed OER might be (111) facet-dependent. Together with Ru, also Ir is very promising in promoting the OER. Despite the lower activity compared to Ru, Ir relies on a striking stability that makes this metal appealing. Apart conventional polyhedral NPs, exotic shaped ones are gaining much attention because of the peculiar features and/or the high specific surface areas. This is the case, for instance, of Ir nanocages that are engineered hollow nanocubes with a surface structure optimized for the atom utilization efficiency. The employment of these nanocages, enclosed in (100) facets with walls of 1.1 nm in thickness, displayed in OER an extremely high performance.[584] The Ir nanocages, in 0.1 M $HClO_4$, required an overpotential of 0.074 V lower than that of commercial Ir/C catalyst to give a current density of 10 mA cm^{-2} (Figure 1.69A). SA and MA of Ir nanocages were 26.2 and 18.1 times higher compared to the commercial catalyst (Figure 1.69B). Finally, durability test performed on both catalysts resulted in a 40% ECSA loss for Ir nanocages and 90% loss for the commercial counterpart after 5000 cycles.

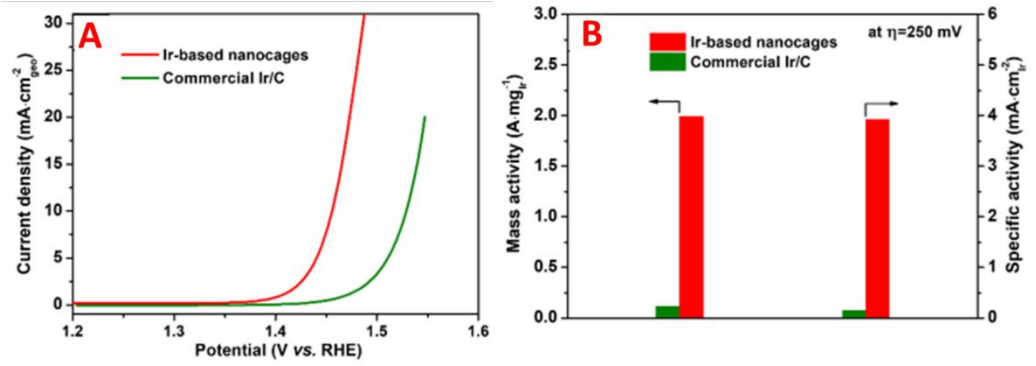

Figure 1.69. Water oxidation polarization curves recorded for Ir nanocages and commercial Ir/C (A). Mass and specific activities for both Ir nanocages and commercial catalyst at 250 mV. Adapted with permission from ref. [584]. Copyright 2019 Wiley-VCH

Hydrogen Evolution Reaction (HER)

The HER is the cathodic half-reaction in water splitting and probably is the most appealing electrocatalytic reaction considering that the generated hydrogen can provide energy for different devices in a green way. Platinum is considered to be one of the most performing metals (Figure 1.70) for HER with fast reaction kinetics and minor overpotentials (in acidic electrolyte) if compared to other metals.[585]

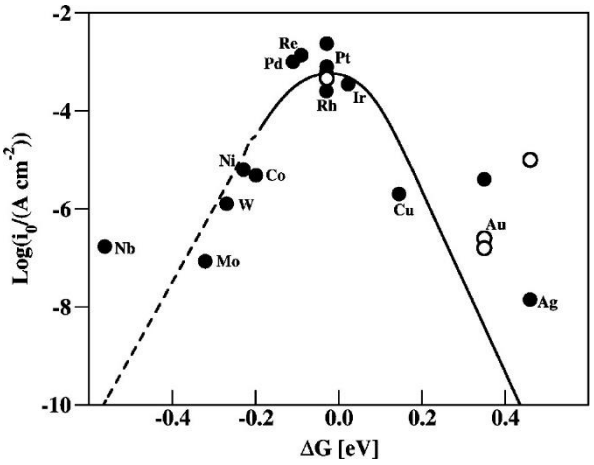

Figure 1.70. Volcano plot for the exchange current density of various metals applied as catalysts in HER as a function of free energy of H adsorption. Metals on the left side are subjected to high H coverage (1 monolayer) while metals on the right side have low H coverage (0.25 monolayer). Reproduced with permission from ref. [585]. Copyright 2010 American Chemical Society.

However, the activity of Pt can decay by 2 orders of magnitude when switching to alkaline solutions.[586] This decrease in activity is caused by the additional water-dissociation steps and the weaker binding energy of H_3O^+ to the metal surface in alkaline media.[586] Therefore, for HER in alkaline electrolytes Pt catalysts are preferred to be replaced by more active metals. Rhodium has risen as one of the best candidates for the activation of H_2O toward HER and the change of activity from acidic to alkaline medium was less relevant compared to Pt which makes Rh a valid catalyst at a large pH range.[587] An interesting study regarding the use of shaped Rh NPs was reported by Huang and co-workers on the use of tetrahedral, concave tetrahedral NPs and nanosheets for HER in 0.1 M KOH.[267] The NPs catalytic activities of these NPs were compared to a commercial Rh/C reference showing improved performances. Specifically, the overpotentials (at 10 mA cm^{-2}) for tetrahedra, concave tetrahedra and nanosheets were reported to be 0.016, 0.014 and 0043 V lower with respect to the commercial Rh/C. In addition, faceted Rh NPs exhibited a remarkable improvement in stress tests. After 5 hours of chronoamperometries at 5 mA cm^{-2} the commercial Rh catalyst presented an increase in overpotential to 0.193 V, whereas tetrahedral and concave tetrahedral NPs slightly increased to 0.122 and 0.168 V, respectively. Of note, for Rh nanosheets an increase in overpotential to only 0.065 V was reported after the 5 hours of chronoamperometric test. These data suggested the critical role of engineered facets in achieving higher performances and stabilities.

1.3.3. Photocatalysis for energy production with metal NCs

Photocatalysis has gained much attention in the last period thanks to the idea of promoting reactions without the need of thermal energy or electrical current sources and has become very relevant in the context of green transition. Solar energy is considered one of the alternatives to fossil fuels as it has infinite availability. In the field of chemistry, light becomes relevant when a material, a photocatalyst, is able to harvest the energy deriving from photons and exploit this energy for chemical transformations. Materials of this kind already exist and have been developed and engineered at the research level and applied in industrial processes. One of the most appealing branches of photocatalysis is the energy production, mainly focused to hydrogen, from biomass-derived oxygenated sources or water. Photocatalytic reactions for hydrogen production are mainly performed in heterogeneous systems with photo-responsive solid materials. Probably the most used and extensively studied photocatalyst of this kind is TiO_2.[588,589] The peculiar properties of titania derive from its semiconductor character that makes it suitable for various applications. The electronic properties of a semiconductor are characterized by its valence band (VB) and conduction band (CB). The VB is formed by the interaction of the highest occupied molecular orbital (HOMO), while the CB is formed by the interaction of the lowest unoccupied molecular orbital (LUMO). The energy range between CB and VB is denoted as bandgap (E_g). The band structure, including the bandgap and the positions of VB and CB, is one of the important properties for a semiconductor photocatalyst, because it determines the light absorption property as well as the redox capability of a semiconductor. When photons, equal or greater in energy respect to the bandgap, are absorbed by the semiconductor the electrons from VB will be excited to the CB creating electron-hole pairs. These electron-hole pairs can give origin to three different processes: can migrate to the semiconductor surface, can be trapped by defects in the bulk or surface and can recombine releasing thermal energy. Charge separation is extremely important for the determination of activity in a photocatalyst. Different strategies can be applied to improve the charge separation based especially on the material synthesis in order to have the minor percentage of defects or based in the introduction of a co-catalyst.[590–593] In this paragraph photocatalytic systems for the production of hydrogen and based on metal co-catalysts modification will be discussed, with a particular focus on NCs.

Since the first study reported in the ’80 providing experimental evidence for the hydrogen production over Pt deposited on TiO_2,[594] various investigations have been carried out on the Pt/TiO_2 photocatalytic activity. Most of these studies have been focused on the preparation method of the catalysts[595] and also on the size effect of Pt NPs.[596] Au has been also investigated as a co-catalyst on

titania for hydrogen production,[597,598] although its efficiency is lower by 30% when compared to platinum.[595] Beside Pt and Au, other metals have been used as co-catalysts for H_2 production including Pd, Rh, Ru, Ir, Ag, Ni, Co and Cu.[599,600] In general, for photocatalytic systems based on the use of metal co-catalysts a size-dependent activity has been observed,[601] with increasing performances at smaller sizes of the co-catalyst. Hence, the use of metal NCs as co-catalysts in photocatalytic systems can be seen as a promising approach toward the improvement of hydrogen production. Indeed, various metal NCs have been studies and employed as semiconductor dopants in photocatalysis, especially for water splitting applications. In order to examine the size effect at the atomic level on photocatalysis, Berr *et al.* relied on Pt NCs with various sizes deposited on CdS nanorods for the study of hydrogen evolution reaction.[602] They found a coverage of 30 NCs per CdS nanorod as minimum loading amount for a high quantum efficiency (QE), while Pt NPs decorating the CdS nanorods displayed lower H_2 production with respect to the clusters, even at high NPs loading. Pt_{46} was found the most performing NC and after deeper investigations on the same system with Pt_8, Pt_{22}, Pt_{34}, Pt_{46} and Pt_{68} the authors established a trend for the activity going from $Pt_8 \approx Pt_{22} < Pt_{34} < Pt_{68} < Pt_{46}$ (Figure 1.71A).[603] The justification for this kind of trend was found in the LUMO position of the clusters, that was fundamental in the electron capture and transfer process for the formation of hydrogen. A suitable LUMO position must be lower than the CB of the semiconductor and higher than the reduction potential of H^+ / H_2 (Figure 1.71B). Among all the Pt NCs in this study Pt_{46} had the proper LUMO energy, thus also the higher catalytic activity.

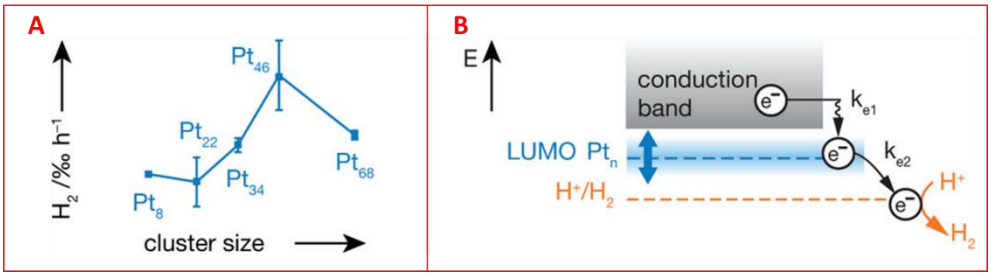

Figure 1.71. Photocatalytic hydrogen evolution trend for the Pt_n NCs (A) and energy level position diagram of the CdS CB, Pt_n LUMO, and H^+/H_2 (B). Reproduced with permission form ref. [603]. Copyright 2013 American Chemical Society.

Although Pt NCs have been widely employed for the photocatalytic hydrogen evolution, they lack in optimal performances as they can also catalyse the oxygen evolution side reaction. Nevertheless, Pt NCs with higher oxidation states (PtO) deposited on TiO_2 have been found to be very efficient in supressing this side reaction.[604] The selectivity of PtO was ascribed to the oxygen dissociation inefficiency of the PtO with respect to metallic Pt.

Regarding the hydrogen evolution from oxygenated molecules, Llorca and co-workers reported a size-dependent study on the photocatalytic hydrogen evolution from aqueous ethanol catalysed by

Pt clusters.[605] The authors prepared Pt NCs of 0.9-1.7 nm in dimension by wet impregnation onto TiO_2, followed by hydrogen reduction and tested the photocatalysts for the ethanol dehydrogenation reaction from a 50/50 %vol ethanol/water. They observed a non-monotonic trend in the performance increase with the cluster size with 1.7 nm Pt NCs being the most active.

Atomically precise Au NCs have also been exploited in photocatalysis. Negishi and co-workers have reported a photocatalytic system with unprotected Au_{25} as co-catalyst deposited on $BaLa_4Ti_4O_{15}$ for hydrogen evolution from water splitting (Figure 1.72A).[606] First, Au_{25} protected by glutathione ligands were mixed with the support to ensure full adsorption followed by calcination at 300 °C (in vacuo) to remove the thiolate ligands. The as-prepared materials were catalytically active and produced both H_2 and O_2 in equal amounts; the activity was then compared to conventional Au NPs supported on $BaLa_4Ti_4O_{15}$ indicating a 2.6-fold higher activity for the Au_{25} NCs with respect to NPs. The same group also studied the size effect on the photocatalytic water splitting of $Au_n(SG)_m$ NCs with n: 10, 15, 18, 22, 25, 29, 33, 39.[607] After deposition on $BaLa_4Ti_4O_{15}$ and calcination for ligand removal, the clusters were carefully selected based on the aggregation-agglomeration effect during calcination. Au_{10}, Au_{15}, Au_{18}, Au_{25}, and Au_{39} (group 1) displayed no dimensional changes while Au_{22}, Au_{29}, and Au_{33} showed a clear increase in size (group 2). From catalytic tests all the Au NCs displayed good activity, superior to Au NPs on the same support, and a trend correlating the increasing performance toward hydrogen production with decreasing size of the NCs could be established (Figure 1.72B). The authors attributed this behaviour to the percentage of exposed metal atoms on the surface, which is higher on the smaller clusters, considering an equivalent amount of metal loading.

Other studies on metal NCs acting as co-catalysts in photocatalytic hydrogen evolution can be found in literature, both in ligand-on and ligand-off modes.[608–610]

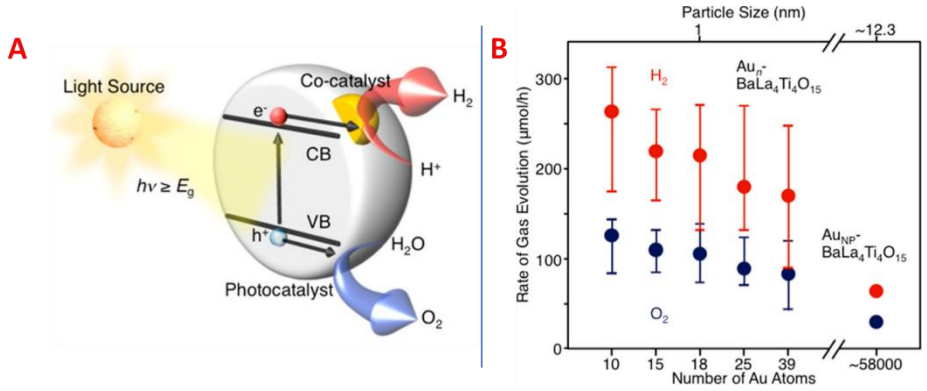

Figure 1.72. Schematic illustration for the photocatalytic hydrogen production from water splitting catalyzed by semiconductor/co-catalyst system (A) and hydrogen and oxygen evolution performances of Au_{10}, Au_{15}, Au_{18}, Au_{25}, Au_{39} and Au NPs supported on $BaLa_4Ti_4O_{15}$. Adapted with permission from ref. [607]. Copyright 2015 American Chemical Society.

2. Characterization techniques

In this chapter, a brief description of the experimental techniques used in the following studies is reported. Different techniques were used to characterize the nanomaterials from a morphological, structural and textural point of view.

2.1.Transmission electron microscopy techniques

In the nanotechnology field and in particular in catalysis performed with nanostructures, the design of materials with enhanced catalytic properties often relies on the precise identification of the active sites. Hence, accurate imaging methods that allow the investigation at the nanometric and atomic level are of paramount importance. Among many characterization techniques, electron microscopy is pivotal in getting information on nanostructured materials and on the components of the material itself. By using modern electron microscopes it is possible to directly observe small NPs, clusters and even single atoms of a sample and their dimensional distribution along with the morphology. Transmission electron microscopy (TEM) techniques easily overcome the limitations of a light microscope for the imaging of small objects thanks to the higher resolution. The resolution on a microscope is defined as the minimum distance between two distinguishable objects in an image and it is related to factors: aberration and diffraction. Aberration is explained by geometrical optics and is limited by enhancing the optical quality of the instrument. Diffraction, on the other hand is tangled to the nature of the wave used for the observation. If considering diffraction only, the maximum theoretical resolution that a microscope can achieve is related to the radiation wavelength, according to the Rayleigh criterion, that puts the resolution limit of any imaging process to the order of the wavelength used. This concept implies that the maximum theoretical resolution of a light microscope is not suitable for the characterization of typical nanomaterials. Contrary, the resolution of an electron microscope is adequate in achieving nanoscale resolution and the maximum theoretical resolution can be obtained referring to the de Broglie's wavelength of the particle:

$$\lambda = \frac{h}{p} \qquad (2.1)$$

where p is the particle momentum, λ is the particle wavelength and h is the Planck's constant. In the TEM instrument the electrons are accelerated by a potential drop, V, acquiring a potential energy eV that is converted to kinetic energy of the electrons at the end of the accelerating section. Equating the two energies the momentum as a function of the potential can be defined:

$$eV = \frac{1}{2} m_0 V^2 \tag{2. 2}$$

$$p = \sqrt{2 m_0 eV} \tag{2. 3}$$

The value of λ can be obtained by substituting equation 2.3 in equation 2.1. For instance, an electron accelerated to 100 keV has a wavelength of about 0.004 nm, that is 100 times smaller than the diameter of an atom. In addition, increasing the accelerating voltage, the electron's wavelength will decrease. However, it must be highlighted that equations 2.2 and 2.3 do not consider the relativistic effect that cannot be neglected for energies above 100 keV. Moreover, practical limitations relative to the microscope construction must be taken into account such as the aberration limits and the homogeneity of the magnetic lenses. Nevertheless, atomic scale resolution is achievable by the use of modern instruments like aberration corrected TEM (AC-TEM) in which spatial and spectral resolution is significantly improved, even when using low accelerating voltages (Figure 2.1).[611]

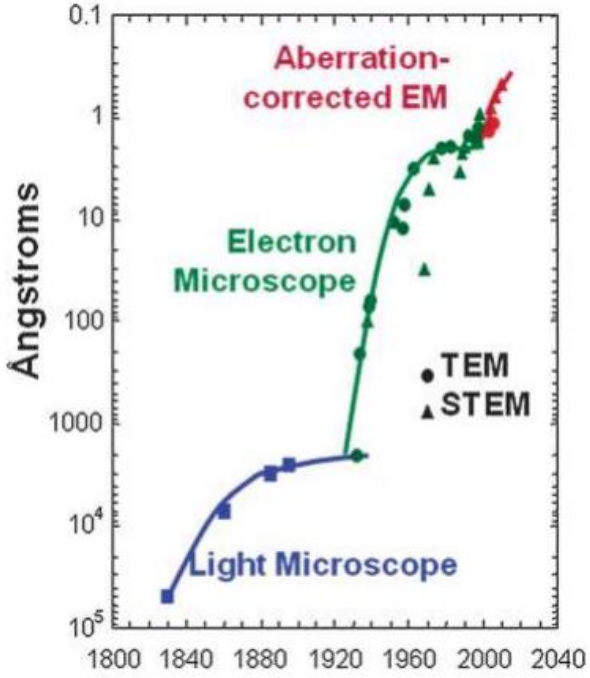

Figure 2.1. Spatial resolution along the years for microscopy instruments.

The achievement of higher resolutions at lower accelerating voltages is particularly advantageous when visualising samples that are sensitive to structural changes under the electron beam.

A typical TEM instrument consists of a vertical column in which an electron beam is generated from a source placed at the top; the electrons are directed at the bottom of the column and in their path hit the sample that is positioned in a sample holder perfectly aligned with the beam (Figure 2.2). The column is kept in ultra-high vacuum (UHV) in order to reduce the scattering effect generated from electrons interacting with gas atoms. Electromagnetic coils, having the function of lenses, are positioned along the column and have the function of focusing and aligning the beam. Apertures of different diameters can be inserted in the column at various positions to narrow the beam spot. Two common types of electron sources are used in a TEM instrument that are thermionic emission source and field emission gun (FEG) and they are characterized by the way electrons are generated. After electrons are generated, they are accelerated by an electrostatic field before entering the column; the strength of the field determines the electron kinetic energy .

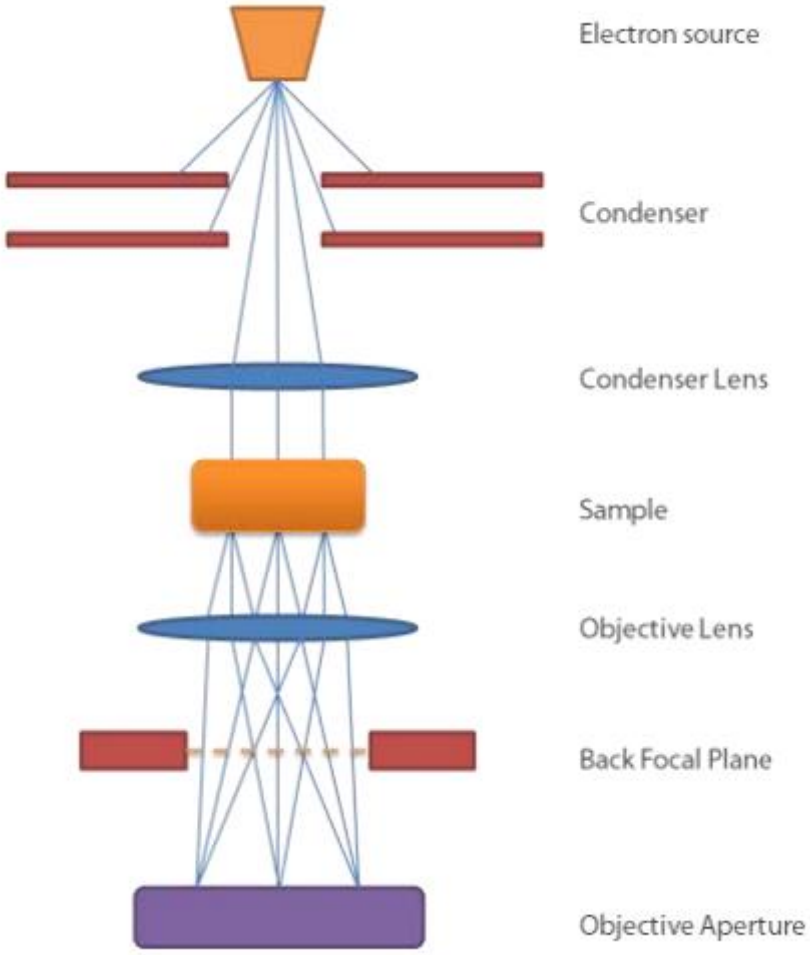

Figure 2.2. Schematic representation of a TEM column.

The condenser apertures and lenses system select and focus the electrons and set the beam diameter to a desired value, then the beam passes through the sample. The incident beam interacts with the internal crystal structure of the sample generating diffracted and non-diffracted electrons. These electrons are focused by another lens to the back focal plane (BFP). In this plane a diffraction pattern is formed in which every spot is related to the reflection of crystal planes in one particular orientation. Images and diffraction patterns are visualized on a fluorescent screen and may be digitally recorded using a camera positioned below this screen. Usually, only a specific area of the sample is selected to contribute to the diffraction pattern in order to reduce the intensity of the diffracted electrons reaching the camera sensor avoiding damage issues. Usually this is performed by focusing the beam with the lenses or by reducing the aperture above the sample. This operation generates the so called selected-area electron diffraction (SAED). After the diffraction pattern area is selected, it is possible to perform two basic imaging operations by selecting the central diffracted electrons or the scattered electrons with detectors positioned at different angles (Figure 2.3). Images collected from the direct diffracted electrons result in bright field (BF) mode while those collected from the scattered electrons result in dark field (DF) mode. The BF detector is aligned to the transmitted electrons while the DF detector is annular and surrounds the BF detector. Another detector, positioned at very high angles with respect to the transmitted beam, can be mounted on the TEM instrument for high-angle annular dark-field (HAADF) mode. In this acquisition method, the detector captures inelastically scattered electrons or thermal diffuse scattering at high angles (50 to 200 mrad). The HAADF acquisition is performed in STEM mode displaying the integrated intensities of the electrons in synchronism with the incident probe position. The signal strength of the high angle scattered electrons is proportional to Z^2 (Z: atomic number), thus making the technique useful particularly for the detection of heavy-metal particles. The HAADF image is easily interpreted as no multiple scattering is involved because the scattering cross section of the thermal diffuse scattering at high angles used for the imaging is negligible and the interference effect of the electrons does not take place for the imaging. The resolution of the HAADF image is almost determined by the incident probe diameter on the specimen. HR-TEM is the working mode of the instrument that consists in the application of high voltages to enhance the resolution. This technique is very useful for the characterization of crystallinity, defect structure, morphology and symmetry. However, the technique presents some limitations related to the high voltage used that might damage the sample or to the purity and thickness of the sample that initiate multiple diffraction phenomena. In addition, HR-TEM images are still 2-D representations of 3-D structures and some morphological information cannot be completely acquired. Recent developments in electron tomography and quantitative STEM have further improved the TEM abilities in reconstructing 3-D

models of the investigated nanomaterials.[612] STEM mode is another way of performing microscopic analyses that consist in scanning a focused convergent beam over the sample by using a system of additional lenses. The STEM mode has the advantage of generating images with low noise.

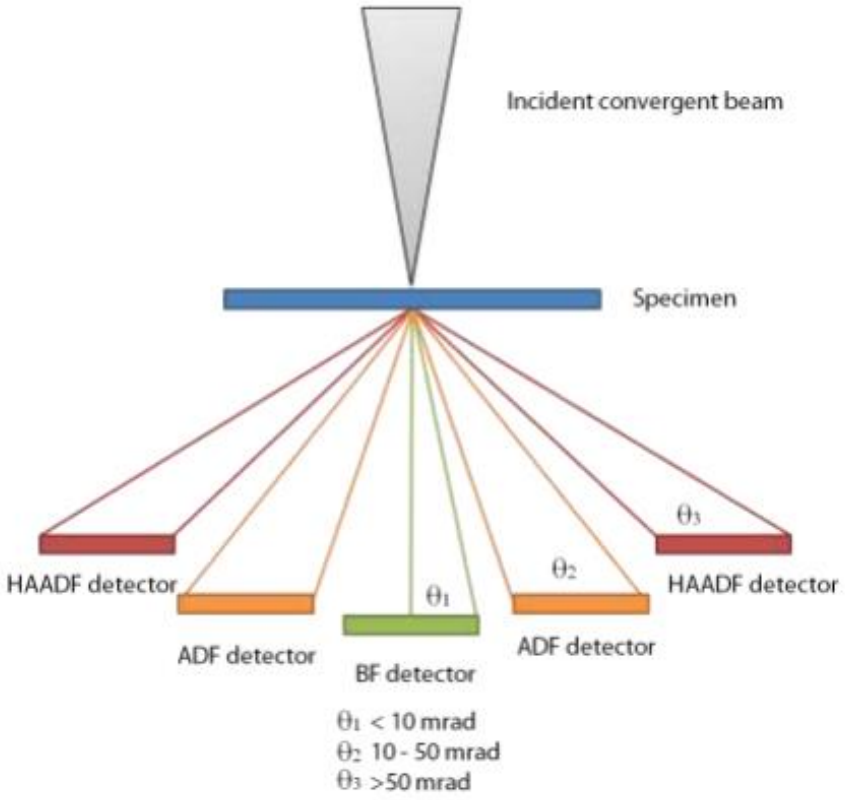

Figure 2.3. Schematic representation of the various detectors present in a TEM instrument based on the angle of collected electrons.

Inelastic interactions of the electrons with the sample, in which energy is transferred, can provide useful complementary information about the composition. Energy transfer from an incoming high energy electron to core electrons of the atom's sample may result in the ionization of the atom itself forming a hole that can recombine with higher energy level electrons releasing the excess under x-ray photons that are characteristic of the atom's nature from which it was emitted. In x-ray energy dispersive spectroscopy (EDX) these photons are collected and counted to build a spectrum of the elemental composition of the sample.

2.2 Physisorption

The activity of a solid phase catalyst (heterogeneous) is closely related to its surface morphology and area. Hence, reactions catalysed by heterogeneous materials occur on active sites distributed along the surface that are accessible to the reactants. If the porosity of the material is appropriate with pore diameters large enough to allow reactants and products diffusion, then the activity of such material will be proportional to the identified active sites. On the contrary, if pores are too narrow (particularly the pore entrance) the reaction will be limited by mass transport and governed by diffusion. In this latter case, the activity of the material could be independent from the surface area or dependent to its square root, based on the diffusion mode. Thus the pore structure design and identification of a heterogeneous catalyst is very important when considering the enhancement of its activity and selectivity. For instance, a particular pore structure may induce a "shape selectivity" to a reaction by limiting the diffusion of one specific reactant or product. Porous character and texture can even vary in the same material, depending on the treatments it was subjected, and pores can vary in shape and dimension as-well. Pores can be divided into three groups on the basis of their dimensions:

- micropores, with diameter smaller than 2 nm
- mesopores, with diameter between 2 and 50 nm (typically amorphous materials)
- macropores, with di diameter larger than 50 nm

Surface area measurements

Among all the known methods for the determination of surface areas in solid nanostructured materials, the most used is the volumetric method. This method is widely used for surface area analyses on various materials such as ceramics, adsorbents and catalysts. The volumetric method relies in measuring the adsorption of an inert gas on the solid surface at a pre-determined constant temperature as a function of the partial pressure of the used gas. An important prerequisite for the correct application of this technique is the choice of the gas that must have a weak interaction with the investigated material, in order to consider only physical interactions. This analysis gives a physisorption isotherm as output and based on the isotherm shape it is possible to extrapolate surface area and pore distribution data, according to empirical equations and adsorption models. Since physisorbed gas molecules are not confined to specific sites on the solid material, they are free to diffuse and cover all the accessible exposed surface. Furthermore, since the interactions that lead to gas adsorption are reversible, the analysis results completely non-destructive or invasive and

do not modify the analysed surfaces. Because of reversibility of the gas-solid interaction both adsorption and desorption processes can be studied. Moreover, as multiple layers of gas adsorbate can be formed, the pore volume can be measured if the amount of gas needed to completely fill the pores can be extrapolated. According to the IUPAC recommendations, physisorption isotherms can be categorized in six types (Figure 2.4A).[613]

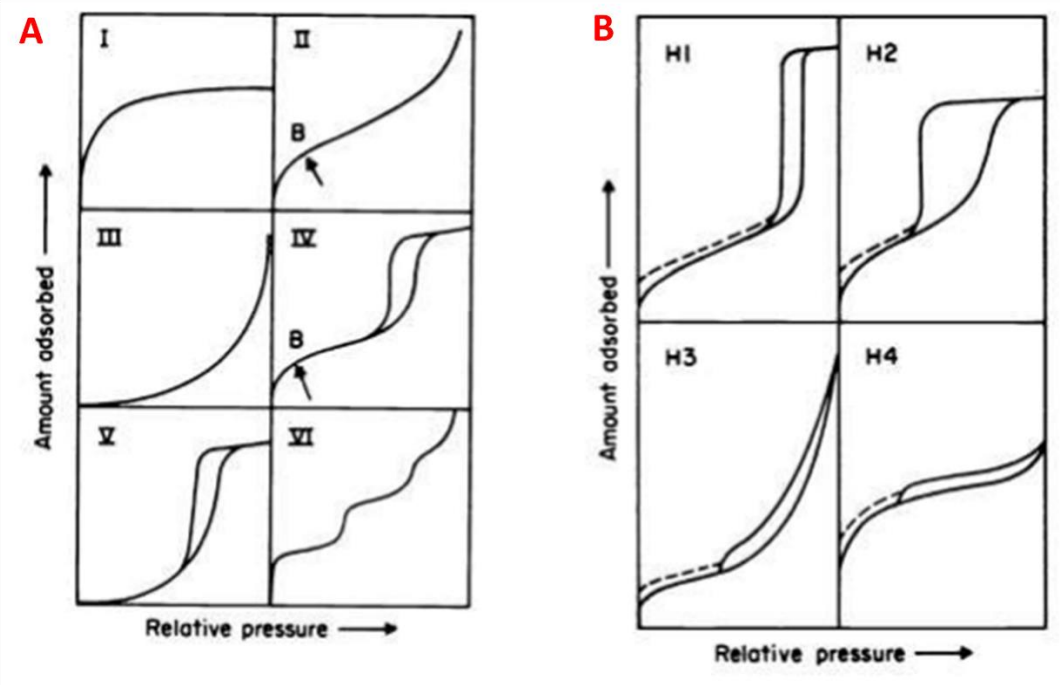

Figure 2.4. Types of physisorption isotherms (A) and hysteresis loops (B) according to the IUPAC classification. Reproduced with permission from ref. [613]. Copyright 1985 IUPAC.

The standard physisorption isotherms can be categorized as follows:

- Type I isotherms are generated by microporous materials with relatively low external surfaces such as activated carbon and zeolites.
- Type II isotherms are common for non-porous or macroporous materials in which unrestricted monolayer-multilayer gas adsorption occurs.
- Type III isotherms are considered to be rare. These isotherms are convex to the relative pressure axis along all their entire range and are not useful for surface area data extrapolation. The adsorbate gas may be replaced by another one to get a more useful isotherm.
- Type IV isotherms are common of many industrial adsorbents. The hysteresis loop present in these isotherms is associated to capillary gas condensation in the mesopores and can differ depending on the pore geometry.

- Type V isotherms are also uncommon and related to type III ones, with a weak adsorbent-adsorbate interaction.
- Type VI isotherms describe stepwise multilayer gas adsorption and are typical for uniform non-porous surfaces.

The hysteresis loop is also relevant in determining the pore distribution of a material and according to IUPAC four types can be described (Figure 2.4B). H1 type results from compact agglomerates of uniform spherical particles with monodisperse size and disposition, while H4 type is common for adsorbents constituted of bidimensional particles. H2 and H3 hysteresis types are usually observed for intermediate situations. However, hysteresis loops are not easily classified as most materials display a random shape and pore size distribution.

To determine the total surface area of a material by volumetric method, a monolayer of adsorbed gas must be achieved and detected from the isotherm shape. This is obtained only for isotherm type I, II and IV. For type I, the gas adsorption is described by the Langmuir equation:

$$\frac{V}{V_m} = \frac{bp}{1 + bp} \tag{2.4}$$

where p is the gas pressure, b is a constant derived from kinetic principles and is related to the temperature and adsorption heat, V is the adsorbed gas volume and V_m is the volume of adsorbed gas needed for the formation of a theoretical monolayer on the material surface. For the determination of V_m the Langmuir equation can be rearranged as:

$$\frac{p}{V} = \frac{P}{V_m} + \frac{1}{bV_m} \tag{2.5}$$

Therefore, a $\frac{p}{V}$ *vs* p plot can be obtained that gives a straight line and the slope of which is $\frac{1}{V_m}$.

For type II and IV isotherms, the Langmuir equation is not suitable as multilayer coverage takes place. The monolayer coverage may be extrapolated by referring to the ordinate value of the isotherms inflection, known as point B in Figure 4A. The point B method is appliable only if the initial isotherm section is defined by a sharp change of the curvature. Otherwise, a sophisticated analysis of the isotherm is needed and the surface area can be determined applying the Brunauer-Emmet-Teller (BET) theory. The BET model assumes the adsorption as a reversible process consisting in the stacking of infinite gas molecule monolayers with the most external layer in equilibrium with the vapor phase. On the basis of this consideration the BET equation is derived:

$$\frac{p}{V(p^0 - p)} = \frac{1}{V_m C} + \frac{C - 1}{V_m C} \cdot \frac{p}{p^0} \quad (2.6)$$

where p is the gas pressure, p^0 is the saturated vapor pressure of the liquid at operating temperature, V is the volume of adsorbed gas, V_m the volume of monolayer coverage and C the BET constant, dependent on the temperature and gas used for the analysis. Plotting $\frac{p}{V(p^0-p)}$ vs $\frac{p}{p^0}$ gives a straight line as output in the range of $0.05 < \frac{p}{p^0} < 0.35$, with the slope and intercept value used to determine the monolayer coverage volume. Once V_m is known, the surface area can be obtained from:

$$S = \frac{V_m}{V_{mol}} \cdot N_A a_m \quad (2.7)$$

where V_{mol} is the molar volume of the adsorbate, N_A the Avogadro number and a_m is the area of one adsorbed molecule (0.162 nm^2 for N_2 at liquid nitrogen temperature).

Pore volume and diameter

Many methods have been developed for the measurement of pore distribution, however, in this study, the gas adsorption method will be used. This method relies on the physisorption process and in particular is focused on the capillary condensation of the adsorbate that occurs at lower pressure with respect to the saturation pressure of the gas. For common cylindrical pores the capillary condensation is described by the Kelvin equation:

$$ln\frac{p^0}{p} = \frac{2V\gamma\, cos\, \alpha}{rRT} \quad (2.8)$$

with V is the molar volume of the gas, α is the contact angle of the liquid on the pore surface, γ is the surface tension of the liquid, r is the radius of the pore, R is the cas constant and T the operating temperature. From this equation, the pore size distribution can be obtained by the volume of adsorbed gas as a function of pore diameters (calculated for each $\frac{p^0}{p}$). This relationship also gives insight on the hysteresis loop formation and relates it to the pore shape. Indeed, in cylindrical pores, for instance, the capillary condensation occurs at the same partial pressure both in adsorption and desorption processes. The hysteresis is caused by the gas evaporation at lower $\frac{p^0}{p}$ values during

desorption, with respect to values in condensation during adsorption. This discordance in values is justified by the bottleneck geometry of the pore entrance that have smaller diameter compared to the internal pore diameter. Although the Kelvin equation is robust in describing the pore distribution, it is not sufficient for the correct interpretation of experimental data obtained via gas adsorption method. Hence other models describing pore structure in nanomaterials are needed. Different model have been developed along the decades however they can drastically differ one from the other based on the pore size range in which they can be applied. One of the most common used methods was developed by Barret, Joyner and Halenda (BJH method) and describes mesopore distributions. By examining the physisorption isotherm between $0.40 < \frac{p^0}{p} < 0.98$ (in which monolayer formation and gas saturation in the pores occur) it is possible to extrapolate the mesopore volume and pore size distribution.

2.3 Chemisorption

Chemisorption analyses are based on a specific interaction between a probe gas molecule and the material subjected to analysis. Usually chemisorption is applied to metal catalysts in which information about the active phase (metal) are extracted. The probe molecule must be able to chemically react with the metal, producing a single layer of chemisorbed molecules. By measuring the volume of the consumed gas for the monolayer formation it is possible to obtain active surface area and the dispersion of the metal in the support. A typical chemisorption isotherm is represented in Figure 2.5.

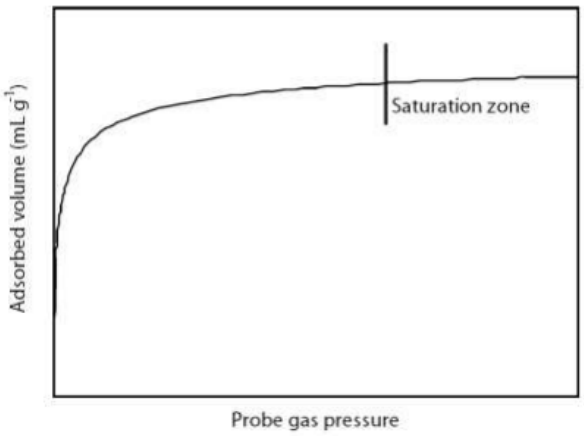

Figure 2.5. Representative chemisorption isotherm.

The number of surface metal atoms $N_{(S)M}$ and the active metal surface area S_M can be obtained from:

$$N_{(s)M} = n\frac{V}{V_m}N_A \quad (2.9)$$

$$S_M = N_{(S)M}a_M \quad (2.10)$$

where V is the volume of adsorbed gas, V_m is the gas molar volume, N_A is the Avogadro number, a_M is the cross sectional area of a single metal atom and n is the stoichiometry of the chemisorption reaction that represents the number of metal atoms needed to bind a single gas molecule.

The most commonly used gasses for chemisorption are hydrogen and carbon monoxide, although other gasses can be employed. The gas choice depends on the metal nature and on the support in which the metal is deposited. Generally the chemisorption stoichiometry with hydrogen is assumed to be 2 as hydrogen dissociates on the surface with each hydrogen atom binding one metal atom. Contrary, when CO is used, the stoichiometry is assumed to be 1 even though is some cases the stoichiometry can vary, like in the case of small metal NPs where geminal di-carbonylic species can be formed on under-coordinated metal atoms.[614] Similarly, hydrogen stoichiometry may also be different especially for extremely small particles (< 1 nm) or because of the formation of metal hydrides and spillover effects on reducible oxides.[615] These phenomena must be considered when performing chemisorption analyses and during data evaluation.

In the case of non-dissociative adsorption (CO gas), the Langmuir equation can be applied, assuming a constant chemisorption energy:

$$n_{a\,ds} = \frac{n^m_{a\,ds}bp}{1+bp} \quad (2.11)$$

where $n_{a\,ds}$ is the quantity of adsorbed gas at pressure p, $n^m_{a\,ds}$ is the quantity of gas needed for the monolayer formation and b is a constant. The saturation limit should correspond to a horizontal plateau in the high gas pressure region; however, this is not always observed as subsequent gas monolayers may be formed by physical adsorption generating an upward increment in the isotherm. In this case, the first monolayer volume can be obtained by extrapolating to zero pressure the linear portion of the isotherm. Another method can also be applied to find the monolayer volume that consists in subtracting the physisorption contribution from the chemisorption one: this is done by first measuring the total isotherm composed by both chemisorption and physisorption contributions,

then the system is evacuated to remove physisorbed gas molecules leaving only the chemisorbed monolayer that is measured by a second analysis. The difference of the two isotherms gives the irreversible adsorption that, by extrapolation to zero of the linear section, determines the monolayer volume associated to the chemisorbed gas. From the chemisorbed volume the metal dispersion (D%) can be obtained along with the average particle diameter d_{part}. To obtain these descriptors, the particle shape must be specified. Assuming a spherical shape for the metal particles:

$$D\% = \frac{N_{(s)M}}{N_{(tot)M}} \tag{2. 12}$$

$$d_{part} = 6\frac{V_M}{a_M} \cdot \frac{N_{(tot)M}}{N_{(S)M}} = 6\frac{V_M}{a_M} \cdot \frac{1}{D\%} \tag{2. 13}$$

where $N_{(S)M}$ is the number of surface metal atoms, $N_{(tot)M}$ is the total number of metal atoms, 6 is the geometrical factor for spherical particles and a_M is the area of one metal atom. V_M is the volume of a metal atom and it can be calculated as:

$$V_M = \frac{MW}{\rho N_A} \tag{2. 14}$$

with MW being the atomic weight of the metal and ρ its density.

2.4 Powder x-ray diffraction (XRD)

X-ray crystallography is a well-established technique for the structure investigation of nanomaterials. XRD is based on the diffraction phenomenon that occurs when x-ray photons are scattered by crystallographic lattice planes. The intensity of the diffracted photons is maximum when a constructive interference occurs, described by the Bragg's law as:

$$n\lambda = 2dsin\theta \tag{2. 15}$$

with n being the diffraction order, λ the wavelength of the incident x-ray, d is the interplanar spacing and θ is the incident angle of the beam.

The x-ray diffractograms obtained by this technique give information about several important properties of a material such as the crystallinity, the crystallite size and the atomic constituents of

the unit cell. The crystallite size is extrapolated from the peaks geometry, in particular from the broadening degree, by applying the Scherrer's equation:

$$\tau = \frac{K\lambda}{\beta \cos\theta} \quad (2.16)$$

where τ is the crystallite mean size, K is a constant related to the peak shape, λ is the x-ray wavelength, β is the full width at half maximum (FWHM) and θ is the Bragg angle.

According to the Scherrer's equation, reflections with larger FWHM are a direct indicator of small crystallite size. Based on the same principle, amorphous materials display no sharp reflections but only broad bands due to the absence of long-range order. However, it should be mentioned that this equation is not always reliable as the reflection broadening may be caused by a variety of other factors besides crystallite size. Other factors contributing to peak broadening may be dislocations, grain boundaries, stacking faults, residual stress and impurities. In addition the β value may be affected by instrumental factors.

2.5 X-ray absorption spectroscopy

X-ray absorption spectroscopy (XAS) is a useful technique employed for the study of local geometric and electronic structure of the matter. XAS measures the energy-dependent fine structure of the x-ray absorption coefficient near the absorption edge of a specific element. According to Beer's law, when incident x-rays hit a sample with intensity I_0, the extent of adsorption will depend on the photon energy *E* and the sample thickness *t*.

$$I_t(t) = I_0 e^{-\mu(E)t} \quad (2.17)$$

Where I_t is the transmitted intensity and $\mu(E)$ is the energy-dependent x-ray absorption coefficient. At larger energy regions, $\mu(E)$ varies approximately as:

$$\mu(E) \approx \frac{dZ^4}{mE^3} \quad (2.18)$$

where *d* is the target density, *Z* the atomic number and *m* the atomic mass.

Therefore $\mu(E)$ decreases with increasing photon energies. However, if the photon energy is equal or bigger than the core electron binding energy, another core electron can be excited and a sharp increase in absorption coefficient is observed. Above the absorption edge, the difference between

photon energy and binding energy is converted to kinetic energy of the photoelectron and $\mu(E)$ keeps decreasing with increased photon energy. Core-hole states have a very short lifetime (10^{-15} s), after which an electron from a higher energy state compensates the hole and releases the energy difference via fluorescence X-ray or Auger electron emission.

According to quantum mechanical perturbation theory, the transition rate between the core level and the final state is proportional to the product of the squared modulus of the matrix element M and the density of states ρ:

$$\mu \propto |M|^2 \rho \propto |\langle f|H_\rho|i\rangle|^2 \rho \qquad (2.19)$$

where |i⟩ and |f⟩ are the initial and final state, respectively, and H_ρ is the x-ray photon electromagnetic field, the Hamiltonian that causes the transition. Both factors can cause a modulation of the absorption coefficient thus creating the x-ray absorption fine structure (XAFS). At the smallest x-ray energies for which the photon can be absorbed, the photoelectron will be excited to unoccupied bound states of the absorbing atom. This can lead to a strong increase of the absorption coefficient at particular X-ray energies corresponding to the energy difference between the core level and the unoccupied states (pre-edge absorption bands). For higher x-ray energies, the photoelectron is promoted to a free or continuum state. The wave consequently created propagates and is scattered at neighbouring atoms. The emitted and scattered waves interfere in ways that depend on the geometry of the absorber environment and on the photoelectron wavelength, which is inversely proportional to the photoelectron momentum and therefore changes with photon energy. Hence, the final state is an energy-dependent superposition of emitted and scattered waves. Because the initial state is highly localized at the absorbing atom, the matrix element *M* in equation (2.19) depends on the magnitude of the final state wave function at the site of the absorbing atom. Thus, constructive or destructive interference of emitted and scattered waves affect the absorption probability, creating an energy-dependent fine structure of the absorption coefficient. Figure 2.6 displays schematically the absorption fine structure as a function of photon energy. Three regions are commonly distinguished: the pre-edge region, the x-ray absorption near edge structure (XANES) and the extended x-ray absorption fine structure (EXAFS).

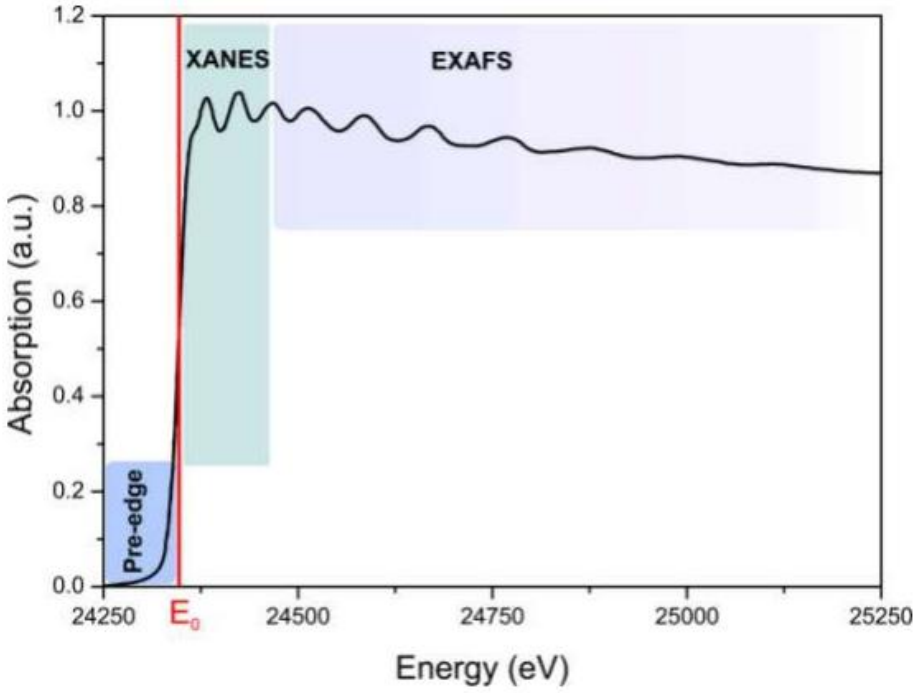

Figure 2.6. Example of a XAS spectrum with the pre-edge, XANES and EXAFS regions highlighted.

XANES is distinguished by photoelectron transitions to unoccupied states and is susceptible to the chemical bonding and depending on it can exhibit features for different oxidation states of the absorbing atom. The XANES features are also affected by strong multiple scattering effects that depend on the local geometry around the absorbing atom. This provides information for the discrimination of different crystal phases. Although great advances have been reported recently, theoretical calculations of the fine structure in the XANES region are intricate and the reliability of such simulations is still limited. Consequently, the acquired spectra are usually compared to known standards and the percentages in which the standards describe the sample are given by linear combination fitting.

In the EXAFS region (photon energies above 30 eV after the edge), the core electron is promoted to a continuum state and the signal depends on the neighbouring environment of the absorbing atom. EXAFS spectra contain information related to the coordination number, interatomic distances in a material, structural and thermal disorder nearby specific species. EXAFS can be advantageous if compared to XRD in giving structural information as the former technique do not require long-rage order to extrapolate useful information. Theoretical models on fine structure for EXAFS have been implemented as-well with great accuracy, however, as for XANES, also EXAFS analyses still rely on standard materials measurement for data fitting. XAS experiments are usually carried out at synchrotron facilities due to the specific requirement of high x-ray intensities and a wide range energy spectrum. In a typical XAFS beamline, x-rays are selected with narrow energy bands by the

use of a double crystal monochromator and Bragg diffraction criteria. Harmonic energies are subtracted from the beam by synchronised detuning of the double crystal that reduces the transmission of the harmonics without losing the primary energy. Otherwise, mirrors can be employed to discard energies below a set value. With this kind of experimental set-ups, the absorption coefficient can be measured as a function of x-ray energy. Generally, the absorption coefficient can be obtained either by the direct measure of the incident and transmitted beam intensities (transmission mode) (Figure 2.7A) or by the measure of the incident photons and the decay ones like fluorescence photons or Auger electrons (fluorescence or electron yield mode) (Figure 2.7B, C).

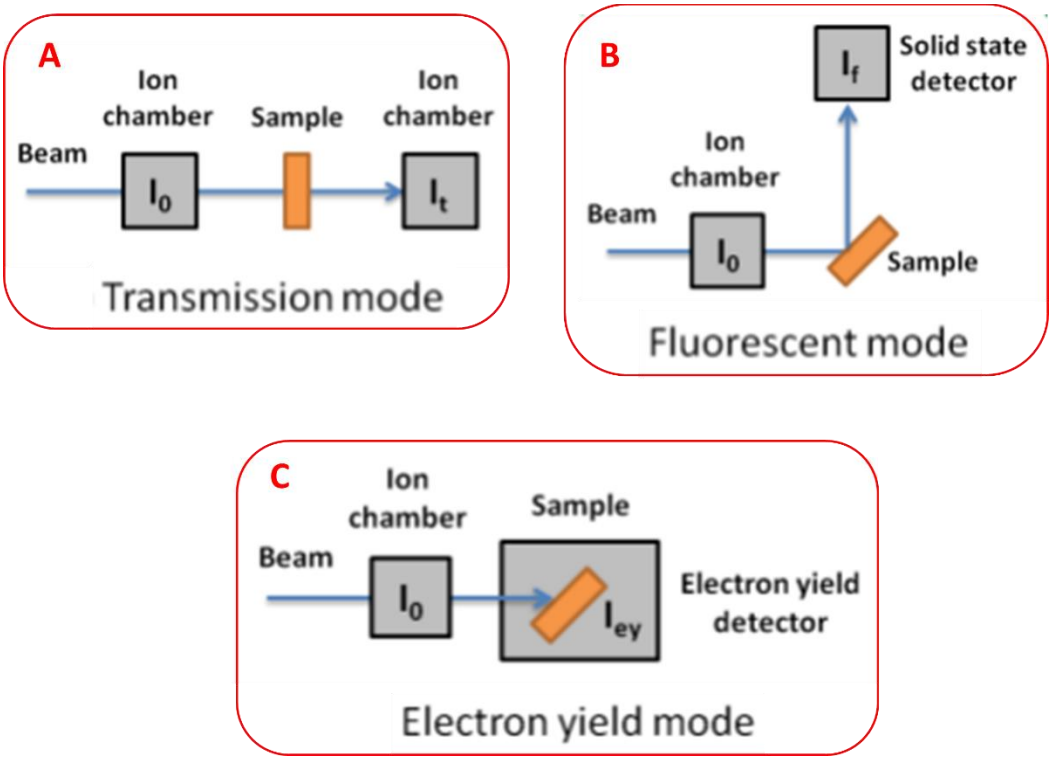

Figure 2.7. Schematic representations of different experimental set-ups for the three detection modes in XAS measurements.

After data acquisition, mathematical analysis must be performed in order to extrapolate the useful information. In general, XANES and EXAFS data are processed separately due to the different information contained in the respective spectral regions. The energy scale adjustment and spectra alignment is important for a correct data interpretation: in XANES for the edge shifts determination and in EXAFS for precise bond length extrapolation. For different absorption edges, the monochromator must be calibrated with a reference which usually consists in a metal foil measured together with each sample. In XANES, prior to fitting process, normalization of the spectrum must be performed in order to remove sample thickness and concentration perturbations improving the comparison of different samples. The region before the absorption edge is usually fitted by linear

pre-edge line, while above the edge, the data is approximated to a quadratic post-edge line. The difference between pre-edge and post-edge lines at the threshold E_0 provides the edge step $\Delta\mu_0$. The normalization of XANES spectra is performed by subtraction of the pre-edge line from measured spectra over the whole energy range and division by $\Delta\mu_0$ prior to levelling the spectrum after the threshold. The relative quantity (in percentage) of the components of interest can be extracted by fitting the normalized spectra with a linear combination of the reference compounds. EXAFS analysis, on the other hand, requires more processing steps. First, the fine structure X(E) is obtained from the absorption background by fitting the pre- and post-edge lines. The pre-edge is subtracted from the experimental spectrum at every energy value and the background $\mu_0(E)$ is approximated by a spline function that approaches the post-edge line at energies over the absorption edge. The difference between absorption coefficient $\mu(E)$ and the background $\mu_0(E)$ is normalized toward $\Delta\mu_0$, resulting in the fine structure X(E). To find X(k) the threshold energy E_0 is needed: this is typically considered as the maximum of the derivative of $\mu(E)$ toward E or as the energy value determined at half height of the step. Following, a Fourier transform (FT) into R-space is applied. EXAFS FT provides information on the scattering contributions. Different scattering contributions, with significant difference in R_j, when subjected to FT result in distinct peaks with amplitudes proportional to N_j/σ_j. However, the FT is an intricate function and for a full and correct interpretation, both real and imaginary part must be considered when processing data. A back-transformation can be applied to recognise different scattering contributions if their signals are well defined in R-space. Unfortunately, this practise usually fails for higher coordination shells due to scattering overlay. To surmount this issue, the path fitting approach can be applied. This approach is based on the cumulative expansion of various single and multiple scattering paths and needs additional pre-existing information about the investigated system. The analysis starts with a built model of the structure in which absorbing atom, position and nature of the neighbouring atoms are specified and included in the fitting process. The great advantage of the path fitting approach resides in the ability to give information about structural parameters beyond the first coordination shell.

2.6 X-ray photoemission spectroscopy

Photoemission spectroscopy usually denotes techniques that measure the kinetic energy and number of photoelectrons emitted from a material (sample) by the photoelectric effect, in order to obtain information about the oxidation state of the species of interest and their relative abundance in the investigated sample. Due to the short inelastic mean free path of the photoelectrons in matter,

photoemission spectroscopies give reliable composition information only at the surface and nearby (1-10 nm thickness); hence, these techniques are relevant in the study of catalytic materials. X-ray photoemission spectroscopy (XPS) is one of the most common techniques of its kind and its chemical analysis power derives from the small chemical shifts possessed by electron core levels that depend on the chemical environment of the ionised atom. XPS analyses give information about the formal oxidation state of atoms, the nature of the nearest neighbours and the hybridization state to the nearest neighbour atoms. This technique is commonly used to study inorganic compounds, alloys, semiconductors, catalysts, organic-inorganic hybrid nanostructures and so on. One major drawback of XPS is that it works at high vacuum (10^{-8} millibar) or ultra-high vacuum ($<10^{-9}$ millibar) conditions that limits its use for in-situ catalysis studies. However, improvements have been made, and modern set-ups have been developed that allow measurements at near ambient pressure (NAP-XPS) (tens of millibar). Another issue related to XPS measurements is the x-ray or vacuum degradation that can cause modifications of the sample during analysis. Analyses are usually performed using conventional XPS systems equipped with Al Kα or Mg Kα x-rays source, alternatively experiments can be carried out with synchrotron-based light source and analysed by special custom-designed electron energy analysers (SRPES). As the energy of an x-ray with precise wavelength is known (1486.7 eV for Al Kα sources) and the kinetic energies of emitted electrons are measured in analysis, their binding energy can be obtained by applying the energy conservation equation:

$$BE = E_p - (E_k + \Phi) \tag{2. 20}$$

with *BE* being the electron binding energy, E_p is the x-ray photon energy, E_k the photoelectron kinetic energy (measured during analysis) and Φ is the work function. The work function considers the small photoelectron's kinetic energy released as surplus that is absorbed by the detector; practically the work function is a fixed constant parameter that rarely needs to be adjusted. The output of an XPS experiment is a spectrum of the detected photoelectrons (counts) as a function of their BE. Each element has a characteristic set of XPS peaks at precise BE ranges that are related to the electronic configurations in the atoms. The number of photoelectron counts is proportional to the amount of the investigated element in the XPS sampling volume, thus a (semi-)quantitative analysis can be performed, upon normalization and correction by a relative sensitivity factor. However, the quantitative accuracy is influenced by various factors such as signal to noise ratio, signal intensity, sample homogeneity, energy dependence corrections on the electron mean free path and sample degradation during analysis. An XPS apparatus (Figure 2.8) is constituted by various parts that include the x-ray source, a pre-chamber for sample introduction a main chamber (kept in

UHV by a series of turbomolecular vacuum pumps), electron collection lenses, an electron energy analyser (composed by two hemispherical conductive magnets for electron selection) and a detector composed by an electron multiplier.

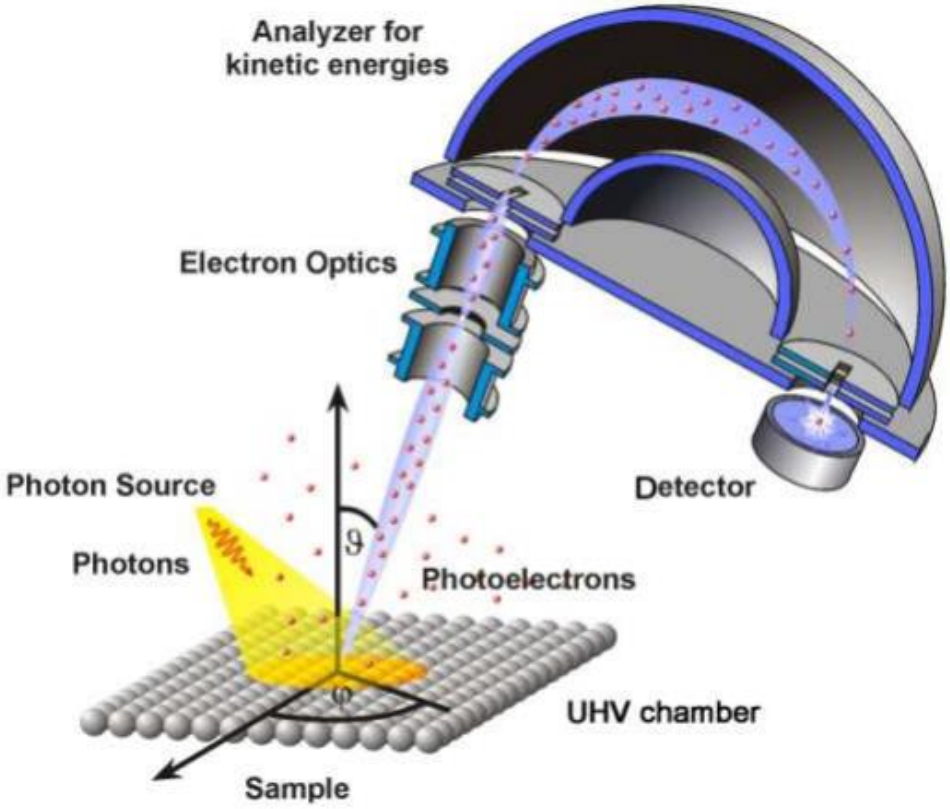

Figure 2.8. Schematic representation of a XPS instrument.

2.7 Photocatalytic reactor line

The photocatalytic activity of the Au_n/TiO_2 and the benchmark catalysts was studied under simulated solar light irradiation in the UV-VIS-NIR range using a Solar Simulator LOT-Oriel, equipped with a 150 W Xe lamp and an atmospheric edge filter with a cut-off at 300 nm. Irradiance was ~ 25 mW cm^{-2} in the UV range (300-400 nm) and ~ 180 mW cm^{-2} in the VIS-NIR range (400-1050 nm). The photocatalytic system is depicted in Figure 2.9. The reactor consisted in a Teflon-lined stainless steel reactor, connected to inert gas line, hermetically sealed with a quartz glass window and thermostated at 20 °C. The photocatalyst is dispersed in 96% ethanol by magnetic stirring at a fixed stirring rate. The generated hydrogen was streamed out of the reactor with an Ar flow of 15 mL min^{-1} and its concentration was measured with an Agilent 7890 gas chromatograph

equipped with a TCD detector, connected to a Carboxen 1010 column (Supelco, 30 m x 0.53 mm ID, 30microm film) using Ar as gas carrier.

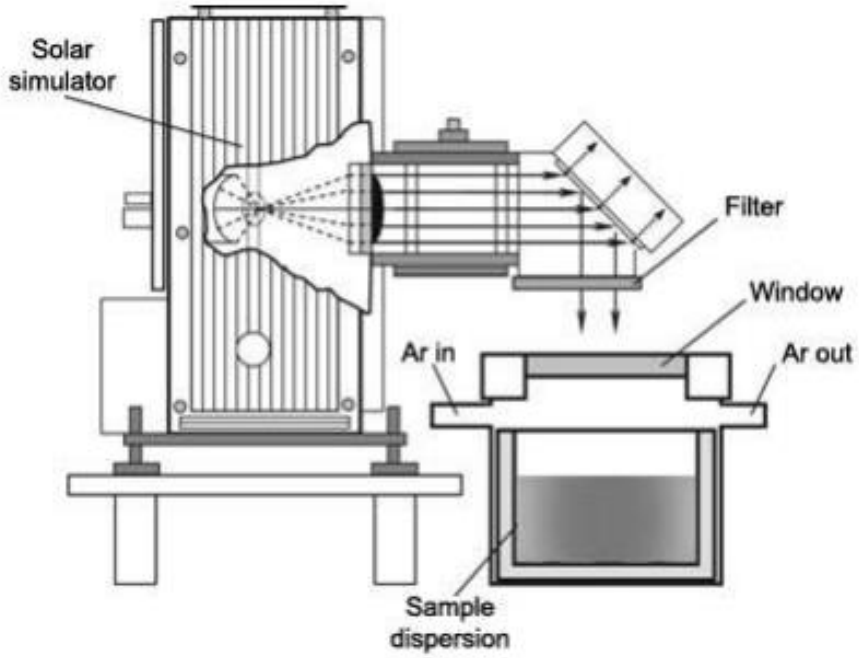

Figure 2.9. Schematic representation of the photocatalytic set-up.

In order to study the photocatalytic performance, specific parameters can be used. In heterogeneous photocatalysis, the turnover number (TON) is the ratio of the number of photoinduced transformations for a given period of time to the number of active sites or photocatalytic centres in their ground state. In this specific case, the photoinduced transformations can be seen as the number of electrons that react to produce hydrogen per active site, before the catalyst deactivates. Hence, the number of electrons is equal to 2 times the produced hydrogen molecules. The catalytic active sites, in this case, are approximated to the number of Au atoms present in the catalyst. The TON may be simplified as:

$$TON = \frac{2n_{H_2}}{n_{Au}} \quad (2.\ 21)$$

where n_{H_2} are the moles of hydrogen produced and n_{Au} are the moles of gold in the catalyst. As TON depends on the irradiation period, its value should be referred to a timescale. The turnover frequency (TOF) is the rate of hydrogen production per active site and can be used to compare photocatalytic activities, as-well. However TON and TOF are influenced by various parameters such as temperature, light intensity and wavelength range. Other parameters commonly used for

comparison of catalytic systems are apparent quantum yield (AQY) and internal quantum yield (IQY). AQY is derived from equation 2.21 by replacing the moles of Au with the number of incident photons:

$$AQY = \frac{2n_{H_2}}{n_{incident\ photons}} \quad (2.\ 22)$$

For AQY extrapolation, $n_{incident\ photons}$ is measured as a function of the wavelength by using a monochromatic source or band-pass filters. In comparative studies, AQY is reported at the same wavelength.

In the IQY, only the absorbed photos that reach the active site are considered:

$$IQY = \frac{2n_{H_2}}{n_{absorbed\ photons}} \quad (2.\ 23)$$

It should be highlighted that AQY ≤ IQY and this latter is rarely used because determination of the real number of absorbed photons is challenging for solid suspensions due to light scattering.

Solar-to-hydrogen (STH) energy conversion efficiency is the efficiency of the system in terms of incoming light energy converted into chemical energy, and for hydrogen production it is:

$$STH = \frac{F_{H_2} \cdot \Delta G^0_{H_2}}{S \cdot A_{irr}} \quad (2.\ 24)$$

where F_{H_2} is the produced hydrogen flow (mol s^{-1}), $\Delta G^0_{H_2}$ is the Gibbs free energy associated with hydrogen production (237 x 10^3 J mol^{-1}), S is the total irradiance (W cm^{-2}) and A_{irr} is the irradiated area (cm^2). Another way to report the conversion efficiency is the light-to-fuel efficiency (LFE):

$$LFE = \frac{F_{H_2} \cdot \Delta H^0_{H_2}}{S \cdot A_{irr}} \quad (2.\ 25)$$

With $\Delta H^0_{H_2}$ being the enthalpy associated with hydrogen combustion (285.8 x 10^3 J mol^{-1}). The STH and LFE descriptors are influenced by experimental conditions and irradiation time, hence comparison of STH and LFE among different studies should be carefully considered. Typical reported values of STH and LFE are below 1% (in most cases, way below).

3. Aim

Heterogeneous catalysis is very sensitive to a great number of variables, especially those related to the catalyst. Therefore, the engineering of well-defined catalysts, by using a rational design approach that priory allows the definition of the catalyst properties, can help in limiting these variables, and in enhancing the performances. In line with this, the objectives of this thesis were set to the development of new catalysts based on metal nanoparticles and nanoclusters that exhibit specific properties related to the surface features of the NPs and to the size control at the atomic level of the NCs.

This general approach will be applied to three different areas of catalysis, namely: the photocatalytic hydrogen generation; electrocatalytic ORR and MOR reactions and thermal catalytic carbon-carbon bond forming reactions. The first two applications go in the direction of energy production from renewable sources that is more and more needed in contemporary society. The third represents instead a more classical application that can nevertheless take advantage from the development of more efficient and cost effective catalytic systems.

For each of these applications, different nanostructured materials will be devised. In particular, porous Pt NPs will be targeted for use in electrocatalysis, considering their high potential in this field. Au NCs will be used in photocatalysis, namely as co-catalysts with titania for the production of hydrogen from ethanol and, finally, the development of Pd NCs will be pursued as catalysts for the thermal cross coupling reactions owing to the well-known activity of palladium in these kinds of organic reactions.

The preparation of porous Pt NPs, enclosed by regular planes, will be based on the facet stabilization properties of organic surfactants like OLAM and OLAC. Porous metal NPs are usually characterized by polycrystalline structures having good catalytic activities that rapidly deteriorate because of the loss of undercoordinated surface atoms during catalytic runs. The development of porous platinum NPs with extended regular surface planes will be undertaken here in order to understand the growth mechanism involved in the definition of such features. This could be done by TEM investigation during all the stages of NPs formation to disentangle the tight interplay of kinetic and thermodynamic factors governing these syntheses. Additionally, the synthesis will be studied through variation of the reaction conditions in order to establish a proper set-up for high reproducibility. Various combinations of OLAM and OLAC surfactants will be investigated, together with the temperature, stirring rate, order of surfactant addition, use of inert atmosphere etc. Platinum was selected for this study because of its exceptional catalytic properties that are

appealing in electrocatalysis. To prove the effective properties control of porous multifaceted Pt NPs, ORR and MOR test will be performed and compared to a commercial Pt catalyst benchmark.

The approach envisioned for the preparation of gold on titania photocatalysts, will rely on the synthesis of thiolate and phosphine protected atomically precise Au NCs. Au on titania nanostructures are widely known and used photocatalysts for hydrogen production, where one of the most performing catalysts is the photodeposited Au/TiO_2. This catalyst is characterized by well-dispersed Au NPs with size around 2-3 nm over the support surface. In pursuing the design of superior photocatalysts with respect to the photodeposited Au/TiO_2 benchmark, we decided to exploit the clusters well-defined atomicity for catalytic purposes, measuring their activity under strictly controlled reaction conditions in order to establish a size/performance correlation. The peculiar properties exhibited by Au NCs are due to the energy bands splitting into distinct levels, thus the addition or subtraction of even one atom from the clusters drastically backlashes on their behaviour. For this study, we set as a target the investigation of atomically precise Au NCs, as co-catalysts, in the photocatalytic production of hydrogen from ethanol. Reported size focusing protocols will be used and possibly adapted to obtain monolayer protected Au_{11}, Au_{18}, Au_{23} and Au_{25} NCs that will be characterized by conventional techniques such as UV-VIS, NMR and TGA. The non-trivial preparation of these atomically precise NCs, is strongly influenced by the structure of the thiolate ligand, solvent, temperature and reducing agent. This represents an enormous benefit because a rich variety of Au NCs are available; our choice of exploring atomicity, ranging from Au_{11} to Au_{25}, instead of focusing on larger particles, is dictated by the higher activities of smaller clusters. The NCs dispersion on the final catalysts will be studied by two different deposition methods based on the use of UV light, to decompose the organic ligands protecting the clusters, and on clusters impregnation prior to photocatalytic tests. The photocatalytic results of this study will be benchmarked to those of a photodeposited Au/TiO_2 catalyst.

Lastly, Pd(II) tiara-like complexes, of well-defined nuclearity, prepared by using thiolate ligands, will be used for the design and preparation of NCs-based solid phase catalysts for Suzuki cross coupling reactions. For this project we envisioned the design of supported small clusters with controlled atomicity starting from a defined Pd complex in order to obtain a catalyst with reproducible catalytic properties. At variance with the case of Au NCs, complexation of the Pd ions in the high oxidation state, to form species with precise poly-nuclearity, is mainly dictated by the ligand choice while other factors are less influencing. In this study, a $Pd_8(SCH_2COOMe)_{16}$ complex will be the primary target; this compound will be subjected to various treatments to enable its dispersion on Al_2O_3. In particular, selected protocols, like the UV irradiation/deposition process and hydrogen reduction at high temperature, will be studied for the atomicity conservation of the Pd

complex in the solid phase. The deposition process of small clusters or complexes is non-trivial and requires tailored procedures to avoid aggregation. Herein, UV light will be applied to induce the $Pd_8(SCH_2COOMe)_{16}$ ligand decomposition in an Al_2O_3 suspension with the consecutive adsorption of the resulting clusters on the support. This pre-catalyst will be subjected to H_2 reduction to deliver the final material that will be characterized by selected techniques, such as TEM, XPS and EXAFS, to confirm the size preservation and effective reduction that determine the final properties of the catalyst. The performance of the Pd_8/Al_2O_3 catalyst will be studied to evaluate its performance in various coupling reactions with substituted bromobenzenes and phenylboronic acid. Moreover, the durability of the catalyst will be subjected to study by recycling and leaching test.

4. Results and discussion

4.1. Synthesis of porous multifaceted Pt NPs for ORR and MOR

4.1.1. Introduction

Platinum has very appealing physico-chemical properties, such as high corrosion resistance and excellent hydrogen and oxygen adsorption capacity,[616] proficiently exploited in homogeneous and heterogenous catalysis.[166,206,538,617–621] Because of this reason, along the decades, great effort has been paid in the preparation of improved platinum-based NPs. As discussed in the introduction section, platinum NPs activity, as-well as all metal-based nanomaterials activity, is mainly attributed to composition,[622] specific surface area[623] and abundance of low coordination number sites.[624] In addition, defects (i.e. twin boundaries, vacancies),[625,626] and the nature of crystallographic planes[95,537,627,628] also affect the activity of heterogeneous catalysts based on transition metals. Considering all this, protocols developed to design platinum NPs with tailored morphology and size are to be preferred since they may provide nanostructures with enhanced catalytic properties. The improvement of methodologies for structural control over size and morphology aiming at enhancing selectivity and activity in tuneable NPs[493] have also increased the interest towards metal nanomaterials in general, especially in the catalysis field.

In this context, porous/dendritic platinum NPs, despite the lack of size confinement, have emerged in the material science and chemistry fields with applications in catalysis for the activation of small molecules.[582,629] The porosity is probably the most interesting feature of these NPs,[630] as pores and channels in the internal structure host a great number of proximal active sites and enhance reactant diffusion, increasing the overall catalytic performances compared to non-porous NPs, with the same dimensions.[631] In addition, large surface areas make these NPs approximable to aggregates of small nanocrystals but with increased stability,[308] with the absence of leaching and sintering issues.[632] Commonly, porous Pt nanostructures are prepared by wet-chemical methods and can be synthesized by various approaches such as hard templating[633–635] or soft templating techniques,[299,566,581,636] dealloying processes[312,637] and electrochemical procedures.[638–640] Among all these strategies, the preparation of porous Pt NPs by chemical reduction in a soft templating agent is more convenient with respect to others because of their facile scalability and cost-effectiveness. In this context, various templating agents have been employed in the design of porous/dendritic NPs such as lyotropic liquids,[299] surfactants[303,579] and polymers[636] giving rise to a variety of protocols that have contributed to the increased interest and availability of these metal NPs. Moreover, the fine tuning

of the reaction conditions widens the possibilities of introducing unique features such as low- and high-index facets and undercoordinated sites in the porous NPs scaffold.[640–642] However, despite the increasing number of reported studies on these metal NPs, aspects like morphology control over lattice planes exposed on the surface and size monodispersity still remain hard to address and are a matter of study.

In this chapter, the synthesis of dendritic multi-faceted platinum NPs enriched in regular planes decorating the surface will be reported. By resorting on transmission electron microscopy to monitor the reaction course, we provide evidence of unprecedented growth process of these NPs. The NPs were produced by the thermolytic reduction of platinum(II) 2,4-pentanedionate in dibenzyl ether as solvent in the presence of oleylamine (OLAM) and oleic acid (OLAC) as directing and templating agents working under argon atmosphere. The platinum NPs were then anchored on a carbon support and subjected to an optimized cleaning treatment consisting in washing steps with alkaline solution of NaOH in methanol[643], necessary to expose the surface[644] without compromising the original morphology/nanostructure. The as-prepared NPs were tested in electrocatalysis for the oxygen reduction reaction (ORR) and the methanol oxidation reaction (MOR) in acidic media as proof of concept of their catalytic activity for future applications.

4.1.2. Synthesis and characterization of porous multifaceted Pt NPs

In this study, the synthesis of porous platinum NPs was performed by a wet-chemical method (Scheme 4.1) in dibenzyl ether, a high boiling point solvent, to easily reach the metal thermal reduction temperature (for platinum ca. 200 °C).

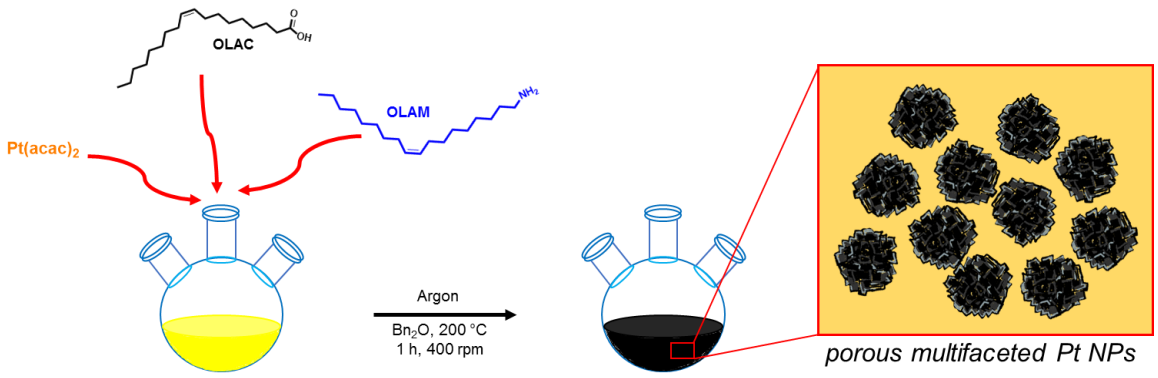

Scheme 4.1. Representative synthetic scheme for the porous multifaceted platinum nanoparticles.

Platinum 2,4-pentanedionate OLAM, OLAC and the solvent were first introduced in the flask and purged in argon at 100 °C for 10 minutes to remove air and moisture that at high temperatures

might generate violent bursts. The temperature was then increased up to 200 °C with a ramp of ca. 5 °C min^{-1} and maintained for 60 minutes. The electron microscopy characterizations for the obtained NPs are presented in Figure 4.1. HAADF-STEM and TEM images (Figure 4.1a, 4.1b respectively) highlight the remarkable uniform size and narrow distribution of the porous NPs. Indeed, as shown in the dimensional distribution histogram (Figure 4.1c) a mean diameter of around 52 ± 2 nm for a set of ~ 400 particles is measured. The most prominent features of these nanostructures are the planes, bordered by edges and corners, that decorate the surface, as observed in Figure 4.1b and 4.1d. The high magnification micrograph of a single particle (Figure 4.1d) emphasizes the porous structure and abundant presence of shaped crystallites with an average size of 10 ± 1 nm. The small nanocrystals are well oriented and hierarchically assembled to constitute the porous NPs themselves. HR-TEM image of the crystallites reveals well-defined extended terraces composed by uniform low-indexed planes as evinced in Figure 4.1e. Besides, from the SAED pattern (Figure 4.1f), diffraction rings of the first reflections for the fcc Pt lattice (111), (200) and (220) can be identified. The marked bright spots seen in the SAED indicate the high crystallinity of the synthesised NPs. To further comprehend the NPs morphology and the evolution to faceted crystallites decorating the NPs surface, the synthesis was monitored at increasing reaction time by TEM analysis.

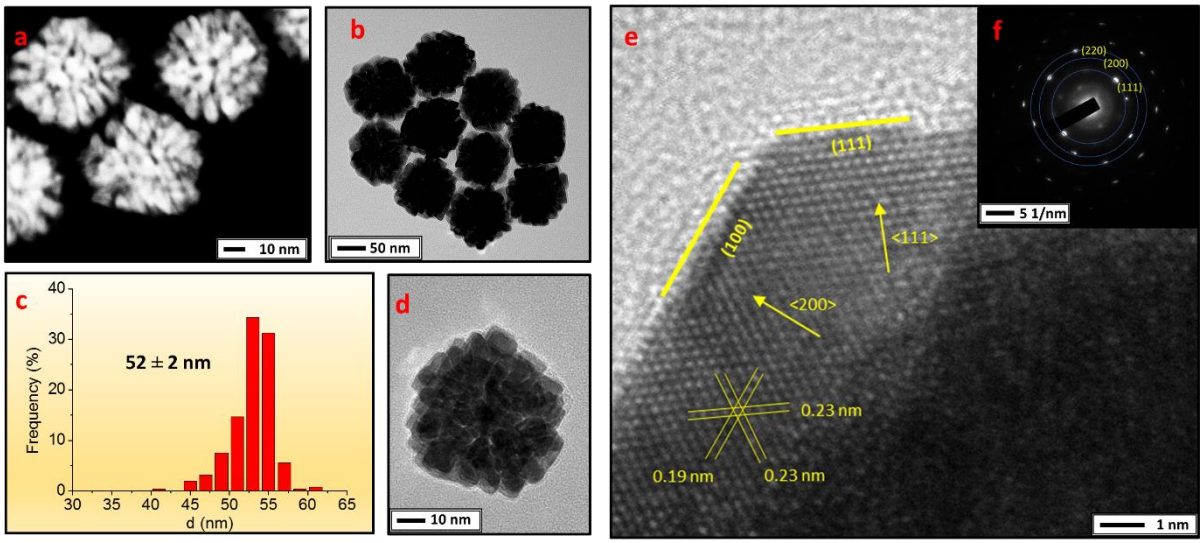

Figure 4.1. Representative HAADF-STEM image of the Pt NPs (a), low mag (b), dimensional analysis (c) and high mag (d) TEM images of the NPs, HR-TEM image of Pt crystallite (e) and selected area ED patterns (f).

The start of temperature ramp from 100 °C to 200 °C was arbitrarily chosen as time zero from which small aliquots (0.2 mL) of the reaction mixture were collected every 5 or 10 minutes and analysed after a quick purification step (hexane/ethanol washing and centrifugation at 15000 rpm). The electron dose rate and the image acquisition conditions were properly set to avoid unwanted beam effects. The growth evolution of the Pt NPs are summarised in Figure 4.2. After 5 minutes of reaction time (Figure 4.2a), small cubic NPs with an average size of 8 ± 1 nm were observed. The nucleation stage of porous Pt nanostructures usually involves the formation of polycrystalline seeds or small dendrites[306,579,645] due to the fast reduction kinetics developed by using excess of reducing agent or uncontrolled temperatures. However, small dendritic seeds were also observed in this study when deviating from the optimized conditions. Addition of OLAM and OLAC to the metal precursor solution performed at 120 °C, rather than at room temperature, and with 5 minutes delay one from the other, independently of the introduction order gave rise to the small polycrystalline dendrimers observed in Figure 4.3. In our optimized procedure, however, the addition of OLAM and OLAC at room temperature, and before the starting of the ramp, might allow the formation of Pt-OLAM complexes[646] that have a slower reduction rate compared to $Pt(acac)_2$. Additionally, the absence on strong reducing agents, but the use of OLAM as reductant,[146] further gave thermodynamic control to the reaction. Furthermore, the control of reduction kinetics was accompanied by the thermodynamic stabilization promoted by the ligands themselves. All this resulted in a synergic combination toward the minimization of surface free energy at the initial growth stage that lead to the formation of the cubic-shaped NPs seen in Figure 4.2a. While seeds may still be produced after 5 minutes, we observed that this process is also accompanied by a morphology change of the already produced nanocubes. Indeed, at this stage the new reduced Pt atoms partially contribute to the formation of new seeds and additionally deposit on the already formed ones originating a preferential growth along the <111> axes, promoted by the ligands, as highlighted by the elongated vertexes of the cubes after 10 minutes (Figure 4.2b). The further growth of the elongated cubes evolve to the star-shaped NPs after 15 minutes (Figure 4.2c).

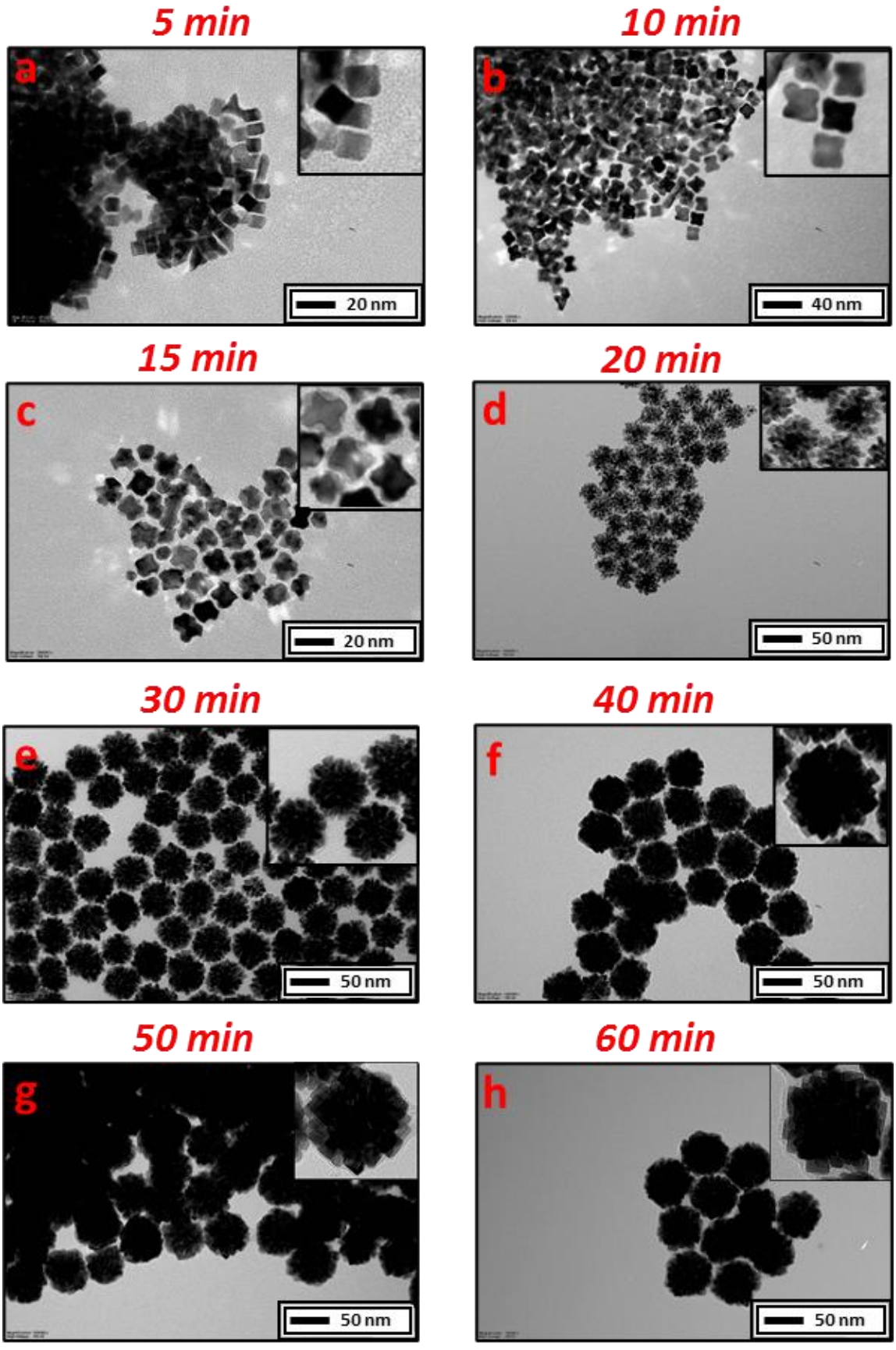

Figure 4.2. Typical TEM images representing the size and shape progression of the porous Pt NPs at 5 (a), 10 (b), 15 (c), 20 (d), 30 (e), 40 (f), 50 (g) and 60 minutes (h).

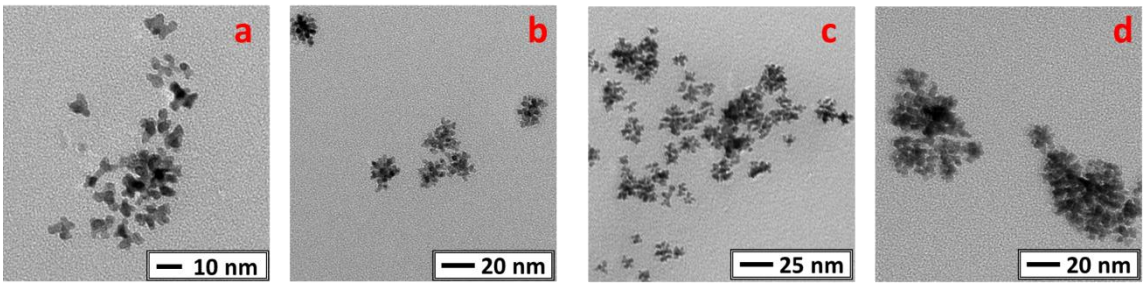

Figure 4.3. Representative TEM images of Pt NPs obtained by delayed addition of the surfactants. (a) OLAM added at 0 minutes and OLAC at 5 minutes, (b) OLAM added at 0 minutes and OLAC at 10 minutes, (c) OLAC added at 0 minutes and OLAM at 5 minutes, (d) OLAC added at 0 minutes and OLAM at 10 minutes.

The TEM images of the sample collected at 20 minutes (Figure 4.2d) mark a change in the NPs morphology evolution, with the deposition of small polycrystalline clusters on the star-shaped NPs that quickly grow in elongated branches giving rise to porous dendrites. This quick change in morphology can be related to the temperature that reaches 200 °C at this stage and remains steady for the rest of the process. At this temperature, the platinum reduction is likely boosted by the high temperature, driving the NPs growth towards a kinetic control and promoting the formation of polycrystalline nanostructures. From 30 to 40 minutes (Figure 4.2e, f), while there are no relevant changes in size of the Pt dendrimers, as seen from the dimensional analysis in Figure 4.4, thickening of their branches is clearly visible. This latter process gives rise to the formation of regular facets on the NPs surface and the overall NPs morphology does not further change at 50 or 60 minutes reaction times (Figure 4.2g, 4.2h). This latter behaviour suggests a thermodynamic stabilization promoted by the capping agents through the reorganization of Pt atoms at the surface in order to achieve a minimum of the surface energy. The time-course TEM analysis in the synthesis of porous faceted Pt NPs played a crucial role in studying the formation of present Pt NPs. As previously established, step-by-step TEM monitoring provides direct feedback useful in addressing the formation mechanisms dominating the different phases of the NPs preparation.[647] In agreement to what already documented for the growth mechanism of porous/dendritic Pt NPs, here a continuous seed formation followed by a fast autocatalytic aggregation-based growth was observed.[310,648,649]

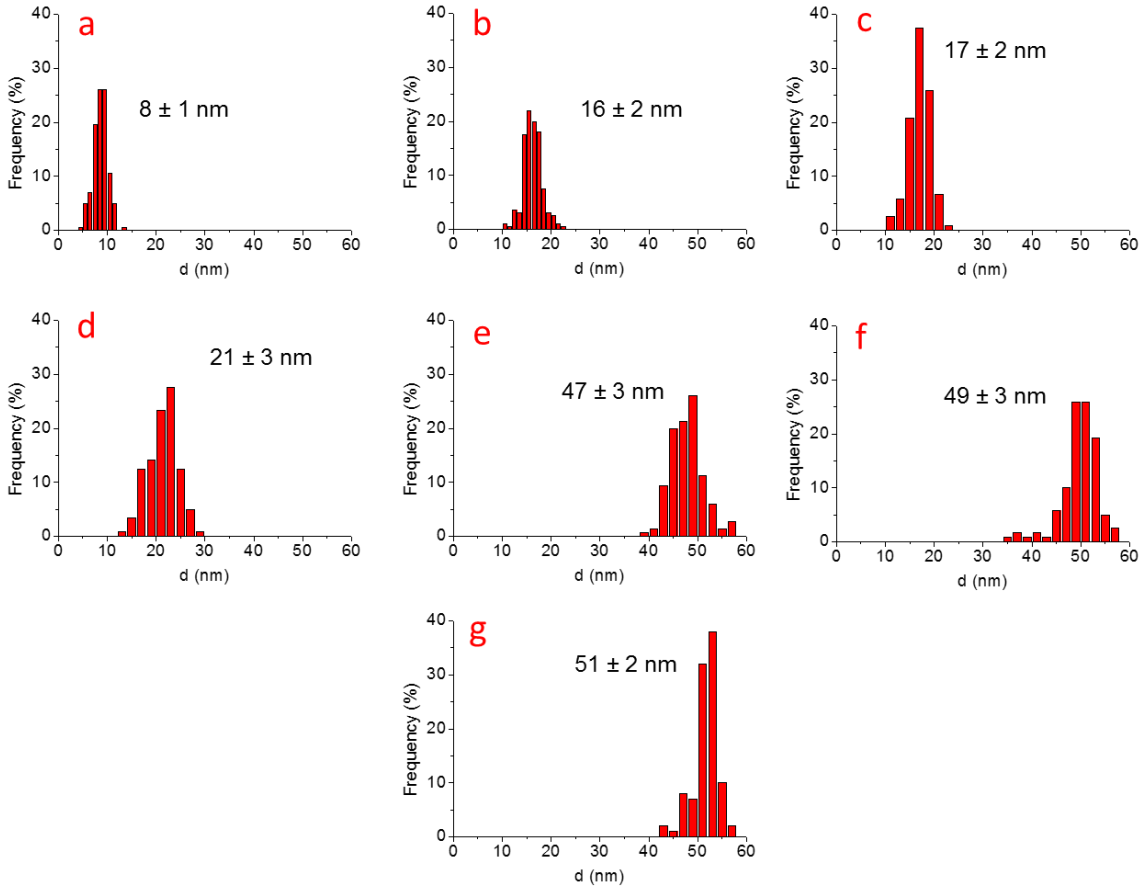

Figure 4.4. Dimensional analysis of the different Pt NPs at 5 minutes (a), 10 minutes (b), 15 minutes (c), 20 minutes (d), 30 minutes (e), 40 minutes (f) and 50 minutes (g) reaction time.

Nevertheless, an additional benefit concerning the narrow size distribution of the nanoparticles was achieved. Monodispersity has been sporadically documented by previous synthetic methodologies for porous NPs,[565,650,651] that usually are reported by ill-defined and large size distribution.[579,649,652]

To investigate the robustness of the synthesis, control experiments were performed in non-optimal conditions. While the effect of precursor concentration was previously investigated showing a correlation with size and morphology changes,[652,653] we focused on different aspects that still affect the synthesis such as temperature, stirring rate, and ligands molar ratio. First, a control experiment in air confirmed the pivotal role of inert gas for the successful production of multifaceted porous NPs. In fact, in air atmosphere, polycrystalline porous NPs were obtained, as seen from Figure 4.5.

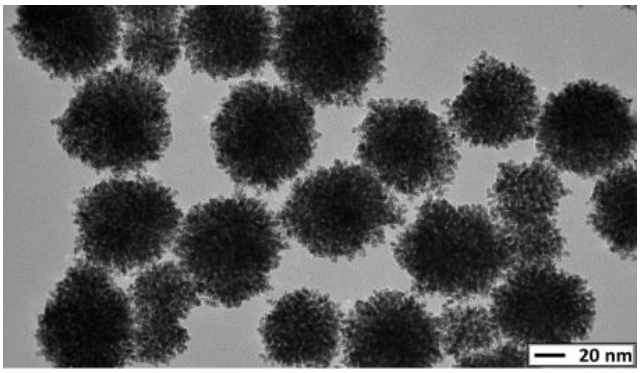

Figure 4.5. Representative TEM image of porous Pt NPs prepared in air. Regular facets are lost without the use of inert gas during reaction.

When the synthesis was performed at 180 °C for 1 hour instead of 200 °C, a dark yellow solution was obtained, delivering a very low quantity of smaller dendritic NPs as reported in Figure 4.6a. Although OLAM can act as a reducing agent for metal precursors at lower temperatures and with very slow kinetics,[654] in our procedure the thermally boosted reduction at 200 °C is critical for the production of these NPs. On the other hand, reaction performed at higher temperatures (210 °C) resulted in bigger and polydispersed NPs (Figure 4.6b), but regular planes can still be detected on the surface (inset Figure 4.6b).

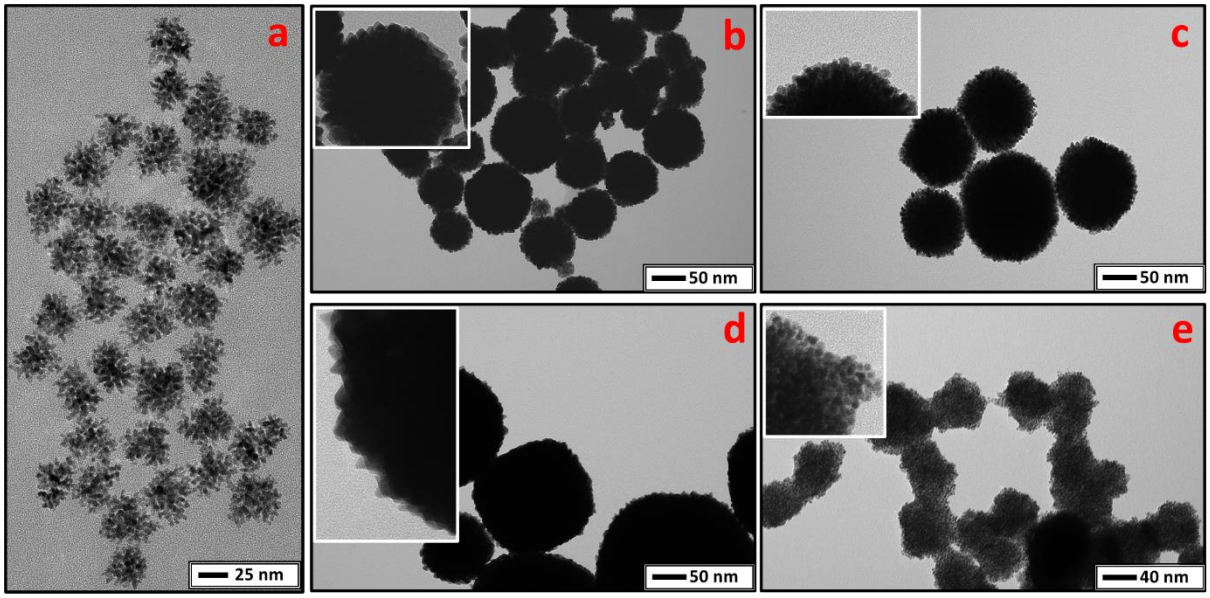

Figure 4.6. Representative TEM images of synthesis performed at 180 °C (a), 210 °C (b), 600 rpm (c), only OLAM as surfactant (d) and only OLAC (e).

Increasing the stirring rate from 400 rpm to 600 rpm, is sufficient to modify the ideal conditions responsible for the minimization of surface energy and deliver polydispersed porous NPs without the shaped features (Figure 4.6c). The use of exclusively OLAM or OLAC as surfactant resulted respectively in large NPs with no distinct porosity (Figure 6d) but highly enriched in regular corners

(inset Figure 4.6d), and in densely packed aggregates of small crystallites (Figure 4.6e and inset). Moreover, screening of different OLAM/OLAC molar ratios (1/3, 1/1.5, 1.5/1, 3/1) resulted in porous but dimensionally polydispersed NPs (Figure 4.7), except OLAM/OLAC = 1/3 that delivered small crystallites (Figure 4.7a, e) like those produced using only OLAC as surfactant. Surprisingly, NPs obtained by different OLAM/OLAC molar ratios do not display the shape uniformity and the facets achieved under the optimised conditions. By plotting the concentration variation of [OLAM] / [OLAM + OLAC] versus the NPs dimension, a monotonic upward trend is observed that correlates higher OLAM concentration to the increasing NPs dimension (Figure 4.8). Considering these aspects, we can speculate a synergistic effect of OLAM and OLAC, when used at the same molarity, in creating the right environment for the formation of uniform and monodisperse porous multifaceted Pt NPs. Moreover, by fine tuning the reaction conditions, it is possible to obtain batches of homogeneous materials with different size and shape and potential different properties.

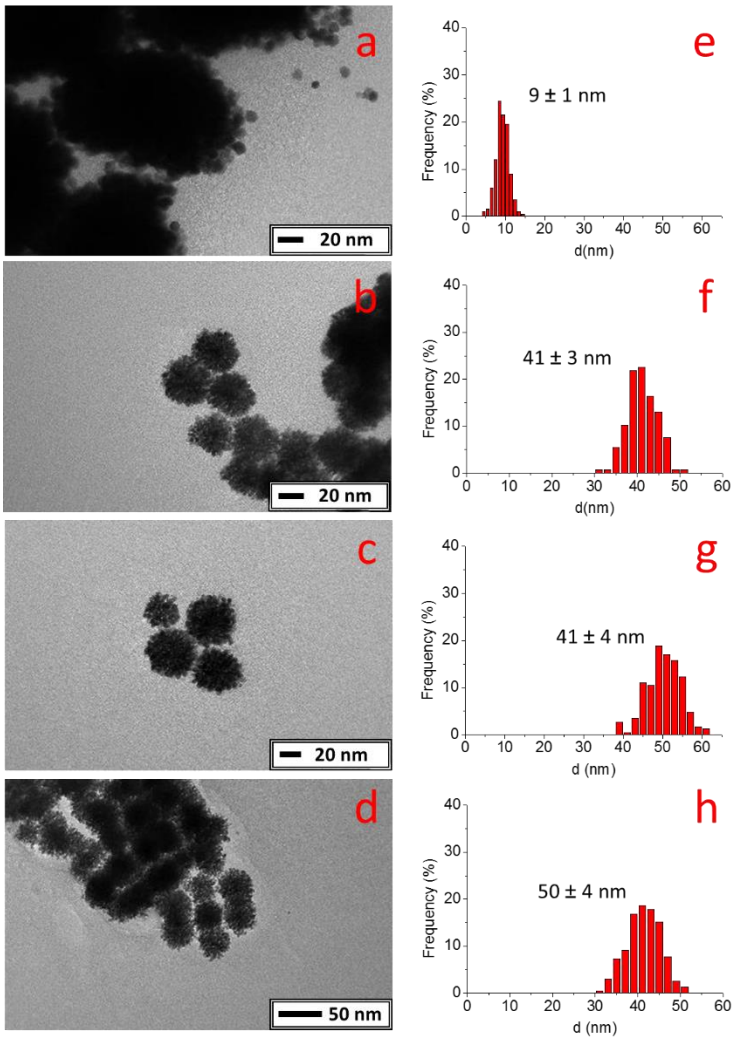

Figure 4.7. Representative TEM images and respective dimensional analysis of reaction performed with 1/3 (a, e), 1/1.5 (b, f), 1.5/1 (c, g) and 3/1 (d, h) OLAM/OLAC molar ratio.

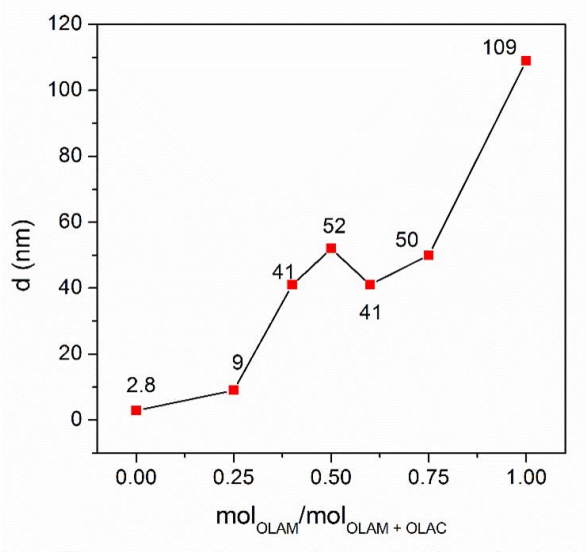

Figure 4.8. NPs dimension as a function of mol$_{(OLAM)}$/mol$_{(OLAM + OLAC)}$ showing a relative size increment with OLAM concentration.

4.1.3. Textural properties

Surface area measurements were performed on the unsupported Pt NPs to evaluate their potential application in catalysis. Nitrogen adsorption/desorption isotherm (Figure 4.9) measured at liquid nitrogen temperature revealed a BET surface area of 15.4 m^2 g^{-1} which is consistent with previously reported syntheses of porous Pt nanostructures in organic phase.[310] Pore size distribution of the unsupported NPs (inset Figure 4.9) gave an average pore diameter of 35 nm that is much larger than the slits and empty space observed in the porous Pt NPs by TEM analyses. This result indicates that the major contribution to pore volume in the dried sample is related to the voids formed by the aggregation of the porous Pt NPs, with the NPs internal porous volume being less highlighted in the analysis. The synthesized porous Pt NPs were deposited on Vulcan XC72R support to obtain suitable materials for electrocatalytic studies. The composite material and a commercial Pt/C material used as reference have been characterized to relate their properties with the electrochemical performances. Notably, the composite porous Pt NPs/Vulcan material was prepared with a metal loading of 15 wt%, as determined by ICP-OES analysis. This value is comparable with the nominal 20 wt% reported for the commercial Pt/C reference material.

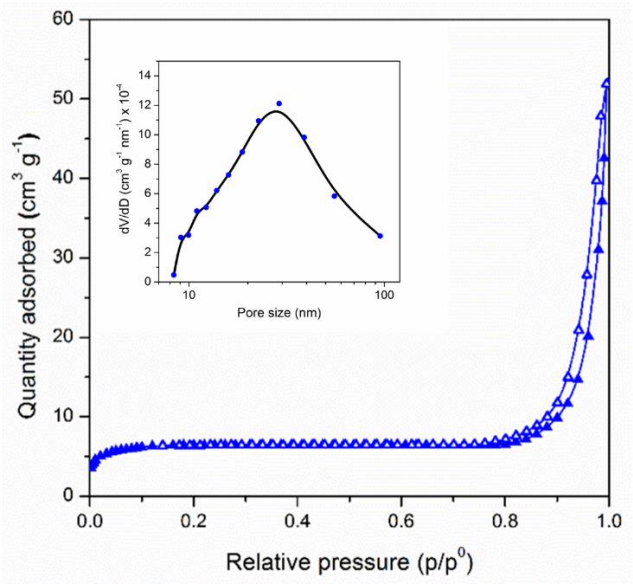

Figure 4.9. Nitrogen physisorption isotherm of the unsupported porous Pt NPs and pore size distribution (inset).

Textural properties of the composite porous Pt NPs/Vulcan and the commercial Pt/C materials are very similar (Figure 4.10 and Table 4.1), with a high surface area and pore volume and an extended mesoporous network around 63 nm. The most relevant differences between these 2 samples are a slightly larger contribution of micropores, a relative maximum centred around 3.6 nm in the mesopore size distribution and a significantly lower cumulative pore volume for the commercial Pt/C material. As expected, the pristine Vulcan XC72R shows a higher surface area and pore volume than the composite porous Pt NPs/Vulcan material, considering the higher density of Pt with respect to carbon support. Notably, after sintering of the composite porous Pt NPs/Vulcan under H_2 at 400 °C, no significant modifications of the textural properties are observed.

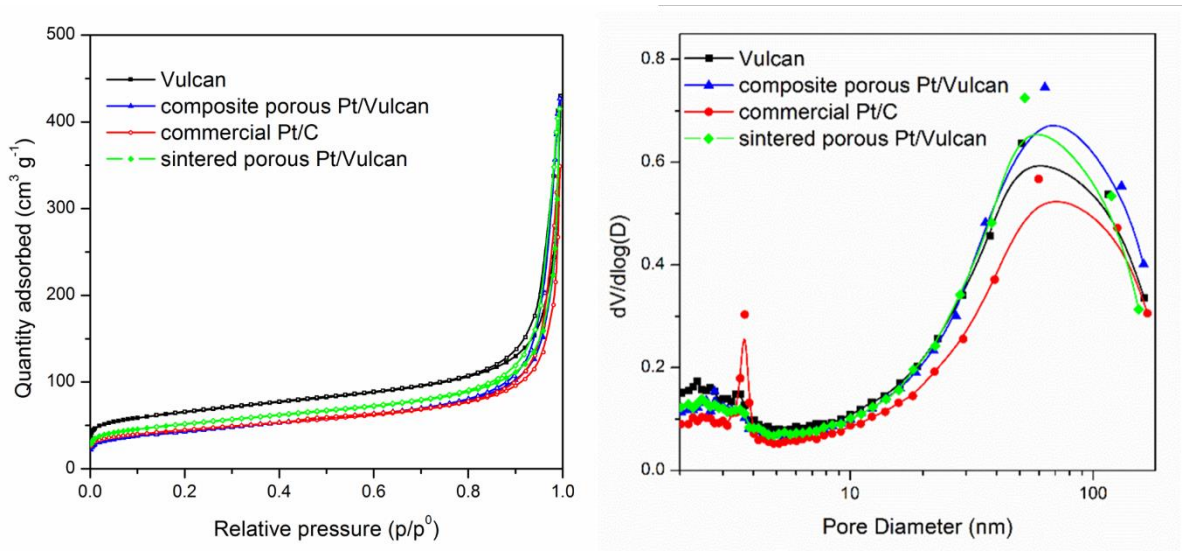

Figure 4.10. N_2 physisorption isotherms and pore size distribution for Vulcan (black), composite porous Pt on Vulcan (blue), sintered porous Pt on Vulcan (green) and commercial Pt on carbon (red).

Table 4.1. Summary of the textural properties of the investigated materials.

	S_{BET} [a] ($m^2\ g^{-1}$)	S_{ext} [b] ($m^2\ g^{-1}$)	S_{micro} [c] ($m^2\ g^{-1}$)	V_{tot} [d] ($cm^3\ g^{-1}$)	V_{micro} [e] ($cm^3\ g^{-1}$)	V_{meso} [f] ($cm^3\ g^{-1}$)	D_M [g] (nm)
Vulcan	200	146	54	0.604	0.036	0.568	51
composite porous Pt/Vulcan	140	125	15	0.627	0.012	0.615	63
comm. Pt/C	138	106	32	0.503	0.022	0.481	59
sintered porous Pt/Vulcan	140	113	27	0.525	0.019	0.506	53

[a] Specific surface area calculated following the BET method.
[b] Specific surface area external to micropores, determined from the t-plot analysis.
[c] Specific surface area of micropores.
[d] Total volume of pores calculated from BJH analysis.
[e] Total volume of micropores, determined from t-plot analysis.
[f] Total volume of mesopores.
[g] Maximum of the pore size distribution, determined by BJH analysis

Hydrogen chemisorption experiments have been performed on the various Pt/C materials to analyse the Pt exposed surface area. H_2 chemisorption isotherms are presented in Figure 4.11 and the obtained results are summarized in Table 4.2.

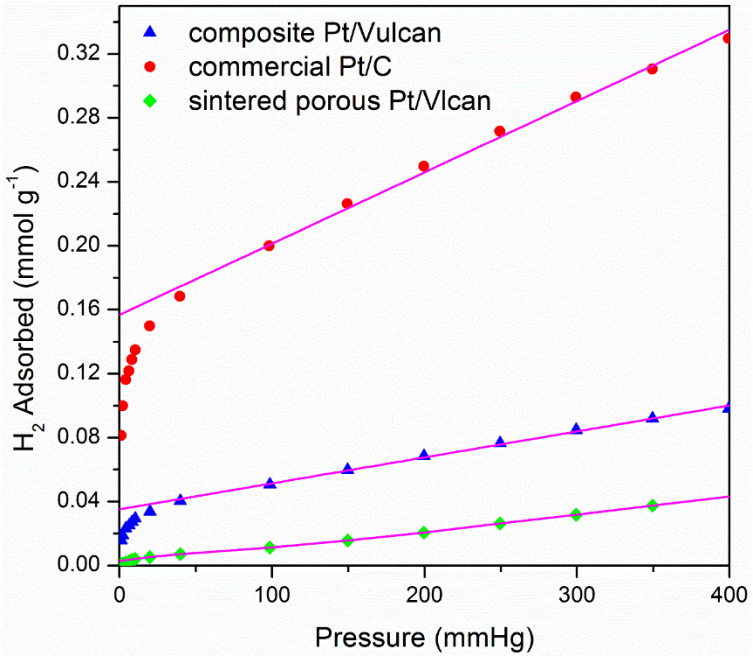

Figure 4.11. H_2 chemisorption measurements for porous multifaceted Pt on Vulcan and commercial Pt on carbon.

Table 4.2. Summary of the metal textural properties of the investigated materials.

	D % [a]	***d part*** [b] ***(nm)***	***EMSA cat*** [c] ***($m^2\ g^{-1}$)***	***EMSA Pt*** [d] ***($m^2\ g^{-1}$)***
comm. Pt/C	23.9	5.0	11.8	59.1
composite porous Pt/Vulcan	7.3	15	2.7	18.1
sintered porous Pt/Vulcan	0.4	280	0.14	0.97

[a] Metal dispersion, calculated assuming a spherical shape of the metal particles.
[b] Apparent particle size.
[c] Exposed metal surface area (EMSA), expressed per quantity of catalyst.
[d] Exposed metal surface area (EMSA), expressed per quantity of platinum.

The composite porous Pt NPs/Vulcan chemisorbed a remarkably lower amount of H_2 with respect to the commercial Pt/C material. As a consequence, metal dispersion and exposed surface areas (reported irrespectively of the mass of the catalyst or to the mass of Pt) are lower, and apparent metal particle size is larger for the composite porous Pt/Vulcan material. It is straightforward to note that, in the composite porous Pt/Vulcan material, the exposed metal surface area reported with respect to the mass of Pt is 18.1 $m^2\ g_{Pt}^{-1}$ that is very close to the value of 15.4 $m^2\ g^{-1}$ measured by N_2 physisorption on the pristine porous Pt NPs, even considering the intrinsic systematic errors of the two different techniques.

Moreover, powder XRD analysis of the composite porous Pt/Vulcan material (Figure 4.12) showed the typical reflection of metal Pt (JCPDS 04–0802), together with a very broad reflection around 26°, due to the crystalline graphitic portion of Vulcan XC72R. The peak broadening of the (111) reflection of Pt is compatible with an average crystallite size of 11 nm, the same measured for the pristine porous Pt NPs. This result suggests that the porous nature of the Pt NPs is preserved during the various steps involved in the preparation of the composite porous Pt NPs/Vulcan (deposition protected porous Pt NPs and washing to remove organic ligands). Notably, after sintering treatment in H_2 at 400°C, the exposed metal surface area drastically decreased, confirming the deep sintering on the Pt nanoparticles.

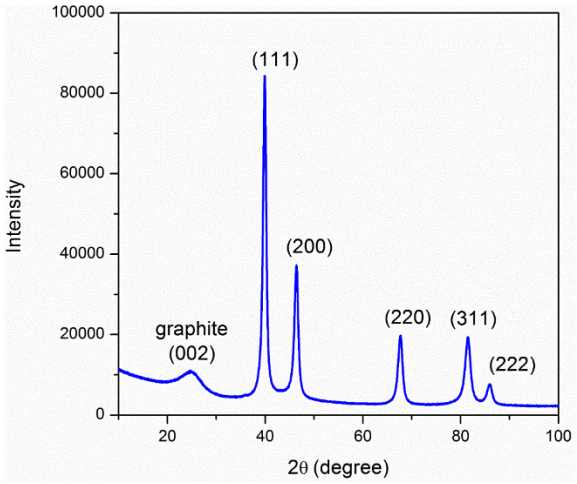

Figure 4.12. Powder x-ray diffraction pattern of the composite porous Pt NPs/Vulcan.

Furthermore, the morphology of the various Pt/C samples was analysed by TEM. A representative TEM image of the commercial Pt/C sample (Figure 4.13a) shows the presence of highly dispersed Pt nanoparticles, with a mean diameter of 3 – 4 nm. On the other hand, TEM images of the composite porous Pt/Vulcan material (Figure 4.13b) shows the presence of the porous Pt NPs deposited on the carbonaceous support: despite the limited contrast due to the thickness of the support around the porous Pt NPs, the aggregation of various Pt crystallites to form a porous particle is clearly visible. After sintering by H_2 treatment at 400°C, TEM analysis (Figure 4.13c) confirms the coalescence of Pt crystallite to form very large metal particles, with spherical shapes. All the results obtained by TEM analysis of the supported Pt/C materials, investigated in electrocatalytic tests, are fully in agreement with the H_2 chemisorption results.

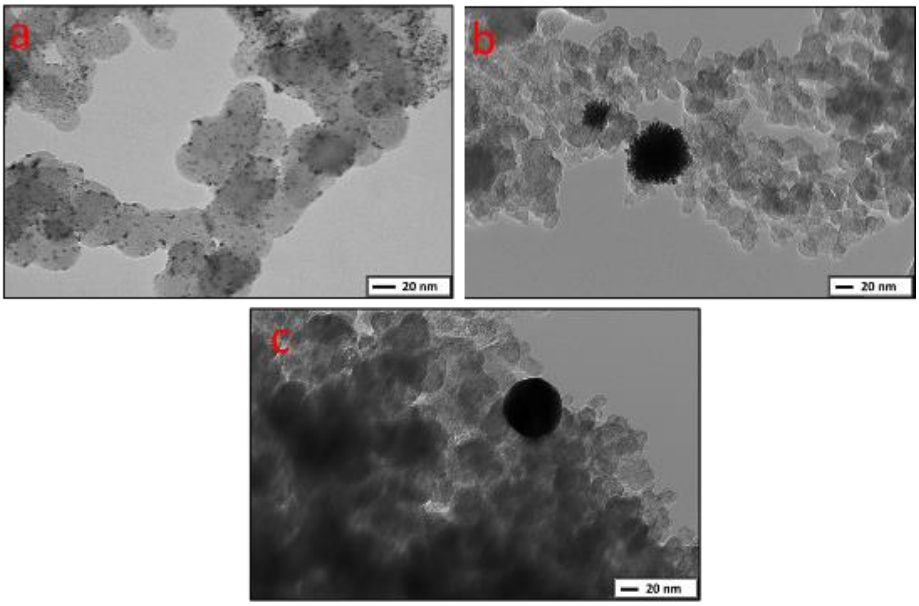

Figure 4.13. TEM images of commercial Pt/C (a), composite porous Pt/Vulcan (b) and sintered Pt/Vulcan (c).

4.1.4. Electrocatalytic investigations

The standard thermal cleaning procedure could not be applied to the present nanostructure Pt based systems as they would be subjected to structural and morphological modifications. After electrode conditioning, all samples were therefore subjected to cyclic voltammetries (CVs) at 0.1 V s^{-1} to clean and investigate the surface of the catalyst. Commonly, platinum-based materials CVs can be divided into three areas accounting for different contributions: the hydrogen region, the double layer (DL) region and the oxide region.[655] The characteristic CVs for the three materials tested are reported in Figure 4.14. The DL region (0.4 – 0.6 V *vs* RHE) is mainly influenced by the carbon support: from the lower capacitive currents, we can infer that the Vulcan XC72R has less surface area accessible to the ions in solution than the carbon used in the commercial Pt/C. In the hydrogen region, the CV peaks can reveal the features of the exposed platinum surfaces. Commercial Pt/C material shows two close peaks at 0.15 and 0.2 V *vs* RHE: while the first can be related to (110) step sites, the origin of the second peak is somewhat still debated and could arise from (111) sites.[656] Similarly, the composite porous Pt/Vulcan shows a peak at 0.13V and one at 0.3V *vs* RHE, with (110) and (100) step sites also present on the surface.[656]

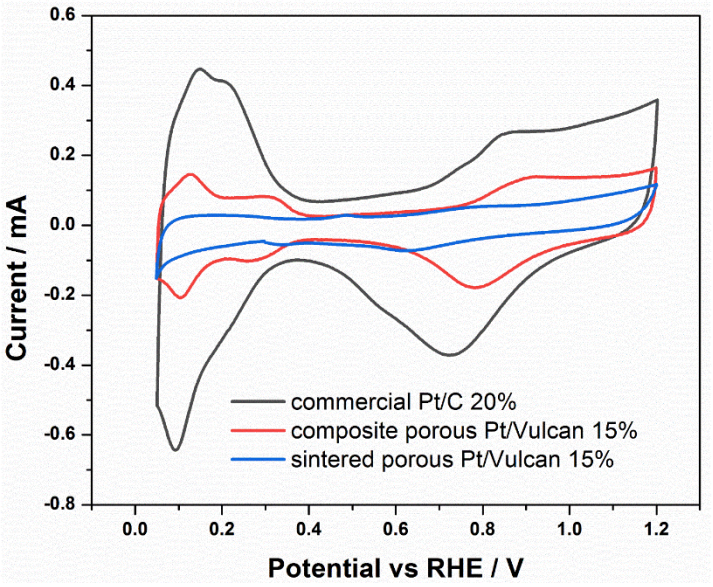

Figure 4.14. CVs of commercial Pt/C (black), composite porous Pt/Vulcan material (red) and sintered porous Pt/Vulcan material (blue), registered at 100 mV s^{-1} in $HClO_4$ 0.1 M.

From the area of the H desorption peaks, ECSAs and roughness factors (RF) can be calculated for the three samples. As expected, the commercial Pt/C material shows the highest electrochemical surface areas, due to the very low dimensions of the Pt nanoparticles. The ECSA for the composite porous Pt NPs/Vulcan is one-half than that of the commercial reference material. After sintering,

only 25% of ECSA is retained (Table 4.3). These results are in good agreement with the trend observed for the exposed metal surface area measured by H_2 chemisorption.

Table 4.3. ECSAs and RFs of the investigated catalysts.

	ECSA / m^2 g^{-1}	***RF***
Commercial Pt/C	6.3	1.9
Composite porous Pt NPs/Vulcan	2.9	0.87
Sintered porous Pt NPs/Vulcan	0.71	0.21

The large difference between the values of metal surface area from electrochemical measurements and H_2 chemisorption can be clearly related to the differences in the techniques: H_2 chemisorption counts for all the exposed surface Pt atoms while ECSA takes into accounts only the atoms that can be reached by diffusion of electrons in the overall assembly of the electrode. Moreover, the cathodic and anodic sweeps of the composite porous Pt NPs/Vulcan material show very good symmetry in the hydrogen region. This indicates high reversibility of the phenomena thanks to the clean surface which was confirmed by IR analysis of the pre- and post-treated catalyst with NaOH (Figure 4.15).[657]

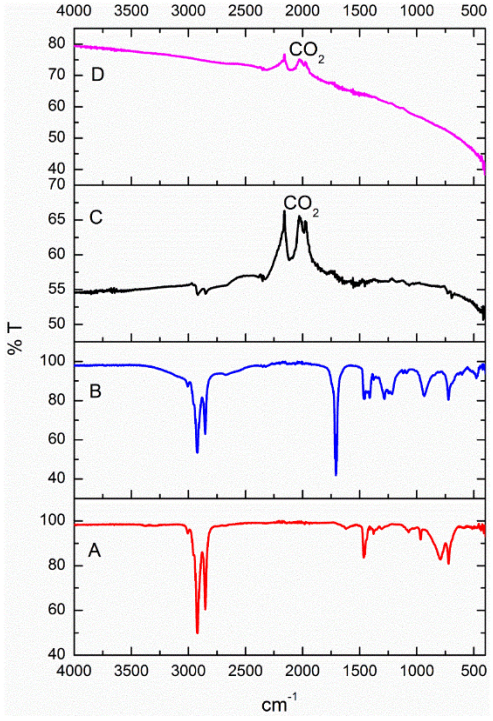

Figure 4.15. IR spectra of OLAM (A), OLAC (B), untreated Pt NPs (C) and NaOH treated Pt NPs (D).

Oxygen Reduction Reaction (ORR)

ORR catalytic activities of the different Pt-C composites were investigated via linear sweep voltammetry (LSV) in acidic electrolyte (0.1 M $HClO_4$) saturated with pure O_2 from 0.1 to 1.1 V *vs* RHE at a scan rate of 10 mV s^{-1}. Catalyst loading varied for the different materials between 153 (for commercial Pt/C) and 187 µg cm^{-2} (for composite porous and sintered Pt NPs/Vulcan), corresponding to a fixed loading of ~ 30 μg_{Pt} cm^{-2}. The LSV results obtained for ORR in $HClO_4$ 0.1 M for the investigated materials are presented in Figure 4.16 while Figure 4.17 summarizes the MAs, normalized with respect to the mass of Pt, and SAs, normalized with respect to ECSA of each material. The comparison of the obtained results highlights the importance of porosity of the Pt NPs in our material. The sweeps of commercial Pt/C and composite porous Pt NPs/Vulcan are very similar, showing higher activities per unit area for the porous nanoparticles. The composite porous Pt NPs/Vulcan shows comparable MA with respect to commercial Pt/C material but, having a lower ECSA, its SA is much higher than that of the reference material. Overall, the material displays higher MA and SA for ORR, compared to other porous or non-porous Pt-based nanomaterials from the literature.[149,637] At the same time, the sintered Pt NPs/Vulcan show a very low MA while SA is closer to that of reference commercial Pt/C. The peculiar performance of the composite porous Pt NPs/Vulcan expressed in terms of SA could arise from the well-defined morphology of the Pt crystallites.

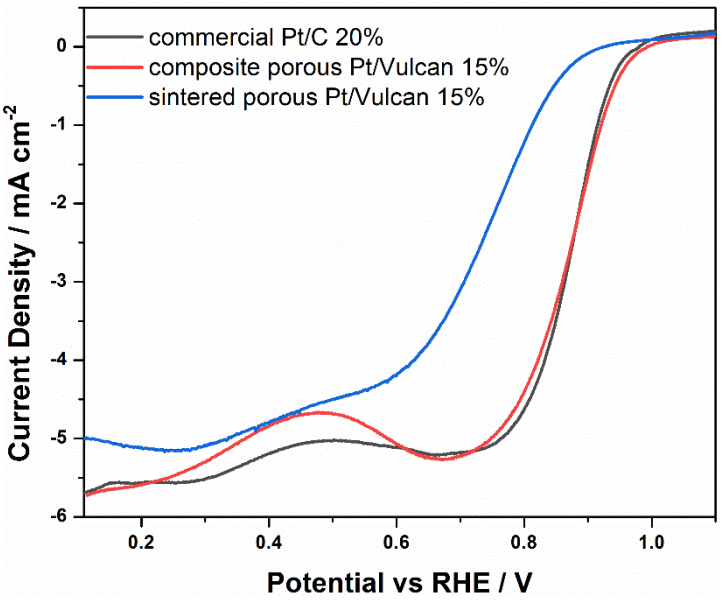

Figure 4.16. LSVs for commercial Pt/C (black), composite porous Pt/Vulcan material (red) and sintered porous Pt/Vulcan material (blue), registered at 10 mV s^{-1} from 0.1 to 1.1 V in 0.1M $HClO_4$ solution at 1600 rpm. Visualised potentials are corrected for pH and ohmic losses.

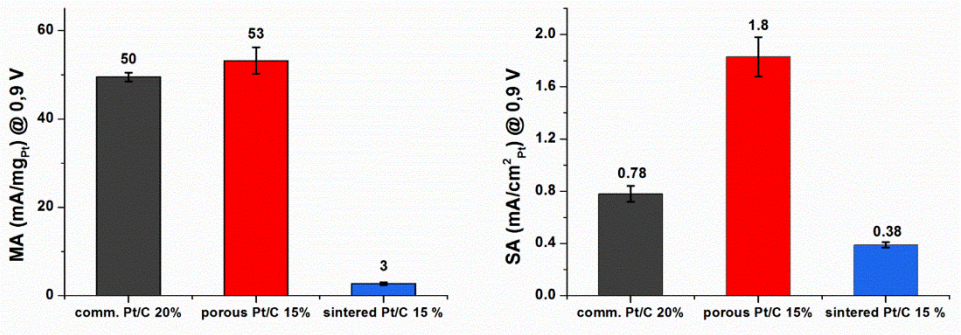

Figure 4.17. Comparison of MAs (a) and SAs (b) for ORR calculated from values at 0.9 V *vs* RHE in Figure 4.16.

Methanol Oxidation Reaction (MOR)

MOR catalytic activities of the different Pt/C composites were investigated via CV in acidic electrolyte (MeOH 10 vol% in 0.1 M $HClO_4$) in Ar between 0.4 and 1.4 V *vs* RHE at a scan rate of 50 mV s^{-1} (Figure 4.18) while normalized activities (MA and SA) are presented in Figure 4.19. Platinum loading was fixed at ~ 30 μg_{Pt} cm^{-2}. The MOR behaviour of the three materials is similar to the case of ORR. In particular, the onset for methanol oxidation in the forward scan is shifted to negative potentials following the order: commercial Pt/C (0.58 V), composite porous Pt/Vulcan (0.60 V) and sintered porous Pt/Vulcan (0.65 V). This suggests a faster CO_{ads} oxidation rate (intermediate) on the commercial Pt/C surface, however, when normalised by mass and ECSAs, composite porous Pt/Vulcan resulted the best performing with a MA of 880 mA mg^{-1}_{Pt} and SA of 30 mA cm^{-2}_{Pt} compared to MA of 860 mA mg^{-1}_{Pt} and SA of 13.6 mA cm^{-2}_{Pt} exhibited by the commercial counterpart. The high current densities at the end of the forward scan (at ca 1.3 V) point out the substantial contribution of the methanol oxidation on the Pt-oxides surface, that originates at high voltages,[658] for the composite porous Pt/Vulcan and the commercial Pt/C. In the backward scan, the onset of the secondary methanol oxidation peak is shifted to positive potentials for the composite porous Pt/Vulcan with respect to the commercial Pt/C outlining a lower surface coverage in reaction intermediates; this can be rationalised by a higher oxidation rate on the porous Pt compared to the commercial Pt/C. As for the sintered porous Pt/Vulcan the current densities result not comparable with the other two tested materials. Specific activities calculated on the forward scan for the non-porous materials (commercial Pt/C and composite sintered Pt/Vulcan) are comparable with normalised current densities of 13.6 mA cm^{-2}_{Pt} and 7.1 mA cm^{-2}_{Pt}, while the porous nature and exposed facets in the composite porous Pt/Vulcan sample results in better performance of the electrocatalyst (30 mA cm^{-2}_{Pt}). Again, mass activities do not show a significant

difference between the commercial Pt/C and composite porous Pt/Vulcan, pointing to a balancing effect between lower ECSA and higher specific activity. Due to different ways of setting up the MOR experiments, it is difficult to compare results with the literature. Where a comparison is possible, our material displays higher mass and specific activities toward MOR, with respect to other porous and non-porous Pt-based nanomaterials.[579,634,659]

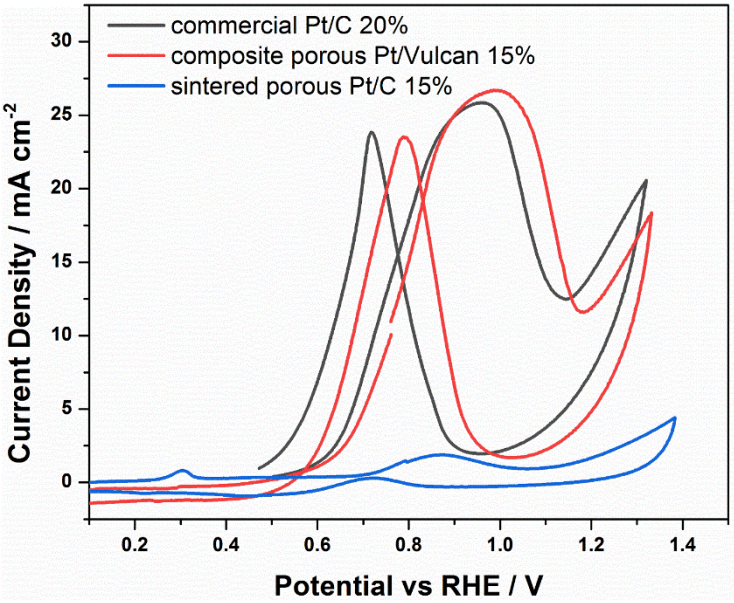

Figure 4.18. CVs of commercial Pt/C (black), composite porous Pt/Vulcan material (red) and sintered porous Pt/Vulcan material (blue), registered at 50 mV s^{-1} in a 10% vol MeOH sol. in 0.1M $HClO_4$ from 0.1 to 1.5 V. Visualised potentials are corrected for pH and ohmic losses.

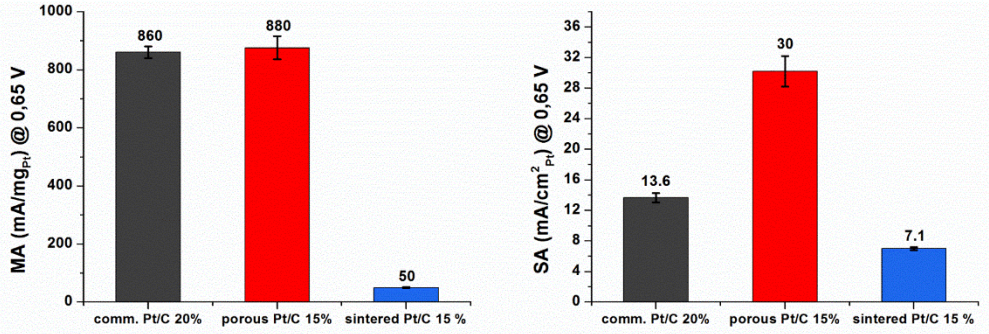

Figure 4.19. Comparison of MAs (a) and SAs (b) for MOR calculated from values at 0.65 V *vs* RHE in Figure 4.18.

4.1.5. Conclusions

A straightforward and rapid synthesis was developed for the preparation of porous multifaceted Pt NPs. The reaction was performed in liquid phase in presence of OLAM and OLAC that showed to be crucial to achieve the complex architecture of the NPs. Various control experiments highlighted

the importance of fine tuning of the optimal reaction conditions. Reduction of the precursor was promoted by the OLAM ligand and aided by the high temperature, without the use of conventional strong reducing agent. The porous multifaceted Pt NPs displayed a remarkable uniformity in shape and narrow monodispersity with a good grade of porosity. The growth mechanism was investigated by TEM analysis which displayed an unusual morphological transition of the NPs shape going from small regular crystallites, to dendrites to porous particles with uniform surface planes. Finally, the NPs were treated to clean the surface and activate them for electrochemical applications toward the reduction of molecular oxygen and the oxidation of methanol. The output of the electrocatalytic tests displayed a higher MA (53 mA mg^{-1}_{Pt}) and SA (1.8 mA cm^{-2}_{Pt}) toward the ORR of the porous multifaceted Pt NPs with respect to the commercial Pt/C benchmark that delivered lower MA (50 mA mg^{-1}_{Pt}) and SA (0.78 mA cm^{-2}_{Pt}). The same behaviour was also observed for the MOR where the porous multifaceted NPs showed higher MA (880 mA mg^{-1}_{Pt}) and SA (30 mA cm^{-2}_{Pt}) with respect to the commercial counterpart which displayed a MA of 860 mA mg^{-1}_{Pt} and a SA of 13.6 mA cm^{-2}_{Pt}. In general, the normalised activities show a trend in both MOR and ORR, favouring our porous platinum NP in respect to the commercial standard.

4.1.6.Experimental

Materials

Oleylamine technical grade 70% (OLAM), oleic acid technical grade 90% (OLAC), benzyl ether 98%, ethanol 99.8%, methanol 99.8%, isopropanol 99.9%, toluene 99.7%, acetone 99.5%, conc. $HClO_4$ 70%, H_2SO_4 99.999% and Nafion 117 5% solution were purchased from Sigma-Aldrich. Platinum(II) 2,4-pentanedionate (49.6% Pt) was purchased from Chempur, Vulcan XC72R was supplied from Cabot. The 20% Pt on Carbon used as standard was bought from Alfa Aesar. All electrochemical experiments were performed with MilliQ water obtained by using a Direct-Q (Millipore) water purification system. All the glassware used for the synthesis and deposition process of porous Platinum NPs were previously cleaned with aqua regia (HCl/HNO_3 = 3/1), then rinsed with MilliQ water.

Synthesis of porous dendritic Pt NPs

Pt NPs were prepared by a surfactant-assisted process inspired by a previous protocol used in our group.[166] In a typical synthetic procedure, a three-necked 25 mL round bottom flask, equipped with

stirring bar and internal thermometer, was flame-dried under vacuum then purged with argon. Subsequently, 20 mg $Pt(acac)_2$ (0.05 mmol), 2 mL OLAM 70% (6.43 mmol), 2 mL OLAC (7.11 mmol) and 10 mL benzyl ether were added under argon flow to the flask and stirred at 100 °C using an oil bath for 10 minutes to completely dissolve the platinum complex and remove water traces. Temperature was then increased at 200 °C (5 °C min^{-1}), the flask was sealed, and argon flow stopped to better control the temperature. The reaction mixture was left to stir at 400 rpm for 1 hour. At reaction completion, the flask was cooled to room temperature and ethanol was added (15 mL), NPs were precipitated by centrifugation at 5000 rpm for 6 minutes and washed with ethanol/*n*-hexane 3 times and centrifuged again. Finally, the product was redispersed in *n*-hexane.

Deposition of Pt NPs on carbon (Vulcan)

Pt on carbon was prepared by a deposition process in organic solvent. Typically, 50 mg Vulcan were dispersed in 50 mL toluene and sonicated for 30 minutes, then dispersion was stirred vigorously. Afterwards, 10 mg of Pt NPs in 10 mL *n*-hexane were added dropwise under constant stirring, the suspension was left to stir for additional 3 hours. The as prepared Pt/C was centrifuged at 5000 rpm for 12 minutes and washed 3 times with methanol before drying in vacuum at 60 °C for 12 hours.

Methanol/NaOH treatment:[643] The dried catalyst was suspended in methanol followed by 150 mg NaOH addition. The suspension was sonicated for 20 minutes until complete NaOH dissolution, then catalyst was collected by centrifugation at 5000 rpm for 12 minutes and washed with acetone (this procedure was repeated 3 times). The last washing step was performed with bi-distilled water and the catalyst was filtered before drying at 60 °C under vacuum for 12 hours.

Preparation of sintered Pt NPs

Sintered Pt NPs on Vulcan were prepared starting from NaOH treated NPs. 20 mg of NaOH treated porous Pt NPs on Vulcan were transferred to a 30 mL quartz tube reactor connected to a H_2/Ar line. The catalyst was first purged with Ar at room temperature for 30 minutes, then heated at 400 °C (ramp 5 °C min^{-1}) under 100 mL min^{-1} H_2/Ar (3 % H_2) flow for 4 hours.

Electrode preparation

All the inks were prepared in a 3:1 H_2O:iPrOH mixture with the addition of 0.05% (v/v) Nafion® 117 5% solution and a catalyst concentration of 5 mg mL^{-1}. The ink was drop casted on the polished GC-RDE in 8 µl drops till a loading of 30 μg_{Pt} cm^{-2} was reached for every experiment and dried in air flow with a RDE rotation rate at 700 rpm.

Electrochemical measurements

All electrochemical characterizations were carried out at room temperature on an Autolab 302N electrochemical workstation (Metrohm, Autolab), by using a standard three-electrode setup. A GC rotating disk electrode (RDE Metrohm, Autolab, geometric SA 0.196 cm^2) was used as the working electrode. A Pt wire and a saturated calomel electrode (SCE, KCl sat.), counter and reference electrodes respectively, were separated from the main chamber via bridges equipped with Vycor® frits. According to recent literature,[660] the use of Pt as CE is strictly recommended to be avoided when the electrochemical study is referred to highlight the activity of nonprecious metal - based catalysts, in particular Pt-free electrocatalysts in acidic media and for prolonged measurements (HER, ORR chronoamperometric studies). In the present case, we investigated Pt based materials. Furthermore, the Pt CE was carefully separated from the main cell chamber to further minimize interferences, as proved by a crosscheck comparison with a carbon- based CE. All the characterizations were done following the procedures reported by Shinozaki *et al.*[657,661] To completely clean the surface of the nanoparticles from any possible residue, 200 cycles of CV were used at 0.5 V s^{-1} between 0 and 1.2 V *vs* RHE. During this conditioning, the hydrogen adsorption and desorption peaks became more accentuated and symmetric, until a stable response from the material was obtained. All electrocatalytic experiments were corrected for ohmic losses and background currents (i.e. capacitive currents). Two parameters were chosen to compare different catalytic results, Specific Activity (SA, mA cm_{Pt}^{-2}) and Mass Activity (MA, mA mg_{Pt}^{-1}), both measured at potentials of interest for the specific catalytic reaction.

To evaluate electrochemically active surface area (ECSA) of the platinum NPs, many different procedures can be found in literature, resulting in high variability in ECSA values (even in orders of magnitude).[662] Here we followed the most straightforward procedure, based on the integration of H_{upd} related peaks in a CV at 0.1 V s^{-1}. ECSA was obtained dividing the as obtained charge with the standard value of 210 µC cm^{-2}, normalized for the Pt NPs mass. Roughness Factors (RF) were calculated as ECSA values times the material loading:

$$ECSA = \frac{Q_{UPD}\ (\mu C)}{210\ \mu C\ cm^{-2}} \frac{1}{m_{Pt}} \qquad RF = ECSA \cdot \frac{m_{Pt}}{SA_{geo}}$$

Characterization

TEM analyses were performed using a Philips EM 208 microscope operating at 100 kV and equipped with a 11 MP bottom-mounted CCD Olympus Quemesa camera. High-Resolution TEM (HR-TEM) images, selected area electron diffraction (SAED) patterns and high angle annular dark field (HAADF) scanning TEM (STEM) were acquired by using a JEOL 2010 UHR field emission gun microscope operated at 200 kV with a measured spherical aberration coefficient Cs of 0.47 ± 0.01 mm. The electron dose rate was $1.5 \cdot 10^{-8}$ e/sÅ^2 for regular and HR-TEM imaging. HAADF-STEM images were acquired using an illumination angle of 12 mrad and a collection angle $88 \leq 2\theta \leq 234$ mrad. Textural properties were analysed by N_2 physisorption at liquid nitrogen temperature using a Micrometrics ASAP 2020 automatic analyzer. All the NPs were degassed at 50 °C for 12 hours at 10 μmHg. The specific surface area was obtained by applying the Brunauer-Emmett-Teller (BET) method equation. Pore size distribution was determined applying the Barrett, Joyner, Halenda (BJH) method equation to the desorption branch of the isotherms. H_2 chemisorption was performed using a Micrometrics ASAP 2020C apparatus. A chemisorption stoichiometry H:M = 1:1 was assumed for the calculation of the exposed metal surface area. The materials have been degassed at 100 °C for 6 hours. H_2 chemisorption isotherms have been recorded in 1 – 400 torr pressure range at room temperature. The Pt concentration in the catalyst was quantified by means of Inductively Coupled Plasma-Optical Emission Spectrometry (ICP-OES) using an Optima 8000 instrument (Perkin Elmer; Waltham, MA, USA) with an integrated S10 autosampler. A five-point standard curve was used for ICP-OES measurements (range 0-10 mg L^{-1}). The limit of detection at the operative wavelength of 228.616 nm was 0.01 mg L^{-1}. Powder X-ray diffraction (XRD) analysis was performed on a X'Pert Philips MPD with monochromatic Cu Kα radiation (λ = 1.5406 Å), the range used was 2θ = 10–120 ° in Bragg-Brentano geometry with a step size of 0.0263 °. The average crystallite size was determined applying Scherrer equation $D = (k * \lambda)/(\beta \cos \theta)$ where D is the mean size of the crystallite, the Scherrer constant k = 0.9354 was obtained by tabulated values for the octahedral crystallites determined for hkl = 111, λ is the x-ray wavelength expressed in Å, β is the full width at half maximum (FWHM) of the first XRD peak expressed in radians and θ is the Bragg angle. IR spectra were recorded in attenuated total reflectance (ATR) mode on a Shimadzu IRAffinity-1S spectrophotometer equipped with a QATR 10 accessory.

4.2. Reduced polynuclear Pd complexes for Suzuki cross coupling reactions

4.2.1. Introduction

Cross coupling reactions are a class of metal catalysed transformations that involve the formation of a carbon-carbon or carbon-heteroatom bond. This class of reactions is very important for various applications and became fundamental in the pharmaceutical industry since, for all the drugs produced, a palladium catalysed coupling is applied at some point of the synthetic process. The palladium catalysed Suzuki cross coupling of aryl halides with boronic acids is one of the most known and used reaction of this class.

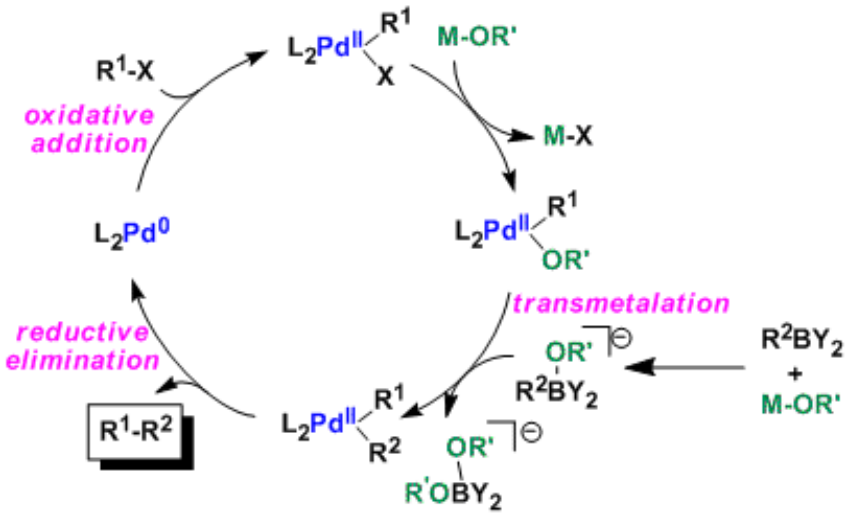

Scheme 4.2. Catalytic cycle for the Pd-catalysed Suzuki cross coupling reaction.

From a mechanistic point of view, the reaction starts with the oxidative addition of a haloarene to Pd(0) generating a Pd(II) intermediate adduct that consecutively engages transmetalation with a base-activated boronic acid giving rise to a secondary intermediate, which finally undergoes reductive elimination restoring the Pd(0) catalyst and delivering the final product (Scheme 4.2). The development of this reaction and its improvement has been mainly restricted to homogeneous catalysis where the Suzuki coupling has flourished with impressive progress.[663–668] Nevertheless, a great variety of heterogeneous systems based on palladium NPs have advanced in the research field.[669–675] A large number of studies in this area targeted the design of efficient heterogeneous systems with a two-fold aim: promote coupling reactions with low metal loadings and to easily recover and recycle the catalyst. However, very often these new supported catalysts were used in Suzuki couplings aiming primarily at a functional characterization of the catalyst itself rather than

to a real reaction optimization to achieve higher yields or wider scope. Suzuki coupling was employed as model reaction to provide evidence for the catalytic activity of various palladium nanostructures deposited on suitable supports. Most of these coupling reactions performed in presence of a heterogeneous catalyst could be run at moderate temperatures or even at room temperature,[676] and photocatalytic variants have been described as-well.[677,678] As discussed in the introduction section, a debate is still active concerning the real active species in the coupling reactions when solid palladium catalysts are used.[679–682]. Nowadays for the cross coupling reactions promoted by Pd NPs, or in general Pd in solid phase, a cocktail-type mechanism is widely accepted (Figure 4.20).[542,683] This cocktail-type mechanism is based on the dissolution and re-deposition of the active species promoting the reaction such as single atoms, clusters and NPs, either deposited on the support or truly in solution because of the leaching phenomena. The generation of smaller active species, in particular, is governed by the leaching process involved during the reaction and promoted by temperature, solvent, ligands and especially reactant molecules (Figure 4.21). Another factor that influences the leaching process is the presence or formation of palladium oxide in the reaction environment. It has been demonstrated that amorphous PdO can be easily leached in solution increasing the amount of homogeneous metal species, thus enhancing the overall activity.[684–686]

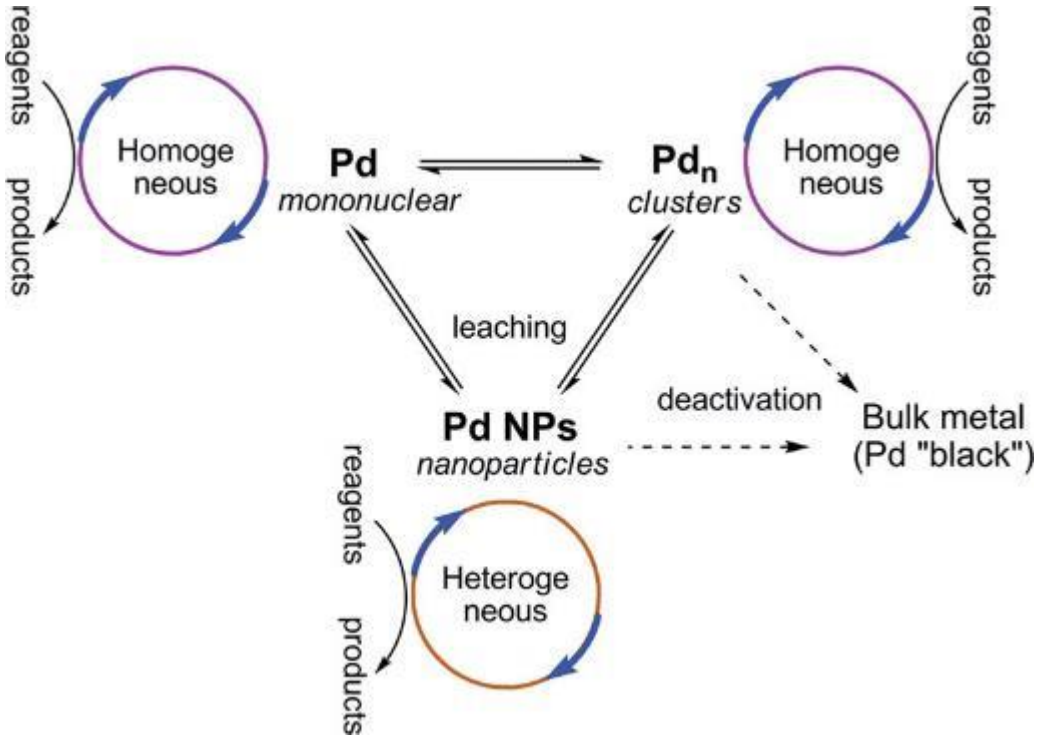

Figure 4.20. Interconversion of various catalyst in a "cocktail" type mechanism. Reproduced with permission from ref. [683]. Copyright 2012 American Chemical Society.

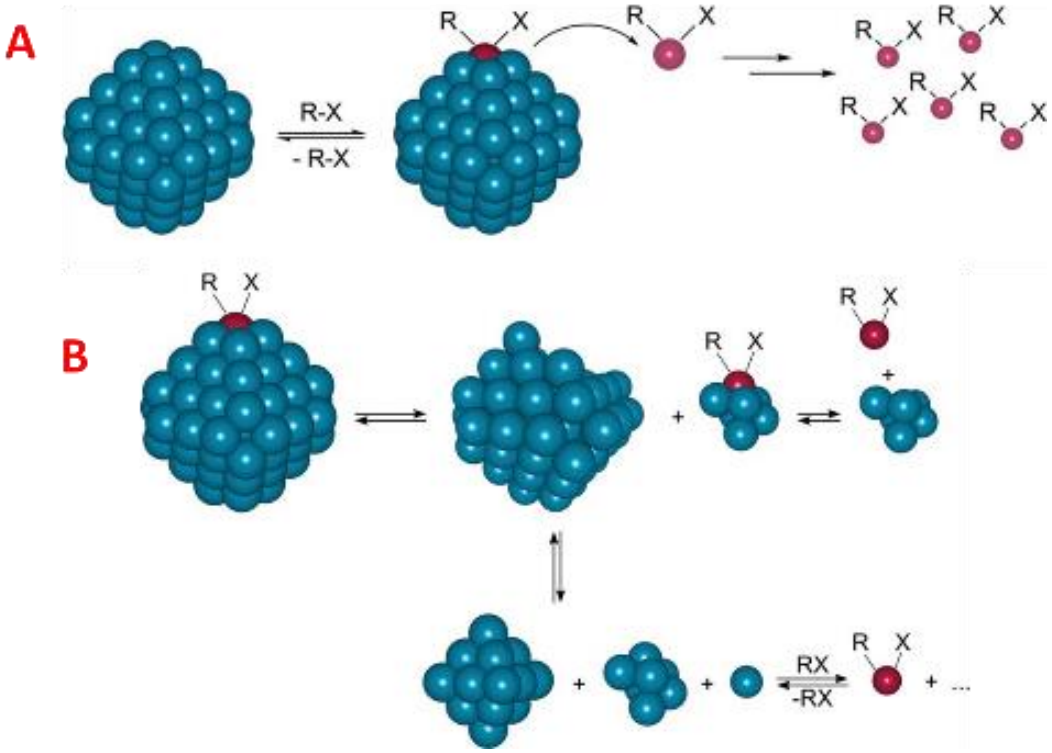

Figure 4.21. Schematic representation of the leaching process by detachment of single atoms (A) and by detachment of clusters (B). Adapted with permission from ref. [683]. Copyright 2012 American Chemical Society.

However, the leaching process raises another concern that is related to the loss in activity of the catalyst. Indeed, when the leached species in solution do not re-deposit on the support, they are lost during the recovery step of the catalyst that is usually performed by filtration and washing. This can lower the performance when recycled catalysts are used and becomes more and more relevant after every additional recycling step. Moreover, leaching without redeposition is also accountable for the contamination of the products that is a problem to be faced, especially in the production of active pharmaceutical ingredients.

Considering all these aspects, it should be pointed out that an optimal heterogeneous catalyst for cross coupling reactions based on solid palladium nanostructures is hardly achievable, especially because the leaching issue is unavoidable and because of the hard discrimination between one type of mechanism with respect to the others in the cocktail-type catalysis. However, good examples of catalyst design have been reported for the minimization of these drawbacks like the one presented by Pérez-Ramírez and co-workers on the Palladium single-atom catalyst (SAC) supported on exfoliated carbon nitride for the Suzuki coupling of arylboronic esters with aryl halides.[687] In general, it should be pointed out that when working on cross coupling reactions catalysed by solid palladium deposited on a support a series of aspects must be taken into account: (i) polycrystalline nanostructured palladium has high leaching rate that can be translated in improved catalytic

activity; (ii) palladium oxide is more susceptible to leaching; (iii) at equal metal loading smaller palladium nanostructure give a higher concentration of leached species with respect to larger NPs; (iv) leaching issues can be excluded by using ligand protected NCs, such in the case of $Au_{25}(SR)_{18}$,[546] or by employing a support with coordinating functional groups; (v) re-deposition is favoured with the use of high specific surface area supports with appropriate pore size; (vi) homogeneous aggregation can be limited by performing the reaction at low palladium concentrations.

Besides having a very peculiar structure, tiara-like clusters can be considered very promising catalysts both in the ligand coordinated or reduced form.[435,688–691] Nickel thiolate tiara-like clusters have been employed as electrocatalysts for the HER[689] and OER[690] and for the photocatalytic hydrogen evolution by water splitting[688,691] with remarkable results. A series of platinum thiolate tiara-like clusters have been reduced in hydrogen to give small bare metal clusters that were exploited for the styrene hydrogenation reaction. Nevertheless, there are very limited catalytic studies on either the native metallacrown complexes, or on their reduced forms where these molecules could express their best performance as unprotected atomically precise clusters. Unfortunately, the reduced form of these complexes is hard to achieve since thiolates, commonly used as ligand to prepare the complexes, might leave metal-sulfide clusters after reduction step deactivating the metal itself.

In this chapter, the study on a reduced octanuclear tiara-like palladium complex coordinated by methyl thioglycolate ligands will be reported for the Suzuki cross coupling reactions. The synthesis of the complex was performed by means of conventional methods used for the preparation of organometallic complexes following an already reported protocol.[434] The complex was characterized to confirm its structure and afterwards it was supported on alumina and subjected to various treatments for the preparation of a final catalyst Pd_8/Al_2O_3, based on dispersed Pd clusters. Deep characterizations of the catalyst were performed by means of TEM analysis to investigate the clusters size preservation and their homogeneous dispersion. Additionally, XPS and EXAFS experiments were carried out to determine the effective reduction and composition of the Pd_8/Al_2O_3 catalyst. The as-prepared catalyst was then tested for the Suzuki cross coupling of arylboronic acids and aryl halides. The scope of the reaction was widely expanded considering a series of *meta*- and *para*-substituted aryl halides. The catalyst displayed a remarkable activity and a good tolerance toward *meta*- and *para*-substituted aromatic substrates. Finally, control experiments were performed to determine the catalyst robustness and performance was evaluated by benchmarking against two different Pd catalysts.

4.2.2. Synthesis and characterization of the catalyst

Pd complex synthesis and catalyst preparation

The assembling of the catalyst started with the synthesis of $Pd_8(SCH_2COOMe)_{16}$ complex (Scheme 4.3). Pd thiolate complexes have been reported in the literature and the reaction mechanism for their synthesis is known to first proceed through the formation of yellow coloured $Pd(SR)_2$ complexes that, in presence of a suitable base, initiate self-condensation delivering small linear oligomers which tend to cyclise when the nuclearity is high enough to give orange/red coloured stable cyclic complexes in solution (Figure 4.22).[437]

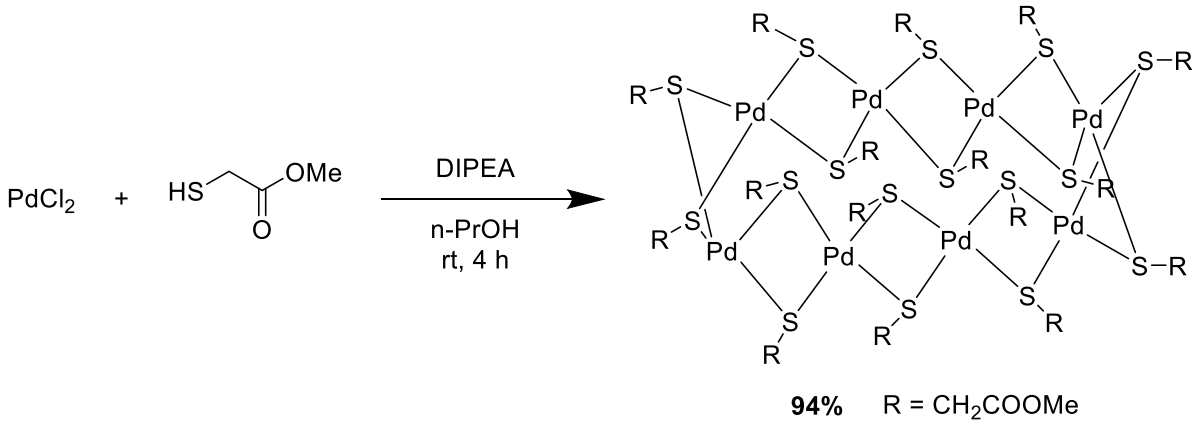

Scheme 4.3. Synthetic scheme of the $Pd_8(SCH_2COOMe)_{16}$ complex.

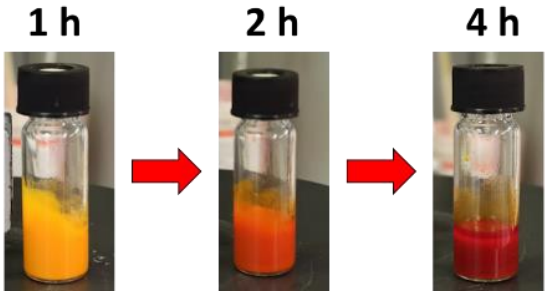

Figure 4.22. Colour progression of the palladium complex during the synthesis of $Pd_8(SCH_2COOMe)_{16}$.

The purity of the product was confirmed by ^{1}H-NMR of the crystalline material that was compared with the literature reference.[434] The spectrum, in chloroform, includes two methylene signals at 3.33 and 3.23 ppm and two methoxy signals at 3.96 and 3.77 ppm (Figure 4.23). These two sets of signals are attributed to the axial and equatorial methoxycarbonylmethyl arms of the cyclic complex. Different NMR signals for the same groups in axial and equatorial positions have been

also observed for cyclic hexameric Pd thiolate complexes.[692,693] The peak at 3.96 ppm appears as a slightly broad singlet due to the dynamic behaviour of the axial arms of the complex.

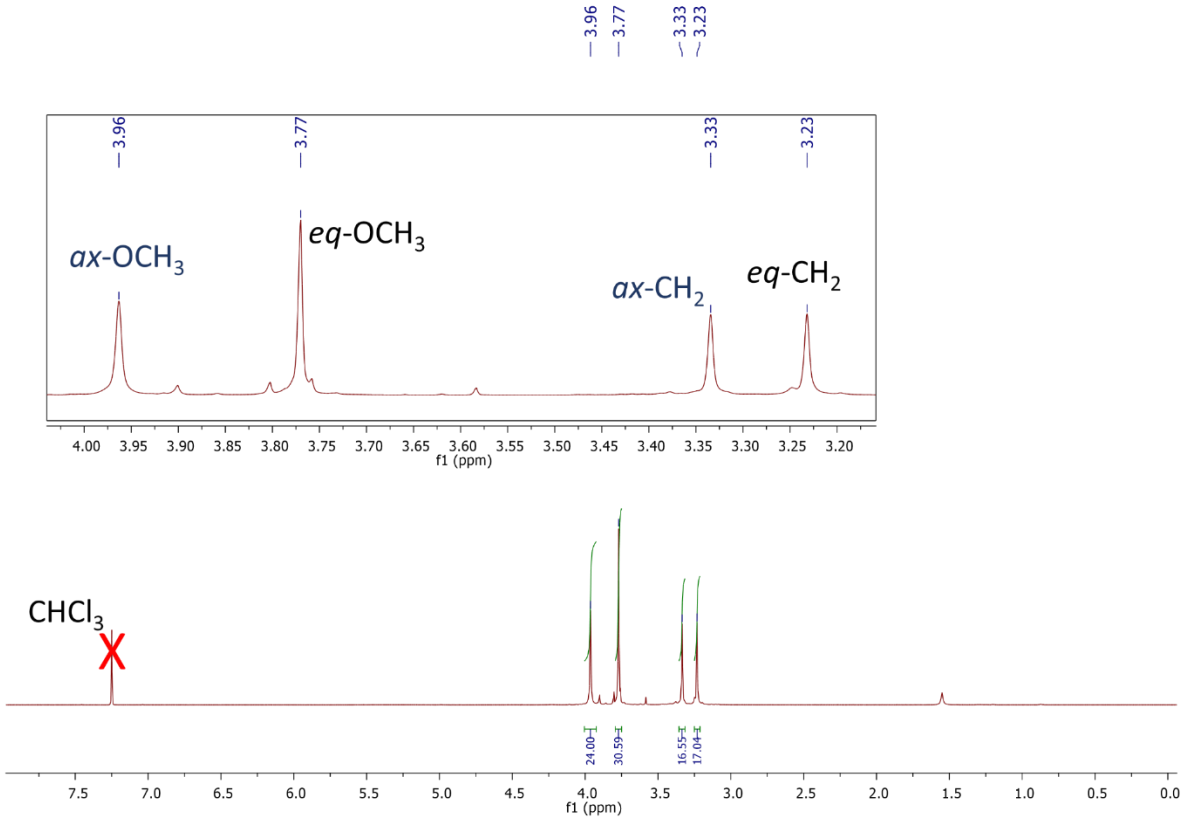

Figure 4.23. ^{1}H-NMR (500 MHz) spectrum of the $Pd_8(SCH_2COOMe)_{16}$ complex performed in $CDCl_3$.

The crystallized complex was then deposited onto Al_2O_3 through an irradiation/deposition process under UV light (Figure 4.24A). The deposition process was performed in order to obtain a nominal 0.2 wt%, as further confirmed by ICP-OES analysis to be in the range of 0.13-0.17 wt% (see Experimental section). It is well known that thiols and sulfides can undergo radical sulfur-carbon bond cleavage under UV light.[694] this was exploited for the formation of PdS clusters that can be adsorbed on alumina by dipole interactions. Without UV irradiation, the thiolate complex failed to adsorb on the support because of the hydrophobicity imparted by the organic ligand. Moreover, the choice of the support was pivotal in avoiding aggregation of the palladium during deposition, with Al_2O_3 being identified as the optimal choice. After irradiation, a slight colour change of both the suspension and the alumina was observed. The last step in the preparation of the catalyst consisted in the high temperature hydrogen reduction of the supported PdS clusters. The pre-catalyst, after being dried under vacuum was finely powdered and treated with H_2/Ar flow at 300 °C for 15 hours resulting in a grey brownish powder hereinafter referred to as Pd_8/Al_2O_3 (Figure 4.24B) .

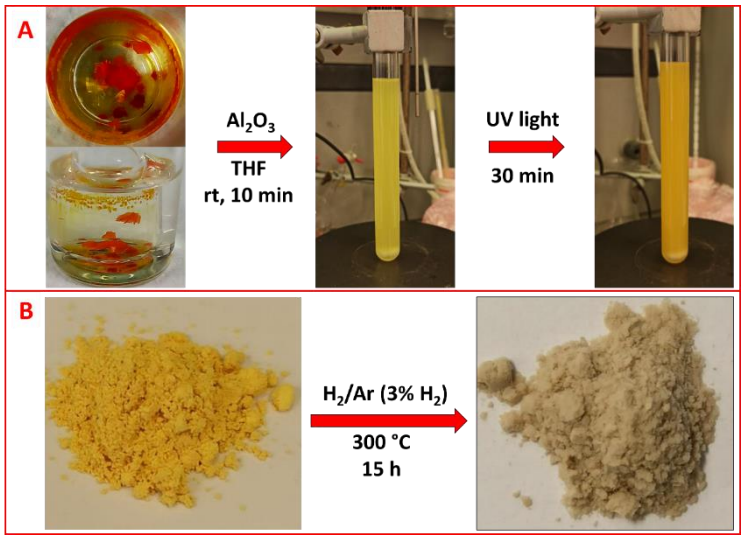

Figure 4.24. Representative images of the irradiation/deposition process (A) and reduction step in H_2/Ar performed on the pre-reduced catalyst.

Catalyst characterization

A preliminary characterization of the Pd_8/Al_2O_3 catalyst was carried out by means of electron microscopy analyses. Figure 4.25 shows an overview of the catalyst observed by TEM in bright field (BF) mode. The detected alumina particles show a dimension in the size range of 50-200 nm (Figure 4.25A) where the porous texture is clearly observable (Figure 4.25B). The alumina particles are composed of smaller crystallites of 10-20 nm in dimension and with high crystallinity as highlighted in Figure 4.25C. Unfortunately, no Pd clusters were detected in BF-TEM mode due to the small size of the clusters. However, switching to dark field STEM mode (DF-STEM), bright spots were detected on the support surface, the small number of spots is consistent with the low metal loading (Figure 4.25D, E). The few bright spots, having dimension around 1-2 nm, were subjected to EDX analysis to investigate the elemental nature. EDX line-profile measurements on two different clusters was performed and, in both cases, a Pd signal considerably higher than the background was detected confirming the metallic nature of the NCs (Figure 4.26).

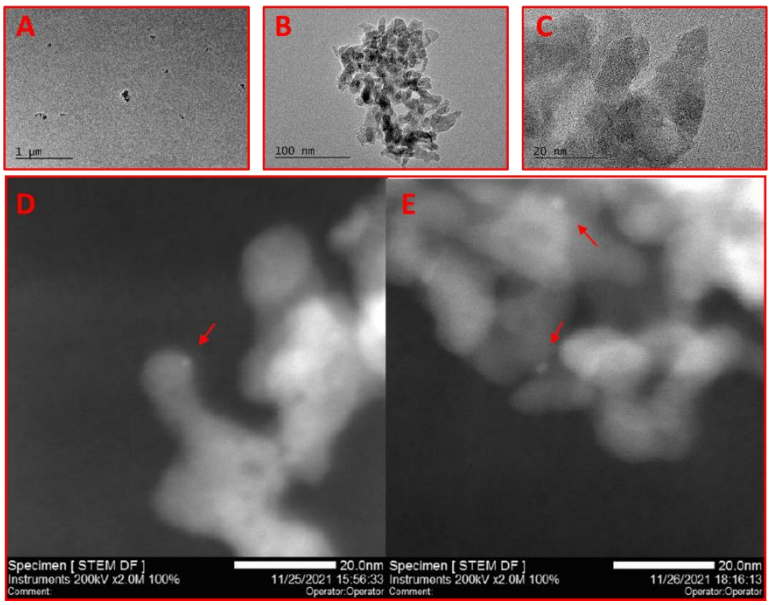

Figure 4.25. Representative BF-TEM micrographs of the Pd_8/Al_2O_3 catalyst (A, B, C) and DF-STEM high magnification micrographs with bright spots highlighted by red arrows (D, E).

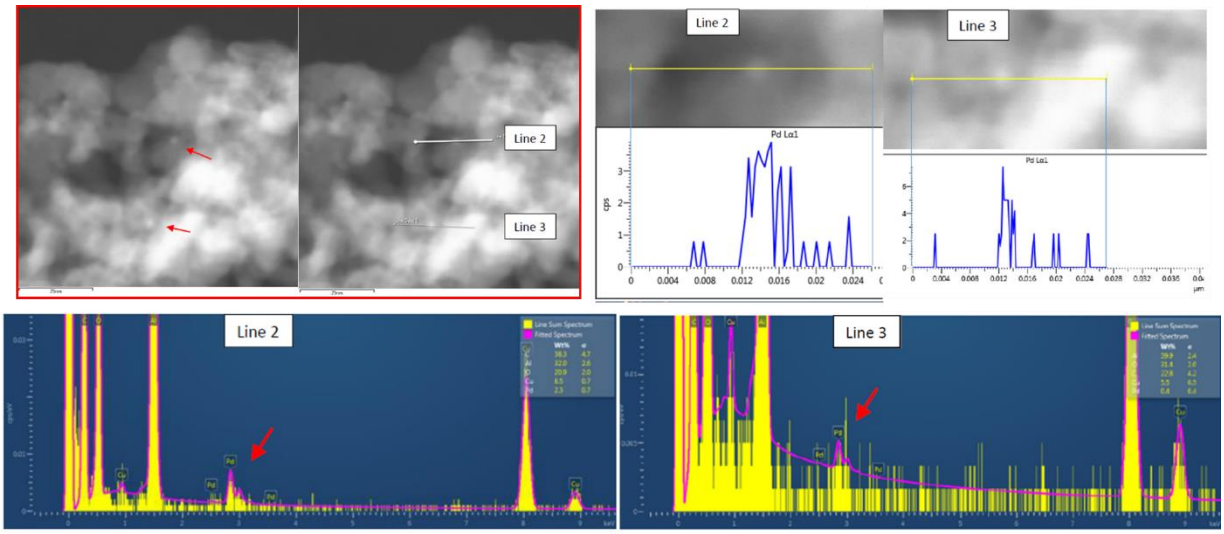

Figure 4.26. Summary of the STEM-EDX analyses on Pd_8/Al_2O_3 catalyst.

To confirm the effective removal of the organic ligands during all the treatments for the catalyst preparation, IR analysis were performed on the pre-reduced and post-reduced catalyst (Figure4.27). First, the $Pd_8(SCH_2COOMe)_{16}$ spectrum was acquired (orange) as a reference to be compared with the irradiated and reduced samples. The impregnated complex on Al_2O_3 still displayed the typical features of the organic ligands (red) as also did the pre-reduced catalyst (blue) but in minor percentage of transmittance suggesting the presence of the ligand in low trace amounts after UV irradiation/deposition treatment. However, the reduced Pd_8/Al_2O_3 (black) spectrum resulted

completely featureless in the range where characteristic peaks of the complex emerged, confirming the removal of organic ligands from the catalyst.

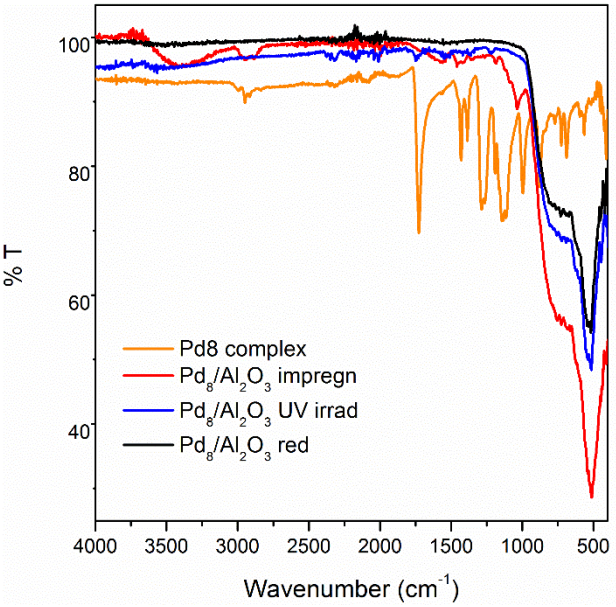

Figure 4.27. Representative IR spectra for the $Pd_8(SCH_2COOMe)_{16}$ complex, impregnated, pre-reduced and post-reduced catalyst.

XPS analyses were performed on the catalyst to investigate the reduction efficiency in generating metallic palladium clusters. Scan survey spectra for the pre-reduced and reduced catalyst are shown in Figure 4.28A and 4.28C. The Pd 3d spectrum falls in the 325 to 350 eV energy region and is not detected in the survey spectra due to its low quantity. High resolution acquisitions on the pre-reduced catalyst (Figure 4.28B) show the oxidised nature of Pd (336.3 eV, $3d^{5/2}$, 341.6 eV $3d^{3/2}$) that is found in the Pd^{+2} oxidation state suggesting its presence as palladium sulfide. This was also confirmed by analysis on sulfur with a binding energy of 164.0 eV (2 $p^{3/2}$) and 164.0 ($2p^{1/2}$) that is consistent with PdS.[695] As expected, the spectra of the Pd_8/Al_2O_3 catalyst after reduction treatment in H_2 (Figure 4.28D) highlight the strong presence of metallic Pd (335.6 eV, $3d^{5/2}$, 341.1 $3d^{3/2}$) while sulfur was below the detection limit, suggesting removal of large fraction of S during H_2 reduction.

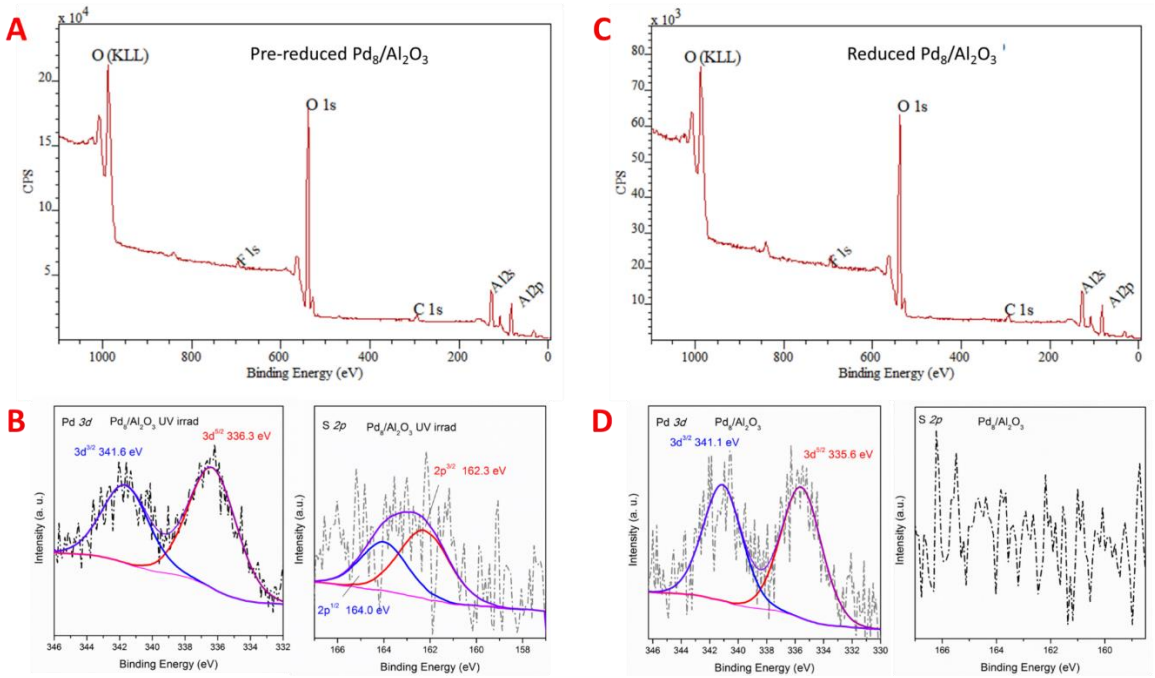

Figure 4.28. XPS analyses for the pre-reduced catalyst (A, B) and the reduced Pd_8/Al_2O_3 catalyst (C, D) with the high resolutions scans of palladium and sulfur.

Next, EXAFS measurements were performed on the catalyst to get insight on the species present in clusters and the coordination environment of Pd. Six samples were subjected to EXAFS analysis: $Pd_8(SCH_2COOMe)_{16}$ complex (denoted $Pd_8(SR)_{16}$), $Pd_8(SCH_2COOMe)_{16}$ impregnated on Al_2O_3 (denoted $Pd_8(SR)_{16}$ impregn), pre-reduced (Pd_8/Al_2O_3 UV irrad) and post-reduced catalyst (Pd_8/Al_2O_3), Pd_8/Al_2O_3 after 1 recycle and after 10 recycles. The obtained results are reported in Table 4.4. As expected, for the $Pd_8(SCH_2COOMe)_{16}$ complex only Pd-S was observed with a fixed coordination number of 4 and a distance of 2.32 Å which is in good agreement with the average Pd-S bond length. The same values were obtained also for the impregnated complex, confirming the retention of the molecular structure after adsorption on the support. The pre-catalyst after irradiation/deposition process (Pd_8/Al_2O_3 UV irrad) still displays the presence of sulfur on palladium although at a slightly reduced distance (2.31 Å) that suggests a small reassessment of the Pd clusters on the alumina support after the organic chain cleavage. A marked change in the Pd environment is observed after the reduction of the catalyst in H_2. Pd-S contribution to EXAFS signal strongly decreases to 0.9, suggesting removal of S from the surface in agreement with XPS analysis. Moreover, Pd-O and Pd-Pd distances appear in the fitting of the FT[k^2 $\chi(k)$]. The Pd-O presence is related to the interaction of Pd clusters with the support oxygens (CN = 2.1). However, the presence of palladium oxide cannot be excluded as the absorption of oxygen increases with the decreasing size of Pd NCs. Notably, the low CN for Pd-Pd (0.2) is a clear indication of the small size of the clusters. Regarding the catalyst used for the reaction, after the first cycle, a significant

increase in the Pd-Pd CN is observed (2.8) accompanied with a decrease for the Pd-O CN (0.4). This behaviour may be interpreted by the fast dissolution of Pd species in the reaction media and redeposition as metallic Pd to form bigger clusters. After the 10th recycle this trend is emphasised even more with the Pd-Pd CN of 6.5 and the disappearing of Pd-O contribution. All the results are well supported by the EXAFS spectra and their corresponding FTs in Figure 4.29 where the modulus of every material investigated is well fitted with the fixed parameters. Notably, the correct fit of the EXAFS signals of the catalysts used for Suzuki coupling still requires the introduction of a Pd-S contribution, with a CN around 1.2. This result suggests that part of S is still retained on the catalyst, probably on the surface of Pd clusters.

Table 4.4. Summary of the results obtained from EXAFS analyses.

		$Pd_8(SR)_{16}$	$Pd_8(SR)_{16}$ *impregn*	Pd_8/Al_2O_3 *UV irrad*	Pd_8/Al_2O_3	Pd_8/Al_2O_3 *1st recycle*	Pd_8/Al_2O_3 *10th recycle*
Pd-S	*CN*	4	4	3.8 ± 0.2	0.9 ± 0.2	1.3 ± 0.2	1.2 ± 0.2
	R (Å)	2.32	2.33	2.31	2.30	2.29	2.27
Pd-O	*CN*				2.1 ± 0.1	0.4	
	R (Å)				2.03	1.81	
Pd-Pd	*CN*				0.2 ± 0.1	2.8	6.5 ± 0.4
	R (Å)				2.76	2.78	2.74

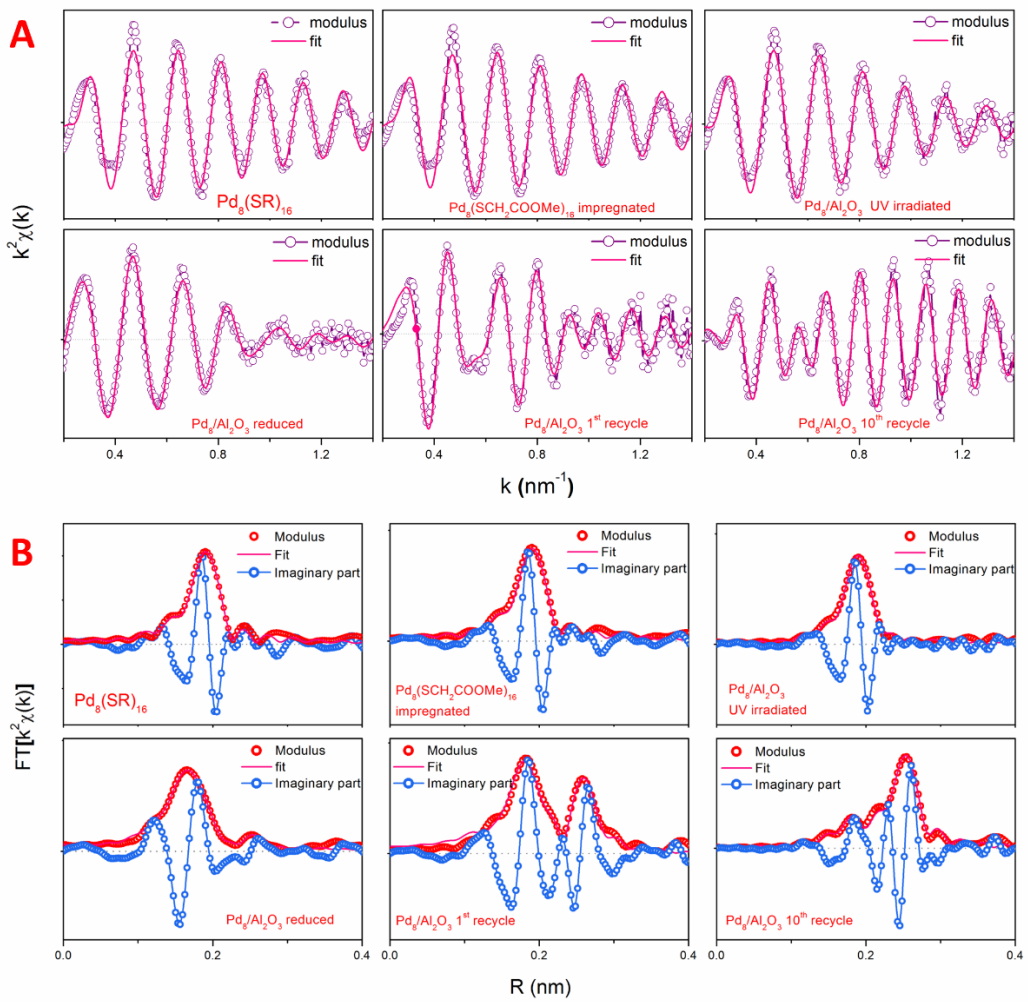

Figure 4.29. Fitted EXAFS (A) and Fourier transforms (B) spectra of the Pd complex, the materials along the preparation steps, after the first and last recycling test.

Before testing the catalyst, textural properties were investigated for the Pd_8/Al_2O_3 nanomaterial. Physisorption measurements were performed on the support and on the pre- and post-reduced catalysts. From the three isotherms shown in Figure 4.30 is it clearly observable the similarity of the materials. The visible hysteresis on the isotherms is a first hint of the preserved mesoporosity of the support during the various treatments. Moreover, the pore size distributions for alumina, UV irradiated pre-catalyst and the reduced catalyst perfectly match with a maxima of pore distribution centred at 28 nm (Figure 4.31). The detailed results of physisorption analysis are shown in Table 4.5. Clearly the high surface area of the support, previously calcinated at 900 °C for 24 hours, was maintained after the UV irradiation and reduction at 300 °C.

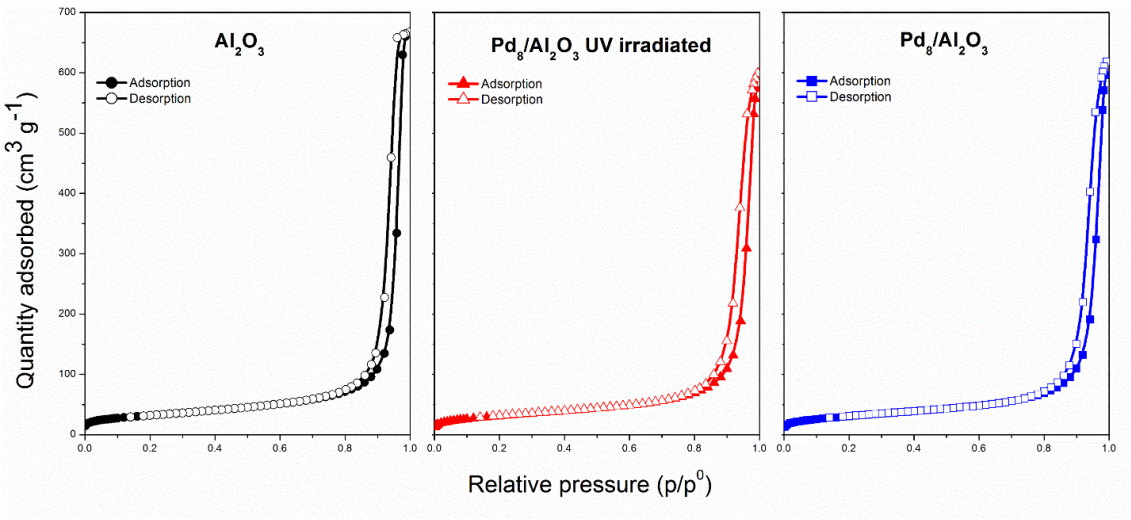

Figure 4.30. Physisorption isotherms for alumina (black), the UV irradiated pre-catalyst (red) and the reduced catalyst (blue).

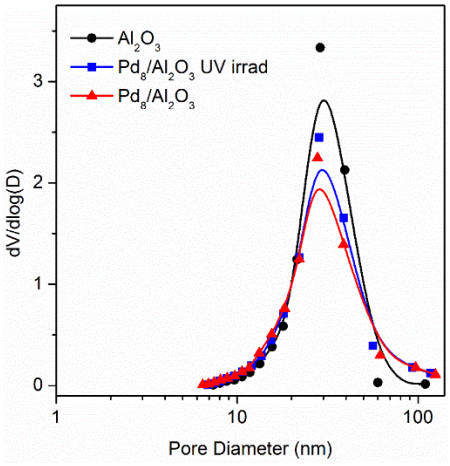

Figure 4.31. Pore size distribution, obtained from the BJH analysis for alumina (black), the UV irradiated pre-catalyst (red) and the reduced catalyst (blue).

Table 4.5. Summary of the textural characterization for, Al_2O_3, Pd_8/Al_2O_3 UV irradiated and Pd_8/Al_2O_3.

	S_{BET} [a] ($m^2\ g^{-1}$)	S_{ext} [b] ($m^2\ g^{-1}$)	V_{tot} [c] ($cm^3\ g^{-1}$)	V_{meso} [d] ($cm^3\ g^{-1}$)	D_M [e] (nm)
Al_2O_3	107	101	1.028	1.024	28
Pd_8/Al_2O_3 UV irradiated	104	110	0.914	0.914	28
Pd_8/Al_2O_3	103	107	0.945	0.945	28

[a] Specific surface area calculated following the BET method.
[b] Specific surface area external to micropores, determined from the t-plot analysis.
[c] Total volume of pores calculated from BJH analysis.
[d] Total volume of mesopores.
[e] Maximum of the pore size distribution, determined by BJH analysis.

4.2.3. Suzuki cross-coupling reactions and catalytic tests

The investigation of Pd_8/Al_2O_3 activity in Suzuki coupling reactions started with the optimization of the reaction conditions by a detailed screening of the solvent, base, temperature and reaction time. The coupling of bromobenzene with phenylboronic acid was selected as model reaction and, as initial parameters, the temperature was set at 50 °C and 30 minutes reaction time for the screening of solvents and bases. Initially, K_2CO_3 was used as a reference base for the solvent screening. As displayed in Table 4.6, water resulted in a poor conversion of the reactants. Although water is a good medium for the dispersion of supported catalysts, the limited solubility of organic reactants hindered diffusion on the catalyst resulting in a poor conversion. Alcohols such as EtOH and MeOH delivered the product with mediocre conversions (40.7% and 24.3% respectively). Indeed, alcohols and organic solvents are extremely efficient in solubilizing the coupling substrates but have poor abilities in homogenising the solid catalyst in solution. Interestingly, a combination of water and ethanol (1/1 v/v) resulted in very high conversion (> 99%) of the biphenyl product. Thanks to the miscibility of the two solvents, their beneficial character was combined synergistically giving a homogeneous suspension of the catalyst and an optimal dissolution and diffusion of the reactants. The employment of other organic solvents resulted again in very low conversions; with some solvents such as THF, 1,4-dioxane and DMSO only negligible conversion could be measured.

Table 4.6. Solvents screening for the optimization of the Suzuki coupling.

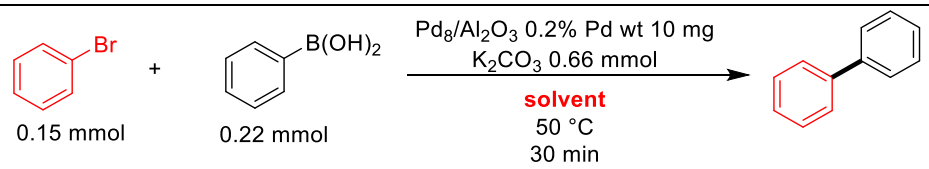

0.15 mmol 0.22 mmol

Entry	Solvent	Conversion (%)[a]
1	H_2O	4.5
2	EtOH	40.7
3	MeOH	24.3
4	EtOH/H_2O 1/1	> 99
5	MeCN	2.7
6	THF	traces
7	1,4-dioxane	traces
8	Acetone	2.2
9	Toluene	7.7
10	DMF	2.5
11	DMSO	traces

[a] Based on the biphenyl product and determined by GC-MS with benzophenone as internal standard.

After the 1:1 mixture of water and ethanol was identified as the best solvent, different inorganic and organic bases were screened (Table 4.7). First, a blank run was performed to highlight the pivotal role of the base in Suzuki coupling. Indeed, the base is involved in the promotion of the transmetalation between the palladium-aryl halide adduct and the boronic acid. Then, inorganic bases were screened displaying poor to discrete conversions. Other carbonates such as Cs_2CO_3 and Na_2CO_3 resulted in acceptable conversions, 40.7% and 60.4 % respectively, while phosphates, K_3PO_4 and Na_3PO_4, performed slightly worse. On the other hand, low activity was observed with the use of bicarbonates and hydroxides with conversions ranging from 11.1% to 15%. A similar behaviour was also observed when organic bases, such as amines, were employed except for DABCO that gave a product conversion of 34.6%. Hence, over all the bases screened, K_2CO_3 resulted the most performing allowing to achieve almost quantitative conversion.

In trying to further optimize the reaction conditions a test reaction was set up at room temperature (25 °C) resulting in decreased activity with a 43.9% conversion. The same behaviour was also noted when the reaction time was reduced from 30 to 20 in achieving 75% conversion only. After these considerations, the initial temperature and reaction time were kept as optimal conditions. The selectivity of the reaction was also investigated by control experiments to determine the homocoupling weight on the catalysed reaction. Two homocoupling catalytic tests were performed by using only one of the two substrates for the coupling reaction, bromobenzene or phenylboronic acid (Scheme 4.4). At the optimised reaction conditions, bromobenzene afforded the product only in traces while phenylboronic acid gave 2.2% conversion to biphenyl. These results suggest a very high selectivity of the catalyst in promoting only the cross coupling reaction with a high discrimination for the homocoupling of the substrates.

Table 4.7. Bases screening for the optimization of the Suzuki coupling.

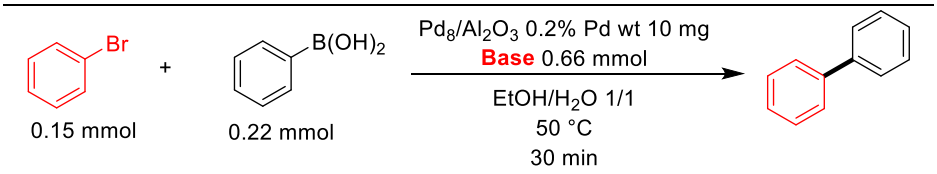

Entry	Base	Conversion (%)[a]
1	none	0
2	K_2CO_3	> 99
3	Cs_2CO_3	40.7
4	Na_2CO_3	60.4
5	$KHCO_3$	11.1
6	$NaHCO_3$	11.6
7	K_3PO_4	43.4
8	Na_3PO_4	24.9
9	KOH	12.3
10	NaOH	15
11	DMAP	traces
12	DABCO	34.6
13	DIPEA	7.3
14	TEA	13

[a] Based on the biphenyl product and determined by GC-MS with benzophenone as internal standard.

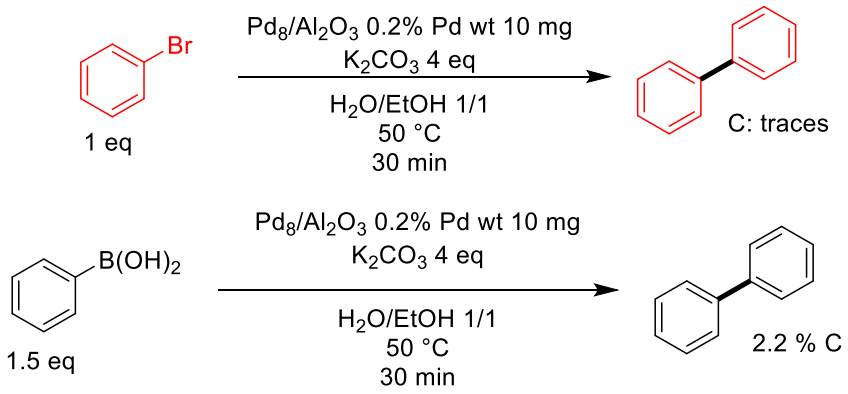

Scheme 4.4. Control experiments for the homocoupling selectivity toward bromobenzene (up) and phenylboronic acid (down).

To validate the high activity of the Pd_8/Al_2O_3 catalyst for the reaction, a crucial control experiment was performed. Along the years various studies have reported metal-free cross coupling reactions that were afterwards recognised to be the result of data misinterpretation.[696–698] It is well known that cross coupling reactions need a metal catalyst to work and when the metal is not provided on

purpose, alleged metal-free cross coupling reactions take place because the metal is already present as contaminant in the reagents. In order to discriminate palladium contamination coming from the reactants or from the base, a catalytic test was performed employing only the Al_2O_3 support without the Pd_8 clusters. As expected, the test failed pointing out no conversion of the reactants to the product, attributing the catalytic activity to the Pd_8 clusters only. Nevertheless, to highlight the importance of the reduction step in delivering an active catalyst, a test was performed with the Pd_8/Al_2O_3 UV irradiated pre-catalyst. The crude reaction mixture was analysed by GC-MS giving a conversion of 4% in biphenyl. Next, the scope of the reaction was expanded to a series of substituted bromoarenes (Scheme 4.5). The yields reported in the following are those of the isolated products after purification of the reaction mixture by flash chromatography. *Para*-substituted bromoarenes were mostly employed because of their availability, while *ortho*-substituted bromoarenes were not considered for the scope after a preliminary test on 2-bromobenzaldehyde that gave only traces of the product. Concerning the functional group (FG) tolerance, the catalyst behaved remarkably well, displaying a good tolerance toward various functional groups of different nature. Alkyl FGs were well tolerated in the catalysis providing the corresponding products **3a**-**3e** in excellent yields (from 87% to 99%). Aromatic substituents on the bromobenzene gave products **3f** and **3g** in high yield while the biphenyl resulting from the coupling of 2-bromo-6-methoxynaphtalene and phenylboronic acid (**3l**) was isolated with 80% yield. Hydroxy and methoxy FGs both in *meta* and *para* also resulted in products **3h**, **3i** and **3j**, **3k**, respectively, with good yield while bromoaniline derivatives delivered products **3n** and **3o** in almost quantitative conversion. Surprisingly, bromobenzenes with electron-withdrawing groups displayed good reactivity although they are known to reduce the kinetics of the oxidative addition step of the catalytic cycle. Bromobenzenes with electron-withdrawing FGs gave products in high to very high yield such as 4-trifluoromethylbiphenyl **3q** (99%), 4-phenylbenzonitrile **3s** (96%), 4-phenylbenzaldehyde **3u** (98%) or 4-biphenylcarboxylic acid **3x** (97%). Overall, the catalyst demonstrated to be well suitable in catalysing different meta- and para-substituted substrates with any difficulty in standard reaction conditions.

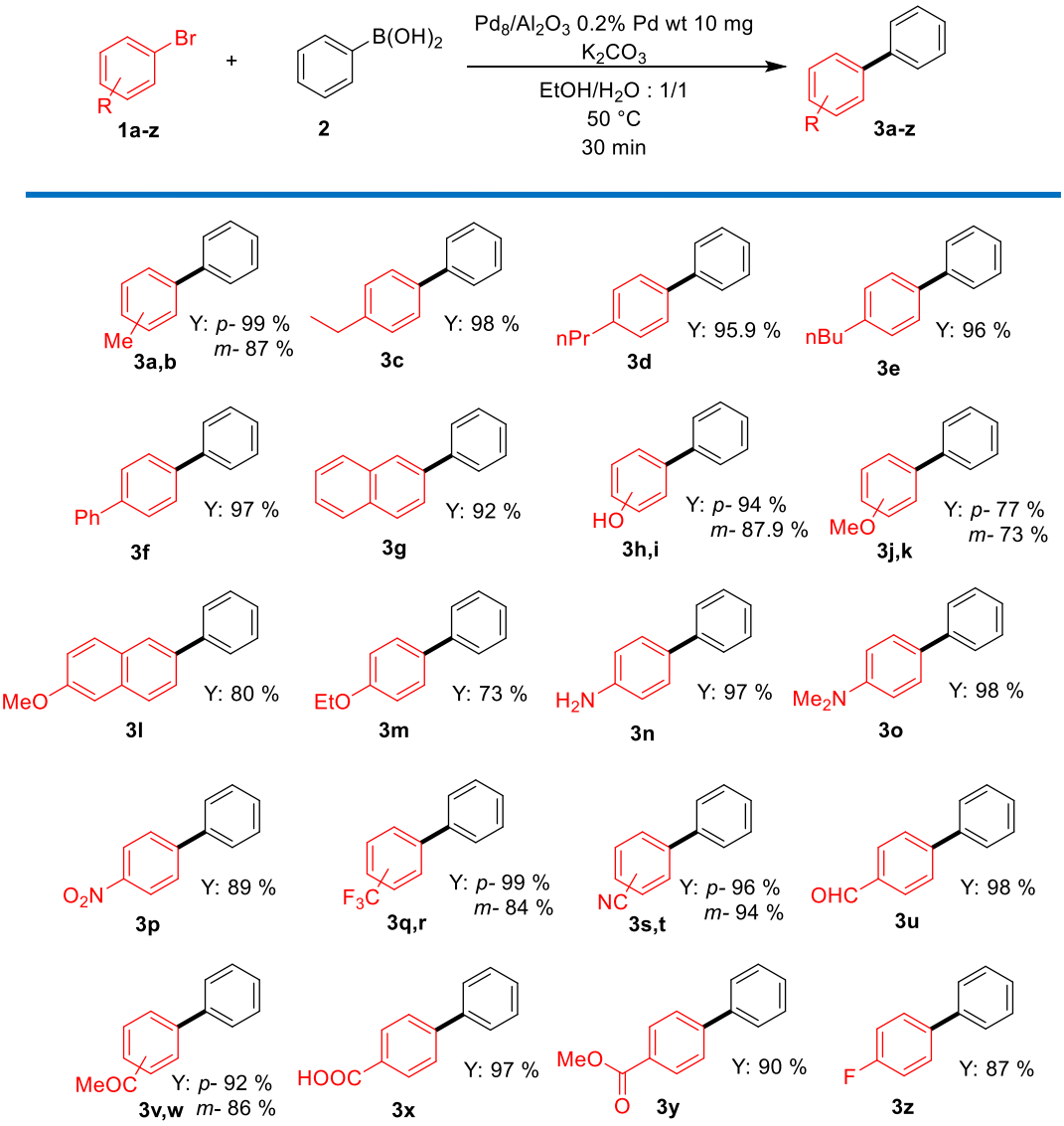

Scheme 4.5. Reaction scope expansion on bromoarenes.

Additional tests were carried out to compare the performance of Pd_8/Al_2O_3 with standard catalysts like the commercial Pd/C 10% and conventional Pd/Al_2O_3 prepared by impregnation and reduced at the same conditions used for the Pd_8/Al_2O_3 treatment. The quantity of catalyst used for the test was the same and was fixed at 0.12 mol% of Pd. As evinced from Scheme 4.6, the commercial Pd/C displayed poor activity (7.4% conversion) toward the Suzuki coupling under the same conditions used for Pd_8/Al_2O_3. The impregnated Pd/Al_2O_3 converted the substrates in product up to 24% which was higher with respect to Pd/C but still not comparable with the Pd_8/Al_2O_3 catalyst.

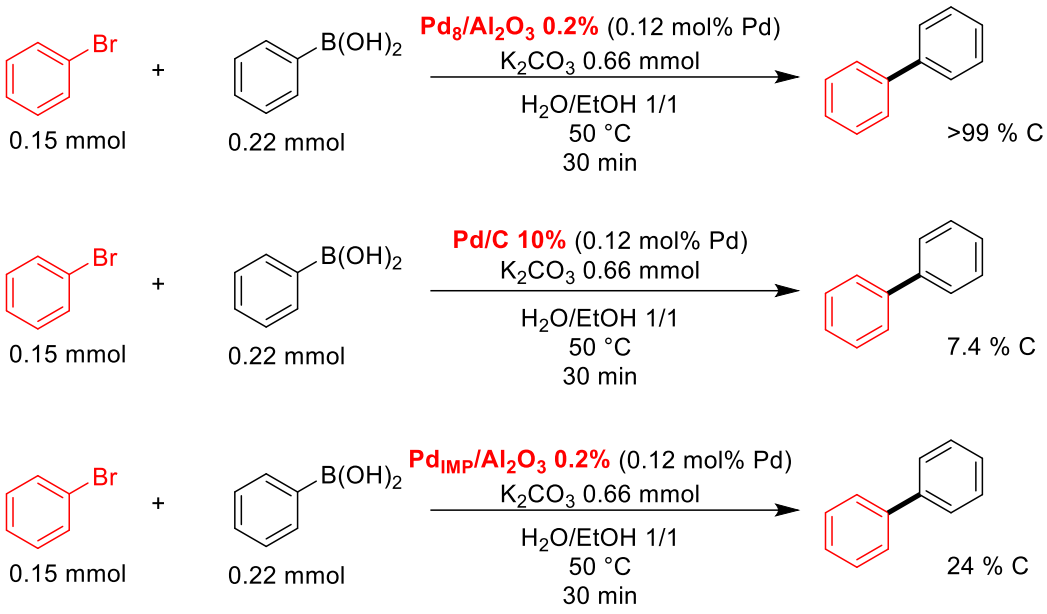

Scheme 4.6. Activity comparison based on the percentage conversion of the reactants to products for Pd_8/Al_2O_3, commercial Pd/C and impregnated Pd/Al_2O_3.

Besides catalytic activity, to estimate the usefulness of a solid phase catalyst, it is also important to consider its reusability and durability. The recycling tests are one of the most performed experiments for this kind of catalysts that can give hints on the stability of the material. For Pd_8/Al_2O_3, recycling tests were performed in the same optimised conditions used for the scope expansion. The results reported in Figure 4.32 represent the conversion of bromobenzene and phenylboronic acid to biphenyl using the same catalyst for 10 recycles. The ability of the catalyst in promoting the reaction with high conversions (between 96% and 99%) was maintained up to 6 recycles, after which conversion displayed a limited decrease down to 87% and 89% at the 9^{th} and 10^{th} recycle, respectively. It is reasonable to think that the high activity maintained for many recycles is the result of a negligible leaching effect on the catalyst. This negligible leaching was corroborated by elemental analysis by ICP-OES of the reaction medium after the catalytic tests. The analysis resulted in a palladium concentration lower than the detection limit of the instrument (20 ppb).

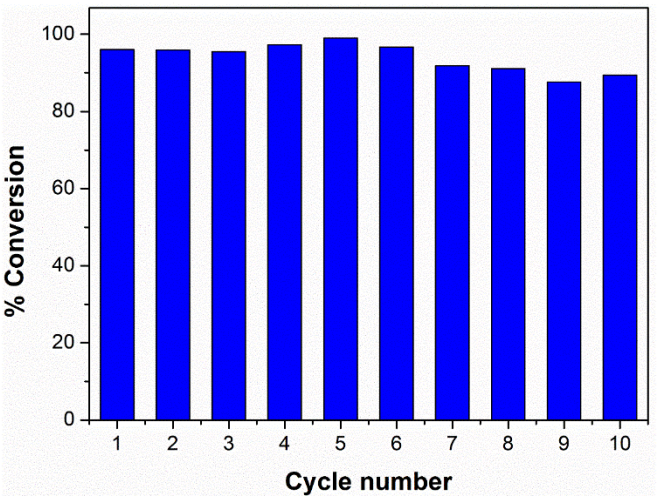

Figure 4.32. Recycling tests for the Pd_8/Al_2O_3 catalyst used in the Suzuki coupling of bromobenzene with phenylboronic acid.

4.2.4. Conclusions

In conclusion, this study exploited palladium polynuclear complexes for the design of a highly active catalyst for the Suzuki cross-coupling reactions. The complex and the catalyst were extensively characterized during all the preparation steps with different techniques. Electron microscopy analyses gave insight of the dispersion of palladium clusters while XPS and EXAFS investigations contributed in determining the composition and evolution of the palladium clusters. The high activity and selectivity of the catalyst was verified by extensive tests and control experiments. The good performance of Pd_8/Al_2O_3 allowed extending the scope of the reaction to include several bromoarenes carrying electron-withdrawing and electron-donating substituents. All the tested substrates were converted to the corresponding substituted biphenyls in excellent yields further confirming the flexibility of this catalyst in Suzuki coupling reactions. The higher performance of the Pd_8/Al_2O_3 was also corroborated by comparison test with a commercial Pd/C that resulted in a very poor conversion (7.4 %) with respect to our catalyst. Lastly the stability of Pd_8/Al_2O_3 was tested by repeated recycling tests, up to 10 recycles, that showed no rapid changes in the activity. This proof of concept study based on Suzuki cross-coupling reactions demonstrates the appealing potential of metal clusters obtained from polynuclear tiara-like complexes in the preparation of solid phase catalysts.

4.2.5. Experimental

Materials

All reagents employed were bought from Merck and Alfa Aesar and used without purification, unless where indicated. Solvents were purchased from Merck and VWR. Deuterated solvents were bought from Merck and Cambridge Isotope Laboratories. Al_2O_3 Puralox TH100/150 was supplied by Sasol. Reactions were monitored by TLC on Merck silica gel plates (0.25 mm) and visualized by UV light, $KMnO_4$ stain or $Ce_2(MoO_4)_3$ stain solutions. Flash chromatography was performed on Normasil silica gel 60® 40-63 μm purchased from VWR. All the glassware employed for the preparation of the materials and for the catalytic tests was cleaned with aqua regia (HCl/HNO_3 3/1 v/v) and rinsed with MilliQ water before use.

Synthesis of $Pd_8(SCH_2COOMe)_{16}$ complex

The synthesis of $Pd_8(SCH_2COOMe)_{16}$ tiara-like complex was performed following an already reported protocol.[434] Briefly, $PdCl_2$ (50 mg, 0.28 mmol) was first finely dispersed in 0.5 mL n-propanol with the aid of a sonication bath for 5 minutes. The as-obtained $PdCl_2$ dispersion was introduced, at room temperature, in a scintillation 4 mL screw capped glass vial, equipped with stirring bar, containing a 0.5 mL *n*-propanol solution containing 51 μL of methyl thioglycolate (0.57 mmol) and 96 μL *N,N*-diisopropylethylamine (DIPEA) (0.56 mmol). The reaction mixture was vigorously stirred at room temperature for 4 hours after which it was filtered on a Gooch funnel with type IV porosity frit. The yellow solid obtained from the filtration was thoroughly washed with methanol directly on the funnel to remove excess thiol and DIPEA. The Pd_8 complex was collected off the frit with DCM and was recrystallised by diffusion of *n*-pentane vapours in DCM at 4 °C for 3 days. Orange-yellow plate shaped crystals and their aggregates in blocks were obtained in 94% yield on Pd basis (84 mg, 0.33 mmol).

$Pd_8(SCH_2COOMe)_{16}$ irradiation/deposition over Al_2O_3 support

The deposition of the $Pd_8(SCH_2COOMe)_{16}$ complexes was performed as described: Alumina (100 mg) was first dispersed in 17 mL inhibitor free THF with the aid of a sonication bath for 10 minutes and vigorously stirred in a screw-capped tube-shaped vial. Subsequently, 1 mg of $Pd_8(SCH_2COOMe)_{16}$ dissolved in 3 mL THF was added dropwise to the suspension and stirred for an additional 10 minutes. The quantity of Pd complex to deposit was chosen in order to achieve a

final 0.2 wt% Pd loading. The as-prepared suspension was then irradiated with UV light (450 W halogen lamp) for 30 minutes under stirring to decompose the ligands and favour adsorption onto the support. After irradiation, the suspension was filtered on a 0.45 μm PVDF filter disk and dried at 60 °C under vacuum overnight. The as-obtained pre-catalyst was finely powdered before being reduced.

Reduction to Pd_8/Al_2O_3

The dried pre-catalyst was introduced in a tube-shaped quartz reactor equipped with a quartz inlet tube, screw-sealed together between rubber gaskets, and connected to H_2/Ar gas line. The reactor was then purged with Ar gas for 30 minutes and placed in a pit furnace where it was heated at 300 °C (5 °C min^{-1} ramp) for 15 hours under H_2/Ar flow (3 % H_2, 100 mL min^{-1}). After this reduction step, the powder was collected for further characterization and catalytic tests.

Suzuki cross coupling reaction general conditions

All the catalytic tests were performed in air (except otherwise stated) as follows: 10 mg Pd_8/Al_2O_3 (0.1% Pd wt), arylboronic acid (0.22 mmol) and K_2CO_3 (0.66 mmol) were introduced in a 10 mL screw-capped tube-shaped vial, equipped with stirring bar. Subsequently, 2 mL ethanol/water (1/1 v/v ratio) were added and stirred at room temperature. After 2 minutes, aryl halide (0.15 mmol) was added to the reaction mixture, the vial was sealed and placed in a preheated water bath at 50 °C for 30 minutes under vigorous stirring. After 30 min the vial was cooled to room temperature and extracted with EtOAc 2 x 5 mL. The EtOAc extracts were washed with water (5 mL) and brine (10 mL) before being dried over Na_2SO_4. After solvent removal, the product was purified by flash chromatography in *n*-Hex/EtOAc to yield the desired product. For the optimization of reaction conditions a calibration curve with internal standard (benzophenone) was created for GC-MS analysis and the reaction crude products were analysed prior to extraction and purification steps.

Characterization

The electron microscopy analysis was performed by Field-Emission Transmission Electron Microscope (JEM-2100 F, JEOL) operated at 200 kV. The microscope was equipped with a scanning transmission electron microscopy (STEM) unit and a detector for Energy-dispersive X-ray (EDX) mapping and spectroscopy (X-MAX80, Oxford). The samples were prepared by drop

casting an ethanol solution of the catalyst on a carbon-coated copper TEM grid and air-dried at room temperature. The images were analysed using ImageJ 1.52a software. ICP-OES analysis has been performed using an Optima 8000 Spectrometer (PerkinElmer) equipped with a S10 autosampler. The total palladium concentration was evaluated using calibration curves obtained by dilution of SpectrascanTM palladium standard solutions for ICP-OES analysis (Teknolab A/S, Norway). All standards (range: 0.1–50.0 mg/L) were prepared using a EtOH 96% solution to compensate the matrix effect. The used emission wavelength was 324.754 nm, the limit of detection 0.03 mg/L and the repeatability of measurements expressed as relative standard deviations (RSD%) and calculated on 6 replicates of various samples was lower than 4%. Calibration curves obtained by means of 5 standard solutions had correlation coefficients higher than 0.998. Textural properties were analysed by N_2 physisorption at liquid nitrogen temperature using a Micrometrics ASAP 2020 automatic analyzer. All the NPs were degassed at 50 °C for 12 hours at 10 µmHg. The specific surface area was obtained by applying the Brunauer-Emmett-Teller (BET) method equation. Pore size distribution was determined applying the Barrett, Joyner, Halenda (BJH) method equation to the desorption branch of the isotherms. The X-ray photoelectron spectroscopy (XPS) measurements were performed in an ultrahigh vacuum (UHV) spectrometer equipped with a RESOLVE 120 MCD5 hemispherical electron analyser. The Al Kα hv=1486.6 eV dual anode X-ray source was used as incident radiation. The constant pass energy mode was used to record both survey and high-resolution spectra, with pass energies 100 and 20 eV, respectively.

X-ray absorption spectra (named here µX both for normalized linear absorption coefficient or fluorescence yield), in the near edge (XANES) and extended (EXAFS) energy ranges, were measured at the SAMBA beamline of Synchrotron SOLEIL. Ex situ samples were analysed after deposition of the powders on polyvinylidene fluoride (PVDF) membrane. Spectra of samples at the Pd K edge were collected by measuring the Kα emission of Pd with a pixelated (6x6) Ge detector (Mirion) with DxMap digital signal processors (XIA). Dead time correction was applied on the basis of the calibrated estimate from DxpMap DSP cards by XIA Ltd. Data on standard materials were measured in transmission mode. EXAFS data analysis was carried out with theoretical standards from Feff 8.455 and with the Demeter software for data handling (Athena) and fitting (Artemis). All fits were carried out in R-space ($3.5 \leq k \leq 13$ Å^{-1} ; $1 \leq r \leq 3.2$ Å; EXAFS data have been k^2 weighted). The amplitude reduction factor (S_0^2) was estimated by fitting the EXAFS signal of finely meshed Pd metallic foil and its value was fixed to 0.87(5).

IR spectra were recorded in attenuated total reflectance (ATR) mode on a Shimadzu IRAffinity-1S spectrophotometer equipped with a QATR 10 accessory. Nuclear magnetic resonance (NMR) spectra were recorded on a Varian 400 spectrometer operating at 400 MHz for proton. The NMR

spectra have been processed by means of MestReNova software. ^{1}H-NMR spectra were referenced to the residual protons in the deuterated solvent. ^{13}C-NMR spectra were referenced to the solvent chemical shift. Chemical shifts (δ) are reported in ppm and the multiplicity of each signal is identified by the conventional abbreviations: s for singlet, d for doublet, t for triplet, q for quartet, dd for doublet of doublets, dt for doublet of triplets, m for multiplet, br for broad peak. Coupling constants (*J*) are reported in Hertz (Hz). GC-MS analyses were performed on a Agilent 7890 GC gas chromatograph equipped with an Agilent 5975C mass spectrometer and mounting a J&D DB-225 m column (60 m, 0.25 mm ID, 0.25 µm film) and using He as carrier. The conversion % in the catalytic tests was determined by interpolation of the product and internals standard peak area ratios in a calibration curve built with standard concentrations of biphenyl and benzophenone.

4.3 Photocatalytic hydrogen production promoted by Au NCs on TiO_2

4.3.1. Introduction

Oxygenated compounds undergo a faster oxidation process, compared to water, under photocatalytic conditions; consequently, the photoreforming of oxygenated compounds is more appreciated with respect to water splitting because of the higher efficiency. Indeed photocatalytic water splitting is very challenging from a thermodynamic perspective and usually sacrificial agents such as alcohols or amines are used to boost the reaction. Methanol has been widely employed as oxygenated molecule for the photocatalytic production of hydrogen thanks to its low activation energy toward oxidation that results in high conversions.[699,700] However, in the sustainable production of hydrogen, also the use of biomass derivatives as sacrificial agents for the photoreforming process are of high interest. Kondarides and co-workers have studied photocatalytic hydrogen production, mainly on titania based photocatalysts, from the oxidation of various biomass-derived feedstocks like ethanol, aldehydes and carboxylates.[701,702] Another interesting alternative relies on the use of glycerol that is obtained as a by-product of the biodiesel production; glycerol has a negative environmental fallout as the glycerol consuming processes are outpaced by the enormous amount produced.[703,704] In general, the advantages in producing hydrogen by photoreforming rely on the catalytic setup that enables reactions performed at room temperature and atmospheric pressure. Under these conditions, the sintering phenomenon, that can occur during the thermal reforming of hydrocarbons performed at high temperatures deactivating the catalyst, is completely avoided. In addition, the photooxidation of alcohols and other oxygenated compounds deliver valuable by-products like acetaldehyde and dihydroxyacetone, parallel to the hydrogen generation. As anticipated in the introduction, suitable materials for the photocatalytic hydrogen production are usually semiconductors with an appropriate band gap. The photogenerated electrons and holes are responsible for the reduction (Figure 4.33A) and oxidation (Figure 4.33B) semi-reactions. However, when the semiconductor is not efficient in propagating the charges all along its structure, a deactivation mechanism can occur because of electrons and holes recombination (Figure 4.33C, D) making ineffective the redox process.

The typical material used for the hydrogen production from oxygenated compounds is TiO_2 that has the great advantage of possessing the right band-gap for the photoreforming of alcohols. In addition titania is cheap, widely available and very stable from the chemical and physical perspective. However, the main drawback of TiO_2 resides on its wide band-gap (3.2 eV), thus TiO_2 needs to

adsorb UV light to generate charge carriers. Because the UV component in sunlight is only 4%, titania needs to be modified in order to improve its activity.

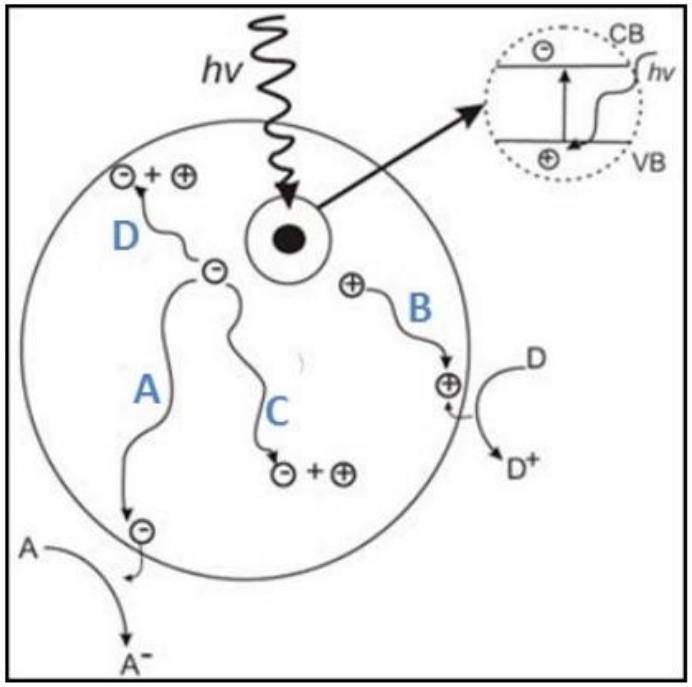

Figure 4.33. Schematic representation of the photogenerated electrons and holes and their involvement in the reduction (A), oxidation (B), bulk (C) and surface (D) recombination.

One of the main methods to enhance the photoactivity of TiO_2 is based on the use of metal NPs to improve the charge separation. Indeed, when a metal is deposited on TiO_2 a Schottky barrier is created at the interphase junction that favours the propagation of electrons on the metal avoiding their recombination with holes. Various studies have been reported based on this strategy and employing various metal NPs for the alcohol photoreforming over TiO_2.[705–708] Au nanostructures on TiO_2, although being less performing compared to Pt, are equally appreciated because of their stability toward oxidation. Au/TiO_2 catalysts have been widely investigated along the years for the production of hydrogen from alcohols with remarkable improvements.[708,709] In recent years, sub-nanometric gold NCs are becoming very appealing for photocatalytic applications and although they have been mainly used for photocatalytic water splitting,[607,609,610] some studies also reported NCs for the production of hydrogen by alcohols photoreforming.[605,710]

In this thesis work, thiolate and phosphine protected Au_n NCs (n: 11, 18, 23, 25) were prepared and used for the hydrogen generation from ethanol photoreforming. The clusters were synthesised by known procedures and were characterized by conventional analyses such as UV-VIS, NMR and TGA. Preparation of the catalyst was performed by irradiation deposition with UV light and by in-situ impregnation of the clusters on TiO_2 P25. The catalysts were tested for the photoreforming and

compared with a photodeposited Au/TiO_2 material. Because this study is still under development, the results reported in the following sections are to be considered preliminary.

4.3.2. Au NCs synthesis and catalyst preparation

Au NCs synthesis

The synthesis of the Au NCs was performed following reported procedures widely described in the literature. For the preparation of $Au_{25}(PET)_{18}^-TOA^+$ a size focusing procedure was followed.[332] The size focusing approach allows to obtain precise NCs by aging a solution of reduced NCs and NPs in presence of a specific thiol. The reaction involves different steps with the formation of different intermediates (Scheme 4.7). First the addition of TOAB results pivotal in delivering the Au_{25} clusters, indeed, it has been demonstrated that the absence of Br^- ions in the reaction environment causes the formation of bigger Au NPs.[711] The effect of the Br^- was ascribed to the stabilization of the charged $Au_{25}(PET)_{18}^-$ preventing its oxidation and agglomeration in larger NPs. Moreover, the darkening of the $HAuCl_4$ solution upon TOAB addition is related to the partial or complete ion exchange between Cl^- and Br^- in the Au(III) salt. The second step consists in the thiol addition to the reaction that delivers Au(I) intermediates. When the first synthetic procedures for thiolate protected Au_{25} NCs were reported, the formation of Au(I)-thiolate polymeric complexes as intermediates was considered plausible. However, this hypothesis was later disproved,[712] as Au(I)-thiolate complexes are almost completely insoluble in most of the common organic solvents and their presence is easily detectable by precipitate formation. Mechanistic studies, supported by NMR analysis and control experiments, disclosed the formation of $Au(I)X_2(TOA)$ as intermediate along with disulfide after the thiol introduction to the reaction mixture.

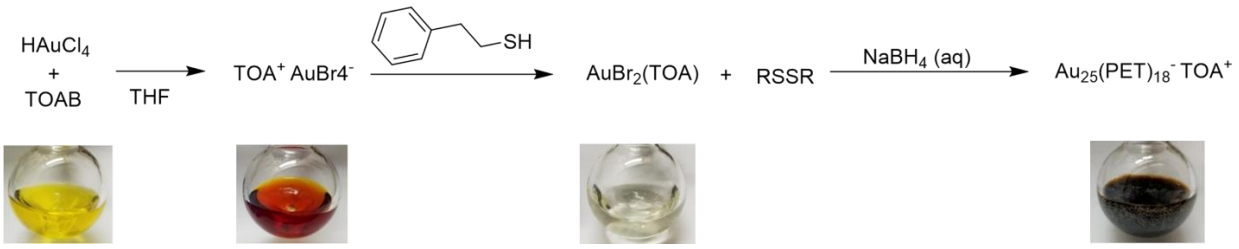

Scheme 4.7. Synthetic scheme for the $Au_{25}(PET)_{18}^-TOA^+$ preparation with the solution colour change upon every step.

In the third step, the Au(I) intermediate is reduced and aged in order to promote size focusing of clusters. Various protocols have reported the need of an inert atmosphere for the successful production of clusters,[331,332] however, it was documented that active oxygenated species, formed in

situ or provided by the solvent, can enhance the thiol etching in the size focusing step, thus oxygen, and in particular peroxide species, are supposed to be beneficial for the formation of small clusters.[711] After the $Au_{25}(PET)_{18}^{-}TOA^{+}$ was prepared and isolated, it was preliminarily characterised by UV-VIS. The spectrum obtained displays the characteristic absorption bands of Au_{25} in its reduced form with three maxima centred at 400, 450 and 670 nm (Figure 4.34). DFT experiment have shown that the absorption bands are related to HOMO-LUMO transitions with the absorption at 670 and 450 nm related to sp intraband transitions while absorption at 400 nm related to interband transition from d band to sp band.[330] ^{1}H-NMR spectroscopy was also performed on the Au_{25} cluster and compared with the literature finding a good match (Figure 4.35). In particular, it is possible to distinguish the inner and outer methylene protons in the dimeric staples for α and β positions with respect to the sulfur atom.

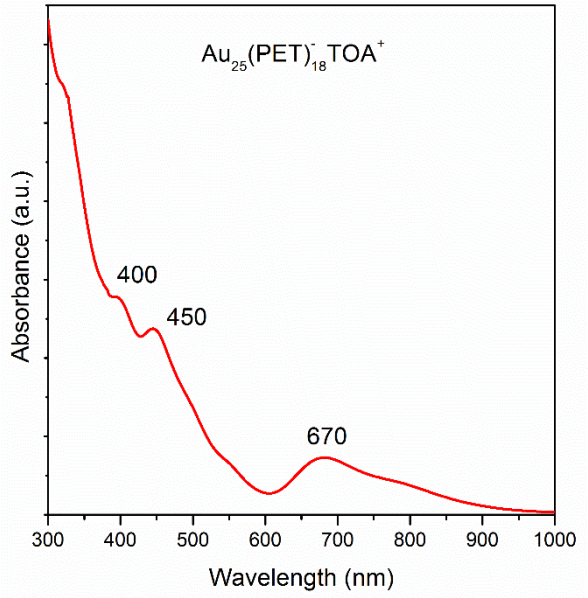

Figure 4.34. UV-VIS spectrum acquired in DCM for the $Au_{25}(PET)_{18}^{-}TOA^{+}$ NCs prepared by size focusing procedure.

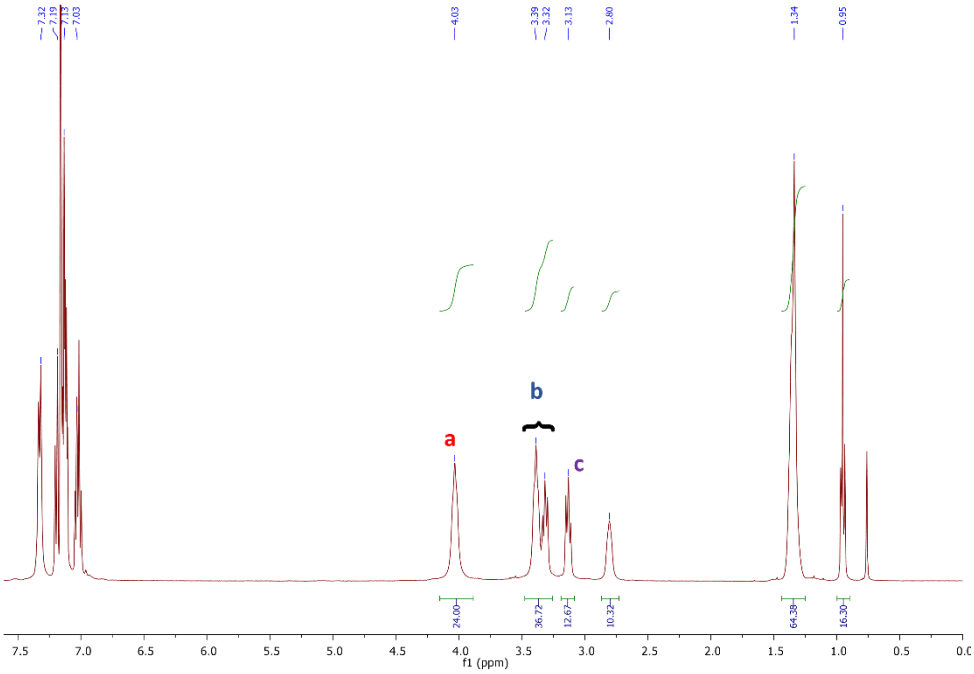

Figure 4.35. ^{1}H-NMR spectrum (400 MHz) recorded in benzene-d_6 of the $Au_{25}(PET)_{18}^{-}TOA^{+}$ NCs with the methylene protons highlighted by the red letters: α-CH_{2in} (a), β-CH_{2in} + α-CH_{2out} (b) and β-CH_{2out} (c).

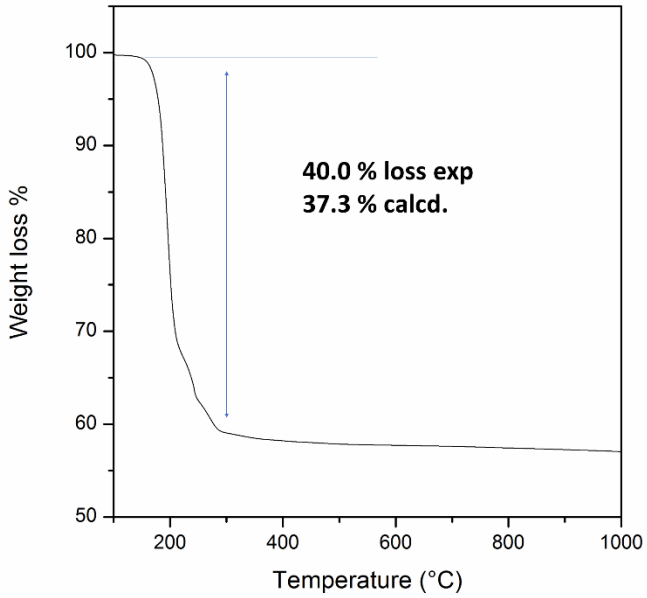

Figure 4.36. TGA analysis for $Au_{25}(PET)_{18}^{-}TOA^{+}$ NCs performed in nitrogen flow.

Moreover TGA analysis (Figure 4.36) was performed on Au_{25} clusters revealing a weight loss of 40.0% that is marginally higher than the calculated one. The higher weight loss is probably observed due to traces of thiol and/or TOAB.

The $Au_{23}(SCy)_{16}^{-}TOA^{+}$ NCs was prepared by reduction of $HAuCl_4$ salt with $NaBH_4$ following a reported procedure in methanol.[713] The formation mechanism is similar to the one described above for the Au_{25} clusters with the exception of using cyclohexanethiol as ligand that during the size

focusing delivered Au_{23} clusters which resulted the most stable under these conditions. The as-prepared cluster was characterized by UV-VIS spectroscopy and the resulting spectrum is reported in Figure 4.37. The spectrum exhibits only one absorption band centred at 570 nm with a small shoulder at 460 nm. This peak involves both the HOMO to LUMO and HOMO to LUMO+1 electronic transitions in the Au_{23} band structure. Additional characterization of the $Au_{23}(SCy)_{16}^{-}TOA^{+}$ NCs was performed by TGA analysis (Figure 4.38) in nitrogen finding a weight loss of 34.9% that is slightly higher than the calculated value, probably due to thiol and/or TOAB traces.

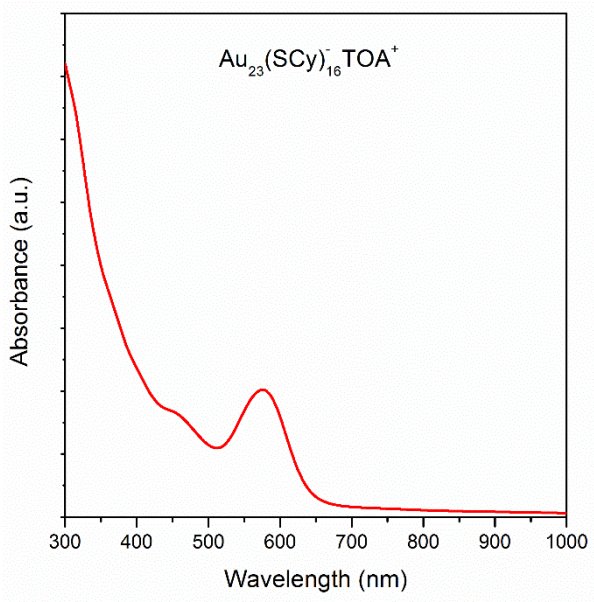

Figure 4.37. UV-VIS spectrum of $Au_{23}(SCy)_{16}^{-}TOA^{+}$ NCs performed in DCM.

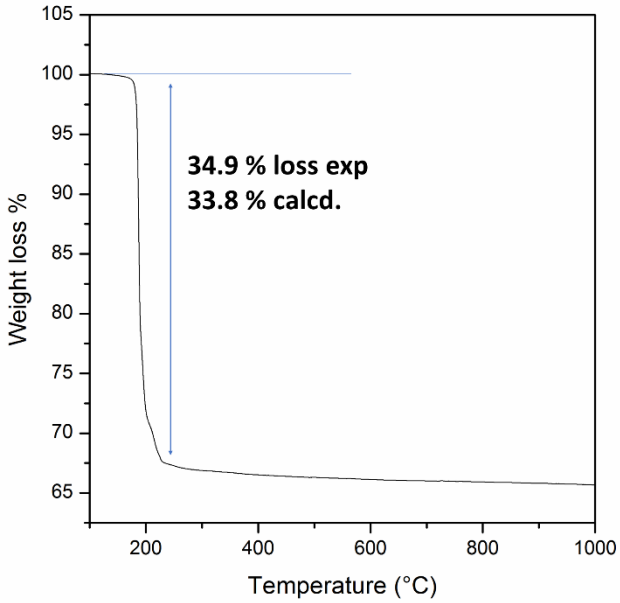

Figure 4.38. TGA analysis of $Au_{23}(SCy)_{16}^{-}TOA^{+}$ NCs performed in nitrogen.

$Au_{18}(SCy)_{14}$ NCs were similarly prepared to Au_{23} NCs but instead of using methanol as solvent, DCM was employed, while thiol and reductant were kept in large excess with respect to Au precursor.[714] It is interesting to note the completely different colour developed during the reaction in comparison to the Au_{23} or Au_{25} synthesis. Here, upon $NaBH_4$ addition, the colour changes from yellow to murky green without development of darker hues (Figure 4.39).

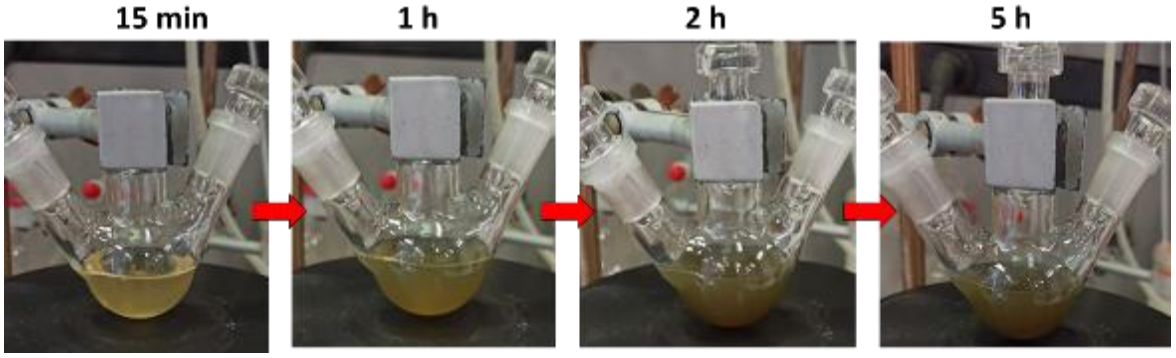

Figure 4.39. Synthesis of $Au_{18}(SCy)_{14}$ clusters: colour progression upon $NaBH_4$ addition to the reaction mixture.

This slower progression could be a preliminary hint of the more sluggish reduction kinetics in DCM. After reaction completion, the clusters were isolated and analysed by UV-VIS spectroscopy. The obtained spectrum (Figure 4.40) displays three absorption bands at 450, 570 and 630 nm correlated to HOMO-LUMO transitions.[714] TGA analysis performed on the Au_{18} clusters (Figure 4.41) revealed a weight loss of 31.5% that is in agreement with the calculated one of 31.3%, confirming the purity of the clusters.

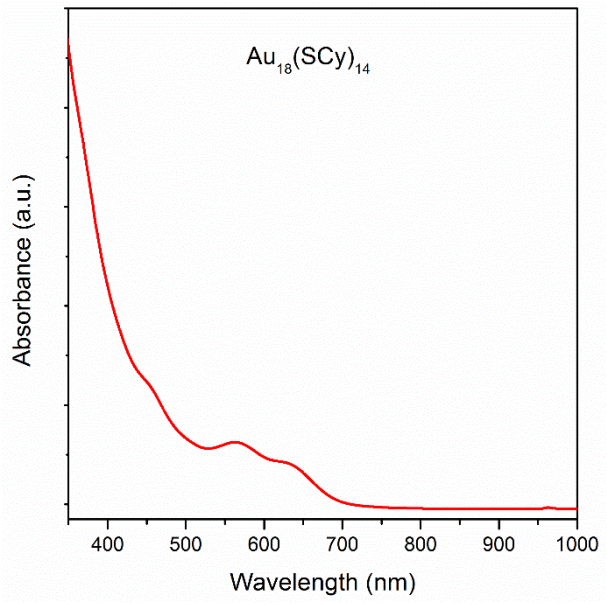

Figure 4.40. UV-VIS spectrum of $Au_{18}(SCy)_{14}$ performed in DCM.

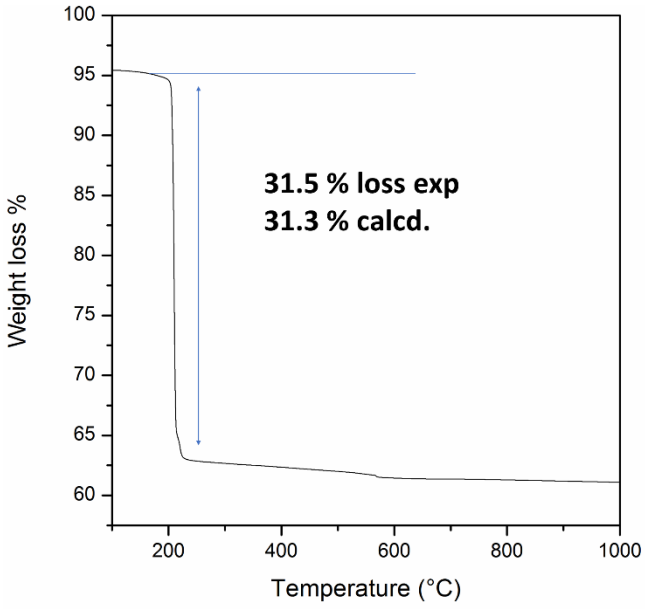

Figure 4.41. TGA analysis of $Au_{18}(SCy)_{14}$ performed in nitrogen.

The last Au cluster prepared was $Au_{11}(PPh_3)_7Cl_3$ that, differently from the previous three, is protected by phosphine ligands. The procedure adopted was reported in literature by Hutchison and co-workers.[358] The $Au_{11}(PPh_3)_7Cl_3$ cluster was usually reported as a by-product in the synthesis of $[Au_{11}(PPh_3)_8Cl_2]Cl$,[359,360] however the discovery of a procedure selective only for $Au_{11}(PPh_3)_7Cl_3$ allowed the isolation of this cluster in high yield. The procedure consisted in using large excess (5 equivalents) of $NaBH_4$ for the reduction of $AuPPh_3Cl$. Using lower reductant excess resulted in the formation of a mixture of $Au_{11}(PPh_3)_7Cl_3$ and $[Au_{11}(PPh_3)_8Cl_2]Cl$. Moreover THF is adopted as solvent to increase the solubility of Au precursor and $NaBH_4$. The Au_{11} clusters were isolated by precipitation of the reaction crude in pentane and dissolved in DCM after filtration. The UV-VIS spectrum $Au_{11}(PPh_3)_7Cl_3$ displays two main absorption peaks at 308 and 420 nm with smaller shoulders at 380 and 290 nm that are characteristic of this phosphine protected cluster (Figure 4.42). In addition the ^{1}H-NMR spectrum, reported in Figure 4.43, was registered and compared with the literature finding a perfect match, although small traces of triphenylphosphine (7.70-7.45 ppm) and $[Au_{11}(PPh_3)_8Cl_2]Cl$ (6.94, 6.84 and 6.70 ppm), as side product, were detected.[358]

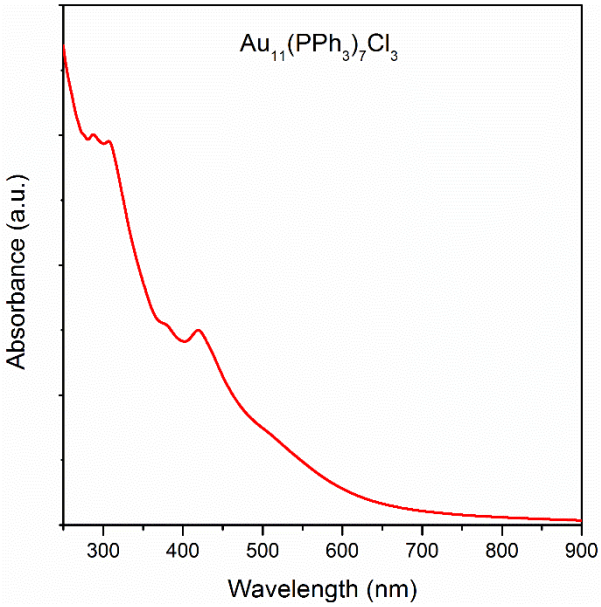

Figure 4.42. UV-VIS spectrum of $Au_{11}(PPh_3)_7Cl_3$ acquired in DCM.

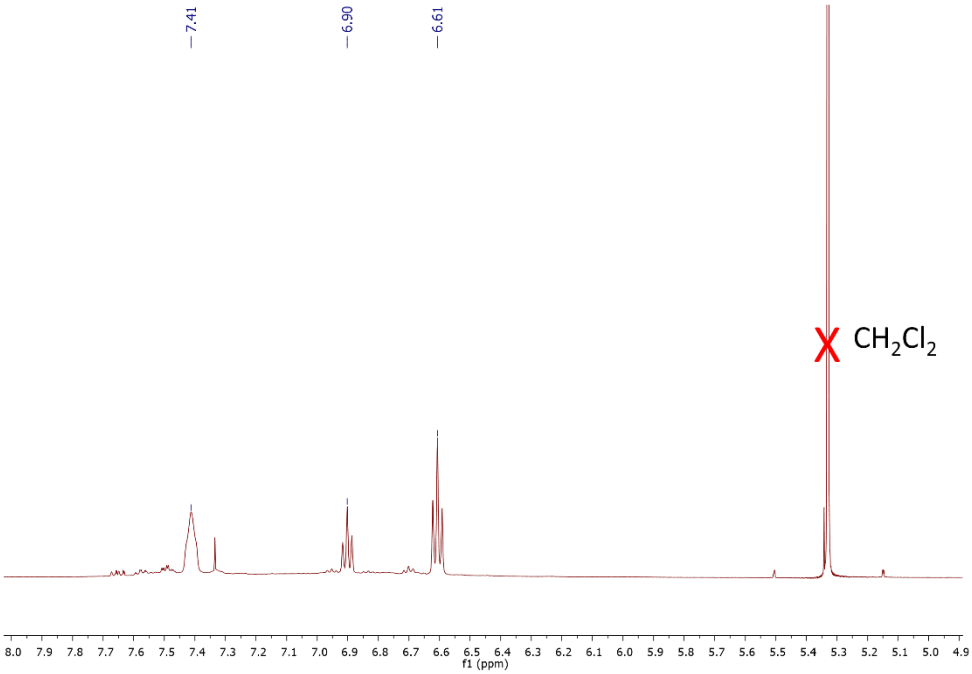

Figure 4.43. ^{1}H-NMR spectrum (400 MHz) of $Au_{11}(PPh_3)_7Cl_3$ performed in CD_2Cl_2.

Catalyst preparation

The catalysts used for the photoreforming of ethanol were prepared by using two protocols. The first protocol involved a UV irradiation deposition process on a TiO_2 dispersion in THF in presence of the desired NCs. UV light is able to promote thiol cleavage in organic molecules,[694] thus gold adsorption on TiO_2 is favoured once the organic ligand is detached from the cluster surface. After the UV irradiation process the catalyst was dried in vacuum and characterized by IR spectroscopy to evaluate the effective ligand removal. The spectra obtained are reported in Figure 4.44A and all four samples (Au_{25}/TiO_2, Au_{23}/TiO_2, Au_{18}/TiO_2, Au_{11}/TiO_2) displayed no particular feature related to the original ligand on the NCs (Figure 4.44B).

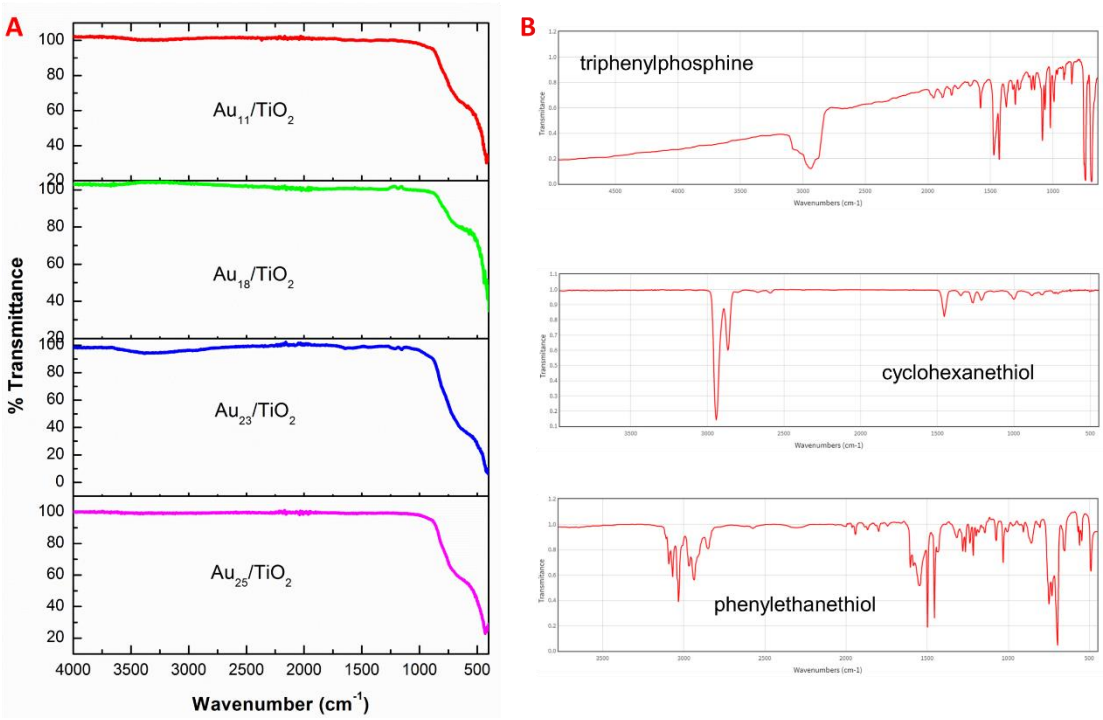

Figure 4.44. IR spectra of Au_{25}/TiO_2, Au_{23}/TiO_2, Au_{18}/TiO_2 and Au_{11}/TiO_2 prepared by UV irradiation deposition (A) and reference spectra for the ligands used in the preparation of the Au NCs (B). Reference spectra for the ligands were obtained from NIST database.

A preliminary microscopic analysis was performed on Au_{11}/TiO_2 after irradiation in order to investigate aggregate formations during the precipitation. The image reported in Figure 4.45 displays the Au_{11}/TiO_2 catalyst deposited on TEM grid but no Au NCs or bigger metal aggregates could be observed. Unfortunately, the low resolution power of the instrument did not allow a proper investigation, hence the detection of such small nanostructures resulted unsuccessful. However, new TEM experiments have been scheduled on advanced instruments.

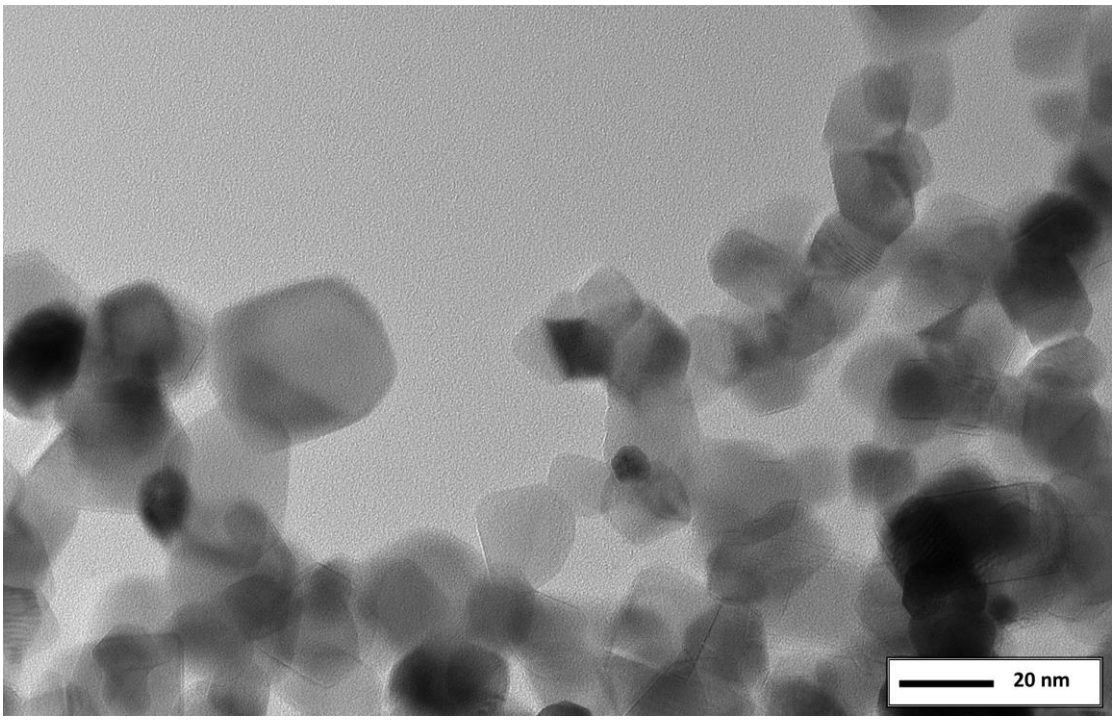

Figure 4.45. TEM image of the Au_{11}/TiO_2 catalyst prepared by UV irradiation deposition protocol.

Another set of catalysts was prepared, using the same Au NCs, by *in-situ* impregnation of the clusters on TiO_2 prior to photocatalytic tests. The Au loading was fixed at 0.1% wt and this value was confirmed by ICP-OES analysis. This strategy was used to investigate the influence of the protected NCs on the hydrogen production and for comparison with the UV irradiated catalysts. The *in-situ* impregnated Au_n/TiO_2 catalysts were characterized post photocatalysis by IR spectroscopy to assess the presence of ligands bonded to the metal cluster. Although other studies have suggested the ligand persistence on the clusters during photocatalysis,[715–717] we observed no ligand traces on the catalyst after the photoreforming (Figure 4.46). This result suggests the ligands removal during photocatalysis, probably due to the light-promoted radical processes. Hence, the catalysts prepared by the two protocols are considered to feature unprotected Au NCs, although deep characterization with other techniques (XPS) is needed to corroborate this hypothesis based on preliminary data. However, during the catalytic tests, with the *in-situ* impregnated catalyst, the thiolate ligands might have a role, at the first stages, before their complete decomposition by light.

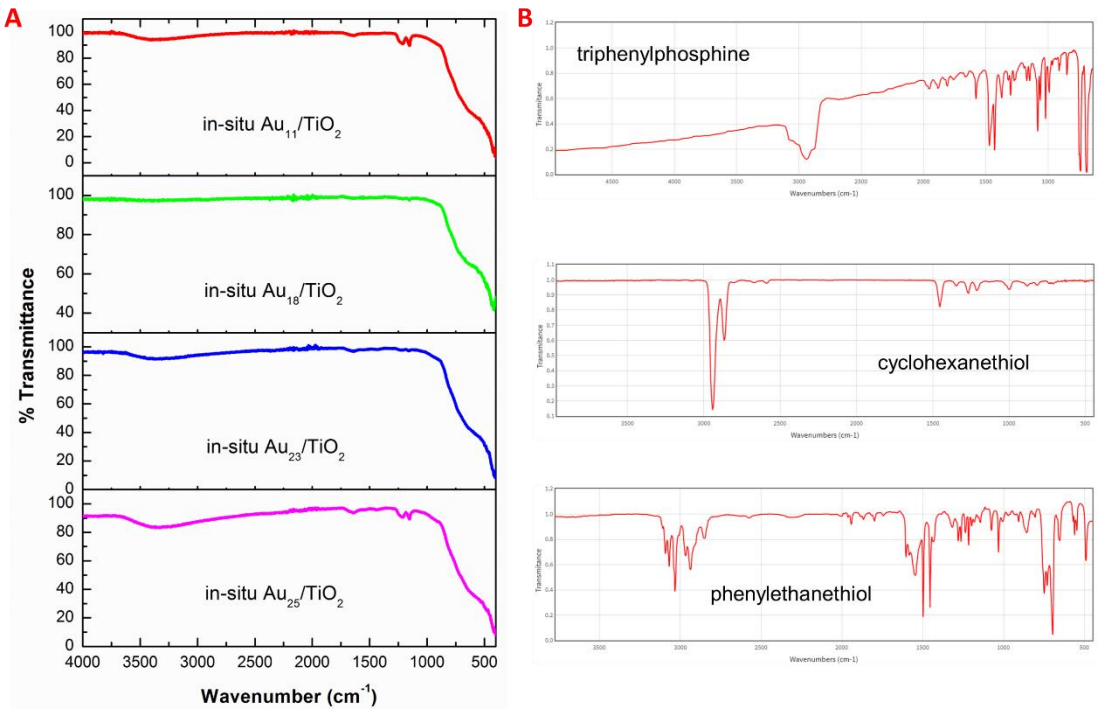

Figure 4.46. IR spectra of Au_{25}/TiO_2, Au_{23}/TiO_2, Au_{18}/TiO_2 and Au_{11}/TiO_2 prepared by *in-situ* impregnation of Au NCs on TiO_2 (A) and reference spectra for the ligands used in the preparation of the Au NCs (B). Reference spectra for the ligands were obtained from NIST database.

4.3.3. Catalytic photoreforming of ethanol for H_2 production

Preliminary catalytic tests were carried out under the same conditions for all the prepared photocatalysts in a thermostated reactor under inert conditions (Ar flow, 15 mL min^{-1}). The reactor was exposed to light generated from a solar simulator positioned at the same distance from the reactor porthole in every experiment. Preliminary tests, conducted to evaluate the hydrogen production, are discussed below.

First the catalysts prepared by UV irradiation/deposition were tested toward the photoreforming of ethanol and the results are reported in Figure 4.47 and Table 4.8. The photoreforming was carried out for 20 hours in order to study the performance stability in the hydrogen production. From the graph in Figure 4.47A, an overall high activity of the catalysts based on Au NCs is displayed by Au_{23}/TiO_2 and Au_{25}/TiO_2, in particular. Au_{23}/TiO_2 resulted the most active with a H_2 production of 1652 μmol g^{-1} h^{-1} at 20 hours. Nevertheless, also Au_{25}/TiO_2 had a comparable activity to Au_{23}/TiO_2 with 1635 μmol g^{-1} h^{-1} at 20 hours. Au_{18}/TiO_2 and Au_{11}/TiO_2 displayed a H_2 production of 1361 and 929 μmol g^{-1} h^{-1} , respectively. Compared to the photodeposited Au catalyst (1069 μmol g^{-1} h^{-1} at 20 hours), Au_{23}/TiO_2, Au_{25}/TiO_2 and Au_{18}/TiO_2 resulted much higher in activity, while Au_{11}/TiO_2 had a slightly lower H_2 production at 20 hours. From the data collected, a reduced activity seems to

correlate with a decreased number of metal atoms in the cluster. This trend was also documented in other studies for the photocatalytic water splitting with Pt clusters.[603] Moreover, another interesting aspect to be considered is the H_2 production stability of the Au_n NCs based catalysts that resulted much more constant along time compared to the photodeposited Au catalyst which had an initial fast upward trend that slowly decreased at longer times. This is also highlighted in the second graph with the production expressed in μmol g^{-1} as a function of time (Figure 4.47B). This behaviour suggested a possible agglomeration of the Au NPs in the photodeposited catalyst. In addition, TiO_2 was also tested in the photoreforming of ethanol as a reference to exclude possible activities deriving from contamination of the support. The TON (turnover number) and LFE (light-to-fuel efficiency) in Table 4.8 for the investigated catalysts are in line with the trends observed in Figure 4.47.

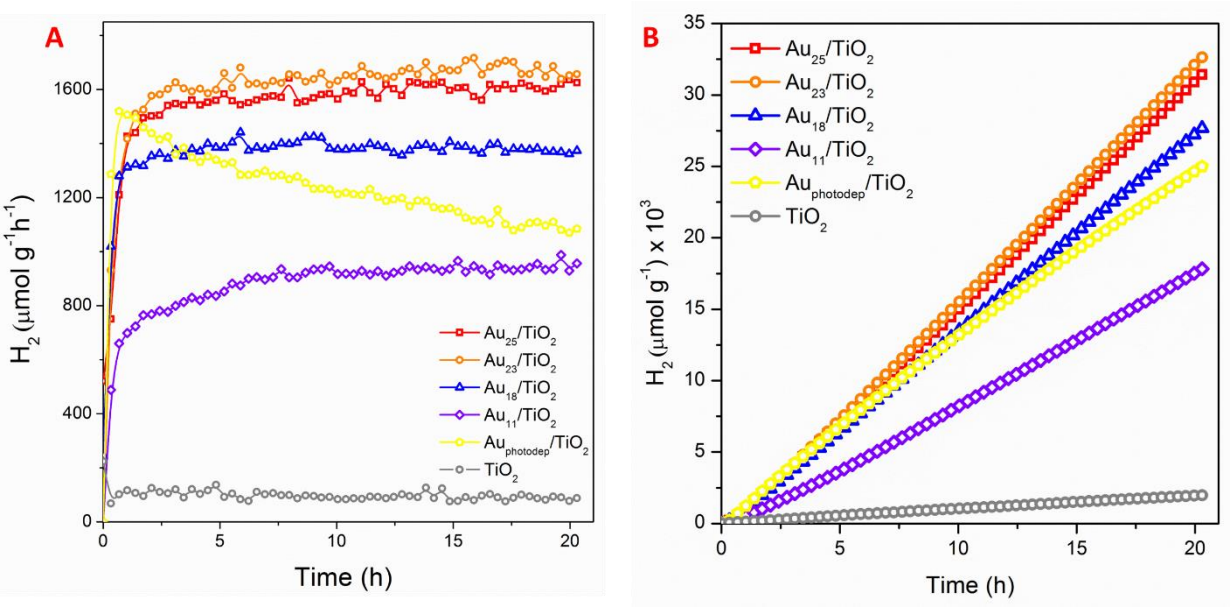

Figure 4.47. Photocatalytic H_2 evolution over time expressed as μmol g^{-1} h^{-1} (A) and as μmol g^{-1} (B) of the Au_n/TiO_2 catalysts, prepared by UV irradiation/deposition and compared with a photodeposited 0.1% wt Au/TiO_2 and TiO_2.

Table 4.8. Summary of the catalytic activities for the UV irradiation/deposition Au_n/TiO_2 catalysts and comparison with $Au_{photodep}/TiO_2$ and TiO_2.

Catalyst	*H_2 amount ($\mu mol\ g^{-1}\ h^{-1}$) @20h*	*H_2 amount ($\mu mol\ g^{-1}$) @20h*	*TON ($\mu mol_{H2}\ \mu mol_{Au}^{-1}$) @20h*	*LFE_{20}[a] (%)*
Au_{25}/TiO_2	1635	31436	6205	0.018
Au_{23}/TiO_2	1652	32644	6443	0.018
Au_{18}/TiO_2	1361	27677	5462	0.015
Au_{11}/TiO_2	929	17825	3518	0.007
$Au_{photodep}/TiO_2$	1069	24995	4933	0.011
TiO_2	77	1976	-	0.0008

[a] Light-to-Fuel efficiency

The catalysts prepared by *in-situ* impregnation were also tested in the same photocatalytic conditions applied to the UV irradiated ones. The results of these experiments are reported in Figure 4.48 and Table 4.9. Surprisingly, all the impregnated Au_n NCs exhibited a superior activity, with respect to the photodeposited Au/TiO_2 catalyst (1069 μmol g^{-1} h^{-1} at 20 hours), toward the H_2 evolution (Figure 4.48A).

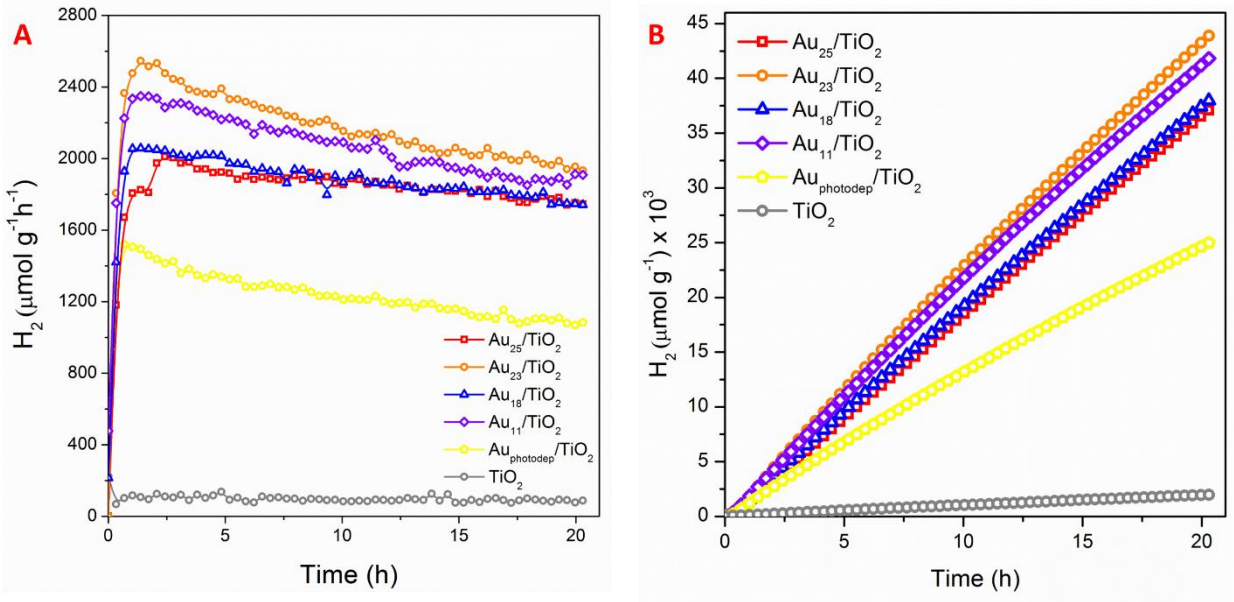

Figure 4.48. Photocatalytic H_2 evolution over time expressed as μmol g^{-1} h^{-1} (A) and as μmol g^{-1} (B) of the Au_n/TiO_2 catalysts, prepared by in-situ impregnation and compared with a photodeposited 0.1% wt Au/TiO_2 and TiO_2.

Table 4.9. Summary of the catalytic activities for the in-situ impregnated Au_n/TiO_2 catalysts and comparison with $Au_{photodep}/TiO_2$ and TiO_2.

Catalyst	*H_2 amount ($\mu mol\ g^{-1}\ h^{-1}$) @20h*	*H_2 amount ($\mu mol\ g^{-1}$) @20h*	*TON ($\mu mol_{H2}\ \mu mol_{Au}^{-1}$) @20h*	*LFE_{20}[a] (%)*
Au_{25}/TiO_2	1752	37095	7321	0.019
Au_{23}/TiO_2	1955	43891	8663	0.021
Au_{18}/TiO_2	1746	37974	7494	0.019
Au_{11}/TiO_2	1913	41815	8253	0.021
$Au_{photodep}/TiO_2$	1069	24995	4933	0.011
TiO_2	77	1976	-	0.0008

[a] Light-to-Fuel efficiency

In particular, Au_{23}/TiO_2 displayed the highest activity among the NCs with a H_2 production rate of 1955 μmol g^{-1} h^{-1} at 20 hours. A similar activity was observed also for Au_{11}/TiO_2 catalyst with 1913 μmol g^{-1} h^{-1} at 20 hours. Au_{25}/TiO_2 and Au_{18}/TiO_2 exhibited slightly decreased H_2 production of 1752 and 1746 μmol g^{-1} h^{-1}, respectively, compared to Au_{23} and Au_{11} catalysts. As seen from the stability tests in Figure 4.48A, Au_{25} and Au_{18} displayed an almost identical trend along time.

Contrary to the Au_n/TiO_2 catalysts obtained by UV irradiation/deposition, the *in-situ* impregnated ones did not follow an activity trend related to the NCs atomicity. In general the *in-situ* impregnated Au_n/TiO_2 catalysts displayed an enhanced activity compared to $Au_{photodep}/TiO_2$ and to the Au_n/TiO_2 catalysts prepared by UV irradiation/deposition. However, their stability was inferior with respect to the UV irradiated counterparts and followed a downward progression, especially at longer reaction times, with a gradual decrease in H_2 production. This trend is also highlighted in the global H_2 production graph reported in Figure 4.48B and was possibly caused by aggregation of the Au clusters during photocatalysis. The marked activity of the *in-situ* impregnated Au_n/TiO_2 catalysts is also supported by the TON and LFE values reported in Table 4.9.

4.3.4. Conclusions

In conclusion a series of Au NCs, namely $Au_{25}(PET)_{18}$-TOA^+, $Au_{23}(SCy)_{16}$-TOA^+, $Au_{18}(SCy)_{14}$ and $Au_{11}(PPh_3)_7Cl_3$, were prepared following robust synthetic protocols with the use of different ligands for the control of atomicity. The NCs were characterized by different techniques such as UV-VIS, ^{1}H-NMR and TGA analyses. The Au NCs were then supported on TiO_2 with two different strategies consisting in UV irradiation of the clusters in a suspension of the support and *in-situ* impregnation performed prior to photocatalytic tests. The two sets of catalysts were tested for the photoreforming of ethanol and their performance compared to a photodeposited catalyst. From the H_2 production monitoring, catalytic activities were extrapolated showing a marked activity of the Au NCs based catalyst. In particular, Au_n/TiO_2 prepared by UV irradiation/deposition method displayed a remarkable stability over time, with H_2 productions slightly superior for Au_{25} (1635 μmol g^{-1} h^{-1} @ 20 h and TON 6205 μmol_{H2} μmol_{Au}^{-1} @ 20 h), Au_{23} (1652 μmol g^{-1} h^{-1} @ 20 h and TON 6443 μmol_{H2} μmol_{Au}^{-1} @ 20 h), Au_{18} (1361 μmol g^{-1} h^{-1} @ 20 h and TON 5462 μmol_{H2} μmol_{Au}^{-1} @ 20 h) with respect to the photodeposited Au catalyst (1069 μmol g^{-1} h^{-1} @ 20 h and TON 4933 μmol_{H2} μmol_{Au}^{-1} @ 20 h), except Au_{11}/TiO_2 (929 μmol g^{-1} h^{-1} @ 20 h and TON 3518 μmol_{H2} μmol_{Au}^{-1} @ 20 h). On the other hand, a significant increase in activity was observed for the *in-situ* impregnated Au_n/TiO_2 catalysts that exhibited superior performance compared to the reference prepared by photodeposition. Au_{23}/TiO_2 (1955 μmol g^{-1} h^{-1} @ 20 h and TON 8663 μmol_{H2} μmol_{Au}^{-1} @ 20 h) and Au_{11}/TiO_2 (1913 μmol g^{-1} h^{-1} @ 20 h and TON 8253 μmol_{H2} μmol_{Au}^{-1} @ 20 h) resulted the most active followed by Au_{25} (1752 μmol g^{-1} h^{-1} @ 20 h and TON 7321 μmol_{H2} μmol_{Au}^{-1} @ 20 h) and Au_{18} (1746 μmol g^{-1} h^{-1} @ 20 h and TON 7494 μmol_{H2} μmol_{Au}^{-1} @ 20 h). Although these results are still preliminary and this study is ongoing, with the need of a detailed characterization of the tested

catalysts, it must be stressed that their performances are very promising. Photodeposited metals on TiO_2 are considered benchmark materials for their high activity and ease of preparation. Despite this, often photodeposition results in broad size distribution of metal nanoparticles.[718–720] Hence, engineered photocatalysts with metal NCs with well-defined nuclearity used as co-catalyst will allow a better understanding of the performances of conventional photodeposited ones in hydrogen production from photoreforming of oxygenated compounds. This knowledge will allow the development of photocatalysts with metal co-catalysts that exhibit superior activity with respect to photodeposited counterparts.

4.3.5. Experimental section

Materials

All reagents employed were bought from Merck and Alfa Aesar and used without purification, unless where indicated. Solvents were purchased from Merck and VWR. Deuterated solvents were bought from Merck and Cambridge Isotope Laboratories. Chlorinated solvents employed for dissolving Au NCs were treated with K_2CO_3. All the glassware employed for the synthesis of Au NCs and the Teflon liners for the photocatalytic tests were cleaned with aqua regia (HCl/HNO_3 1/1 v/v) and rinsed with MilliQ water before use.

Synthesis of $Au_{25}(PET)_{18}^{-}TOA^{+}$

In a three-neck round bottom flask 61 mg of $HAuCl_4 \cdot 3H_2O$ (0.15 mmol) in 4.5 mL of THF were introduced. Subsequently, 102 mg (0.19 mmol) of TOAB were added to the flask under argon obtaining a deep orange/red solution. The mixture was left to stir 10 min at room temperature and then was cooled at 0 °C by water/ice bath. After 30 minutes of stirring at 0 °C, 100 μL (0.75 mmol) of 2-penylethanethiol (PET) were added to the reaction mixture and kept stirring at 0 °C for 1 hour at low stirring speed (100 rpm). After 1 hour the ice bath was removed and stirring was kept at 100 rpm. Upon thiol addition the solution colour started do faint until it become completely colourless in 2 h. The reaction was left to age overnight at room temperature after which it was cooled to 0 °C again with a water/ice bath and the stirring was increased to the maximum speed. A freshly prepared $NaBH_4$ aqueous solution, obtained from 58 mg (1.5 mmol) $NaBH_4$ dissolved in 1.5 ice cold MilliQ water, was quickly added to the reaction at 0 °C. The solution colour immediately changed from colourless to dark brown and gas was generated upon addition. The reaction was left

to stir for 1 day after which THF was evaporated by argon stream under the fume-hood. Dark oil droplets in water were left, after THF removal, that were copiously washed with different methanol/water mixtures (7/3, 8/2, 9/1, only methanol) in order to remove thiol and TOAB excess. The resulting crude was dissolved in DCM and centrifuged at 5000 rpm for 15 min to remove solid precipitate. The DCM supernatant was collected and dried under Ar stream and Au_{25} clusters were collected by washing the brown film/oil with acetonitrile. Acetonitrile was dried under Ar leaving a brown/orange film (18 mg, yield 37% based on Au) that was stored at -18 °C for further characterization. The purity of $Au_{25}(PET)_{18}^{-}TOA^{+}$ was confirmed by UV-VIS spectroscopy and ^{1}H-NMR. UV-VIS: (DCM) λ_{max}: 325, 405, 445, 681, 800 nm. ^{1}H-NMR (benzene-*d*6, 400 MHz): δ: 7.37-6.93 (m, 90H, Ph_{in} + Ph_{out}); 4.02 (br, 24H, α-CH_{2in}) 3.48-3.03 (br + dt, 36H, β-CH_{2in} + α-CH_{2out}); 3.13 (br, 12H, β-CH_{2out}); 2.80 (br, 10H, (25% excess respect to theoretical 8H), CH_2N+); 1.34 (br, 61H (27% excess respect to theoretical 48H), oct-CH_2); 0.95 (br, 16H, (33% excess respect to theoretical 12H), oct-CH_3).

Synthesis of $Au_{23}(SCy)_{16}^{-}TOA^{+}$

In a three-neck 50 mL round-bottom flask $HAuCl_4 \cdot 3H_2O$ (118 mg, 0.3 mmol) and TOAB (190 mg, 0.348 mmol) were dissolved in 15 mL methanol. After vigorously stirring for 15 min, a colour changed from yellow to dark reddish orange was observed. Then, stirring speed was reduced to 100 rpm and excess cyclohexanethiol (196 μL, 1.6 mmol) was added to the mixture at room temperature. The reddish orange solution turned yellowish in 15 minutes and completely colourless in 40 minutes indicating the conversion of Au(III) to Au(I) complexes. After 1 hour, stirring speed was increased to the maximum and $NaBH_4$ (114 mg, 3 mmol dissolved freshly in 6 mL of ice-cold MilliQ water) was rapidly added to the reaction. The solution turned black immediately indicating formation of Au NCs and NPs, which were present as precipitate as in methanol solution resulted insoluble. The reaction mixture was further stirred overnight at room temperature, after which the methanol solution was pipetted out of the flask and the precipitate was washed with methanol/water mixture (7/3, 8/2, 9/1, only methanol to remove excess thiol and TOAB. The resulting black precipitate was dissolved in DMC and centrifuged at 5000 rpm for 10 min and the supernatant was evaporated in Ar stream leaving a black/dark red film (15 mg, 17 % based on Au). UV-VIS (DCM) λ_{max}: 570 nm.

Synthesis of $Au_{18}(SCy)_{14}$

In a three-neck round bottom flask, TOAB (127 mg, 0.2 mmol) dissolved in 10 mL DCM were introduced, followed by $HAuCl_4$ (78 mg, 0.2 mmol) dissolved in 0.5 mL ethanol. After 15 min of vigorous stirring at room temperature, cyclohexanethiol (125 μL, 1 mmol) was added at low stirring speed and at room temperature. The reaction was kept at low stirring speed until the complete disappearance of the yellow colour. Then, $NaBH_4$ (19 mg, 0.5 mmol) freshly dissolved in 1.5 mL ethanol was added dropwise to the reaction mixture with increased stirring speed . The solution slowly turned deep green indicating the formation of Au clusters. The reaction was further stirred for 5 hours, after which it was allowed to precipitate and the ethanol supernatant was removed. Precipitate was washed with methanol/water (7/3, 8/2, 9/1, only methanol) to remove thiol and TOAB excess, then it was dissolved in DCM and centrifuged to remove insoluble precipitate. The DCM supernatant was evaporated with Ar stream leaving a dark green film (10 mg, yield 15% based on Au). UV-VIS (DCM) λ_{max}: 450, 570, 630 nm.

Synthesis of $Au_{11}(PPh_3)_7Cl_3$

In a three-neck 25 mL round bottom flask, $Au(PPh_3)Cl$ (180 mg, 0.36 mmol) was dissolved in 8 mL THF and stirred at room temperature. $NaBH_4$ (68 mg, 1.8 mmol) dissolved in 8 mL of absolute ethanol was added to this solution in one portion under stirring at room temperature. The clear colourless solution immediately became dark brown, and gas evolution was observed. The reaction mixture was stirred at room temperature for 2 hours and then was poured into a beaker containing 200 mL pentane and allowed to precipitate for 2 hours. The orange/brown precipitate was collected on a medium-porosity fritted funnel and washed with *n*-hexane (4 × 7.5 mL) and DCM/*n*-hexane (1:1, 4 × 5 mL). The remaining solid was then dissolved and washed through the frit into a tared vial using 5 mL portions of DCM until no colour was observed in the extracting solution. The solvent was evaporated by Ar stream to dryness obtaining a dark red film mixed with solid (50 mg, yield 37% based on Au). UV-VIS (DCM) λ_{max}: 308, 420 nm. ^{1}H-NMR (400 MHz, CD_2Cl_2) δ: 7.41 (br, 2H), 6.90 (t, J: 7.5 Hz, 1H), 6.61 (t, J: 7.6 Hz, 2H).

Impregnation of Au NCs on TiO_2 P25

The impregnation of Au NCs was performed directly on the photocatalytic reactor as follows: An appropriate amount of Au NCs was dissolved in 0.5 mL DCM and added to ca 60 mg TiO_2

dispersed in 80 mL EtOH 96 % in the Teflon liner in order to get a 0.1% wt Au loading. The liner was closed in the photocatalytic reactor and purged with Ar for 30 minutes before catalytic tests.

Deposition/irradiation of Au NC on TiO_2 P25

The deposition/irradiation of Au NCs was performed by UV irradiation as follows: 100 mg TiO_2 P25 were suspended in 17 mL THF and sonicated for 15 min to homogenise the dispersion. 1-2 mg of Au NCs were dissolved in THF and added to the TiO2 suspension under fast stirring speed at room temperature and stirred for 15 minutes, after which the suspension was irradiated with UV light (450 W halogen lamp) for 20 minutes to favour the cleavage on thiolate ligands. Subsequently, the suspension was filtered on a 0.45 μm PVDF Millipore filter disk and dried at 60 °C under vacuum overnight. The as-prepared catalyst was used without further treatments.

Photocatalytic tests

The activity of the prepared materials was evaluated in terms of hydrogen production by photoreforming of ethanol 96%. In a Teflon-lined photoreactor, 60 mg ca of the Au NCs/TiO_2 (0.1% wt Au) were suspended into 80 mL of alcohol solution Before starting the photocatalysis, the reactor was thermostated at 20 °C and purged with Ar (15 mL min^{-1}) for at least 30 minutes. The photoreactor was illuminated with a Lot-Oriel Solar Simulator equipped with a 150 W Xe lamp and an Atmospheric Edge Filter with a cut-off at 300 nm. This results in a surface power density of ~25 mW cm^{-2} in the UV range (300–400 nm) and ~180 mW cm^{-2} in the visible range (400–100 nm), approaching the conditions used in a solar concentrator. The on-line detection of volatile products was carried out using an Agilent 7890A Gas Chromatograph equipped with two analytical lines. A 10 way-two loops injection valve was employed for injection during on-line analysis of the gaseous products. A Carboxen 1010 PLOT (Supelco, 30 m × 0.53 mm ID, 30 μm film) column followed by a Thermal Conductivity Detector (TCD) was used for gaseous products quantification using Ar as carrier and a DB-225ms column (J&W, 60 m × 0.32 mm ID, 20 μm film) using He as carrier followed by a mass spectrometer (MS) HP 5975C was employed for the detection of the volatile organic compounds.

Characterizations

UV-VIS spectroscopy analyses were carried out on a Perkin Elmer Lambda 35 spectrophotometer having a scanning speed of 240 nm min^{-1} and a slit amplitude of 2 nm, using quartz cuvettes whose optical path was 10 mm. ^{1}H-NMR spectra were recorded on a Varian 400 spectrometer and a Varian 500 spectrometer, operating respectively at 400 MHz and 500 MHz for proton. The NMR spectra have been processed by means of MestReNova software. Chemical shifts (δ) are reported in ppm and the multiplicity of each signal is identified by the conventional abbreviations: s for singlet, d for doublet, t for triplet, q for quartet, m for multiplet, br for broad peak. Coupling constants (*J*) are reported in Hertz. Thermogravimetric analysis (TGA) was performed on TGA Q500 (TA Instruments) under nitrogen, equilibrating at 100°C, and following a ramp of 10 °C min^{-1} up to 900 °C. IR spectra were recorded in attenuated total reflectance (ATR) mode on a Shimadzu IRAffinity-1S spectrophotometer equipped with a QATR 10 accessory. Transmission electron microscopic (TEM) images were collected by means of a Philips EM 208 Electron Microscope operating at 100 kV equipped with 11 MegaPixel bottom-mounted CCD Olympus Quemesa camera. ICP-OES analysis has been performed using an Optima 8000 Spectrometer (PerkinElmer) equipped with a S10 autosampler. The total gold concentration was evaluated using calibration curves obtained by dilution of SpectrascanTM gold standard solutions for ICP-OES analysis (Teknolab A/S, Norway). All standards (range: 0.1–50.0 mg/L) were prepared using a 96% EtOH solution to compensate the matrix effect. The used emission wavelength was 324.754 nm, the limit of detection 0.03 mg/L and the repeatability of measurements expressed as relative standard deviations (RSD%) and calculated on 6 replicates of various samples was lower than 4%. Calibration curves obtained by means of 5 standard solutions had correlation coefficients higher than 0.998.

5. Conclusions

The research work developed during this PhD thesis provides some new insights into the development of nanomaterials based catalysts with well-defined properties dictated by the engineering of metal NPs and NCs. The manipulation at the nanoscale level of such nanomaterials was achieved by means of solid synthetic protocols modified for the preparation of new materials through the control of exposed surface features in NPs and atomicity in small NCs. Three nanomaterials were subjected to a thorough study with the purpose of enriching the state of the art in catalysis with nanostructured catalysts.

Porous multifaceted Pt NPs were prepared, characterized and applied in electrocatalytic ORR and MOR. In particular a new protocol was developed for the synthesis of porous NPs with regular planes/facets exposed on the surface. The Pt NPs were obtained in monodisperse size and with a good degree of porosity that was consistent with the applied protocol. Detailed studies were performed on the synthetic procedure through microscopic analyses for the monitoring of the NPs morphological progression in order to support a coherent formation mechanism. TEM experiments provided structural information on the porous multifaceted NPs and allowed to determine the dendritic nature of the material that evolved in the aggregation of small regular and highly crystalline nanocrystals. Various kinetic and thermodynamic aspects were considered in the different stages of the reaction that were consistent with the microscopic observations. Moreover, a series of control experiment were performed in support of the optimised reaction conditions by variations of experimental parameters. Experiments performed with different OLAM/OLAC ratios emphasised the importance of using an equimolar ratio of the surfactants and suggested a correlation for size increase to the increased OLAM mole fraction. The porous multifaceted Pt NPs were anchored to a carbonaceous support and subjected to various treatments for removal of the organic surfactants that passivated the active surface. Electrocatalytic investigations on the material revealed a marked activity toward the ORR that was superior to commercial Pt/C despite the higher ECSA of the latter. Enhanced activities were also displayed toward the MOR that, again, resulted higher with respect to the commercial counterpart. The synthesis and catalytic applications of porous multifaceted Pt NPs reported in this work contributes to the development of better catalysts to be employed in electrocatalytic systems for cleaner energy production.

Regarding the control of catalytic properties through atomic precision engineering palladium and gold were exploited for the development of nanostructured catalysts starting from NCs. Palladium clusters were designed in the form of Pd_8 by various treatments of a thiolate-protected tiara-like

octanuclear Pd complexes and used in catalysis for Suzuki cross coupling reactions. The $Pd_8(SCH_2COOMe)_{16}$ complex was prepared using an already reported protocol very useful in providing high yield of the starting material for the catalyst assembling. After NMR characterization of the Pd complex, a UV irradiation/deposition protocol was applied for its heterogenization (at 0.1% wt of Pd) on highly porous Al_2O_3 through photoinduced ligand C-S cleavage. The supported clusters in form of PdS were treated under H_2 at high temperature to reduce Pd(II) and remove sulfur obtaining an active Pd_8/Al_2O_3 catalyst. The effective deposition of the clusters in form of PdS and the reduction were confirmed by EXAFS analyses that revealed a final catalyst composition consisting of PdO, PdS and Pd(0). Microscopic analyses confirmed the small size of the Pd clusters and their uniform distribution over the support. The textural properties were maintained during all the catalyst treatment and were characterized by physisorption analyses. The as-prepared Pd_8/Al_2O_3 catalyst was subjected to catalytic tests for the Suzuki coupling in which it displayed excellent performances. The catalytic system was optimized through extensive screening of the reaction conditions by solvent, base, temperature and time variations. Remarkably, Pd_8/Al_2O_3 was reported to catalyse the coupling of phenylboronic acid with substituted bromobenzenes bearing FGs of various nature in the meta- and para- position. The activity of Pd_8/Al_2O_3 was compared to a commercial Pd/C catalyst and an impregnated Pd/Al_2O_3, reduced in the same conditions used for Pd_8/Al_2O_3, demonstrating superior activity under the same reaction conditions. Since it is known that the mechanism of Suzuki coupling reactions, involving solid phase catalysts, proceeds through dissolution and redeposition of atomic Pd, dedicated tests were performed on the Pd_8/Al_2O_3 system displaying a very low metal leaching. Finally, in order to assess the activity of the catalyst over time, recycling test were performed. The catalyst ensured a high conversion up to the 6^{th} recycle, after which a slow decrease was observed. The results obtained in this study of Pd_8/Al_2O_3 on Suzuki coupling reactions display how reduction of Pd thiolate complexes with high and well-defined nuclearity to achieve small Pd clusters may be a useful strategy for the preparation of novel, highly performant catalysts.

In line with the atomic control of heterogeneous catalysts, Au NCs with precise nuclearity have also been prepared and exploited for the photocatalytic hydrogen production from ethanol oxidation. The control of nuclearity was applied by size focusing protocols to deliver the thiolate or phosphine protected NCs Au_{25}, Au_{23}, Au_{18} and Au_{11} that were characterized by conventional analytic techniques. Two procedures were applied for the anchoring of the Au NCs on TiO_2 in order to maximise the dispersity and avoid metal agglomeration. A UV irradiation/deposition method was applied to generate a first set of catalysts that displayed a high photocatalytic activity comparable to a benchmark photodeposited Au/TiO_2, but with improved stability on prolonged time in hydrogen

production. Another set of photocatalysts was prepared directly in-situ by impregnating with a cluster solution the TiO_2 suspended in ethanol prior to light irradiation. This set of photocatalysts gave hydrogen production values remarkably higher compared to the benchmark catalyst, however, their stability over time slowly decreased still remaining significantly more performing than the photodeposited benchmark Au/TiO_2. Worth to be mentioned, the UV irradiated/deposited Au_n/TiO_2 catalysts displayed higher activity at higher cluster atomicity, while for in-situ prepared catalysts no such a correlation could be observed.

The objectives of this work were targeted by the use of nanotechnology for the control of nanostructured materials that exhibited different properties and were employed in separate branches of catalysis (electro-, thermo- and photocatalysis), giving an indication of possible application and, hopefully, future studies.

Acknowledgements

Vorrei esprimere la mia gratitudine alla Prof. Lucia Pasquato ed al Prof. Paolo Fornasiero per avermi accolto nei loro rispettivi gruppi di ricerca e per avermi guidato in questi tre anni con la loro esperienza ed i loro saggi consigli, a loro va tutta la mia riconoscenza. Ringrazio altresì il Prof. Paolo Pengo ed il Prof. Tiziano Montini, che mi hanno seguito più da vicino, dal lato pratico e teorico; mi avete fatto capire che, anche quando le cose non vanno per il verso giusto se ne guadagna sempre qualcosa di buono.

A tutti i componenti dei due gruppi, grazie per le belle giornate passate insieme, tra una risata e molti caffè, senza di voi il tempo passato qui sarebbe stato una scala di grigi.

Un affettuoso ringraziamento va anche a tutti gli amici delle avventure triestine, che lontano dal laboratorio, sono riusciti a tirar fuori la mia parte migliore.

Infine, il grazie più importante va alla mia famiglia, che mi ha sempre supportato in tutte le mie scelte ed i miei percorsi, spronandomi a dare il massimo, sempre.

Appendix A. Suzuki cross couplings

General information

^{1}H and ^{13}C NMR spectra were recorded on a Varian 400 spectrometer operating at 400 MHz. The NMR spectra were processed by means of MestReNova software. ^{1}H-NMR spectra were referenced to the residual protons in the deuterated solvent. ^{13}C-NMR spectra were referenced to the solvent chemical shift. Chemical shifts (δ) are reported in ppm and the multiplicity of each signal is identified by the conventional abbreviations: s for singlet, d for doublet, t for triplet, q for quartet, dd for doublet of doublets, dt doublet of tripets, m for multiplet, br for broad peak. Coupling constants (J) are reported in Hertz (Hz). Mass spectrometry measurements were carried out on GC-MS system with an Agilent 7890A Gas Chromatograph equipped with 10 way-two loops injection valve and a DB-225ms column (J&W, 60 m × 0.32 mm ID, 20 μm film) followed by a mass spectrometer (MS) HP 5975C. Compound injections were performed by first dissolving the products in methanol or acetonitrile.

Synthesis of substituted biphenyls

General procedure

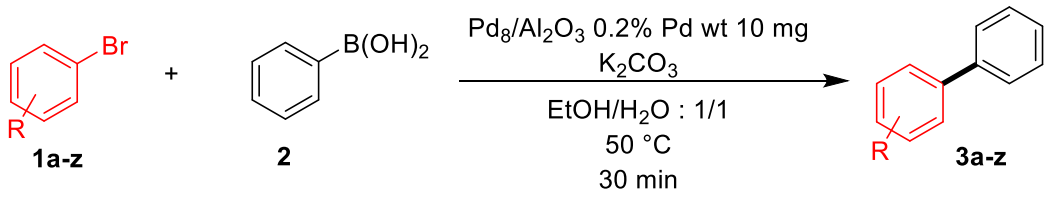

10 mg Pd8/Al2O3 (0.1% Pd wt), arylboronic acid (0.22 mmol) and K2CO3 (0.66 mmol) were introduced in a 10 mL screw-capped tube-shaped vial, equipped with stirring bar. Subsequently, 2 mL ethanol/water (1/1 v/v ratio) were added and stirred at room temperature. After 2 min, aryl halide (0.15 mmol) was added to the reaction mixture, the vial was sealed and placed in a preheated water bath at 50 °C for 30 min under vigorous stirring. After 30 min the vial was cooled to room temperature and extracted with EtOAc 2 x 5 mL. The EtOAc extracts were washed with water (5

mL) and brine (10 mL) before being dried over Na2SO4. After solvent removal, the product was purified by flash chromatography in n-Hex/EtOAc to yield the desired product.

1,1'-biphenyl (3)

^{1}H-NMR (400 MHz, $CDCl_3$) δ (ppm): 7.63 (d, *J*: 7.2, 4 H), 7.48 (t, *J*: 7.4 Hz, 4 H), 7.33 (t, *J*: 7.4 Hz, 2 H); ^{13}C-NMR (100 MHz, $CDCl_3$) δ: 141.2, 128.8, 127.3, 127.2. m/z 154

Data for substituted biphenyls

4-methyl-1,1'-biphenyl (3a)

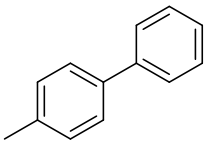

Crude product was purified by flash chromatography (n-hexane/EtOAc 99.5/0.5). ^{1}H-NMR (400 MHz, $CDCl_3$) δ (ppm): 7.63-7.59 (m, 2 H), 7.54-7.51 (m, 2 H), 7.48-7.43 (m, 2 H), 7.37-7.33 (m, 1 H), 7.30-7.26 (d, *J*: 2.7 Hz, 2 H), 2.34 (s, 3 H); ^{13}C-NMR (100 MHz, $CDCl_3$) δ (ppm): 141.15, 138.32, 137.00, 129.44, 128.69, 126.98, 126.96, 126.95, 21.09; m/z 168.

3-methyl-1,1'-biphenyl (3b)

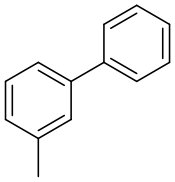

Crude product was purified by flash chromatography (n-hexane/EtOAc 99/1). ^{1}H-NMR (400 MHz, $CDCl_3$) δ (ppm): 7.62-7.59 (m, 2 H), 7.47-7.40 (m, 4 H), 7.38-7.33 (m, 2 H), 7.19 (d, *J*: 7.5 Hz, 1 H), 2.44 (s, 3 H); ^{13}C-NMR (100 MHz, $CDCl_3$) δ (ppm): 141.35, 141.23, 138.31, 128.68, 128.65, 127.98, 127.97, 127.17, 127.14, 124.26, 21.54; m/z 168.

4-ethyl-1,1'-biphenyl (3c)

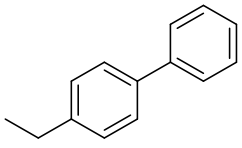

Crude product was purified by flash chromatography (n-hexane/EtOAc 99/1). ^{1}H-NMR (400 MHz, $CDCl_3$) δ (ppm): 7.63-7.60 (m, 2 H), 7.57-7.53 (m, 2 H), 7.48-7.43 (m, 2 H), 7.37-7.33 (m, 1 H), 7.30 (d, *J*: 8 Hz, 2 H), 2.73 (q, J: 7.6 Hz, 2H), 1.31 (t, J: 7.6 Hz, 3H); ^{13}C-NMR (100 MHz, $CDCl_3$) δ (ppm): 143.38, 141.18, 138.55, 128.70, 128.28, 127.08, 127.01, 126.96, 28.52, 15.62; m/z 182.

4-propyl-1,1'-biphenyl (3d)

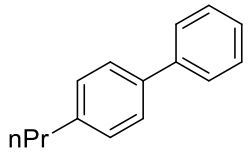

Crude product was purified by flash chromatography (n-hexane/EtOAc 99/1). ^{1}H-NMR (400 MHz, $CDCl_3$) δ (ppm): 7.61-7.58 (m, 2 H), 7.54-7.50 (m, 2 H), 7.46-7.41 (m, 2 H), 7.35-7.31 (m, 1 H), 7.28-7.24 (m, 2 H), 2.64 (m, 2 H), 1.70 (dq, *J*: 14.8, 7.4 Hz, 2 H), 0.99 (t, *J*: 7.3 Hz), 3 H); ^{13}C-NMR (100 MHz, $CDCl_3$) δ (ppm): 141.82, 141.17, 138.56, 128.85, 128.67, 126.97, 126.94, 126.92, 37.69, 24.55, 13.88; m/z 196.

4-butyl-1,1'-biphenyl (3e)

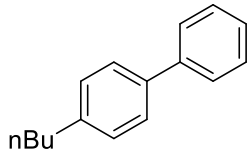

Crude product was purified by flash chromatography (n-hexane/EtOAc 99/1). ^{1}H-NMR (400 MHz, $CDCl_3$) δ (ppm): 7.60 (m, 2 H), 7.53 (m, 2 H), 7.44 (m, 2 H), 7.28 (m, 1 H), 7.26 (d, *J*: 7.6 Hz, 2 H), 2.67 (t, 2 H), 1.65 (m, 2 H), 1.41 (dq, *J*: 14.6, 7.3 Hz, 2 H), 0.96 (t, *J*: 7.3 Hz, 3 H); ^{13}C-NMR (100 MHz, $CDCl_3$) δ (ppm): 142.05, 141.18, 138.52, 128.81, 128.67, 126.98, 126.96, 126.92, 35.29, 33.64, 22.41, 13.98; m/z 210.

1,1':4',1''-terphenyl (3f)

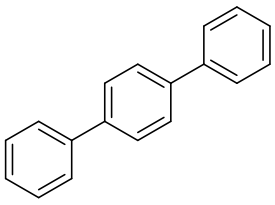

Crude product was purified by flash chromatography (n-hexane/EtOAc 99/1). ^{1}H-NMR (400 MHz, $CDCl_3$) δ (ppm): 7.70 (s, 4 H), 7.68-7.64 (m, 4 H), 7.50-7.44 (m, 4 H), 7.40-7.35 (m, 2 H); ^{13}C-NMR (100 MHz, $CDCl_3$) δ (ppm): 140.69, 140.11, 128.81, 127.49, 127.33, 127.04; m/z 230.

2-phenylnaphthalene (3g)

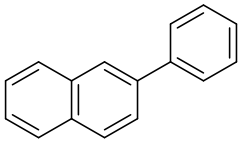

Crude product was purified by flash chromatography (n-hexane/EtOAc 99.5/0.5). ^{1}H-NMR (400 MHz, $CDCl_3$) δ (ppm): 8.08 (s, 1 H), 7.96-7.88 (m, 3 H), 7.79-7.74 (m, 3 H), 7.55-7.49 (m, 4 H), 7.43-7.39 (m, 1 H); ^{13}C-NMR (100 MHz, $CDCl_3$) δ (ppm): 141.31, 138.74, 133.86, 132.81, 129.03, 128.59, 128.37, 127.82, 127.61, 127.52, 126.46, 126.10, 125.98, 125.77; m/z 204.

[1,1'-biphenyl]-4-ol (3h)

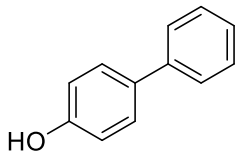

Crude product was purified by flash chromatography (n-hexane/EtOAc 90/10). ^{1}H-NMR (400 MHz, $CDCl_3$) δ (ppm): 7.57-7.52 (m, 2 H), 7.51-7.46 (m, 2 H), 7.45-7.39 (m, 2 H), 7.34-7.28 (m, 1 H), 6.93-6.89 (m, 2 H); ^{13}C-NMR (100 MHz, $CDCl_3$) δ (ppm): 155.04, 140.71, 138.38, 134.11, 128.72, 128.39, 126.71, 115.63; m/z 170.

[1,1'-biphenyl]-3-ol (3i)

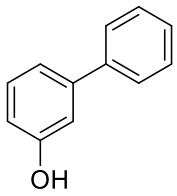

Crude product was purified by flash chromatography (n-hexane/EtOAc 90/10). ^{1}H-NMR (400 MHz, $CDCl_3$) δ (ppm): 7.60-7.56 (m, 2 H), 7.46-7.42 (m, 2 H), 7.37-7.29 (m, 2 H), 7.20-7.16 (m, 1 H), 7.09-7.05 (m, 1 H), 6.85-6.81 (m, 1 H); ^{13}C-NMR (100 MHz, $CDCl_3$) δ (ppm): 155.79, 143.07, 140.71, 129.95, 128.81, 127.45, 127.15, 119.81, 114.16, 114.08, m/z 170.

4-methoxy-1,1'-biphenyl (3j)

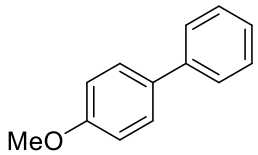

Crude product was purified by flash chromatography (n-hexane/EtOAc 95/5). ^{1}H-NMR (400 MHz, $CDCl_3$) δ (ppm): 7.58-7.52 (m, 4 H), 7.45-7.39 (m, 2 H), 7.34-7.28 (m, 1 H), 7.00-6.96 (m, 2 H), 3.86 (s, 3 H); ^{13}C-NMR (100 MHz, $CDCl_3$) δ (ppm): 159.12, 140.81, 137.76, 128.70, 128.14, 126.72, 126.64, 114.18, 55.33; m/z 184.

3-methoxy-1,1'-biphenyl (3k)

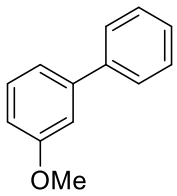

Crude product was purified by flash chromatography (n-hexane/EtOAc 95/5). ^{1}H-NMR (400 MHz, $CDCl_3$) δ (ppm): 7.61-7.57 (m, 2 H), 7.47-7.41 (m, 2 H), 7.39-7.33 (m, 2 H), 7.22-7.17 (m, 1 H), 7.14 (dd, J: 2.4, 1.8 Hz, 1 H), 6.93-6.89 (m, 1 H), 3.87 (s, 3 H); ^{13}C-NMR (100 MHz, $CDCl_3$) δ (ppm): 159.91, 142.76, 141.09, 129.72, 128.71, 127.39, 127.18, 119.67, 112.89, 112.66, 55.29; m/z 184.

2-methoxy-6-phenylnaphthalene (3l)

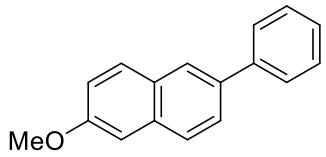

Crude product was purified by flash chromatography (n-hexane/EtOAc 98/2). ^{1}H-NMR (400 MHz, $CDCl_3$) δ (ppm): 7.99 (d, *J*: 1.6 Hz, 1 H), 7.83-7.78 (m, 2 H), 7.75-7.70 (m, 3 H), 7.51-7.46 (m, 2 H), 7.39-7.34 (m, 1 H), 7.21-7.15 (m, 2 H); ^{13}C-NMR (100 MHz, $CDCl_3$) δ (ppm): 157.75, 141.19, 136.39, 133.78, 129.70, 128.81, 127.24, 127.21, 127.05,126.03, 119.14, 105.56 55.33; m/z 234.

4-ethoxy-1,1'-biphenyl (3m)

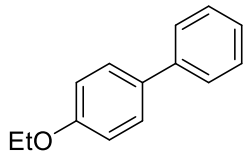

Crude product was purified by flash chromatography (n-hexane/EtOAc 95/5). ^{1}H-NMR (400 MHz, $CDCl_3$) δ (ppm): 7.58-7.52 (m, 4 H), 7.45-7.41 (m, 2 H), 7.33-7.29 (m, 1 H), 7.01-6.96 (m, 2 H), 4.09 (d, *J*: 7.0 Hz, 2 H), 1.46 (t, 3 H); ^{13}C-NMR (100 MHz, $CDCl_3$) δ (ppm): 158.51, 140.86, 133.60, 128.69, 128.11, 126.70, 126.59, 114.75, 63.51, 14.88; m/z 198.

[1,1'-biphenyl]-4-amine (3n)

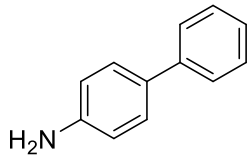

Crude product was purified by flash chromatography (n-hexane/EtOAc 75/25). ^{1}H-NMR (400 MHz, $CDCl_3$) δ (ppm): 7.57-7.52 (m, 2 H), 7.46-7.37 (m, 4 H), 7.31-7.22 (m, 1 H), 6.78-6.73 (m, 2 H), 3.72 (s, 2 H); ^{13}C-NMR (100 MHz, $CDCl_3$) δ (ppm): 145.81, 141.13, 131.57, 128.64, 127.99, 126.39, 126.24, 115.42; m/z 169.

N,N-dimethyl-[1,1'-biphenyl]-4-amine (3o)

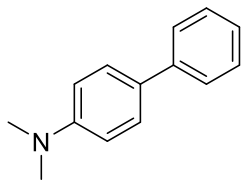

Crude product was purified by flash chromatography (n-hexane/EtOAc 8/2). ^{1}H-NMR (400 MHz, $CDCl_3$) δ (ppm): 7.61-7.52 (m, 4 H), 7.45-7.39 (m, 2 H), 7.31-7.25 (m, 1 H), 6.88-6.82 (d, *J*: 8.7 Hz, 2 H), 3.02 (s, 6 H); ^{13}C-NMR (100 MHz, $CDCl_3$) δ (ppm): 141.20, 128.65, 127.72, 126.3, 126.02, 112.88, 40.73; m/z 197.

4-nitro-1,1'-biphenyl (3p)

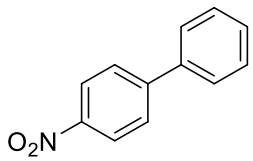

Crude product was purified by flash chromatography (n-hexane/EtOAc 98/2). ^{1}H-NMR (400 MHz, $CDCl_3$) δ (ppm): 8.32-8.28 (m, 2 H), 7.76-7.71 (m, 2 H), 7.65-7.60 (m, 2 H), 7.53-7.42 (m, 3 H); ^{13}C-NMR (100 MHz, $CDCl_3$) δ (ppm): 147.59, 138.76, 129.13, 128.89, 127.78, 127.36, 124.09; m/z 199.

4-(trifluoromethyl)-1,1'-biphenyl (3q)

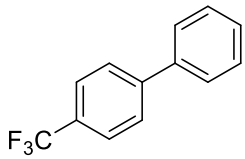

Crude product was purified by flash chromatography (n-hexane/EtOAc 99/1). ^{1}H-NMR (400 MHz, $CDCl_3$) δ (ppm): 7.71 (s, 4 H), 7.63-7.60 (m, 2 H), 7.52-7.47 (m, 2 H), 7.45-7.40 (m, 1 H); ^{13}C-NMR (100 MHz, $CDCl_3$) δ (ppm): 144.72, 139.76, 129.00, 128.17, 127.41, 127.27, 125.68, 123.22; m/z 222.

3-(trifluoromethyl)-1,1'-biphenyl (3r)

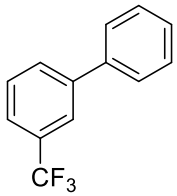

Crude product was purified by flash chromatography (n-hexane/EtOAc 99/1). ^{1}H-NMR (400 MHz, $CDCl_3$) δ (ppm): 7.85 (s, 1 H), 7.77 (d, J: 7.6 Hz, 1 H), 7.64-7.53 (m, 4 H), 7.51-7.45 (m, 2 H), 7.44-7.37 (m, 1H); ^{13}C-NMR (100 MHz, $CDCl_3$) δ (ppm): 141.96, 139.75, 130.40, 129.20, 128.97, 128.01, 127.20, 123.92; m/z 222.

[1,1'-biphenyl]-4-carbonitrile (3s)

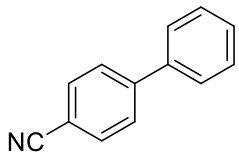

Crude product was purified by flash chromatography (n-hexane/EtOAc 96/4). ^{1}H-NMR (400 MHz, $CDCl_3$) δ (ppm): 7.75-7.66 (m, 4 H), 7.61-7.56 (m, 2 H), 7.51-7.40 (m, 3 H); ^{13}C-NMR (100 MHz, $CDCl_3$) δ (ppm): 145.65, 139.16, 132.58, 129.10, 128.64, 127.72, 127.21, 118.92, 110.90; m/z 179.

[1,1'-biphenyl]-3-carbonitrile (3t)

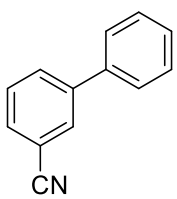

Crude product was purified by flash chromatography (n-hexane/EtOAc 96/4). ^{1}H-NMR (400 MHz, $CDCl_3$) δ (ppm): 7.87 (s, 1 H), 7.82 (d, J: 7.9 Hz, 1 H), 7.63 (d, 9.2 Hz 1 H), 7.58-7.54 (m, 3 H), 7.51-7.46 (m, 2 H), 7.44-7.40 (m, 1 H); ^{13}C-NMR (100 MHz, $CDCl_3$) δ (ppm): 142.46, 138.86, 131.47, 130.69, 129.62, 129.11, 128.38, 127.07, 118.83, 112.93; m/z 179.

[1,1'-biphenyl]-4-carbaldehyde (3u)

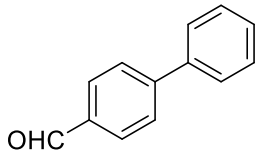

Crude product was purified by flash chromatography (n-hexane/EtOAc 98/2). ^{1}H-NMR (400 MHz, $CDCl_3$) δ (ppm): 10.06 (s, 1 H), 7.96 (d, *J*: 8.4 Hz, 2 H), 7.76 (d, *J*: 8.2 Hz, 2 H), 7.64 (d, *J*: 7.2 Hz, 2 H), 7.52-7.39 (m, 3 H); ^{13}C-NMR (100 MHz, $CDCl_3$) δ (ppm): 191.90, 147.18, 139.70, 135.18, 130.25, 129.00, 128.46, 127.67, 127.35; m/z 182

1-([1,1'-biphenyl]-4-yl)ethan-1-one (3v)

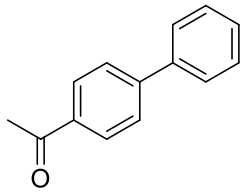

Crude product was purified by flash chromatography (n-hexane/EtOAc 95/5). ^{1}H-NMR (400 MHz, $CDCl_3$) δ (ppm): 8.05-8.00 (m, 2 H), 7.71-7.66 (m, 2 H), 765-7.60 (m, 2 H), 7.50-7.44 (m, 2 H), 7.43-7.37 (m, 1 H), 2.64 (s, 3 H); ^{13}C-NMR (100 MHz, $CDCl_3$) δ (ppm): 197.72, 145.76, 139.85, 135.84, 128.94, 128.89, 128.21, 127.25, 127.20, 26.66; m/z 196.

1-([1,1'-biphenyl]-3-yl)ethan-1-one (3w)

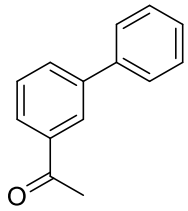

Crude product was purified by flash chromatography (n-hexane/EtOAc 95/5). ^{1}H-NMR (400 MHz, $CDCl_3$) δ (ppm): 8.19 (t, *J*: 1.8 Hz, 1 H), 7.95-7.93 (m, 1 H), 7.81-7.79 (m, 1 H), 7.63 (dt, *J*: 3.1, 1.8 Hz, 2 H, 7.55 (t, *J*: 7.7 Hz, 1 H), 7.50-7.45 (m, 2 H), 7.42-7.38 (m, 1 H), 2.67 (s, 3 H); ^{13}C-NMR (100 MHz, $CDCl_3$) δ (ppm): 196.59, 138.77, 135.93, 131.72, 131.36, 130.17, 128.90, 127.79, 127.17, 126.82, 122.93, 26.60; m/z 196.

[1,1'-biphenyl]-4-carboxylic acid (3x)

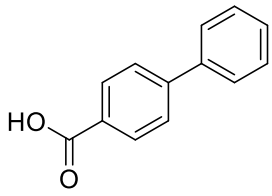

Crude product was purified by recrystallization in EtOH. ^{1}H-NMR (400 MHz, DMSO-d_6) δ (ppm): 12.94 (s, 1 H), 8.05-7.96 (m, 2 H), 7.82-7.75 (m, 2 H), 7.75-7.69 (m, 2 H), 7.53-7.45 (m, 2 H), 7.44-7.38 (m, 1 H); ^{13}C-NMR (100 MHz, DMSO-d_6) δ (ppm): 167.57, 144.75, 139.47, 130.40, 130.05, 129.52, 128.73, 127.40, 127.26; m/z 198.

Methyl [1,1'-biphenyl]-4-carboxylate (3y)

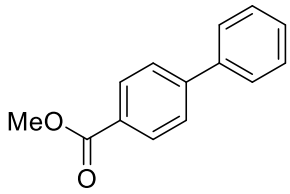

Crude product was purified by flash chromatography (n-hexane/EtOAc 95/5). ^{1}H-NMR (400 MHz, $CDCl_3$) δ (ppm): 8.14-8.08 (m, 2 H), 7.69-7.61 (m, 4 H), 7.50-7.44 (m, 2 H), 7.42-7.37 (m, 1 H), 3.94 (s, 3 H); ^{13}C-NMR (100 MHz, $CDCl_3$) δ (ppm): 166.98, 145.61, 139.98, 130.08, 128.90, 128.88, 128.12, 127.26, 127.03, 52.11; m/z 212.

4-fluoro-1,1'-biphenyl (3z)

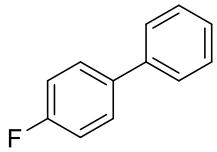

Crude product was purified by flash chromatography (n-hexane/EtOAc 99/1). ^{1}H-NMR (400 MHz, $CDCl_3$) δ (ppm): 7.58-7.52 (m, 4 H), 7.47-7.41 (m, 2 H), 7.38-7.32 (m, 1 H), 7.17-7.09 (m, 2 H); ^{13}C-NMR (100 MHz, $CDCl_3$) δ (ppm): 171.14, 163.67, 161.22, 140.24, 137.34, 128.79, 128.70, 128.62, 127.23, 126.99, 115.69, 115.48; m/z 172.

NMR spectra

4-methyl-1,1'-biphenyl (3a)

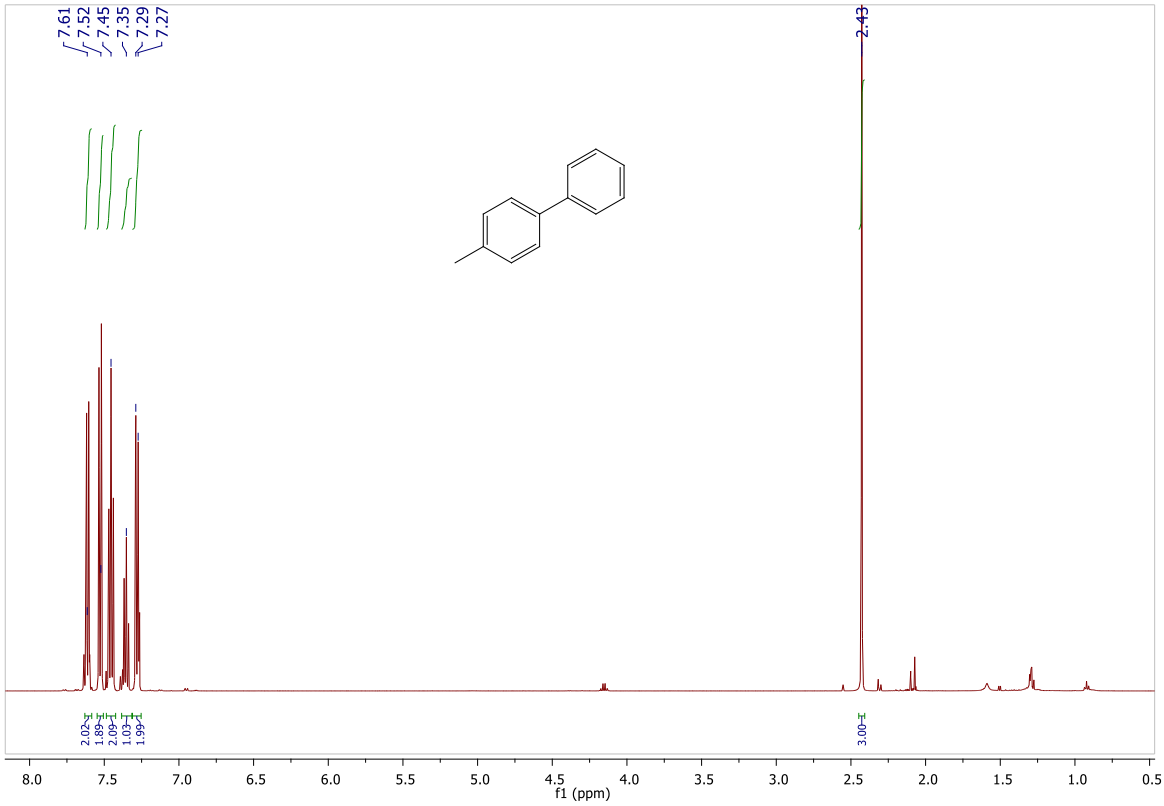

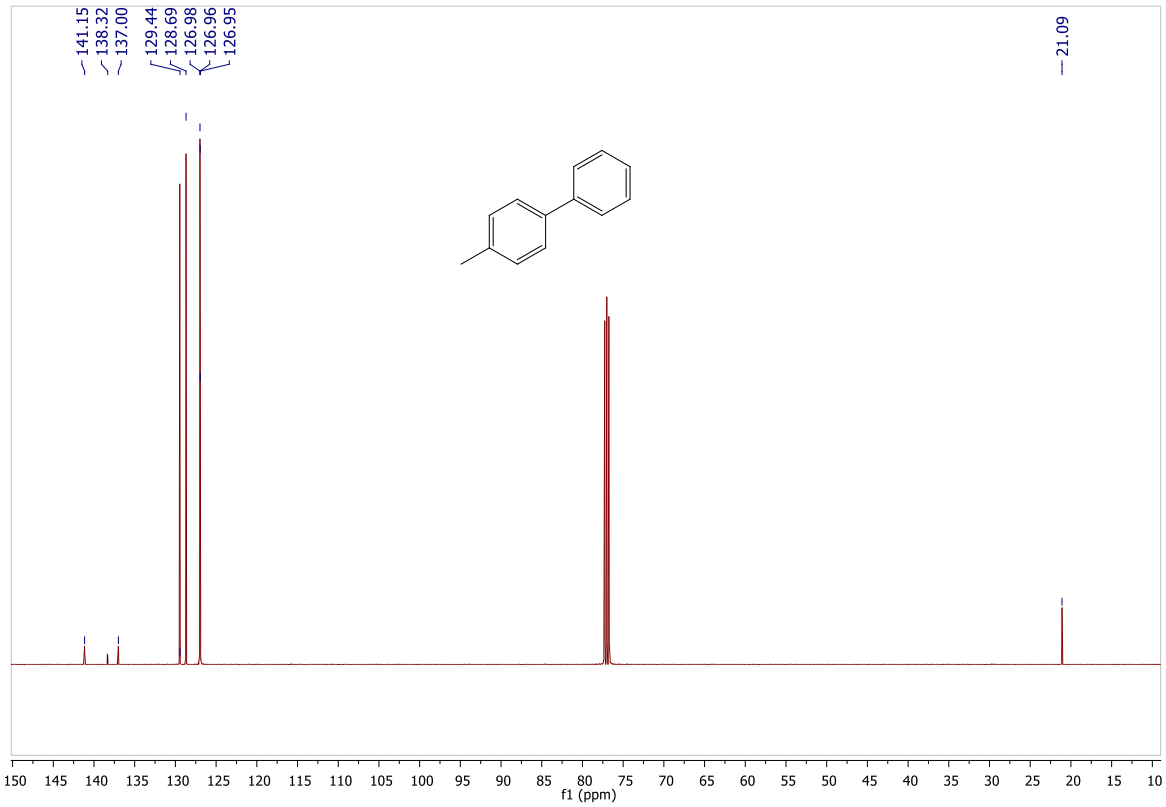

3-methyl-1,1'-biphenyl (3b)

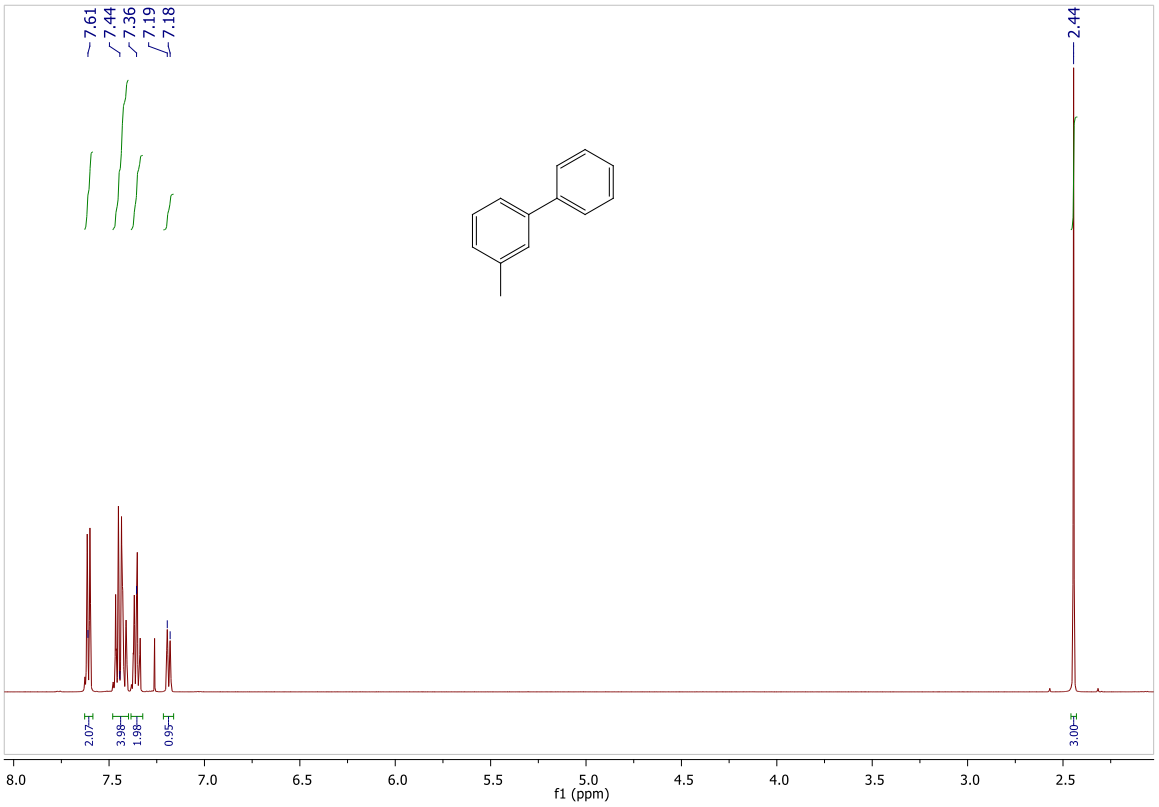

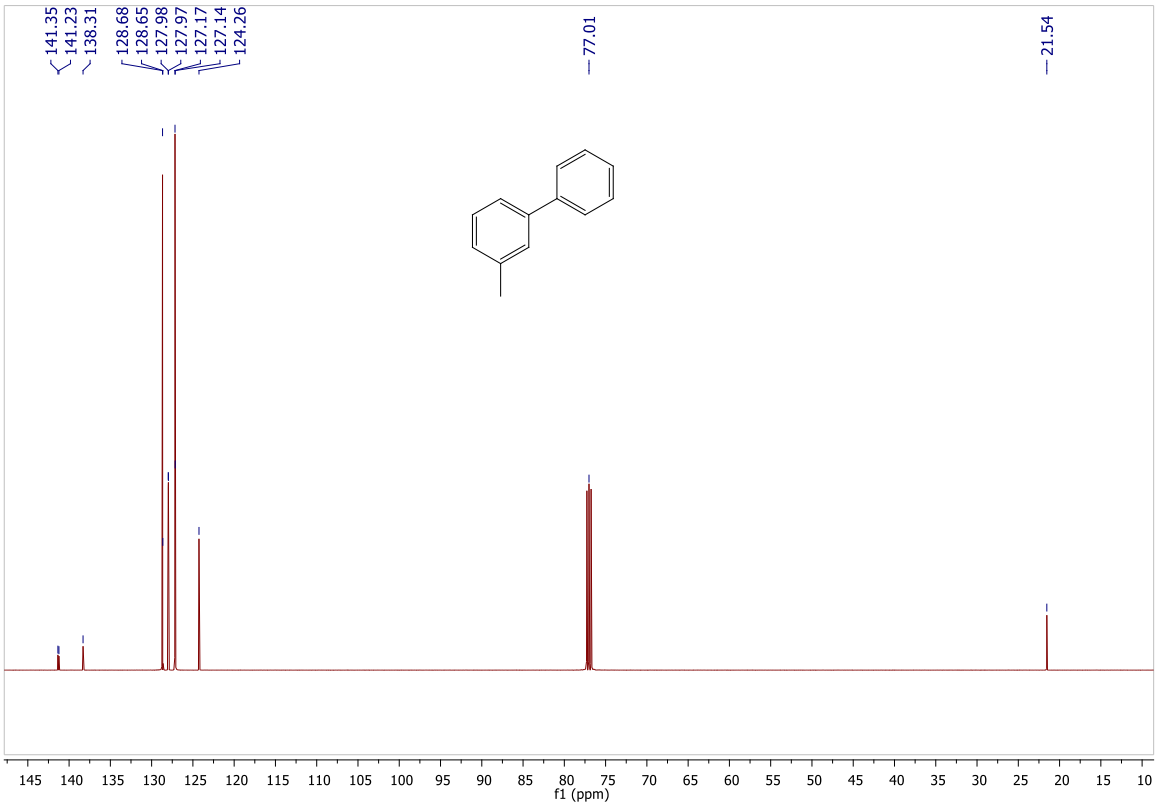

4-ethyl-1,1'-biphenyl (3c)

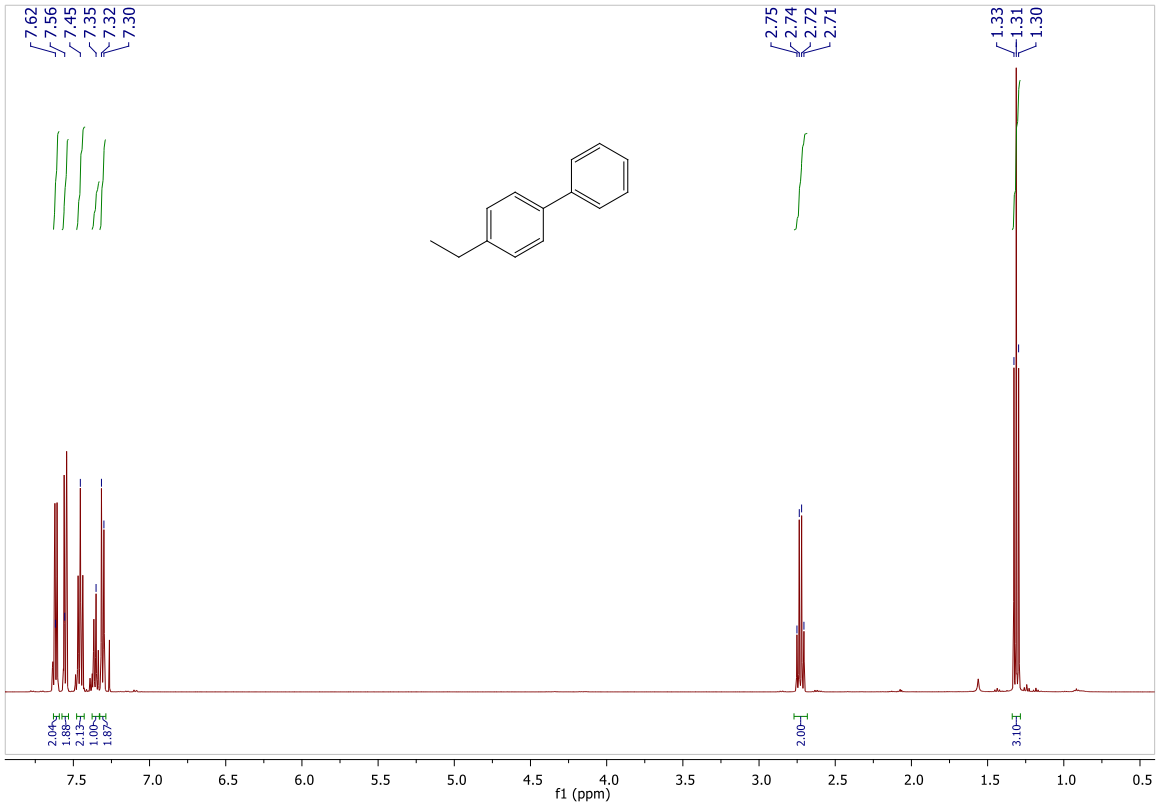

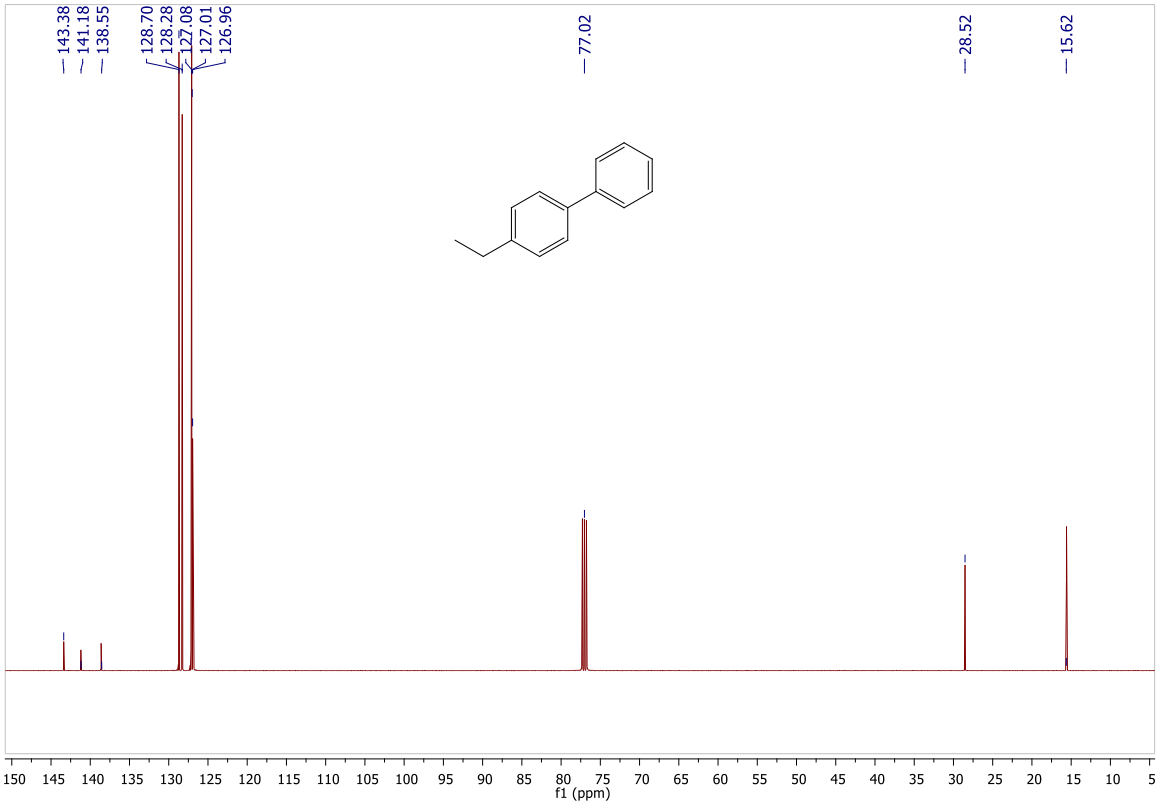

4-propyl-1,1'-biphenyl (3d)

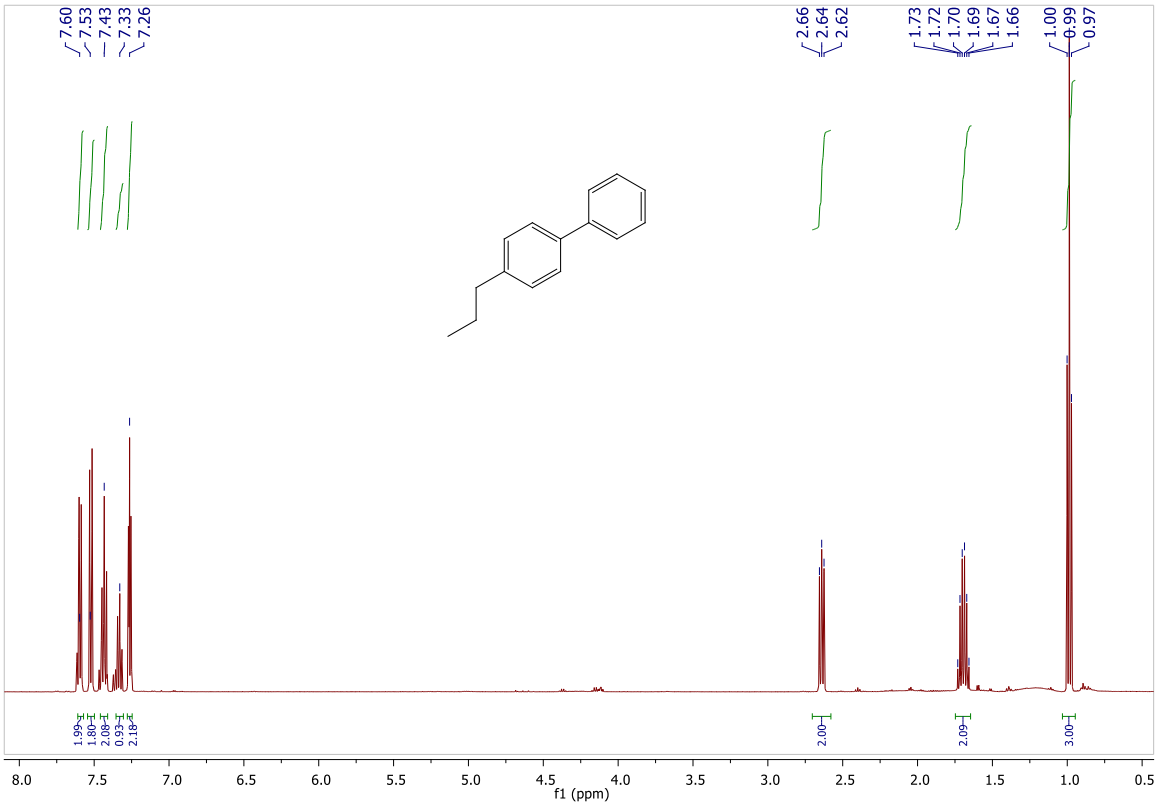

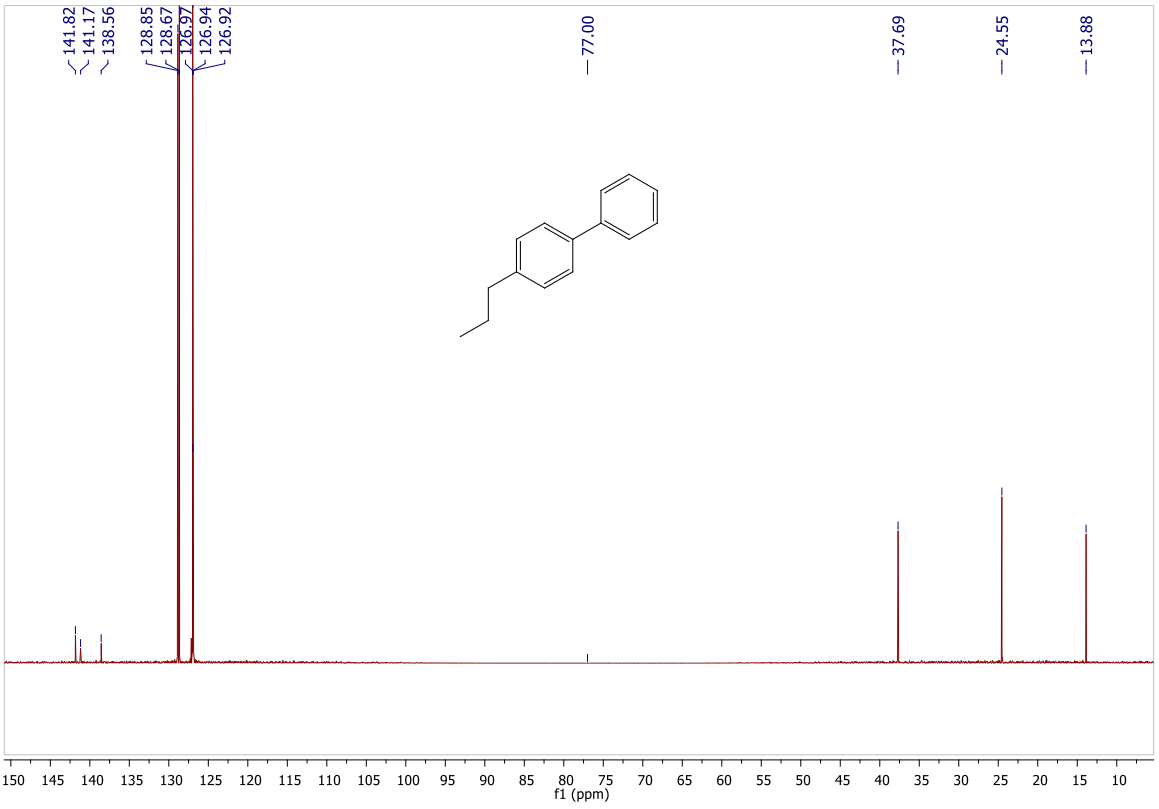

4-butyl-1,1'-biphenyl (3e)

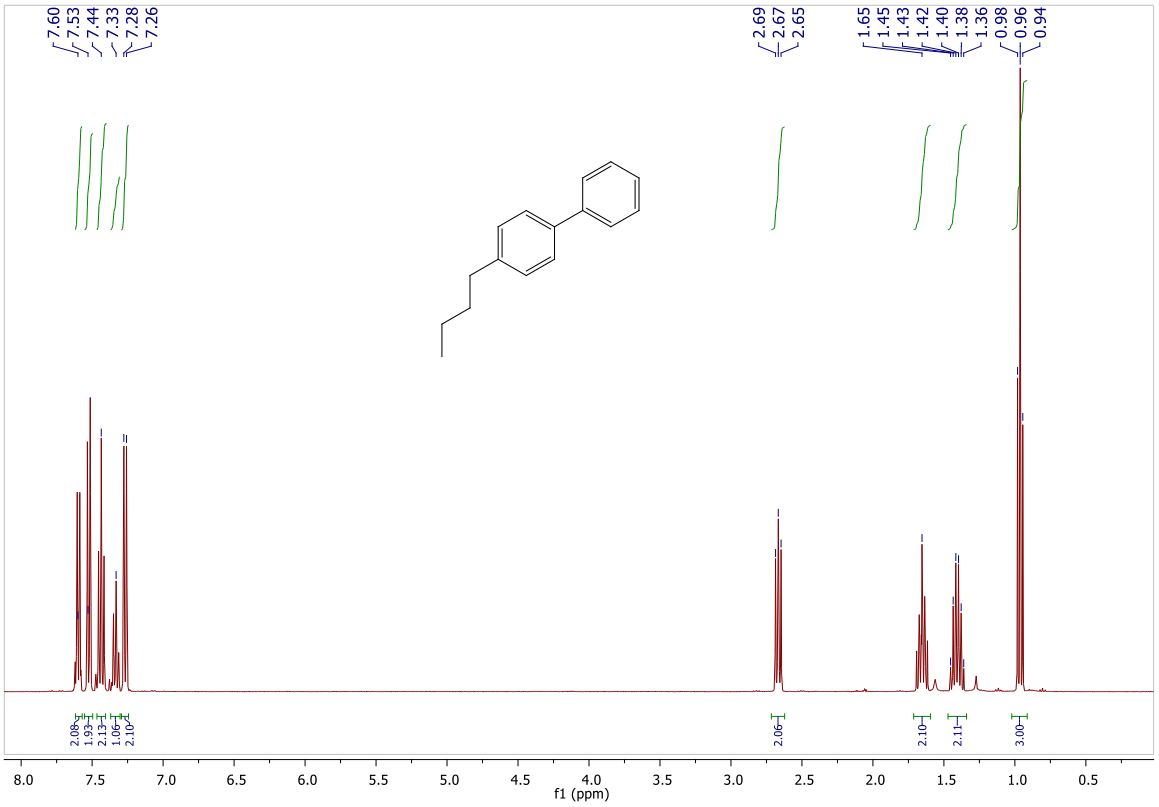

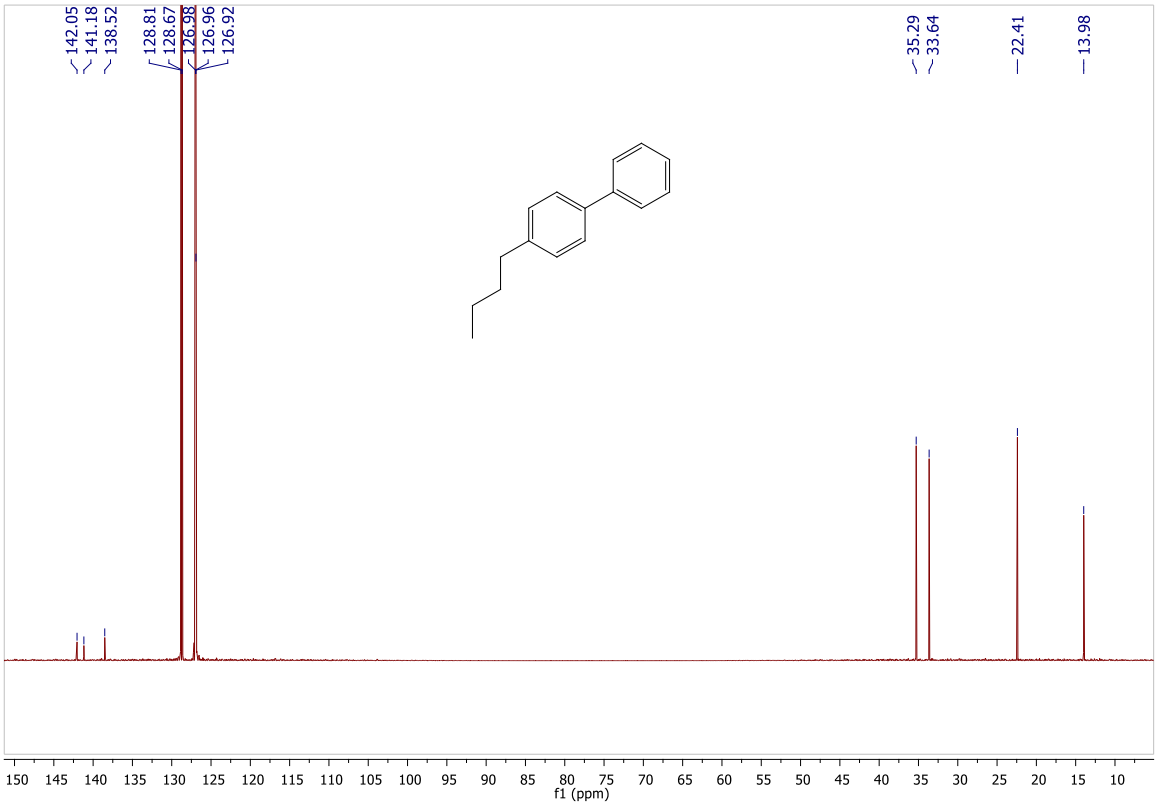

1,1':4',1''-terphenyl (3f)

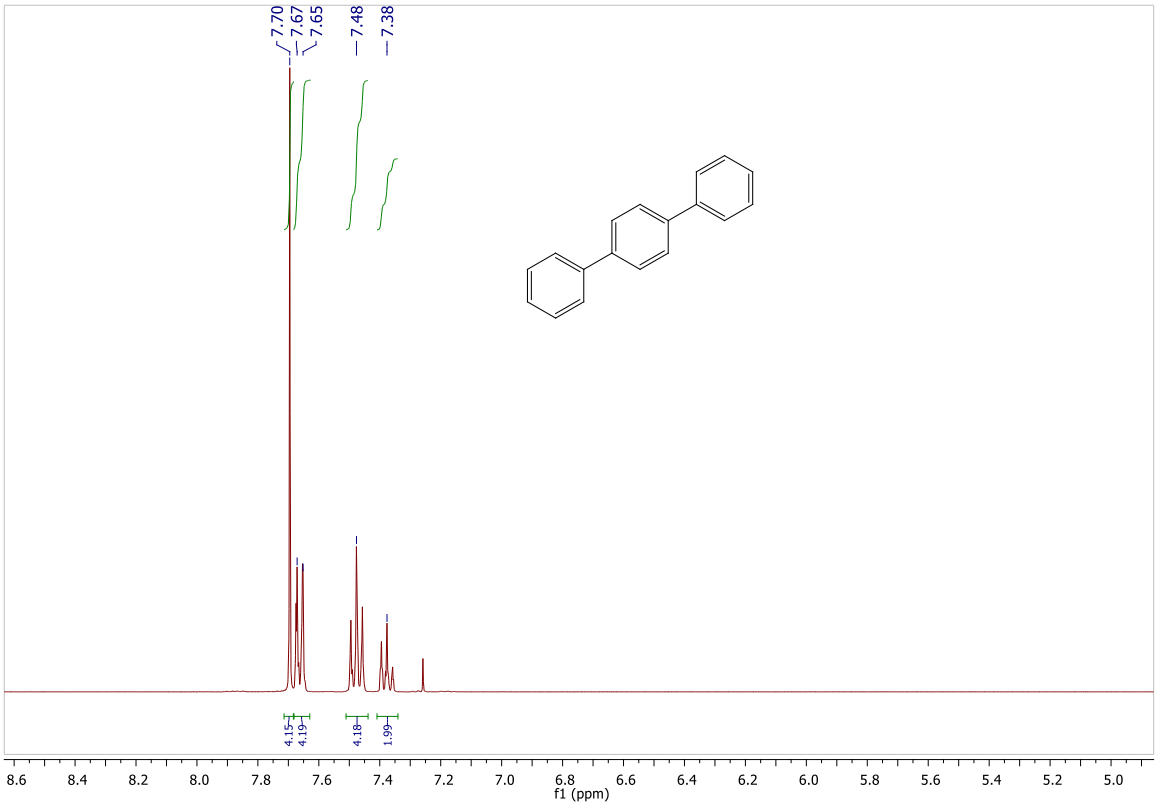

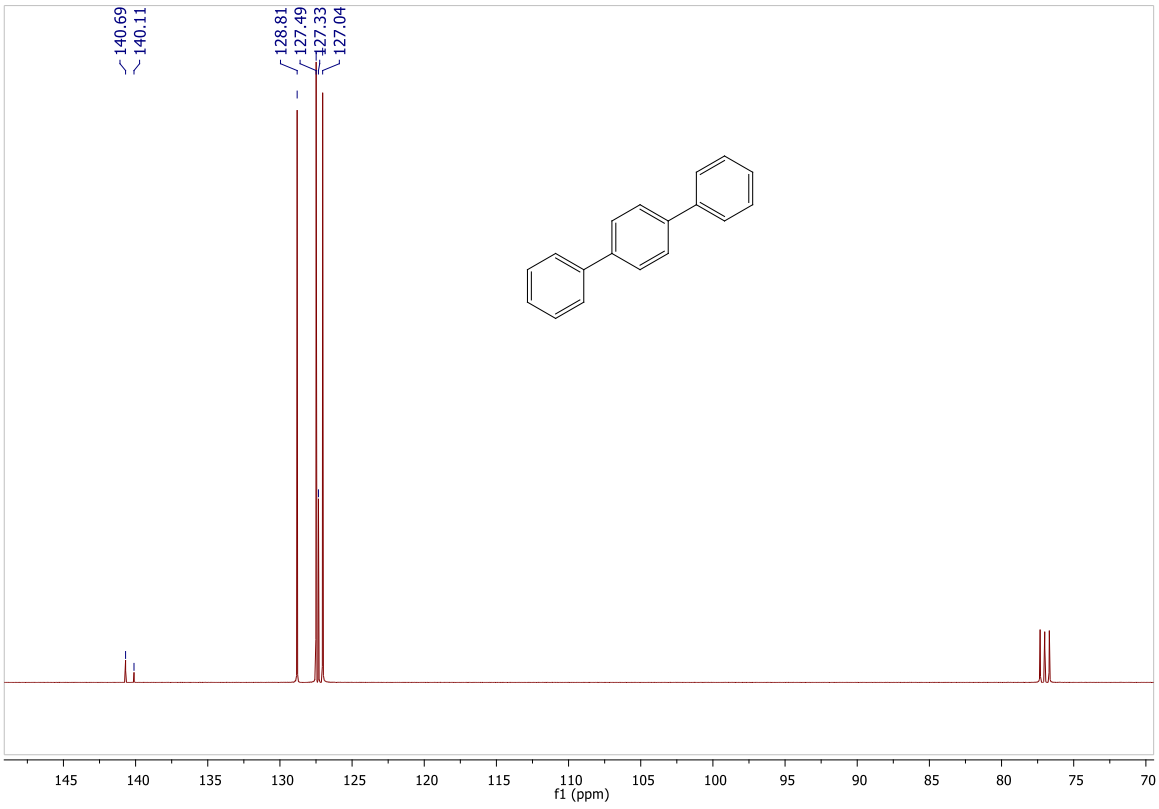

2-phenylnaphthalene (3g)

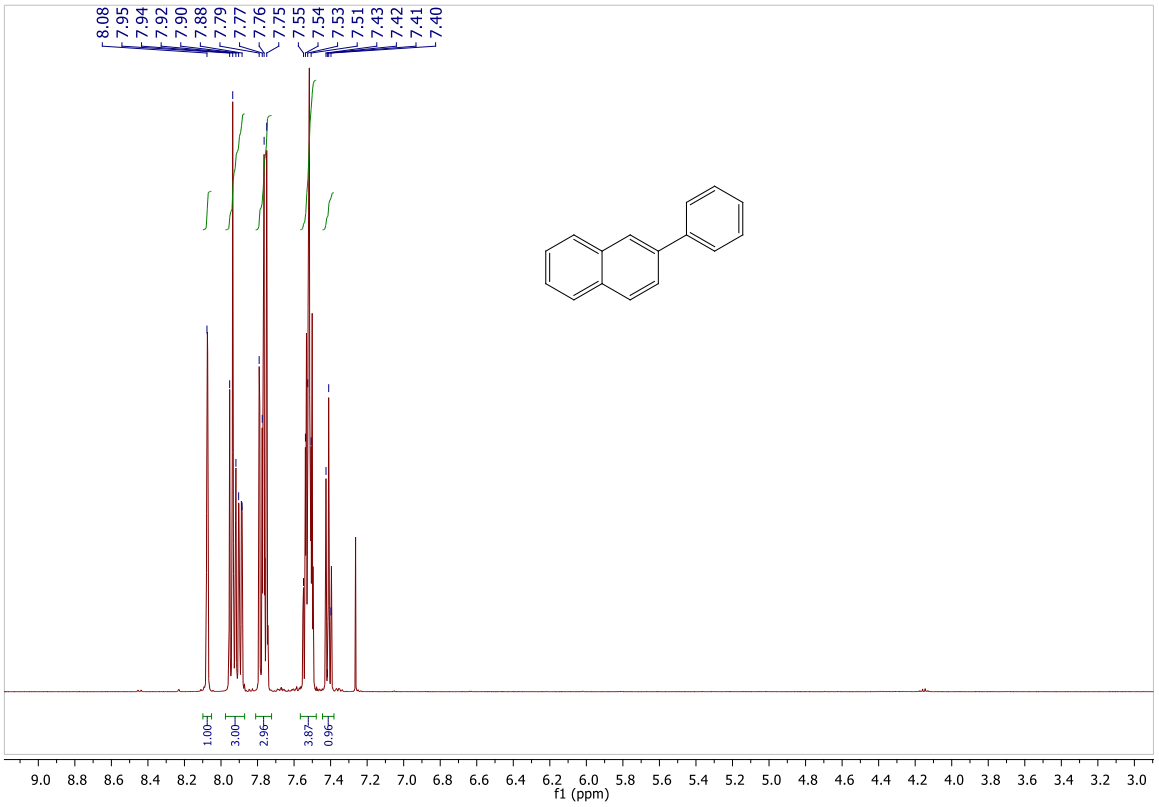

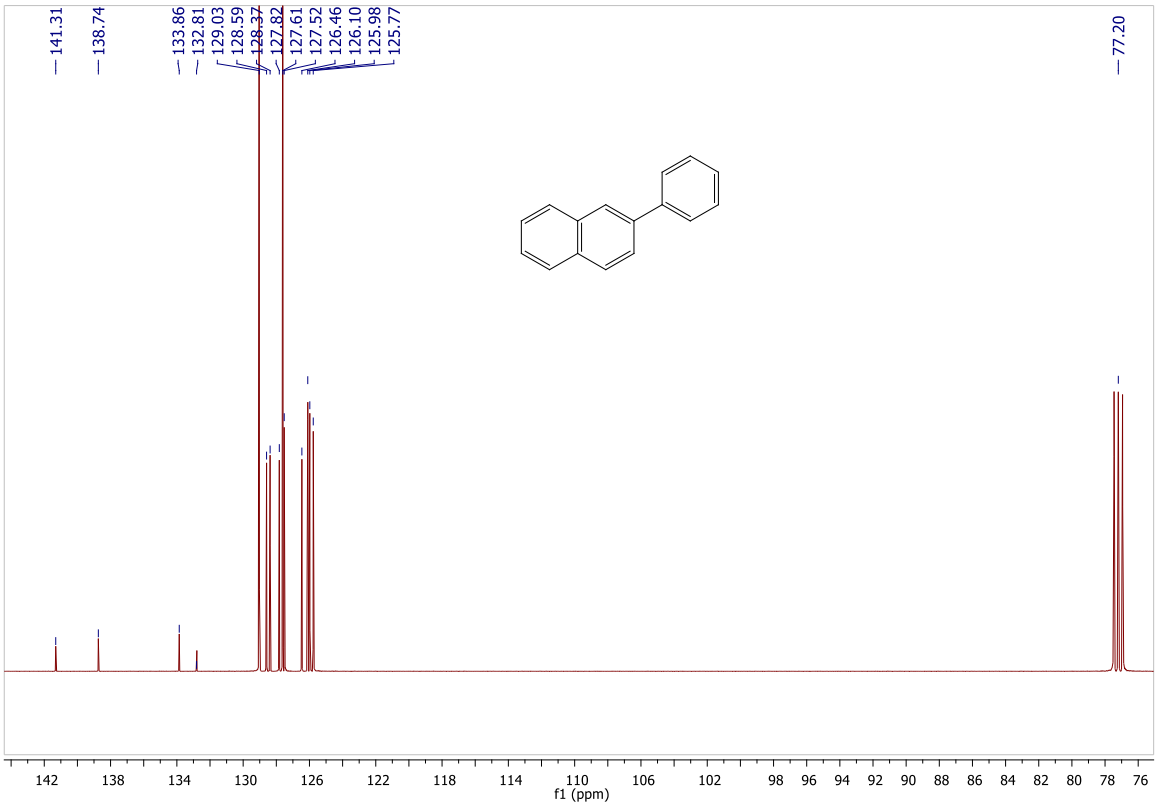

[1,1'-biphenyl]-4-ol (3h)

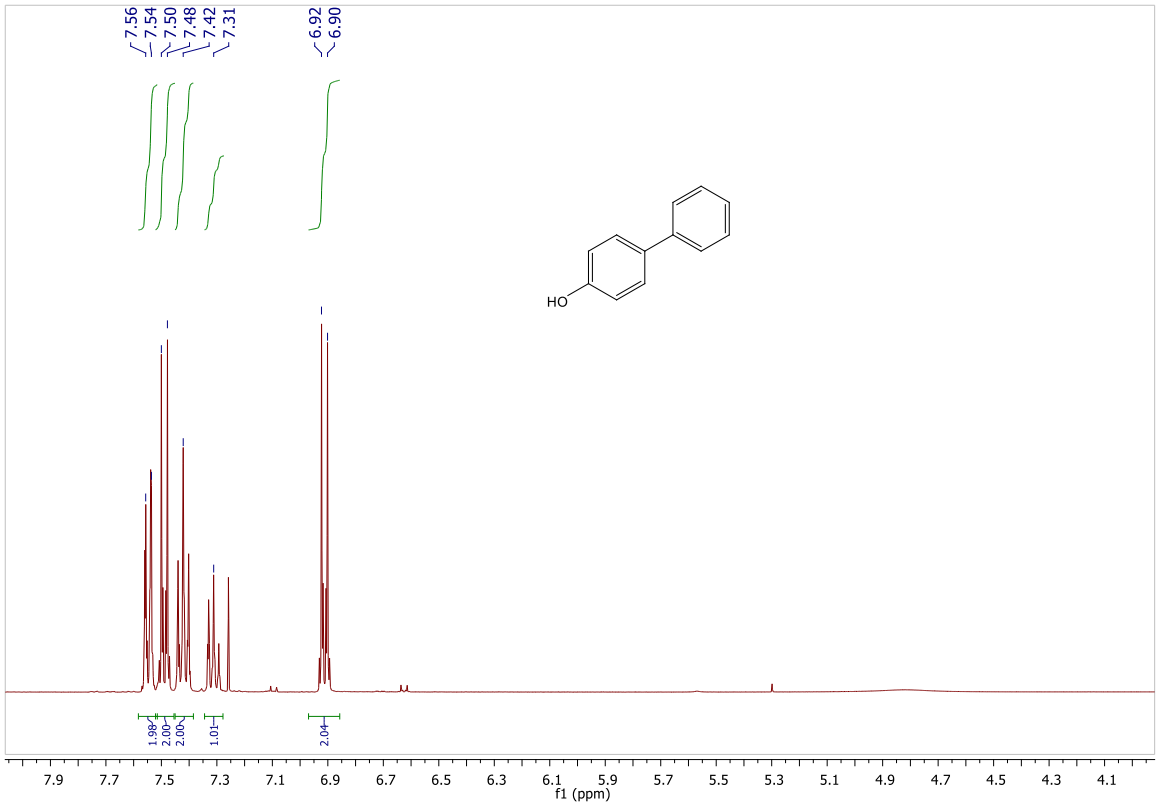

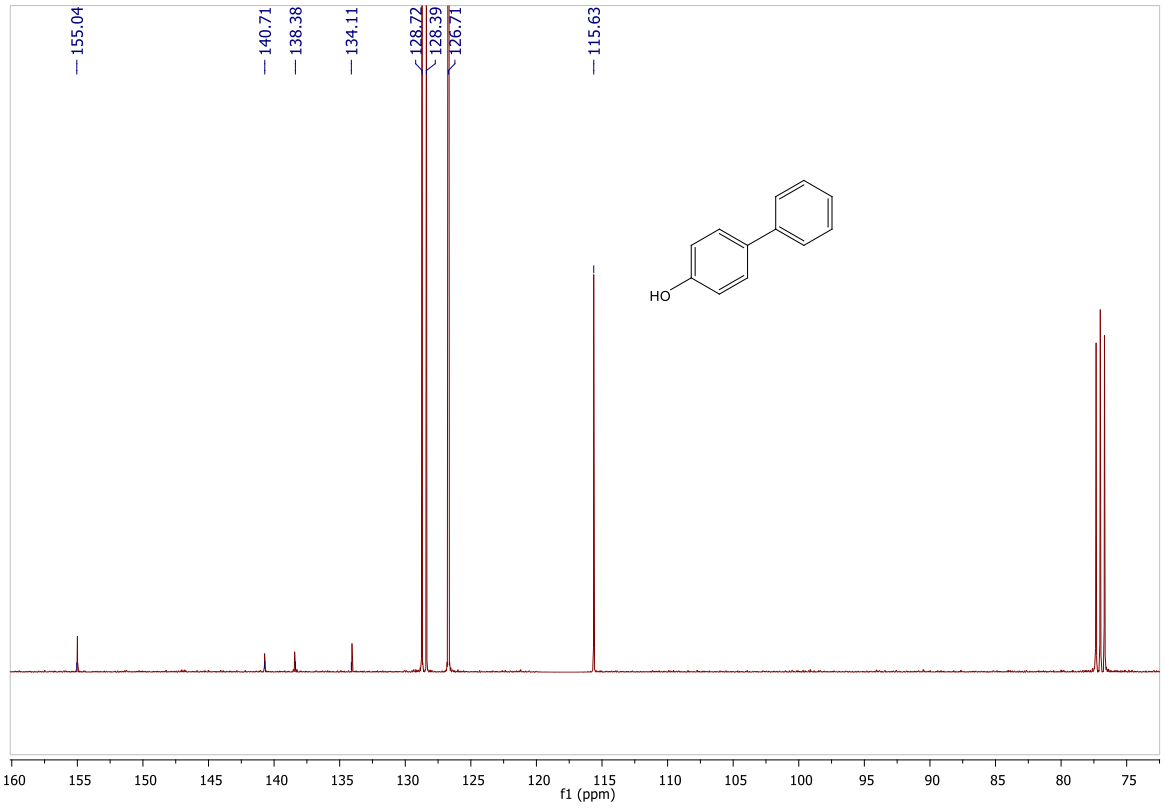

[1,1'-biphenyl]-3-ol (3i)

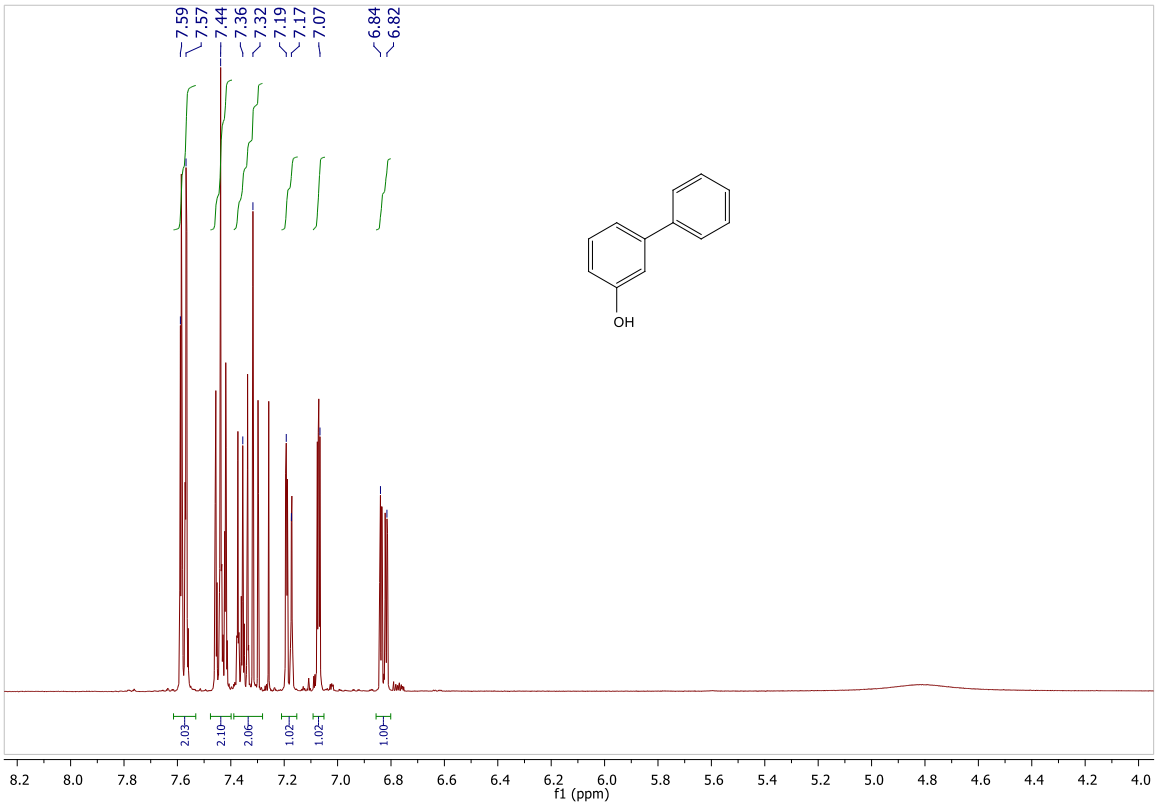

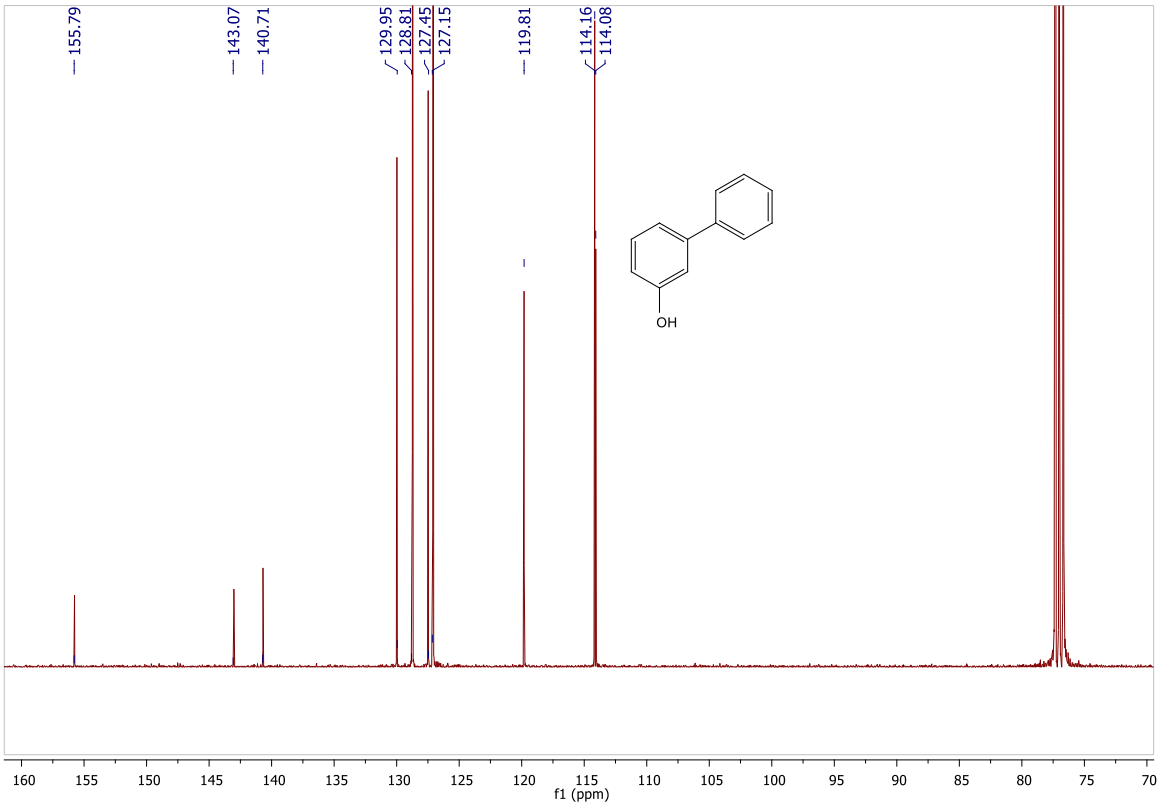

4-methoxy-1,1'-biphenyl (3j)

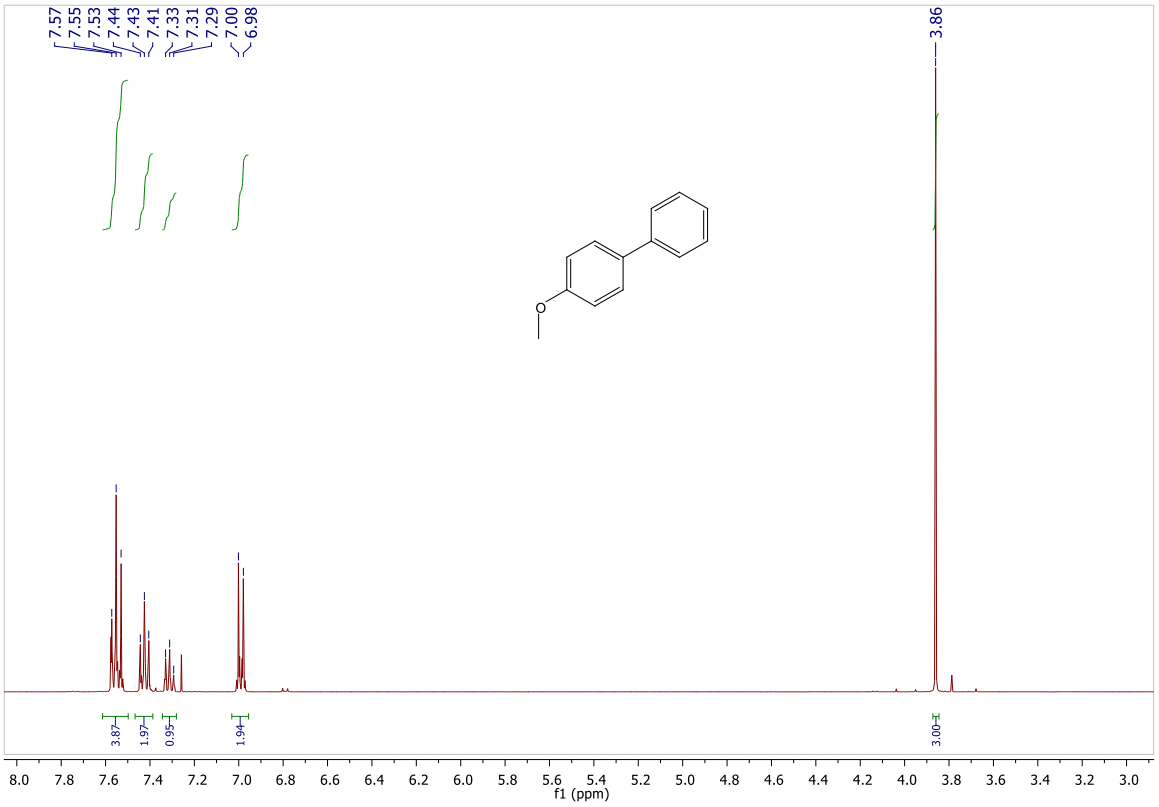

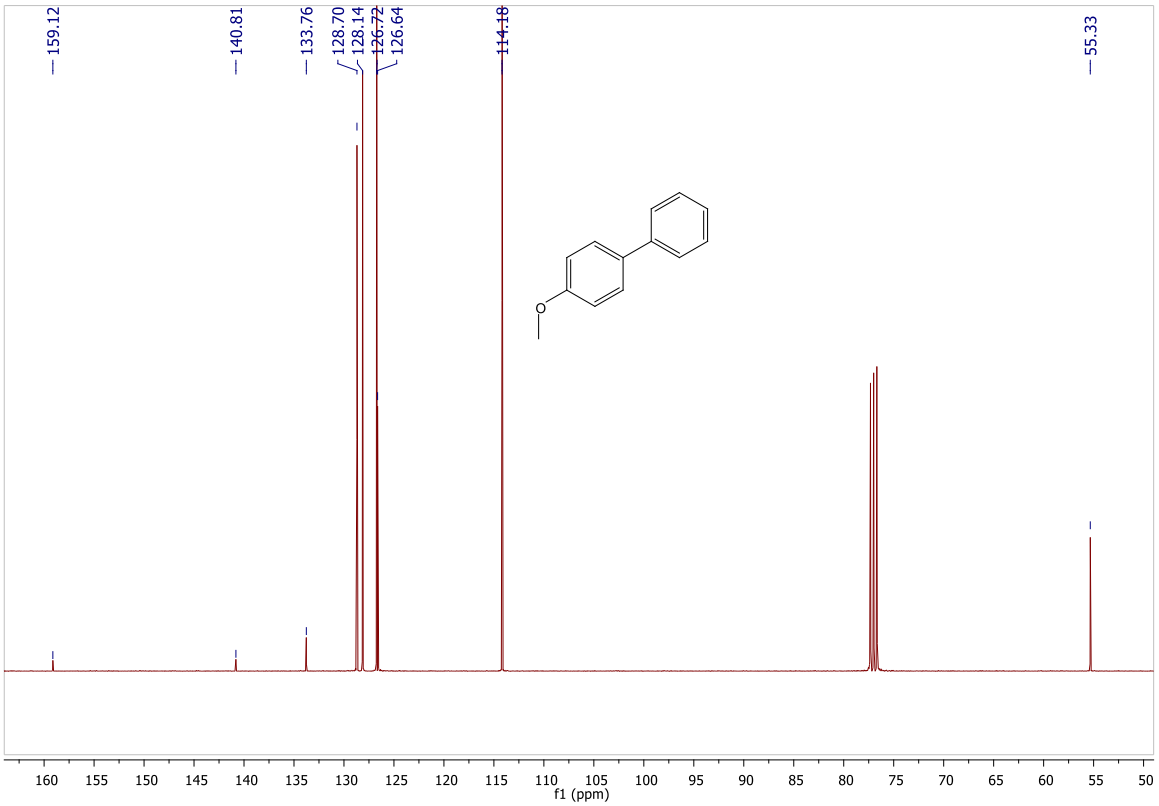

3-methoxy-1,1'-biphenyl (3k)

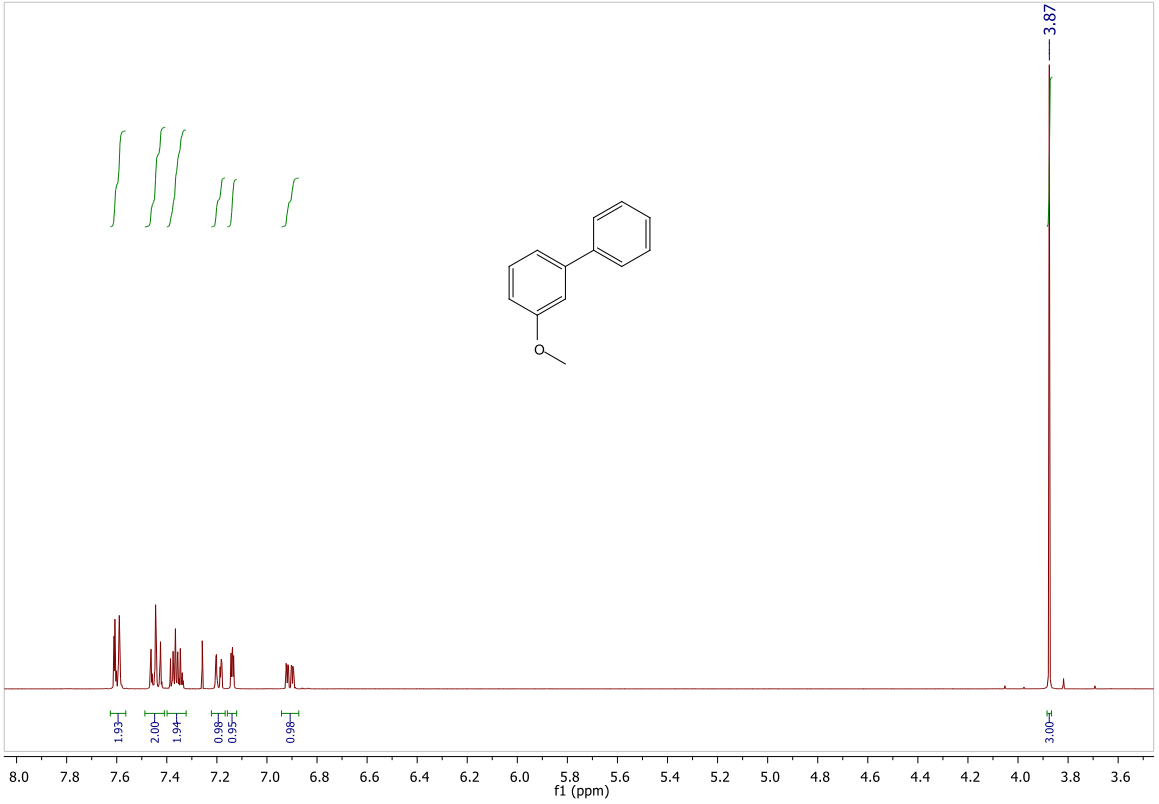

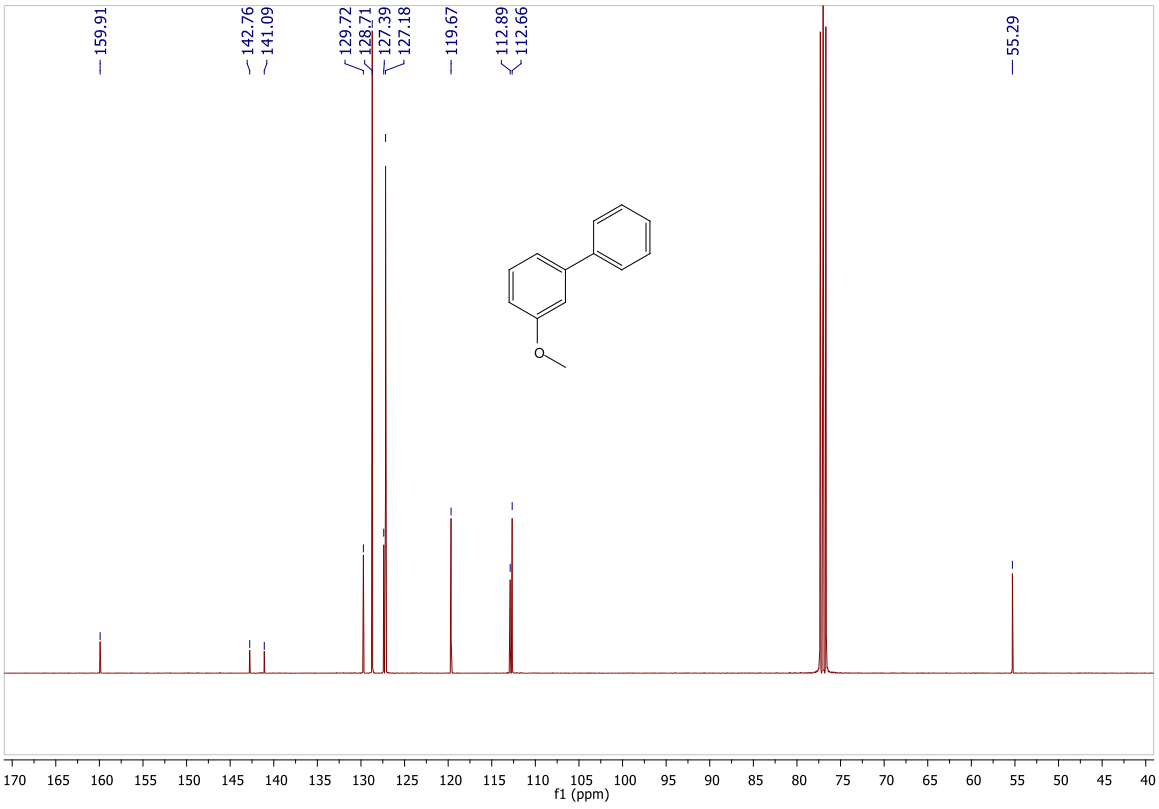

2-methoxy-6-phenylnaphthalene (3l)

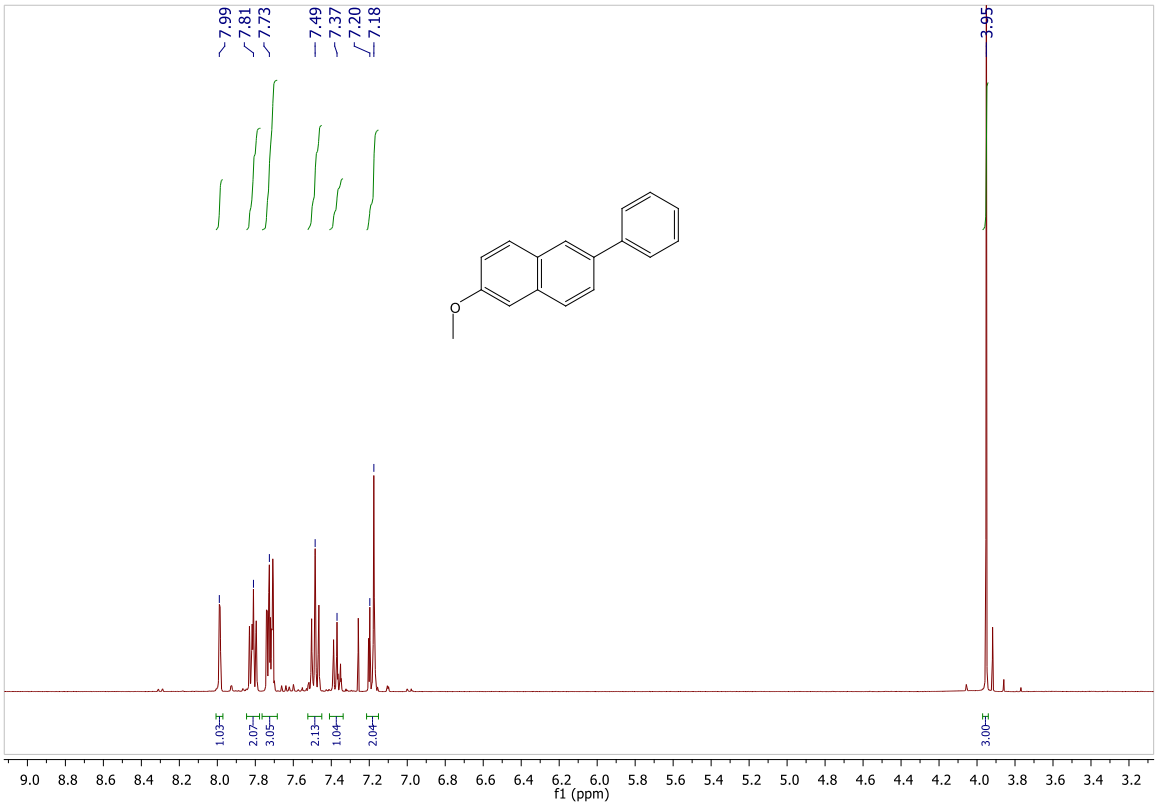

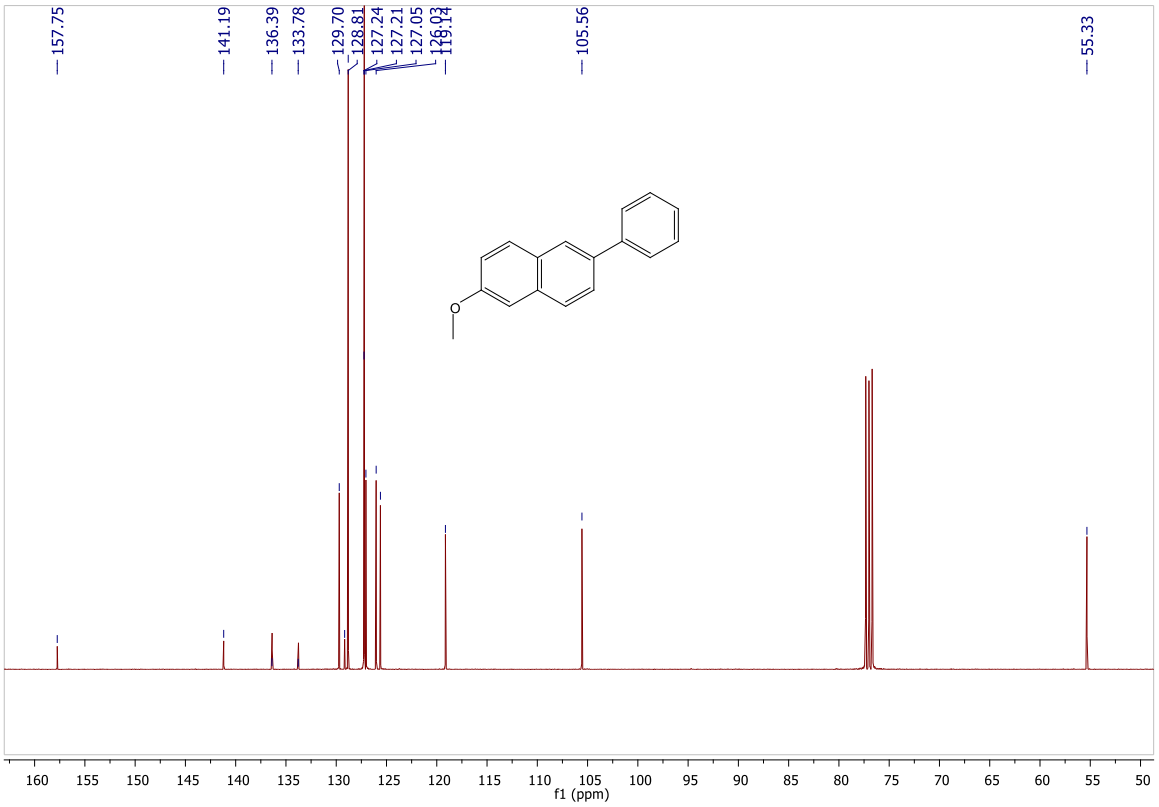

4-ethoxy-1,1'-biphenyl (3m)

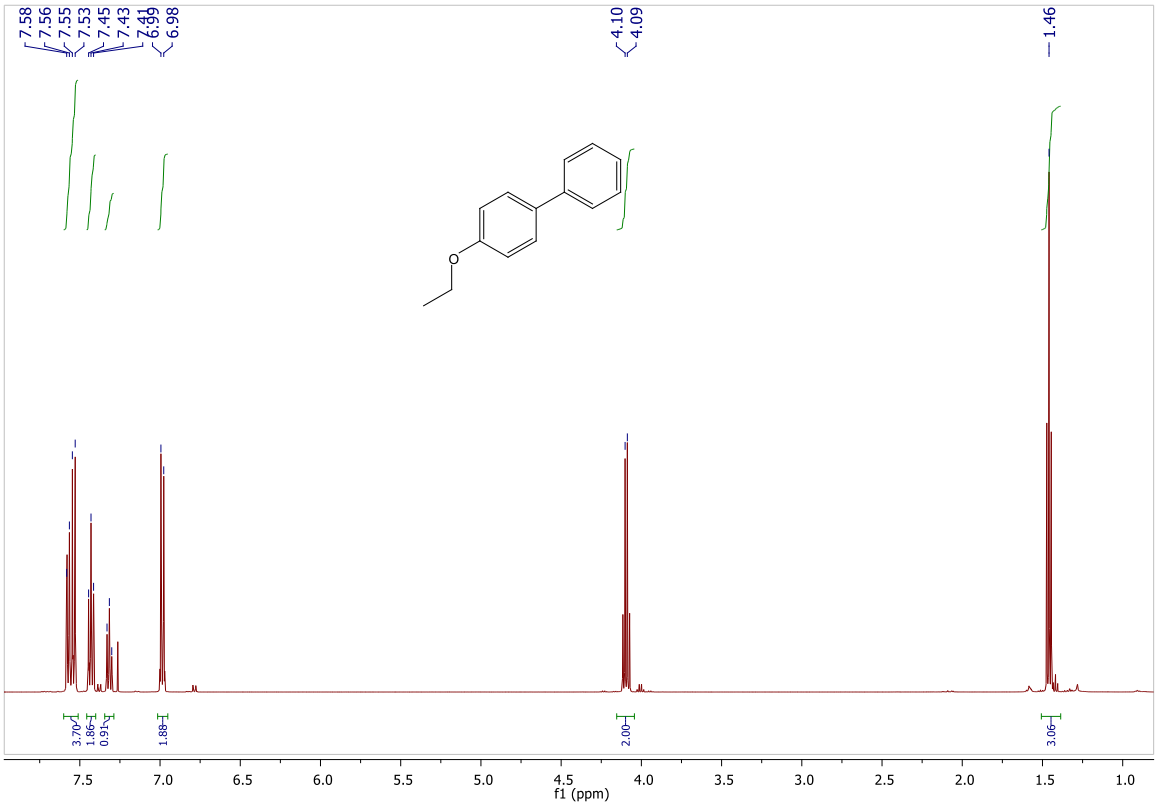

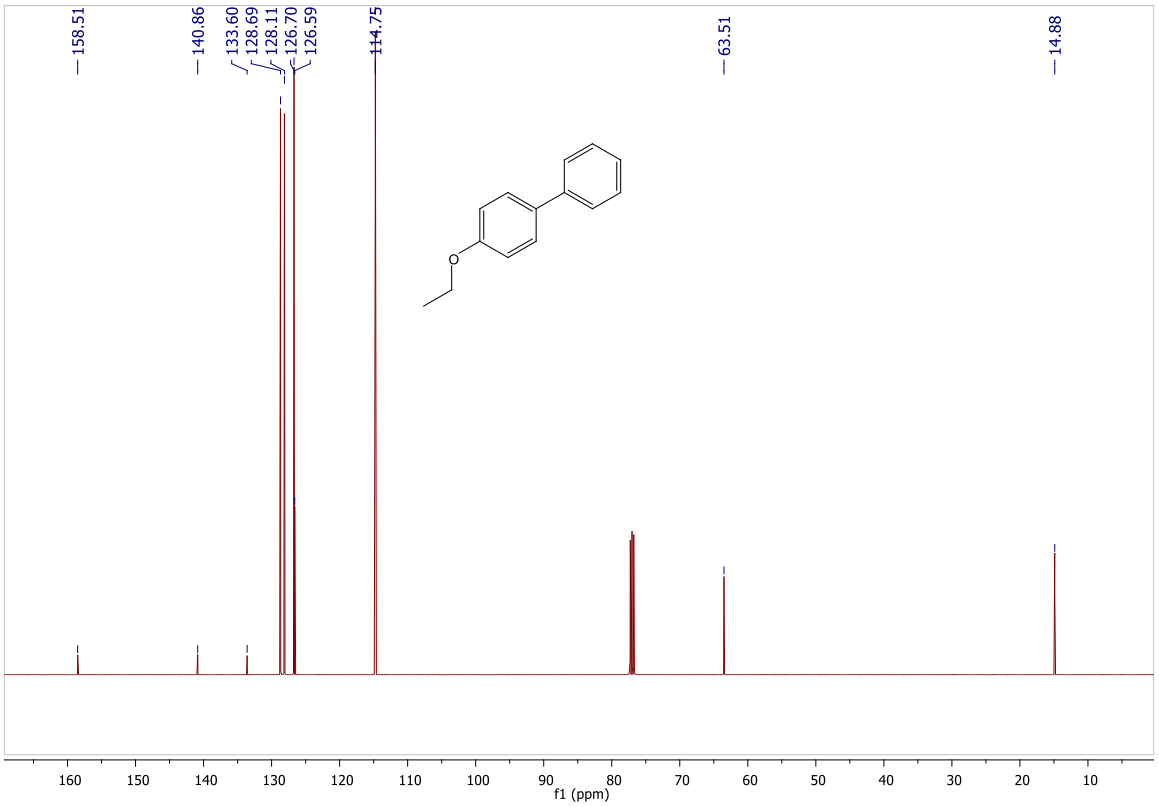

[1,1'-biphenyl]-4-amine (3n)

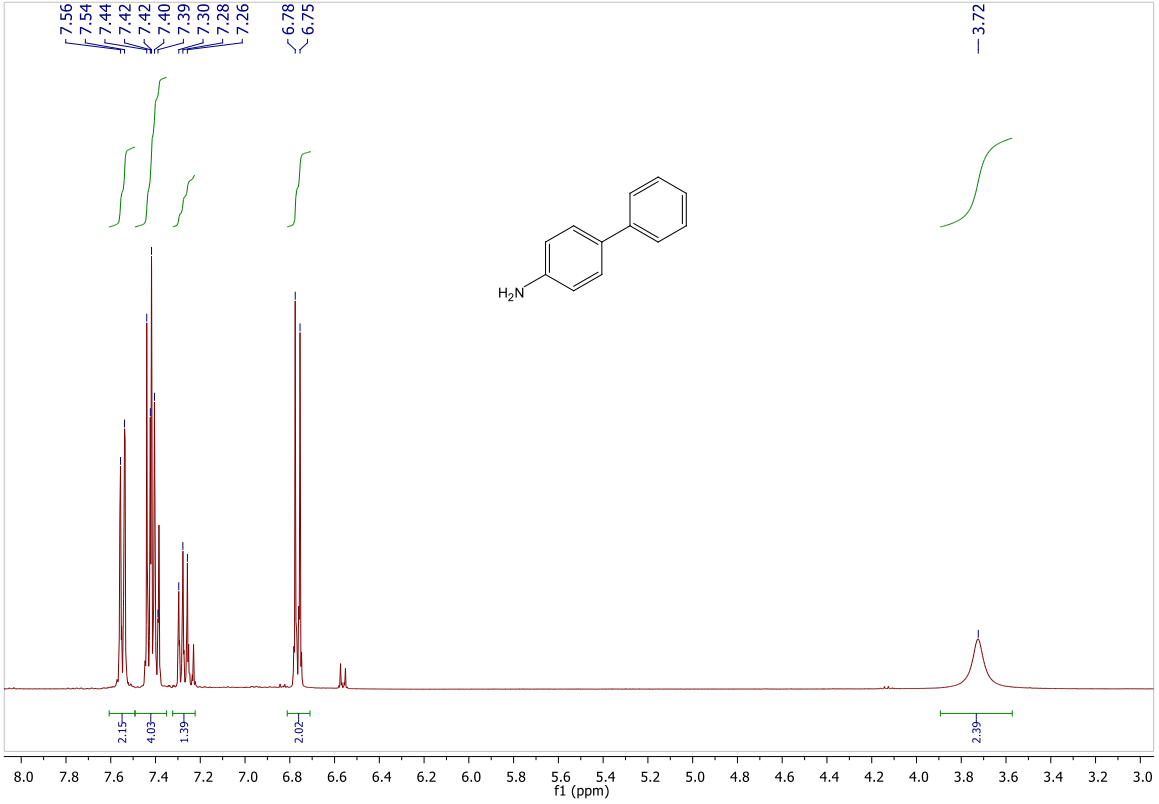

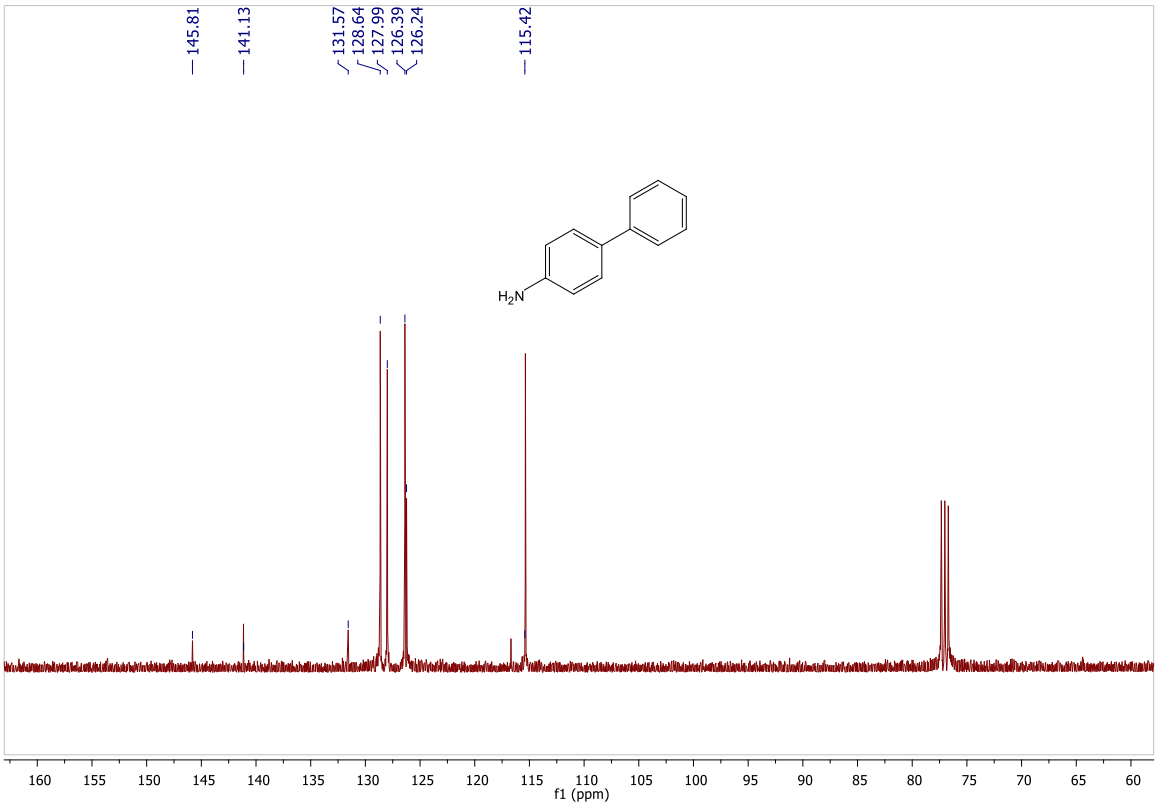

N,N-dimethyl-[1,1'-biphenyl]-4-amine (3o)

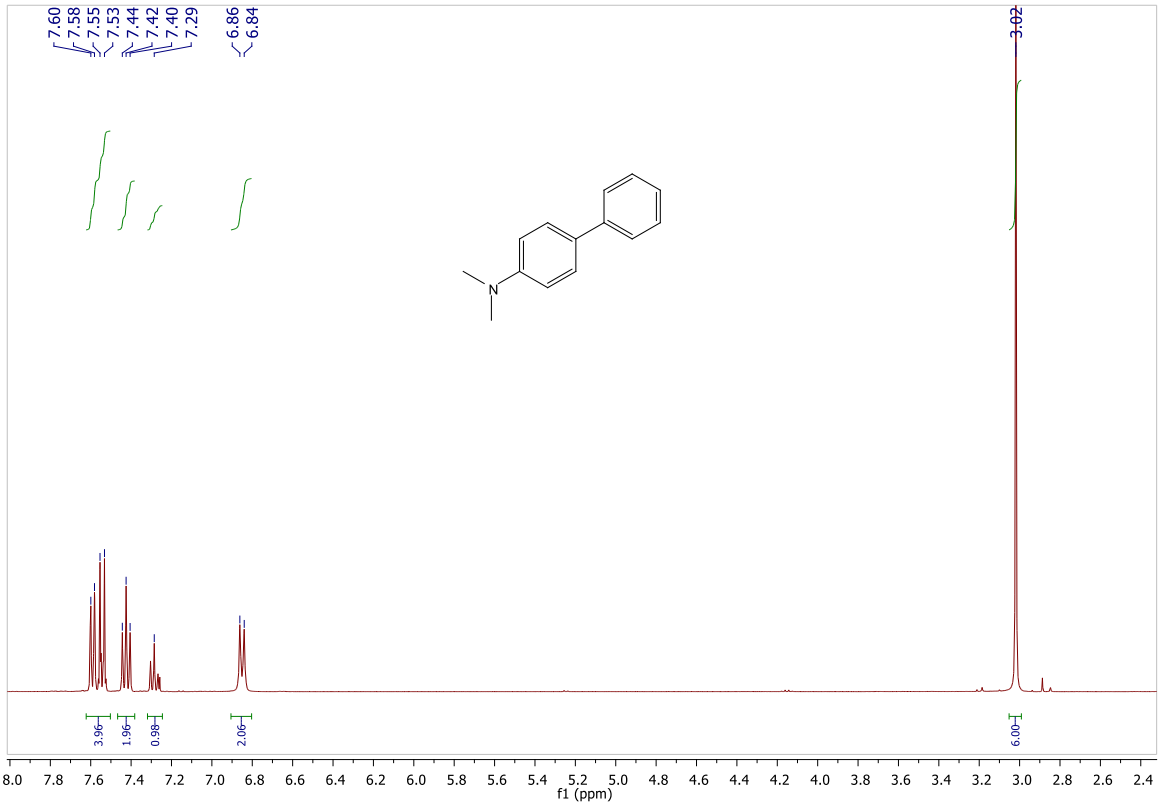

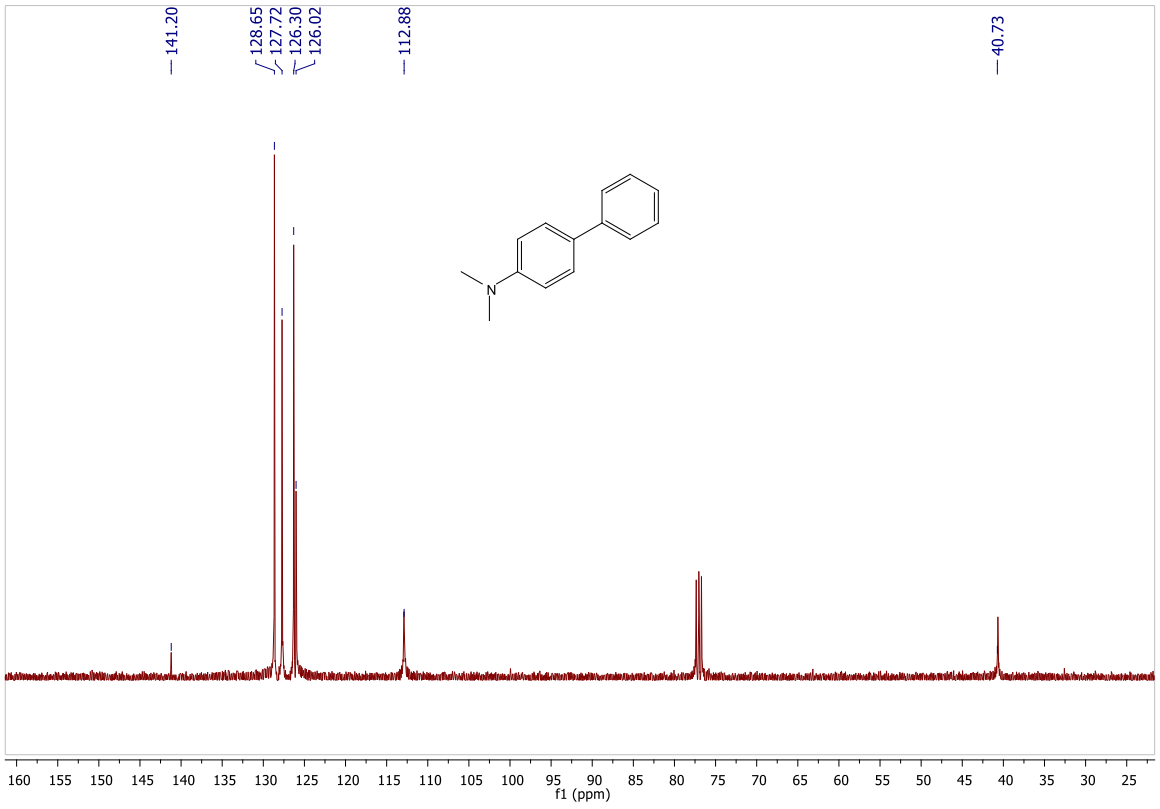

4-nitro-1,1'-biphenyl (3p)

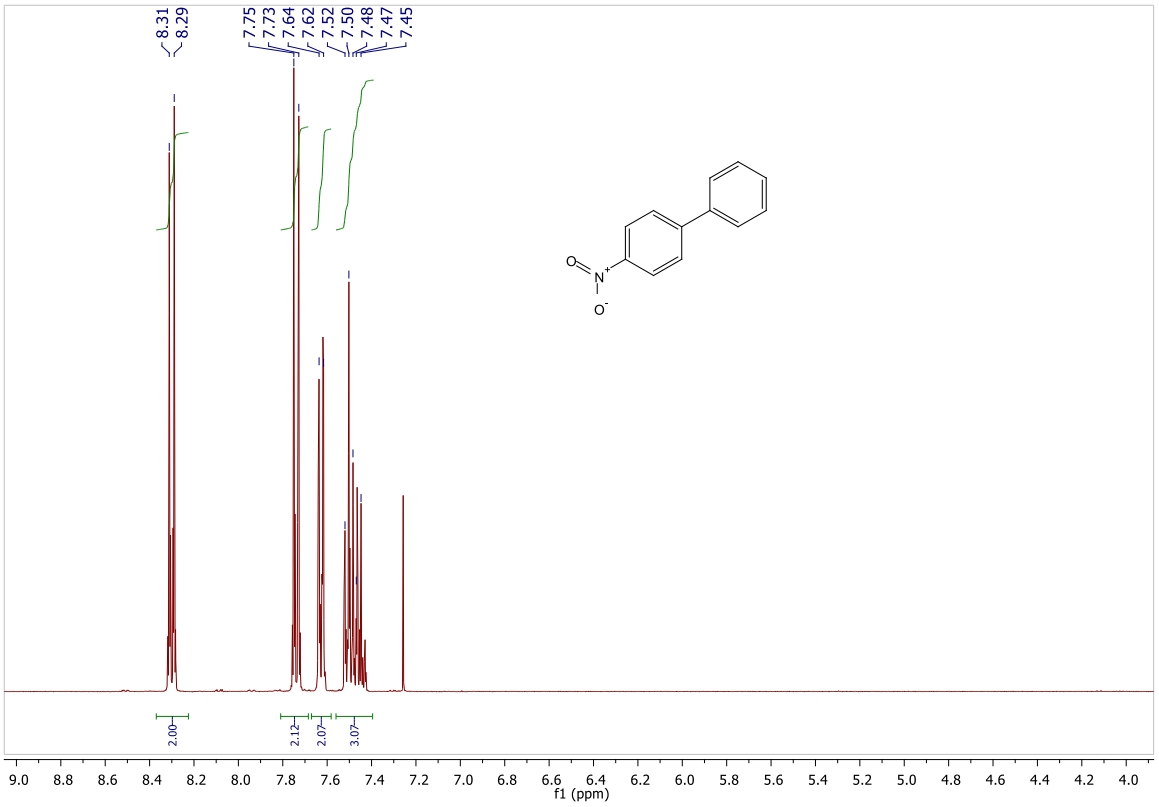

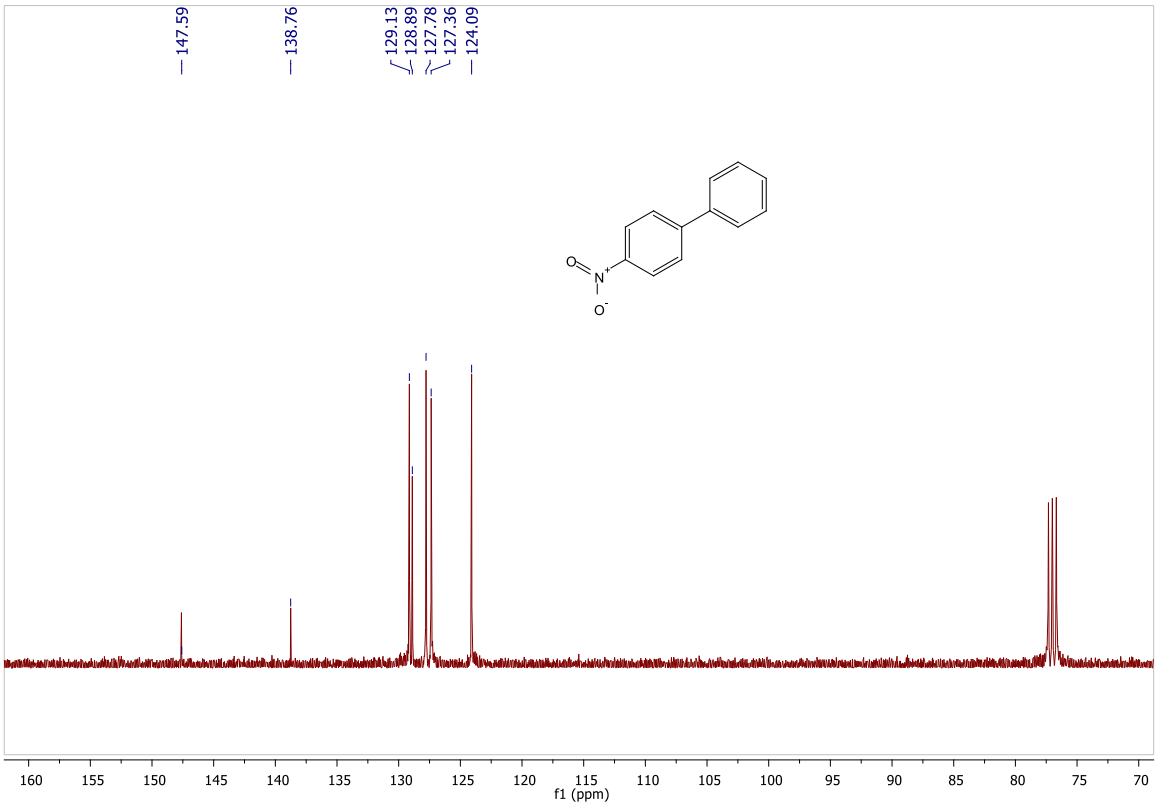

4-(trifluoromethyl)-1,1'-biphenyl (3q)

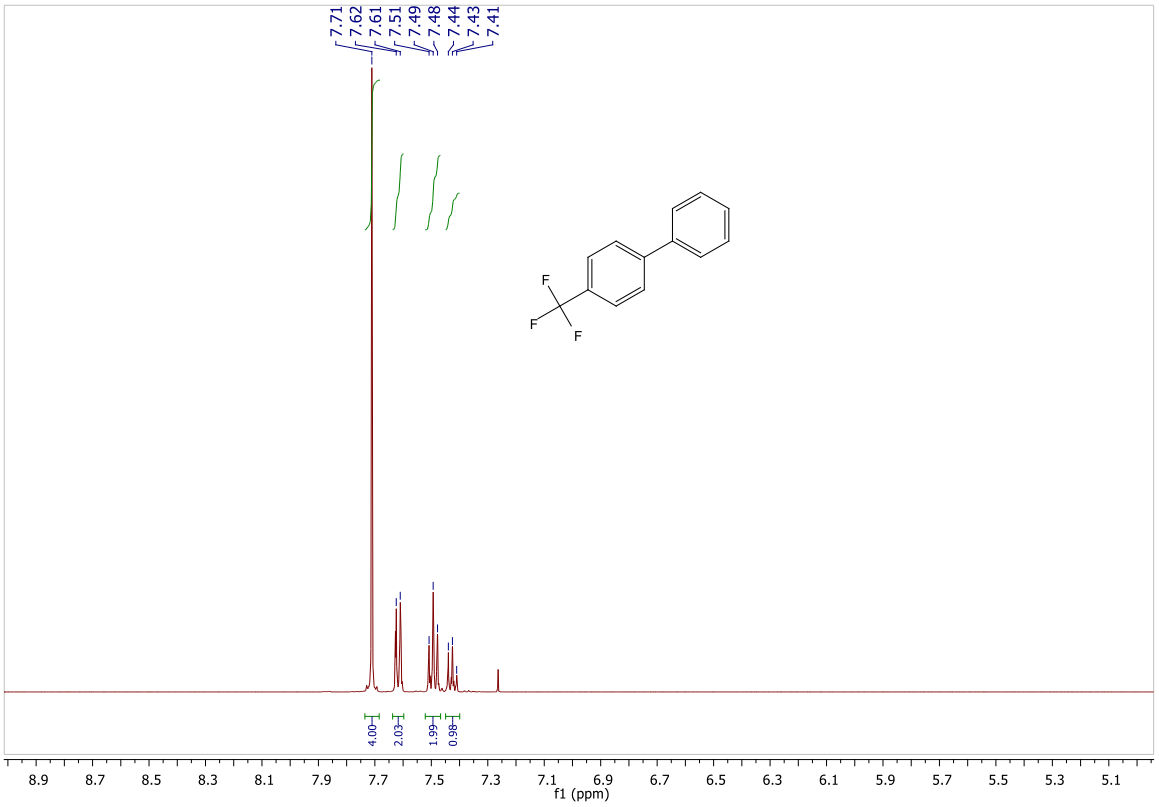

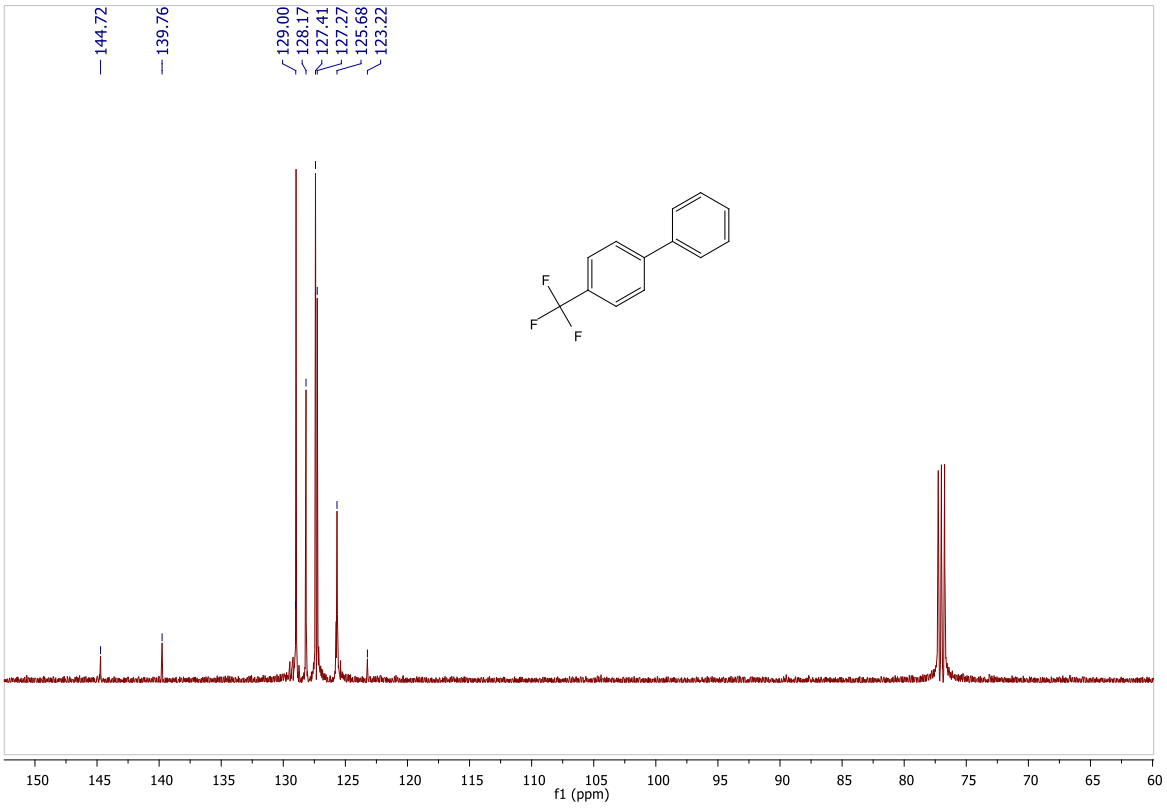

3-(trifluoromethyl)-1,1'-biphenyl (3r)

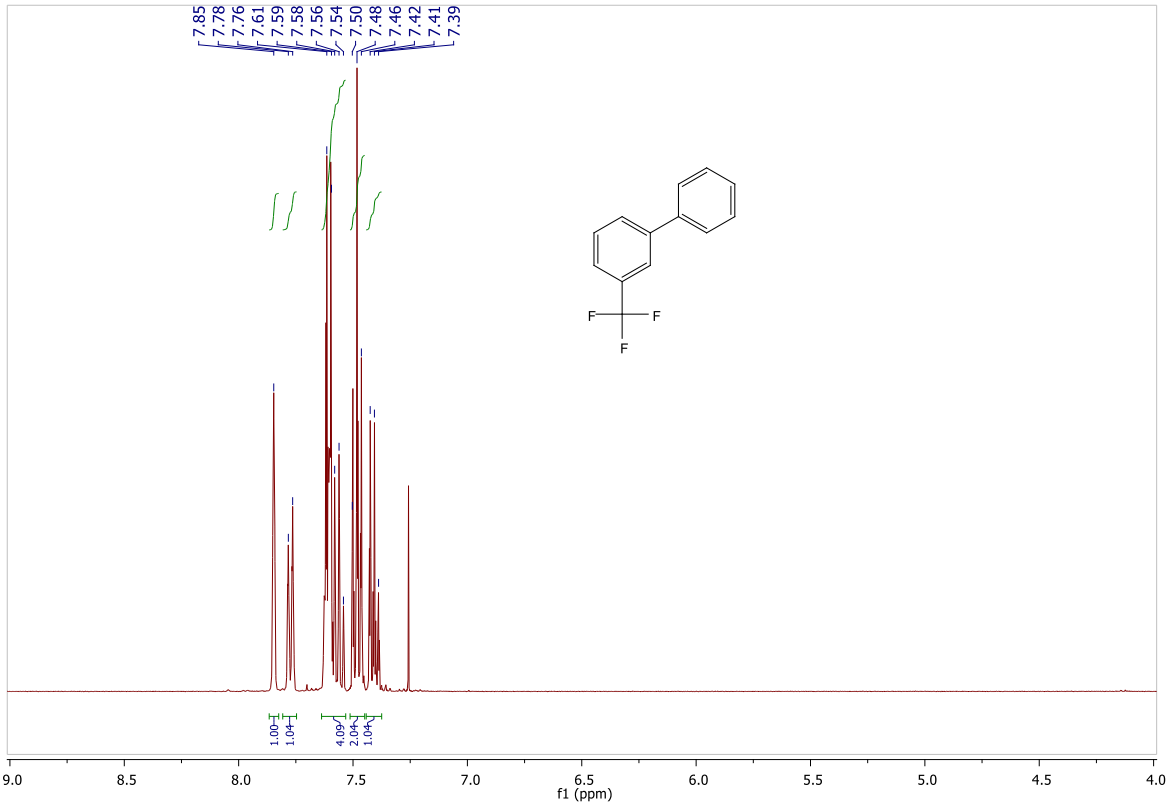

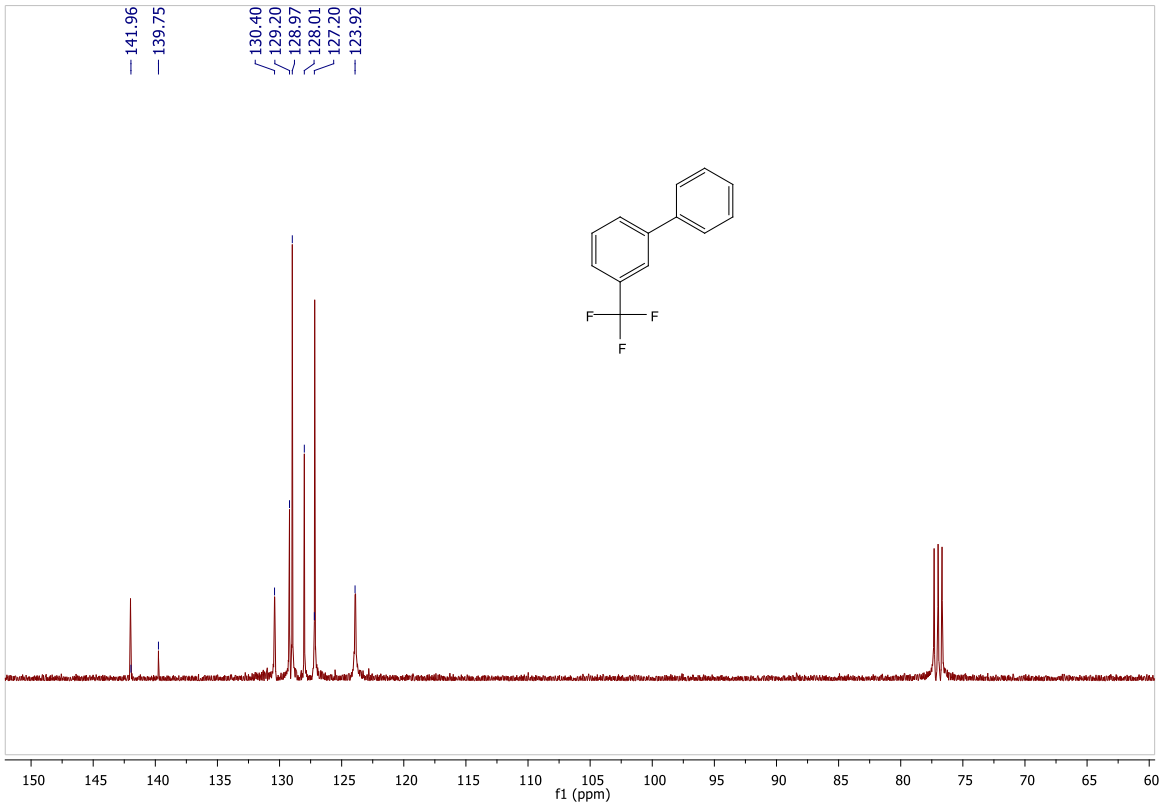

[1,1'-biphenyl]-4-carbonitrile (3s)

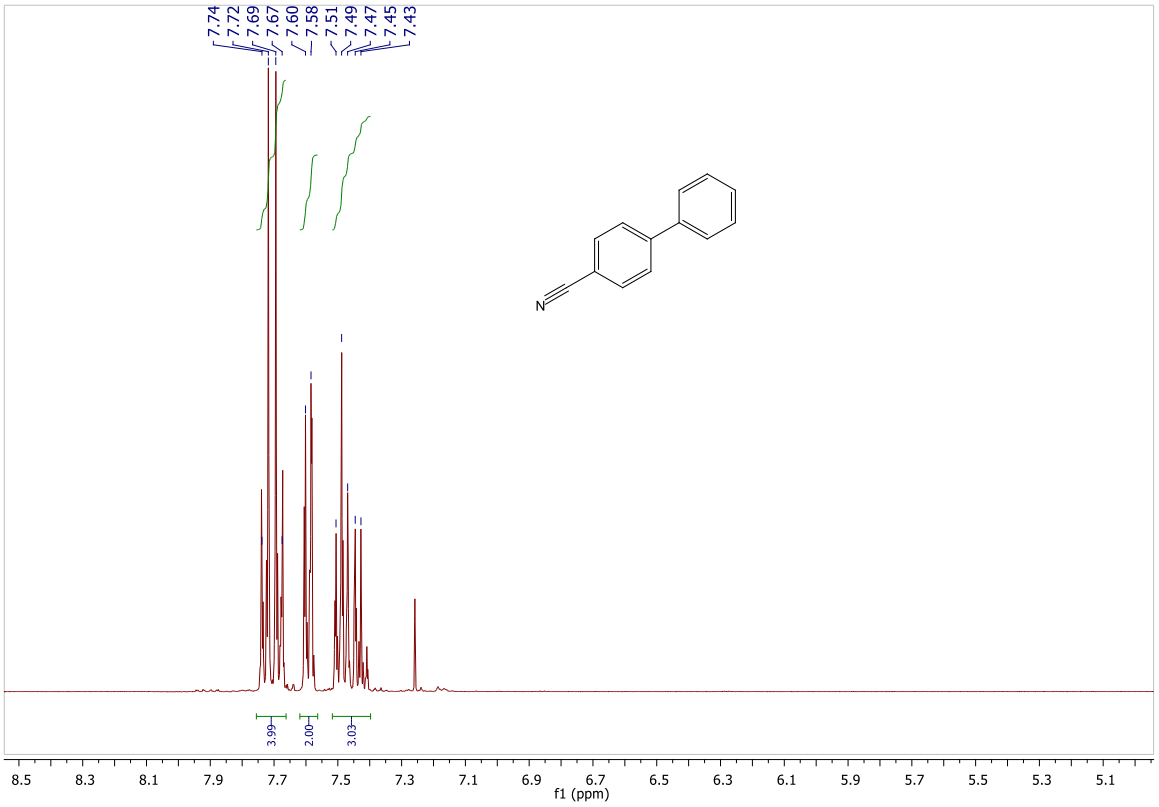

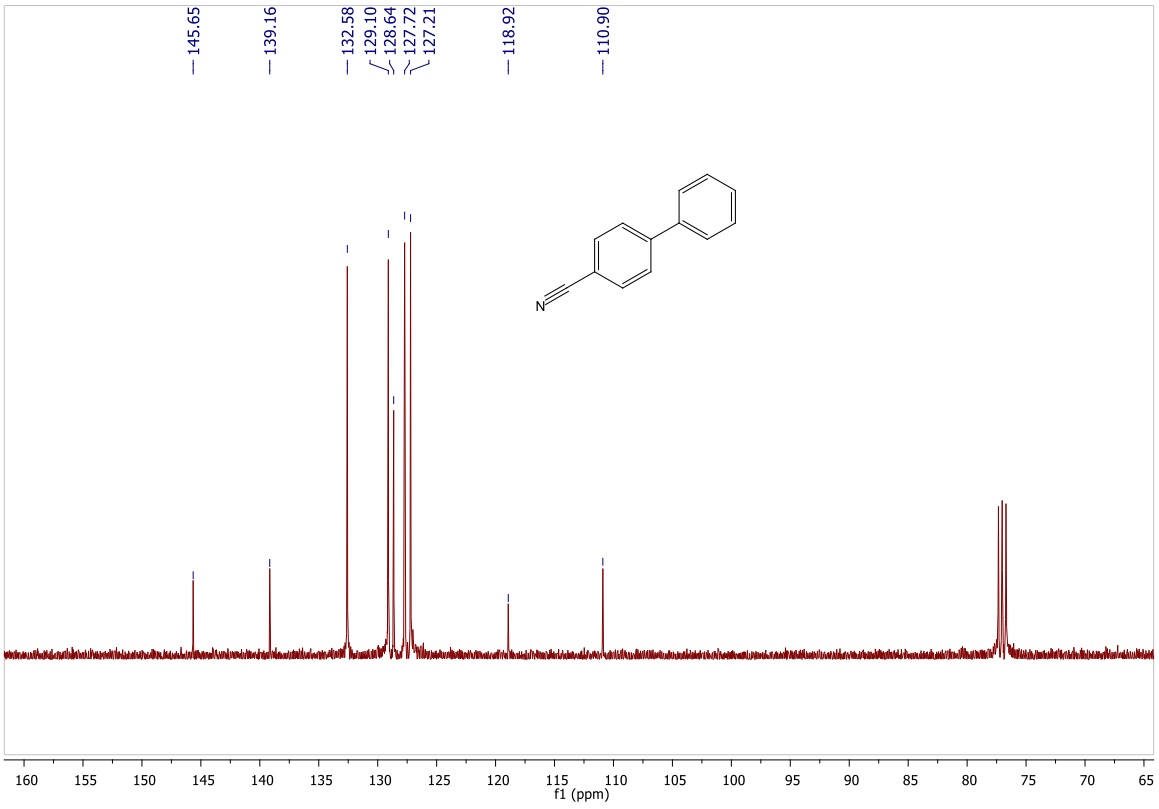

[1,1'-biphenyl]-3-carbonitrile (3t)

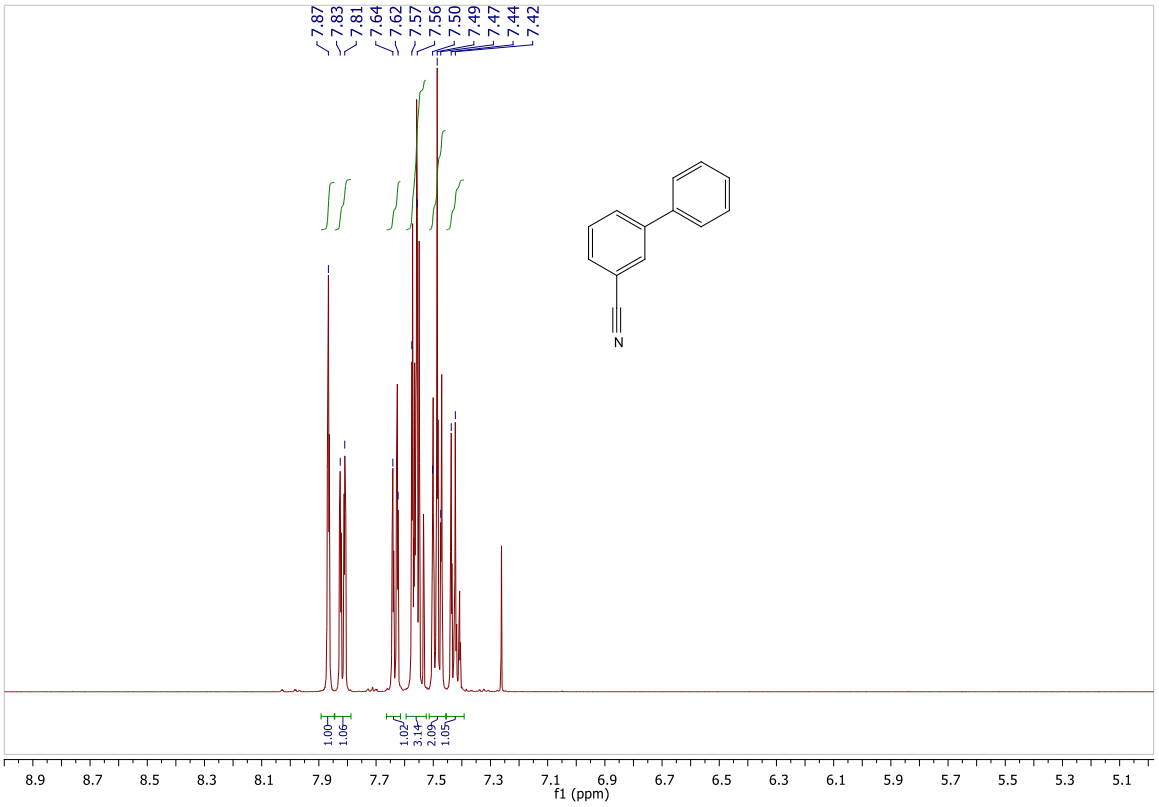

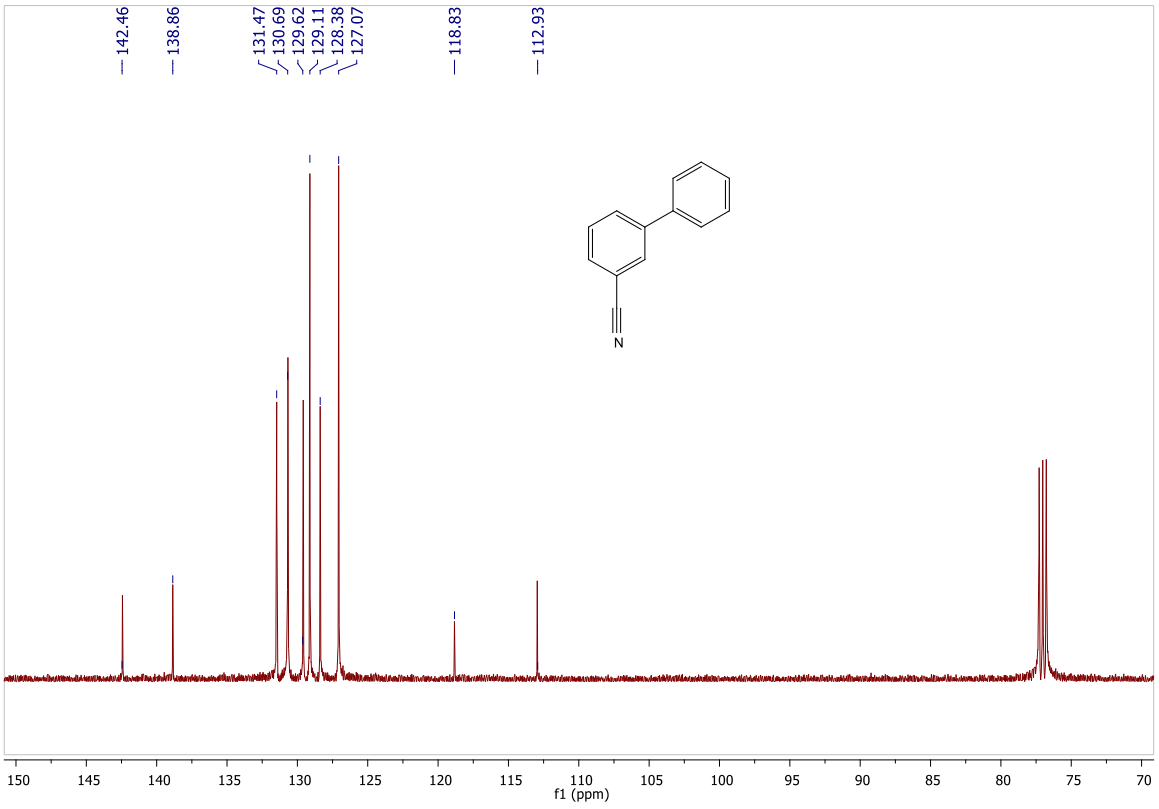

[1,1'-biphenyl]-4-carbaldehyde (3u)

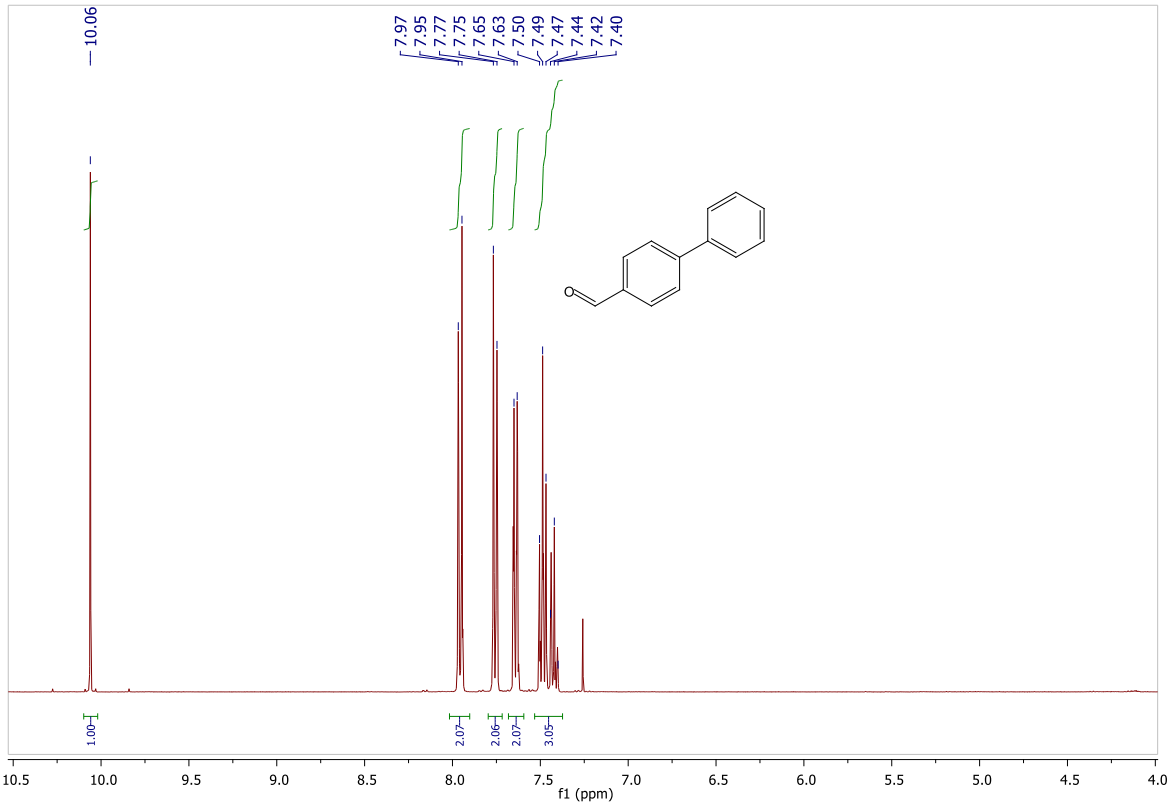

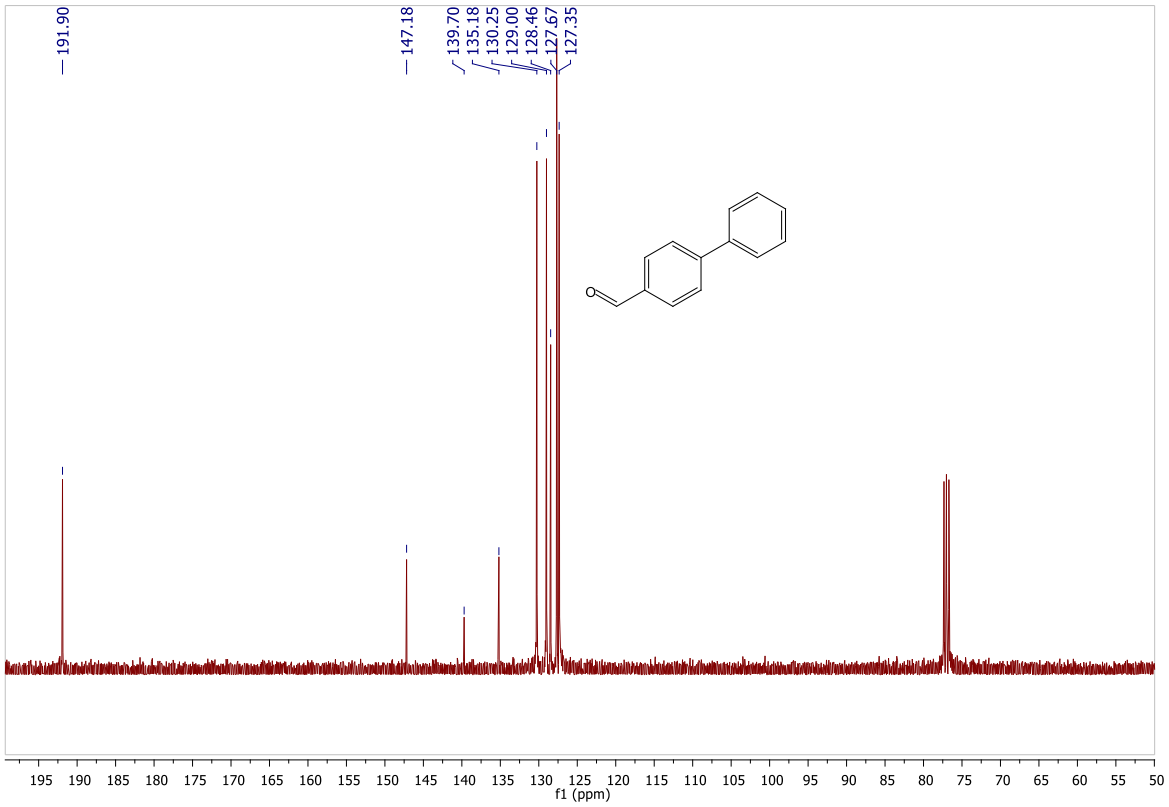

1-([1,1'-biphenyl]-4-yl)ethan-1-one (3v)

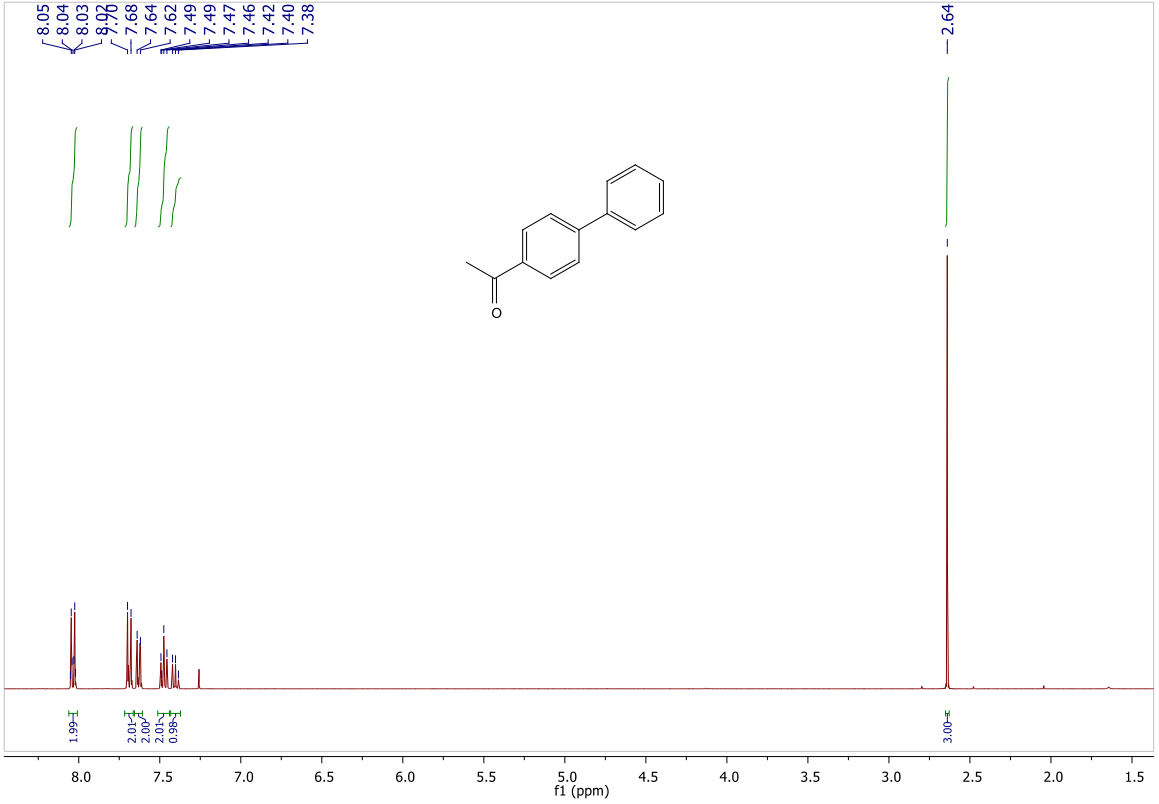

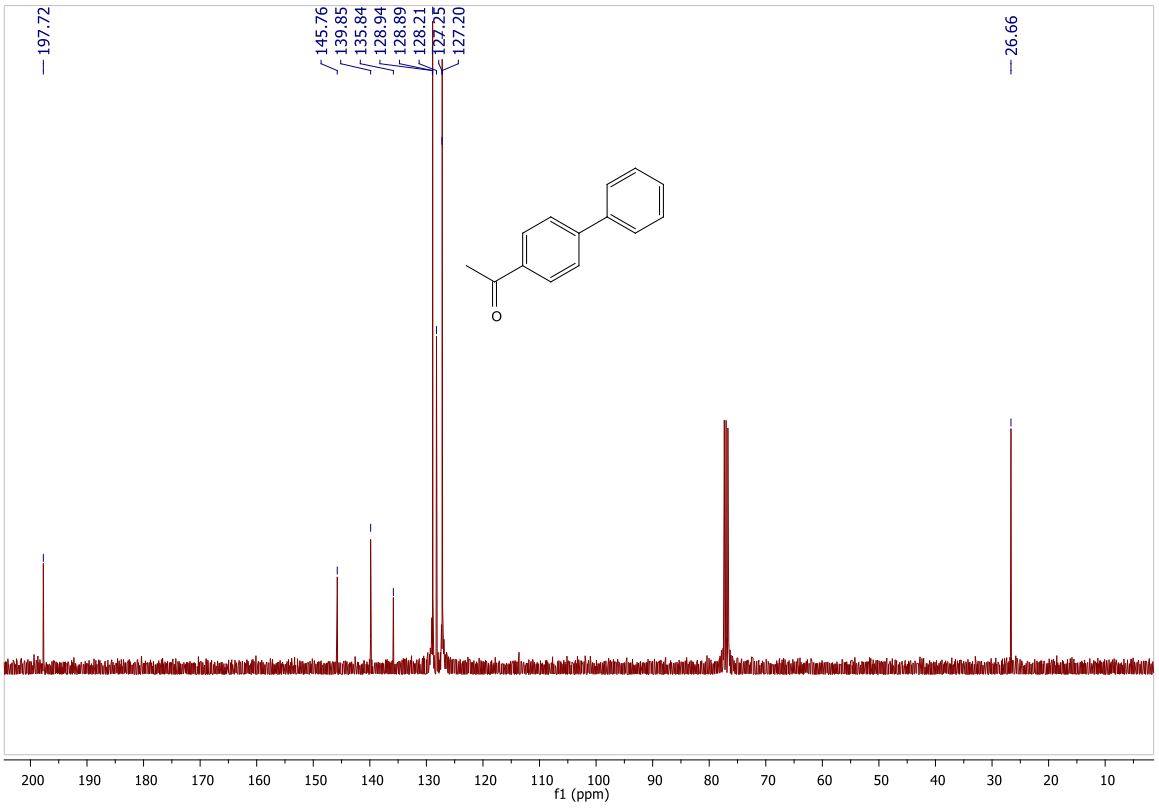

1-([1,1'-biphenyl]-3-yl)ethan-1-one (3w)

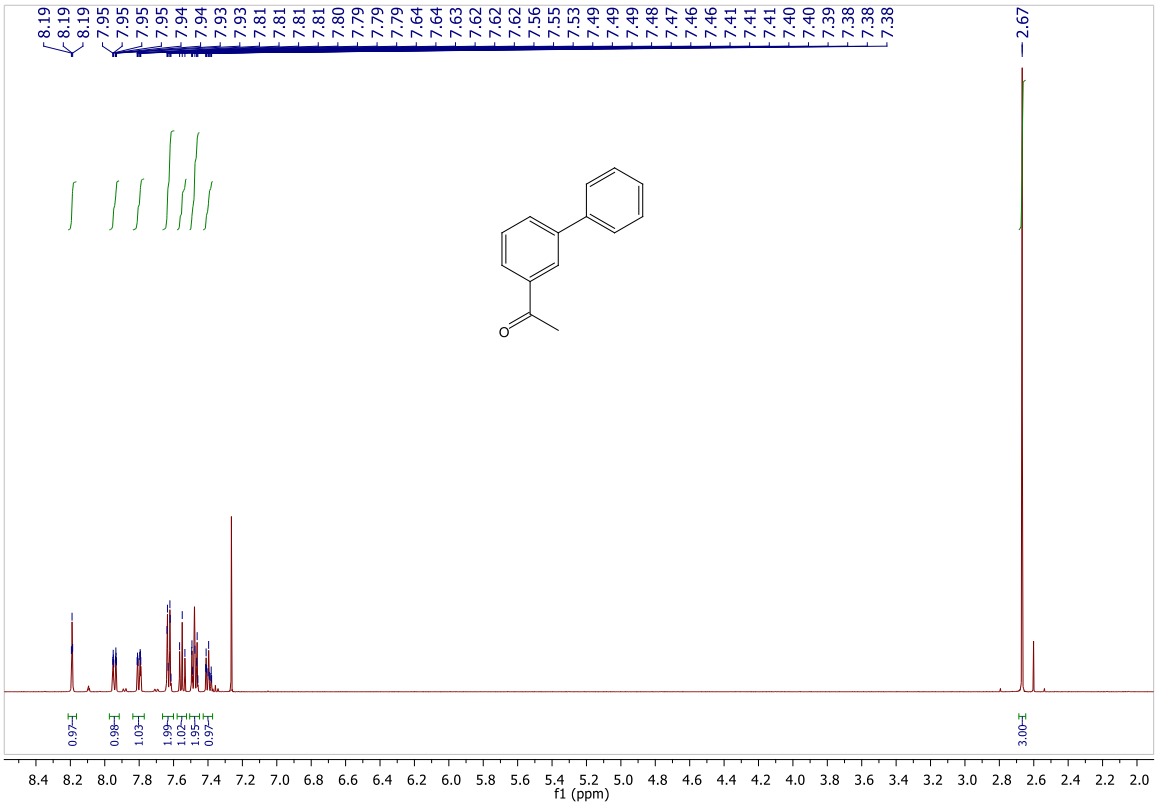

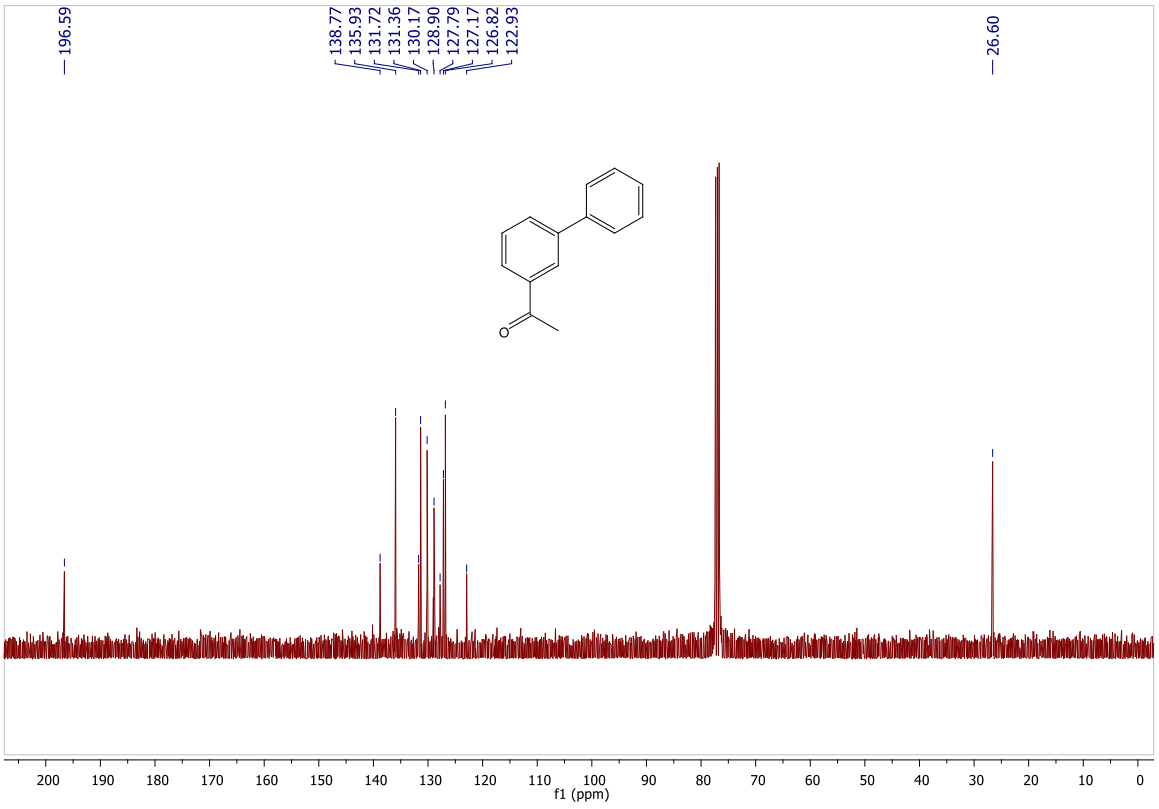

[1,1'-biphenyl]-4-carboxylic acid (3x)

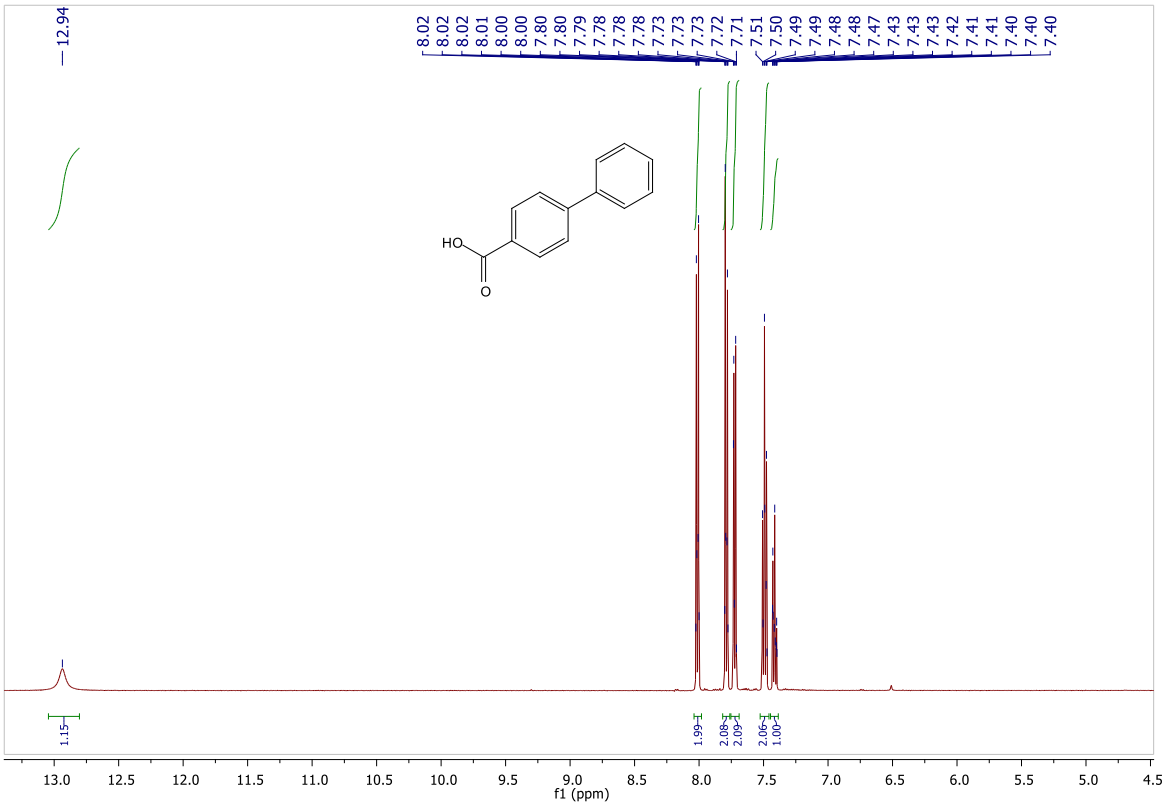

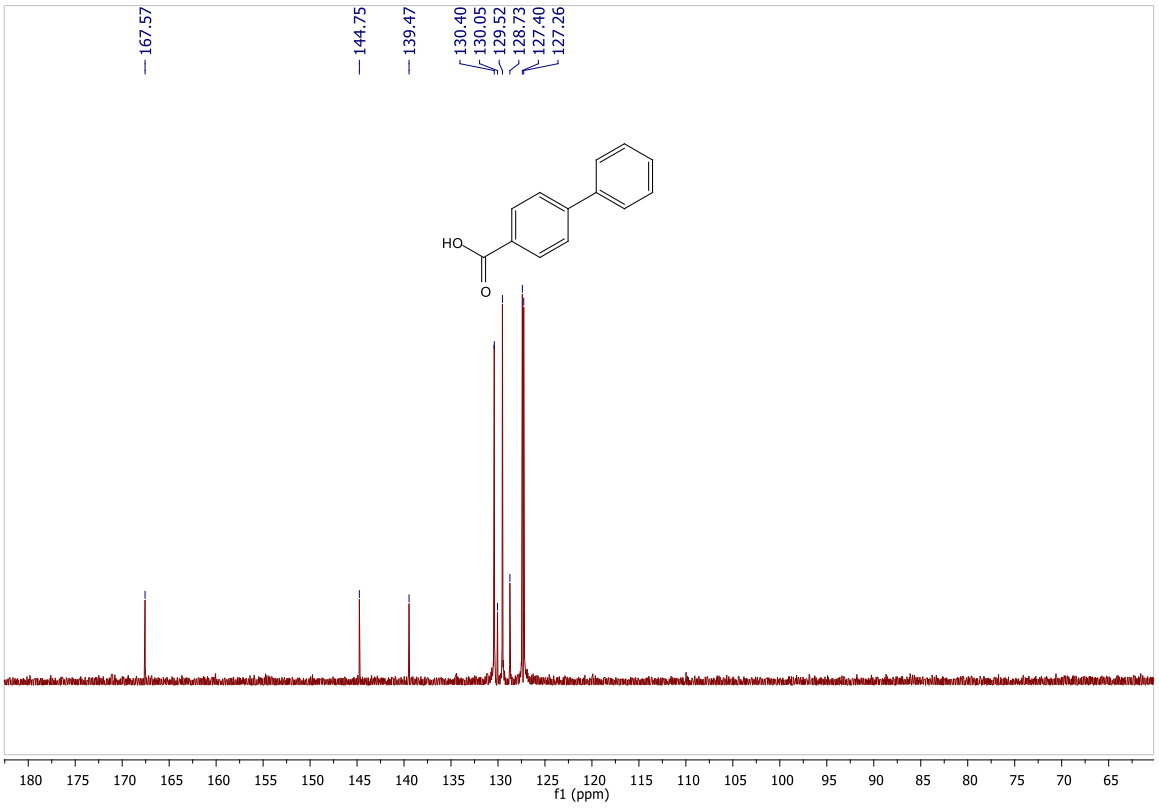

Methyl [1,1'-biphenyl]-4-carboxylate (3y)

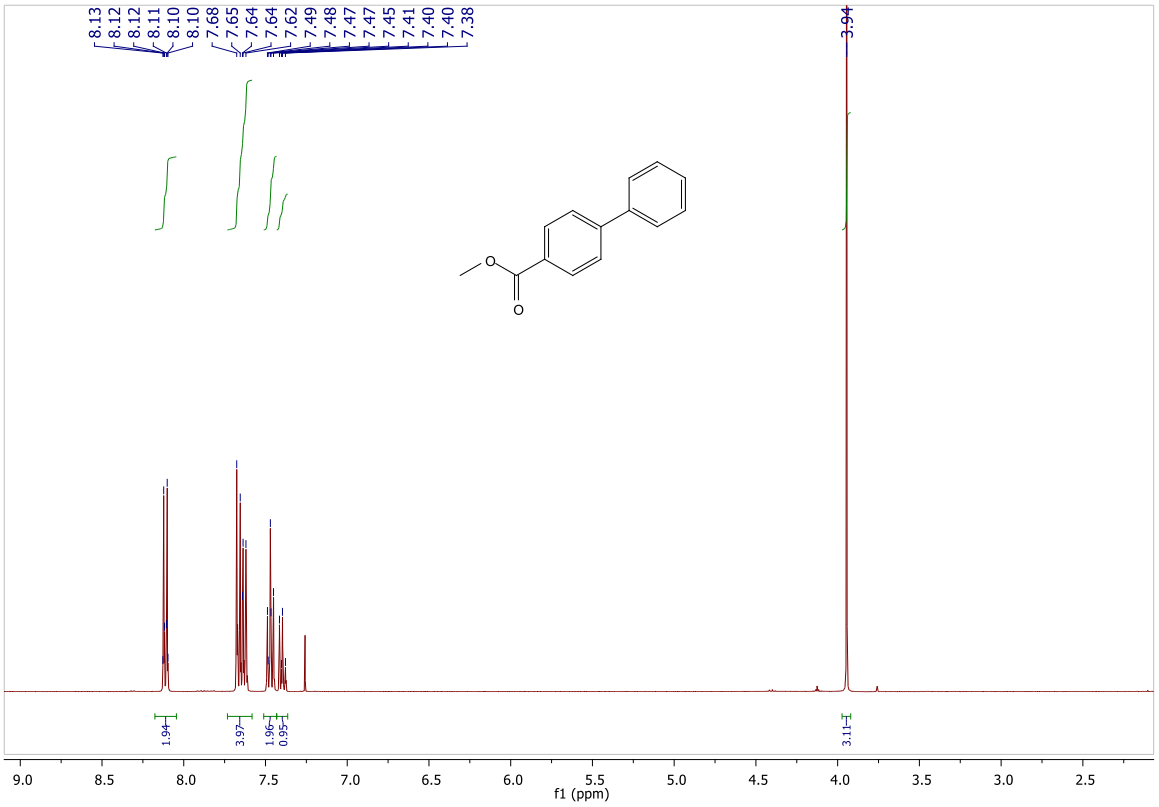

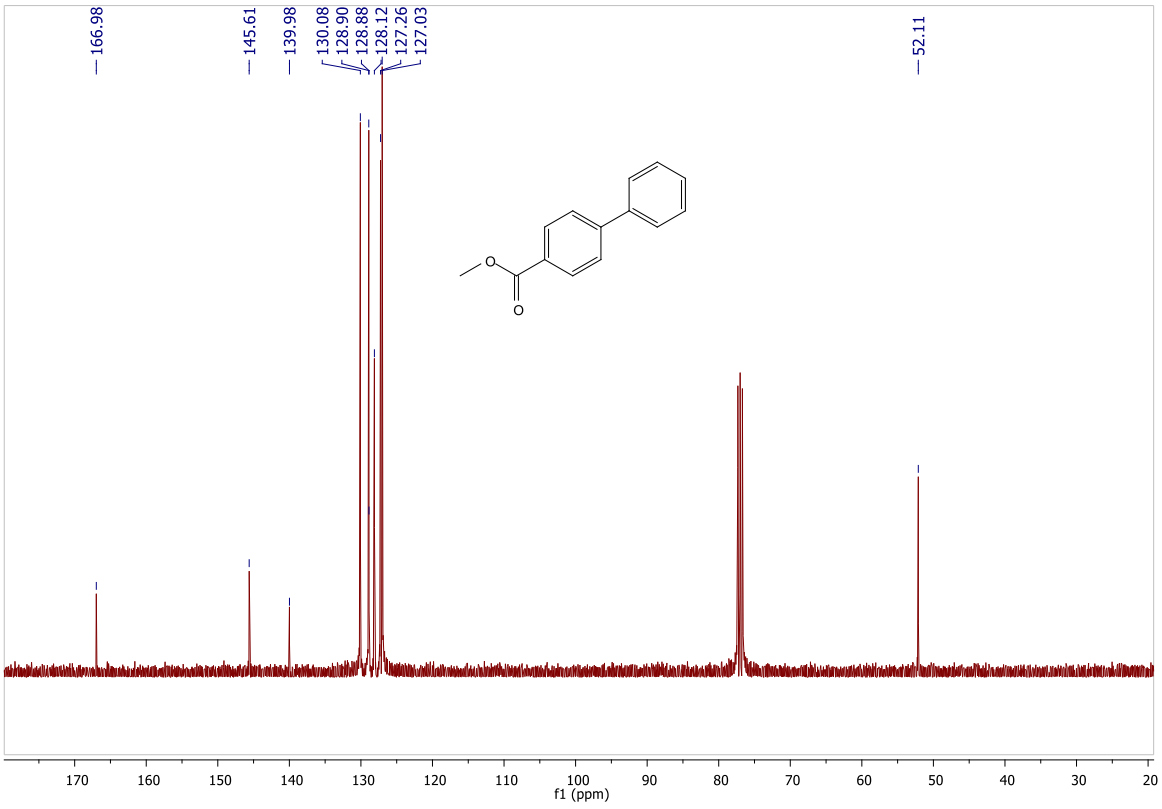

4-fluoro-1,1'-biphenyl (3z)

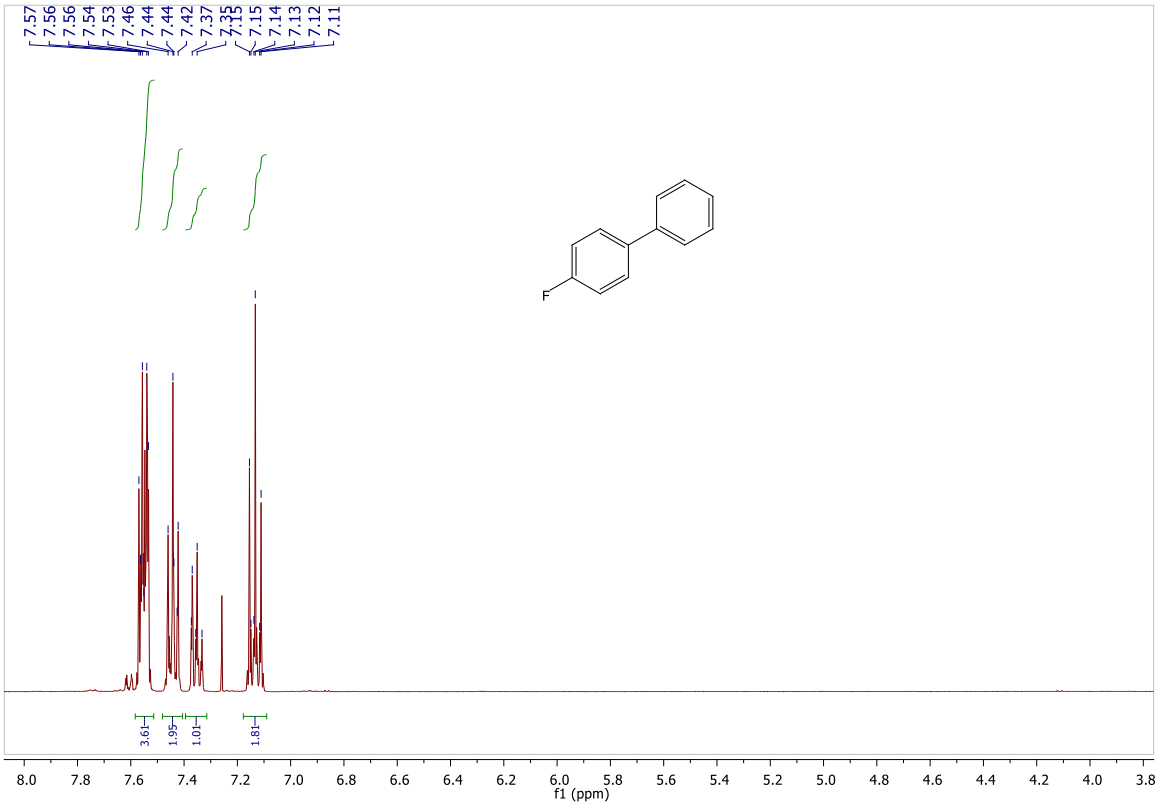

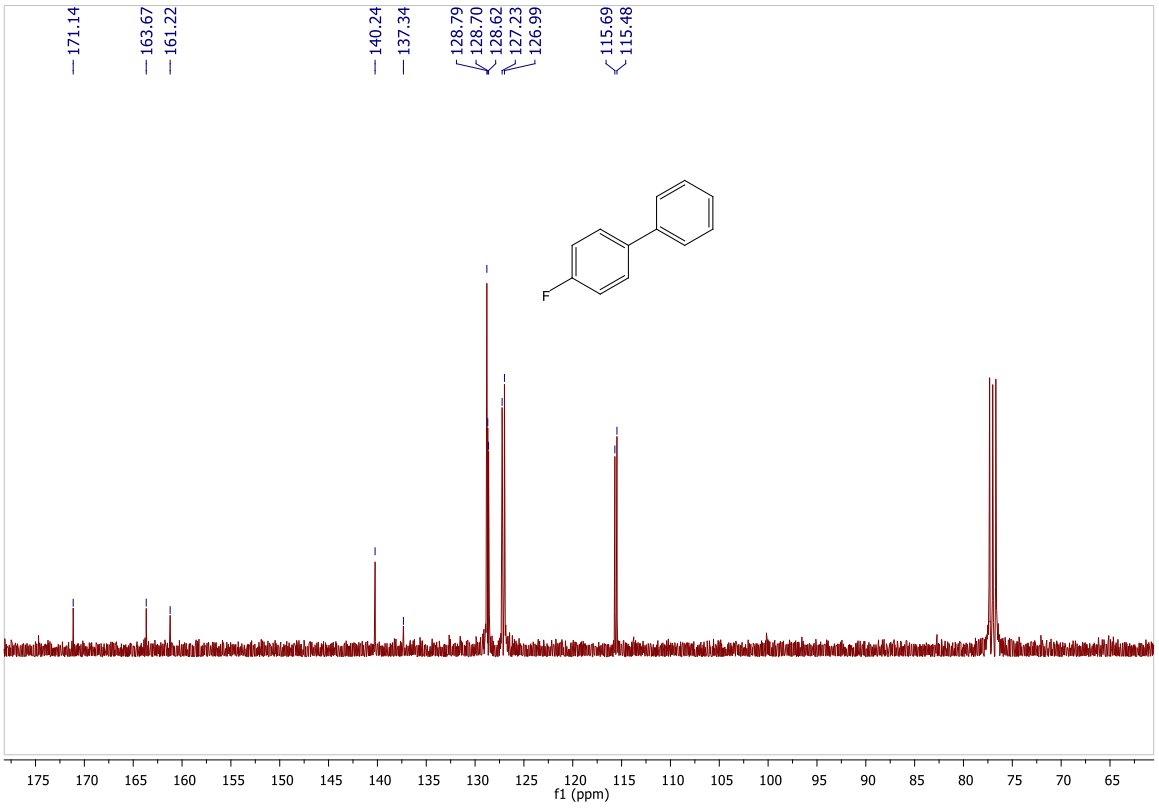

Bibliography

(1) Feynman, R. P. There's Plenty of Room at the Bottom. *Engineering and Science* **1960**, 22–36. https://doi.org/10.1201/9780429500459.

(2) Allen, T. M.; Cullis, P. R. Liposomal Drug Delivery Systems: From Concept to Clinical Applications. *Advanced Drug Delivery Reviews* **2013**, *65* (1), 36–48. https://doi.org/10.1016/j.addr.2012.09.037.

(3) Patra, J. K.; Das, G.; Fraceto, L. F.; Campos, E. V. R.; Rodriguez-Torres, M. D. P.; Acosta-Torres, L. S.; Diaz-Torres, L. A.; Grillo, R.; Swamy, M. K.; Sharma, S.; Habtemariam, S.; Shin, H. S. Nano Based Drug Delivery Systems: Recent Developments and Future Prospects. *Journal of Nanobiotechnology* **2018**, *16* (1), 1–33. https://doi.org/10.1186/s12951-018-0392-8.

(4) Sun, T.; Zhang, Y. S.; Pang, B.; Hyun, D. C.; Yang, M.; Xia, Y. Engineered Nanoparticles for Drug Delivery in Cancer Therapy. *Angewandte Chemie - International Edition* **2014**, *53* (46), 12320–12364. https://doi.org/10.1002/anie.201403036.

(5) Panwar, N.; Soehartono, A. M.; Chan, K. K.; Zeng, S.; Xu, G.; Qu, J.; Coquet, P.; Yong, K. T.; Chen, X. Nanocarbons for Biology and Medicine: Sensing, Imaging, and Drug Delivery. *Chemical Reviews* **2019**, *119* (16), 9559–9656. https://doi.org/10.1021/acs.chemrev.9b00099.

(6) Choi, W.; Choudhary, N.; Han, G. H.; Park, J.; Akinwande, D.; Lee, Y. H. Recent Development of Two-Dimensional Transition Metal Dichalcogenides and Their Applications. *Materials Today* **2017**, *20* (3), 116–130. https://doi.org/10.1016/j.mattod.2016.10.002.

(7) Fan, F. R.; Tang, W.; Wang, Z. L. Flexible Nanogenerators for Energy Harvesting and Self-Powered Electronics. *Advanced Materials* **2016**, *28* (22), 4283–4305. https://doi.org/10.1002/adma.201504299.

(8) Ozbay, E. Plasmonics: Merging Photonics and Electronics at Nanoscale Dimensions. *Science (1979)* **2006**, *311* (5758), 189–193. https://doi.org/10.1126/science.1114849.

(9) Priolo, F.; Gregorkiewicz, T.; Galli, M.; Krauss, T. F. Silicon Nanostructures for Photonics and Photovoltaics. *Nature Nanotechnology* **2014**, *9* (1), 19–32. https://doi.org/10.1038/nnano.2013.271.

(10) Stark, W. J.; Stoessel, P. R.; Wohlleben, W.; Hafner, A. Industrial Applications of Nanoparticles. *Chemical Society Reviews* **2015**, *44* (16), 5793–5805. https://doi.org/10.1039/c4cs00362d.

(11) Serrano, E.; Rus, G.; García-Martínez, J. Nanotechnology for Sustainable Energy. *Renewable and Sustainable Energy Reviews* **2009**, *13* (9), 2373–2384. https://doi.org/10.1016/j.rser.2009.06.003.

(12) Yetisen, A. K.; Qu, H.; Manbachi, A.; Butt, H.; Dokmeci, M. R.; Hinestroza, J. P.; Skorobogatiy, M.; Khademhosseini, A.; Yun, S. H. Nanotechnology in Textiles. *ACS Nano* **2016**, *10* (3), 3042–3068. https://doi.org/10.1021/acsnano.5b08176.

(13) Lee, J.; Mahendra, S.; Alvarez, P. J. J. Nanomaterials in the Construction Industry: A Review of Their Applications and Environmental Health and Safety Considerations. *ACS Nano* **2010**, *4* (7), 3580–3590. https://doi.org/10.1021/nn100866w.

(14) Atalla, M. M.; Kahng, D. A New "Hot Electron" Triode Structure with Semiconductor-Metal Emitter. *IRE Transactions on Electron Devices* **1962**, *9* (6), 507–508. https://doi.org/10.1109/T-ED.1962.15048.

(15) Schmid, G. Metal Clusters - New Perspectives in Future Nanoelectronics. *Current Opinion in Solid State and Materials Science* **1997**, *2* (2), 204–212. https://doi.org/10.1016/S1359-0286(97)80067-8.

(16) Schmid, G. Nanoclusters - Building Blocks for Future Nanoelectronic Devices? *Advanced Engineering Materials* **2001**, *3* (10), 737–743. https://doi.org/10.1002/1527-2648(200110)3:10<737::AID-ADEM737>3.0.CO;2-8.
(17) Choi, Y. H.; Han, H. K. Nanomedicines: Current Status and Future Perspectives in Aspect of Drug Delivery and Pharmacokinetics. *Journal of Pharmaceutical Investigation* **2018**, *48* (1), 43–60. https://doi.org/10.1007/s40005-017-0370-4.
(18) Hare, J. I.; Lammers, T.; Ashford, M. B.; Puri, S.; Storm, G.; Barry, S. T. Challenges and Strategies in Anti-Cancer Nanomedicine Development: An Industry Perspective. *Advanced Drug Delivery Reviews* **2017**, *108*, 25–38. https://doi.org/10.1016/j.addr.2016.04.025.
(19) Ventola, C. L. Progress in Nanomedicine: Approved and Investigational Nanodrugs. *P and T* **2017**, *42* (12), 742–755.
(20) Zhou, Y.; Huang, W.; Liu, J.; Zhu, X.; Yan, D. Self-Assembly of Hyperbranched Polymers and Its Biomedical Applications. *Advanced Materials* **2010**, *22* (41), 4567–4590. https://doi.org/10.1002/adma.201000369.
(21) Calderón, M.; Quadir, M. A.; Sharma, S. K.; Haag, R. Dendritic Polyglycerols for Biomedical Applications. *Advanced Materials* **2010**, *22* (2), 190–218. https://doi.org/10.1002/adma.200902144.
(22) Giljohann, D. A.; Seferos, D. S.; Daniel, W. L.; Massich, M. D.; Patel, P. C.; Mirkin, C. A. Gold Nanoparticles for Biology and Medicine. *Angewandte Chemie - International Edition* **2010**, *49* (19), 3280–3294. https://doi.org/10.1002/anie.200904359.
(23) Kango, S.; Kalia, S.; Celli, A.; Njuguna, J.; Habibi, Y.; Kumar, R. Surface Modification of Inorganic Nanoparticles for Development of Organic-Inorganic Nanocomposites - A Review. *Progress in Polymer Science* **2013**, *38* (8), 1232–1261. https://doi.org/10.1016/j.progpolymsci.2013.02.003.
(24) Bozzuto, G.; Molinari, A. Liposomes as Nanomedical Devices. *International Journal of Nanomedicine* **2015**, *10*, 975–999. https://doi.org/10.2147/IJN.S68861.
(25) Zhang, L.; Chan, J. M.; Gu, F. X.; Rhee, J. W.; Wang, A. Z.; Radovic-Moreno, A. F.; Alexis, F.; Langer, R.; Farokhzad, O. C. Self-Assembled Lipid-Polymer Hybrid Nanoparticles: A Robust Drug Delivery Platform. *ACS Nano* **2008**, *2* (8), 1696–1702. https://doi.org/10.1021/nn800275r.
(26) Al-Jamal, W. T.; Kostarelos, K. Liposomes: From a Clinically Established Drug Delivery System to a Nanoparticle Platform for Theranostic Nanomedicine. *Accounts of Chemical Research* **2011**, *44* (10), 1094–1104. https://doi.org/10.1021/ar200105p.
(27) Huynh, N. T.; Passirani, C.; Saulnier, P.; Benoit, J. P. Lipid Nanocapsules: A New Platform for Nanomedicine. *International Journal of Pharmaceutics* **2009**, *379* (2), 201–209. https://doi.org/10.1016/j.ijpharm.2009.04.026.
(28) Oerlemans, C.; Bult, W.; Bos, M.; Storm, G.; Nijsen, J. F. W.; Hennink, W. E. Polymeric Micelles in Anticancer Therapy: Targeting, Imaging and Triggered Release. *Pharmaceutical Research* **2010**, *27* (12), 2569–2589. https://doi.org/10.1007/s11095-010-0233-4.
(29) Cabral, H.; Miyata, K.; Osada, K.; Kataoka, K. Block Copolymer Micelles in Nanomedicine Applications. *Chemical Reviews* **2018**, *118* (14), 6844–6892. https://doi.org/10.1021/acs.chemrev.8b00199.
(30) Danhier, F.; Ansorena, E.; Silva, J. M.; Coco, R.; le Breton, A.; Préat, V. PLGA-Based Nanoparticles: An Overview of Biomedical Applications. *Journal of Controlled Release* **2012**, *161* (2), 505–522. https://doi.org/10.1016/j.jconrel.2012.01.043.
(31) Prabhu, R. H.; Patravale, V. B.; Joshi, M. D. Polymeric Nanoparticles for Targeted Treatment in Oncology: Current Insights. *International Journal of Nanomedicine* **2015**, *10*, 1001–1018. https://doi.org/10.2147/IJN.S56932.
(32) Dawidczyk, C. M.; Russell, L. M.; Searson, P. C. Nanomedicines for Cancer Therapy: State-of-the-Art and Limitations to Pre-Clinical Studies That Hinder Future Developments. *Frontiers in Chemistry* **2014**, *2* (AUG), 1–13. https://doi.org/10.3389/fchem.2014.00069.

(33) Villena de Francisco, E.; García-Estepa, R. M. Nanotechnology in the Agrofood Industry. *Journal of Food Engineering* **2018**, *238* (May), 1–11. https://doi.org/10.1016/j.jfoodeng.2018.05.024.
(34) Sharma, Y. C.; Srivastava, V.; Singh, V. K.; Kaul, S. N.; Weng, C. H. Nano-Adsorbents for the Removal of Metallic Pollutants from Water and Wastewater. *Environmental Technology* **2009**, *30* (6), 583–609. https://doi.org/10.1080/09593330902838080.
(35) Hua, M.; Zhang, S.; Pan, B.; Zhang, W.; Lv, L.; Zhang, Q. Heavy Metal Removal from Water/Wastewater by Nanosized Metal Oxides: A Review. *Journal of Hazardous Materials* **2012**, *211–212*, 317–331. https://doi.org/10.1016/j.jhazmat.2011.10.016.
(36) Chong, M. N.; Jin, B.; Chow, C. W. K.; Saint, C. Recent Developments in Photocatalytic Water Treatment Technology: A Review. *Water Research* **2010**, *44* (10), 2997–3027. https://doi.org/10.1016/j.watres.2010.02.039.
(37) Lee, K. M.; Lai, C. W.; Ngai, K. S.; Juan, J. C. Recent Developments of Zinc Oxide Based Photocatalyst in Water Treatment Technology: A Review. *Water Research* **2016**, *88*, 428–448. https://doi.org/10.1016/j.watres.2015.09.045.
(38) Smith, S. C.; Rodrigues, D. F. Carbon-Based Nanomaterials for Removal of Chemical and Biological Contaminants from Water: A Review of Mechanisms and Applications. *Carbon N Y* **2015**, *91*, 122–143. https://doi.org/10.1016/j.carbon.2015.04.043.
(39) Nasrollahzadeh, M.; Sajjadi, M.; Iravani, S.; Varma, R. S. Carbon-Based Sustainable Nanomaterials for Water Treatment: State-of-Art and Future Perspectives. *Chemosphere* **2021**, *263*, 128005. https://doi.org/10.1016/j.chemosphere.2020.128005.
(40) Mauter, M. S.; Elimelech, M. Environmental Applications of Carbon-Based Nanomaterials. *Environmental Science & Technology* **2008**, *42* (16), 5843–5859. https://doi.org/10.1021/es8006904.
(41) Yin, J.; Deng, B. Polymer-Matrix Nanocomposite Membranes for Water Treatment. *Journal of Membrane Science* **2015**, *479*, 256–275. https://doi.org/10.1016/j.memsci.2014.11.019.
(42) Barrejón, M.; Prato, M. Carbon Nanotube Membranes in Water Treatment Applications. *Advanced Materials Interfaces* **2022**, *9* (1). https://doi.org/10.1002/admi.202101260.
(43) Jat, S. K.; Bhattacharya, J.; Sharma, M. K. Nanomaterial Based Gene Delivery: A Promising Method for Plant Genome Engineering. *Journal of Materials Chemistry B* **2020**, *8* (19), 4165–4175. https://doi.org/10.1039/d0tb00217h.
(44) Sanzari, I.; Leone, A.; Ambrosone, A. Nanotechnology in Plant Science: To Make a Long Story Short. *Frontiers in Bioengineering and Biotechnology* **2019**, *7* (May), 1–12. https://doi.org/10.3389/fbioe.2019.00120.
(45) Lau, H. Y.; Wu, H.; Wee, E. J. H.; Trau, M.; Wang, Y.; Botella, J. R. Specific and Sensitive Isothermal Electrochemical Biosensor for Plant Pathogen DNA Detection with Colloidal Gold Nanoparticles as Probes. *Scientific Reports* **2017**, *7* (October 2016), 1–7. https://doi.org/10.1038/srep38896.
(46) Serik, O.; Ainur, I.; Murat, K.; Tetsuo, M.; Masaki, I. Silicon Carbide Fiber-Mediated DNA Delivery into Cells of Wheat (Triticum Aestivum L.) Mature Embryos. *Plant Cell Reports* **1996**, *16* (3–4), 133–136. https://doi.org/10.1007/BF01890853.
(47) Zhao, X.; Meng, Z.; Wang, Y.; Chen, W.; Sun, C.; Cui, B.; Cui, J.; Yu, M.; Zeng, Z.; Guo, S.; Luo, D.; Cheng, J. Q.; Zhang, R.; Cui, H. Pollen Magnetofection for Genetic Modification with Magnetic Nanoparticles as Gene Carriers. *Nature Plants* **2017**, *3* (12), 956–964. https://doi.org/10.1038/s41477-017-0063-z.
(48) Demirer, G. S.; Zhang, H.; Matos, J. L.; Goh, N. S.; Cunningham, F. J.; Sung, Y.; Chang, R.; Aditham, A. J.; Chio, L.; Cho, M. J.; Staskawicz, B.; Landry, M. P. High Aspect Ratio Nanomaterials Enable Delivery of Functional Genetic Material without DNA Integration in Mature Plants. *Nature Nanotechnology* **2019**, *14* (5), 456–464. https://doi.org/10.1038/s41565-019-0382-5.

(49) Wang, Q.; Chen, J.; Zhang, H.; Lu, M.; Qiu, D.; Wen, Y.; Kong, Q. Synthesis of Water Soluble Quantum Dots for Monitoring Carrier-DNA Nanoparticles in Plant Cells. *Journal of Nanoscience and Nanotechnology* **2011**, *11* (3), 2208–2214. https://doi.org/10.1166/jnn.2011.3560.
(50) Diaz, R. J.; Rosenberg, R. Spreading Dead Zones and Consequences for Marine Ecosystems. *Science (1979)* **2008**, *321* (5891), 926–929. https://doi.org/10.1126/science.1156401.
(51) Kottegoda, N.; Sandaruwan, C.; Priyadarshana, G.; Siriwardhana, A.; Rathnayake, U. A.; Berugoda Arachchige, D. M.; Kumarasinghe, A. R.; Dahanayake, D.; Karunaratne, V.; Amaratunga, G. A. J. Urea-Hydroxyapatite Nanohybrids for Slow Release of Nitrogen. *ACS Nano* **2017**, *11* (2), 1214–1221. https://doi.org/10.1021/acsnano.6b07781.
(52) Marcińczyk, M.; Oleszczuk, P. Biochar and Engineered Biochar as Slow- and Controlled-Release Fertilizers. *Journal of Cleaner Production* **2022**, *339* (September 2021). https://doi.org/10.1016/j.jclepro.2022.130685.
(53) Duhan, J. S.; Kumar, R.; Kumar, N.; Kaur, P.; Nehra, K.; Duhan, S. Nanotechnology: The New Perspective in Precision Agriculture. *Biotechnology Reports* **2017**, *15* (December 2016), 11–23. https://doi.org/10.1016/j.btre.2017.03.002.
(54) Aktar, W.; Sengupta, D.; Chowdhury, A. Impact of Pesticides Use in Agriculture: Their Benefits and Hazards. *Interdisciplinary Toxicology* **2009**, *2* (1), 1–12. https://doi.org/10.2478/v10102-009-0001-7.
(55) Geiger, F.; Bengtsson, J.; Berendse, F.; Weisser, W. W.; Emmerson, M.; Morales, M. B.; Ceryngier, P.; Liira, J.; Tscharntke, T.; Winqvist, C.; Eggers, S.; Bommarco, R.; Pärt, T.; Bretagnolle, V.; Plantegenest, M.; Clement, L. W.; Dennis, C.; Palmer, C.; Oñate, J. J.; Guerrero, I.; Hawro, V.; Aavik, T.; Thies, C.; Flohre, A.; Hänke, S.; Fischer, C.; Goedhart, P. W.; Inchausti, P. Persistent Negative Effects of Pesticides on Biodiversity and Biological Control Potential on European Farmland. *Basic and Applied Ecology* **2010**, *11* (2), 97–105. https://doi.org/10.1016/j.baae.2009.12.001.
(56) van Bruggen, A. H. C.; He, M. M.; Shin, K.; Mai, V.; Jeong, K. C.; Finckh, M. R.; Morris, J. G. Environmental and Health Effects of the Herbicide Glyphosate. *Science of the Total Environment* **2018**, *616–617*, 255–268. https://doi.org/10.1016/j.scitotenv.2017.10.309.
(57) Kah, M.; Kookana, R. S.; Gogos, A.; Bucheli, T. D. A Critical Evaluation of Nanopesticides and Nanofertilizers against Their Conventional Analogues. *Nature Nanotechnology* **2018**, *13* (8), 677–684. https://doi.org/10.1038/s41565-018-0131-1.
(58) Graham, J. H.; Johnson, E. G.; Myers, M. E.; Young, M.; Rajasekaran, P.; Das, S.; Santra, S. Potential of Nano-Formulated Zinc Oxide for Control of Citrus Canker on Grapefruit Trees. *Plant Disease* **2016**, *100* (12), 2442–2447. https://doi.org/10.1094/PDIS-05-16-0598-RE.
(59) Liang, J.; Yu, M.; Guo, L.; Cui, B.; Zhao, X.; Sun, C.; Wang, Y.; Liu, G.; Cui, H.; Zeng, Z. Bioinspired Development of P(St-MAA)-Avermectin Nanoparticles with High Affinity for Foliage to Enhance Folia Retention. *Journal of Agricultural and Food Chemistry* **2018**, *66* (26), 6578–6584. https://doi.org/10.1021/acs.jafc.7b01998.
(60) Petosa, A. R.; Rajput, F.; Selvam, O.; Öhl, C.; Tufenkji, N. Assessing the Transport Potential of Polymeric Nanocapsules Developed for Crop Protection. *Water Research* **2017**, *111*, 10–17. https://doi.org/10.1016/j.watres.2016.12.030.
(61) Li, Z.-Z.; Chen, J.-F.; Liu, F.; Liu, A.-Q.; Wang, Q.; Sun, H.-Y.; Wen, L.-X. Study of UV-Shielding Properties of Novel Porous Hollow Silica Nanoparticle Carriers for Avermectin. *Pest Management Science* **2007**, *63* (3), 241–246. https://doi.org/10.1002/ps.1301.
(62) Song, S.; Liu, X.; Jiang, J.; Qian, Y.; Zhang, N.; Wu, Q. Stability of Triazophos in Self-Nanoemulsifying Pesticide Delivery System. *Colloids and Surfaces A: Physicochemical and Engineering Aspects* **2009**, *350* (1–3), 57–62. https://doi.org/10.1016/j.colsurfa.2009.08.034.
(63) Kah, M.; Machinski, P.; Koerner, P.; Tiede, K.; Grillo, R.; Fraceto, L. F.; Hofmann, T. Analysing the Fate of Nanopesticides in Soil and the Applicability of Regulatory Protocols

Using a Polymer-Based Nanoformulation of Atrazine. *Environmental Science and Pollution Research* **2014**, *21* (20), 11699–11707. https://doi.org/10.1007/s11356-014-2523-6.
(64) Torabian, S.; Zahedi, M.; Khoshgoftar, A. H. Effects of Foliar Spray of Nano-Particles of FeSO4 on the Growth and Ion Content of Sunflower under Saline Condition. *Journal of Plant Nutrition* **2017**, *40* (5), 615–623. https://doi.org/10.1080/01904167.2016.1240187.
(65) Shalaby, T. A.; Bayoumi, Y.; Abdalla, N.; Taha, H.; Alshaal, T.; Shehata, S.; Amer, M.; Domokos-Szabolcsy, É.; El-Ramady, H. Nanoparticles, Soils, Plants and Sustainable Agriculture. **2016**, 283–312. https://doi.org/10.1007/978-3-319-39303-2_10.
(66) Lu, L.; Huang, M.; Huang, Y.; Corvini, P. F. X.; Ji, R.; Zhao, L. Mn3O4 Nanozymes Boost Endogenous Antioxidant Metabolites in Cucumber (Cucumis Sativus) Plant and Enhance Resistance to Salinity Stress. *Environmental Science: Nano* **2020**, *7* (6), 1692–1703. https://doi.org/10.1039/d0en00214c.
(67) Chaudhry, Q.; Scotter, M.; Blackburn, J.; Ross, B.; Boxall, A.; Castle, L.; Aitken, R.; Watkins, R. Applications and Implications of Nanotechnologies for the Food Sector. *Food Additives and Contaminants - Part A Chemistry, Analysis, Control, Exposure and Risk Assessment* **2008**, *25* (3), 241–258. https://doi.org/10.1080/02652030701744538.
(68) Dasgupta, N.; Ranjan, S.; Mundekkad, D.; Ramalingam, C.; Shanker, R.; Kumar, A. Nanotechnology in Agro-Food: From Field to Plate. *Food Research International* **2015**, *69*, 381–400. https://doi.org/10.1016/j.foodres.2015.01.005.
(69) Wang, H.; Qian, J.; Ding, F. Emerging Chitosan-Based Films for Food Packaging Applications. *Journal of Agricultural and Food Chemistry* **2018**, *66* (2), 395–413. https://doi.org/10.1021/acs.jafc.7b04528.
(70) Azeredo, H. M. C.; Rosa, M. F.; Mattoso, L. H. C. Nanocellulose in Bio-Based Food Packaging Applications. *Industrial Crops and Products* **2017**, *97*, 664–671. https://doi.org/10.1016/j.indcrop.2016.03.013.
(71) Zubair, M.; Ullah, A. Recent Advances in Protein Derived Bionanocomposites for Food Packaging Applications. *Critical Reviews in Food Science and Nutrition* **2020**, *60* (3), 406–434. https://doi.org/10.1080/10408398.2018.1534800.
(72) de Azeredo, H. M. C. Antimicrobial Nanostructures in Food Packaging. *Trends in Food Science and Technology* **2013**, *30* (1), 56–69. https://doi.org/10.1016/j.tifs.2012.11.006.
(73) Li, X.; Li, W.; Jiang, Y.; Ding, Y.; Yun, J.; Tang, Y.; Zhang, P. Effect of Nano-ZnO-Coated Active Packaging on Quality of Fresh-Cut "Fuji" Apple. *International Journal of Food Science and Technology* **2011**, *46* (9), 1947–1955. https://doi.org/10.1111/j.1365-2621.2011.02706.x.
(74) Dobrucka, R.; Ankiel, M. Possible Applications of Metal Nanoparticles in Antimicrobial Food Packaging. *Journal of Food Safety* **2019**, *39* (2), 1–7. https://doi.org/10.1111/jfs.12617.
(75) Song, K. *Micro- and Nano-Fillers Used in the Rubber Industry*; Elsevier Ltd, 2017. https://doi.org/10.1016/B978-0-08-100409-8.00002-4.
(76) Hardman, N. J. The New Carbon Black and Its Role in the United States Manufacturing Renaissance. *Reinforced Plastics* **2017**, *61* (3), 145–148. https://doi.org/10.1016/j.repl.2017.02.002.
(77) Serpone, N.; Dondi, D.; Albini, A. Inorganic and Organic UV Filters: Their Role and Efficacy in Sunscreens and Suncare Products. *Inorganica Chimica Acta* **2007**, *360* (3), 794–802. https://doi.org/10.1016/j.ica.2005.12.057.
(78) Nussbaumer, R. J.; Caseri, W. R.; Smith, P.; Tervoort, T. Polymer-TiO2 Nanocomposites: A Route towards Visually Transparent Broadband UV Filters and High Refractive Index Materials. *Macromolecular Materials and Engineering* **2003**, *288* (1), 44–49. https://doi.org/10.1002/mame.200290032.
(79) T. D. Manning, G. R. Hurst, G. R. Nichol, M. W. and G. B. G. WO2013014423 A1. *PCT Int. Pat.* **2011**.

(80) Go, M. R.; Bae, S. H.; Kim, H. J.; Yu, J.; Choi, S. J. Interactions between Food Additive Silica Nanoparticles and Food Matrices. *Frontiers in Microbiology* **2017**, *8* (JUN), 1–12. https://doi.org/10.3389/fmicb.2017.01013.
(81) Védrine, J. C. Heterogeneous Catalysis on Metal Oxides. *Catalysts* **2017**, *7* (11). https://doi.org/10.3390/catal7110341.
(82) Burke, M. S.; Enman, L. J.; Batchellor, A. S.; Zou, S.; Boettcher, S. W. Oxygen Evolution Reaction Electrocatalysis on Transition Metal Oxides and (Oxy)Hydroxides: Activity Trends and Design Principles. *Chemistry of Materials* **2015**, *27* (22), 7549–7558. https://doi.org/10.1021/acs.chemmater.5b03148.
(83) Chaturvedi, S.; Dave, P. N.; Shah, N. K. Applications of Nano-Catalyst in New Era. *Journal of Saudi Chemical Society* **2012**, *16* (3), 307–325. https://doi.org/10.1016/j.jscs.2011.01.015.
(84) Schmal, M. *Heterogeneous Catalysis and Its Industrial Applications*; 2016. https://doi.org/10.1007/978-3-319-09250-8.
(85) Kwon H. M., Yun H. W., Kang S. C., Kim I. J., G. S. S. EP 1 609 826 A3. *European Patent Office* **2005**.
(86) Cao, J. J.; Huang, Y.; Zhang, Q. Ambient Air Purification by Nanotechnologies: From Theory to Application. *Catalysts* **2021**, *11* (11), 1–41. https://doi.org/10.3390/catal11111276.
(87) Lahtinen, E.; Kukkonen, E.; Kinnunen, V.; Lahtinen, M.; Kinnunen, K.; Suvanto, S.; Vaïsänen, A.; Haukka, M. Gold Nanoparticles on 3D-Printed Filters: From Waste to Catalysts. *ACS Omega* **2019**, *4* (16), 16891–16898. https://doi.org/10.1021/acsomega.9b02113.
(88) Sinha, A. K.; Suzuki, K.; Takahara, M.; Azuma, H.; Nonaka, T.; Fukumoto, K. Mesostructured Manganese Oxide/Gold Nanoparticle Composites for Extensive Air Purification. *Angewandte Chemie - International Edition* **2007**, *46* (16), 2891–2894. https://doi.org/10.1002/anie.200605048.
(89) Haruta, M. Size- and Support-Dependency in the Catalysis of Gold. *Catalysis Today* **1997**, *36* (1), 153–166. https://doi.org/10.1016/S0920-5861(96)00208-8.
(90) Valden, M.; Lai, X.; Goodman, D. W. Onset of Catalytic Activity of Gold Clusters on Titania with the Appearance of Nonmetallic Properties. *Science (1979)* **1998**, *281* (5383), 1647–1650. https://doi.org/10.1126/science.281.5383.1647.
(91) Campbell, C. T.; Parker, S. C.; Starr, D. E. The Effect of Size-Dependent Nanoparticle Energetics on Catalyst Sintering. *Science (1979)* **2002**, *298* (5594), 811–814. https://doi.org/10.1126/science.1075094.
(92) Shi, A. C.; Masel, R. I. The Effects of Gas Adsorption on Particle Shapes in Supported Platinum Catalysts. *Journal of Catalysis* **1989**, *120* (2), 421–431. https://doi.org/10.1016/0021-9517(89)90282-0.
(93) Narayanan, R.; El-Sayed, M. A. Catalysis with Transition Metal Nanoparticles in Colloidal Solution: Nanoparticle Shape Dependence and Stability. *The Journal of Physical Chemistry B* **2005**, *109* (26), 12663–12676. https://doi.org/10.1021/jp051066p.
(94) Falicov, L. M.; Somorjai, G. A. Correlation between Catalytic Activity and Bonding and Coordination Number of Atoms and Molecules on Transition Metal Surfaces: Theory and Experimental Evidence. *Proceedings of the National Academy of Sciences* **1985**, *82* (8), 2207–2211. https://doi.org/10.1073/pnas.82.8.2207.
(95) Bratlie, K. M.; Lee, H.; Komvopoulos, K.; Yang, P.; Somorjai, G. A. Platinum Nanoparticle Shape Effects on Benzene Hydrogenation Selectivity. *Nano Letters* **2007**, *7* (10), 3097–3101. https://doi.org/10.1021/nl0716000.
(96) Lyu, H.; Gao, B.; He, F.; Ding, C.; Tang, J.; Crittenden, J. C. Ball-Milled Carbon Nanomaterials for Energy and Environmental Applications. *ACS Sustainable Chemistry and Engineering* **2017**, *5* (11), 9568–9585. https://doi.org/10.1021/acssuschemeng.7b02170.
(97) Zhuang, S.; Lee, E. S.; Lei, L.; Nunna, B. B.; Kuang, L.; Zhang, W. Synthesis of Nitrogen-Doped Graphene Catalyst by High-Energy Wet Ball Milling for Electrochemical Systems.

International Journal of Energy Research **2016**, *40* (15), 2136–2149. https://doi.org/10.1002/er.3595.
(98) Matsumoto, R.; Adachi, S.; Sadki, E. H. S.; Yamamoto, S.; Tanaka, H.; Takeya, H.; Takano, Y. Maskless Patterning of Gallium-Irradiated Superconducting Silicon Using Focused Ion Beam. *ACS Applied Electronic Materials* **2020**, *2* (3), 677–682. https://doi.org/10.1021/acsaelm.9b00781.
(99) Xu, K.; Chen, J. High-Resolution Scanning Probe Lithography Technology: A Review. *Applied Nanoscience (Switzerland)* **2020**, *10* (4), 1013–1022. https://doi.org/10.1007/s13204-019-01229-5.
(100) Kuo, C. W.; Shiu, J. Y.; Cho, Y. H.; Chen, P. Fabrication of Large-Area Periodic Nanopillar Arrays for Nanoimprint Lithography Using Polymer Colloid Masks. *Advanced Materials* **2003**, *15* (13), 1065–1068. https://doi.org/10.1002/adma.200304824.
(101) Szabó, Z.; Volk, J.; Fülöp, E.; Deák, A.; Bársony, I. Regular ZnO Nanopillar Arrays by Nanosphere Photolithography. *Photonics and Nanostructures - Fundamentals and Applications* **2013**, *11* (1), 1–7. https://doi.org/10.1016/j.photonics.2012.06.009.
(102) Nam, J. H.; Jang, M. J.; Jang, H. Y.; Park, W.; Wang, X.; Choi, S. M.; Cho, B. Room-Temperature Sputtered Electrocatalyst WSe2 Nanomaterials for Hydrogen Evolution Reaction. *Journal of Energy Chemistry* **2020**, *47*, 107–111. https://doi.org/10.1016/j.jechem.2019.11.027.
(103) Wender, H.; Migowski, P.; Feil, A. F.; Teixeira, S. R.; Dupont, J. Sputtering Deposition of Nanoparticles onto Liquid Substrates: Recent Advances and Future Trends. *Coordination Chemistry Reviews* **2013**, *257* (17–18), 2468–2483. https://doi.org/10.1016/j.ccr.2013.01.013.
(104) Kumar, P. S.; Sundaramurthy, J.; Sundarrajan, S.; Babu, V. J.; Singh, G.; Allakhverdiev, S. I.; Ramakrishna, S. Hierarchical Electrospun Nanofibers for Energy Harvesting, Production and Environmental Remediation. *Energy Environ. Sci.* **2014**, *7* (10), 3192–3222. https://doi.org/10.1039/C4EE00612G.
(105) Duque, J. S.; Madrigal, B. M.; Riascos, H.; Avila, Y. P. Colloidal Metal Oxide Nanoparticles Prepared by Laser Ablation Technique and Their Antibacterial Test. *Colloids and Interfaces* **2019**, *3* (1). https://doi.org/10.3390/colloids3010025.
(106) Park, H.; Reddy, D. A.; Kim, Y.; Lee, S.; Ma, R.; Kim, T. K. Synthesis of Ultra-Small Palladium Nanoparticles Deposited on CdS Nanorods by Pulsed Laser Ablation in Liquid: Role of Metal Nanocrystal Size in the Photocatalytic Hydrogen Production. *Chemistry - A European Journal* **2017**, *23* (53), 13112–13119. https://doi.org/10.1002/chem.201702304.
(107) Zheng, J.; Yang, R.; Xie, L.; Jianglan, Q.; Yang, L.; Xingguo, L. Plasma-Assisted Approaches in Inorganic Nanostructure Fabrication. *Advanced Materials* **2010**, *22* (13), 1451–1473. https://doi.org/10.1002/adma.200903147.
(108) Okumura, M.; Nakamura, S.; Tsubota, S.; Toshiko, N.; Azuma, M.; Haruta, M. Chemical Vapor Deposition of Gold on Al_2O_3,SiO_2,and TiO_2 for the Oxidation of CO and of H_2. *Catalysis Letters* **1998**, *51* (1–2), 53–58.
(109) Fukui, T.; Ando, S.; Tokura, Y.; Toriyama, T. GaAs Tetrahedral Quantum Dot Structures Fabricated Using Selective Area Metalorganic Chemical Vapor Deposition. *Applied Physics Letters* **1991**, *58* (18), 2018–2020. https://doi.org/10.1063/1.105026.
(110) Mohanty, U. S. Electrodeposition: A Versatile and Inexpensive Tool for the Synthesis of Nanoparticles, Nanorods, Nanowires, and Nanoclusters of Metals. *Journal of Applied Electrochemistry* **2011**, *41* (3), 257–270. https://doi.org/10.1007/s10800-010-0234-3.
(111) D'Amato, R.; Falconieri, M.; Gagliardi, S.; Popovici, E.; Serra, E.; Terranova, G.; Borsella, E. Synthesis of Ceramic Nanoparticles by Laser Pyrolysis: From Research to Applications. *Journal of Analytical and Applied Pyrolysis* **2013**, *104*, 461–469. https://doi.org/10.1016/j.jaap.2013.05.026.

(112) Wallace, R.; Brown, A. P.; Brydson, R.; Wegner, K.; Milne, S. J. Synthesis of ZnO Nanoparticles by Flame Spray Pyrolysis and Characterisation Protocol. *Journal of Materials Science* **2013**, *48* (18), 6393–6403. https://doi.org/10.1007/s10853-013-7439-x.
(113) Xia, Y.; Xia, X.; Peng, H. C. Shape-Controlled Synthesis of Colloidal Metal Nanocrystals: Thermodynamic versus Kinetic Products. *J Am Chem Soc* **2015**, *137* (25), 7947–7966. https://doi.org/10.1021/jacs.5b04641.
(114) Sau, T. K.; Rogach, A. L.; Jäckel, F.; Klar, T. A.; Feldmann, J. Properties and Applications of Colloidal Nonspherical Noble Metal Nanoparticles. *Advanced Materials* **2010**, *22* (16), 1805–1825. https://doi.org/10.1002/adma.200902557.
(115) Boles, M. A.; Engel, M.; Talapin, D. v. Self-Assembly of Colloidal Nanocrystals: From Intricate Structures to Functional Materials. *Chemical Reviews* **2016**, *116* (18), 11220–11289. https://doi.org/10.1021/acs.chemrev.6b00196.
(116) Shi, Y.; Lyu, Z.; Zhao, M.; Chen, R.; Nguyen, Q. N.; Xia, Y. Noble-Metal Nanocrystals with Controlled Shapes for Catalytic and Electrocatalytic Applications. *Chemical Reviews* **2021**, *121* (2), 649–735. https://doi.org/10.1021/acs.chemrev.0c00454.
(117) Xia, Y.; Xiong, Y.; Lim, B.; Skrabalak, S. E. Shape-Controlled Synthesis of Metal Nanocrystals: Simple Chemistry Meets Complex Physics? *Angewandte Chemie - International Edition* **2009**, *48* (1), 60–103. https://doi.org/10.1002/anie.200802248.
(118) LaMer, V. K.; Dinegar, R. H. Theory, Production and Mechanism of Formation of Monodispersed Hydrosols. *J Am Chem Soc* **1950**, *72* (11), 4847–4854. https://doi.org/10.1021/ja01167a001.
(119) Vekilov, P. G. The Two-Step Mechanism of Nucleation of Crystals in Solution. *Nanoscale* **2010**, *2* (11), 2346–2357. https://doi.org/10.1039/c0nr00628a.
(120) Loh, N. D.; Sen, S.; Bosman, M.; Tan, S. F.; Zhong, J.; Nijhuis, C. A.; Král, P.; Matsudaira, P.; Mirsaidov, U. Multistep Nucleation of Nanocrystals in Aqueous Solution. *Nature Chemistry* **2017**, *9* (1), 77–82. https://doi.org/10.1038/nchem.2618.
(121) Yao, T.; Sun, Z.; Li, Y.; Pan, Z.; Wei, H.; Xie, Y.; Nomura, M.; Niwa, Y.; Yan, W.; Wu, Z.; Jiang, Y.; Liu, Q.; Wei, S. Insights into Initial Kinetic Nucleation of Gold Nanocrystals. *J Am Chem Soc* **2010**, *132* (22), 7696–7701. https://doi.org/10.1021/ja101101d.
(122) Barnard, A. S.; Young, N. P.; Kirkland, A. I.; van Huis, M. A.; Xu, H. Nanogold: A Quantitative Phase Map. *ACS Nano* **2009**, *3* (6), 1431–1436. https://doi.org/10.1021/nn900220k.
(123) Wang, Y.; Peng, H. C.; Liu, J.; Huang, C. Z.; Xia, Y. Use of Reduction Rate as a Quantitative Knob for Controlling the Twin Structure and Shape of Palladium Nanocrystals. *Nano Letters* **2015**, *15* (2), 1445–1450. https://doi.org/10.1021/acs.nanolett.5b00158.
(124) Wiley, B.; Herricks, T.; Sun, Y.; Xia, Y. Polyol Synthesis of Silver Nanoparticles: Use of Chloride and Oxygen to Promote the Formation of Single-Crystal, Truncated Cubes and Tetrahedrons. *Nano Letters* **2004**, *4* (9), 1733–1739. https://doi.org/10.1021/nl048912c.
(125) Smith, D. K.; Korgel, B. A. The Importance of the CTAB Surfactant on the Colloidal Seed-Mediated Synthesis of Gold Nanorods. *Langmuir* **2008**, *24* (3), 644–649. https://doi.org/10.1021/la703625a.
(126) Song, H.; Kim, F.; Connor, S.; Somorjai, G. A.; Yang, P. Pt Nanocrystals: Shape Control and Langmuir-Blodgett Monolayer Formation. *Journal of Physical Chemistry B* **2005**, *109* (1), 188–193. https://doi.org/10.1021/jp0464775.
(127) Skrabalak, S. E.; Au, L.; Li, X.; Xia, Y. Facile Synthesis of Ag Nanocubes and Au Nanocages. *Nature Protocols* **2007**, *2* (9), 2182–2190. https://doi.org/10.1038/nprot.2007.326.
(128) Aherne, D.; Ledwith, D. M.; Gara, M.; Kelly, J. M. Optical Properties and Growth Aspects of Silver Nanoprisms Produced by a Highly Reproducible and Rapid Synthesis at Room Temperature. *Advanced Functional Materials* **2008**, *18* (14), 2005–2016. https://doi.org/10.1002/adfm.200800233.

(129) Sau, T. K.; Murphy, C. J. Role of Ions in the Colloidal Synthesis of Gold Nanowires. *Philosophical Magazine* **2007**, *87* (14–15), 2143–2158. https://doi.org/10.1080/14786430601110356.
(130) Hee Song, J.; Kim, F.; Kim, D.; Yang, P. Crystal Overgrowth on Gold Nanorods: Tuning the Shape, Facet, Aspect Ratio, and Composition of the Nanorods. *Chemistry - A European Journal* **2005**, *11* (3), 910–916. https://doi.org/10.1002/chem.200400805.
(131) Xiong, Y.; Cai, H.; Yin, Y.; Xia, Y. Synthesis and Characterization of Fivefold Twinned Nanorods and Right Bipyramids of Palladium. *Chemical Physics Letters* **2007**, *440* (4–6), 273–278. https://doi.org/10.1016/j.cplett.2007.04.074.
(132) Sun, J.; Guan, M.; Shang, T.; Gao, C.; Xu, Z.; Zhu, J. Selective Synthesis of Gold Cuboid and Decahedral Nanoparticles Regulated and Controlled by Cu2+ Ions. *Crystal Growth and Design* **2008**, *8* (3), 906–910. https://doi.org/10.1021/cg070635a.
(133) Filankembo, A.; Giorgio, S.; Lisiecki, I.; Pileni, M. P. Is the Anion the Major Parameter in the Shape Control of Nanocrystals? *Journal of Physical Chemistry B* **2003**, *107* (30), 7492–7500. https://doi.org/10.1021/jp022282q.
(134) Murphy, C. J.; Sau, T. K.; Gole, A. M.; Orendorff, C. J.; Gao, J.; Gou, L.; Hunyadi, S. E.; Li, T. Anisotropic Metal Nanoparticles: Synthesis, Assembly, and Optical Applications. *Journal of Physical Chemistry B* **2005**, *109* (29), 13857–13870. https://doi.org/10.1021/jp0516846.
(135) Kuo, C. H.; Huang, M. H. Synthesis of Branched Gold Nanocrystals by a Seeding Growth Approach. *Langmuir* **2005**, *21* (5), 2012–2016. https://doi.org/10.1021/la0476332.
(136) Hu, J.; Zhang, Y.; Liu, B.; Liu, J.; Zhou, H.; Xu, Y.; Jiang, Y.; Yang, Z.; Tian, Z. Q. Synthesis and Properties Tadpole-Shaped Gold Nanoparticles. *J Am Chem Soc* **2004**, *126* (31), 9470–9471. https://doi.org/10.1021/ja049738x.
(137) Sun, Y.; Zhang, L.; Zhou, H.; Zhu, Y.; Sutter, E.; Ji, Y.; Rafailovich, M. H.; Sokolov, J. C. Seedless and Templateless Synthesis of Rectangular Palladium Nanoparticles. *Chemistry of Materials* **2007**, *19* (8), 2065–2070. https://doi.org/10.1021/cm0623209.
(138) Kuwahara, Y.; Yoshimori, K.; Tomita, K.; Sakai, M.; Sawada, T.; Niidome, Y.; Yamada, S.; Shosenji, H. Novel Effects of Twin-Tailed Cationic Surfactants on the Formation of Gold Nanorods. *Chemistry Letters* **2007**, *36* (10), 1230–1231. https://doi.org/10.1246/cl.2007.1230.
(139) Chiang, C. L.; Hsu, M. B.; Lai, L. B. Control of Nucleation and Growth of Gold Nanoparticles in AOT/Span80/Isooctane Mixed Reverse Micelles. *Journal of Solid State Chemistry* **2004**, *177* (11), 3891–3895. https://doi.org/10.1016/j.jssc.2004.07.003.
(140) Li, C.; Shuford, K. L.; Chen, M.; Lee, E. J.; Cho, S. O. A Facile Polyol Route to Uniform Gold Octahedra with Tailorable Size and Their Optical Properties. *ACS Nano* **2008**, *2* (9), 1760–1769. https://doi.org/10.1021/nn800264q.
(141) Love, J. C.; Estroff, L. A.; Kriebel, J. K.; Nuzzo, R. G.; Whitesides, G. M. *Self-Assembled Monolayers of Thiolates on Metals as a Form of Nanotechnology*; 2005; Vol. 105. https://doi.org/10.1021/cr0300789.
(142) Ip, A. H.; Thon, S. M.; Hoogland, S.; Voznyy, O.; Zhitomirsky, D.; Debnath, R.; Levina, L.; Rollny, L. R.; Carey, G. H.; Fischer, A.; Kemp, K. W.; Kramer, I. J.; Ning, Z.; Labelle, A. J.; Chou, K. W.; Amassian, A.; Sargent, E. H. Hybrid Passivated Colloidal Quantum Dot Solids. *Nature Nanotechnology* **2012**, *7* (9), 577–582. https://doi.org/10.1038/nnano.2012.127.
(143) Ma, N.; Grigory, T.; Kelley, S. O. Nucleic Acid-Passivated Semiconductor Nanocrystals: Biomolecular Templating of Form and Function. *Accounts of Chemical Research* **2010**, *43* (2), 173–180. https://doi.org/10.1021/ar900046n.
(144) Peng, S.; Wang, C.; Xie, J.; Sun, S. Synthesis and Stabilization of Monodisperse Fe Nanoparticles. *J Am Chem Soc* **2006**, *128* (33), 10676–10677. https://doi.org/10.1021/ja063969h.
(145) Ramirez, E.; Jansat, S.; Philippot, K.; Lecante, P.; Gomez, M.; Masdeu-Bultó, A. M.; Chaudret, B. Influence of Organic Ligands on the Stabilization of Palladium Nanoparticles.

Journal of Organometallic Chemistry **2004**, *689* (24 SPEC. ISS.), 4601–4610. https://doi.org/10.1016/j.jorganchem.2004.09.006.
(146) Mourdikoudis, S.; Liz-Marzán, L. M. Oleylamine in Nanoparticle Synthesis. *Chemistry of Materials*. 2013, pp 1465–1476. https://doi.org/10.1021/cm4000476.
(147) Harris, R. A.; Shumbula, P. M.; van der Walt, H. Analysis of the Interaction of Surfactants Oleic Acid and Oleylamine with Iron Oxide Nanoparticles through Molecular Mechanics Modeling. *Langmuir* **2015**, *31* (13), 3934–3943. https://doi.org/10.1021/acs.langmuir.5b00671.
(148) Kang, Y.; Ye, X.; Murray, C. B. Size- and Shape-Selective Synthesis of Metal Nanocrystals and Nanowires Using CO as a Reducing Agent. *Angewandte Chemie - International Edition* **2010**, *49* (35), 6156–6159. https://doi.org/10.1002/anie.201003383.
(149) Xia, B. Y.; Wu, H. bin; Wang, X.; Lou, X. W. Highly Concave Platinum Nanoframes with High-Index Facets and Enhanced Electrocatalytic Properties. *Angewandte Chemie - International Edition* **2013**, *52* (47), 12337–12340. https://doi.org/10.1002/anie.201307518.
(150) Saldias, C.; Bonardd, S.; Quezada, C.; Radic, D.; Leiva, A. The Role of Polymers in the Synthesis of Noble Metal Nanoparticles: A Review. *Journal of Nanoscience and Nanotechnology* **2017**, *17* (1), 87–114. https://doi.org/10.1166/jnn.2017.13016.
(151) Madkour, M.; Bumajdad, A.; Al-Sagheer, F. To What Extent Do Polymeric Stabilizers Affect Nanoparticles Characteristics? *Advances in Colloid and Interface Science* **2019**, *270*, 38–53. https://doi.org/10.1016/j.cis.2019.05.004.
(152) Koczkur, K. M.; Mourdikoudis, S.; Polavarapu, L.; Skrabalak, S. E. Polyvinylpyrrolidone (PVP) in Nanoparticle Synthesis. *Dalton Transactions* **2015**, *44* (41), 17883–17905. https://doi.org/10.1039/c5dt02964c.
(153) Zeng, J.; Zheng, Y.; Rycenga, M.; Tao, J.; Li, Z. Y.; Zhang, Q.; Zhu, Y.; Xia, Y. Controlling the Shapes of Silver Nanocrystals with Different Capping Agents. *J Am Chem Soc* **2010**, *132* (25), 8552–8553. https://doi.org/10.1021/ja103655f.
(154) Al-Saidi, W. A.; Feng, H.; Fichthorn, K. A. Adsorption of Polyvinylpyrrolidone on Ag Surfaces: Insight into a Structure-Directing Agent. *Nano Letters* **2012**, *12* (2), 997–1001. https://doi.org/10.1021/nl2041113.
(155) Ahmadi, T. S.; Wang, Z. L.; Green, T. C.; Henglein, A.; El-Sayed, M. A. Shape-Controlled Synthesis of Colloidal Platinum Nanoparticles. *Science (1979)* **1996**, *272* (5270), 1924–1925. https://doi.org/10.1126/science.272.5270.1924.
(156) Petroski, J. M.; Wang, Z. L.; Green, T. C.; El-Sayed, M. A. Kinetically Controlled Growth and Shape Formation Mechanism of Platinum Nanoparticles. *Journal of Physical Chemistry B* **1998**, *102* (18), 3316–3320. https://doi.org/10.1021/jp981030f.
(157) Yang, W.; Yin, Q.; Chen, C. L. Designing Sequence-Defined Peptoids for Biomimetic Control over Inorganic Crystallization. *Chemistry of Materials* **2021**, *33* (9), 3047–3065. https://doi.org/10.1021/acs.chemmater.1c00243.
(158) Berti, L.; Burley, G. A. Nucleic Acid and Nucleotide-Mediated Synthesis of Inorganic Nanoparticles. *Nature Nanotechnology* **2008**, *3* (2), 81–87. https://doi.org/10.1038/nnano.2007.460.
(159) Chiu, C. Y.; Li, Y.; Ruan, L.; Ye, X.; Murray, C. B.; Huang, Y. Platinum Nanocrystals Selectively Shaped Using Facet-Specific Peptide Sequences. *Nature Chemistry* **2011**, *3* (5), 393–399. https://doi.org/10.1038/nchem.1025.
(160) Turkevich, J.; Stevenson, P. C.; Hillier, J. A Study of the Nucleation and Growth Processes in the Synthesis of Colloidal Gold. *Discuss Faraday Soc* **1951**, *11* (c), 55. https://doi.org/10.1039/df9511100055.
(161) Turkevich, J.; Kim, G. Palladium: Preparation and Catalytic Properties of Particles of Uniform Size. *Science (1979)* **1970**, *169* (3948), 873–879. https://doi.org/10.1126/science.169.3948.873.

(162) Turkevich, J. Colloidal Gold. Part I. *Gold Bulletin* **1985**, *18* (3), 86–91. https://doi.org/10.1007/BF03214690.
(163) Turkevich, J. Colloidal Gold. Part II. *Gold Bulletin* **1985**, *18* (4), 125–131. https://doi.org/10.1007/bf03214694.
(164) Janssens, T. V. W.; Clausen, B. S.; Hvolbæk, B.; Falsig, H.; Christensen, C. H.; Bligaard, T.; Nørskov, J. K. Insights into the Reactivity of Supported Au Nanoparticles: Combining Theory and Experiments. *Topics in Catalysis* **2007**, *44* (1–2), 15–26. https://doi.org/10.1007/s11244-007-0335-3.
(165) Hvolbæk, B.; Janssens, T. V. W.; Clausen, B. S.; Falsig, H.; Christensen, C. H.; Nørskov, J. K. Catalytic Activity of Au Nanoparticles. *Nano Today* **2007**, *2* (4), 14–18. https://doi.org/10.1016/S1748-0132(07)70113-5.
(166) Cargnello, M.; Doan-Nguyen, V. V. T.; Gordon, T. R.; Diaz, R. E.; Stach, E. A.; Gorte, R. J.; Fornasiero, P.; Murray, C. B. Control of Metal Nanocrystal Size Reveals Metal-Support Interface Role for Ceria Catalysts. *Science (1979)* **2013**, *341* (6147), 771–773. https://doi.org/10.1126/science.1240148.
(167) Boronat, M.; Leyva-Pérez, A.; Corma, A. Theoretical and Experimental Insights into the Origin of the Catalytic Activity of Subnanometric Gold Clusters: Attempts to Predict Reactivity with Clusters and Nanoparticles of Gold. *Accounts of Chemical Research* **2014**, *47* (3), 834–844. https://doi.org/10.1021/ar400068w.
(168) Kelly, K. L.; Coronado, E.; Zhao, L. L.; Schatz, G. C. The Optical Properties of Metal Nanoparticles: The Influence of Size, Shape, and Dielectric Environment. *The Journal of Physical Chemistry B* **2003**, *107* (3), 668–677. https://doi.org/10.1021/jp026731y.
(169) Subramanian, V.; Wolf, E. E.; Kamat, P. v. Catalysis with TiO2/Gold Nanocomposites. Effect of Metal Particle Size on the Fermi Level Equilibration. *J Am Chem Soc* **2004**, *126* (15), 4943–4950. https://doi.org/10.1021/ja0315199.
(170) Li, Y.; Boone, E.; El-Sayed, M. A. Size Effects of PVP-Pd Nanoparticles on the Catalytic Suzuki Reactions in Aqueous Solution. *Langmuir* **2002**, *18* (12), 4921–4925. https://doi.org/10.1021/la011469q.
(171) le Bars, J.; Specht, U.; Bradley, J. S.; Blackmond, D. G. Catalytic Probe of the Surface of Colloidal Palladium Particles Using Heck Coupling Reactions. *Langmuir* **1999**, *15* (22), 7621–7625. https://doi.org/10.1021/la990144v.
(172) Song, H.; Rioux, R. M.; Hoefelmeyer, J. D.; Komor, R.; Niesz, K.; Grass, M.; Yang, P.; Somorjai, G. A. Hydrothermal Growth of Mesoporous SBA-15 Silica in the Presence of PVP-Stabilized Pt Nanoparticles: Synthesis, Characterization, and Catalytic Properties. *J Am Chem Soc* **2006**, *128* (9), 3027–3037. https://doi.org/10.1021/ja057383r.
(173) Teranishi, T.; Miyake, M. Size Control of Palladium Nanoparticles and Their Crystal Structures. *Chemistry of Materials* **1998**, *10* (2), 594–600. https://doi.org/10.1021/cm9705808.
(174) Rioux, R. M.; Song, H.; Hoefelmeyer, J. D.; Yang, P.; Somorjai, G. A. High-Surface-Area Catalyst Design: Synthesis, Characterization, and Reaction Studies of Platinum Nanoparticles in Mesoporous SBA-15 Silica. *Journal of Physical Chemistry B* **2005**, *109* (6), 2192–2202. https://doi.org/10.1021/jp048867x.
(175) Zhang, Y.; Grass, M. E.; Habas, S. E.; Tao, F.; Zhang, T.; Yang, P.; Somorjai, G. A. One-Step Polyol Synthesis and Langmuir-Blodgett Monolayer Formation of Size-Tunable Monodisperse Rhodium Nanocrystals with Catalytically Active (111) Surface Structures. *Journal of Physical Chemistry C* **2007**, *111* (33), 12243–12253. https://doi.org/10.1021/jp073350h.
(176) Daniel, M. C.; Astruc, D. Gold Nanoparticles: Assembly, Supramolecular Chemistry, Quantum-Size-Related Properties, and Applications Toward Biology, Catalysis, and Nanotechnology. *Chemical Reviews* **2004**, *104* (1), 293–346. https://doi.org/10.1021/cr030698+.

(177) Templeton, A. C.; Wuelfing, W. P.; Murray, R. W. Monolayer-Protected Cluster Molecules. *Accounts of Chemical Research* **2000**, *33* (1), 27–36. https://doi.org/10.1021/ar9602664.
(178) Malinsky, M. D.; Kelly, K. L.; Schatz, G. C.; van Duyne, R. P. Chain Length Dependence and Sensing Capabilities of the Localized Surface Plasmon Resonance of Silver Nanoparticles Chemically Modified with Alkanethiol Self-Assembled Monolayers. *J Am Chem Soc* **2001**, *123* (7), 1471–1482. https://doi.org/10.1021/ja003312a.
(179) Shon, Y. S.; Dawson, G. B.; Porter, M.; Murray, R. W. Monolayer-Protected Bimetal Cluster Synthesis by Core Metal Galvanic Exchange Reaction. *Langmuir* **2002**, *18* (10), 3880–3885. https://doi.org/10.1021/la025586c.
(180) Yee, C. K.; Jordan, R.; Ulman, A.; White, H.; King, A.; Rafailovich, M.; Sokolov, J. Novel One-Phase Synthesis of Thiol-Functionalized Gold, Palladium, and Iridium Nanoparticles Using Superhydride. *Langmuir* **1999**, *15* (10), 3486–3491. https://doi.org/10.1021/la990015e.
(181) Gomez, S.; Erades, L.; Philippot, K.; Chaudret, B.; Collière, V.; Balmes, O.; Bovin, J. O. Platinum Colloids Stabilized by Bifunctional Ligands : Self-Organization and Connection to Gold. *Chemical Communications* **2001**, *1* (16), 1474–1475. https://doi.org/10.1039/b103781c.
(182) Viau, G.; Brayner, R.; Poul, L.; Chakroune, N.; Lacaze, E.; Fiévet-Vincent, F.; Fiévet, F. Ruthenium Nanoparticles: Size, Shape, and Self-Assemblies. *Chemistry of Materials* **2003**, *15* (2), 486–494. https://doi.org/10.1021/cm0212109.
(183) Monai, M.; Montini, T.; Fonda, E.; Crosera, M.; Delgado, J. J.; Adami, G.; Fornasiero, P. Nanostructured Pd-Pt Nanoparticles: Evidences of Structure/Performance Relations in Catalytic H2 Production Reactions. *Applied Catalysis B: Environmental* **2018**, *236* (March), 88–98. https://doi.org/10.1016/j.apcatb.2018.05.019.
(184) Cargnello, M.; Wieder, N. L.; Montini, T.; Gorte, R. J.; Fornasiero, P. Synthesis of Dispersible Pd@CeO2 Core-Shell Nanostructures by Self-Assembly. *J Am Chem Soc* **2010**, *132* (4), 1402–1409. https://doi.org/10.1021/ja909131k.
(185) Cargnello, M.; Delgado Jaén, J. J.; Hernández Garrido, J. C.; Bakhmutsky, K.; Montini, T.; Calvino Gámez, J. J.; Gorte, R. J.; Fornasiero, P. Exceptional Activity for Methane Combustion over Modular Pd@CeO2 Subunits on Functionalized Al2O3. *Science (1979)* **2012**, *337* (6095), 713–717. https://doi.org/10.1126/science.1222887.
(186) Shchukin, D. G.; Sukhorukov, G. B. Nanoparticle Synthesis in Engineered Organic Nanoscale Reactors. *Advanced Materials* **2004**, *16* (8), 671–682. https://doi.org/10.1002/adma.200306466.
(187) Porta, F.; Prati, L.; Rossi, M.; Scari, G. Synthesis of Au(0) Nanoparticles from W/O Microemulsions. *Colloids and Surfaces A: Physicochemical and Engineering Aspects* **2002**, *211* (1), 43–48. https://doi.org/10.1016/S0927-7757(02)00220-0.
(188) Eriksson, S.; Nylén, U.; Rojas, S.; Boutonnet, M. Preparation of Catalysts from Microemulsions and Their Applications in Heterogeneous Catalysis. *Applied Catalysis A: General* **2004**, *265* (2), 207–219. https://doi.org/10.1016/j.apcata.2004.01.014.
(189) Chen, D. H.; Wang, C. C.; Huang, T. C. Preparation of Palladium Ultrafine Particles in Reverse Micelles. *Journal of Colloid and Interface Science* **1999**, *210* (1), 123–129. https://doi.org/10.1006/jcis.1998.5795.
(190) Chen, Y.; Fan, Z.; Zhang, Z.; Niu, W.; Li, C.; Yang, N.; Chen, B.; Zhang, H. Two-Dimensional Metal Nanomaterials: Synthesis, Properties, and Applications. *Chemical Reviews* **2018**, *118* (13), 6409–6455. https://doi.org/10.1021/acs.chemrev.7b00727.
(191) Huo, D.; Kim, M. J.; Lyu, Z.; Shi, Y.; Wiley, B. J.; Xia, Y. One-Dimensional Metal Nanostructures: From Colloidal Syntheses to Applications. *Chemical Reviews* **2019**, *119* (15), 8972–9073. https://doi.org/10.1021/acs.chemrev.8b00745.

(192) Zhang, H.; Jin, M.; Xia, Y. Noble-Metal Nanocrystals with Concave Surfaces: Synthesis and Applications. *Angewandte Chemie - International Edition* **2012**, *51* (31), 7656–7673. https://doi.org/10.1002/anie.201201557.
(193) Tao, A. R.; Habas, S.; Yang, P. Shape Control of Colloidal Metal Nanocrystals. *Small* **2008**, *4* (3), 310–325. https://doi.org/10.1002/smll.200701295.
(194) Li, Z.; Ji, S.; Liu, Y.; Cao, X.; Tian, S.; Chen, Y.; Niu, Z.; Li, Y. Well-Defined Materials for Heterogeneous Catalysis: From Nanoparticles to Isolated Single-Atom Sites. *Chemical Reviews* **2020**, *120* (2), 623–682. https://doi.org/10.1021/acs.chemrev.9b00311.
(195) Quan, Z.; Wang, Y.; Fang, J. High-Index Faceted Noble Metal Nanocrystals. *Accounts of Chemical Research* **2013**, *46* (2), 191–202. https://doi.org/10.1021/ar200293n.
(196) Li, Y. R.; Li, M. X.; Li, S. N.; Liu, Y. J.; Chen, J.; Wang, Y. A Review of Energy and Environment Electrocatalysis Based on High-Index Faceted Nanocrystals. *Rare Metals* **2021**, *40* (12), 3406–3441. https://doi.org/10.1007/s12598-021-01747-8.
(197) Huang, L.; Liu, M.; Lin, H.; Xu, Y.; Wu, J.; Dravid, V. P.; Wolverton, C.; Mirkin, C. A. Shape Regulation of High-Index Facet Nanoparticles by Dealloying. *Science (1979)* **2019**, *365* (6458), 1159–1163. https://doi.org/10.1126/science.aax5843.
(198) Xiaoqing Huang, Zipeng Zhao, Jingmin Fan, Yueming Tan, and N. Z. Amine-Assisted Synthesis of Concave Polyhedral Platinum. *J Am Chem Soc* **2010**, *133*, 4718–4721.
(199) Ren, J.; Tilley, R. D. Preparation, Self-Assembly, and Mechanistic Study of Highly Monodispersed Nanocubes. *J Am Chem Soc* **2007**, *129* (11), 3287–3291. https://doi.org/10.1021/ja067636w.
(200) Wu, B.; Zheng, N.; Fu, G. Small Molecules Control the Formation of Pt Nanocrystals: A Key Role of Carbon Monoxide in the Synthesis of Pt Nanocubes. *Chemical Communications* **2011**, *47* (3), 1039–1041. https://doi.org/10.1039/c0cc03671d.
(201) Kang, Y.; Pyo, J. B.; Ye, X.; Diaz, R. E.; Gordon, T. R.; Stach, E. A.; Murray, C. B. Shape-Controlled Synthesis of Pt Nanocrystals: The Role of Metal Carbonyls. *ACS Nano* **2013**, *7* (1), 645–653. https://doi.org/10.1021/nn3048439.
(202) Wang, C.; Daimon, H.; Lee, Y.; Kim, J.; Sun, S. Synthesis of Monodisperse Pt Nanocubes and Their Enhanced Catalysis for Oxygen Reduction. *J Am Chem Soc* **2007**, *129* (22), 6974–6975. https://doi.org/10.1021/ja070440r.
(203) Niesz, K.; Grass, M.; Somorjai, G. A. Precise Control of the Pt Nanoparticle Size by Seeded Growth Using EO 13PO30EO13 Triblock Copolymers as Protective Agents. *Nano Letters* **2005**, *5* (11), 2238–2240. https://doi.org/10.1021/nl051561x.
(204) Xiong, Y.; Cai, H.; Wiley, B. J.; Wang, J.; Kim, M. J.; Xia, Y. Synthesis and Mechanistic Study of Palladium Nanobars and Nanorods. *J Am Chem Soc* **2007**, *129* (12), 3665–3675. https://doi.org/10.1021/ja0688023.
(205) Li, Y.; Bian, T.; Du, J.; Xiong, Y.; Zhan, F.; Zhang, H.; Yang, D. Facile Synthesis of High-Quality Pt Nanostructures with a Controlled Aspect Ratio for Methanol Electro-Oxidation. *CrystEngComm* **2014**, *16* (36), 8340–8343. https://doi.org/10.1039/c4ce00713a.
(206) Kang, Y.; Li, M.; Cai, Y.; Cargnello, M.; Diaz, R. E.; Gordon, T. R.; Wieder, N. L.; Adzic, R. R.; Gorte, R. J.; Stach, E. A.; Murray, C. B. Heterogeneous Catalysts Need Not Be so "Heterogeneous": Monodisperse Pt Nanocrystals by Combining Shape-Controlled Synthesis and Purification by Colloidal Recrystallization. *J Am Chem Soc* **2013**, *135* (7), 2741–2747. https://doi.org/10.1021/ja3116839.
(207) Lee, C. T.; Yang, X.; Vara, M.; Gilroy, K. D.; Xia, Y. Water-Based Synthesis of Sub-10 Nm Pt Octahedra and Their Performance towards the Oxygen Reduction Reaction. *ChemNanoMat* **2017**, *3* (12), 879–884. https://doi.org/10.1002/cnma.201700189.
(208) Moglianetti, M.; Solla-Gullón, J.; Donati, P.; Pedone, D.; Debellis, D.; Sibillano, T.; Brescia, R.; Giannini, C.; Montiel, V.; Feliu, J. M.; Pompa, P. P. Citrate-Coated, Size-Tunable Octahedral Platinum Nanocrystals: A Novel Route for Advanced Electrocatalysts. *ACS*

Applied Materials and Interfaces **2018**, *10* (48), 41608–41617. https://doi.org/10.1021/acsami.8b11774.
(209) Gisbert-González, J. M.; Feliu, J. M.; Ferre-Vilaplana, A.; Herrero, E. Why Citrate Shapes Tetrahedral and Octahedral Colloidal Platinum Nanoparticles in Water. *Journal of Physical Chemistry C* **2018**, *122* (33), 19004–19014. https://doi.org/10.1021/acs.jpcc.8b05195.
(210) Ruan, L.; Chiu, C. Y.; Li, Y.; Huang, Y. Synthesis of Platinum Single-Twinned Right Bipyramid and {111}-Bipyramid through Targeted Control over Both Nucleation and Growth Using Specific Peptides. *Nano Letters* **2011**, *11* (7), 3040–3046. https://doi.org/10.1021/nl201958w.
(211) Zhu, W.; Yin, A. X.; Zhang, Y. W.; Yan, C. H. Highly Shape-Selective Synthesis of Monodispersed Fivefold Twinned Platinum Nanodecahedrons and Nanoicosahedrons. *Chemistry - A European Journal* **2012**, *18* (39), 12222–12226. https://doi.org/10.1002/chem.201201099.
(212) Zhou, W.; Wu, J.; Yang, H. Highly Uniform Platinum Icosahedra Made by Hot Injection-Assisted GRAILS Method. *Nano Letters* **2013**, *13* (6), 2870–2874. https://doi.org/10.1021/nl401214d.
(213) Zhao, M.; Holder, J.; Chen, Z.; Xie, M.; Cao, Z.; Chi, M.; Xia, Y. Facile Synthesis of Pt Icosahedral Nanocrystals with Controllable Sizes for the Evaluation of Size-Dependent Activity toward Oxygen Reduction. *ChemCatChem* **2019**, *11* (10), 2458–2463. https://doi.org/10.1002/cctc.201900239.
(214) Lim, B.; Jiang, M.; Tao, J.; Camargo, P. H. C.; Zhu, Y.; Xia, Y. Shape-Controlled Synthesis of Pd Nanocrystals in Aqueous Solutions. *Advanced Functional Materials* **2009**, *19* (2), 189–200. https://doi.org/10.1002/adfm.200801439.
(215) Jin, M.; Liu, H.; Zhang, H.; Xie, Z.; Liu, J.; Xia, Y. Synthesis of Pd Nanocrystals Enclosed by {100} Facets and with Sizes <10 Nm for Application in CO Oxidation. *Nano Research* **2011**, *4* (1), 83–91. https://doi.org/10.1007/s12274-010-0051-3.
(216) Lim, B.; Kobayashi, H.; Camargo, P. H. C.; Allard, L. F.; Liu, J.; Xia, Y. New Insights into the Growth Mechanism and Surface Structure of Palladium Nanocrystals. *Nano Research* **2010**, *3* (3), 180–188. https://doi.org/10.1007/s12274-010-1021-5.
(217) Zeng, J.; Zhu, C.; Tao, J.; Jin, M.; Zhang, H.; Li, Z. Y.; Zhu, Y.; Xia, Y. Controlling the Nucleation and Growth of Silver on Palladium Nanocubes by Manipulating the Reaction Kinetics. *Angewandte Chemie - International Edition* **2012**, *51* (10), 2354–2358. https://doi.org/10.1002/anie.201107061.
(218) Wang, Y.; Xie, S.; Liu, J.; Park, J.; Huang, C. Z.; Xia, Y. Shape-Controlled Synthesis of Palladium Nanocrystals: A Mechanistic Understanding of the Evolution from Octahedrons to Tetrahedrons. *Nano Letters* **2013**, *13* (5), 2276–2281. https://doi.org/10.1021/nl400893p.
(219) Lim, B.; Xiong, Y.; Xia, Y. A Water-Based Synthesis of Octahedral, Decahedral, and Icosahedral Pd Nanocrystals. *Angewandte Chemie - International Edition* **2007**, *46* (48), 9279–9282. https://doi.org/10.1002/anie.200703755.
(220) Liu, M.; Zheng, Y.; Zhang, L.; Guo, L.; Xia, Y. Transformation of Pd Nanocubes into Octahedra with Controlled Sizes by Maneuvering the Rates of Etching and Regrowth. *J Am Chem Soc* **2013**, *135* (32), 11752–11755. https://doi.org/10.1021/ja406344j.
(221) Ma, X. Y.; Chen, Y.; Wang, H.; Li, Q. X.; Lin, W. F.; Cai, W. bin. Electrocatalytic Oxidation of Ethanol and Ethylene Glycol on Cubic, Octahedral and Rhombic Dodecahedral Palladium Nanocrystals. *Chemical Communications* **2018**, *54* (20), 2562–2565. https://doi.org/10.1039/c7cc08793d.
(222) Niu, W.; Zhang, L.; Xu, G. Shape-Controlled Synthesis of Single-Crystalline Palladium Nanocrystals. *ACS Nano* **2010**, *4* (4), 1987–1996. https://doi.org/10.1021/nn100093y.
(223) Li, L.; Zhang, N.; He, H.; Zhang, G.; Song, L.; Qiu, W. Shape-Controlled Synthesis of Pd Nanocrystals with Exposed {110} Facets and Their Catalytic Applications. *Catalysis Today* **2019**, *327* (January 2018), 28–36. https://doi.org/10.1016/j.cattod.2018.07.038.

(224) Huang, H.; Wang, Y.; Ruditskiy, A.; Peng, H. C.; Zhao, X.; Zhang, L.; Liu, J.; Ye, Z.; Xia, Y. Polyol Syntheses of Palladium Decahedra and Icosahedra as Pure Samples by Maneuvering the Reaction Kinetics with Additives. *ACS Nano* **2014**, *8* (7), 7041–7050. https://doi.org/10.1021/nn501919e.
(225) Xiong, Y.; McLellan, J. M.; Chen, J.; Yin, Y.; Li, Z. Y.; Xia, Y. Kinetically Controlled Synthesis of Triangular and Hexagonal Nanoplates of Palladium and Their SPR/SERS Properties. *J Am Chem Soc* **2005**, *127* (48), 17118–17127. https://doi.org/10.1021/ja056498s.
(226) Huang, X.; Tang, S.; Mu, X.; Dai, Y.; Chen, G.; Zhou, Z.; Ruan, F.; Yang, Z.; Zheng, N. Freestanding Palladium Nanosheets with Plasmonic and Catalytic Properties. *Nature Nanotechnology* **2011**, *6* (1), 28–32. https://doi.org/10.1038/nnano.2010.235.
(227) Zhang, Q.; Li, W.; Moran, C.; Zeng, J.; Chen, J.; Wen, L.-P.; Xia, Y. Seed-Mediated Synthesis of Ag Nanocubes with Controllable Edge Lengths in the Range of 30−200 Nm and Comparison of Their Optical Properties. *J Am Chem Soc* **2010**, *132* (32), 11372–11378. https://doi.org/10.1021/ja104931h.
(228) Sang, H. I.; Yun, T. L.; Wiley, B.; Xia, Y. Large-Scale Synthesis of Silver Nanocubes: The Role of HCl in Promoting Cube Perfection and Monodispersity. *Angewandte Chemie - International Edition* **2005**, *44* (14), 2154–2157. https://doi.org/10.1002/anie.200462208.
(229) Bi, Y.; Lu, G. Morphology-Controlled Preparation of Silver Nanocrystals and Their Application in Catalysis. *Chemistry Letters* **2008**, *37* (5), 514–515. https://doi.org/10.1246/cl.2008.514.
(230) Wang, Y.; Zheng, Y.; Huang, C. Z.; Xia, Y. Synthesis of Ag Nanocubes 18-32 Nm in Edge Length: The Effects of Polyol on Reduction Kinetics, Size Control, and Reproducibility. *J Am Chem Soc* **2013**, *135* (5), 1941–1951. https://doi.org/10.1021/ja311503q.
(231) Tao, A.; Sinsermsuksakul, P.; Yang, P. Polyhedral Silver Nanocrystals with Distinct Scattering Signatures. *Angewandte Chemie International Edition* **2006**, *45* (28), 4597–4601. https://doi.org/10.1002/anie.200601277.
(232) Chen, Z.; Chang, J. W.; Balasanthiran, C.; Milner, S. T.; Rioux, R. M. Anisotropic Growth of Silver Nanoparticles Is Kinetically Controlled by Polyvinylpyrrolidone Binding. *J Am Chem Soc* **2019**, *141* (10), 4328–4337. https://doi.org/10.1021/jacs.8b11295.
(233) Siekkinen, A. R.; McLellan, J. M.; Chen, J.; Xia, Y. Rapid Synthesis of Small Silver Nanocubes by Mediating Polyol Reduction with a Trace Amount of Sodium Sulfide or Sodium Hydrosulfide. *Chemical Physics Letters* **2006**, *432* (4–6), 491–496. https://doi.org/10.1016/j.cplett.2006.10.095.
(234) Zhang, Q.; Li, W.; Wen, L.-P.; Chen, J.; Xia, Y. Facile Synthesis of Ag Nanocubes of 30 to 70 Nm in Edge Length with CF 3 COOAg as a Precursor. *Chemistry - A European Journal* **2010**, *16* (33), 10234–10239. https://doi.org/10.1002/chem.201000341.
(235) Wang, Y.; Wan, D.; Xie, S.; Xia, X.; Huang, C. Z.; Xia, Y. Synthesis of Silver Octahedra with Controlled Sizes and Optical Properties via Seed-Mediated Growth. *ACS Nano* **2013**, *7* (5), 4586–4594. https://doi.org/10.1021/nn401363e.
(236) Wiley, B. J.; Xiong, Y.; Li, Z.-Y.; Yin, Y.; Xia, Y. Right Bipyramids of Silver: A New Shape Derived from Single Twinned Seeds. *Nano Letters* **2006**, *6* (4), 765–768. https://doi.org/10.1021/nl060069q.
(237) Gao, Y.; Jiang, P.; Song, L.; Wang, J. X.; Liu, L. F.; Liu, D. F.; Xiang, Y. J.; Zhang, Z. X.; Zhao, X. W.; Dou, X. Y.; Luo, S. D.; Zhou, W. Y.; Xie, S. S. Studies on Silver Nanodecahedrons Synthesized by PVP-Assisted N,N-Dimethylformamide (DMF) Reduction. *Journal of Crystal Growth* **2006**, *289* (1), 376–380. https://doi.org/10.1016/j.jcrysgro.2005.11.123.
(238) Wang, W.; Zhou, S.; Shen, M.; Hood, Z. D.; Xiao, K.; Xia, Y. Facile Synthesis of Silver Icosahedral Nanocrystals with Uniform and Controllable Sizes. *ChemNanoMat* **2018**, *4* (10), 1071–1077. https://doi.org/10.1002/cnma.201800255.

(239) Zhang, Q.; Xie, J.; Yang, J.; Lee, J. Y. Monodisperse Icosahedral Ag, Au, and Pd Nanoparticles: Size Control Strategy and Superlattice Formation. *ACS Nano* **2009**, *3* (1), 139–148. https://doi.org/10.1021/nn800531q.
(240) Niu, Z.; Cui, F.; Kuttner, E.; Xie, C.; Chen, H.; Sun, Y.; Dehestani, A.; Schierle-Arndt, K.; Yang, P. Synthesis of Silver Nanowires with Reduced Diameters Using Benzoin-Derived Radicals to Make Transparent Conductors with High Transparency and Low Haze. *Nano Letters* **2018**, *18* (8), 5329–5334. https://doi.org/10.1021/acs.nanolett.8b02479.
(241) Sun, Y.; Mayers, B.; Xia, Y. Transformation of Silver Nanospheres into Nanobelts and Triangular Nanoplates through a Thermal Process. *Nano Letters* **2003**, *3* (5), 675–679. https://doi.org/10.1021/nl034140t.
(242) Tsuji, M.; Ogino, M.; Matsuo, R.; Kumagae, H.; Hikino, S.; Kim, T.; Yoon, S.-H. Stepwise Growth of Decahedral and Icosahedral Silver Nanocrystals in DMF. *Crystal Growth & Design* **2010**, *10* (1), 296–301. https://doi.org/10.1021/cg9009042.
(243) Rocha, T. C. R.; Winnischofer, H.; Westphal, E.; Zanchet, D. Formation Kinetics of Silver Triangular Nanoplates. *The Journal of Physical Chemistry C* **2007**, *111* (7), 2885–2891. https://doi.org/10.1021/jp0660637.
(244) Kim, F.; Connor, S.; Song, H.; Kuykendall, T.; Yang, P. Platonic Gold Nanocrystals. *Angewandte Chemie International Edition* **2004**, *43* (28), 3673–3677. https://doi.org/10.1002/anie.200454216.
(245) Park, J. E.; Lee, Y.; Nam, J. M. Precisely Shaped, Uniformly Formed Gold Nanocubes with Ultrahigh Reproducibility in Single-Particle Scattering and Surface-Enhanced Raman Scattering. *Nano Letters* **2018**, *18* (10), 6475–6482. https://doi.org/10.1021/acs.nanolett.8b02973.
(246) Seo, D.; Yoo, C. il; Park, J. C.; Park, S. M.; Ryu, S.; Song, H. Directed Surface Overgrowth and Morphology Control of Polyhedral Gold Nanocrystals. *Angewandte Chemie International Edition* **2008**, *47* (4), 763–767. https://doi.org/10.1002/anie.200704094.
(247) Cao, C.; Park, S.; Sim, S. J. Seedless Synthesis of Octahedral Gold Nanoparticles in Condensed Surfactant Phase. *Journal of Colloid and Interface Science* **2008**, *322* (1), 152–157. https://doi.org/10.1016/j.jcis.2008.03.031.
(248) Jeong, G. H.; Kim, M.; Lee, Y. W.; Choi, W.; Oh, W. T.; Park, Q.-H.; Han, S. W. Polyhedral Au Nanocrystals Exclusively Bound by {110} Facets: The Rhombic Dodecahedron. *J Am Chem Soc* **2009**, *131* (5), 1672–1673. https://doi.org/10.1021/ja809112n.
(249) Niu, W.; Zheng, S.; Wang, D.; Liu, X.; Li, H.; Han, S.; Chen, J.; Tang, Z.; Xu, G. Selective Synthesis of Single-Crystalline Rhombic Dodecahedral, Octahedral, and Cubic Gold Nanocrystals. *J Am Chem Soc* **2009**, *131* (2), 697–703. https://doi.org/10.1021/ja804115r.
(250) Sánchez-Iglesias, A.; Pastoriza-Santos, I.; Pérez-Juste, J.; Rodríguez-González, B.; García de Abajo, F. J.; Liz-Marzán, L. M. Synthesis and Optical Properties of Gold Nanodecahedra with Size Control. *Advanced Materials* **2006**, *18* (19), 2529–2534. https://doi.org/10.1002/adma.200600475.
(251) Seo, D.; Yoo, C. il; Chung, I. S.; Park, S. M.; Ryu, S.; Song, H. Shape Adjustment between Multiply Twinned and Single-Crystalline Polyhedral Gold Nanocrystals: Decahedra, Icosahedra, and Truncated Tetrahedra. *The Journal of Physical Chemistry C* **2008**, *112* (7), 2469–2475. https://doi.org/10.1021/jp7109498.
(252) Yang, H.-J.; He, S.-Y.; Chen, H.-L.; Tuan, H.-Y. Monodisperse Copper Nanocubes: Synthesis, Self-Assembly, and Large-Area Dense-Packed Films. *Chemistry of Materials* **2014**, *26* (5), 1785–1793. https://doi.org/10.1021/cm403098d.
(253) Loiudice, A.; Lobaccaro, P.; Kamali, E. A.; Thao, T.; Huang, B. H.; Ager, J. W.; Buonsanti, R. Tailoring Copper Nanocrystals towards C2 Products in Electrochemical CO2 Reduction. *Angewandte Chemie - International Edition* **2016**, *55* (19), 5789–5792. https://doi.org/10.1002/anie.201601582.

(254) Jin, M.; He, G.; Zhang, H.; Zeng, J.; Xie, Z.; Xia, Y. Shape-Controlled Synthesis of Copper Nanocrystals in an Aqueous Solution with Glucose as a Reducing Agent and Hexadecylamine as a Capping Agent. *Angewandte Chemie International Edition* **2011**, *50* (45), 10560–10564. https://doi.org/10.1002/anie.201105539.
(255) Lu, S. C.; Hsiao, M. C.; Yorulmaz, M.; Wang, L. Y.; Yang, P. Y.; Link, S.; Chang, W. S.; Tuan, H. Y. Single-Crystalline Copper Nano-Octahedra. *Chemistry of Materials* **2015**, *27* (24), 8187–8188. https://doi.org/10.1021/acs.chemmater.5b03519.
(256) Strach, M.; Mantella, V.; Pankhurst, J. R.; Iyengar, P.; Loiudice, A.; Das, S.; Corminboeuf, C.; van Beek, W.; Buonsanti, R. Insights into Reaction Intermediates to Predict Synthetic Pathways for Shape-Controlled Metal Nanocrystals. *J Am Chem Soc* **2019**, *141* (41), 16312–16322. https://doi.org/10.1021/jacs.9b06267.
(257) Choi, C.; Cheng, T.; Flores Espinosa, M.; Fei, H.; Duan, X.; Goddard, W. A.; Huang, Y. A Highly Active Star Decahedron Cu Nanocatalyst for Hydrocarbon Production at Low Overpotentials. *Advanced Materials* **2019**, *31* (6), 1–7. https://doi.org/10.1002/adma.201805405.
(258) Luo, M.; Zhou, M.; Rosa da Silva, R.; Tao, J.; Figueroa-Cosme, L.; Gilroy, K. D.; Peng, H.-C.; He, Z.; Xia, Y. Pentatwinned Cu Nanowires with Ultrathin Diameters below 20 Nm and Their Use as Templates for the Synthesis of Au-Based Nanotubes. *ChemNanoMat* **2017**, *3* (3), 190–195. https://doi.org/10.1002/cnma.201600337.
(259) Lee, J. W.; Han, J.; Lee, D. S.; Bae, S.; Lee, S. H.; Lee, S. K.; Moon, B. J.; Choi, C. J.; Wang, G.; Kim, T. W. 2D Single-Crystalline Copper Nanoplates as a Conductive Filler for Electronic Ink Applications. *Small* **2018**, *14* (8), 1–7. https://doi.org/10.1002/smll.201703312.
(260) Kim, M. J.; Alvarez, S.; Chen, Z.; Fichthorn, K. A.; Wiley, B. J. Single-Crystal Electrochemistry Reveals Why Metal Nanowires Grow. *J Am Chem Soc* **2018**, *140* (44), 14740–14746. https://doi.org/10.1021/jacs.8b08053.
(261) Pastoriza-Santos, I.; Sánchez-Iglesias, A.; Rodríguez-González, B.; Liz-Marzán, L. M. Aerobic Synthesis of Cu Nanoplates with Intense Plasmon Resonances. *Small* **2009**, *5* (4), 440–443. https://doi.org/10.1002/smll.200801088.
(262) Hoefelmeyer, J. D.; Niesz, K.; Somorjai, G. A.; Tilley, T. D. Radial Anisotropic Growth of Rhodium Nanoparticles. *Nano Letters* **2005**, *5* (3), 435–438. https://doi.org/10.1021/nl048100g.
(263) Zhang, Y.; Grass, M. E.; Kuhn, J. N.; Tao, F.; Habas, S. E.; Huang, W.; Yang, P.; Somorjai, G. A. Highly Selective Synthesis of Catalytically Active Monodisperse Rhodium Nanocubes. *J Am Chem Soc* **2008**, *130* (18), 5868–5869. https://doi.org/10.1021/ja801210s.
(264) Biacchi, A. J.; Schaak, R. E. The Solvent Matters: Kinetic versus Thermodynamic Shape Control in the Polyol Synthesis of Rhodium Nanoparticles. *ACS Nano* **2011**, *5* (10), 8089–8099. https://doi.org/10.1021/nn2026758.
(265) Long, N. V.; Chien, N. D.; Hirata, H.; Matsubara, T.; Ohtaki, M.; Nogami, M. Highly Monodisperse Cubic and Octahedral Rhodium Nanocrystals: Their Evolutions from Sharp Polyhedrons into Branched Nanostructures and Surface-Enhanced Raman Scattering. *Journal of Crystal Growth* **2011**, *320* (1), 78–89. https://doi.org/10.1016/j.jcrysgro.2011.02.006.
(266) Park, K. H.; Jang, K.; Kim, H. J.; Son, S. U. Near-Monodisperse Tetrahedral Rhodium Nanoparticles on Charcoal: The Shape-Dependent Catalytic Hydrogenation of Arenes. *Angewandte Chemie International Edition* **2007**, *46* (7), 1152–1155. https://doi.org/10.1002/anie.200603961.
(267) Zhang, N.; Shao, Q.; Pi, Y.; Guo, J.; Huang, X. Solvent-Mediated Shape Tuning of Well-Defined Rhodium Nanocrystals for Efficient Electrochemical Water Splitting. *Chemistry of Materials* **2017**, *29* (11), 5009–5015. https://doi.org/10.1021/acs.chemmater.7b01588.

(268) Lee, S. R.; Vara, M.; Hood, Z. D.; Zhao, M.; Gilroy, K. D.; Chi, M.; Xia, Y. Rhodium Decahedral Nanocrystals: Facile Synthesis, Mechanistic Insights, and Experimental Controls. *ChemNanoMat* **2018**, *4* (1), 66–70. https://doi.org/10.1002/cnma.201700327.
(269) Choi, S.-I.; Lee, S. R.; Ma, C.; Oliy, B.; Luo, M.; Chi, M.; Xia, Y. Facile Synthesis of Rhodium Icosahedra with Controlled Sizes up to 12 Nm. *ChemNanoMat* **2016**, *2* (1), 61–66. https://doi.org/10.1002/cnma.201500122.
(270) Jin, M.; Zhang, H.; Xie, Z.; Xia, Y. Palladium Concave Nanocubes with High-Index Facets and Their Enhanced Catalytic Properties. *Angewandte Chemie International Edition* **2011**, *50* (34), 7850–7854. https://doi.org/10.1002/anie.201103002.
(271) Zhang, J.; Zhang, L.; Xie, S.; Kuang, Q.; Han, X.; Xie, Z.; Zheng, L. Synthesis of Concave Palladium Nanocubes with High-Index Surfaces and High Electrocatalytic Activities. *Chemistry - A European Journal* **2011**, *17* (36), 9915–9919. https://doi.org/10.1002/chem.201100868.
(272) Zhou, Z.-Y.; Tian, N.; Huang, Z.-Z.; Chen, D.-J.; Sun, S.-G. Nanoparticlecatalysts with High Energy Surfaces and Enhanced Activity Synthesized by Electrochemical Method. *Faraday Discuss.* **2009**, *140*, 81–92. https://doi.org/10.1039/B803716G.
(273) Wei, L.; Xu, C. D.; Huang, L.; Zhou, Z. Y.; Chen, S. P.; Sun, S. G. Electrochemically Shape-Controlled Synthesis of Pd Concave-Disdyakis Triacontahedra in Deep Eutectic Solvent. *Journal of Physical Chemistry C* **2016**, *120* (29), 15569–15577. https://doi.org/10.1021/acs.jpcc.5b03580.
(274) Tian, N.; Zhou, Z.-Y.; Yu, N.-F.; Wang, L.-Y.; Sun, S.-G. Direct Electrodeposition of Tetrahexahedral Pd Nanocrystals with High-Index Facets and High Catalytic Activity for Ethanol Electrooxidation. *J Am Chem Soc* **2010**, *132* (22), 7580–7581. https://doi.org/10.1021/ja102177r.
(275) Qian, J.; Shen, M.; Zhou, S.; Lee, C.-T.; Zhao, M.; Lyu, Z.; Hood, Z. D.; Vara, M.; Gilroy, K. D.; Wang, K.; Xia, Y. Synthesis of Pt Nanocrystals with Different Shapes Using the Same Protocol to Optimize Their Catalytic Activity toward Oxygen Reduction. *Materials Today* **2018**, *21* (8), 834–844. https://doi.org/10.1016/j.mattod.2018.08.005.
(276) Zhang, Z.; Hui, J.; Liu, Z.-C.; Zhang, X.; Zhuang, J.; Wang, X. Glycine-Mediated Syntheses of Pt Concave Nanocubes with High-Index { Hk 0} Facets and Their Enhanced Electrocatalytic Activities. *Langmuir* **2012**, *28* (42), 14845–14848. https://doi.org/10.1021/la302973r.
(277) Wei, L.; Fan, Y.-J.; Tian, N.; Zhou, Z.-Y.; Zhao, X.-Q.; Mao, B.-W.; Sun, S.-G. Electrochemically Shape-Controlled Synthesis in Deep Eutectic Solvents—A New Route to Prepare Pt Nanocrystals Enclosed by High-Index Facets with High Catalytic Activity. *The Journal of Physical Chemistry C* **2012**, *116* (2), 2040–2044. https://doi.org/10.1021/jp209743h.
(278) Wei, L.; Zhou, Z. Y.; Chen, S. P.; Xu, C. D.; Su, D.; Schuster, M. E.; Sun, S. G. Electrochemically Shape-Controlled Synthesis in Deep Eutectic Solvents: Triambic Icosahedral Platinum Nanocrystals with High-Index Facets and Their Enhanced Catalytic Activity. *Chemical Communications* **2013**, *49* (95), 11152–11154. https://doi.org/10.1039/c3cc46473c.
(279) Li, Y.; Jiang, Y.; Chen, M.; Liao, H.; Huang, R.; Zhou, Z.; Tian, N.; Chen, S.; Sun, S. Electrochemically Shape-Controlled Synthesis of Trapezohedral Platinum Nanocrystals with High Electrocatalytic Activity. *Chemical Communications* **2012**, *48* (76), 9531–9533. https://doi.org/10.1039/c2cc34322c.
(280) Tian, N.; Zhou, Z.-Y.; Sun, S.-G.; Ding, Y.; Wang, Z. L. Synthesis of Tetrahexahedral Platinum Nanocrystals with High-Index Facets and High Electro-Oxidation Activity. *Science (1979)* **2007**, *316* (5825), 732–735. https://doi.org/10.1126/science.1140484.
(281) Xiao, J.; Liu, S.; Tian, N.; Zhou, Z.-Y.; Liu, H.-X.; Xu, B.-B.; Sun, S.-G. Synthesis of Convex Hexoctahedral Pt Micro/Nanocrystals with High-Index Facets and Electrochemistry-

Mediated Shape Evolution. *J Am Chem Soc* **2013**, *135* (50), 18754–18757. https://doi.org/10.1021/ja410583b.
(282) Zhang, L.; Chen, D.; Jiang, Z.; Zhang, J.; Xie, S.; Kuang, Q.; Xie, Z.; Zheng, L. Facile Syntheses and Enhanced Electrocatalytic Activities of Pt Nanocrystals with {hkk} High-Index Surfaces. *Nano Research* **2012**, *5* (3), 181–189. https://doi.org/10.1007/s12274-012-0198-1.
(283) Zhang, J.; Langille, M. R.; Personick, M. L.; Zhang, K.; Li, S.; Mirkin, C. A. Concave Cubic Gold Nanocrystals with High-Index Facets. *J Am Chem Soc* **2010**, *132* (40), 14012–14014. https://doi.org/10.1021/ja106394k.
(284) Ma, Y.; Kuang, Q.; Jiang, Z.; Xie, Z.; Huang, R.; Zheng, L. Synthesis of Trisoctahedral Gold Nanocrystals with Exposed High-Index Facets by a Facile Chemical Method. *Angewandte Chemie International Edition* **2008**, *47* (46), 8901–8904. https://doi.org/10.1002/anie.200802750.
(285) Huo, D.; Ding, H.; Zhou, S.; Li, J.; Tao, J.; Ma, Y.; Xia, Y. Facile Synthesis of Gold Trisoctahedral Nanocrystals with Controllable Sizes and Dihedral Angles. *Nanoscale* **2018**, *10* (23), 11034–11042. https://doi.org/10.1039/C8NR02949K.
(286) Ming, T.; Feng, W.; Tang, Q.; Wang, F.; Sun, L.; Wang, J.; Yan, C. Growth of Tetrahexahedral Gold Nanocrystals with High-Index Facets. *J Am Chem Soc* **2009**, *131* (45), 16350–16351. https://doi.org/10.1021/ja907549n.
(287) Niu, W.; Duan, Y.; Qing, Z.; Huang, H.; Lu, X. Shaping Gold Nanocrystals in Dimethyl Sulfoxide: Toward Trapezohedral and Bipyramidal Nanocrystals Enclosed by {311} Facets. *J Am Chem Soc* **2017**, *139* (16), 5817–5826. https://doi.org/10.1021/jacs.7b00036.
(288) Niu, W.; Chua, Y. A. A.; Zhang, W.; Huang, H.; Lu, X. Highly Symmetric Gold Nanostars: Crystallographic Control and Surface-Enhanced Raman Scattering Property. *J Am Chem Soc* **2015**, *137* (33), 10460–10463. https://doi.org/10.1021/jacs.5b05321.
(289) Beck, J. S.; Vartuli, J. C.; Roth, W. J.; Leonowicz, M. E.; Kresge, C. T.; Schmitt, K. D.; Chu, C. T. W.; Olson, D. H.; Sheppard, E. W.; McCullen, S. B.; Higgins, J. B.; Schlenker, J. L. A New Family of Mesoporous Molecular Sieves Prepared with Liquid Crystal Templates. *J Am Chem Soc* **1992**, *114* (27), 10834–10843. https://doi.org/10.1021/ja00053a020.
(290) Shin, H. J.; Ryoo, R.; Liu, Z.; Terasaki, O. Template Synthesis of Asymmetrically Mesostructured Platinum Networks. *J Am Chem Soc* **2001**, *123* (6), 1246–1247. https://doi.org/10.1021/ja003461t.
(291) Wang, D.; Zhou, W. L.; McCaughy, B. F.; Hampsey, J. E.; Ji, X.; Jiang, Y.-B.; Xu, H.; Tang, J.; Schmehl, R. H.; O'Connor, C.; Brinker, C. J.; Lu, Y. Electrodeposition of Metallic Nanowire Thin Films Using Mesoporous Silica Templates. *Advanced Materials* **2003**, *15* (2), 130–133. https://doi.org/10.1002/adma.200390025.
(292) Liu, Z.; Sakamoto, Y.; Ohsuna, T.; Hiraga, K.; Terasaki, O.; Ko, C. H.; Shin, H. J.; Ryoo, R. TEM Studies of Platinum Nanowires Fabricated in Mesoporous Silica MCM-41. *Angewandte Chemie* **2000**, *39* (17), 3107–3110. https://doi.org/10.1002/1521-3773(20000901)39:17<3107::AID-ANIE3107>3.0.CO;2-J.
(293) Takai, A.; Doi, Y.; Yamauchi, Y.; Kuroda, K. Soft-Chemical Approach of Noble Metal Nanowires Templated from Mesoporous Silica (SBA-15) through Vapor Infiltration of a Reducing Agent. *The Journal of Physical Chemistry C* **2010**, *114* (17), 7586–7593. https://doi.org/10.1021/jp910288x.
(294) Doi, Y.; Takai, A.; Sakamoto, Y.; Terasaki, O.; Yamauchi, Y.; Kuroda, K. Tailored Synthesis of Mesoporous Platinum Replicas Using Double Gyroid Mesoporous Silica (KIT-6) with Different Pore Diameters via Vapor Infiltration of a Reducing Agent. *Chemical Communications* **2010**, *46* (34), 6365–6367. https://doi.org/10.1039/c0cc01196g.
(295) Guo, X.-J.; Yang, C.-M.; Liu, P.-H.; Cheng, M.-H.; Chao, K.-J. Formation and Growth of Platinum Nanostructures in Cubic Mesoporous Silica. *Crystal Growth & Design* **2005**, *5* (1), 33–36. https://doi.org/10.1021/cg0499414.

(296) Wang, H.; Jeong, H. Y.; Imura, M.; Wang, L.; Radhakrishnan, L.; Fujita, N.; Castle, T.; Terasaki, O.; Yamauchi, Y. Shape- and Size-Controlled Synthesis in Hard Templates: Sophisticated Chemical Reduction for Mesoporous Monocrystalline Platinum Nanoparticles. *J Am Chem Soc* **2011**, *133* (37), 14526–14529. https://doi.org/10.1021/ja2058617.
(297) Ding, J. H.; Gin, D. L. Catalytic Pd Nanoparticles Synthesized Using a Lyotropic Liquid Crystal Polymer Template. *Chemistry of Materials* **2000**, *12* (1), 22–24. https://doi.org/10.1021/cm990603d.
(298) Kijima, T.; Yoshimura, T.; Uota, M.; Ikeda, T.; Fujikawa, D.; Mouri, S.; Uoyama, S. Noble-Metal Nanotubes (Pt, Pd, Ag) from Lyotropic Mixed-Surfactant Liquid-Crystal Templates. *Angewandte Chemie* **2004**, *116* (2), 230–234. https://doi.org/10.1002/ange.200352630.
(299) Attard, G. S.; Bartlett, P. N.; Coleman, N. R. B.; Elliott, J. M.; Owen, J. R.; Wang, J. H. Mesoporous Platinum Films from Lyotropic Liquid Crystalline Phases. *Science (1979)* **1997**, *278* (5339), 838–840. https://doi.org/10.1126/science.278.5339.838.
(300) Bartlett, P. N.; Gollas, B.; Guerin, S.; Marwan, J. The Preparation and Characterisation of H1-e Palladium Films with a Regular Hexagonal Nanostructure Formed by Electrochemical Deposition from Lyotropic Liquid Crystalline Phases. *Physical Chemistry Chemical Physics* **2002**, *4* (15), 3835–3842. https://doi.org/10.1039/b201845d.
(301) Bender, F.; Mankelow, R. K.; Hibbert, D. B.; Gooding, J. J. Lyotropic Liquid Crystal Templating of Groups 11 and 12 Metal Films. *Electroanalysis* **2006**, *18* (16), 1558–1563. https://doi.org/10.1002/elan.200603585.
(302) Luo, K.; Walker, C. T.; Edler, K. J. Mesoporous Silver Films from Dilute Mixed-Surfactant Solutions by Using Dip-Coating. *Advanced Materials* **2007**, *19* (11), 1506–1509. https://doi.org/10.1002/adma.200601244.
(303) Ullah, M. H.; Chung, W.-S.; Kim, I.; Ha, C.-S. PH-Selective Synthesis of Monodisperse Nanoparticles and 3D Dendritic Nanoclusters of CTAB-Stabilized Platinum for Electrocatalytic O2 Reduction. *Small* **2006**, *2* (7), 870–873. https://doi.org/10.1002/smll.200600071.
(304) Kani, K.; Zakaria, M. B.; Lin, J.; Alshehri, A. A.; Kim, J.; Bando, Y.; You, J.; Hossain, M. S. A.; Bo, J.; Yamauchi, Y. Synthesis and Characterization of Dendritic Pt Nanoparticles by Using Cationic Surfactant. *Bull Chem Soc Jpn* **2018**, *91* (9), 1333–1336. https://doi.org/10.1246/bcsj.20180129.
(305) Wang, L.; Yamauchi, Y. Synthesis of Mesoporous Pt Nanoparticles with Uniform Particle Size from Aqueous Surfactant Solutions toward Highly Active Electrocatalysts. *Chemistry - A European Journal* **2011**, *17* (32), 8810–8815. https://doi.org/10.1002/chem.201100386.
(306) Jiang, B.; Li, C.; Malgras, V.; Imura, M.; Tominaka, S.; Yamauchi, Y. Mesoporous Pt Nanospheres with Designed Pore Surface as Highly Active Electrocatalyst. *Chemical Science* **2016**, *7* (2), 1575–1581. https://doi.org/10.1039/c5sc03779d.
(307) Li, Y.; Liu, Y.; Yamauchi, Y.; Kaneti, Y. V.; Alsheri, S. M.; Ahamad, T.; Alhokbany, N.; Kim, J.; Ariga, K.; Wu, N.; Xu, J. Micelle-Assisted Strategy for the Direct Synthesis of Large-Sized Mesoporous Platinum Catalysts by Vapor Infiltration of a Reducing Agent. *Nanomaterials* **2018**, *8* (10), 1–10. https://doi.org/10.3390/nano8100841.
(308) Wang, L.; Imura, M.; Yamauchi, Y. Tailored Design of Architecturally Controlled Pt Nanoparticles with Huge Surface Areas toward Superior Unsupported Pt Electrocatalysts. *ACS Applied Materials and Interfaces* **2012**, *4* (6), 2865–2869. https://doi.org/10.1021/am300574e.
(309) Lim, B.; Xia, Y. Metal Nanocrystals with Highly Branched Morphologies. *Angewandte Chemie - International Edition*. 2011, pp 76–85. https://doi.org/10.1002/anie.201002024.
(310) Teng, X.; Liang, X.; Maksimuk, S.; Yang, H. Synthesis of Porous Platinum Nanoparticles. *Small* **2006**, *2* (2), 249–253. https://doi.org/10.1002/smll.200500244.
(311) Yang, S.; Luo, X. Mesoporous Nano/Micro Noble Metal Particles: Synthesis and Applications. *Nanoscale* **2014**, *6* (9), 4438–4457. https://doi.org/10.1039/C3NR06858G.

(312) Erlebacher, J.; Aziz, M. J.; Karma, A.; Dimitrov, N.; Sieradzki, K. Evolution of Nanoporosity in Dealloying. *Nature* **2001**, *410* (6827), 450–453. https://doi.org/10.1038/35068529.
(313) Juarez, T.; Biener, J.; Weissmüller, J.; Hodge, A. M. Nanoporous Metals with Structural Hierarchy: A Review. *Advanced Engineering Materials* **2017**, *19* (12), 1–23. https://doi.org/10.1002/adem.201700389.
(314) Brust, M.; Walker, M.; Bethell, D.; Schiffrin, D. J.; Whyman, R. Synthesis of Thiol-Derivatised Gold Nanoparticles in a Two-Phase Liquid–Liquid System. *J. Chem. Soc., Chem. Commun.* **1994**, No. 7, 801–802. https://doi.org/10.1039/C39940000801.
(315) Jin, R.; Qian, H.; Wu, Z.; Zhu, Y.; Zhu, M.; Mohanty, A.; Garg, N. Size Focusing: A Methodology for Synthesizing Atomically Precise Gold Nanoclusters. *The Journal of Physical Chemistry Letters* **2010**, *1* (19), 2903–2910. https://doi.org/10.1021/jz100944k.
(316) Zeng, C.; Chen, Y.; Das, A.; Jin, R. Transformation Chemistry of Gold Nanoclusters: From One Stable Size to Another. *Journal of Physical Chemistry Letters* **2015**, *6* (15), 2976–2986. https://doi.org/10.1021/acs.jpclett.5b01150.
(317) Aiken, J. D.; Finke, R. G. A Review of Modern Transition-Metal Nanoclusters: Their Synthesis, Characterization, and Applications in Catalysis. *Journal of Molecular Catalysis A: Chemical* **1999**, *145* (1–2), 1–44. https://doi.org/10.1016/S1381-1169(99)00098-9.
(318) Chakraborty, I.; Pradeep, T. Atomically Precise Clusters of Noble Metals: Emerging Link between Atoms and Nanoparticles. *Chemical Reviews* **2017**, *117* (12), 8208–8271. https://doi.org/10.1021/acs.chemrev.6b00769.
(319) Jin, R.; Zeng, C.; Zhou, M.; Chen, Y. Atomically Precise Colloidal Metal Nanoclusters and Nanoparticles: Fundamentals and Opportunities. *Chemical Reviews*. 2016, pp 10346–10413. https://doi.org/10.1021/acs.chemrev.5b00703.
(320) Du, Y.; Sheng, H.; Astruc, D.; Zhu, M. Atomically Precise Noble Metal Nanoclusters as Efficient Catalysts: A Bridge between Structure and Properties. *Chemical Reviews* **2020**, *120* (2), 526–622. https://doi.org/10.1021/acs.chemrev.8b00726.
(321) Jin, R. Quantum Sized, Thiolate-Protected Gold Nanoclusters. *Nanoscale* **2010**, *2* (3), 343–362. https://doi.org/10.1039/b9nr00160c.
(322) Terrill, R. H.; Postlethwaite, T. A.; Chen, C. H.; Poon, C. D.; Terzis, A.; Chen, A.; Hutchison, J. E.; Clark, M. R.; Wignall, G.; Londono, J. D.; Falvo, M.; Johnson, C. S.; Samulski, E. T.; Murray, R. W.; Wignall, G.; Londono, J. D.; Terrill, R. H.; Postlethwaite, T. A.; Poon, C. D.; Terzis, A.; Chen, A.; Hutchison, J. E.; Clark, M. R.; Wignall, G.; Londono, J. D.; Superfine, R.; Falvo, M.; Johnson, C. S.; Samulski, E. T.; Murray, R. W. Monolayers in Three Dimensions: NMR, SAXS, Thermal, and Electron Hopping Studies of Alkanethiol Stabilized Gold Clusters. *J Am Chem Soc* **1995**, *117* (50), 12537–12548. https://doi.org/10.1021/ja00155a017.
(323) Alvarez, M. M.; Khoury, J. T.; Schaaff, T. G.; Shafigullin, M.; Vezmar, I.; Whetten, R. L. Critical Sizes in the Growth of Au Clusters. *Chemical Physics Letters* **1997**, *266* (1–2), 91–98. https://doi.org/10.1016/S0009-2614(96)01535-7.
(324) Donkers, R. L.; Lee, D.; Murray, R. W. Synthesis and Isolation of the Molecule-like Cluster Au38(PhCH2CH2S)24. *Langmuir* **2004**, *20* (5), 1945–1952. https://doi.org/10.1021/la035706w.
(325) Tracy, J. B.; Kalyuzhny, G.; Crowe, M. C.; Balasubramanian, R.; Choi, J.-P.; Murray, R. W. Poly(Ethylene Glycol) Ligands for High-Resolution Nanoparticle Mass Spectrometry. *J Am Chem Soc* **2007**, *129* (21), 6706–6707. https://doi.org/10.1021/ja071042r.
(326) Tracy, J. B.; Crowe, M. C.; Parker, J. F.; Hampe, O.; Fields-Zinna, C. A.; Dass, A.; Murray, R. W. Electrospray Ionization Mass Spectrometry of Uniform and Mixed Monolayer Nanoparticles: Au 25 [S(CH 2) 2 Ph] 18 and Au 25 [S(CH 2) 2 Ph] 18 - x (SR) x. *J Am Chem Soc* **2007**, *129* (51), 16209–16215. https://doi.org/10.1021/ja076621a.

(327) Negishi, Y.; Nobusada, K.; Tsukuda, T. Glutathione-Protected Gold Clusters Revisited: Bridging the Gap between Gold(I)-Thiolate Complexes and Thiolate-Protected Gold Nanocrystals. *J Am Chem Soc* **2005**, *127* (14), 5261–5270. https://doi.org/10.1021/ja042218h.
(328) Jadzinsky, P. D.; Calero, G.; Ackerson, C. J.; Bushnell, D. A.; Kornberg, R. D. Structure of a Thiol Monolayer-Protected Gold Nanoparticle at 1.1 Å Resolution. *Science (1979)* **2007**, *318* (5849), 430–433. https://doi.org/10.1126/science.1148624.
(329) Heaven, M. W.; Dass, A.; White, P. S.; Holt, K. M.; Murray, R. W. Crystal Structure of the Gold Nanoparticle [N(C 8 H 17) 4][Au 25 (SCH 2 CH 2 Ph) 18]. *J Am Chem Soc* **2008**, *130* (12), 3754–3755. https://doi.org/10.1021/ja800561b.
(330) Zhu, M.; Aikens, C. M.; Hollander, F. J.; Schatz, G. C.; Jin, R. Correlating the Crystal Structure of A Thiol-Protected Au25 Cluster and Optical Properties. *J Am Chem Soc* **2008**, *130* (18), 5883–5885. https://doi.org/10.1021/ja801173r.
(331) Zhu, M.; Lanni, E.; Garg, N.; Bier, M. E.; Jin, R. Kinetically Controlled, High-Yield Synthesis of Au25 Clusters. *J Am Chem Soc* **2008**, *130* (4), 1138–1139. https://doi.org/10.1021/ja0782448.
(332) Wu, Z.; Suhan, J.; Jin, R. One-Pot Synthesis of Atomically Monodisperse, Thiol-Functionalized Au 25 Nanoclusters. *Journal of Materials Chemistry* **2009**, *19* (5), 622–626. https://doi.org/10.1039/b815983a.
(333) Chaki, N. K.; Negishi, Y.; Tsunoyama, H.; Shichibu, Y.; Tsukuda, T. Ubiquitous 8 and 29 KDa Gold:Alkanethiolate Cluster Compounds: Mass-Spectrometric Determination of Molecular Formulas and Structural Implications. *J Am Chem Soc* **2008**, *130* (27), 8608–8610. https://doi.org/10.1021/ja8005379.
(334) Qian, H.; Zhu, Y.; Jin, R. Size-Focusing Synthesis, Optical and Electrochemical Properties of Monodisperse Au 38 (SC 2 H 4 Ph) 24 Nanoclusters. *ACS Nano* **2009**, *3* (11), 3795–3803. https://doi.org/10.1021/nn901137h.
(335) Qian, H.; Zhu, M.; Andersen, U. N.; Jin, R. Facile, Large-Scale Synthesis of Dodecanethiol-Stabilized Au 38 Clusters. *The Journal of Physical Chemistry A* **2009**, *113* (16), 4281–4284. https://doi.org/10.1021/jp810893w.
(336) Qian, H.; Jin, R. Controlling Nanoparticles with Atomic Precision: The Case of Au 144(SCH2CH2Ph)60. *Nano Letters* **2009**, *9* (12), 4083–4087. https://doi.org/10.1021/nl902300y.
(337) Dreier, T. A.; Ackerson, C. J. Radicals Are Required for Thiol Etching of Gold Particles. *Angewandte Chemie - International Edition* **2015**, *54* (32), 9249–9252. https://doi.org/10.1002/anie.201502934.
(338) Zeng, C.; Chen, Y.; Li, G.; Jin, R. Magic Size Au 64 (S- c -C 6 H 11) 32 Nanocluster Protected by Cyclohexanethiolate. *Chemistry of Materials* **2014**, *26* (8), 2635–2641. https://doi.org/10.1021/cm500139t.
(339) Liu, C.; Lin, J.; Shi, Y.; Li, G. Efficient Synthesis of Au99(SR)42 Nanoclusters. *Nanoscale* **2015**, *7* (14), 5987–5990. https://doi.org/10.1039/c5nr00543d.
(340) Li, G.; Zeng, C.; Jin, R. Thermally Robust Au 99 (SPh) 42 Nanoclusters for Chemoselective Hydrogenation of Nitrobenzaldehyde Derivatives in Water. *J Am Chem Soc* **2014**, *136* (9), 3673–3679. https://doi.org/10.1021/ja500121v.
(341) Qian, H.; Zhu, Y.; Jin, R. Atomically Precise Gold Nanocrystal Molecules with Surface Plasmon Resonance. *Proc Natl Acad Sci U S A* **2012**, *109* (3), 696–700. https://doi.org/10.1073/pnas.1115307109.
(342) Tvedte, L. M.; Ackerson, C. J. Size-Focusing Synthesis of Gold Nanoclusters with p -Mercaptobenzoic Acid. *Journal of Physical Chemistry A* **2014**, *118* (37), 8124–8128. https://doi.org/10.1021/jp5001946.

(343) Kumar, S.; Jin, R. Water-Soluble Au25(Capt)18 Nanoclusters: Synthesis, Thermal Stability, and Optical Properties. *Nanoscale* **2012**, *4* (14), 4222–4227. https://doi.org/10.1039/c2nr30833a.
(344) Chen, Y.; Zeng, C.; Kauffman, D. R.; Jin, R. Tuning the Magic Size of Atomically Precise Gold Nanoclusters via Isomeric Methylbenzenethiols. *Nano Letters* **2015**, *15* (5), 3603–3609. https://doi.org/10.1021/acs.nanolett.5b01122.
(345) Nimmala, P. R.; Dass, A. Au 99 (SPh) 42 Nanomolecules: Aromatic Thiolate Ligand Induced Conversion of Au 144 (SCH 2 CH 2 Ph) 60. *J Am Chem Soc* **2014**, *136* (49), 17016–17023. https://doi.org/10.1021/ja5103025.
(346) Zeng, C.; Chen, Y.; Das, A.; Jin, R. Transformation Chemistry of Gold Nanoclusters: From One Stable Size to Another. *Journal of Physical Chemistry Letters* **2015**, *6* (15), 2976–2986. https://doi.org/10.1021/acs.jpclett.5b01150.
(347) Zeng, C.; Li, T.; Das, A.; Rosi, N. L.; Jin, R. Chiral Structure of Thiolate-Protected 28-Gold-Atom Nanocluster Determined by X-Ray Crystallography. *J Am Chem Soc* **2013**, *135* (27), 10011–10013. https://doi.org/10.1021/ja404058q.
(348) Zeng, C.; Liu, C.; Chen, Y.; Rosi, N. L.; Jin, R. Gold-Thiolate Ring as a Protecting Motif in the Au20(SR) 16 Nanocluster and Implications. *J Am Chem Soc* **2014**, *136* (34), 11922–11925. https://doi.org/10.1021/ja506802n.
(349) Zeng, C.; Qian, H.; Li, T.; Li, G.; Rosi, N. L.; Yoon, B.; Barnett, R. N.; Whetten, R. L.; Landman, U.; Jin, R. Total Structure and Electronic Properties of the Gold Nanocrystal Au 36 (SR) 24. *Angewandte Chemie International Edition* **2012**, *51* (52), 13114–13118. https://doi.org/10.1002/anie.201207098.
(350) Zeng, C.; Chen, Y.; Kirschbaum, K.; Appavoo, K.; Sfeir, M. Y.; Jin, R. Structural Patterns at All Scales in a Nonmetallic Chiral Au133(SR)52 Nanoparticle. *Science Advances* **2015**, *1* (2), 1–7. https://doi.org/10.1126/sciadv.1500045.
(351) McPartlin, M.; Mason, R.; Malatesta, L. Novel Cluster Complexes of Gold(0)–Gold(I). *J. Chem. Soc. D* **1969**, No. 7, 334–334. https://doi.org/10.1039/C29690000334.
(352) Briant, C. E.; Theobald, B. R. C.; White, J. W.; Bell, L. K.; Mingos, D. M. P.; Welch, A. J. Synthesis and X-Ray Structural Characterization of the Centred Icosahedral Gold Cluster Compound [Au13(PMe2Ph)10Cl2](PF6)3; the Realization of a Theoretical Prediction. *Journal of the Chemical Society, Chemical Communications* **1981**, No. 5, 201. https://doi.org/10.1039/c39810000201.
(353) Shichibu, Y.; Konishi, K. HCl-Induced Nuclearity Convergence in Diphosphine-Protected Ultrasmall Gold Clusters: A Novel Synthetic Route to "Magic-Number" Au13 Clusters. *Small* **2010**, *6* (11), 1216–1220. https://doi.org/10.1002/smll.200902398.
(354) Kamei, Y.; Shichibu, Y.; Konishi, K. Generation of Small Gold Clusters with Unique Geometries through Cluster-to-Cluster Transformations: Octanuclear Clusters with Edge-Sharing Gold Tetrahedron Motifs. *Angewandte Chemie* **2011**, *123* (32), 7580–7583. https://doi.org/10.1002/ange.201102901.
(355) Shichibu, Y.; Zhang, M.; Kamei, Y.; Konishi, K. [Au7]3+: A Missing Link in the Four-Electron Gold Cluster Family. *J Am Chem Soc* **2014**, *136* (37), 12892–12895. https://doi.org/10.1021/ja508005x.
(356) Shichibu, Y.; Konishi, K. Electronic Properties of [Core+ Exo]-Type Gold Clusters: Factors Affecting the Unique Optical Transitions. *Inorganic Chemistry* **2013**, *52* (11), 6570–6575. https://doi.org/10.1021/ic4005592.
(357) Shichibu, Y.; Kamei, Y.; Konishi, K. Unique [Core+two] Structure and Optical Property of a Dodeca-Ligated Undecagold Cluster: Critical Contribution of the Exo Gold Atoms to the Electronic Structure. *Chemical Communications* **2012**, *48* (61), 7559–7561. https://doi.org/10.1039/c2cc30251a.
(358) McKenzie, L. C.; Zaikova, T. O.; Hutchison, J. E. Structurally Similar Triphenylphosphine-Stabilized Undecagolds, Au11(PPh3)7Cl3and [Au11(PPh3)8Cl2]Cl, Exhibit Distinct Ligand

Exchange Pathways with Glutathione. *J Am Chem Soc* **2014**, *136* (38), 13426–13435. https://doi.org/10.1021/ja5075689.
(359) Sarkar, A. K.; Pal, T. Thiol-Functionalized Undecagold Clusters by Ligand Exchange: Synthesis, Mechanism, and Properties. *Chemtracts* **2007**, *19* (5), 180–185.
(360) Woehrle, G. H.; Warner, M. G.; Hutchison, J. E. Ligand Exchange Reactions Yield Subnanometer, Thiol-Stabilized Gold Particles with Defined Optical Transitions. *Journal of Physical Chemistry B* **2002**, *106* (39), 9979–9981. https://doi.org/10.1021/jp025943s.
(361) Wan, X. K.; Yuan, S. F.; Lin, Z. W.; Wang, Q. M. A Chiral Gold Nanocluster Au20 Protected by Tetradentate Phosphine Ligands. *Angewandte Chemie - International Edition* **2014**, *53* (11), 2923–2926. https://doi.org/10.1002/anie.201308599.
(362) Chen, J.; Zhang, Q. F.; Williard, P. G.; Wang, L. S. Synthesis and Structure Determination of a New Au20 Nanocluster Protected by Tripodal Tetraphosphine Ligands. *Inorganic Chemistry* **2014**, *53* (8), 3932–3934. https://doi.org/10.1021/ic500562r.
(363) Chen, J.; Zhang, Q. F.; Bonaccorso, T. A.; Williard, P. G.; Wang, L. S. Controlling Gold Nanoclusters by Diphospine Ligands. *J Am Chem Soc* **2014**, *136* (1), 92–95. https://doi.org/10.1021/ja411061e.
(364) Maity, P.; Tsunoyama, H.; Yamauchi, M.; Xie, S.; Tsukuda, T. Organogold Clusters Protected by Phenylacetylene. *J Am Chem Soc* **2011**, *133* (50), 20123–20125. https://doi.org/10.1021/ja209236n.
(365) Maity, P.; Wakabayashi, T.; Ichikuni, N.; Tsunoyama, H.; Xie, S.; Yamauchi, M.; Tsukuda, T. Selective Synthesis of Organogold Magic Clusters Au54(C≡CPh)26. *Chemical Communications* **2012**, *48* (49), 6085–6087. https://doi.org/10.1039/c2cc18153c.
(366) Wan, X.-K.; Tang, Q.; Yuan, S.-F.; Jiang, D.; Wang, Q.-M. Au 19 Nanocluster Featuring a V-Shaped Alkynyl–Gold Motif. *J Am Chem Soc* **2015**, *137* (2), 652–655. https://doi.org/10.1021/ja512133a.
(367) Wan, X. K.; Yuan, S. F.; Tang, Q.; Jiang, D. E.; Wang, Q. M. Alkynyl-Protected Au23 Nanocluster: A 12-Electron System. *Angewandte Chemie - International Edition* **2015**, *54* (20), 5977–5980. https://doi.org/10.1002/anie.201500590.
(368) Wan, X. K.; Xu, W. W.; Yuan, S. F.; Gao, Y.; Zeng, X. C.; Wang, Q. M. A Near-Infrared-Emissive Alkynyl-Protected Au24 Nanocluster. *Angewandte Chemie - International Edition* **2015**, *54* (33), 9683–9686. https://doi.org/10.1002/anie.201503893.
(369) Wu, Z.; Lanni, E.; Chen, W.; Bier, M. E.; Ly, D.; Jin, R. High Yield, Large Scale Synthesis of Thiolate-Protected Ag7 Clusters. *J Am Chem Soc* **2009**, *131* (46), 16672–16674. https://doi.org/10.1021/ja907627f.
(370) Cathcart, N.; Mistry, P.; Makra, C.; Pietrobon, B.; Coombs, N.; Jelokhani-Niaraki, M.; Kitaev, V. Chiral Thiol-Stabilized Silver Nanoclusters with Well-Resolved Optical Transitions Synthesized by a Facile Etching Procedure in Aqueous Solutions. *Langmuir* **2009**, *25* (10), 5840–5846. https://doi.org/10.1021/la9005967.
(371) Cathcart, N.; Kitaev, V. Silver Nanoclusters: Single-Stage Scaleable Synthesis of Monodisperse Species and Their Chirooptical Properties. *Journal of Physical Chemistry C* **2010**, *114* (38), 16010–16017. https://doi.org/10.1021/jp101764q.
(372) Harkness, K. M.; Tang, Y.; Dass, A.; Pan, J.; Kothalawala, N.; Reddy, V. J.; Cliffel, D. E.; Demeler, B.; Stellacci, F.; Bakr, O. M.; McLean, J. A. Ag44(SR)304-: A Silver-Thiolate Superatom Complex. *Nanoscale* **2012**, *4* (14), 4269–4274. https://doi.org/10.1039/c2nr30773a.
(373) Bakr, O. M.; Amendola, V.; Aikens, C. M.; Wenseleers, W.; Li, R.; Negro, L. D.; Schatz, G. C.; Stellacci, F. Silver Nanoparticles with Broad Multiband Linear Optical Absorption. *Angewandte Chemie - International Edition* **2009**, *48* (32), 5921–5926. https://doi.org/10.1002/anie.200900298.

(374) Udaya Bhaskara Rao, T.; Pradeep, T. Luminescent Ag7 and Ag8 Clusters by Interfacial Synthesis. *Angewandte Chemie - International Edition* **2010**, *49* (23), 3925–3929. https://doi.org/10.1002/anie.200907120.
(375) Rao, T. U. B.; Nataraju, B.; Pradeep, T. Ag9 Quantum Cluster through a Solid-State Route. *J Am Chem Soc* **2010**, *132* (46), 16304–16307. https://doi.org/10.1021/ja105495n.
(376) Bootharaju, M. S.; Burlakov, V. M.; Besong, T. M. D.; Joshi, C. P.; Abdulhalim, L. G.; Black, D. M.; Whetten, R. L.; Goriely, A.; Bakr, O. M. Reversible Size Control of Silver Nanoclusters via Ligand-Exchange. *Chemistry of Materials* **2015**, *27* (12), 4289–4297. https://doi.org/10.1021/acs.chemmater.5b00650.
(377) Yuan, S. F.; Li, P.; Tang, Q.; Wan, X. K.; Nan, Z. A.; Jiang, D. E.; Wang, Q. M. Alkynyl-Protected Silver Nanoclusters Featuring an Anticuboctahedral Kernel. *Nanoscale* **2017**, *9* (32), 11405–11409. https://doi.org/10.1039/c7nr02687k.
(378) Qu, M.; Li, H.; Xie, L. H.; Yan, S. T.; Li, J. R.; Wang, J. H.; Wei, C. Y.; Wu, Y. W.; Zhang, X. M. Bidentate Phosphine-Assisted Synthesis of an All-Alkynyl-Protected Ag74 Nanocluster. *J Am Chem Soc* **2017**, *139* (36), 12346–12349. https://doi.org/10.1021/jacs.7b05243.
(379) Yang, H.; Yan, J.; Wang, Y.; Deng, G.; Su, H.; Zhao, X.; Xu, C.; Teo, B. K.; Zheng, N. From Racemic Metal Nanoparticles to Optically Pure Enantiomers in One Pot. *J Am Chem Soc* **2017**, *139* (45), 16113–16116. https://doi.org/10.1021/jacs.7b10448.
(380) Wang, Z. Y.; Wang, M. Q.; Li, Y. L.; Luo, P.; Jia, T. T.; Huang, R. W.; Zang, S. Q.; Mak, T. C. W. Atomically Precise Site-Specific Tailoring and Directional Assembly of Superatomic Silver Nanoclusters. *J Am Chem Soc* **2018**, *140* (3), 1069–1076. https://doi.org/10.1021/jacs.7b11338.
(381) Shen, X.-T.; Ma, X.-L.; Ni, Q.-L.; Ma, M.-X.; Gui, L.-C.; Hou, C.; Hou, R.-B.; Wang, X.-J. [Ag 15 (N-Triphos) 4 (Cl 4)](NO 3) 3 : A Stable Ag–P Superatom with Eight Electrons (N-Triphos = Tris((Diphenylphosphino)Methyl)Amine). *Nanoscale* **2018**, *10* (2), 515–519. https://doi.org/10.1039/C7NR07308A.
(382) Liu, C.; Li, T.; Abroshan, H.; Li, Z.; Zhang, C.; Kim, H. J.; Li, G.; Jin, R. Chiral Ag 23 Nanocluster with Open Shell Electronic Structure and Helical Face-Centered Cubic Framework. *Nature Communications* **2018**, *9* (1). https://doi.org/10.1038/s41467-018-03136-9.
(383) Du, W.; Jin, S.; Xiong, L.; Chen, M.; Zhang, J.; Zou, X.; Pei, Y.; Wang, S.; Zhu, M. Ag 50 (Dppm) 6 (SR) 30 and Its Homologue Au x Ag 50– x (Dppm) 6 (SR) 30 Alloy Nanocluster: Seeded Growth, Structure Determination, and Differences in Properties. *J Am Chem Soc* **2017**, *139* (4), 1618–1624. https://doi.org/10.1021/jacs.6b11681.
(384) Chen, S.; Kimura, K. Synthesis of Thiolate-Stabilized Platinum Nanoparticles in Protolytic Solvents as Isolable Colloids. *The Journal of Physical Chemistry B* **2001**, *105* (23), 5397–5403. https://doi.org/10.1021/jp0037798.
(385) Kawasaki, H.; Yamamoto, H.; Fujimori, H.; Arakawa, R.; Inada, M.; Iwasaki, Y. Surfactant-Free Solution Synthesis of Fluorescent Platinum Subnanoclusters. *Chemical Communications* **2010**, *46* (21), 3759–3761. https://doi.org/10.1039/b925117k.
(386) le Guével, X.; Trouillet, V.; Spies, C.; Jung, G.; Schneider, M. Synthesis of Yellow-Emitting Platinum Nanoclusters by Ligand Etching. *The Journal of Physical Chemistry C* **2012**, *116* (10), 6047–6051. https://doi.org/10.1021/jp211672t.
(387) Tanaka, S. I.; Miyazaki, J.; Tiwari, D. K.; Jin, T.; Inouye, Y. Fluorescent Platinum Nanoclusters: Synthesis, Purification, Characterization, and Application to Bioimaging. *Angewandte Chemie - International Edition* **2011**, *50* (2), 431–435. https://doi.org/10.1002/anie.201004907.
(388) Chakraborty, I.; Bhuin, R. G.; Bhat, S.; Pradeep, T. Blue Emitting Undecaplatinum Clusters. *Nanoscale* **2014**, *6* (15), 8561–8564. https://doi.org/10.1039/c4nr02778g.

(389) Takahashi, M.; Imaoka, T.; Hongo, Y.; Yamamoto, K. Formation of a Pt12 Cluster by Single-Atom Control That Leads to Enhanced Reactivity: Hydrogenation of Unreactive Olefins. *Angewandte Chemie - International Edition* **2013**, *52* (29), 7419–7421. https://doi.org/10.1002/anie.201302860.
(390) Imaoka, T.; Kitazawa, H.; Chun, W. J.; Yamamoto, K. Finding the Most Catalytically Active Platinum Clusters with Low Atomicity. *Angewandte Chemie - International Edition* **2015**, *54* (34), 9810–9815. https://doi.org/10.1002/anie.201504473.
(391) Zhuang, Z.; Du, C.; Li, P.; Zhang, Z.; Fang, Z.; Guo, J.; Chen, W. Pt21(C4O4SH5)21 Clusters: Atomically Precise Synthesis and Enhanced Electrocatalytic Activity for Hydrogen Generation. *Electrochimica Acta* **2021**, *368*, 137608. https://doi.org/10.1016/j.electacta.2020.137608.
(392) Wang, X.; Zhao, L.; Li, X.; Liu, Y.; Wang, Y.; Yao, Q.; Xie, J.; Xue, Q.; Yan, Z.; Yuan, X.; Xing, W. Atomic-Precision Pt6 Nanoclusters for Enhanced Hydrogen Electro-Oxidation. *Nature Communications* **2022**, *13* (1), 1–10. https://doi.org/10.1038/s41467-022-29276-7.
(393) Chen, D.; Zhao, C.; Ye, J.; Li, Q.; Liu, X.; Su, M.; Jiang, H.; Amatore, C.; Selke, M.; Wang, X. In Situ Biosynthesis of Fluorescent Platinum Nanoclusters: Toward Self-Bioimaging-Guided Cancer Theranostics. *ACS Applied Materials and Interfaces* **2015**, *7* (32), 18163–18169. https://doi.org/10.1021/acsami.5b05805.
(394) Hackendorn, R. A.; Virkar, A. v. Synthesis of Platinum Nanoclusters and Electrochemical Investigation of Their Stability. *Journal of Power Sources* **2013**, *240*, 618–629. https://doi.org/10.1016/j.jpowsour.2013.05.028.
(395) Wettergren, K.; Schweinberger, F. F.; Deiana, D.; Ridge, C. J.; Crampton, A. S.; Rötzer, M. D.; Hansen, T. W.; Zhdanov, V. P.; Heiz, U.; Langhammer, C. High Sintering Resistance of Size-Selected Platinum Cluster Catalysts by Suppressed Ostwald Ripening. *Nano Letters* **2014**, *14* (10), 5803–5809. https://doi.org/10.1021/nl502686u.
(396) Huang, X.; Ishitobi, H.; Inouye, Y. Formation of Fluorescent Platinum Nanoclusters Using Hyper-Branched Polyethylenimine and Their Conjugation to Antibodies for Bio-Imaging. *RSC Advances* **2016**, *6* (12), 9709–9716. https://doi.org/10.1039/c5ra24522b.
(397) Zhao, J.; Liu, J.; Jin, C.; Wang, F. Subnanoscale Platinum by Repeated UV Irradiation: From One and Few Atoms to Clusters for the Automotive PEMFC. *ACS Applied Materials and Interfaces* **2021**, *13* (7), 8395–8404. https://doi.org/10.1021/acsami.0c20935.
(398) Zamborini, F. P.; Gross, S. M.; Murray, R. W. Synthesis, Characterization, Reactivity, and Electrochemistry of Palladium Monolayer Protected Clusters. *Langmuir* **2001**, *17* (2), 481–488. https://doi.org/10.1021/la0010525.
(399) Negishi, Y.; Murayama, H.; Tsukuda, T. Formation of Pdn(SR)m Clusters (N<60) in the Reactions of PdCl2 and RSH (R=n-C18H37, n-C12H25). *Chemical Physics Letters* **2002**, *366* (5–6), 561–566. https://doi.org/10.1016/S0009-2614(02)01643-3.
(400) Zhao, S.; Zhang, H.; House, S. D.; Jin, R.; Yang, J. C.; Jin, R. Ultrasmall Palladium Nanoclusters as Effective Catalyst for Oxygen Reduction Reaction. *ChemElectroChem* **2016**, *3* (8), 1225–1229. https://doi.org/10.1002/celc.201600053.
(401) Zhang, L.; Hu, Q.; Li, Z.; Zhang, Y.; Lu, D.; Shuang, S.; Choi, M. M. F.; Dong, C. Chromatographic Separation and Mass Spectrometric Analysis of: N -Acetyl-l-Cysteine-Protected Palladium Nanoparticles. *Analytical Methods* **2017**, *9* (31), 4539–4546. https://doi.org/10.1039/c7ay01146f.
(402) Eswaramoorthy, S. K.; Dass, A. Atomically Precise Palladium Nanoclusters with 21 and 38 Pd Atoms Protected by Phenylethanethiol. *Journal of Physical Chemistry C* **2022**, *126* (1), 444–450. https://doi.org/10.1021/acs.jpcc.1c09453.
(403) Zhuang, Z.; Yang, Q.; Chen, W. One-Step Rapid and Facile Synthesis of Subnanometer-Sized Pd6(C12H25S)11 Clusters with Ultra-High Catalytic Activity for 4-Nitrophenol Reduction. *ACS Sustainable Chemistry and Engineering* **2019**, *7* (3), 2916–2923. https://doi.org/10.1021/acssuschemeng.8b06637.

(404) Mednikov, E. G.; Dahl, L. F. Syntheses, Structures and Properties of Primarily Nanosized Homo/Heterometallic Palladium CO/PR 3-Ligated Clusters. *Philosophical Transactions of the Royal Society A: Mathematical, Physical and Engineering Sciences* **2010**, *368* (1915), 1301–1332. https://doi.org/10.1098/rsta.2009.0272.
(405) Erickson, J. D.; Mednikov, E. G.; Ivanov, S. A.; Dahl, L. F. Isolation and Structural Characterization of a Mackay 55-Metal-Atom Two-Shell Icosahedron of Pseudo-Ih Symmetry, Pd55L12(M3-CO)20 (L = PR3, R = Isopropyl): Comparative Analysis with Interior Two-Shell Icosahedral Geometries in Capped Three-Shell Pd145, Pt. *J Am Chem Soc* **2016**, *138* (5), 1502–1505. https://doi.org/10.1021/jacs.5b13076.
(406) Mednikov, E. G.; Dahl, L. F. Palladium: It Forms Unique Nanosized Carbonyl Clusters. *Journal of Chemical Education* **2009**, *86* (10), 1135. https://doi.org/10.1021/ed086p1135.
(407) Mednikov, E. G.; Jewell, M. C.; Dahl, L. F. Nanosized (M12-Pt)Pd164-XPtx(CO) 72(PPh3)20 (x ≈ 7) Containing Pt-Centered Four-Shell 165-Atom Pd-Pt Core with Unprecedented Intershell Bridging Carbonyl Ligands: Comparative Analysis of Icosahedral Shell-Growth Patterns with Geometrically Related (...). *J Am Chem Soc* **2007**, *129* (37), 11619–11630. https://doi.org/10.1021/ja073945q.
(408) Jain, V. K.; Jain, L. The Chemistry of Tri- and High-Nuclearity Palladium(II) and Platinum(II) Complexes. *Coordination Chemistry Reviews* **2010**, *254* (23–24), 2848–2903. https://doi.org/10.1016/j.ccr.2010.05.010.
(409) Hayter, R. G.; Humiec, F. S. Some Mercaptides and Mercaptide Complexes of Nickel and Palladium. *Journal of Inorganic and Nuclear Chemistry* **1964**, *26* (5), 807–810. https://doi.org/10.1016/0022-1902(64)80326-2.
(410) Mann, F. G.; Purdie, D. The Constitution of Complex Metallic Salts. Part III. The Parachors of Palladium and Mercury in Simple and Complex Compounds. *Journal of the Chemical Society (Resumed)* **1935**, 1549. https://doi.org/10.1039/jr9350001549.
(411) Woodward, P.; Dahl, L. F.; Abel, E. W.; Crosse, B. C. A New Type of Cyclic Transition Metal Complex, [Ni(SC 2 H 5) 2] 6. *J Am Chem Soc* **1965**, *87* (22), 5251–5253. https://doi.org/10.1021/ja00950a049.
(412) Abel, E. W.; Crosse, B. C. Cyclic Hexameric Mercaptides of Nickel. *Journal of the Chemical Society A: Inorganic, Physical, Theoretical* **1966**, 1377–1378. https://doi.org/10.1039/J19660001377.
(413) Dance, I. G.; Scudder, M. L.; Secomb, R. C-Ni8(SCH2COOEt)16, a Receptive Octagonal Toroid. *Inorganic Chemistry* **1985**, *24* (8), 1201–1208. https://doi.org/10.1021/ic00202a018.
(414) Bowmaker, G.; Tan, L. The Preparation and Low-Frequency Vibrational Spectra of Some Copper(I) and Silver(I) Alkane- and Arene-Monothiolate Complexes. *Australian Journal of Chemistry* **1979**, *32* (7), 1443. https://doi.org/10.1071/CH9791443.
(415) Koo, B. K.; Block, E.; Kang, H.; Liu, S.; Zubieta, J. Syntheis and Structural Characterization of Cyclo-Pentakis [Bis(μ-Trimethylsilylthiomethane)Nickel(II)], [Ni(SCH2SiMe3)2]5, a Pentametallic Tiara Structure. *Polyhedron* **1988**, *7* (15), 1397–1399. https://doi.org/10.1016/S0277-5387(00)80392-7.
(416) Dance, I. G. The Hepta(μ-BenzenethioIato)Pentametallate(I) Dianions of Copper and Silver: Formation and Crystal Structures. *Australian Journal of Chemistry* **1978**, *31* (10), 2195–2206. https://doi.org/10.1071/CH9782195.
(417) Gould, R. O.; Harding, M. M. Nickel and Palladium Complexes of 1-Hydroxyethane-2-Thiol and Analogues. Part I. Crystal Structure of Cyclohexakis[Bis-(μ-1-Hydroxyethane-2-Thiolato)-Nickel(<scp>II</Scp>)]. *J. Chem. Soc. A* **1970**, 875–881. https://doi.org/10.1039/J19700000875.
(418) Abel, E. W.; Jenkins, C. R. Interaction of Thiosilanes and Disilthianes with Some Transitional and Post-Transitional Metal Halides. *Journal of Organometallic Chemistry* **1968**, *14* (2), 285–289. https://doi.org/10.1016/S0022-328X(00)87668-8.

(419) Akerstrom, S. Silver Alkylmercaptides. *Acta Chem. Scand.* **1964**, *18*, 1308. https://doi.org/10.3891/acta.chem.scand.18-1308.
(420) Higgins, J. D.; William Suggs, J. Preparation, Structure and Spectroscopic Studies of the Palladium Mercaptides Pd8(S-NPr)16 and Pd6(S-NPr)12. *Inorganica Chimica Acta* **1988**, *145* (2), 247–252. https://doi.org/10.1016/S0020-1693(00)83966-3.
(421) Handa, M.; Mikuriya, M.; Okawa, H.; Kida, S. Thiolate-Bridged Binuclear Nickel(II) Complex with Thioether Pendant Groups. *Chemistry Letters* **1988**, *17* (9), 1555–1558. https://doi.org/10.1246/cl.1988.1555.
(422) Capdevila, M.; González-Duarte, P.; Sola, J.; Foces-Foces, C.; Cano, F. H.; Martínez-Ripoll, M. Preparation and X-Ray Crystal Structure of [Ni6{μ-S(CH2)3N(CH3)2}12], a Cyclic Hexameric Homothiolate of Nickel. *Polyhedron* **1989**, *8* (10), 1253–1259. https://doi.org/10.1016/S0277-5387(00)86522-5.
(423) Krebs, B.; Henkel, G. Übergangsmetallthiolate - von Molekularen Fragmenten Sulfidischer Festkörper Zu Modellen Aktiver Zentren in Biomolekülen. *Angewandte Chemie* **1991**, *103* (7), 785–804. https://doi.org/10.1002/ange.19911030708.
(424) Power, P. P.; Shoner, S. C. Die Neutralen Übergangsmetallthiolate [{M(SAr)2}2] (M = Mn, Fe, Co; Ar = 2,4,6-TBu3C6H2). *Angewandte Chemie* **1991**, *103* (3), 308–309. https://doi.org/10.1002/ange.19911030310.
(425) Chen, J.; Liu, L.; Liu, X.; Liao, L.; Zhuang, S.; Zhou, S.; Yang, J.; Wu, Z. Gold-Doping of Double-Crown Pd Nanoclusters. *Chemistry - A European Journal* **2017**, *23* (72), 18187–18192. https://doi.org/10.1002/chem.201704413.
(426) Lee, S. C.; Holm, R. H. The Clusters of Nitrogenase: Synthetic Methodology in the Construction of Weak-Field Clusters. *Chemical Reviews* **2004**, *104* (2), 1135–1157. https://doi.org/10.1021/cr0206216.
(427) Henkel, G.; Krebs, B. Metallothioneins: Zinc, Cadmium, Mercury, and Copper Thiolates and Selenolates Mimicking Protein Active Site Features - Structural Aspects and Biological Implications. *Chemical Reviews* **2004**, *104* (2), 801–824. https://doi.org/10.1021/cr020620d.
(428) Zhang, C.; Takada, S.; Kölzer, M.; Matsumoto, T.; Tatsumi, K. Nickel(II) Thiolate Complexes with a Flexible Cyclo-{Ni10S 20} Framework. *Angewandte Chemie - International Edition* **2006**, *45* (23), 3768–3772. https://doi.org/10.1002/anie.200600319.
(429) Tan, C.; Jin, M.; Ma, X.; Zhu, Q.; Huang, Y.; Wang, Y.; Hu, S.; Sheng, T.; Wu, X. In Situ Synthesis of Nickel Tiara-like Clusters with Two Different Thiolate Bridges. *Dalton Transactions* **2012**, *41* (27), 8472–8476. https://doi.org/10.1039/c2dt30524k.
(430) Chui, S. S. Y.; Low, K. H.; Lu, J.; Roy, V. A. L.; Chan, S. L. F.; Che, C. M. Homoleptic Platinum(II) and Palladium(II) Organothiolates and Phenylselenolates: Solvothermal Synthesis, Structural Determination, Optical Properties, and Single-Source Precursors for PdSe and PdS Nanocrystals. *Chemistry - An Asian Journal* **2010**, *5* (9), 2062–2074. https://doi.org/10.1002/asia.201000233.
(431) Rauchfuss, T. B.; Shu, J. Shing.; Roundhill, D. Max. Synthesis and Chemistry of New Nickel, Palladium, and Platinum Complexes of 1,2-Ethanedithiol, 1,3-Propanedithiol, 1,4-Butanedithiol, 1,4,8-Trithianonane, and 1,4,8,11-Tetrathiaundecane. *Inorganic Chemistry* **1976**, *15* (9), 2096–2101. https://doi.org/10.1021/ic50163a017.
(432) Peach, M. E. Thermal Decomposition of Some Metal Mercaptides, M(SC6Hal5), Hal = F, Cl. *Journal of Inorganic and Nuclear Chemistry* **1973**, *35* (3), 1046–1048. https://doi.org/10.1016/0022-1902(73)80483-X.
(433) Beck, W.; Stetter, K. H.; Tadros, S.; Schwarzhans, K. E. Darstellung, IR- Und 19 F-KMR-Spektren von Pentafluorphenylmercapto-Metallkomplexen. *Chem Ber* **1967**, *100* (12), 3944–3954. https://doi.org/10.1002/cber.19671001215.
(434) Yamashina, Y.; Kataoka, Y.; Ura, Y. Tiara-like Octanuclear Palladium(II) and Platinum(II) Thiolates and Their Inclusion Complexes with Dihalo- or Iodoalkanes. *Inorganic Chemistry* **2014**, *53* (7), 3558–3567. https://doi.org/10.1021/ic403050c.

(435) Imaoka, T.; Akanuma, Y.; Haruta, N.; Tsuchiya, S.; Ishihara, K.; Okayasu, T.; Chun, W. J.; Takahashi, M.; Yamamoto, K. Platinum Clusters with Precise Numbers of Atoms for Preparative-Scale Catalysis. *Nature Communications* **2017**, *8* (1), 1–8. https://doi.org/10.1038/s41467-017-00800-4.
(436) Shichibu, Y.; Yoshida, K.; Konishi, K. Hexanuclear Platinum(II) Thiolate Macrocyclic Host: Charge-Transfer- Driven Inclusion of a AgI Ion Guest. *Inorganic Chemistry* **2016**, *55* (18), 9147–9149. https://doi.org/10.1021/acs.inorgchem.6b01579.
(437) Chen, J.; Liu, L.; Weng, L.; Lin, Y.; Liao, L.; Wang, C.; Yang, J.; Wu, Z. Synthesis and Properties Evolution of a Family of Tiara-like Phenylethanethiolated Palladium Nanoclusters. *Scientific Reports* **2015**, *5* (October), 4–11. https://doi.org/10.1038/srep16628.
(438) Chen, J.; Pan, Y.; Wang, Z.; Zhao, P. The Fluorescence Properties of Tiara like Structural Thiolated Palladium Clusters. *Dalton Transactions* **2017**, *46* (38), 12964–12970. https://doi.org/10.1039/c7dt02836a.
(439) Pembere, A. M. S.; Cui, C.; Anumula, R.; Wu, H.; An, P.; Liang, T.; Luo, Z. A Hexagonal Ni 6 Cluster Protected by 2-Phenylethanethiol for Catalytic Conversion of Toluene to Benzaldehyde. *Physical Chemistry Chemical Physics* **2019**, *21* (32), 17933–17938. https://doi.org/10.1039/C9CP02964H.
(440) Maman, M. P.; Nath, A.; Anjusree S; Das, B. C.; Mandal, S. Reversible Polymorphic Structural Transition of Crown-like Nickel Nanoclusters and Its Effect on Conductivity. *Chemical Communications* **2021**, *57* (23), 2935–2938. https://doi.org/10.1039/d1cc00402f.
(441) Kauffman, D. R.; Alfonso, D.; Tafen, D. N.; Lekse, J.; Wang, C.; Deng, X.; Lee, J.; Jang, H.; Lee, J. S.; Kumar, S.; Matranga, C. Electrocatalytic Oxygen Evolution with an Atomically Precise Nickel Catalyst. *ACS Catalysis* **2016**, *6* (2), 1225–1234. https://doi.org/10.1021/acscatal.5b02633.
(442) Chan, S. L.-F.; Shek, L.; Huang, J.-S.; Chui, S. S.-Y.; Sun, R. W.-Y.; Che, C.-M. Molecular Wheels of Ruthenium and Osmium with Bridging Chalcogenolate Ligands: Edge-Shared-Octahedron Structures and Metal-Ion Binding. *Angewandte Chemie* **2012**, *124* (11), 2668–2671. https://doi.org/10.1002/ange.201106065.
(443) Wang, J.; Jian, F.; Huang, B.; Bai, Z. Two Molecular Wheels 12-MC-6 Complexes: Synthesis, Structure and Magnetic Property of [Co(M2-SEt)2]6 and [Fe(M2-SEt)2]6. *Journal of Solid State Chemistry* **2013**, *204*, 272–277. https://doi.org/10.1016/j.jssc.2013.06.007.
(444) Taylor, H. S. A Theory of the Catalytic Surface. *Proceedings of the Royal Society of London. Series A* **1925**, *108* (745), 105–111. https://doi.org/10.1098/rspa.1925.0061.
(445) Védrine, J. C. Revisiting Active Sites in Heterogeneous Catalysis: Their Structure and Their Dynamic Behaviour. *Applied Catalysis A: General* **2014**, *474*, 40–50. https://doi.org/10.1016/j.apcata.2013.05.029.
(446) Han, P.; Axnanda, S.; Lyubinetsky, I.; Goodman, D. W. Atomic-Scale Assembly of a Heterogeneous Catalytic Site. *J Am Chem Soc* **2007**, *129* (46), 14355–14361. https://doi.org/10.1021/ja074891n.
(447) Neurock, M. Perspectives on the First Principles Elucidation and the Design of Active Sites. *Journal of Catalysis* **2003**, *216* (1–2), 73–88. https://doi.org/10.1016/S0021-9517(02)00115-X.
(448) Langmuir, I. THE CONSTITUTION AND FUNDAMENTAL PROPERTIES OF SOLIDS AND LIQUIDS. PART I. SOLIDS. *J Am Chem Soc* **1916**, *38* (11), 2221–2295. https://doi.org/10.1021/ja02268a002.
(449) Somorjai, G. A.; Li, Y. Impact of Surface Chemistry. *Proc Natl Acad Sci U S A* **2011**, *108* (3), 917–924. https://doi.org/10.1073/pnas.1006669107.
(450) Jin, R.; Li, G.; Sharma, S.; Li, Y.; Du, X. Toward Active-Site Tailoring in Heterogeneous Catalysis by Atomically Precise Metal Nanoclusters with Crystallographic Structures. *Chemical Reviews* **2021**, *121* (2), 567–648. https://doi.org/10.1021/acs.chemrev.0c00495.

(451) Herman, R. G.; Klier, K.; Simmons, G. W.; Finn, B. P.; Bulko, J. B.; Kobylinski, T. P. Catalytic Synthesis of Methanol from CO/H2. I. Phase Composition, Electronic Properties and Activity of the Cu/ZnO/M2O3 Catalysts. *Preprints (Basel)* **1978**, *23* (2), 595–615.
(452) Grabow, L. C.; Mavrikakis, M. Mechanism of Methanol Synthesis on Cu through CO2 and CO Hydrogenation. *ACS Catalysis* **2011**, *1* (4), 365–384. https://doi.org/10.1021/cs200055d.
(453) Jacobsen, C. J. H.; Dahl, S.; Hansen, P. L.; Törnqvist, E.; Jensen, L.; Topsøe, H.; Prip, D. v.; Møenshaug, P. B.; Chorkendorff, I. Structure Sensitivity of Supported Ruthenium Catalysts for Ammonia Synthesis. *Journal of Molecular Catalysis A: Chemical* **2000**, *163* (1–2), 19–26. https://doi.org/10.1016/S1381-1169(00)00396-4.
(454) Miyazaki, A.; Balint, I.; Aika, K. I.; Nakano, Y. Preparation of Ru Nanoparticles Supported on γ-Al2O3 and Its Novel Catalytic Activity for Ammonia Synthesis. *Journal of Catalysis* **2001**, *204* (2), 364–371. https://doi.org/10.1006/jcat.2001.3418.
(455) Molnár, Á.; Sárkány, A.; Varga, M. Hydrogenation of Carbon-Carbon Multiple Bonds: Chemo-, Regio- and Stereo-Selectivity. *Journal of Molecular Catalysis A: Chemical* **2001**, *173* (1–2), 185–221. https://doi.org/10.1016/S1381-1169(01)00150-9.
(456) Lin, S. D.; Vannice, M. A. Hydrogenation of Aromatic Hydrocarbons over Supported Pt Catalysts .I. Benzene Hydrogenation. *Journal of Catalysis* **1993**, *143* (2), 539–553. https://doi.org/10.1006/jcat.1993.1297.
(457) Campbell, C. T.; Paffett, M. T. Model Studies of Ethylene Epoxidation Catalyzed by the Ag(110) Surface. *Surface Science* **1984**, *139* (2–3), 396–416. https://doi.org/10.1016/0039-6028(84)90059-1.
(458) Tollefson, J. Worth Its Weight in Platinum. *Nature* **2007**, *450* (7168), 334–335. https://doi.org/10.1038/450334a.
(459) Debe, M. K. Electrocatalyst Approaches and Challenges for Automotive Fuel Cells. *Nature* **2012**, *486* (7401), 43–51. https://doi.org/10.1038/nature11115.
(460) Hansen, T. W.; Delariva, A. T.; Challa, S. R.; Datye, A. K. Sintering of Catalytic Nanoparticles: Particle Migration or Ostwald Ripening? *Accounts of Chemical Research* **2013**, *46* (8), 1720–1730. https://doi.org/10.1021/ar3002427.
(461) Spencer, N. D.; Schoonmaker, R. C.; Somorjai, G. A. Structure Sensitivity in the Iron Single-Crystal Catalysed Synthesis of Ammonia. *Nature* **1981**, *294* (5842), 643–644. https://doi.org/10.1038/294643a0.
(462) Furuya, N.; Koide, S. Hydrogen Adsorption on Platinum Single-Crystal Surfaces. *Surface Science* **1989**, *220* (1), 18–28. https://doi.org/10.1016/0039-6028(89)90460-3.
(463) McCabe, R. W.; Schmidt, L. D. Binding States of CO on Single Crystal Planes of Pt. *Surface Science* **1977**, *66* (1), 101–124. https://doi.org/10.1016/0039-6028(77)90402-2.
(464) Marković, N. M.; Adžić, R. R.; Cahan, B. D.; Yeager, E. B. Structural Effects in Electrocatalysis: Oxygen Reduction on Platinum Low Index Single-Crystal Surfaces in Perchloric Acid Solutions. *Journal of Electroanalytical Chemistry* **1994**, *377* (1–2), 249–259. https://doi.org/10.1016/0022-0728(94)03467-2.
(465) Munnik, P.; de Jongh, P. E.; de Jong, K. P. Recent Developments in the Synthesis of Supported Catalysts. *Chemical Reviews* **2015**, *115* (14), 6687–6718. https://doi.org/10.1021/cr500486u.
(466) An, K.; Somorjai, G. A. Size and Shape Control of Metal Nanoparticles for Reaction Selectivity in Catalysis. *ChemCatChem* **2012**, *4* (10), 1512–1524. https://doi.org/10.1002/cctc.201200229.
(467) Sun, Y.; Xia, Y. Shape-Controlled Synthesis of Gold and Silver Nanoparticles. *Science (1979)* **2002**, *298* (5601), 2176–2179. https://doi.org/10.1126/science.1077229.
(468) Liz-Marzán, L. M. Nanometals: Formation and Color. *Materials Today*. February 2004, pp 26–31. https://doi.org/10.1016/S1369-7021(04)00080-X.
(469) Ding, K.; Cullen, D. A.; Zhang, L.; Cao, Z.; Roy, A. D.; Ivanov, I. N.; Cao, D. A General Synthesis Approach for Supported Bimetallic Nanoparticles via Surface Inorganometallic

Chemistry. *Science (1979)* **2018**, *362* (6414), 560–564. https://doi.org/10.1126/science.aau4414.
(470) Shi, S.; Qin, D. Bifunctional Metal Nanocrystals for Catalyzing and Reporting on Chemical Reactions. *Angewandte Chemie International Edition* **2020**, *59* (10), 3782–3792. https://doi.org/10.1002/anie.201909615.
(471) Zeng, C.; Chen, Y.; Zhao, S.; Jin, R. Atomically Precise Gold and Bimetal Nanoclusters as New Model Catalysts. *Studies in Surface Science and Catalysis* **2017**, *177* (8), 359–408. https://doi.org/10.1016/B978-0-12-805090-3.00010-3.
(472) Tian, S.; Cao, Y.; Chen, T.; Zang, S.; Xie, J. Ligand-Protected Atomically Precise Gold Nanoclusters as Model Catalysts for Oxidation Reactions. *Chemical Communications* **2020**, *56* (8), 1163–1174. https://doi.org/10.1039/c9cc08215h.
(473) Che, M. Nobel Prize in Chemistry 1912 to Sabatier: Organic Chemistry or Catalysis? *Catalysis Today* **2013**, *218–219* (April), 162–171. https://doi.org/10.1016/j.cattod.2013.07.006.
(474) Medford, A. J.; Vojvodic, A.; Hummelshøj, J. S.; Voss, J.; Abild-Pedersen, F.; Studt, F.; Bligaard, T.; Nilsson, A.; Nørskov, J. K. From the Sabatier Principle to a Predictive Theory of Transition-Metal Heterogeneous Catalysis. *Journal of Catalysis* **2015**, *328*, 36–42. https://doi.org/10.1016/j.jcat.2014.12.033.
(475) Neue, C. Interaction of Formic Acid Vapour with Tungsten. *Zeitschrift für Physikalische Chemie* **1960**, *26* (1_2), 16–26. https://doi.org/10.1524/zpch.1960.26.1_2.016.
(476) Hammer, B.; Nørskov, J. K. Electronic Factors Determining the Reactivity of Metal Surfaces. *Surface Science* **1995**, *343* (3), 211–220. https://doi.org/10.1016/0039-6028(96)80007-0.
(477) Liu, P.; Qin, R.; Fu, G.; Zheng, N. Surface Coordination Chemistry of Metal Nanomaterials. *J Am Chem Soc* **2017**, *139* (6), 2122–2131. https://doi.org/10.1021/jacs.6b10978.
(478) Haruta, M.; Kobayashi, T.; Sano, H.; Yamada, N. Novel Gold Catalysts for the Oxidation of Carbon Monoxide at a Temperature Far Below 0 °C. *Chemistry Letters* **1987**, *16* (2), 405–408. https://doi.org/10.1246/cl.1987.405.
(479) Sanchez, A.; Abbet, S.; Heiz, U.; Schneider, W. D.; Häkkinen, H.; Barnett, R. N.; Landman, U. When Gold Is Not Noble: Nanoscale Gold Catalysts. *Journal of Physical Chemistry A* **1999**, *103* (48), 9573–9578. https://doi.org/10.1021/jp9935992.
(480) Lee, S.; Fan, C.; Wu, T.; Anderson, S. L. CO Oxidation on Aun/TiO2 Catalysts Produced by Size-Selected Cluster Deposition. *J Am Chem Soc* **2004**, *126* (18), 5682–5683. https://doi.org/10.1021/ja049436v.
(481) Herzing, A. A.; Kiely, C. J.; Carley, A. F.; Landon, P.; Hutchings, G. J. Identification of Active Gold Nanoclusters on Iron Oxide Supports for CO Oxidation. *Science (1979)* **2008**, *321* (5894), 1331–1335. https://doi.org/10.1126/science.1159639.
(482) He, Q.; Freakley, S. J.; Edwards, J. K.; Carley, A. F.; Borisevich, A. Y.; Mineo, Y.; Haruta, M.; Hutchings, G. J.; Kiely, C. J. Population and Hierarchy of Active Species in Gold Iron Oxide Catalysts for Carbon Monoxide Oxidation. *Nature Communications* **2016**, *7*, 1–8. https://doi.org/10.1038/ncomms12905.
(483) Kaden, W. E.; Wu, T.; Kunkel, W. A.; Anderson, S. L. Electronic Structure Controls Reactivity of Size-Selected Pd Clusters Adsorbed on TiO 2 Surfaces. *Science (1979)* **2009**, *326* (5954), 826–829. https://doi.org/10.1126/science.1180297.
(484) Bonanni, S.; Aït-Mansour, K.; Harbich, W.; Brune, H. Reaction-Induced Cluster Ripening and Initial Size-Dependent Reaction Rates for CO Oxidation on Ptn/TiO2(110)-(1×1). *J Am Chem Soc* **2014**, *136* (24), 8702–8707. https://doi.org/10.1021/ja502867r.
(485) Nie, X.; Qian, H.; Ge, Q.; Xu, H.; Jin, R. CO Oxidation Catalyzed by Oxide-Supported Au 25(SR) 18 Nanoclusters and Identification of Perimeter Sites as Active Centers. *ACS Nano* **2012**, *6* (7), 6014–6022. https://doi.org/10.1021/nn301019f.

(486) Nie, X.; Zeng, C.; Ma, X.; Qian, H.; Ge, Q.; Xu, H.; Jin, R. CeO2-Supported Au38(SR)24 Nanocluster Catalysts for CO Oxidation: A Comparison of Ligand-on and -off Catalysts. *Nanoscale* **2013**, *5* (13), 5912–5918. https://doi.org/10.1039/c3nr00970j.
(487) Wu, Z.; Jiang, D. E.; Mann, A. K. P.; Mullins, D. R.; Qiao, Z. A.; Allard, L. F.; Zeng, C.; Jin, R.; Overbury, S. H. Thiolate Ligands as a Double-Edged Sword for CO Oxidation on CeO 2 Supported Au25(SCH2CH2Ph) 18 Nanoclusters. *J Am Chem Soc* **2014**, *136* (16), 6111–6122. https://doi.org/10.1021/ja5018706.
(488) Wu, Z.; Hu, G.; Jiang, D. E.; Mullins, D. R.; Zhang, Q. F.; Allard, L. F.; Wang, L. S.; Overbury, S. H. Diphosphine-Protected Au22 Nanoclusters on Oxide Supports Are Active for Gas-Phase Catalysis without Ligand Removal. *Nano Letters* **2016**, *16* (10), 6560–6567. https://doi.org/10.1021/acs.nanolett.6b03221.
(489) Widmann, D.; Behm, R. J. Activation of Molecular Oxygen and the Nature of the Active Oxygen Species for Co Oxidation on Oxide Supported Au Catalysts. *Accounts of Chemical Research* **2014**, *47* (3), 740–749. https://doi.org/10.1021/ar400203e.
(490) Green, I. X.; Tang, W.; Neurock, M.; Yates, J. T. Spectroscopic Observation of Dual Catalytic Sites During Oxidation of CO on a Au/TiO 2 Catalyst. *Science (1979)* **2011**, *333* (6043), 736–739. https://doi.org/10.1126/science.1207272.
(491) Cargnello, M.; Doan-Nguyen, V. V. T.; Gordon, T. R.; Diaz, R. E.; Stach, E. A.; Gorte, R. J.; Fornasiero, P.; Murray, C. B. Control of Metal Nanocrystal Size Reveals Metal-Support Interface Role for Ceria Catalysts. *Science (1979)* **2013**, *341* (6147), 771–773. https://doi.org/10.1126/science.1240148.
(492) Bokhimi, X.; Zanella, R.; Morales, A. Au/Rutile Catalysts: Effect of Support Dimensions on the Gold Crystallite Size and the Catalytic Activity for CO Oxidation. *Journal of Physical Chemistry C* **2007**, *111* (42), 15210–15216. https://doi.org/10.1021/jp0746547.
(493) Xie, S.; Choi, S. il; Xia, X.; Xia, Y. Catalysis on Faceted Noble-Metal Nanocrystals: Both Shape and Size Matter. *Current Opinion in Chemical Engineering*. Elsevier Ltd 2013, pp 142–150. https://doi.org/10.1016/j.coche.2013.02.003.
(494) Zheng, Y.; Tao, J.; Liu, H.; Zeng, J.; Yu, T.; Ma, Y.; Moran, C.; Wu, L.; Zhu, Y.; Liu, J.; Xia, Y. Facile Synthesis of Gold Nanorice Enclosed by High-Index Facets and Its Application for CO Oxidation. *Small* **2011**, *7* (16), 2307–2312. https://doi.org/10.1002/smll.201100106.
(495) Sreedhala, S.; Sudheeshkumar, V.; Vinod, C. P. CO Oxidation on Large High-Index Faceted Pd Nanostructures. *Journal of Catalysis* **2016**, *337*, 138–144. https://doi.org/10.1016/j.jcat.2016.01.017.
(496) Qadir, K.; Joo, S. H.; Mun, B. S.; Butcher, D. R.; Renzas, J. R.; Aksoy, F.; Liu, Z.; Somorjai, G. A.; Park, J. Y. Intrinsic Relation between Catalytic Activity of CO Oxidation on Ru Nanoparticles and Ru Oxides Uncovered with Ambient Pressure XPS. *Nano Letters* **2012**, *12* (11), 5761–5768. https://doi.org/10.1021/nl303072d.
(497) Kusada, K.; Kobayashi, H.; Yamamoto, T.; Matsumura, S.; Sumi, N.; Sato, K.; Nagaoka, K.; Kubota, Y.; Kitagawa, H. Discovery of Face-Centered-Cubic Ruthenium Nanoparticles: Facile Size-Controlled Synthesis Using the Chemical Reduction Method. *J Am Chem Soc* **2013**, *135* (15), 5493–5496. https://doi.org/10.1021/ja311261s.
(498) Caron, S.; Dugger, R. W.; Ruggeri, S. G.; Ragan, J. A.; Brown Ripin, D. H. Large-Scale Oxidations in the Pharmaceutical Industry. *Chemical Reviews* **2006**, *106* (7), 2943–2989. https://doi.org/10.1021/cr040679f.
(499) Ishida, T.; Murayama, T.; Taketoshi, A.; Haruta, M. Importance of Size and Contact Structure of Gold Nanoparticles for the Genesis of Unique Catalytic Processes. *Chemical Reviews* **2020**, *120* (2), 464–525. https://doi.org/10.1021/acs.chemrev.9b00551.
(500) Mallat, T.; Baiker, A. Oxidation of Alcohols with Molecular Oxygen on Solid Catalysts. *Chemical Reviews* **2004**, *104* (6), 3037–3058. https://doi.org/10.1021/cr0200116.

(501) Carabineiro, S. A. C. Supported Gold Nanoparticles as Catalysts for the Oxidation of Alcohols and Alkanes. *Frontiers in Chemistry* **2019**, *7* (November). https://doi.org/10.3389/fchem.2019.00702.
(502) Yoskamtorn, T.; Yamazoe, S.; Takahata, R.; Nishigaki, J. I.; Thivasasith, A.; Limtrakul, J.; Tsukuda, T. Thiolate-Mediated Selectivity Control in Aerobic Alcohol Oxidation by Porous Carbon-Supported Au25 Clusters. *ACS Catalysis* **2014**, *4* (10), 3696–3700. https://doi.org/10.1021/cs501010x.
(503) Adnan, R. H.; Golovko, V. B. Benzyl Alcohol Oxidation Using Gold Catalysts Derived from Au 8 Clusters on TiO 2. *Catalysis Letters* **2019**, *149* (2), 449–455. https://doi.org/10.1007/s10562-018-2625-8.
(504) Shahin, Z.; Ji, H.; Chiriac, R.; Essayem, N.; Rataboul, F.; Demessence, A. Thermal Control of the Defunctionalization of Supported Au 25 (Glutathione) 18 Catalysts for Benzyl Alcohol Oxidation. *Beilstein Journal of Nanotechnology* **2019**, *10* (1), 228–237. https://doi.org/10.3762/bjnano.10.21.
(505) Zhang, B.; Fang, J.; Li, J.; Lau, J. J.; Mattia, D.; Zhong, Z.; Xie, J.; Yan, N. Soft, Oxidative Stripping of Alkyl Thiolate Ligands from Hydroxyapatite-Supported Gold Nanoclusters for Oxidation Reactions. *Chemistry - An Asian Journal* **2016**, *11* (4), 532–539. https://doi.org/10.1002/asia.201501074.
(506) Vargaftik, M. N.; Zagorodnikov, V. P.; Stolarov, I. P.; Moiseev, I. I.; Kochubey, D. I.; Likholobov, V. A.; Chuvilin, A. L.; Zamaraev, K. I. Giant Palladium Clusters as Catalysts of Oxidative Reactions of Olefins and Alcohols. *Journal of Molecular Catalysis* **1989**, *53* (3), 315–348. https://doi.org/10.1016/0304-5102(89)80066-5.
(507) Qiao, Z. A.; Zhang, P.; Chai, S. H.; Chi, M.; Veith, G. M.; Gallego, N. C.; Kidder, M.; Dai, S. Lab-in-a-Shell: Encapsulating Metal Clusters for Size Sieving Catalysis. *J Am Chem Soc* **2014**, *136* (32), 11260–11263. https://doi.org/10.1021/ja505903r.
(508) Lei, L.; Wu, Z.; Wang, R.; Qin, Z.; Chen, C.; Liu, Y.; Wang, G.; Fan, W.; Wang, J. Controllable Decoration of Palladium Sub-Nanoclusters on Reduced Graphene Oxide with Superior Catalytic Performance in Selective Oxidation of Alcohols. *Catalysis Science and Technology* **2017**, *7* (23), 5650–5661. https://doi.org/10.1039/c7cy01732d.
(509) Kaizuka, K.; Miyamura, H.; Kobayashi, S. Remarkable Effect of Bimetallic Nanocluster Catalysts for Aerobic Oxidation of Alcohols: Combining Metals Changes the Activities and the Reaction Pathways to Aldehydes/Carboxylic Acids or Esters. *J Am Chem Soc* **2010**, *132* (43), 15096–15098. https://doi.org/10.1021/ja108256h.
(510) Dun, R.; Wang, X.; Tan, M.; Huang, Z.; Huang, X.; Ding, W.; Lu, X. Quantitative Aerobic Oxidation of Primary Benzylic Alcohols to Aldehydes Catalyzed by Highly Efficient and Recyclable P123-Stabilized Pd Nanoclusters in Acidic Aqueous Solution. *ACS Catalysis* **2013**, *3* (12), 3063–3066. https://doi.org/10.1021/cs400788f.
(511) Pérez, Y.; Ruiz-González, M. L.; González-Calbet, J. M.; Concepción, P.; Boronat, M.; Corma, A. Shape-Dependent Catalytic Activity of Palladium Nanoparticles Embedded in SiO2 and TiO2. *Catalysis Today* **2012**, *180* (1), 59–67. https://doi.org/10.1016/j.cattod.2011.09.011.
(512) Henning, A. M.; Watt, J.; Miedziak, P. J.; Cheong, S.; Santonastaso, M.; Song, M.; Takeda, Y.; Kirkland, A. I.; Taylor, S. H.; Tilley, R. D. Gold-Palladium Core-Shell Nanocrystals with Size and Shape Control Optimized for Catalytic Performance. *Angewandte Chemie - International Edition* **2013**, *52* (5), 1477–1480. https://doi.org/10.1002/anie.201207824.
(513) Wang, F.; Lu, Z.; Yang, L.; Zhang, Y.; Tang, Q.; Guo, Y.; Ma, X.; Yang, Z. Palladium Nanoparticles with High Energy Facets as a Key Factor in Dissociating O2 in the Solvent-Free Selective Oxidation of Alcohols. *Chemical Communications* **2013**, *49* (59), 6626–6628. https://doi.org/10.1039/c3cc42674b.

(514) Dai, X.; Rasamani, K. D.; Wu, S.; Sun, Y. Enabling Selective Aerobic Oxidation of Alcohols to Aldehydes by Hot Electrons in Quantum-Sized Rh Nanocubes. *Materials Today Energy* **2018**, *10*, 15–22. https://doi.org/10.1016/j.mtener.2018.08.003.
(515) Lu, X.; Ren, W.; Wu, G. CO 2 Copolymers from Epoxides: Catalyst Activity, Product Selectivity, and Stereochemistry Control. *Accounts of Chemical Research* **2012**, *45* (10), 1721–1735. https://doi.org/10.1021/ar300035z.
(516) Rebsdat, S.; Mayer, D. Ethylene Glycol. In *Ullmann's Encyclopedia of Industrial Chemistry*; Wiley-VCH Verlag GmbH & Co. KGaA: Weinheim, Germany, 2000; Vol. 22, pp 39–40. https://doi.org/10.1002/14356007.a10_101.
(517) Serafin, J. G.; Liu, A. C.; Seyedmonir, S. R. Surface Science and the Silver-Catalyzed Epoxidation of Ethylene: An Industrial Perspective. *Journal of Molecular Catalysis A: Chemical* **1998**, *131* (1–3), 157–168. https://doi.org/10.1016/S1381-1169(97)00263-X.
(518) Srinivasan, K.; Michaud, P.; Kochi, J. K. Epoxidation of Olefins with Cationic (Salen)Manganese(III) Complexes. The Modulation of Catalytic Activity by Substituents. *J Am Chem Soc* **1986**, *108* (9), 2309–2320. https://doi.org/10.1021/ja00269a029.
(519) Katsuki, T. Mn-Salen Catalyst, Competitor of Enzymes, for Asymmetric Epoxidation. *Journal of Molecular Catalysis A: Chemical* **1996**, *113* (1–2), 87–107. https://doi.org/10.1016/S1381-1169(96)00106-9.
(520) Carter, E. A.; Goddard, W. A. Chemisorption of Oxygen, Chlorine, Hydrogen, Hydroxide, and Ethylene on Silver Clusters: A Model for the Olefin Epoxidation Reaction. *Surface Science* **1989**, *209* (1–2), 243–289. https://doi.org/10.1016/0039-6028(89)90071-X.
(521) Yong, Y. S.; Cant, N. W. Ethene Epoxidation over Silver Catalysts in the Presence of Carbon Monoxide and Hydrogen. *Applied Catalysis* **1990**, *62* (1), 189–203. https://doi.org/10.1016/S0166-9834(00)82247-2.
(522) Sachtler, W. M. H.; Backx, C.; van Santen, R. A. On the Mechanism of Ethylene Epoxidation. *Catalysis Reviews* **1981**, *23* (1–2), 127–149. https://doi.org/10.1080/03602458108068072.
(523) CAMPBELL, C.; PAFFETT, M. The Role of Chlorine Promoters in Catalytic Ethylene Epoxidation over the Ag(110) Surface. *Applied Surface Science* **1984**, *19* (1–4), 28–42. https://doi.org/10.1016/0169-4332(84)90051-5.
(524) Bukhtiyarov, V. I.; Knop-Gericke, A. Chapter 9. Ethylene Epoxidation over Silver Catalysts. In *Kinetics and Catalysis*; 2011; Vol. 40, pp 214–247. https://doi.org/10.1039/9781847559876-00214.
(525) Christopher, P.; Linic, S. Engineering Selectivity in Heterogeneous Catalysis: The Impact of Ag Surface Structure on Ethylene Epoxidation Selectivity. *AIChE Annual Meeting, Conference Proceedings* **2008**, No. 100, 11264–11265.
(526) Christopher, P.; Linic, S. Shape- and Size-Specific Chemistry of Ag Nanostructures in Catalytic Ethylene Epoxidation. *ChemCatChem* **2010**, *2* (1), 78–83. https://doi.org/10.1002/cctc.200900231.
(527) Min, B. K.; Friend, C. M. Heterogeneous Gold-Based Catalysis for Green Chemistry: Low-Temperature CO Oxidation and Propene Oxidation. *Chemical Reviews* **2007**, *107* (6), 2709–2724. https://doi.org/10.1021/cr050954d.
(528) Sinha, A. K.; Seelan, S.; Tsubota, S.; Haruta, M. Catalysis by Gold Nanoparticles: Epoxidation of Propene. *Topics in Catalysis* **2004**, *29* (3/4), 95–102. https://doi.org/10.1023/B:TOCA.0000029791.69935.53.
(529) Hartung, W. H. CATALYTIC REDUCTION OF NITRILES AND OXIMES. *J Am Chem Soc* **1928**, *50* (12), 3370–3374. https://doi.org/10.1021/ja01399a033.
(530) Beccat, P.; Bertolini, J. C.; Gauthier, Y.; Massardier, J.; Ruiz, P. Crotonaldehyde and Methylcrotonaldehyde Hydrogenation over Pt(111) and Pt80Fe20(111) Single Crystals. *Journal of Catalysis* **1990**, *126* (2), 451–456. https://doi.org/10.1016/0021-9517(90)90011-8.

(531) Weiss, P. S.; Eigler, D. M. Site Dependence of the Apparent Shape of a Molecule in Scanning Tunneling Micoscope Images: Benzene on Pt{111}. *Physical Review Letters* **1993**, *71* (19), 3139–3142. https://doi.org/10.1103/PhysRevLett.71.3139.
(532) Zaera, F.; Somorjai, G. A. Hydrogenation of Ethylene over Platinum (111) Single-Crystal Surfaces. *J Am Chem Soc* **1984**, *106* (8), 2288–2293. https://doi.org/10.1021/ja00320a013.
(533) Bratlie, K. M.; Flores, L. D.; Somorjai, G. A. In Situ Sum Frequency Generation Vibrational Spectroscopy Observation of a Reactive Surface Intermediate during High-Pressure Benzene Hydrogenation. *Journal of Physical Chemistry B* **2006**, *110* (20), 10051–10057. https://doi.org/10.1021/jp0612735.
(534) Kliewer, C. J.; Somorjai, G. A. Structure Effects on Pyridine Hydrogenation over Pt(111) and Pt(100) Studied with Sum Frequency Generation Vibrational Spectroscopy. *Catalysis Letters* **2010**, *137* (3–4), 118–122. https://doi.org/10.1007/s10562-010-0353-9.
(535) Tsung, C. K.; Kuhn, J. N.; Huang, W.; Aliaga, C.; Hung, L. I.; Somorjai, G. A.; Yang, P. Sub-10 Nm Platinum Nanocrystals with Size and Shape Control: Catalytic Study for Ethylene and Pyrrole Hydrogenation. *J Am Chem Soc* **2009**, *131* (16), 5816–5822. https://doi.org/10.1021/ja809936n.
(536) Crespo-Quesada, M.; Yarulin, A.; Jin, M.; Xia, Y.; Kiwi-Minsker, L. Structure Sensitivity of Alkynol Hydrogenation on Shape- and Size-Controlled Palladium Nanocrystals: Which Sites Are Most Active and Selective? *J Am Chem Soc* **2011**, *133* (32), 12787–12794. https://doi.org/10.1021/ja204557m.
(537) Schmidt, E.; Vargas, A.; Mallat, T.; Baiker, A. Shape-Selective Enantioselective Hydrogenation on Pt Nanoparticles. *J Am Chem Soc* **2009**, *131* (34), 12358–12367. https://doi.org/10.1021/ja9043328.
(538) Meemken, F.; Baiker, A. Recent Progress in Heterogeneous Asymmetric Hydrogenation of C=O and C=C Bonds on Supported Noble Metal Catalysts. *Chemical Reviews* **2017**, *117* (17), 11522–11569. https://doi.org/10.1021/acs.chemrev.7b00272.
(539) Liu, X.; Astruc, D. Development of the Applications of Palladium on Charcoal in Organic Synthesis. *Advanced Synthesis and Catalysis* **2018**, *360* (18), 3426–3459. https://doi.org/10.1002/adsc.201800343.
(540) Phan, N. T. S.; van der Sluys, M.; Jones, C. W. On the Nature of the Active Species in Palladium Catalyzed Mizoroki-Heck and Suzuki-Miyaura Couplings - Homogeneous or Heterogeneous Catalysis, a Critical Review. *Advanced Synthesis and Catalysis* **2006**, *348* (6), 609–679. https://doi.org/10.1002/adsc.200505473.
(541) Shi, W.; Niu, Y.; Li, S.; Zhang, L.; Zhang, Y.; Botton, G. A.; Wan, Y.; Zhang, B. Revealing the Structure Evolution of Heterogeneous Pd Catalyst in Suzuki Reaction via the Identical Location Transmission Electron Microscopy. *ACS Nano* **2021**, *15* (5), 8621–8637. https://doi.org/10.1021/acsnano.1c00486.
(542) Eremin, D. B.; Ananikov, V. P. Understanding Active Species in Catalytic Transformations: From Molecular Catalysis to Nanoparticles, Leaching, "Cocktails" of Catalysts and Dynamic Systems. *Coordination Chemistry Reviews* **2017**, *346*, 2–19. https://doi.org/10.1016/j.ccr.2016.12.021.
(543) Narayanan, R.; El-Sayed, M. A. Effect of Colloidal Nanocatalysis on the Metallic Nanoparticle Shape: The Suzuki Reaction. *Langmuir* **2005**, *21* (5), 2027–2033. https://doi.org/10.1021/la047600m.
(544) Collins, G.; Schmidt, M.; O'Dwyer, C.; Holmes, J. D.; McGlacken, G. P. The Origin of Shape Sensitivity in Palladium-Catalyzed Suzuki-Miyaura Cross Coupling Reactions. *Angewandte Chemie - International Edition* **2014**, *53* (16), 4142–4145. https://doi.org/10.1002/anie.201400483.
(545) Chen, Y.; Liu, C.; Abroshan, H.; Li, Z.; Wang, J.; Li, G.; Haruta, M. Phosphine/Phenylacetylide-Ligated Au Clusters for Multicomponent Coupling Reactions. *Journal of Catalysis* **2016**, *340*, 287–294. https://doi.org/10.1016/j.jcat.2016.05.023.

(546) Abroshan, H.; Li, G.; Lin, J.; Kim, H. J.; Jin, R. Molecular Mechanism for the Activation of Au25(SCH2CH2Ph)18 Nanoclusters by Imidazolium-Based Ionic Liquids for Catalysis. *Journal of Catalysis* **2016**, *337*, 72–79. https://doi.org/10.1016/j.jcat.2016.01.011.
(547) Li, G.; Liu, C.; Lei, Y.; Jin, R. Au25 Nanocluster-Catalyzed Ullmann-Type Homocoupling Reaction of Aryl Iodides. *Chemical Communications* **2012**, *48* (98), 12005–12007. https://doi.org/10.1039/c2cc34765b.
(548) Li, G.; Jiang, D. E.; Liu, C.; Yu, C.; Jin, R. Oxide-Supported Atomically Precise Gold Nanocluster for Catalyzing Sonogashira Cross-Coupling. *Journal of Catalysis* **2013**, *306*, 177–183. https://doi.org/10.1016/j.jcat.2013.06.017.
(549) Li, Z.; Yang, X.; Liu, C.; Wang, J.; Li, G. Effects of Doping in 25-Atom Bimetallic Nanocluster Catalysts for Carbon–Carbon Coupling Reaction of Iodoanisole and Phenylacetylene. *Progress in Natural Science: Materials International* **2016**, *26* (5), 477–482. https://doi.org/10.1016/j.pnsc.2016.09.007.
(550) Wu, B.; Zheng, N. Surface and Interface Control of Noble Metal Nanocrystals for Catalytic and Electrocatalytic Applications. *Nano Today* **2013**, *8* (2), 168–197. https://doi.org/10.1016/j.nantod.2013.02.006.
(551) Gómez-Marín, A. M.; Rizo, R.; Feliu, J. M. Oxygen Reduction Reaction at Pt Single Crystals: A Critical Overview. *Catalysis Science and Technology* **2014**, *4* (6), 1685–1698. https://doi.org/10.1039/c3cy01049j.
(552) Trasatti, S.; Petrii, O. A. Real Surface Area Measurements in Electrochemistry. *Journal of Electroanalytical Chemistry* **1992**, *327* (1–2), 353–376. https://doi.org/10.1016/0022-0728(92)80162-W.
(553) Welch, C. M.; Compton, R. G. The Use of Nanoparticles in Electroanalysis: A Review. *Analytical and Bioanalytical Chemistry* **2006**, *384* (3), 601–619. https://doi.org/10.1007/s00216-005-0230-3.
(554) Koper, M. T. M. Structure Sensitivity and Nanoscale Effects in Electrocatalysis. *Nanoscale* **2011**, *3* (5), 2054–2073. https://doi.org/10.1039/c0nr00857e.
(555) Zhu, J.; Hu, L.; Zhao, P.; Lee, L. Y. S.; Wong, K. Y. Recent Advances in Electrocatalytic Hydrogen Evolution Using Nanoparticles. *Chemical Reviews* **2020**, *120* (2), 851–918. https://doi.org/10.1021/acs.chemrev.9b00248.
(556) Shao, M.; Chang, Q.; Dodelet, J. P.; Chenitz, R. Recent Advances in Electrocatalysts for Oxygen Reduction Reaction. *Chemical Reviews* **2016**, *116* (6), 3594–3657. https://doi.org/10.1021/acs.chemrev.5b00462.
(557) Nørskov, J. K.; Rossmeisl, J.; Logadottir, A.; Lindqvist, L.; Kitchin, J. R.; Bligaard, T.; Jónsson, H. Origin of the Overpotential for Oxygen Reduction at a Fuel-Cell Cathode. *Journal of Physical Chemistry B* **2004**, *108* (46), 17886–17892. https://doi.org/10.1021/jp047349j.
(558) Stamenkovic, V. R.; Fowler, B.; Mun, B. S.; Wang, G.; Ross, P. N.; Lucas, C. A.; Markovic, N. M. Improved Oxygen Reduction Activity on Pt3Ni(111) via Increased Surface Site Availability. *Science (1979)* **2007**, *315* (5811), 493–497. https://doi.org/10.1126/science.1135941.
(559) Dong, J. C.; Zhang, X. G.; Briega-Martos, V.; Jin, X.; Yang, J.; Chen, S.; Yang, Z. L.; Wu, D. Y.; Feliu, J. M.; Williams, C. T.; Tian, Z. Q.; Li, J. F. In Situ Raman Spectroscopic Evidence for Oxygen Reduction Reaction Intermediates at Platinum Single-Crystal Surfaces. *Nature Energy* **2019**, *4* (1), 60–67. https://doi.org/10.1038/s41560-018-0292-z.
(560) Wang, Y.-J.; Long, W.; Wang, L.; Yuan, R.; Ignaszak, A.; Fang, B.; Wilkinson, D. P. Unlocking the Door to Highly Active ORR Catalysts for PEMFC Applications: Polyhedron-Engineered Pt-Based Nanocrystals. *Energy & Environmental Science* **2018**, *11* (2), 258–275. https://doi.org/10.1039/C7EE02444D.

(561) Wang, L.; Holewinski, A.; Wang, C. Prospects of Platinum-Based Nanostructures for the Electrocatalytic Reduction of Oxygen. *ACS Catalysis* **2018**, *8* (10), 9388–9398. https://doi.org/10.1021/acscatal.8b02906.
(562) Wang, C.; Daimon, H.; Onodera, T.; Koda, T.; Sun, S. A General Approach to the Size- and Shape-Controlled Synthesis of Platinum Nanoparticles and Their Catalytic Reduction of Oxygen. *Angewandte Chemie* **2008**, *120* (19), 3644–3647. https://doi.org/10.1002/ange.200800073.
(563) Li, C.; Jiang, B.; Miyamoto, N.; Kim, J. H.; Malgras, V.; Yamauchi, Y. Surfactant-Directed Synthesis of Mesoporous Pd Films with Perpendicular Mesochannels as Efficient Electrocatalysts. *J Am Chem Soc* **2015**, *137* (36), 11558–11561. https://doi.org/10.1021/jacs.5b06278.
(564) Zhong, P.; Liu, H.; Zhang, J.; Yin, Y.; Gao, C. Controlled Synthesis of Octahedral Platinum-Based Mesocrystals by Oriented Aggregation. *Chemistry - A European Journal* **2017**, *23* (28), 6803–6810. https://doi.org/10.1002/chem.201606023.
(565) Gao, Q.; Gao, M. R.; Liu, J. W.; Chen, M. Y.; Cui, C. H.; Li, H. H.; Yu, S. H. One-Pot Synthesis of Branched Palladium Nanodendrites with Superior Electrocatalytic Performance. *Nanoscale* **2013**, *5* (8), 3202–3207. https://doi.org/10.1039/c2nr33345g.
(566) Lu, S.; Eid, K.; Li, W.; Cao, X.; Pan, Y.; Guo, J.; Wang, L.; Wang, H.; Gu, H. Gaseous NH3 Confers Porous Pt Nanodendrites Assisted by Halides. *Scientific Reports* **2016**, *6*, 1–11. https://doi.org/10.1038/srep26196.
(567) Ye, H.; Crooks, J. A.; Crooks, R. M. Effect of Particle Size on the Kinetics of the Electrocatalytic Oxygen Reduction Reaction Catalyzed by Pt Dendrimer-Encapsulated Nanoparticles. *Langmuir* **2007**, *23* (23), 11901–11906. https://doi.org/10.1021/la702297m.
(568) Ye, H.; Crooks, R. M. Electrocatalytic O2 Reduction at Glassy Carbon Electrodes Modified with Dendrimer-Encapsulated Pt Nanoparticles. *J Am Chem Soc* **2005**, *127* (13), 4930–4934. https://doi.org/10.1021/ja0435900.
(569) Yamamoto, K.; Imaoka, T.; Chun, W. J.; Enoki, O.; Katoh, H.; Takenaga, M.; Sonoi, A. Size-Specific Catalytic Activity of Platinum Clusters Enhances Oxygen Reduction Reactions. *Nature Chemistry* **2009**, *1* (5), 397–402. https://doi.org/10.1038/nchem.288.
(570) Wang, L.; Tang, Z.; Yan, W.; Yang, H.; Wang, Q.; Chen, S. Porous Carbon-Supported Gold Nanoparticles for Oxygen Reduction Reaction: Effects of Nanoparticle Size. *ACS Applied Materials and Interfaces* **2016**, *8* (32), 20635–20641. https://doi.org/10.1021/acsami.6b02223.
(571) Lu, Y.; Jiang, Y.; Gao, X.; Chen, W. Charge State-Dependent Catalytic Activity of [Au25(SC12H25)18] Nanoclusters for the Two-Electron Reduction of Dioxygen to Hydrogen Peroxide. *Chemical Communications* **2014**, *50* (62), 8464–8467. https://doi.org/10.1039/c4cc01841a.
(572) Jeyabharathi, C.; Kumar, S. S.; Kiruthika, G. V. M.; Phani, K. L. N. Aqueous CTAB-Assisted Electrodeposition of Gold Atomic Clusters and Their Oxygen Reduction Electrocatalytic Activity in Acid Solutions. *Angewandte Chemie - International Edition* **2010**, *49* (16), 2925–2928. https://doi.org/10.1002/anie.200905614.
(573) Kwak, K.; Azad, U. P.; Choi, W.; Pyo, K.; Jang, M.; Lee, D. Efficient Oxygen Reduction Electrocatalysts Based on Gold Nanocluster–Graphene Composites. *ChemElectroChem* **2016**, *3* (8), 1253–1260. https://doi.org/10.1002/celc.201600154.
(574) Yang, X.; Gan, L.; Zhu, C.; Lou, B.; Han, L.; Wang, J.; Wang, E. A Dramatic Platform for Oxygen Reduction Reaction Based on Silver Nanoclusters. *Chemical Communications* **2014**, *50* (2), 234–236. https://doi.org/10.1039/c3cc47712f.
(575) Liu, M.; Chen, W. Green Synthesis of Silver Nanoclusters Supported on Carbon Nanodots: Enhanced Photoluminescence and High Catalytic Activity for Oxygen Reduction Reaction. *Nanoscale* **2013**, *5* (24), 12558–12564. https://doi.org/10.1039/c3nr04054b.

(576) Clausmeyer, J.; Botz, A.; Öhl, D.; Schuhmann, W. The Oxygen Reduction Reaction at the Three-Phase Boundary: Nanoelectrodes Modified with Ag Nanoclusters. *Faraday Discussions* **2016**, *193*, 241–250. https://doi.org/10.1039/c6fd00101g.
(577) Ma, X. Y.; Chen, Y.; Wang, H.; Li, Q. X.; Lin, W. F.; Cai, W. bin. Electrocatalytic Oxidation of Ethanol and Ethylene Glycol on Cubic, Octahedral and Rhombic Dodecahedral Palladium Nanocrystals. *Chemical Communications* **2018**, *54* (20), 2562–2565. https://doi.org/10.1039/c7cc08793d.
(578) Mao, J.; Chen, J.; Ren, M.; Wei, M.; Zhao, J. Surfactant-Free Platinum Nanocubes with Greatly Enhanced Activity towards Methanol/Ethanol Electrooxidation. *RSC Advances* **2014**, *4* (55), 28832. https://doi.org/10.1039/c4ra03446e.
(579) Wang, S.; Kuai, L.; Huang, Y.; Yu, X.; Liu, Y.; Li, W.; Chen, L.; Geng, B. A Highly Efficient, Clean-Surface, Porous Platinum Electrocatalyst and the Inhibition Effect of Surfactants on Catalytic Activity. *Chemistry - A European Journal* **2013**, *19* (1), 240–248. https://doi.org/10.1002/chem.201203398.
(580) Iqbal, M.; Kaneti, Y. V.; Kim, J.; Yuliarto, B.; Kang, Y. M.; Bando, Y.; Sugahara, Y.; Yamauchi, Y. Chemical Design of Palladium-Based Nanoarchitectures for Catalytic Applications. *Small*. 2019, pp 1–27. https://doi.org/10.1002/smll.201804378.
(581) Mourdikoudis, S.; Chirea, M.; Altantzis, T.; Pastoriza-Santos, I.; Pérez-Juste, J.; Silva, F.; Bals, S.; Liz-Marzán, L. M. Dimethylformamide-Mediated Synthesis of Water-Soluble Platinum Nanodendrites for Ethanol Oxidation Electrocatalysis. *Nanoscale* **2013**, *5* (11), 4776–4784. https://doi.org/10.1039/c3nr00924f.
(582) Kucernak, A.; Jiang, J. Mesoporous Platinum as a Catalyst for Oxygen Electroreduction and Methanol Electrooxidation. *Chemical Engineering Journal* **2003**, *93* (1), 81–90. https://doi.org/10.1016/S1385-8947(02)00111-0.
(583) Zhao, M.; Chen, Z.; Lyu, Z.; Hood, Z. D.; Xie, M.; Vara, M.; Chi, M.; Xia, Y. Ru Octahedral Nanocrystals with a Face-Centered Cubic Structure, {111} Facets, Thermal Stability up to 400 °C, and Enhanced Catalytic Activity. *J Am Chem Soc* **2019**, *141* (17), 7028–7036. https://doi.org/10.1021/jacs.9b01640.
(584) Zhu, J.; Chen, Z.; Xie, M.; Lyu, Z.; Chi, M.; Mavrikakis, M.; Jin, W.; Xia, Y. Iridium-Based Cubic Nanocages with 1.1-Nm-Thick Walls: A Highly Efficient and Durable Electrocatalyst for Water Oxidation in an Acidic Medium. *Angewandte Chemie - International Edition* **2019**, *58* (22), 7244–7248. https://doi.org/10.1002/anie.201901732.
(585) Skúlason, E.; Tripkovic, V.; Björketun, M. E.; Gudmundsdóttir, S.; Karlberg, G.; Rossmeisl, J.; Bligaard, T.; Jónsson, H.; Nørskov, J. K. Modeling the Electrochemical Hydrogen Oxidation and Evolution Reactions on the Basis of Density Functional Theory Calculations. *Journal of Physical Chemistry C* **2010**, *114* (42), 18182–18197. https://doi.org/10.1021/jp1048887.
(586) Zheng, J.; Sheng, W.; Zhuang, Z.; Xu, B.; Yan, Y. Universal Dependence of Hydrogen Oxidation and Evolution Reaction Activity of Platinum-Group Metals on PH and Hydrogen Binding Energy. *Science Advances* **2016**, *2* (3), 1–9. https://doi.org/10.1126/sciadv.1501602.
(587) Mahmood, N.; Yao, Y.; Zhang, J. W.; Pan, L.; Zhang, X.; Zou, J. J. Electrocatalysts for Hydrogen Evolution in Alkaline Electrolytes: Mechanisms, Challenges, and Prospective Solutions. *Advanced Science* **2018**, *5* (2). https://doi.org/10.1002/advs.201700464.
(588) Montini, T.; Monai, M.; Beltram, A.; Romero-Ocaña, I.; Fornasiero, P. H2 Production by Photocatalytic Reforming of Oxygenated Compounds Using TiO2-Based Materials. *Materials Science in Semiconductor Processing* **2016**, *42*, 122–130. https://doi.org/10.1016/j.mssp.2015.06.069.
(589) Ma, Y.; Wang, X.; Jia, Y.; Chen, X.; Han, H.; Li, C. Titanium Dioxide-Based Nanomaterials for Photocatalytic Fuel Generations. *Chemical Reviews* **2014**, *114* (19), 9987–10043. https://doi.org/10.1021/cr500008u.

(590) Kumar Singh, A.; Das, C.; Indra, A. Scope and Prospect of Transition Metal-Based Cocatalysts for Visible Light-Driven Photocatalytic Hydrogen Evolution with Graphitic Carbon Nitride. *Coordination Chemistry Reviews* **2022**, *465*, 214516. https://doi.org/10.1016/j.ccr.2022.214516.
(591) Li, J.; Zhao, T.; Chen, T.; Liu, Y.; Ong, C. N.; Xie, J. Engineering Noble Metal Nanomaterials for Environmental Applications. *Nanoscale* **2015**, *7* (17), 7502–7519. https://doi.org/10.1039/c5nr00857c.
(592) Yang, X.; Wang, D. Photocatalysis: From Fundamental Principles to Materials and Applications. *ACS Applied Energy Materials* **2018**, *1* (12), 6657–6693. https://doi.org/10.1021/acsaem.8b01345.
(593) Bai, S.; Wang, L.; Li, Z.; Xiong, Y. Facet-Engineered Surface and Interface Design of Photocatalytic Materials. *Advanced Science* **2017**, *4* (1). https://doi.org/10.1002/advs.201600216.
(594) Nakabayashi, S.; Fujishima, A.; Honda, K. Experimental Evidence for the Hydrogen Evolution Site in Photocatalytic Process on Pt/TiO2. *Chemical Physics Letters* **1983**, *102* (5), 464–465. https://doi.org/10.1016/0009-2614(83)87447-8.
(595) Bamwenda, G. R.; Tsubota, S.; Nakamura, T.; Haruta, M. Photoassisted Hydrogen Production from a Water-Ethanol Solution: A Comparison of Activities of Au□TiO2 and Pt□TiO2. *Journal of Photochemistry and Photobiology A: Chemistry* **1995**, *89* (2), 177–189. https://doi.org/10.1016/1010-6030(95)04039-I.
(596) Ikuma, Y.; Bessho, H. Effect of Pt Concentration on the Production of Hydrogen by a TiO2 Photocatalyst. *International Journal of Hydrogen Energy* **2007**, *32* (14), 2689–2692. https://doi.org/10.1016/j.ijhydene.2006.09.024.
(597) Primo, A.; Corma, A.; García, H. Titania Supported Gold Nanoparticles as Photocatalyst. *Physical Chemistry Chemical Physics* **2011**, *13* (3), 886–910. https://doi.org/10.1039/c0cp00917b.
(598) Greaves, J.; Al-Mazroai, L.; Nuhu, A.; Davies, P.; Bowker, M. Photocatalytic Methanol Reforming on Au/TiO2 for Hydrogen Production. *Gold Bulletin* **2006**, *39* (4), 216–219. https://doi.org/10.1007/BF03215557.
(599) Chiarello, G. L.; Aguirre, M. H.; Selli, E. Hydrogen Production by Photocatalytic Steam Reforming of Methanol on Noble Metal-Modified TiO2. *Journal of Catalysis* **2010**, *273* (2), 182–190. https://doi.org/10.1016/j.jcat.2010.05.012.
(600) Kim, J.; Monllor-Satoca, D.; Choi, W. Simultaneous Production of Hydrogen with the Degradation of Organic Pollutants Using TiO2 Photocatalyst Modified with Dual Surface Components. *Energy and Environmental Science* **2012**, *5* (6), 7647–7656. https://doi.org/10.1039/c2ee21310a.
(601) Murdoch, M.; Waterhouse, G. I. N.; Nadeem, M. A.; Metson, J. B.; Keane, M. A.; Howe, R. F.; Llorca, J.; Idriss, H. The Effect of Gold Loading and Particle Size on Photocatalytic Hydrogen Production from Ethanol over Au/TiO2 Nanoparticles. *Nature Chemistry* **2011**, *3* (6), 489–492. https://doi.org/10.1038/nchem.1048.
(602) Berr, M. J.; Schweinberger, F. F.; Döblinger, M.; Sanwald, K. E.; Wolff, C.; Breimeier, J.; Crampton, A. S.; Ridge, C. J.; Tschurl, M.; Heiz, U.; Jäckel, F.; Feldmann, J. Size-Selected Subnanometer Cluster Catalysts on Semiconductor Nanocrystal Films for Atomic Scale Insight into Photocatalysis. *Nano Letters* **2012**, *12* (11), 5903–5906. https://doi.org/10.1021/nl3033069.
(603) Schweinberger, F. F.; Berr, M. J.; Döblinger, M.; Wolff, C.; Sanwald, K. E.; Crampton, A. S.; Ridge, C. J.; Jäckel, F.; Feldmann, J.; Tschurl, M.; Heiz, U. Cluster Size Effects in the Photocatalytic Hydrogen Evolution Reaction. *J Am Chem Soc* **2013**, *135* (36), 13262–13265. https://doi.org/10.1021/ja406070q.
(604) Hang Li, Y.; Xing, J.; Jia Chen, Z.; Li, Z.; Tian, F.; Rong Zheng, L.; Feng Wang, H.; Hu, P.; Jun Zhao, H.; Gui Yang, H. Unidirectional Suppression of Hydrogen Oxidation on Oxidized

Platinum Clusters. *Nature Communications* **2013**, *4*, 1–7. https://doi.org/10.1038/ncomms3500.
(605) Dessal, C.; Martínez, L.; Maheu, C.; Len, T.; Morfin, F.; Rousset, J. L.; Puzenat, E.; Afanasiev, P.; Aouine, M.; Soler, L.; Llorca, J.; Piccolo, L. Influence of Pt Particle Size and Reaction Phase on the Photocatalytic Performances of Ultradispersed Pt/TiO2 Catalysts for Hydrogen Evolution. *Journal of Catalysis* **2019**, *375*, 155–163. https://doi.org/10.1016/j.jcat.2019.05.033.
(606) Negishi, Y.; Mizuno, M.; Hirayama, M.; Omatoi, M.; Takayama, T.; Iwase, A.; Kudo, A. Enhanced Photocatalytic Water Splitting by BaLa4Ti4O15 Loaded with ∼1 Nm Gold Nanoclusters Using Glutathione-Protected Au25 Clusters. *Nanoscale* **2013**, *5* (16), 7188. https://doi.org/10.1039/c3nr01888a.
(607) Negishi, Y.; Matsuura, Y.; Tomizawa, R.; Kurashige, W.; Niihori, Y.; Takayama, T.; Iwase, A.; Kudo, A. Controlled Loading of Small Au n Clusters (n = 10–39) onto BaLa 4 Ti 4 O 15 Photocatalysts: Toward an Understanding of Size Effect of Cocatalyst on Water-Splitting Photocatalytic Activity. *The Journal of Physical Chemistry C* **2015**, *119* (20), 11224–11232. https://doi.org/10.1021/jp5122432.
(608) Chen, Y.; Soler, L.; Armengol-Profitós, M.; Xie, C.; Crespo, D.; Llorca, J. Enhanced Photoproduction of Hydrogen on Pd/TiO2 Prepared by Mechanochemistry. *Applied Catalysis B: Environmental* **2022**, *309*. https://doi.org/10.1016/j.apcatb.2022.121275.
(609) Wang, C.; Lv, P.; Xue, D.; Cai, Y.; Yan, X.; Xu, L.; Fang, J.; Yang, Y. Zero-Dimensional/Two-Dimensional Au25(Cys)18 Nanoclusters/g-C3N4 Nanosheets Composites for Enhanced Photocatalytic Hydrogen Production under Visible Light. *ACS Sustainable Chemistry and Engineering* **2018**, *6* (7), 8447–8457. https://doi.org/10.1021/acssuschemeng.8b00643.
(610) Wang, D.; Liu, Z. P.; Yang, W. M. Revealing the Size Effect of Platinum Cocatalyst for Photocatalytic Hydrogen Evolution on TiO2 Support: A DFT Study. *ACS Catalysis* **2018**, *8* (8), 7270–7278. https://doi.org/10.1021/acscatal.8b01886.
(611) Saghi, Z.; Midgley, P. A. Electron Tomography in the (S)TEM: From Nanoscale Morphological Analysis to 3D Atomic Imaging. *Annual Review of Materials Research* **2012**, *42* (April), 59–79. https://doi.org/10.1146/annurev-matsci-070511-155019.
(612) Yang, J. C.; Small, M. W.; Grieshaber, R. v.; Nuzzo, R. G. Recent Developments and Applications of Electron Microscopy to Heterogeneous Catalysis. *Chemical Society Reviews* **2012**, *41* (24), 8179–8194. https://doi.org/10.1039/c2cs35371g.
(613) Sing, K. S. W. Reporting Physisorption Data for Gas/Solid Systems with Special Reference to the Determination of Surface Area and Porosity (Recommendations 1984). *Pure and Applied Chemistry* **1985**, *57* (4), 603–619. https://doi.org/10.1351/pac198557040603.
(614) Dulaurent, O.; Bianchi, D. Adsorption Isobars for CO on a Pt/Al2O3 Catalyst at High Temperatures Using FTIR Spectroscopy: Isosteric Heat of Adsorption and Adsorption Model. *Applied Catalysis A: General* **2000**, *196* (2), 271–280. https://doi.org/10.1016/S0926-860X(99)00472-X.
(615) Gatica, J. M.; Baker, R. T.; Fornasiero, P.; Bernal, S.; Kašpar, J. Characterization of the Metal Phase in NM/Ce 0.68 Zr 0.32 O 2 (NM: Pt and Pd) Catalysts by Hydrogen Chemisorption and HRTEM Microscopy: A Comparative Study. *The Journal of Physical Chemistry B* **2001**, *105* (6), 1191–1199. https://doi.org/10.1021/jp003632g.
(616) van Muylde, J.; de Zoubov, N. Electrochemical Properties of the Platinum Metals. *Platinum Metals Review* **1959**, *3* (3), 100–106.
(617) Labinger, J. A. Platinum-Catalyzed C − H Functionalization. *Chemical Reviews* **2017**, *117* (13), 8483–8496. https://doi.org/10.1021/acs.chemrev.6b00583.
(618) Sabyrov, K.; Jiang, J.; Yaghi, O. M.; Somorjai, G. A. Hydroisomerization of N-Hexane Using Acidified Metal-Organic Framework and Platinum Nanoparticles. *J Am Chem Soc* **2017**, *139* (36), 12382–12385. https://doi.org/10.1021/jacs.7b06629.

(619) Sakai, K.; Ozawa, H. Homogeneous Catalysis of Platinum(II) Complexes in Photochemical Hydrogen Production from Water. *Coordination Chemistry Reviews* **2007**, *251* (21–24), 2753–2766. https://doi.org/10.1016/j.ccr.2007.08.014.
(620) Liu, K.; Wang, A.; Zhang, T. Recent Advances in Preferential Oxidation of Co Reaction over Platinum Group Metal Catalysts. *ACS Catalysis* **2012**, *2* (6), 1165–1178. https://doi.org/10.1021/cs200418w.
(621) Holton, O. T.; Stevenson, J. W. The Role of Platinum in Proton Exchange Membrane Fuel Cells Evaluation of Platinum's Unique Properties for Use in Both the Anode and Cathode of a Proton Exchange Membrane Fuel Cell. *@BULLETPlatinum Metals Rev* **2013**, *57* (4), 259–271.
(622) Kim, H.; Yoo, T. Y.; Bootharaju, M. S.; Kim, J. H.; Chung, D. Y.; Hyeon, T. Noble Metal-Based Multimetallic Nanoparticles for Electrocatalytic Applications. *Advanced Science* **2022**, *9* (1), 1–36. https://doi.org/10.1002/advs.202104054.
(623) Meher, S. K.; Cargnello, M.; Troiani, H.; Montini, T.; Rao, G. R.; Fornasiero, P. Alcohol Induced Ultra-Fine Dispersion of Pt on Tuned Morphologies of CeO2 for CO Oxidation. *Applied Catalysis B: Environmental* **2013**, *130–131*, 121–131. https://doi.org/10.1016/j.apcatb.2012.10.022.
(624) Lopez, N.; Janssens, T. V. W.; Clausen, B. S.; Xu, Y.; Mavrikakis, M.; Bligaard, T.; Nørskov, J. K. On the Origin of the Catalytic Activity of Gold Nanoparticles for Low-Temperature CO Oxidation. *Journal of Catalysis* **2004**, *223* (1), 232–235. https://doi.org/10.1016/j.jcat.2004.01.001.
(625) Xie, C.; Yan, D.; Li, H.; Du, S.; Chen, W.; Wang, Y.; Zou, Y.; Chen, R.; Wang, S. Defect Chemistry in Heterogeneous Catalysis : Recognition , Understanding , and Utilization. *ACS Catalysis* **2020**, *10* (19), 11082–11098. https://doi.org/10.1021/acscatal.0c03034.
(626) Shi, R.; Zhao, Y.; Waterhouse, G. I. N.; Zhang, S.; Zhang, T. Defect Engineering in Photocatalytic Nitrogen Fixation. *ACS Catalysis*. 2019, pp 9739–9750. https://doi.org/10.1021/acscatal.9b03246.
(627) Valério Neto, E. S.; Almeida, C. V. S.; Russell, A. E.; Salazar-Banda, G. R.; Eguiluz, K. I. B. Realising the Activity Benefits of Pt Preferential (111) Surfaces for Ethanol Oxidation in a Nanowire Electrocatalyst. *Electrochimica Acta* **2020**, *348*, 1–11. https://doi.org/10.1016/j.electacta.2020.136206.
(628) Bennett, D. A.; Cargnello, M.; Diroll, B. T.; Murray, C. B.; Vohs, J. M. Shape-Dependence of the Thermal and Photochemical Reactions of Methanol on Nanocrystalline Anatase TiO2. *Surface Science* **2016**, *654*, 1–7. https://doi.org/10.1016/j.susc.2016.07.009.
(629) Peng, Z.; Yang, H. Synthesis and Oxygen Reduction Electrocatalytic Property of Pt-on-Pd. *J Am Chem Soc* **2009**, *131* (22), 7542–7543. https://doi.org/10.1021/ja902256a.
(630) Yu, W.; Batchelor-mcauley, C.; Compton, R. G. Porosity Controls the Catalytic Activity of Platinum Nanoparticles. *Physical Chemistry Chemical Physics* **2019**, *21* (36), 20415–20421. https://doi.org/10.1039/c9cp03887f.
(631) Mohanty, A.; Garg, N.; Jin, R. Zuschriften A Universal Approach to the Synthesis of Noble Metal Nanodendrites and Their Catalytic Properties **. *Angewandte Chemie* **2010**, *122* (29), 5082–5086. https://doi.org/10.1002/ange.201000902.
(632) Hansen, T. W.; Delariva, A. T.; Challa, S. R.; Datye, A. K. Sintering of Catalytic Nanoparticles : Particle Migration or Ostwald Ripening ? *Accounts of Chemical Research* **2013**, *46* (8), 1720–1730. https://doi.org/10.1021/ar3002427.
(633) Shin, H. J.; Ryoo, R.; Liu, Z. Template Synthesis of Asymmetrically Mesostructured Platinum Networks. *J Am Chem Soc* **2001**, *123* (11), 1246–1247. https://doi.org/10.1021/ja003461t.
(634) Koo, J. H.; Kumar, A.; Lee, S.; Jin, X.; Jeong, H.; Kim, J.; Lee, I. S. Pore-Engineered Silica Nanoreactors for Chemical Interaction-Guided Confined Synthesis of Porous Platinum

Nanodendrites. *Chemistry of Materials* **2018**, *30* (9), 3010–3018. https://doi.org/10.1021/acs.chemmater.8b00628.
(635) Han, Y.; Kim, J. M.; Stucky, G. D. Preparation of Noble Metal Nanowires Using Hexagonal Mesoporous Silica SBA-15. *Chemistry of Materials* **2000**, *12* (9), 2068–2069. https://doi.org/10.1021/cm0010553.
(636) Self-assembly, C.; Gruner, S. M.; Disalvo, F. J.; Wiesner, U. Ordered Mesoporous Materials from Metal Nanoparticle – Block Copolymer Self-Assembly. *Science (1979)* **2008**, *320* (June), 1748–1753. https://doi.org/10.1126/science.1159950.
(637) Shui, J. L.; Chen, C.; Li, J. C. M. Evolution of Nanoporous Pt-Fe Alloy Nanowires by Dealloying and Their Catalytic Property for Oxygen Reduction Reaction. *Advanced Functional Materials* **2011**, *21* (17), 3357–3362. https://doi.org/10.1002/adfm.201100723.
(638) Elliott, J. M.; Squires, A. M. Optimum Conditions for Electrochemical Deposition of 3-D Mesoporous Platinum Framework. *Journal of Nanoparticle Research* **2020**, *22* (6). https://doi.org/10.1007/s11051-020-04912-9.
(639) Zhang, W.; Yang, J.; Lu, X. Tailoring Galvanic Replacement Reaction for the Preparation of Pt/Ag Bimetallic Hollow Nanostructures with Controlled Number of Voids. *ACS Nano* **2012**, *6* (8), 7397–7405. https://doi.org/10.1021/nn302590k.
(640) Ye, F.; Hu, W.; Zhang, T.; Yang, J.; Ding, Y. Enhanced Electrocatalytic Activity of Pt-Nanostructures Prepared by Electrodeposition Using Poly(Vinyl Pyrrolidone) as a Shape-Control Agent. *Electrochimica Acta* **2012**, *83*, 383–386. https://doi.org/10.1016/j.electacta.2012.08.022.
(641) Lim, B.; Lu, X.; Jiang, M.; Camargo, P. H. C.; Cho, E. C.; Lee, E. P.; Xia, Y. Facile Synthesis of Highly Faceted Multioctahedral Pt Nanocrystals through Controlled Overgrowth. *Nano Letters* **2008**, *8* (11), 4043–4047. https://doi.org/10.1021/nl802959b.
(642) Lacroix, L. M.; Gatel, C.; Arenal, R.; Garcia, C.; Lachaize, S.; Blon, T.; Warot-Fonrose, B.; Snoeck, E.; Chaudret, B.; Viau, G. Tuning Complex Shapes in Platinum Nanoparticles: From Cubic Dendrites to Fivefold Stars. *Angewandte Chemie - International Edition* **2012**, *51* (19), 4690–4694. https://doi.org/10.1002/anie.201107425.
(643) Arán-Ais, R. M.; Vidal-Iglesias, F. J.; Solla-Gullón, J.; Herrero, E.; Feliu, J. M. Electrochemical Characterization of Clean Shape-Controlled Pt Nanoparticles Prepared in Presence of Oleylamine/Oleic Acid. *Electroanalysis* **2015**, *27* (4), 945–956. https://doi.org/10.1002/elan.201400619.
(644) Khan, M. D.; Opallo, M.; Revaprasadu, N. Colloidal Synthesis of Metal Chalcogenide Nanomaterials from Metal-Organic Precursors and Capping Ligand Effect on Electrocatalytic Performance: Progress, Challenges and Future Perspectives. *Dalton Transactions* **2021**, *50* (33), 11347–11359. https://doi.org/10.1039/d1dt01742j.
(645) Pasricha, R.; Bala, T.; Biradar, A. v; Umbarkar, S.; Sastry, M. Synthesis of Catalytically Active Porous Platinum Nanoparticles by Transmetallation Reaction and Proposition of the Mechanism. *Small* **2009**, *5* (12), 1467–1473. https://doi.org/10.1002/smll.200801863.
(646) Yin, X.; Shi, M.; Wu, J.; Pan, Y. T.; Gray, D. L.; Bertke, J. A.; Yang, H. Quantitative Analysis of Different Formation Modes of Platinum Nanocrystals Controlled by Ligand Chemistry. *Nano Letters* **2017**, *17* (10), 6146–6150. https://doi.org/10.1021/acs.nanolett.7b02751.
(647) Teng, X.; Yang, H. Synthesis of Platinum Multipeds: An Induced Anisotropic Growth. *Nano Letters* **2005**, *5* (5), 885–891. https://doi.org/10.1021/nl0503072.
(648) Chen, J.; Herricks, T.; Geissler, M.; Xia, Y. Single-Crystal Nanowires of Platinum Can Be Synthesized by Controlling the Reaction Rate of a Polyol Process. *J Am Chem Soc* **2004**, *126* (35), 10854–10855. https://doi.org/10.1021/ja0468224.
(649) Song, Y.; Yang, Y.; Medforth, C. J.; Pereira, E.; Singh, A. K.; Xu, H.; Jiang, Y.; Brinker, C. J.; Swol, F. van; Shelnutt, J. A.; Uni, V. Controlled Synthesis of 2-D and 3-D Dendritic

Platinum Nanostructures. *J Am Chem Soc* **2004**, *126* (2), 1924–1926. https://doi.org/10.1021/ja037474t.
(650) Mourdikoudis, S.; Montes-García, V.; Rodal-Cedeira, S.; Winckelmans, N.; Pérez-Juste, I.; Wu, H.; Bals, S.; Pérez-Juste, J.; Pastoriza-Santos, I. Highly Porous Palladium Nanodendrites: Wet-Chemical Synthesis, Electron Tomography and Catalytic Activity. *Dalton Transactions* **2019**, *48* (11), 3758–3767. https://doi.org/10.1039/c9dt00107g.
(651) Wen, X.; Lerch, S.; Wang, Z.; Aboudiab, B.; Tehrani-Bagha, A. R.; Olsson, E.; Moth-Poulsen, K. Synthesis of Palladium Nanodendrites Using a Mixture of Cationic and Anionic Surfactants. *Langmuir* **2020**, *36* (7), 1745–1753. https://doi.org/10.1021/acs.langmuir.9b03804.
(652) Wang, L.; Yamauchi, Y. Facile Synthesis of Three-Dimensional Dendritic Platinum Nanoelectrocatalyst. *Chemistry of Materials* **2009**, *21* (c), 3562–3569. https://doi.org/10.1021/cm901161g.
(653) Wang, L.; Wang, H.; Nemoto, Y.; Yamauchi, Y. Rapid and Efficient Synthesis of Platinum Nanodendrites with High Surface Area by Chemical Reduction with Formic Acid. *Chemistry of Materials* **2010**, *22* (12), 2835–2841. https://doi.org/10.1021/cm9038889.
(654) Lu, X.; Tuan, H. Y.; Korgel, B. A.; Xia, Y. Facile Synthesis of Gold Nanoparticles with Narrow Size Distribution by Using AuCl or AuBr as the Precursor. *Chemistry - A European Journal* **2008**, *14* (5), 1584–1591. https://doi.org/10.1002/chem.200701570.
(655) Angerstein-Kozlowska H.; Conway B. E.; Sharp W. B. A. Faraday Trans. I, 1973. *Langmuir* **1973**, *43*, 9–36.
(656) Diaz-Morales, O.; Hersbach, T. J. P.; Badan, C.; Garcia, A. C.; Koper, M. T. M. Hydrogen Adsorption on Nano-Structured Platinum Electrodes. *Faraday Discussions* **2018**, *210*, 301–315. https://doi.org/10.1039/c8fd00062j.
(657) Shinozaki, K.; Zack, J. W.; Richards, R. M.; Pivovar, B. S.; Kocha, S. S. Oxygen Reduction Reaction Measurements on Platinum Electrocatalysts Utilizing Rotating Disk Electrode Technique. *Journal of The Electrochemical Society* **2015**, *162* (10), F1144–F1158. https://doi.org/10.1149/2.1071509jes.
(658) Chung, D. Y.; Lee, K. J.; Sung, Y. E. Methanol Electro-Oxidation on the Pt Surface: Revisiting the Cyclic Voltammetry Interpretation. *Journal of Physical Chemistry C* **2016**, *120* (17), 9028–9035. https://doi.org/10.1021/acs.jpcc.5b12303.
(659) Lai, J.; Niu, W.; Qi, W.; Zhao, J.; Li, S.; Gao, W.; Luque, R.; Xu, G. A Platinum Highly Concave Cube with One Leg on Each Vertex as an Advanced Nanocatalyst for Electrocatalytic Applications. *ChemCatChem* **2015**, *7* (7), 1064–1069. https://doi.org/10.1002/cctc.201403042.
(660) Chen, R.; Yang, C.; Cai, W.; Wang, H. Y.; Miao, J.; Zhang, L.; Chen, S.; Liu, B. Use of Platinum as the Counter Electrode to Study the Activity of Nonprecious Metal Catalysts for the Hydrogen Evolution Reaction. *ACS Energy Letters* **2017**, *2* (5), 1070–1075. https://doi.org/10.1021/acsenergylett.7b00219.
(661) Shinozaki, K.; Zack, J. W.; Pylypenko, S.; Pivovar, B. S.; Kocha, S. S. Oxygen Reduction Reaction Measurements on Platinum Electrocatalysts Utilizing Rotating Disk Electrode Technique. *Journal of The Electrochemical Society* **2015**, *162* (12), F1384–F1396. https://doi.org/10.1149/2.0551512jes.
(662) Rudi, S.; Cui, C.; Gan, L.; Strasser, P. Comparative Study of the Electrocatalytically Active Surface Areas (ECSAs) of Pt Alloy Nanoparticles Evaluated by Hupd and CO-Stripping Voltammetry. *Electrocatalysis* **2014**, *5* (4), 408–418. https://doi.org/10.1007/s12678-014-0205-2.
(663) Miyaura, N.; Suzuki, A. Palladium-Catalyzed Cross-Coupling Reactions of Organoboron Compounds. *Chemical Reviews* **1995**, *95* (7), 2457–2483. https://doi.org/10.1021/cr00039a007.

(664) García-Melchor, M.; Braga, A. A. C.; Lledós, A.; Ujaque, G.; Maseras, F. Computational Perspective on Pd-Catalyzed C–C Cross-Coupling Reaction Mechanisms. *Accounts of Chemical Research* **2013**, *46* (11), 2626–2634. https://doi.org/10.1021/ar400080r.
(665) Martin, R.; Buchwald, S. L. Palladium-Catalyzed Suzuki-Miyaura Cross-Coupling Reactions Employing Dialkylbiaryl Phosphine Ligands. *Accounts of Chemical Research* **2008**, *41* (11), 1461–1473. https://doi.org/10.1021/ar800036s.
(666) Marion, N.; Nolan, S. P. Well-Defined N-Heterocyclic Carbenes−Palladium(II) Precatalysts for Cross-Coupling Reactions. *Accounts of Chemical Research* **2008**, *41* (11), 1440–1449. https://doi.org/10.1021/ar800020y.
(667) Suzuki, A. Cross-Coupling Reactions of Organoboranes: An Easy Way to Construct C-C Bonds (Nobel Lecture). *Angewandte Chemie - International Edition* **2011**, *50* (30), 6722–6737. https://doi.org/10.1002/anie.201101379.
(668) Kadu, B. S. Suzuki-Miyaura Cross Coupling Reaction: Recent Advancements in Catalysis and Organic Synthesis. *Catalysis Science and Technology* **2021**, *11* (4), 1186–1221. https://doi.org/10.1039/d0cy02059a.
(669) Hong, K.; Sajjadi, M.; Suh, J. M.; Zhang, K.; Nasrollahzadeh, M.; Jang, H. W.; Varma, R. S.; Shokouhimehr, M. Palladium Nanoparticles on Assorted Nanostructured Supports: Applications for Suzuki, Heck, and Sonogashira Cross-Coupling Reactions. *ACS Applied Nano Materials* **2020**, *3* (3), 2070–2103. https://doi.org/10.1021/acsanm.9b02017.
(670) Zhao, M.; Wu, Y.; Cao, J. P. Carbon-Based Material-Supported Palladium Nanocatalysts in Coupling Reactions: Discussion on Their Stability and Heterogeneity. *Applied Organometallic Chemistry* **2020**, *34* (4), 1–28. https://doi.org/10.1002/aoc.5539.
(671) Lamblin, M.; Nassar-Hardy, L.; Hierso, J. C.; Fouquet, E.; Felpin, F. X. Recyclable Heterogeneous Palladium Catalysts in Pure Water: Sustainable Developments in Suzuki, Heck, Sonogashira and Tsuji-Trost Reactions. *Advanced Synthesis and Catalysis* **2010**, *352* (1), 33–79. https://doi.org/10.1002/adsc.200900765.
(672) Hussain, I.; Capricho, J.; Yawer, M. A. Synthesis of Biaryls via Ligand-Free Suzuki–Miyaura Cross-Coupling Reactions: A Review of Homogeneous and Heterogeneous Catalytic Developments. *Advanced Synthesis and Catalysis* **2016**, *358* (21), 3320–3349. https://doi.org/10.1002/adsc.201600354.
(673) Pérez-Lorenzo, M. Palladium Nanoparticles as Efficient Catalysts for Suzuki Cross-Coupling Reactions. *Journal of Physical Chemistry Letters* **2012**, *3* (2), 167–174. https://doi.org/10.1021/jz2013984.
(674) Yin, L.; Liebscher, J. Carbon-Carbon Coupling Reactions Catalyzed by Heterogeneous Palladium Catalysts. *Chemical Reviews* **2007**, *107* (1), 133–173. https://doi.org/10.1021/cr0505674.
(675) Narayanan, R. Recent Advances in Noble Metal Nanocatalysts for Suzuki and Heck Cross-Coupling Reactions. *Molecules* **2010**, *15* (4), 2124–2138. https://doi.org/10.3390/molecules15042124.
(676) Sun, J.; Fu, Y.; He, G.; Sun, X.; Wang, X. Green Suzuki-Miyaura Coupling Reaction Catalyzed by Palladium Nanoparticles Supported on Graphitic Carbon Nitride. *Applied Catalysis B: Environmental* **2015**, *165*, 661–667. https://doi.org/10.1016/j.apcatb.2014.10.072.
(677) Li, X. H.; Baar, M.; Blechert, S.; Antonietti, M. Facilitating Room-Temperature Suzuki Coupling Reaction with Light: Mott-Schottky Photocatalyst for C-C-Coupling. *Scientific Reports* **2013**, *3*, 23–24. https://doi.org/10.1038/srep01743.
(678) Xiao, Q.; Sarina, S.; Bo, A.; Jia, J.; Liu, H.; Arnold, D. P.; Huang, Y.; Wu, H.; Zhu, H. Visible Light-Driven Cross-Coupling Reactions at Lower Temperatures Using a Photocatalyst of Palladium and Gold Alloy Nanoparticles. *ACS Catalysis* **2014**, *4* (6), 1725–1734. https://doi.org/10.1021/cs5000284.

(679) Schmidt, A. F.; Kurokhtina, A. A. Distinguishing between the Homogeneous and Heterogeneous Mechanisms of Catalysis in the Mizoroki-Heck and Suzuki-Miyaura Reactions: Problems and Prospects. *Kinetics and Catalysis* **2012**, *53* (6), 714–730. https://doi.org/10.1134/S0023158412060109.
(680) Fang, P.-P.; Jutand, A.; Tian, Z.-Q.; Amatore, C. Au-Pd Core-Shell Nanoparticles Catalyze Suzuki-Miyaura Reactions in Water through Pd Leaching. *Angewandte Chemie* **2011**, *123* (51), 12392–12396. https://doi.org/10.1002/ange.201103465.
(681) Ellis, P. J.; Fairlamb, I. J. S.; Hackett, S. F. J.; Wilson, K.; Lee, A. F. Evidence for the Surface-Catalyzed Suzuki-Miyaura Reaction over Palladium Nanoparticles: An Operando XAS Study. *Angewandte Chemie - International Edition* **2010**, *49* (10), 1820–1824. https://doi.org/10.1002/anie.200906675.
(682) Narayanan, R.; Tabor, C.; El-Sayed, M. A. Can the Observed Changes in the Size or Shape of a Colloidal Nanocatalyst Reveal the Nanocatalysis Mechanism Type: Homogeneous or Heterogeneous? *Topics in Catalysis* **2008**, *48* (1–4), 60–74. https://doi.org/10.1007/s11244-008-9057-4.
(683) Ananikov, V. P.; Beletskaya, I. P. Toward the Ideal Catalyst: From Atomic Centers to a "Cocktail" of Catalysts. *Organometallics* **2012**, *31* (5), 1595–1604. https://doi.org/10.1021/om201120n.
(684) del Zotto, A.; Zuccaccia, D. Metallic Palladium, PdO, and Palladium Supported on Metal Oxides for the Suzuki-Miyaura Cross-Coupling Reaction: A Unified View of the Process of Formation of the Catalytically Active Species in Solution. *Catalysis Science and Technology* **2017**, *7* (18), 3934–3951. https://doi.org/10.1039/c7cy01201b.
(685) Joucla, L.; Cusati, G.; Pinel, C.; Djakovitch, L. One-Pot Suzuki/Heck Sequence for the Synthesis of (E)-Stilbenes Featuring a Recyclable Silica-Supported Palladium Catalyst via a Multi-Component Reaction in 1,3-Propanediol. *Advanced Synthesis and Catalysis* **2010**, *352* (11–12), 1993–2001. https://doi.org/10.1002/adsc.201000028.
(686) Soomro, S. S.; Ansari, F. L.; Chatziapostolou, K.; Köhler, K. Palladium Leaching Dependent on Reaction Parameters in Suzuki-Miyaura Coupling Reactions Catalyzed by Palladium Supported on Alumina under Mild Reaction Conditions. *Journal of Catalysis* **2010**, *273* (2), 138–146. https://doi.org/10.1016/j.jcat.2010.05.007.
(687) Chen, Z.; Vorobyeva, E.; Mitchell, S.; Fako, E.; Ortuño, M. A.; López, N.; Collins, S. M.; Midgley, P. A.; Richard, S.; Vilé, G.; Pérez-Ramírez, J. A Heterogeneous Single-Atom Palladium Catalyst Surpassing Homogeneous Systems for Suzuki Coupling. *Nature Nanotechnology*. Springer US 2018. https://doi.org/10.1038/s41565-018-0167-2.
(688) Zhang, W.; Hong, J.; Zheng, J.; Huang, Z.; Zhou, J. (Steve); Xu, R. Nickel–Thiolate Complex Catalyst Assembled in One Step in Water for Solar H 2 Production. *J Am Chem Soc* **2011**, *133* (51), 20680–20683. https://doi.org/10.1021/ja208555h.
(689) Angamuthu, R.; Bouwman, E. Reduction of Protons Assisted by a Hexanuclear Nickel Thiolate Metallacrown: Protonation and Electrocatalytic Dihydrogen Evolution. *Physical Chemistry Chemical Physics* **2009**, *11* (27), 5578–5583. https://doi.org/10.1039/b904932k.
(690) Kauffman, D. R.; Alfonso, D.; Tafen, D. N.; Lekse, J.; Wang, C.; Deng, X.; Lee, J.; Jang, H.; Lee, J. S.; Kumar, S.; Matranga, C. Electrocatalytic Oxygen Evolution with an Atomically Precise Nickel Catalyst. *ACS Catalysis* **2016**, *6* (2), 1225–1234. https://doi.org/10.1021/acscatal.5b02633.
(691) Kagalwala, H. N.; Gottlieb, E.; Li, G.; Li, T.; Jin, R.; Bernhard, S. Photocatalytic Hydrogen Generation System Using a Nickel-Thiolate Hexameric Cluster. *Inorganic Chemistry* **2013**, *52* (15), 9094–9101. https://doi.org/10.1021/ic4013069.
(692) Yang, Z.; Smetana, A. B.; Sorensen, C. M.; Klabunde, K. J. Synthesis and Characterization of a New Tiara Pd(II) Thiolate Complex, [Pd(SC12H25)2]6, and Its Solution-Phase Thermolysis to Prepare Nearly Monodisperse Palladium Sulfide Nanoparticles. *Inorganic Chemistry* **2007**, *46* (7), 2427–2431. https://doi.org/10.1021/ic061242o.

(693) Ananikov, V. P.; Orlov, N. v.; Zalesskiy, S. S.; Beletskaya, I. P.; Khrustalev, V. N.; Morokuma, K.; Musaev, D. G. Catalytic Adaptive Recognition of Thiol (SH) and Selenol (SeH) Groups toward Synthesis of Functionalized Vinyl Monomers. *J Am Chem Soc* **2012**, *134* (15), 6637–6649. https://doi.org/10.1021/ja210596w.
(694) Bonesi, S. M.; Fagnoni, M.; Dondi, D.; Albini, A. Photochemical Carbon-Sulfur Bond Cleavage in Some Alkyl and Benzyl Sulfides. *Inorganica Chimica Acta* **2007**, *360* (3), 1230–1234. https://doi.org/10.1016/j.ica.2006.07.022.
(695) Du, C.; Li, P.; Yang, F.; Cheng, G.; Chen, S.; Luo, W. Monodisperse Palladium Sulfide as Efficient Electrocatalyst for Oxygen Reduction Reaction. *ACS Applied Materials and Interfaces* **2018**, *10* (1), 753–761. https://doi.org/10.1021/acsami.7b16359.
(696) Novák, Z.; Adamik, R.; Csenki, J. T.; Béke, F.; Gavaldik, R.; Varga, B.; Nagy, B.; May, Z.; Daru, J.; Gonda, Z.; Tolnai, G. L. Revisiting the Amine-Catalysed Cross-Coupling. *Nature Catalysis* **2021**, *4* (12), 991–993. https://doi.org/10.1038/s41929-021-00709-8.
(697) Liu, W.; Cao, H.; Zhang, H.; Zhang, H.; Chung, K. H.; He, C.; Wang, H.; Kwong, F. Y.; Lei, A. Organocatalysis in Cross-Coupling: DMEDA-Catalyzed Direct C-H Arylation of Unactivated Benzene. *J Am Chem Soc* **2010**, *132* (47), 16737–16740. https://doi.org/10.1021/ja103050x.
(698) Leadbeater, N. E.; Marco, M. Transition-Metal-Free Suzuki-Type Coupling Reactions: Scope and Limitations of the Methodology. *Journal of Organic Chemistry* **2003**, *68* (14), 5660–5667. https://doi.org/10.1021/jo034230i.
(699) Cargnello, M.; Gasparotto, A.; Gombac, V.; Montini, T.; Barreca, D.; Fornasiero, P. Photocatalytic H2 and Added-Value by-Products-the Role of Metal Oxide Systems in Their Synthesis from Oxygenates. *European Journal of Inorganic Chemistry* **2011**, No. 28, 4309–4323. https://doi.org/10.1002/ejic.201100532.
(700) Kawai, T.; Sakata, T. Photocatalytic Hydrogen Production from Liquid Methanol and Water. *Journal of the Chemical Society, Chemical Communications* **1980**, *764* (15), 694. https://doi.org/10.1039/c39800000694.
(701) Patsoura, A.; Kondarides, D. I.; Verykios, X. E. Photocatalytic Degradation of Organic Pollutants with Simultaneous Production of Hydrogen. *Catalysis Today* **2007**, *124* (3–4), 94–102. https://doi.org/10.1016/j.cattod.2007.03.028.
(702) Kondarides, D. I.; Patsoura, A.; Verykios, X. E. Anaerobic Photocatalytic Oxidation of Carbohydrates in Aqueous Pt/TiO 2 Suspensions with Simultaneous Production of Hydrogen. *Journal of Advanced Oxidation Technologies* **2010**, *13* (1), 116–123. https://doi.org/10.1515/jaots-2010-0115.
(703) Aresta, M.; Dibenedetto, A.; Nocito, F.; Ferragina, C. Valorization of Bio-Glycerol: New Catalytic Materials for the Synthesis of Glycerol Carbonate via Glycerolysis of Urea. *Journal of Catalysis* **2009**, *268* (1), 106–114. https://doi.org/10.1016/j.jcat.2009.09.008.
(704) Sivasamy, A.; Cheah, K. Y.; Fornasiero, P.; Kemausuor, F.; Zinoviev, S.; Miertus, S. Catalytic Applications in the Production of Biodiesel from Vegetable Oils. *ChemSusChem* **2009**, *2* (4), 278–300. https://doi.org/10.1002/cssc.200800253.
(705) Chen, W. T.; Chan, A.; Sun-Waterhouse, D.; Llorca, J.; Idriss, H.; Waterhouse, G. I. N. Performance Comparison of Ni/TiO2 and Au/TiO2 Photocatalysts for H2 Production in Different Alcohol-Water Mixtures. *Journal of Catalysis* **2018**, *367*, 27–42. https://doi.org/10.1016/j.jcat.2018.08.015.
(706) Chen, W. T.; Dong, Y.; Yadav, P.; Aughterson, R. D.; Sun-Waterhouse, D.; Waterhouse, G. I. N. Effect of Alcohol Sacrificial Agent on the Performance of Cu/TiO2 Photocatalysts for UV-Driven Hydrogen Production. *Applied Catalysis A: General* **2020**, *602* (June), 117703. https://doi.org/10.1016/j.apcata.2020.117703.
(707) Gallo, A.; Montini, T.; Marelli, M.; Minguzzi, A.; Gombac, V.; Psaro, R.; Fornasiero, P.; Dal Santo, V. H2 Production by Renewables Photoreforming on Pt-Au/TiO 2 Catalysts Activated

by Reduction. *ChemSusChem* **2012**, *5* (9), 1800–1811. https://doi.org/10.1002/cssc.201200085.
(708) Puga, A. v.; Forneli, A.; García, H.; Corma, A. Production of H2 by Ethanol Photoreforming on Au/TiO2. *Advanced Functional Materials* **2014**, *24* (2), 241–248. https://doi.org/10.1002/adfm.201301907.
(709) Primo, A.; Corma, A.; García, H. Titania Supported Gold Nanoparticles as Photocatalyst. *Physical Chemistry Chemical Physics* **2011**, *13* (3), 886–910. https://doi.org/10.1039/c0cp00917b.
(710) Ni, D.; Shen, H.; Li, H.; Ma, Y.; Zhai, T. Synthesis of High Efficient Cu/TiO 2 Photocatalysts by Grinding and Their Size-Dependent Photocatalytic Hydrogen Production. *Applied Surface Science* **2017**, *409*, 241–249. https://doi.org/10.1016/j.apsusc.2017.03.046.
(711) Parker, J. F.; Weaver, J. E. F.; McCallum, F.; Fields-Zinna, C. A.; Murray, R. W. Synthesis of Monodisperse [Oct4N+][Au 25(SR)18-] Nanoparticles, with Some Mechanistic Observations. *Langmuir* **2010**, *26* (16), 13650–13654. https://doi.org/10.1021/la1020466.
(712) Goulet, P. J. G.; Lennox, R. B. New Insights into Brust-Schiffrin Metal Nanoparticle Synthesis. *J Am Chem Soc* **2010**, *132* (28), 9582–9584. https://doi.org/10.1021/ja104011b.
(713) Das, A.; Li, T.; Nobusada, K.; Zeng, C.; Rosi, N. L.; Jin, R. Nonsuperatomic [Au23(SC6H11) 16]- Nanocluster Featuring Bipyramidal Au15 Kernel and Trimeric Au3(Sr)4 Motif. *J Am Chem Soc* **2013**, *135* (49), 18264–18267. https://doi.org/10.1021/ja409177s.
(714) Das, A.; Liu, C.; Byun, H. Y.; Nobusada, K.; Zhao, S.; Rosi, N.; Jin, R. Structure Determination of [Au18(SR)14]. *Angewandte Chemie - International Edition* **2015**, *54* (10), 3140–3144. https://doi.org/10.1002/anie.201410161.
(715) Yu, C.; Li, G.; Kumar, S.; Kawasaki, H.; Jin, R. Stable Au25(SR)18/TiO2 Composite Nanostructure with Enhanced Visible Light Photocatalytic Activity. *Journal of Physical Chemistry Letters* **2013**, *4* (17), 2847–2852. https://doi.org/10.1021/jz401447w.
(716) Abbas, M. A.; Kim, T. Y.; Lee, S. U.; Kang, Y. S.; Bang, J. H. Exploring Interfacial Events in Gold-Nanocluster-Sensitized Solar Cells: Insights into the Effects of the Cluster Size and Electrolyte on Solar Cell Performance. *J Am Chem Soc* **2016**, *138* (1), 390–401. https://doi.org/10.1021/jacs.5b11174.
(717) Chen, Y. S.; Choi, H.; Kamat, P. v. Metal-Cluster-Sensitized Solar Cells. A New Class of Thiolated Gold Sensitizers Delivering Efficiency Greater than 2%. *J Am Chem Soc* **2013**, *135* (24), 8822–8825. https://doi.org/10.1021/ja403807f.
(718) Beltram, A.; Romero-Ocaña, I.; Josè Delgado Jaen, J.; Montini, T.; Fornasiero, P. Photocatalytic Valorization of Ethanol and Glycerol over TiO2 Polymorphs for Sustainable Hydrogen Production. *Applied Catalysis A: General* **2016**, *518*, 167–175. https://doi.org/10.1016/j.apcata.2015.09.022.
(719) Montini, T.; Gombac, V.; Delgado, J. J.; Venezia, A. M.; Adami, G.; Fornasiero, P. Sustainable Photocatalytic Synthesis of Benzimidazoles. *Inorganica Chimica Acta* **2021**, *520* (February), 120289. https://doi.org/10.1016/j.ica.2021.120289.
(720) Montini, T.; Gombac, V.; Sordelli, L.; Delgado, J. J.; Chen, X.; Adami, G.; Fornasiero, P. Nanostructured Cu/TiO2 Photocatalysts for H2 Production from Ethanol and Glycerol Aqueous Solutions. *ChemCatChem* **2011**, *3* (3), 574–577. https://doi.org/10.1002/cctc.201000289.